Concept and Applications of Carrier Pocket Engineering to Design Useful Thermoelectric Materials Using Superlattice Structures

A thesis presented

by

Takaaki Koga

to

The Division of Engineering and Applied Sciences
in partial fulfillment of the requirements
for the degree of
Doctor of Philosophy
in the subject of
Applied Physics

Harvard University
Cambridge, Massachusetts
April, 2000

Abstract

In this thesis, a general optimization approach to maximize the values of the thermoelectric figure of merit $Z_{3D}T$ is proposed using semiconducting superlattice systems. This optimization process, denoted by the "Carrier Pocket Engineering concept" in the text, takes the following four stages of actual investigation : (I) theoretical predictions for the materials combinations to be used and for the detailed structure of the superlattices in order to achieve the maximum value of $Z_{3D}T$ for the whole superlattice, using the simplest possible models; (II) experimental proof-of-principle study of the theoretical predictions made in (I) and give feedback to the theoretical concept and its explicit implementation; (III) improvement of the theoretical models to understand the experimental results obtained in (II) and to make improved theoretical predictions; and (IV) application of the knowledge acquired for the mechanisms responsible for enhancing $Z_{3D}T$ during the investigation of one materials system, to another materials system that may provide even larger values of $Z_{3D}T$ after incorporating the newly acquired knowledge for enhancing $Z_{3D}T$.

To demonstrate the above optimization process, a series of theoretical and experimental investigations were carried out using the following materials systems : (1) (111) oriented PbTe/$Pb_{1-x}Eu_xTe$ multiple-quantum-well superlattices to clarify the detailed mechanisms responsible for the previously observed enhancement in the thermoelectric power S in this system; (2) GaAs/AlAs short-period superlattices to propose the new concept of Carrier Pocket Engineering, where unconventional X- and L-point valleys, that do not contribute to the thermoelectric transport in the bulk form, can be made to contribute to the thermoelectric transport in the superlattice form, enhancing the values of $Z_{3D}T$ significantly relative to those for the corresponding bulk materials; (3) Si/Ge short-period superlattices to propose a yet new concept of lattice strain engineering to further increase the values of $Z_{3D}T$ in this superlattice system, and to provide an experimental proof-of-principle study of the Carrier Pocket Engineering concept using this materials system.

Besides the above main stream of this thesis, the properties of (111) oriented

PbTe/Te and $PbSe_{0.98}Te_{0.02}$/PbTe "quantum-dot" superlattices, (001) oriented short-period superlattices of PbTe/$Pb_{1-x}Eu_xTe$, and (111) oriented Bi/$Pb_{1-x}Eu_xTe$ superlattices are also discussed as possible candidates for the future high ZT materials.

Acknowledgments

This thesis is a summary of my work carried out at MIT (Massachusetts Institution of Technology) under the supervision of Professor Mildred S. Dresselhaus (MIT) during the period between January 1997 and March 2000.

First, I would like to thank Professor Mildred S. Dresselhaus for introducing me to the world of low-dimensional thermoelectricity as well as for her academic guidance, continuous encouragement, trust and patience throughout my thesis work that was carried out in the Dresselhaus group (MGM). I am also obliged to Dr. Gene Dresselhaus and Ms. Laura Doughty in MGM, respectively, for various academic support and for her professional administrative support that were provided to me during my stay in MGM.

Mr. Theodore C. Harman of MIT Lincoln Laboratory and Professor Henry Ehrenreich of Harvard University have been two of the most respected scientists to me, respectively, in experiment and in theory. Their physical insights into the research problems were precise and concrete, and taught me how to look at the problems from various different angles. I would also like to thank Ted for sharing his precious, high-quality superlattice samples with us for the experimental investigations carried out in this thesis.

Professor David A. Broido of Boston College and Dr. Thomas L. Reinecke of Naval Research Laboratory have provided an additional source for theoretical insights throughout the thesis work. I would also like to thank them for teaching me how to do the computer calculation that is necessary to solve the Boltzmann transport equation numerically, and I would like to thank Professor Broido for kindly answering all the questions I asked during my computer simulation work.

I would like to thank Professor Venkatesh Narayanamurti and Professor Frans A. Spaepen of Harvard University for being on my thesis committee at Harvard, and for monitoring my thesis work at MIT on a regular basis.

I would like to thank all our collaborators under the DOD/ONR MURI program on "Quantum Structures for Thermoelectric Applications". Especially, Profes-

sor Gang Chen, Professor Kang L. Wang, Dr. Jianlin Liu and Mr. Theodorian Borca-Tasciuc of UCLA (University of California at Los Angeles) for numerous scientific discussions, and Professor Wang and Jianlin for growing the highest quality Si/Ge superlattice samples in the world for the experimental proof-of-principle study carried out in this thesis.

I am also indebted to Professor Gunther Bauer and Dr. Gunther Springholz of the Johannes Kepler Universität, Linz, Austria, for growing the PbTe/$Pb_{1-x}Eu_xTe$ multiple-quantum-well samples for the supplemental study carried out in this thesis and for giving us scientific inputs.

I would like to thank all the members in MGM : Dr. Xiangzhong Sun for sharing his expertise in physics and computer science with me, Mr. Stephen B. Cronin for providing me with various technical and scientific help, and all other MGM members including Dr. Manyalibo J. Matthews, Dr. Dmitry Gekhtman, Dr. Zhibo Zhang, Ms. Sandra Brown, Dr. Marcos Pimenta, Dr. Alessandra Marucci, Mr. Hao Xin, Dr. Paola Corio, Mr. Yuming Lin, Ms. Marcie R. Black, Mr. Oded Rabin, Dr. Ado Jorio, and others, for various scientific discussions, their friendship, and creating an excellent research atmosphere in MGM.

Finally, I would like to thank my parents, Tatsuhiko and Masayo, and my sister, Tamaki, for their warm love, continuous help, and all kind of encouragement they provided to me during my stay in the United States.

Contents

List of Figures

List of Tables

Chapter 1

Introduction

1.1 Thermoelectric coefficients

1.1.1 The Seebeck effect

When a temperature gradient is maintained in a material and no electric current is allowed to flow, there will be a steady-state electrostatic potential difference between the high- and low-temperature regions of the specimen. The electromotive force $\boldsymbol{\mathcal{E}}$[†] created by this potential drop inside the specimen is known as the thermoelectric field and is conventionally written as

$$\boldsymbol{\mathcal{E}} = \mathbf{S} \cdot \boldsymbol{\nabla} T, \tag{1.1}$$

where the proportionality constant $\mathbf{S}$ is known as the Seebeck coefficient or the thermoelectric power of the material, which in general is a second rank symmetric tensor for anisotropic materials.

To measure the thermoelectric voltage, one must use a circuit of two different materials (denoted by a and b, respectively), where the two materials are connected together to form a junction at one end (denoted as junction ab) and the other ends of

[†] $\boldsymbol{\mathcal{E}}$ is defined as $\mathbf{E} + \frac{\nabla \zeta}{|e|}$, where $\mathbf{E}$ is the electrical field, $|e|$ is the absolute value of electron charge, and $\nabla \zeta$ is the gradient of the chemical potential ζ (see Ref. [1] for more discussion).

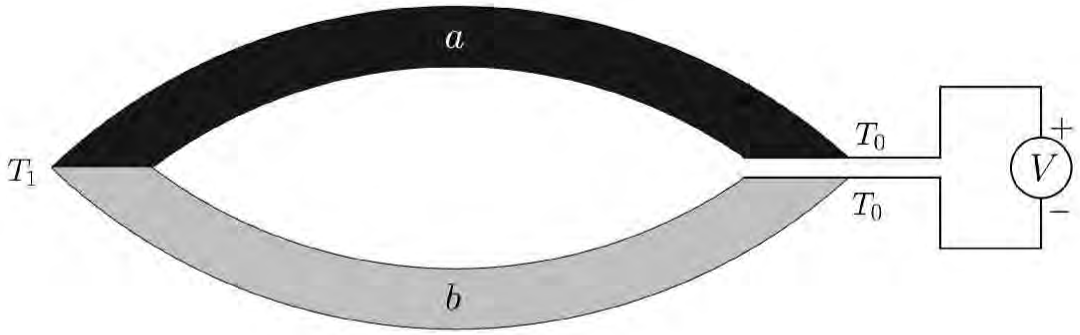

Figure 1-1: Circuit for measuring the difference in thermoelectric voltage developed in two different materials (a and b), in each of which the temperature varies from T_0 to T_1.

the two materials are connected to a voltmeter as shown in Fig. 1-1. It is necessary to use the same kind of metals for the leads connecting materials a and b to the voltmeter. In this circuit, the temperature at junction ab is maintained at T_1, while the temperatures at the other junctions (junctions formed between materials a b and the metal leads to the voltmeter) are maintained at T_0. It is assumed that the voltmeter is placed in a homogeneous temperature background to avoid any temperature gradient within the circuitry of the meter itself. Then, the thermoelectric voltage measured across the voltmeter is

$$\Delta V = -\int \boldsymbol{\mathcal{E}} \cdot d\mathbf{l} = S_{ab}\Delta T, \tag{1.2}$$

where S_{ab} is the differential Seebeck coefficient between the elements a and b, i.e., $S_{ab} = S_a - S_b$, and ΔT is defined as $T_1 - T_0$. Therefore, if the value of the Seebeck coefficient for material a is negligibly small compared to that for material b ($S_a \ll S_b$) as in the case of material a being a superconductor ($S_a = 0$), the Seebeck coefficient of material b is given by,

$$S_b = -\frac{\Delta V}{\Delta T}. \tag{1.3}$$

1.1.2 The Peltier effect

If an electrical current is driven in a circuit of two dissimilar materials that is maintained at a uniform temperature, then heat will be evolved at one junction and

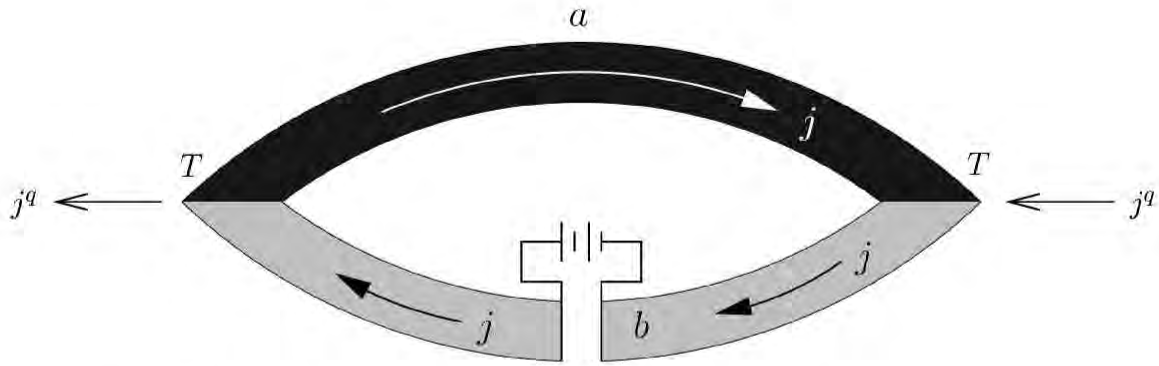

Figure 1-2: The Peltier effect. A current $\mathbf{j}$ is driven in a circuit of two dissimilar materials at uniform temperature T. Thermal current q is evolved at one junction and supplied at the other.

absorbed at the other (Fig. 1-2). This is because an isothermal electric current in a material is accompanied by a thermal current,

$$\mathbf{j}^q = \mathbf{\Pi} \cdot \mathbf{j}, \tag{1.4}$$

where $\mathbf{j}$ and $\mathbf{j}^q$ are the electrical and thermal current densities, respectively, and $\mathbf{\Pi}$ is known as the Peltier coefficient which in general is a second rank symmetric tensor for anisotropic materials. Because the electric current is uniform in a closed circuit and the Peltier coefficient differs from one material to another, the thermal current in the two materials will not be equal, and the difference must be evolved at one junction and supplied to the other if a uniform temperature is to be maintained.

In the circuit shown in Fig. 1-2, a thermal flow j^q is generated according to the differential Peltier coefficient between the two elements $\Pi_{ab} = \Pi_a - \Pi_b$ ($j^q = -\Pi_{ab} j$). The absolute value of the Peltier coefficient for a single element is determined when one of the two branches is a superconductor.

It should be noted that the application of the theory of thermodynamics [2] leads to the following relation between the Seebeck and Peltier coefficients :

$$\mathbf{\Pi} = \mathbf{S}T, \tag{1.5}$$

where T is the absolute temperature. Therefore, measuring either $\mathbf{S}$ or $\mathbf{\Pi}$ only pro-

vides us with the information of the other as well.

1.1.3 The Thomson effect

Consider a homogeneous conductor in which thermal and electric current flow simultaneously. The rate at which heat is generated in a unit volume of the conductor is given by [3]

$$\frac{dQ}{dt} = \rho \mathbf{j} \cdot \mathbf{j} + \boldsymbol{\nabla} \cdot (\mathbf{K} \cdot \boldsymbol{\nabla} T) - \mathbf{j} \cdot \boldsymbol{\tau} \cdot \boldsymbol{\nabla} T, \tag{1.6}$$

where $\mathbf{j}$ (first rank tensor), $\mathbf{K}$ (second rank tensor) and $\boldsymbol{\tau}$ (second rank tensor) are the electrical current density, the thermal conductivity, and a quantity called the "Thomson coefficient", respectively. In Eq. 1.6, the first term corresponds to joule heating, and second term denotes the rate at which heat is flowing into the unit volume due to thermal conduction. The Thomson effect states that there is an additional term (the third term) in Eq. 1.6 which is related to the heat generation due to the Peltier heat current.[†] It should be noted that this third term in Eq. 1.6 is dependent on the direction of the applied electrical current. Therefore, the value of the Thomson coefficient is experimentally determined by measuring the change in the heat generation in the pertinent conductor by flipping the direction of the electrical current for a fixed temperature gradient.

It can be shown [3] that the Thomson coefficient $\boldsymbol{\tau}$ is related to the temperature derivative of the Seebeck coefficient by the following equation :

$$\boldsymbol{\tau} = T \frac{d\mathbf{S}}{dT}, \tag{1.8}$$

where T is the absolute temperature.

[†]The third term in Eq. 1.6 is not a simple divergence of the Peltier heat current, because

$$\boldsymbol{\nabla} \cdot (T\mathbf{S} \cdot \mathbf{j}) = \boldsymbol{\nabla} T \cdot \mathbf{S} \cdot \mathbf{j} + T \boldsymbol{\nabla} \cdot \mathbf{S} \cdot \mathbf{j}. \tag{1.7}$$

The trick here comes from the fact that the Peltier heat current is defined in a uniform temperature background. Therefore the first term in the right hand side of Eq. 1.7 is set to be identically zero.

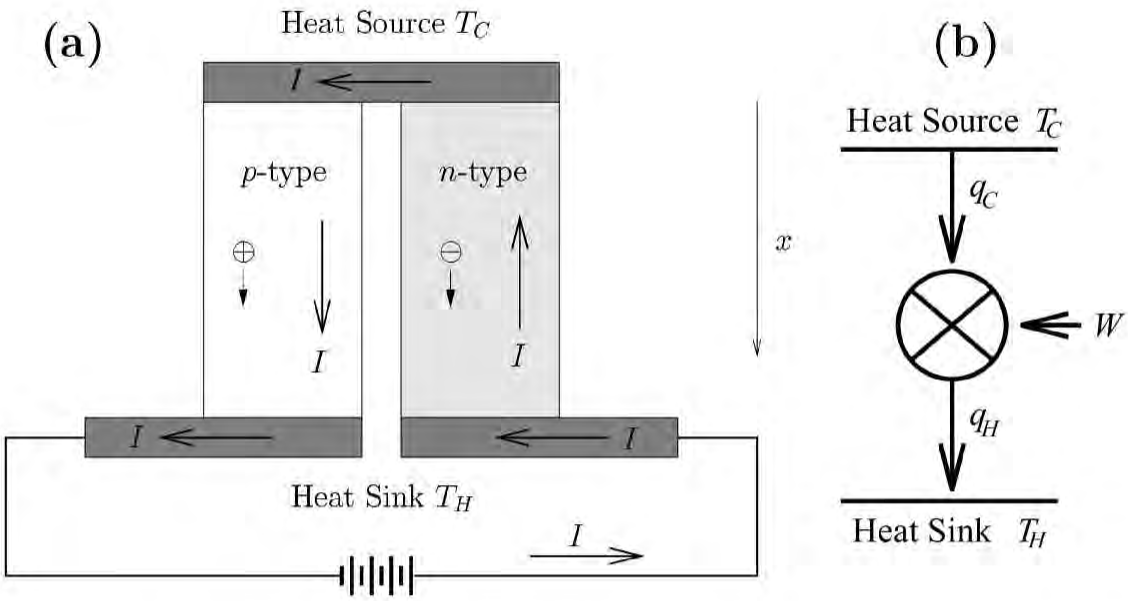

Figure 1-3: (a) Simple thermoelectric refrigerator. (b) Simple diagram for a heat engine that corresponds to (a).

1.2 Principle of thermoelectric energy conversion

In this section, we will discuss the basic theory of thermoelectric energy conversion. Shown in Figs. 1-3 and 1-4 are schematic diagrams for a simple thermoelectric refrigerator and a simple thermoelectric power generator, respectively, together with the corresponding simplified heat engines. It should be noted that there are obvious differences in the definitions of the symbols for the heat flows q_C and q_H, for the temperatures T_C and T_H, and for the work W between our thermoelectric refrigerator and power generator as shown in Figs. 1-3 and 1-4. The basic principles for thermoelectric refrigeration and power generation are explained as follows. For thermoelectric refrigeration, an electrical current is passed through the thermoelectric device which is made of a pair of p- and n-type semiconductors as shown in Fig. 1-3. This electrical current creates flows of electrons and holes, respectively, in the n-type and p-type legs of the thermoelectric device. Since the directions of these particle currents created by the electrical current are opposite between the electrons and the holes, the heat flows carried by these particles are always directed from the cold end (denoted as the heat source in Fig. 1-3) to the hot end (denoted as the heat sink

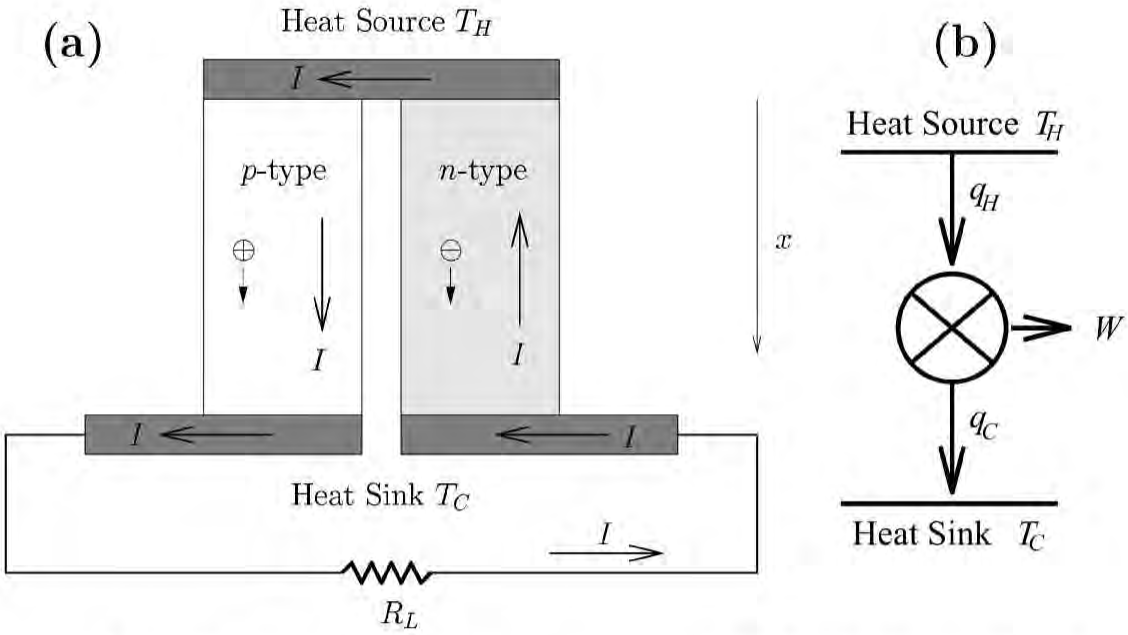

Figure 1-4: (a) Simple thermoelectric power generator. (b) Simple diagram for a heat engine that corresponds to (a).

in Fig. 1-4). Therefore, we can cool the cold end of the thermoelectric device. For thermoelectric power generation, the electromotive force is generated by the thermal gradient established across the thermoelectric device as shown in Fig. 1-4. Since the sign of the electromotive force (emf) is opposite between the p- and n-type materials for a given direction of the temperature gradient, the emfs generated in the p- and n-type legs of the thermoelectric device add up for power generation. In this way, the thermal energy applied to the thermoelectric device is converted to electrical energy. Finally, the electrical energy thus generated is consumed by an external load resistance denoted by R_L in Fig. 1-4.

Now, we are particularly interested in the following two quantities, respectively, for thermoelectric refrigeration and for thermoelectric power generation :

(1) **Thermoelectric coefficient of performance ϕ** for thermoelectric refrigeration, defined by

$$\phi \equiv \frac{q_C}{W} = \frac{(S_p - S_n)IT_C - \frac{1}{2}I^2R - K(T_H - T_C)}{(S_p - S_n)I(T_H - T_C) + I^2R}, \tag{1.9}$$

where q_C is the heat flow into the system at the cold end (heat source) of the thermoelectric device, W is the work given to the system (device) by the electricity (by

the battery), I is the electrical current passed through the device, R is the internal resistance (impedance) of the thermoelectric device, K is the thermal conductance across the thermoelectric device [from the cold end (heat source) to the hot end (heat sink) of the device], S_p and S_n are the Seebeck coefficients for the p- and n-type legs of the pertinent thermoelectric device, respectively. The derivation of the third expression in Eq. 1.9 is given in §1.2.1.

(2) **Thermal efficiency η** for thermoelectric power generation is given by

$$\eta \equiv \frac{W}{q_H} = \frac{I^2 R_L}{(S_p - S_n) I T_H + K(T_H - T_C) - \frac{1}{2} I^2 R}, \tag{1.10}$$

where q_H is the heat flow into the system at the hot end (heat source) of the thermoelectric device, W is the work taken out of the thermoelectric device and fed into the load resistance R_L, I is the electrical current generated in the device, R is the internal resistance (impedance) of the thermoelectric device, K is the thermal conductance between the hot end and the cold end of the pertinent device, S_p and S_n are the Seebeck coefficients for the p- and n-type legs of the pertinent thermoelectric device, respectively. The derivation of the third expression in Eq. 1.10 is given in §1.2.2.

1.2.1 Thermoelectric refrigeration

Our goal in this subsection is to find expressions for the coefficient of performance for a thermoelectric cooling device for a given temperature difference between the cold and hot ends of the pertinent device. The thermoelectric coefficient of performance is defined as the ratio of the rate at which heat is extracted from the source to the rate at which electrical energy is consumed from the battery. Another quantity of interest is the maximum temperature difference that can be achieved when no heat has to be extracted from the source.

The rate of heat flow q_i within one of the conductors i ($i = p, n$) at a distance x from the heat source is given by

$$q_{p,n} = \pm \Pi_{p,n} I - \kappa_{p,n} A_{p,n} \frac{dT}{dx} = \pm S_{p,n} I T - \kappa_{p,n} A_{p,n} \frac{dT}{dx}, \tag{1.11}$$

where the plus and minus signs in front of the first term are for the p- and n-type legs in the pertinent thermoelectric device, respectively, and $\Pi_{p,n}$, $\kappa_{p,n}$ and $A_{p,n}$ are the Peltier coefficient, the thermal conductivity and the cross-sectional area for the p- and n-type legs of the thermoelectric device, respectively. It is noted that, in Eq. 1.11, the first term denotes the heat flow due to the Peltier effect and second term denotes the heat flow due to the thermal conduction, respectively. The second term in Eq. 1.11 can be most easily evaluated when the pertinent thermoelectric device is in a steady state (i.e., $\frac{dQ}{dt} = 0$ in Eq. 1.6) and if the Thomson effect is to be ignored (i.e., $\boldsymbol{\tau} = \mathbf{0}$). In this case, integrating the right hand side of Eq. 1.6, we obtain

$$\kappa_{p,n} A_{p,n} \frac{dT}{dx} = -\frac{I^2 (x - \frac{1}{2} L_{p,n})}{\sigma_{p,n} A_{p,n}} + \frac{\kappa_{p,n} A_{p,n} (T_H - T_C)}{L_{p,n}}, \tag{1.12}$$

where $\sigma_{p,n}$ and $L_{p,n}$ are the electrical conductivities and the lengths of the p- and n-type legs of the pertinent thermoelectric device, respectively. By substituting this equation into Eq. (1.11) at $x = 0$, we obtain

$$q_{p,n}|_{x=0} = \pm S_{p,n} I T_C - \frac{\kappa_{p,n} A_{p,n} (T_H - T_C)}{L_{p,n}} - \frac{I^2 L_{p,n}}{2\sigma_{p,n} A_{p,n}}. \tag{1.13}$$

The cooling power, q_C, at the source is the sum of q_p and q_n at $x = 0$:[†]

$$q_C = (S_p - S_n) I T_C - K(T_H - T_C) - \frac{1}{2} I^2 R. \tag{1.14}$$

The electrical power consumed in the p- and n-type legs of the thermoelectric device is given by

$$W_{p,n} = \pm S_{p,n} I (T_H - T_C) + \frac{I^2 L_{p,n}}{\sigma_{p,n} A_{p,n}}, \tag{1.16}$$

where the first term denotes the portion of the electrical power that is used to pump the heat from the heat source to the heat sink, and the second term denotes the

[†]The thermal conductance K and the electrical resistance R for the thermoelectric device are given by

$$K = \frac{\kappa_p A_p}{L_p} + \frac{\kappa_n A_n}{L_n} \qquad \text{and} \qquad R = \frac{L_p}{\sigma_p A_p} + \frac{L_n}{\sigma_n A_n}, \tag{1.15}$$

respectively.

portion of the electrical power that is dissipated into the system. The total power input is then given by

$$W = W_p + W_n = (S_p - S_n)I(T_H - T_C) + I^2R. \tag{1.17}$$

Therefore, the thermoelectric coefficient of performance, ϕ, is finally obtained by the following equation :

$$\phi \equiv \frac{q_C}{W} = \frac{(S_p - S_n)IT_C - \frac{1}{2}I^2R - K(T_H - T_C)}{(S_p - S_n)I(T_H - T_C) + I^2R}. \tag{1.9}$$

It should be noted that the thermoelectric coefficient of performance ϕ depends on the value of the electrical current I. Two cases of special interest are (1) the current I_q for the maximum cooling power and (2) the current I_ϕ for the maximum coefficient of performance.

We determine I_q for the maximum cooling power by setting $dq_C/dI = 0$ in Eq. 1.14 :

$$I_q = \frac{(S_p - S_n)T_C}{R}. \tag{1.18}$$

The corresponding coefficient of performance is given by

$$\phi_q = \frac{\frac{1}{2}ZT_C - (T_H/T_C - 1)}{ZT_H}, \tag{1.19}$$

where[†]

$$Z = \frac{(S_p - S_n)^2}{KR}. \tag{1.20}$$

If the heat source is removed, the coefficient of performance falls to zero and the temperature difference $(T_H - T_C)$ rises to its maximum value

$$(T_H - T_C)_{\max} = \frac{1}{2}ZT_C^2. \tag{1.21}$$

We determine the current I_ϕ for the maximum coefficient of performance by setting

[†]Note that $S_p > 0$ and $S_n < 0$.

$d\phi/dI = 0$ in Eq. 1.9, and we find that

$$I_\phi = \frac{(S_p - S_n)(T_H - T_C)}{R(\sqrt{1 + ZT_M} - 1)}, \tag{1.22}$$

where $T_M = \frac{1}{2}(T_H + T_C)$ is the mean temperature. The maximum coefficient of performance is

$$\phi_{\max} = \frac{T_C(\sqrt{1 + ZT_M} - T_H/T_C)}{(T_H - T_C)(\sqrt{1 + ZT_M} + 1)}. \tag{1.23}$$

Since the quantity Z determines both the maximum temperature difference and the maximum coefficient of performance, it is called the figure of merit for the thermoelectric device. It is easy to see in Eqs. 1.19, 1.21 and 1.23 that $(T_H - T_C)_{\max}$, ϕ_q and $\phi_{\max}$ are all monotonically increasing functions of Z as long as $T_H > T_C$, and $\phi_{\max}$ in Eq. 1.23 renders the value of the Carnot coefficient of performance

$$\phi_{\text{Carnot}} = \frac{T_C}{T_H - T_C} \tag{1.24}$$

as $Z \to \infty$.

The figure of merit Z is not a fixed quantity for a given pair of thermoelectric materials but depends on the relative geometries of the branches. It has its maximum value when the product RK in Eq. (1.20) is a minimum, which occurs when

$$\frac{L_p/A_p}{L_n/A_n} = \sqrt{\frac{\sigma_p \kappa_p}{\sigma_n \kappa_n}}. \tag{1.25}$$

When the dimensions are optimized, the figure of merit becomes

$$Z = \frac{(S_p - S_n)^2}{[(\kappa_p/\sigma_p)^{1/2} + (\kappa_n/\sigma_n)^{1/2}]^2}. \tag{1.26}$$

Although the figure of merit Z of a cooling device depends on the properties of the materials in both branches, it is convenient to define a figure of merit for a single material as

$$Z_{p,n} = \frac{S_{p,n}^2 \sigma_{p,n}}{\kappa_{p,n}}. \tag{1.27}$$

In practice, at most temperatures of interest, the materials for the p- and n-type legs of the thermoelectric device are chosen so that the properties of these materials are comparable to each other. Therefore,

$$Z \simeq \frac{Z_p + Z_n}{2}. \tag{1.28}$$

The treatment shown above assumes that the parameters S, σ and κ are independent of temperature. The errors that originate from this assumption are likely to be important for devices that are operated with large temperature differences between the source and sink. The basic differential equation for the problem including the temperature dependence of the parameters at a steady state ($\frac{dQ}{dt} = 0$) takes the form (see Eq. 1.6) :

$$\frac{d}{dx}\left[\kappa_{p,n}(T) A_{p,n} \frac{dT}{dx}\right] \pm IT \frac{dS_{p,n}(T)}{dT} \frac{dT}{dx} + \frac{I^2}{\sigma_{p,n}(T) A_{p,n}} = 0. \tag{1.29}$$

In general, the best that one can hope for is a numerical solution following the substitution of empirical temperature dependences for the parameters. However, by taking average values over the two branches, one finds [2]

$$Z \simeq \frac{\langle S_p - S_n \rangle^2}{(\langle \kappa_p/\sigma_p \rangle^{1/2} + \langle \kappa_n/\sigma_n \rangle^{1/2})^2}, \tag{1.30}$$

where the angular brackets indicate temperature-averaged quantities. The numerical solution [4] of Eq. 1.29 indicates that this method gives an accuracy that is good enough for most purposes.

1.2.2 Thermoelectric power generation

The device shown in Fig. 1-3 can also be used as a thermoelectric power generator as shown in Fig. 1-4. Following the same argument as given in §1.2.1 (leading to Eq. 1.14), the thermal power input to the hot junction from the heat source is given

by

$$q_H = (S_p - S_n)IT_H + K(T_H - T_C) - \frac{1}{2}I^2R, \tag{1.31}$$

where K and R are the geometry-dependent thermal conductance and electrical resistance, respectively, of the device as in Eq. 1.15 (see the footnote on page 59). The electrical power output is

$$W = I^2R_L, \tag{1.32}$$

where R_L is the load resistance. The current I is given by[†]

$$I = \frac{(S_p - S_n)(T_H - T_C)}{R + R_L}, \tag{1.33}$$

since the open-circuit voltage is $(S_p - S_n)(T_H - T_C)$. Thus the thermal efficiency for the thermoelectric power generation is given by

$$\eta \equiv \frac{W}{q_H} = \frac{I^2R_L}{(S_p - S_n)IT_H + K(T_H - T_C) - \frac{1}{2}I^2R}. \tag{1.10}$$

Eq. 1.10 states that the thermal efficiency η depends on the value of the load resistance R_L. Two cases of the special interest are (1) the value of the load resistance for which the maximum power output is obtained from the thermoelectric device and (2) the value of the load resistance for which the maximum thermal efficiency for the thermoelectric power generation is achieved.

The load resistance which maximizes the power output W is obtained by setting its total derivative (see Eqs. 1.32 and 1.33) equal to zero with respect to the load resistance R_L. The result obtained is $R_L = R$, and the thermal efficiency at maximum power output is found to be

$$\eta_W = \frac{2Z(T_H - T_C)}{Z(3T_H + T_C) + 8}, \tag{1.34}$$

where Z is the thermoelectric figure of merit of the thermoelectric device as defined

[†]Note that $S_p > 0$ and $S_n < 0$, and therefore both the p-branch and the n-branch contribute to the current generation.

in Eq. 1.20.

The load resistance which maximizes the thermal efficiency η is determined by setting $d\eta/dR_L = 0$ in Eq. 1.10, so that we obtain $R_L = \sqrt{ZT_M + 1}R$. The corresponding expression for the maximum thermal efficiency is given by

$$\eta_{\max} = \frac{(T_H - T_C)(\sqrt{1 + ZT_M} - 1)}{T_H(\sqrt{1 + ZT_M} + T_C/T_H)}, \tag{1.35}$$

where $T_M = \frac{1}{2}(T_H + T_C)$ is the mean temperature. The thermoelectric figure of merit Z again determines both the maximum thermal efficiency $\eta_{\max}$ and the thermal efficiency at maximum power output η_W. It is easy to see that both η_W in Eq. 1.34 and $\eta_{\max}$ in Eq. 1.35 are monotonically increasing functions of Z as long as $T_H > T_C$, and the value of $\eta_{\max}$ in Eq. 1.35 approaches the Carnot efficiency

$$\eta_{\text{Carnot}} = \frac{T_H - T_C}{T_H} \tag{1.36}$$

as $Z \to \infty$.

1.3 Low-dimensional thermoelectricity

As we discussed in §1.2, the usefulness of thermoelectric materials for the refrigeration or power generation applications is expressed in terms of the thermoelectric figure of merit Z,

$$Z = \frac{S^2\sigma}{\kappa}, \tag{1.37}$$

where S is the thermoelectric power or Seebeck coefficient, σ is the electrical conductivity, and κ is the thermal conductivity. Since Z is a function of temperature and the values of ϕ_q, $\phi_{\max}$, η_W and $\eta_{\max}$ for a given thermoelectric device (see Eqs. 1.19, 1.23, 1.34 and 1.35) are all expressed in terms of ZT rather than Z itself, where T is the absolute temperature, the dimensionless quantity ZT is the quantity that is more widely used as the measure of the usefulness for a given thermoelectric material than Z.

Now, in order to increase the value of ZT, one needs to increase the values of S and σ, and decrease the value of κ. In semiconductors, it is possible to vary the values of the thermoelectric transport coefficients individually by adjusting the doping level of the material. For non-degenerate semiconductors,[†] the value of σ is roughly proportional to the carrier concentration of the pertinent material, whose value can be controlled by doping. The value of S for a given material is also determined by its doping level. Since the value of S, for non-degenerate semiconductors, is a linear function of the chemical potential ζ [i.e., $S = a\zeta + b$, where a is a positive number for both p- and n-type materials, and b is a negative (positive) number for n-type (p-type) materials], it is logarithmically dependent on the carrier concentration [i.e., $|S|$ (absolute value of S) is a monotonically decreasing function of the carrier concentration]. These features for S and σ are schematically shown in Fig. 1-5.

Another approach for increasing the value of Z is to reduce the value of κ. Since κ can be written as a sum of the lattice thermal conductivity (denoted by $\kappa_{\rm ph}$) and the electronic contribution to the thermal conductivity (denoted by κ_e), reducing the value of either $\kappa_{\rm ph}$ or κ_e would contribute to increasing the value of Z. However, reducing the value of $\kappa_{\rm ph}$ implies an increased crystalline disorder (and therefore the carrier mobility μ is reduced) in the pertinent system, and reducing the value of κ_e also implies the reduction of σ via the Wiedemann-Franz law ($\kappa_e = L_0\sigma T$, where L_0 is the Lorenz number). Therefore, it is generally difficult to increase the value Z for a given materials system.

The best commercial 3D thermoelectric material is in the $Bi_{2(1-x)}Sb_{2x}Te_{3(1-y)}Se_{3y}$ family with a room temperature $ZT \sim 1$ for the composition $Bi_{0.5}Sb_{1.5}Te_3$ [5]. It should be also noted that $ZT \sim 3$ would rival conventional refrigeration techniques in terms of efficiency. It is believed that only incremental improvements in the value of ZT are possible in the generalized Bi_2Te_3 system. For this reason, efforts are being expended in the identification of new families of materials with a high electronic density of states at the Fermi level [6–8] and with cage-like structures partially occupied

[†]A non-degenerate semiconductor means a semiconductor whose chemical potential is below (or 'above' for p-type materials) the band edge of the pertinent material.

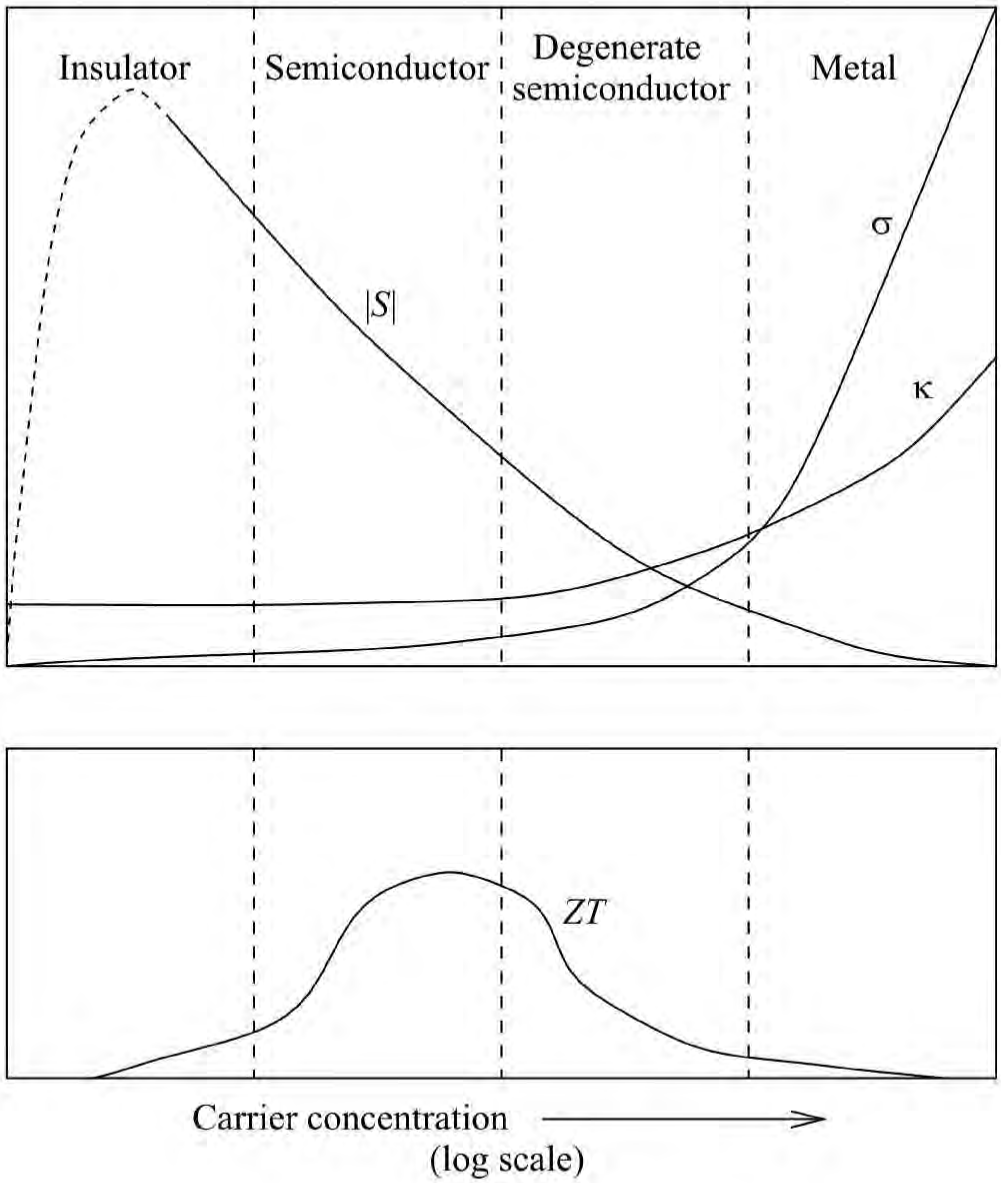

Figure 1-5: What materials can have high ZT?

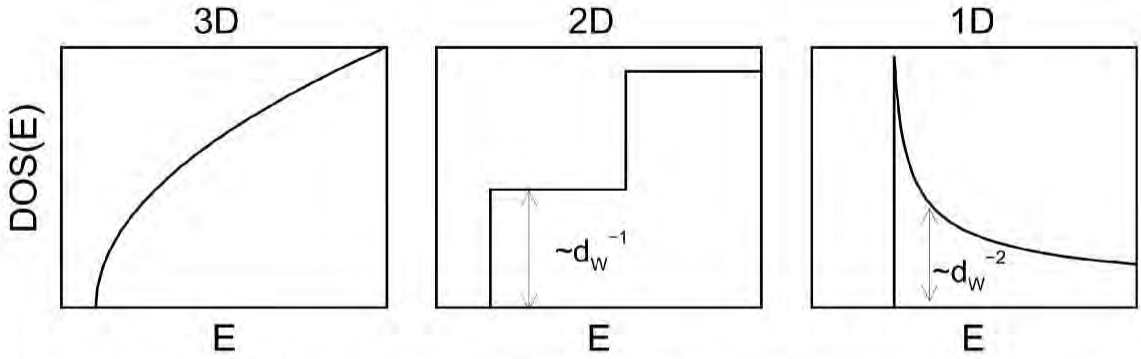

Figure 1-6: The 3D density of states DOS(E) for 3D, 2D and 1D systems. The dependence on d_{W} of the step height in the DOS(E) for a 2D system, and of the relative magnitude of the DOS(E) for a 1D system is indicated, where d_{W} is the quantum well width or quantum wire diameter, for 2D and 1D systems, respectively.

by constituent rattling atoms [9, 10].

Reduced dimensionality, as occurs in quantum wells (2D) or quantum wires (1D), offers another strategy for enhancing ZT [11–22]. This approach primarily takes advantage of the enhanced 3D density of states[†] for electrons near the Fermi level due to the reduced dimensionality. For instance, consider an isolated sheet of a 2D quantum well with a thickness of d_{W}. Since the wavefunction along the z-direction (perpendicular to the plane of the quantum well) is quantized, the number of electronic states available for the lowest subband is independent of the thickness of the quantum well. Therefore, for a given chemical potential ζ, the 3D carrier concentration n increases with decreasing d_{W} (inversely proportional to the value of d_{W}). Since the value of the Seebeck coefficient is roughly a function of the chemical potential only for a given dimensional system (if we ignore the details of the scattering mechanisms), we can also increase the value of $S^2 n$, where n is the 3D carrier concentration of the system, to any values that we want just by reducing the value of d_{W} in an ideal quantum well system (here, we assume that the material used for this 2D quantum well consists of a continuous medium rather than of atoms as in the actual materials, in this thought experiment). This is the first reason why we can expect a large enhancement in the

[†]The 3D density of states here denotes the number of the electronic states per unit energy per unit volume. While the 2D density of states (the number of electronic states per unit energy per unit area) is constant with respect to the thickness of the pertinent 2D quantum well, the 3D density of states for a given 2D quantum well system is inversely proportional to the thickness of the quantum well (see Fig. 1-6).

thermoelectric figure of merit ZT in low-dimensional systems.[†]

The second reason why the values of ZT are expected be enhanced in the low-dimensional systems is that the size (width) of the 2D quantum wells or 1D quantum wires, in the regime where we start observing the effects of the quantum confinement for electrons ($d_{\rm W}$ being in the Å to nm range), tends to be smaller than the length of the phonon mean free path, especially at reduced temperatures ($T < 300$ K). The values of the lattice thermal conductivity $\kappa_{\rm ph}$ is generally expressed by the kinetic formula,

$$\kappa_{\rm ph} = \frac{1}{3} C_{\rm v} v \ell, \tag{1.38}$$

where $C_{\rm v}$ is the heat capacity of the sample, v is the speed of sound and ℓ is the phonon mean free path. The values of $\kappa_{\rm ph}$ for isolated quantum wells and wires are expected to be reduced relative to the corresponding bulk values when the values of $d_{\rm W}$ are smaller than the length of the phonon mean free path ℓ [23]. Therefore, the value of ZT for low-dimensional systems is expected to be enhanced not only through the enhanced $S^2 n$, but also through the reduced $\kappa_{\rm ph}$. This is the basic principle for enhancing the values of ZT using low dimensional structures (denoted as the basic principle of low-dimensional thermoelectricity, hereafter).

To make use of the basic principle of low-dimensional thermoelectricity for actual materials design to achieve enhanced values of ZT, we have to consider several additional issues, as discussed below. For example, in deriving the above basic principle, we have assumed that the details of the scattering mechanisms are not affected by changing the thickness of the quantum well $d_{\rm W}$. This is not the case for actual materials systems. For example, for strictly confined 2D electron systems, such as isolated 2D quantum wells as discussed above, the scattering probabilities for the two-dimensionally confined electrons (due to either three-dimensional phonons or ionized impurities) tend to increase with decreasing the value of $d_{\rm W}$ (see Chapters 3 and 6

[†]It should be noted that we can expect even larger enhancements in $S^2 n$ in one-dimensional systems than in two-dimensional systems, because in 1D systems the 3D carrier density n for a given value of the chemical potential is inversely proportional to $d_{\rm W}^2$, i.e., $n \sim \frac{1}{d_{\rm W}^2}$, rather than $n \sim \frac{1}{d_{\rm W}}$, which is valid for 2D systems (see Fig. 1-6).

for more discussion). Therefore, the resultant value for the carrier mobility, for a strongly confined 2D system, tends to decrease with decreasing size of d_W. Secondly, it is practically impossible to fabricate isolated sheets of 2D quantum wells, where the values of d_W are required to be in an Å to nm range. Therefore, the actual materials have to be designed in the form of a superlattice or multiple-quantum-wells. Since the conditions for the quantum confinement are more relaxed in the superlattice form of the material (the wavefunction along the superlattice growth axis is less confined) relative to the isolated quantum well case, the resultant scattering probabilities (and hence the values of the carrier mobility) for the confined carriers in a superlattice (or in multiple-quantum-wells) are not a simple function of the quantum well width d_W, but are given by a complicated function that depends on the detailed properties of the superlattice.

The main theme of this thesis is to develop a systematic approach to design materials, using superlattice structures, that have enhanced values of ZT, based on the basic principle of low-dimensional thermoelectricity that was discussed above. We are specifically interested in the following effects : (1) the effect of quantum confinement on enhancing the absolute values of the Seebeck coefficient for a given carrier concentration, (2) the effect of quantum confinement on the values of the carrier mobility in two-dimensionally confined electron systems, (3) the effect of δ- and modulation-doping schemes on increasing the values of the carrier mobility, (4) the effect of interface scattering of phonons on reducing the values of the lattice thermal conductivity, and (5) the effect of impurity scattering on increasing the absolute value of the Seebeck coefficient S. Our ultimate goal is to integrate these effects in a given materials system, using a superlattice structure as a basic tool, to achieve a practically useful value of ZT for various thermoelectric applications.

1.4 Road map

Following this introductory chapter, we will discuss, in Chapter 2, the phenomenological aspect of low-dimensional thermoelectricity in (111) oriented PbTe(20 Å)/$Pb_{1-x}Eu_xTe$(400

Å) multiple-quantum-well (MQW) superlattices, whose thermoelectric properties are observed to be enhanced within the quantum well relative to the corresponding bulk PbTe due to quantum confinement effects of the conduction carriers.

In Chapter 3, the detailed scattering mechanisms for electrons are investigated for (111) oriented PbTe(20 Å)/$Pb_{1-x}Eu_xTe$(400 Å) MQWs, in order to resolve the origins of the observed enhancement in the Seebeck coefficient that is discussed in Chapter 2. We will specifically identify the roles of longitudinal acoustic phonon deformation potential scattering and polar optical phonon scattering on the observed temperature-dependent phenomena of the Seebeck coefficient in this system, by solving the Boltzmann equation numerically, including these scattering mechanisms explicitly.

Chapter 4 is devoted to the development of a new concept, namely "Carrier Pocket Engineering", to design superlattice structures that have enhanced values of ZT, where we distinguish the values of ZT for the whole superlattice from the values of ZT that is assigned only to the quantum well part of the superlattice by denoting the former by $Z_{3D}T$ and the latter by $Z_{2D}T$. The Carrier Pocket Engineering concept, which is developed in Chapter 4, denotes a systematic optimization process to maximize the value of the thermoelectric figure of merit $Z_{3D}T$ for a given material system using a rational materials design approach. Though we specifically chose the GaAs/AlAs superlattice system to develop this concept of Carrier Pocket Engineering in Chapter 4 (since various band parameters for the GaAs/AlAs system are readily available in the literature), the same basic concept can be applicable both to other materials systems to optimize the value of $Z_{3D}T$ and to other optimization processes (other than optimizing the value of $Z_{3D}T$) for any given materials system using superlattice structures.

In Chapter 5, the concept of the Carrier Pocket Engineering developed in Chapter 4 is applied to Si/Ge superlattice systems. We will predict that the best thermoelectric performance in this materials system can be achieved in (111) oriented short period Si/Ge superlattices. The predicted values of $Z_{3D}T$ for a (111) oriented Si(20 Å)/Ge(20 Å) superlattice and for a (001) oriented Si(20 Å)/Ge(20 Å) superlat-

tice are, respectively, 0.96 and 0.24 at 300 K, using a model based on the constant relaxation time approximation. The second half of Chapter 5 is devoted to an experimental proof-of-principle study to test the predictions that are made in the first half of this chapter. Since samples of (111) oriented Si/Ge superlattices are not yet available to us, we used (001) oriented Si/Ge superlattices to test our theoretical predictions. We observe fairly good agreement between the experimental results and the theoretical predictions that are obtained using semi-classical models, which are developed in Chapter 6. Thus, the basic concept of Carrier Pocket Engineering has been proven to work with (001) oriented Si/Ge superlattices.

In Chapter 6, more detailed theoretical modeling of the thermoelectric transport coefficients is performed for (001) oriented Si/Ge superlattices, including some specific scattering mechanisms (ionized impurity scattering and longitudinal acoustic phonon deformation potential scattering) for the conduction carriers. We will also consider, theoretically, the effects of δ- and modulation-doping techniques on enhancing the values of the carrier mobilities. These values of the carrier mobilities, for δ-doped or modulation-doped, (001) oriented Si(20 Å)/Ge(20 Å) superlattices, are predicted to be a factor of about two larger than the corresponding values for a homogeneously doped, (001) oriented Si(20 Å)/Ge(20 Å) superlattice. The development of the corresponding models for the (111) oriented Si/Ge superlattices to predict enhanced values of $Z_{3D}T$, including δ- and modulation-doping schemes, is left for the future work, where naive estimations based on the results obtained in Chapter 5 (the constant relaxation time approximation) and in Chapter 6 (the effect of the δ- and modulation doping techniques) predict very large values of $Z_{3D}T$ ($Z_{3D}T \approx 2$ at 300 K) for a δ- or modulation-doped, (111) oriented Si(20 Å)/Ge(20 Å) superlattice at the optimum carrier concentration.

Chapter 7 is devoted to the investigation of materials systems that are not included in the previous chapters of this thesis, but are of future interest for research on low-dimensional thermoelectricity. In this chapter, the properties of (111) oriented PbTe/Te and $PbSe_{0.98}Te_{0.02}$/PbTe "quantum-dot" superlattices, (001) oriented short-period superlattices of PbTe/$Pb_{1-x}Eu_xTe$, and (111) oriented Bi/$Pb_{1-x}Eu_xTe$

superlattices are discussed as possible candidates for future high ZT materials, besides the above main stream topics of this thesis.

Finally, in Chapter 8, we summarize the main results of this thesis, and some remarks on future research directions are also given.

Chapter 2

Thermoelectric properties of n-type $PbTe/Pb_{1-x}Eu_xTe$ multiple quantum wells I — Constant relaxation time approximation —

In this chapter, the temperature dependences of various thermoelectric properties (Seebeck coefficient, carrier mobility, electrical conductivity and Hall coefficient) of a two-dimensionally confined electron gas in (111) oriented n-type $PbTe/Pb_{1-x}Eu_xTe$ multiple-quantum-wells (MQW) are investigated both theoretically and experimentally. It is found that $Z_{2D}T > 2$ is obtainable at elevated temperatures (> 400 K), where $Z_{2D}T$ denotes the thermoelectric figure of merit within the quantum wells. The experimental results for the Seebeck coefficient and the Hall carrier concentration are successfully modeled as a function of temperature based on parabolic energy bands and the constant relaxation time (τ) approximation, assuming independent τ values for longitudinal and oblique subbands. We find that the actual carrier mobilities in the quantum wells, which are deconvolved from the Hall carrier mobilities, are

enhanced over those of bulk PbTe, consistent with the quantum confinement of the conduction carriers and the use of modulation doping for the introduction of the n-type carriers. Better thermoelectric properties, especially at low temperatures, are also predicted for (001) oriented PbTe MQWs using the same basic theoretical model.

2.1 Introduction

It has been theoretically predicted by Hicks *et al.* [16] and experimentally demonstrated by Harman *et al.* and Hicks *et al.* [15, 16] that the thermoelectric figure of merit Z can be enhanced in (111) oriented n-type PbTe/$Pb_{1-x}Eu_xTe$ MQWs ($x \approx 0.073$) relative to the corresponding values for Z in bulk PbTe. $ZT \sim 1.2$ has been obtained within the quantum well, denoted as $Z_{2D}T$, at room temperature in this system [15]. PbTe is an attractive system for studying the effects of low-dimensionalities on the thermoelectric properties, as we will discuss in this and the following sections. To list a few reasons briefly: (1) bulk PbTe itself is already a reasonably good thermoelectric material ($ZT \sim 0.4$ at 300 K), (2) the multiplicity and high anisotropy of the constant energy surfaces allow us to explore the effect of this extra degree of freedom on the thermoelectric properties, as discussed below, and (3) well-established band parameters, necessary for theoretical modeling, are readily available in the literature.

A large multiplicity and anisotropy of the carrier valleys are important factors for good thermoelectric materials. This is generally true in both 3D bulk and 2D MQW (multiple-quantum-well) systems, although there are certain distinctions between 3D and 2D systems, as described below. In 3D bulk systems, good thermoelectric materials, such as Bi_2Te_3, have multiple disk-shaped constant energy surfaces (carrier pockets) that have a small effective mass in one direction and large effective masses in the other two directions. A small effective mass usually leads to a high carrier mobility in that direction, whereas large effective masses in the other two directions lead to a high density of states. The multiplicity of the carrier pockets is directly related to the density of states as a proportionality factor. Since the key idea of hav-

ing enhanced thermoelectric properties in 2D MQW systems is to artificially make the effective mass along the quantum well growth axis (z-direction) very large, while keeping the carrier mobility in the plane high, good materials for testing this idea should have both a large (which ensures a large density of states) and a small (which leads to a high mobility in the plane) effective mass component in the xy-plane. The 3D effective mass component along the z-axis can be either small or large, but the smaller the effective mass along the z-axis, the larger the enhancement of the thermoelectric properties over the bulk. Also, the small mass component along the z-direction helps to keep us in a regime of a single subband. It is to our advantage in making MQW structures that we can choose the quantum well growth direction which optimizes the expected thermoelectric properties [14].

Of particular interest, that is from a more general than specific thermoelectric applications point of view, in PbTe/$Pb_{1-x}Eu_xTe$ MQWs are recently published experimental results by Harman *et al.* [15], showing that the Hall mobilities (μ_{Hall}) for PbTe/$Pb_{1-x}Eu_xTe$ MQW samples are higher than those for similarly grown bulk PbTe. The highest μ_{Hall} found in their MQWs (1420 $\text{cm}^2/\text{V}\cdot\text{s}$ at $n_{\text{Hall}} \sim 10^{19}$ cm^{-3} within the quantum wells) is very close to the generally known bulk value (~1700 $\text{cm}^2/\text{V}\cdot\text{s}$ for $n_{\text{Hall}} < 10^{18}$ cm^{-3}) for undoped samples. We will show in this chapter that after corrections for the multi-carrier types and anisotropic constant energy surfaces are made, the observed carrier mobilities for the PbTe MQWs are even greater than those for the high quality bulk PbTe.

The work in this chapter addresses a detailed study of the thermoelectric properties of n-type PbTe MQWs. Various thermoelectric properties, including the Seebeck coefficient, electrical conductivity, and low field Hall coefficient, are measured along the quantum well planes as a function of temperature. These experimental results are interpreted using the theory developed by Hicks *et al.* [11, 12, 14, 16, 17]. For simplicity, we use the constant relaxation time approximation [3] in this chapter, and will postpone the more exact treatment of the Boltzmann equation assuming some specific scattering mechanisms until the next chapter. The detailed analysis of the Hall carrier concentration n_{Hall} is developed in an attempt to assess the actual carrier

mobility in MQWs. It is well known that, in the case of 3D bulk materials [3, 24, 25], the low field Hall carrier concentration $n_{\rm Hall}$ is not equal to the actual carrier concentration unless: (1) the constant energy surfaces are totally spherical, and (2) there exists only one type of carrier (either electrons or holes of a single type with energy-independent effective masses). The corresponding argument in the case of the 2D electron gas is given in the present chapter.

This chapter is arranged in the following way. In the next section (§2.2), we summarize the bulk properties of PbTe and $Pb_{1-x}Eu_xTe$ alloys. It is based on these properties that the models for PbTe/$Pb_{1-x}Eu_xTe$ MQWs are built, and various transport coefficients for these quantum wells are calculated. In §2.3 we show the resulting formula for our theoretical models, based on the constant relaxation time approximation and parabolic energy bands. We also discuss the importance of the correction of the Hall carrier concentration to the actual carrier concentration in the low field limit to interpret the observed experimental data in terms of the actual carrier concentration and to evaluate the actual carrier mobility for 2D PbTe MQWs. In §2.4, various thermoelectric properties are investigated as a function of temperature for (111) oriented PbTe MQWs. The observed experimental results are discussed in detail in terms of our theoretical models. In §2.5, the optimum properties of both (111) and (001) oriented PbTe MQWs are investigated theoretically as a function of temperature. The theoretical results for the (111) oriented PbTe MQWs are compared with the experimental results, and the prediction is made that (001) oriented PbTe MQWs have better thermoelectric properties than the (111) oriented PbTe MQWs. Finally, concluding remarks are given in §2.6.

2.2 Review of the bulk properties of PbTe and $Pb_{1-x}Eu_xTe$ alloys

Several books and review articles exist on the bulk properties of lead chalcogenides [24, 26–28], where one can find some detailed information on the properties of bulk PbTe.

A series of careful systematic research studies on PbTe/$Pb_{1-x}Eu_xTe$ MQWs and bulk $Pb_{1-x}Eu_xTe$ films grown by the molecular-beam epitaxy (MBE) technique has been carried out by the group of Professor G. Bauer at the Johannes Kepler Universität, Linz, Austria, [29–32], from which we can draw a lot of useful information on PbTe/$Pb_{1-x}Eu_xTe$ MQWs and bulk $Pb_{1-x}Eu_xTe$ alloys that is necessary for our modeling and gaining an understanding of the experimental data obtained in our research. In this section, we will summarize the minimum required knowledge on the properties of bulk lead chalcogenides and $Pb_{1-x}Eu_xTe$ alloys needed to help readers understand the subsequent sections in this chapter and the next chapter of this thesis in some depth.

2.2.1 Chemical properties vs. Electronic properties

Crystals of the lead chalcogenides have a cubic (NaCl-type) rock-salt structure, that is group-theoretically classified as the $m3m$ symmetry class. The unit cell is face-centered cubic and the coordination number for all the atoms is six. The nature of the chemical binding in the lead chalcogenides is mixed ionic-covalent, i.e., they are usually classified as polar semiconductors. In contrast to the purely covalent compounds, in which an electron pair is shared equally by both interacting atoms, in polar bonds, the electrons reside for a longer time in the field of one or other of the two nuclei [24]. The polar nature of lead chalcogenides manifests itself in the composition dependence of the electron and hole mobilities in the $PbTe_{1-x}Se_x$ solid solution. It is found that the *hole* mobility for such a solid solution ($x \approx 0.5$) is decreased by a factor of 2.5 from that for pure PbTe ($x = 0$), whereas the *electron* mobility in the solid solution is decreased only by 25 % relative to that for pure PbTe, i.e. the decrease in the electron mobility is much smaller than that in the hole mobility for the same amount of Te substitution with Sn ($x \approx 0.5$) [24]. This is because electrons are considered to travel mainly in the cation (Pb) sublattice, while holes are considered to travel mainly in the anion (chalcogen) sublattice [24]. For the same reason, we can expect a large reduction in electron mobility in the $Pb_{1-x}Eu_xTe$ alloys, since, in $Pb_{1-x}Eu_xTe$, the atoms in the cation sublattice (i.e., Pb in PbTe), that constitutes

the dominant conduction path for the electrons, are substituted with another type of atoms (Eu in $Pb_{1-x}Eu_xTe$) that act as effective scattering centers for electrons.

Evidences for the covalent nature of the chemical bonding in the lead chalcogenides is found in the details of the scattering mechanisms for electrons that are dominant in these crystals. According to Ref. [24], crystals with a predominantly ionic type of binding should, theoretically, exhibit carrier scattering mainly by one of the optical types of phonons. Investigations of the carrier scattering in lead chalcogenides have shown that carriers are scattered both by the optical and acoustic phonons, and the role of the acoustic scattering is very important from relatively low ($\sim$5 K) to relatively high (>400 K) temperatures [24, 26, 27].

2.2.2 Lattice properties vs. Electronic properties

The lattice properties of lead chalcogenides are also found to be closely related with their electronic properties. One such correlation between the lattice properties and the electronic properties is found in the pressure dependence of the energy band gap (E_g), where we find $\partial E_g/\partial P = -8 \times 10^{-6}$ eV·cm^2·kg^{-1} for PbTe [24]. Such a linear coefficient for E_g with pressure, when combined with the bulk modulus of PbTe ($B = -VdP/dV \sim 3.9 \times 10^6$ Ncm^{-2}, where V is the volume of the crystal [33]), provides a relation between the lattice constant d and the energy band gap E_g for the crystal, i.e., the larger the lattice constant, the larger the energy band gap. This feature is qualitatively consistent with the relation between d and E_g in $Pb_{1-x}Eu_xTe$ alloys, as we discuss below, where d is controlled by changing x in this case. Thus, part of the mechanisms responsible for the observed relation between x and E_g in $Pb_{1-x}Eu_xTe$ is considered to be caused by the effect of changing the lattice constant on E_g that is observed in PbTe by applying a pressure.

A very systematic and thorough study of various (chemical, structural, optical, electronic and magnetic) properties of MBE-grown $Pb_{1-x}Eu_xTe$ alloys was performed as a function of Eu content x ($0 < x < 1$) by Ueta *et al.* [32]. Shown in Fig. 2-1 is the relation between the lattice constant d and the Eu content x in $Pb_{1-x}Eu_xTe$ alloys that is reproduced from Ref. [32], where the lattice constants d are determined from

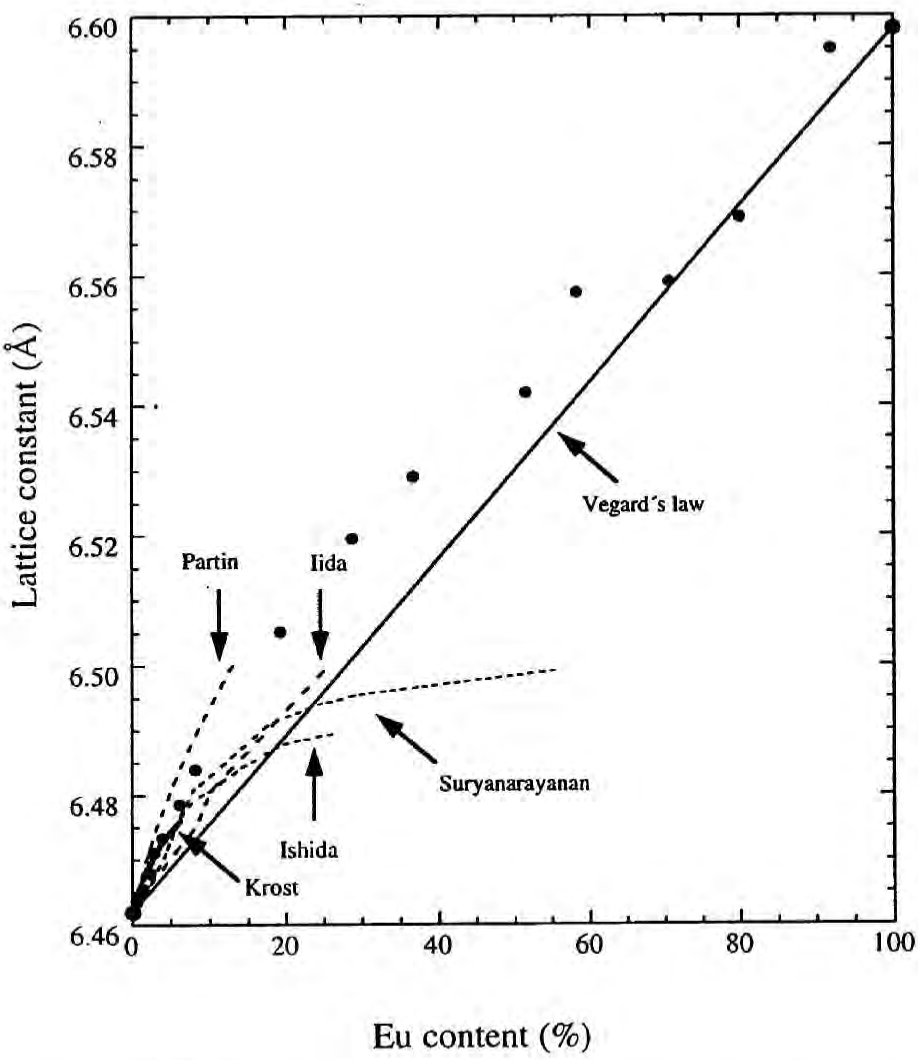

Figure 2-1: Plot for the lattice constant d as a function of Eu content in $Pb_{1-x}Eu_xTe$ alloy [32]. The solid dots indicate the experimental data obtained by Ueta *et al.* [32]. See Ref. [32] and references therein for the curves obtained by various people.

the X-ray measurement and Eu contents x are determined from the ICP (Inductively Coupled Plasma) chemical analysis. In Fig. 2-1, we find that lattice mismatch between PbTe and $Pb_{1-x}Eu_xTe$ alloys is as small as 0.4 % for $x \approx 0.1$. Such a small lattice mismatch is desirable in growing superlattice structures using alternating layers of PbTe and $Pb_{1-x}Eu_xTe$. In addition, other features such as almost negligible electron mobility compared to that for pure PbTe [15] and wide energy band gaps relative to that for pure PbTe ($E_g \simeq 635$ meV for $x \simeq 0.09$ as we discuss below) make $Pb_{1-x}Eu_xTe$ an ideal material for the barrier layers of PbTe MQWs because the large degree of the quantum confinement and the negligible electrical conduction in the barrier layers are expected, respectively, due to the large potential barrier height in the barrier layers and due to the small carrier mobility in the barrier layers. Other advantages of using the $Pb_{1-x}Eu_xTe$ alloys for the barrier layers of the PbTe MQWs include the thermal stability of the PbTe/$Pb_{1-x}Eu_xTe$ interfaces, partially due to the small lattice mismatch between PbTe and $Pb_{1-x}Eu_xTe$ for $x \approx 0.1$.

2.2.3 Electronic band structure

As is common to all the lead chalcogenides, including PbS, PbSe and PbTe, PbTe and $Pb_{1-x}Eu_xTe$ alloys have their conduction band minima at the L-point (the zone boundary along the [111] and equivalent $\langle 111 \rangle$ directions) in the Brillouin zone (see Fig. 2-2). The effective mass component along the main axis of the constant energy ellipsoid (along the $\langle 111 \rangle$ direction) is about ten times as large as the perpendicular component as we discuss below. The temperature dependence for the components of the effective mass tensor in PbTe, and that for the energy band gap for both PbTe and $Pb_{1-x}Eu_xTe$ alloys that are used in our calculation are given in §2.3.5.

It is known that the energy band gap E_g for $Pb_{1-x}Eu_xTe$ is rapidly increased relative to E_g for pure PbTe, if one increases the value of x even slightly from $x = 0$ (see Fig. 2-3) [29, 31]. Recently, it was found that the Eu content x can be varied continuously from 0 (PbTe) to 1 (EuTe) by growing $Pb_{1-x}Eu_xTe$ films on a (111) oriented BaF_2 substrate, using the molecular-beam epitaxy technique (MBE) [31]. The optical spectroscopy investigation revealed that the energy band gap for these

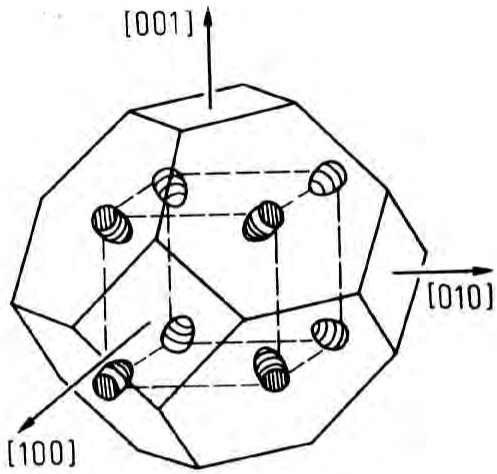

Figure 2-2: Constant energy ellipsoids at L-point in the Brillouin zone for PbTe and $Pb_{1-x}Eu_xTe$ alloys.

materials is also varied from $E_g = 320$ meV (PbTe, i.e., $x = 0$) to $E_g = 2000$ meV (EuTe, i.e., $x = 1$) continuously at 300 K. The results of these investigation are reproduced from Ref. [32] in Fig.2-3.

The most general form for the energy dispersion relation at the L-point in the Brillouin zone derived by $\mathbf{k} \cdot \mathbf{p}$ perturbation theory for pure PbTe and $Pb_{1-x}Eu_xTe$ alloys is given by the following formula [17, 30] :

$$\left\{\frac{\hbar^2\left(k_x^2+k_y^2\right)}{2m_l^c}+\frac{\hbar^2k_z^2}{2m_l^c}-\left(E-\frac{E_g}{2}\right)\right\}\left\{-\frac{\hbar^2\left(k_x^2+k_y^2\right)}{2m_l^v}-\frac{\hbar^2k_z^2}{2m_l^v}-\left(E+\frac{E_g}{2}\right)\right\}$$

$$=\frac{\hbar^2}{m_0}\left\{\frac{P_t^2}{m_0}\left(k_x^2+k_y^2\right)+\frac{P_l^2}{m_0}k_z^2\right\}. \tag{2.1}$$

In Eq. 2.1, m_t^c, m_l^c, m_t^v and m_l^v are the components for the far band effective mass tensor, where the superscripts c and v denote the conduction and valence bands, respectively, and the subscripts t and l denote the transverse and longitudinal components of the effective mass tensor, respectively, P_t and P_l are the transverse and longitudinal components of the momentum matrix element, respectively, and E is the energy of the electron measured from the middle of the energy band gap. It is noted that, in the subsequent sections and chapters, the energy of the electron E

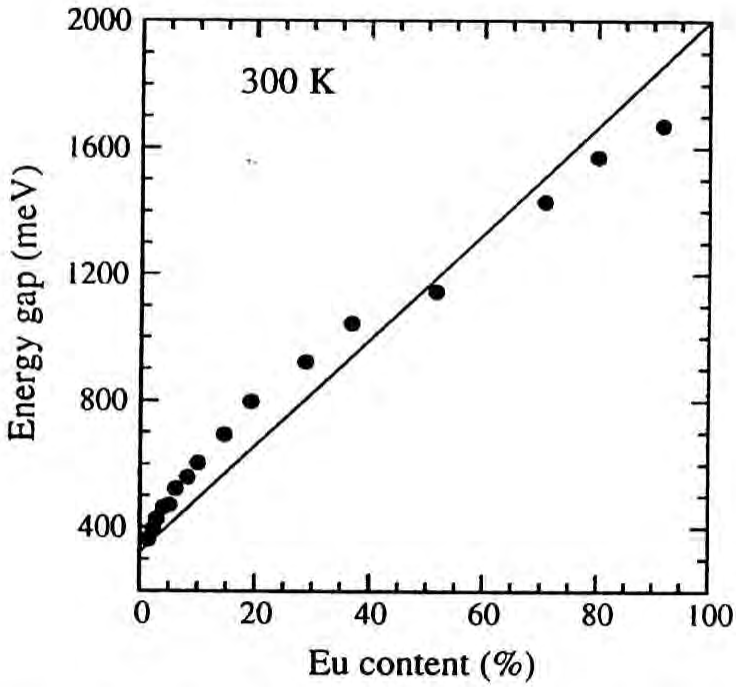

Figure 2-3: Plot for the energy band gap determined by the optical spectroscopy as a function of Eu content in $Pb_{1-x}Eu_xTe$ alloy (the figure is taken from Ref. [32]).

Table 2.1: Band parameters of bulk PbTe and $Pb_{1-x}Eu_xTe$ used in Eq. 2.1 [30].

	E_g (meV)	$2P_t^2/m_0$ (eV)	P_t/P_l	m_t^c/m_0	m_l^c/m_0	m_t^v/m_0	m_l^v/m_0
PbTe	Eq. 2.31	6.02	3.42	0.060	0.505	0.102	0.920
$Pb_{1-x}Eu_xTe$	Eq. 2.31	8.23	3.86	0.060	0.505	0.102	0.920

is measured from the lowest lying conduction (sub)band edge unless otherwise mentioned. The parameters used in Eq. 2.1 are summarized in Table 2.1 for bulk PbTe and $Pb_{1-x}Eu_xTe$ from Ref. [30].

It is of interest to calculate the components of the band edge mass tensor and the density of the electronic states as a function of energy, from the energy dispersion relation given in Eq. 2.1. The components of the band edge effective mass tensor are

Table 2.2: Components for the band edge effective mass tensor for bulk PbTe and $Pb_{1-x}Eu_xTe$ ($x \approx 0.09$) calculated using Eq. 2.2 for 300 K.

	$\tilde{m}_t^c/m_0$	$\tilde{m}_l^c/m_0$	$\lvert\tilde{m}_t^v\rvert/m_0$	$\lvert\tilde{m}_l^v\rvert/m_0$
PbTe	0.0282	0.279	0.0350	0.372
$Pb_{1-x}Eu_xTe$	0.0338	0.35	0.0439	0.511

obtained by evaluating the second derivative of Eq. 2.1 at $k_x = k_y = k_z = 0$ [†] :

$$\frac{m_0}{\tilde{m}_\nu^\lambda} = \frac{1}{\hbar^2}\frac{\partial^2 E}{\partial k_\nu^2} = \pm\left(\frac{2P_\nu^2}{m_0 E_g} + \frac{m_0}{m_\nu^\lambda}\right), \tag{2.2}$$

where + and − signs are for the conduction and valence band, respectively, ν stands for t (transverse) or l (longitudinal), λ stands for c (conduction band) or v (valence band), m_0 is the free electron mass, and $\tilde{m}_\nu^\lambda$ is the component of the effective mass tensor that we are interested in. It is also noted that, in Eq. 2.2, k_t and k_l denote the x (or y) and z components of the $\mathbf{k}$ vector for the [111]-valley, respectively. At 300 K, Eq. 2.31 predicts that $E_g = 321$ meV for bulk PbTe and that $E_g = 635$ meV for $Pb_{1-x}Eu_xTe$ with $x \approx 0.09$ (see the footnote on page 99). The components for the band edge effective mass tensor calculated using these values for E_g and other parameters in Table 2.1 are listed in Table 2.2 and their temperature dependences are plotted in Fig. 2-4.

The density of electronic states as a function of energy corresponding to the energy dispersion relation given by Eq. 2.1 is calculated by taking the energy derivative of the number of electronic states within the constant energy ellipsoid defined by Eq. 2.1.

$$DOS(E) \equiv \frac{d\,n(E)}{dE} = \frac{1}{V}\frac{d\,N(E)}{dE}, \tag{2.3}$$

where

$$N(E) = \frac{4}{3}\pi k_x^0 k_y^0 k_z^0 \times \frac{V}{8\pi^3} \times 4 \times 2. \tag{2.4}$$

[†]Readers should be reminded that the origin for the vector $\mathbf{k}$ here ($k_x = k_y = k_z = 0$) is at the L-point in the Brillouin zone.

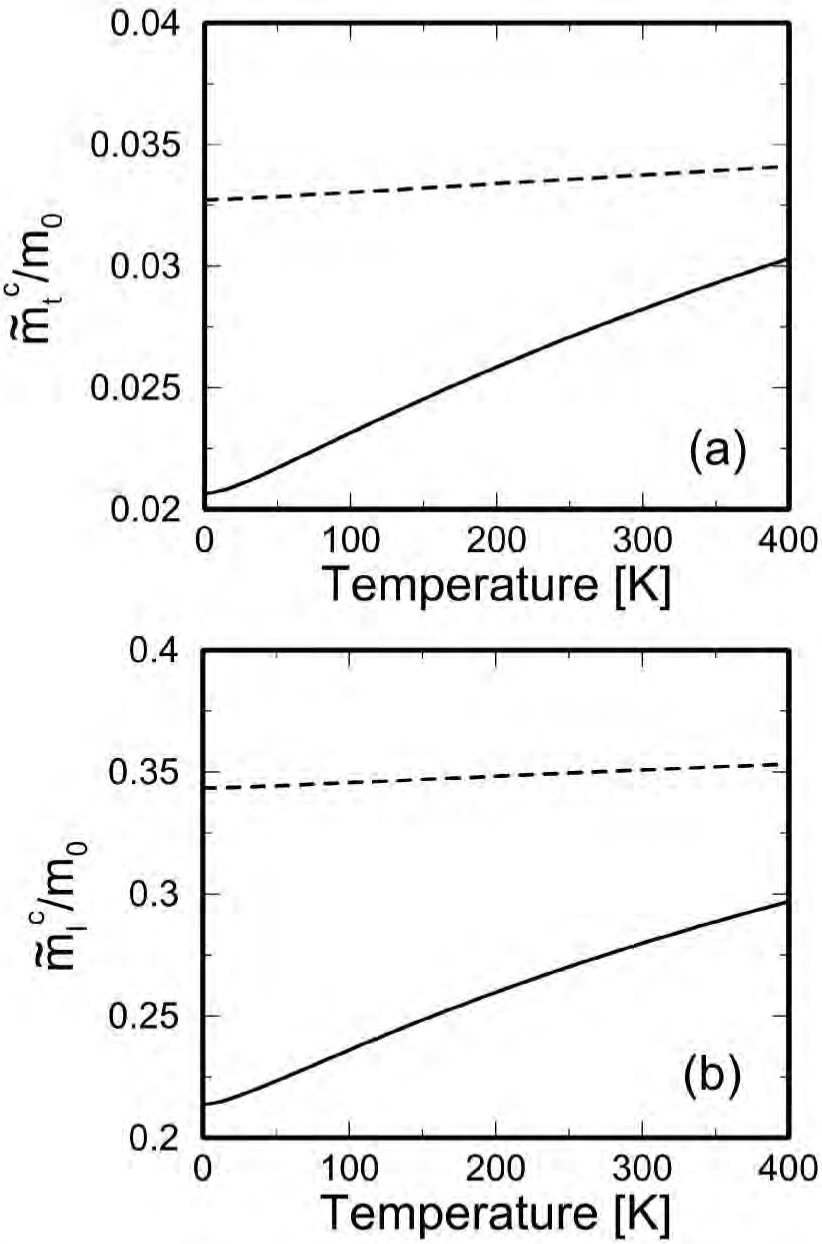

Figure 2-4: Transverse (a) and longitudinal (b) components of the band edge effective mass tensor as a function of temperature calculated using Eq. 2.2 for the conduction band of bulk PbTe (solid curve) and that of $Pb_{1-x}Eu_xTe$ alloy (dashed curve) for $x \simeq 0.09$.

In Eqs. 2.3 and 2.4, V is the volume of the crystal, the factor 4 in Eq. 2.4 comes from the number of the equivalent valleys at the L-points in the Brillouin zone and the factor 2 comes from the spin degeneracy. In Eq. 2.3, k_x^0, for example, is obtained by solving Eq. 2.1 for k_x with other components of $\mathbf{k}$ being set to zero ($k_y = k_z = 0$). k_y^0 and k_z^0 are obtained in a similar way. We list the results blow, noting that ν denotes either t (transverse) or l (longitudinal) and that $k_x^0 = k_y^0 = k_t^0$ and $k_z^0 = k_l^0$:

$$k_\nu^0 = \sqrt{\frac{1}{2}\left(A_\nu(E) + \sqrt{A_\nu(E)^2 + 4B_\nu(E)}\right)}, \tag{2.5}$$

where

$$A_\nu(E) = \frac{m_0}{\hbar^2}\left\{2E\left(\frac{m_\nu^c}{m_0} - \frac{m_\nu^v}{m_0}\right) - E_g\left(\frac{m_\nu^c}{m_0} + \frac{m_\nu^v}{m_0}\right) - 2\frac{2P_\nu^2}{m_0}\frac{m_\nu^c m_\nu^v}{m_0^2}\right\}, \tag{2.6}$$

and

$$B_\nu(E) = \frac{4m_\nu^c m_\nu^v}{\hbar^4}\left(E^2 - \frac{E_g^2}{4}\right). \tag{2.7}$$

Using Eqs. 2.3-2.7, the density of the electronic states $DOS(E)$ is calculated numerically as a function of E for the conduction band of PbTe and $Pb_{1-x}Eu_xTe$ ($x \simeq 0.09$) at 300 K. These results are plotted in Fig. 2-5, together with the results for a parabolic energy band approximation using the components of the effective mass tensor at 300 K given in Table 2.4 (see §2.3.5) for comparison.

2.2.4 Existence of a second valence band

The existence of a second valence, whose maxima are believed to be located at equivalent Σ-points (points along the axes parallel to [110] and equivalent $\langle 110 \rangle$ directions) in the Brillouin zone (see Fig. 2-7), was first surmised by Allgaier [34] from analyzing the temperature dependence of the Hall effect and suggestion was subsequently confirmed by several investigators (see Refs. [24] and [28] and references therein). The existence of such a second valence band is also inferred by the investigation of the temperature dependence of the optical absorption edge, which showed that the optical energy gap becomes independent of temperature above 450 K in PbTe [24].

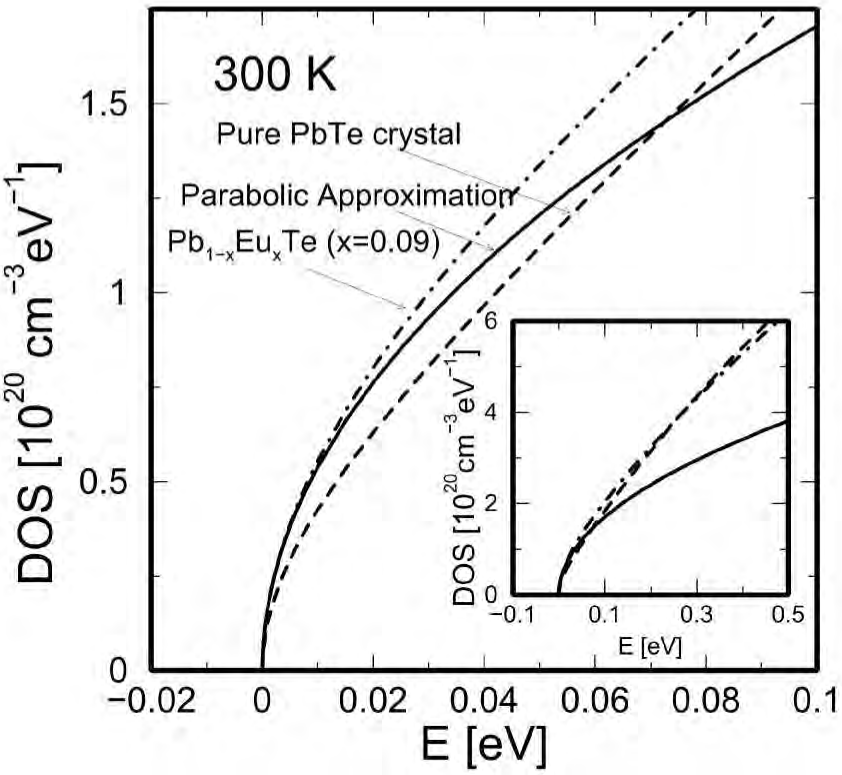

Figure 2-5: Densities of electronic states (DOS) as a function of energy E for the conduction band of PbTe (dashed curve) and $Pb_{1-x}Eu_xTe$ alloy for $x = 0.09$ (dash-dotted curve) at 300 K, that are calculated using Eq. 2.1. The solid curve denotes the parabolic dispersion approximation assuming $m_t = 0.03345$ and $m_l = 0.35$ that are the values and the approximation used in the theoretical calculation in this chapter (see Table 2.4 in §2.3.5). Each curve in this figure is shifted in energy so that $E = 0$ at the conduction band edge to make the comparison easier among these three curves. Note that the parabolic approximation is approximately valid for $E < 0.1$ eV. The inset shows the same data with wider energy range.

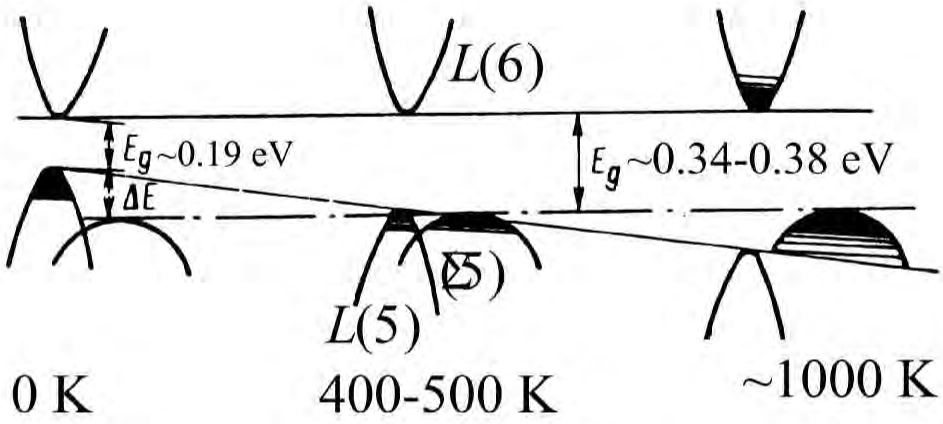

Figure 2-6: Changes in the positions of the valence and conduction band edges of PbTe as a function of temperature. The left, middle, and right diagrams denote the situations at 0 K, 400-500 K, and 1000 K, respectively. The indirect band gap $E_g' = E^{L(6)} - E^{\Sigma(5)}$ is almost temperature independent, whereas the direct band gap $E_g = E^{L(6)} - E^{L(5)}$ increases linearly with increasing temperature. The $\Sigma(5)$ valence band overtakes $L(5)$ valence band above 450 K [35] regarding optical and transport properties.

The temperature dependence of the relative energy for this second valence band edge is qualitatively explained as follows. At low temperatures, the position of the second valence band edge, denoted as $\Sigma(5)$, is lower in energy than that of the first valence band edge, denoted as $L(5)$. The indirect band gap $E_g' = E^{L(6)} - E^{\Sigma(5)}$, where $E^{\Sigma(5)}$ and $E^{L(6)}$ are the energies for the $\Sigma(5)$ edge and for the conduction band edge [denoted as $L(6)$], respectively, is nearly temperature independent. Because of the positive temperature coefficient for the direct energy gap $E_g = E^{L(6)} - E^{L(5)}$ as we discuss in §2.3.5, the second valence band $\Sigma(5)$ overtakes the first valence band $L(5)$ at higher temperatures (above 450 K). A sketch of such a behavior is reproduced from Ref. [35] in Fig. 2-6.

The position and orientation for the $\Sigma(5)$ valleys were investigated by Sitter *et al.* [36] by measuring the anisotropy of the conductivity and the magneto-resistance of the carriers that are excited to the second valence band [$\Sigma(5)$] using p-type PbTe. They found that the constant energy ellipsoids at the second valence band edge are oriented in [100] or equivalent $\langle 100 \rangle$ directions, and that they have a highly anisotropic effective mass tensor [$m_l/m_t \simeq 10$, where m_l and m_t are longitudinal (parallel to the main axis of the constant energy ellipsoid) and transverse (perpendicular to the main

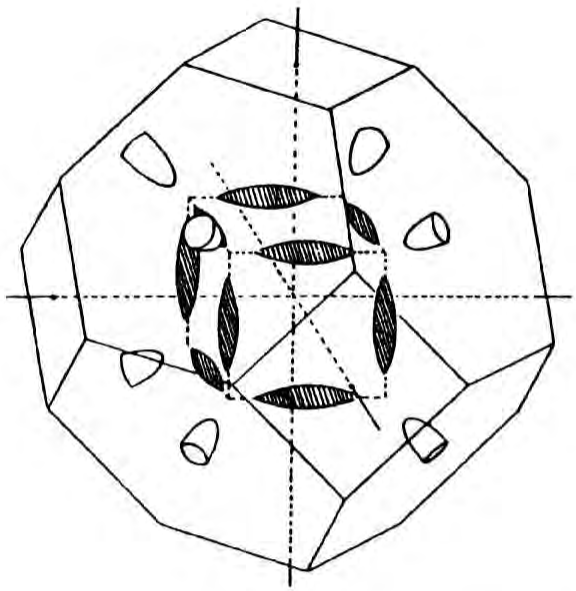

Figure 2-7: Model for the constant energy surfaces of the valence bands for PbTe. $\langle 111 \rangle$ oriented half-ellipsoids at the L-point in the Brillouin zone and $\langle 100 \rangle$ oriented ellipsoids at the Σ-point in the Brillouin zone are shown (the figure is taken from Ref. [36]).

axis of the constant energy ellipsoid) components of the effective mass tensor]. It is also found that the density of states mass for the second valence band edge is quite large, i.e., $m_d^* = N^{2/3} \left(m_t^2 m_l\right)^{1/3} > 1.0$, where N is the number of the equivalent sites for $\Sigma(5)$ ($N = 12$). A sketch of such constant energy ellipsoids within the Brillouin zone is reproduced in Fig. 2-7 from Ref. [36].

2.3 Theoretical Models for the transport coefficients

The theoretical models used in the present work are summarized in this section. The basic framework of these models was developed by Hicks and Dresselhaus [12, 14, 17, 37] for a parabolic single-band material using the constant relaxation time approximation (see Appendix A). Below, we reorganize their formulation in a form more relevant to n-type bulk PbTe and PbTe MQWs.

2.3.1 Transport coefficients for bulk PbTe

Bulk PbTe (either n- or p- type) has four ellipsoidal valleys at the L points in the Brillouin zone, as we discussed in the previous section. The transport coefficients for such a system are isotropic in the absence of a magnetic field because of the cubic symmetry of the lead chalcogenides. In the constant relaxation time approximation, assuming a parabolic energy dispersion relation, the S (Seebeck coefficient), σ (electrical conductivity), and κ_e (electronic contribution to the thermal conductivity), for such materials are described by [3, 17],

$$S_{3D} = -\frac{k_B}{e}\left(\frac{5F_{3/2}(\zeta^*)}{3F_{1/2}(\zeta^*)} - \zeta^*\right), \tag{2.8}$$

$$\sigma_{3D} = N \times \frac{\sqrt{2}(m_t^2 m_l)^{1/2} e}{\pi^2 \hbar^3}(k_B T)^{3/2} \mu F_{1/2}(\zeta^*), \tag{2.9}$$

$$\kappa_{e(3D)} = N \times \frac{\sqrt{2}(m_t^2 m_l)^{1/2} k_B^2 T}{3\pi^2 \hbar^3 e}(k_B T)^{3/2} \mu \left(7F_{5/2}(\zeta^*) - \frac{25}{3}\frac{F_{3/2}(\zeta^*)^2}{F_{1/2}(\zeta^*)}\right), \tag{2.10}$$

respectively, where the subscript 3D indicates the properties of bulk materials for our later convenience in comparing these expressions with those for 2D MQWs. In Eqs. 2.8-2.10, N is the number of equivalent carrier pockets within the Brillouin zone, k_B is the Boltzmann constant, $\hbar$ is Planck's constant divided by 2π ($\hbar = h/2\pi$), e is the absolute value of the electron charge, μ is the carrier mobility in the direction of measurement, m_t and m_l are the transverse and longitudinal effective mass components, respectively, ζ^* is the reduced chemical potential ($\zeta^* = \zeta/k_B T$) measured from the conduction band edge, and $F_j(\zeta^*)$ is a Fermi-related integral function defined by,

$$F_j(\zeta^*) = \int_0^\infty \frac{\xi^j d\xi}{e^{(\xi-\zeta^*)} + 1}. \tag{2.11}$$

Generally, κ_e is related to σ via the Wiedemann-Franz law,

$$\kappa_e = L_0 \sigma T, \tag{2.12}$$

where L_0 is called the Lorenz number. It is implied from Eqs. 2.9 and 2.10 that L_0 in 3D is given by

$$L_{0(3D)} = \frac{k_B^2}{e^2}\left(\frac{7F_{5/2}(\zeta^*)}{3F_{1/2}(\zeta^*)} - \frac{25F_{3/2}(\zeta^*)^2}{9F_{1/2}(\zeta^*)^2}\right). \tag{2.13}$$

The value for $L_{0(3D)}$ is plotted as a function of ζ^* in Fig. 2-8 (solid curve). It is shown in this figure that $L_{0(3D)}$ for a non-degenerate semiconductor ($\zeta^* < 0$) is 21-24 % smaller than the value traditionally used for metals and degenerate semiconductors (2.45×10^{-8} WΩ/K^2). It is noted that the actual Lorenz number L_0 for bulk PbTe should be even lower than the values predicted by Eq. 2.13 because [24]: (1) the inclusion of the effects of non-parabolic energy bands and an energy-dependent relaxation time $\tau(E)$ into our model would further decrease $L_{0(3D)}$ by about 30 % in the non-degenerate regime ($\zeta^* < 0$), and (2) the carrier-carrier scattering, which has little effect on the electrical conductivity but has a significant effect on the electronic thermal conductivity, would lead to a 40-60 % reduction of L_0 from $L_{0(3D)}$ (Eq. 2.13) at low temperature (below ~200 K). For these reasons, our estimation of $\kappa_{e(3D)}$ using Eq. 2.13 is conservative. The same argument should also apply to $L_{0(2D)}$ in 2D which will be discussed in §2.3.3.

2.3.2 Conversion of the Hall carrier density to the actual carrier density in bulk PbTe

The Hall carrier concentration n_{Hall}, which can be determined experimentally, is defined by,

$$n_{\text{Hall}} = -\frac{1}{R_H e}, \tag{2.14}$$

where R_H is the Hall coefficient. Theoretical formulation of the Hall carrier concentration follows from the equation of motion for an electron in an electric and magnetic field,

$$-e\left(\vec{E} + \vec{v} \times \vec{B}\right) = \frac{m^*\vec{v}}{\tau}, \tag{2.15}$$

where $\vec{v}$ is the velocity of the electron, c is the speed of light, m^* is the effective mass of the electron, τ is the (scattering) relaxation time for the electron, and $\vec{E}$

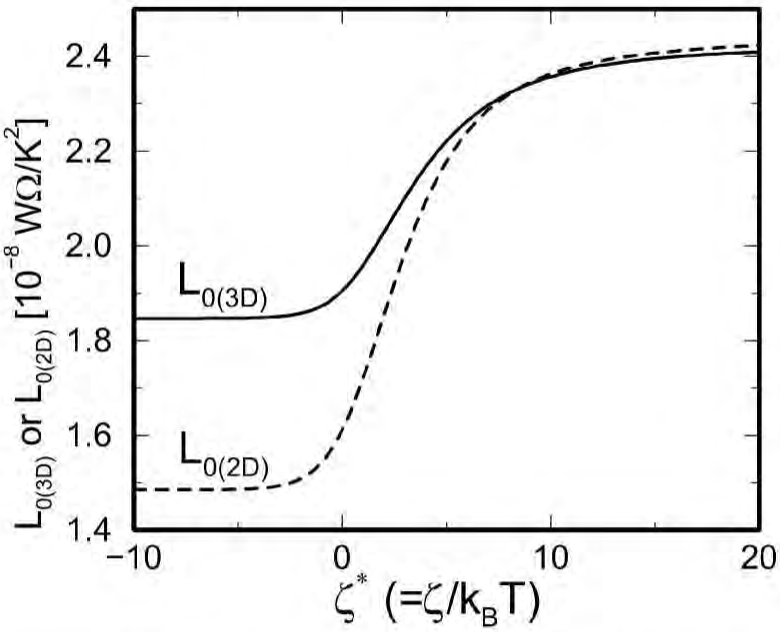

Figure 2-8: Lorenz number $L_{0(3D)}$ (solid curve) and $L_{0(2D)}$ (dashed curve) defined by Eqs. 2.13 and 2.22, respectively, as a function of reduced chemical potential ζ^* $(= \zeta/k_BT)$. $L_{0(3D)}$ and $L_{0(2D)}$ approach the traditional value for metals at large ζ^*.

and $\vec{B}$ are the electric and magnetic fields, respectively. For anisotropic (ellipsoidal) constant energy surfaces, the effective mass m^* in the above equation is replaced by the corresponding effective mass tensor.

For bulk n-type PbTe, four equivalent carrier pockets about the L-points are oriented along the [111] or an equivalent $\langle 111 \rangle$ direction. Assuming that the magnetic field $\vec{B}$ is applied in the (111) direction (along the growth direction of the superlattice), as is the case in our experiments, and the relaxation time τ is a function of energy only, we obtain the following expression for $n_{\mathrm{Hall(3D)}}$ in the low field limit ($\omega_c\tau \approx \mu B \ll 1$, where $\omega_c = eB/m^*$) [24, 25, 34],

$$n_{\mathrm{Hall(3D)}} = \frac{(2K_{3D}+1)^2}{3K_{3D}(K_{3D}+2)} r_H^{-1} n_{3D} \equiv G_{3D}^{-1} r_H^{-1} n_{3D}, \tag{2.16}$$

where K_{3D} is the ratio between the longitudinal- and transverse- effective mass components for the ellipsoidal carrier pockets ($K_{3D} = m_l/m_t$), n_{3D} is the actual carrier concentration in the 3D material, G_{3D} is the geometrical factor defined by the above

equation, and r_H is the Hall scattering factor defined by [24, 25],

$$r_H = \frac{\langle \tau^2 \rangle}{\langle \tau \rangle^2}. \tag{2.17}$$

Here $\langle\rangle$ denotes the energy average of the indicated quantity defined by

$$< A(E) >= \frac{\int_0^\infty A(E)(-\partial f/\partial E)k^3 dE}{\int_0^\infty (-\partial f/\partial E)k^3 dE}, \tag{2.18}$$

for the pertinent 3D parabolic band. Since G_{3D} has a negligible temperature dependence in PbTe, we evaluate it only at 300 K. Using the bulk effective mass values found in the literature [28] ($m_t = 0.033\ m$ and $m_l = 0.35\ m$ at 300 K), we obtain the value of the geometric factor $G_{3D}^{-1} = 1.23$. It is known that, in non-degenerate statistics, $r_H = 1.18$ for acoustic deformation potential scattering ($\tau \sim E^{-1/2}$) and $r_H = 1.93$ for ionized impurity scattering ($\tau \sim E^{3/2}$) [24, 25]. Note that, in degenerate statistics, $r_H \to 1$ when $\zeta^* \to \infty$ for either scattering mechanism (See Fig. 2-9). It is noted that the carrier scattering by the Coulomb potential of ionized impurities is very weak in PbTe due to the large static dielectric constant ($\epsilon_S \sim 400$) [28]. Therefore, choosing $r_H = 1.18$ (acoustic phonon deformation potential scattering), we obtain 0.96 for the total correction factor $G_{3D} r_H$. This shows that $n_{\rm Hall}$ should be very close to n_{3D} in n-type bulk 3D PbTe.

Using this result, we plot in Fig. 2-10 the theoretical results for $|S|$ as a function of $n_{\rm Hall}$ at 300 K (dashed line), where we use $n_{\rm Hall} = 1.04\, n_{3D}$. In this figure, we compare our theoretical results obtained using Eqs. 2.8 and 2.16 with the experimental results taken from Ref. [15]. Also plotted in the figure are the experimental and theoretical results for the (111) oriented n-type PbTe MQWs which will be discussed in §2.3.3 and §2.3.4. Fig. 2-10 shows that the experimental results (open circles) [15] agree very well with the theoretical results (dashed curve) for the case of 3D bulk n-type PbTe.

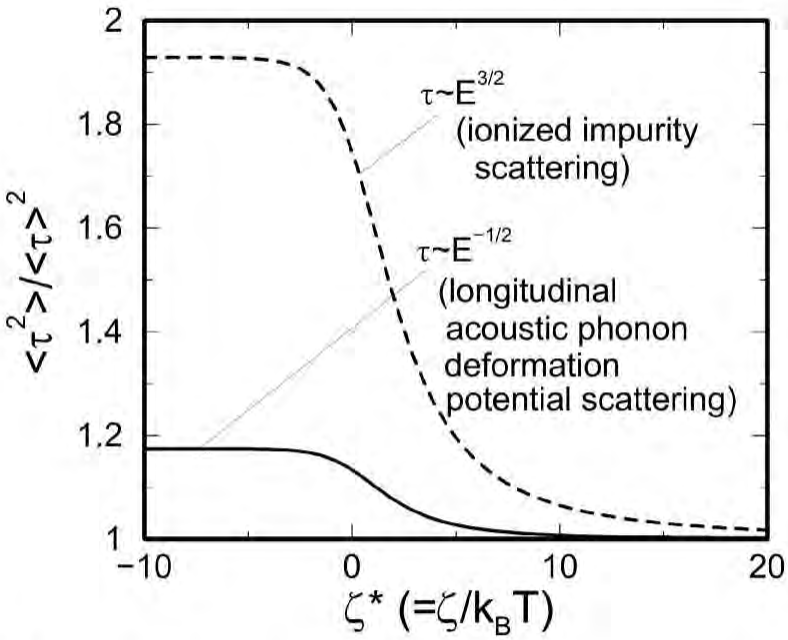

Figure 2-9: Hall scattering factor r_H (defined by $\langle\tau^2\rangle/\langle\tau\rangle^2$) as a function of reduced chemical potential ζ^* for a 3D parabolic energy band. The solid curve denotes the results for longitudinal acoustic phonon deformation potential scattering ($\tau \sim E^{-1/2}$) and the dashed curve denotes the result for ionized impurity scattering ($\tau \sim E^{3/2}$).

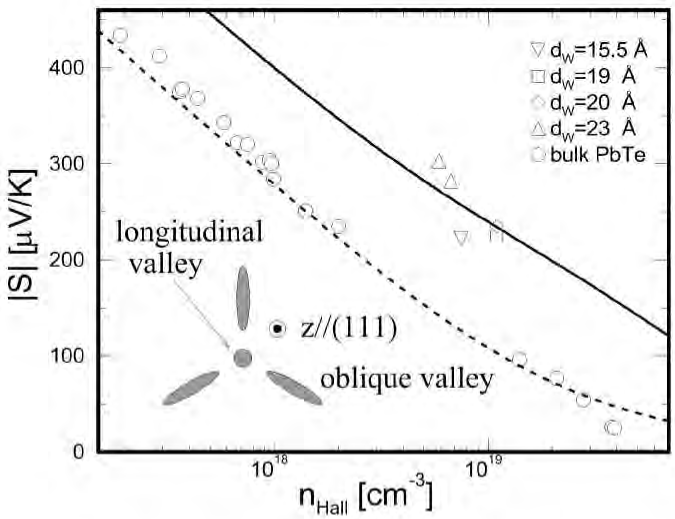

Figure 2-10: The Seebeck coefficient of n-type bulk PbTe and (111) oriented PbTe MQWs as a function of Hall carrier concentration at 300 K. The experimental results for bulk PbTe and for the (111) oriented MQWs taken from Ref. [15] are plotted with various symbols according to the quantum well thickness d_W. Also shown are the theoretical results for bulk PbTe (dashed curve) and for the (111) oriented MQWs ($d_W = 20$ Å, $\Delta E_{\text{longt-obliq}} = 65$ meV) assuming $\mu_{\text{longt}} = \mu_{\text{obliq}}$ (solid curves). Shown in the inset is a schematic picture for the constant energy surfaces for the (111) oriented PbTe MQWs. See §2.3.3 and §2.3.4 for details.

2.3.3 Transport coefficients for PbTe MQWs

In the constant relaxation time approximation, S, σ and κ_e for a single subband quantum well (2D electron gas) are given by [14, 17]

$$S_{2D} = -\frac{k_B}{e}\left(\frac{2F_1(\zeta^*)}{F_0(\zeta^*)} - \zeta^*\right), \tag{2.19}$$

$$\sigma_{2D} = N \times \frac{(m_t m_l)^{1/2} e}{\pi\hbar^2 d_W}(k_B T)\mu F_0(\zeta^*), \tag{2.20}$$

$$\kappa_{e(2D)} = N \times \frac{(m_t m_l)^{1/2} k_B^2 T}{\pi\hbar^2 d_W e}(k_B T)\mu\left(3F_2(\zeta^*) - \frac{4F_1(\zeta^*)^2}{F_0(\zeta^*)}\right), \tag{2.21}$$

respectively, where d_W is the quantum well thickness and the subscript 2D specifically indicates that these expressions are for 2D MQW systems. A quantum well thickness d_W of 20 Å, a typical value in our experiments, is usually used in our calculations unless mentioned otherwise explicitly. The above equations also imply that

$$L_{0(2D)} = \frac{k_B^2}{e^2}\left(\frac{3F_2(\zeta^*)}{F_0(\zeta^*)} - \frac{4F_1(\zeta^*)^2}{F_0(\zeta^*)^2}\right), \tag{2.22}$$

where $L_{0(2D)}$ is the Lorenz number for a 2D electron gas system (see Fig. 2-8). It is noted that $L_{0(2D)}$ is about 20 % smaller than $L_{0(3D)}$ in the absence of degeneracy. It is expected that the Lorenz number L_0 for actual 2D MQW systems is even smaller than $L_{0(2D)}$ in Eq. 2.22 due to band non-parabolicity and carrier-carrier scattering as discussed in §2.3.1 for bulk PbTe. Smaller L_0 is desirable for obtaining higher ZT.

If the sample has multiple types of (sub)bands as in (111) oriented PbTe MQWs (namely, the longitudinal- and oblique-subbands, as schematically shown in the inset of Fig. 2-10), the overall transport coefficients are given by the following sums and weighted average,

$$S_{(\mathrm{tot})} = \frac{\sum \sigma_i S(\zeta_i^*)}{\sum \sigma_i}, \tag{2.23}$$

$$\sigma_{(\mathrm{tot})} = \sum \sigma_i, \tag{2.24}$$

$$\kappa_{e(\mathrm{tot})} = \sum \kappa_{ei}, \tag{2.25}$$

where the summations are taken over the different types of bands, or subbands in the case of MQWs, and σ_i and κ_{ei} are the electrical conductivity and the electronic contribution to the thermal conductivity for the ith (sub)band, respectively. The reduced chemical potential ζ_i^* $(= \zeta_i/k_BT)$ is measured from each (sub)band edge. Equations 2.24 and 2.25 also imply that the Lorenz number L_0 for multiple-(sub)band materials is no longer a simple function of ζ^* only, but involves sums and division of transport coefficients defined for each subband.

2.3.4 Conversion of the Hall carrier density to the actual carrier density in PbTe MQWs

From the same formulation as was developed in §2.3.2, the Hall carrier concentration for (111) oriented 2D PbTe MQWs in the low field limit ($\omega_c\tau \approx \mu B \ll 1$) is given by the following expression using the two-carrier model [3, 24, 25],

$$n_{\mathrm{Hall(2D)}} = \frac{(n_{\mathrm{longt}}\mu_{\mathrm{longt}} + n_{\mathrm{obliq}}\mu_{\mathrm{obliq}})^2}{n_{\mathrm{longt}}\mu_{\mathrm{longt}}^2 r_{H\mathrm{longt}} + \frac{4K_{\mathrm{2D}}}{(K_{\mathrm{2D}}+1)^2} n_{\mathrm{obliq}}\mu_{\mathrm{obliq}}^2 r_{H\mathrm{obliq}}} \tag{2.26}$$

where n, μ and r_H are the carrier concentration, carrier mobility and the Hall scattering factor (see Eq. 2.17), respectively. The subscripts 'longt' and 'obliq' denote the longitudinal- and the oblique- subbands, respectively, where the longitudinal subband arises from the [111] carrier pocket which is oriented along the quantum well growth direction (z-direction) and the oblique subband arises from three equivalent $\langle 111 \rangle$ carrier pockets which are at an oblique angle with respect to the z-direction (see the inset of Fig. 2-10). The carrier mobilities for the longitudinal and oblique subbands are given by

$$\mu_{\mathrm{longt}} = \frac{e\tau_{\mathrm{longt}}}{m_{t(\mathrm{2D})}}, \tag{2.27}$$

and

$$\mu_{\mathrm{obliq}} = \frac{1}{2}\left(\frac{1}{m_{t(\mathrm{2D})}} + \frac{1}{m_{l(\mathrm{2D})}}\right) e\tau_{\mathrm{obliq}}, \tag{2.28}$$

respectively, where τ_{longt} and τ_{obliq} are the relaxation times for the longitudinal and the oblique subbands, respectively. Using the 2D effective masses [$m_{t(\mathrm{2D})} = 0.033\, m$

and $m_{l(2D)} = 0.315\,m$] which are obtained from the projection of the 3D constant energy surfaces on the (111) quantum well plane, we obtain the transport masses $0.033\,m$ and $0.060\,m$ for the longitudinal and the oblique subbands, respectively. It is noted that the transport mass for the oblique subband here is quite different from the corresponding density-of-states mass for the oblique subband [$m^*_{\rm obliq} = 3 \times (m_{t(2D)} m_{l(2D)})^{1/2} = 0.308\,m$] because of the anisotropy and the multiplicity of the carrier pockets for the oblique subbands. The Hall scattering factors in the case of 2D MQWs are $r_{H\rm longt} = r_{H\rm obliq} = 1$ for the longitudinal acoustic phonon deformation potential (LADP) scattering since the relaxation time τ is constant with energy.[†] K_{2D} is the ratio between the longitudinal and transverse effective mass components ($K_{2D} = m_{l(2D)}/m_{t(2D)}$) for an oblique (elliptical) pocket. Substituting Eqs. 2.27 and 2.28, the 2D effective mass components and $r_{H\rm longt} = r_{H\rm obliq} = 1$ into Eq. 2.26, we obtain,

$$n_{\rm Hall(2D)} = \frac{(1.81\gamma_\tau n_{\rm longt} + n_{\rm obliq})^2}{3.27\gamma_\tau^2 n_{\rm longt} + 0.347 n_{\rm obliq}} \tag{2.29}$$

for n-type (111) oriented PbTe quantum wells at 300 K, where $\gamma_\tau = \tau_{\rm longt}/\tau_{\rm obliq}$. Since both $n_{\rm Hall(2D)}$ (Eq. 2.29) and $S_{\rm 2D(tot)}$ (Eq. 2.23) are a function of γ_τ and ζ^* only, at fixed temperatures, we can determine the ratio of the relaxation times between the two subbands ($\tau_{\rm longt}/\tau_{\rm obliq}$) and the electro-chemical potential (hence the carrier occupation in each subband) for the pertinent sample by measuring both S and $n_{\rm Hall}$ experimentally. The values for $n_{\rm longt}$, $n_{\rm obliq}$ and $\tau_{\rm longt}/\tau_{\rm obliq}$ thus obtained are summarized in Table 2.3 together with the estimated *actual* carrier mobility $\sigma/en_{\rm QW} = \sigma/e(n_{\rm longt} + n_{\rm obliq})$. It is noted that, in these calculations, the energy of the valley-splitting ($\Delta E_{\rm longt-obliq}$) is determined from the square well approximation as will be discussed in the next subsection. The large scatter in the values for $\tau_{\rm longt}/\tau_{\rm obliq}$ found in Table 2.3 suggests that this quantity may be rather sensitive to extrinsic factors such as sample quality. Various conditions for intra- and inter-valley scattering that lead to various values

[†]In the longitudinal acoustic phonon deformation potential (LADP) scattering, $\tau(E)$ is inversely proportional to the density of states (DOS) for the electron at the given energy E. Since the DOS is constant with energy for a 2D parabolic energy dispersion relation, the resulting $\tau(E)$ is constant with energy as well for the LADP scattering in a 2D electron gas.

Table 2.3: Properties of PbTe/$Pb_{0.927}Eu_{0.073}Te$ MQW samples at 300 K [15].

Sample #	d_W† [Å]	n_{Hall}† [cm^{-3}]	n_{longt} [cm^{-3}]	n_{obliq} [cm^{-3}]	μ_{Hall}† [cm^2/V·s]	σ/en_{QW} [cm^2/V·s]	S† [μV/K]	τ_{longt} τ_{obliq}
T-225	19	1.1×10^{19}	3.0×10^{18}	4.1×10^{18}	1420	2180	−225	0.603
T-229	20	1.1×10^{19}	2.9×10^{18}	3.7×10^{18}	710	1200	−235	0.483
T-235	23	5.9×10^{18}	1.7×10^{18}	1.5×10^{18}	650	1210	−303	0.232
T-246	15.5	7.5×10^{18}	2.8×10^{18}	4.4×10^{18}	1150	1200	−222	1.185
T-236	23	6.7×10^{18}	1.9×10^{18}	1.8×10^{18}	640	1170	−282	0.465

†Data taken from Ref. [15].

for $\tau_{longt}/\tau_{obliq}$ (from 0.4 to 3.3) [38] are discussed in §3.4.1, where we consider the conditions for $\tau_{longt}/\tau_{obliq}$ by fitting the experimental data using the equations developed in this and the last subsections. In Appendix B, we examine the validity of our model by studying the lightly doped PbTe/$Pb_{1-x}Eu_xTe$ MQW samples experimentally. These samples are grown by Dr. G. Springholz and Professor G. Bauer at the Johannes Kepler Universität, Linz, Austria, specifically for this purpose. We expect that, for lightly doped PbTe MQW samples, the majority of carriers reside in the longitudinal subband, and that the experimental results are more easily modeled and interpreted in terms of our models. It is indeed seen that the experimental results agree well with the theoretical prediction when the majority of carriers reside in the longitudinal subband.

In the present and next chapter, we will focus on our best sample (T-225), which we expect to have properties closest to those of intrinsic PbTe quantum wells. In the subsequent sections in this chapter, we therefore analyze the observed properties of this particular sample as a function of temperature in terms of our models that have been discussed thus far.

2.3.5 Modeling of temperature dependent transport coefficients

Theoretical modeling of the temperature dependent transport coefficients involves knowledge of the temperature dependent band parameters. Such information on the

Table 2.4: Temperature dependent band parameters.

Band parameter	Temperature dependence	Ref.
m_t/m	$0.024 + 3.15 \times 10^{-5}T$	[28]
m_l/m	$0.25 + 3.33 \times 10^{-4}T$	[28]
E_g(PbTe)	Eq. 2.30	[29]
$E_g(Pb_{0.927}Eu_{0.073}Te)$	630 meV†	[16]

† See the footnote on page 99.

bulk PbTe/$Pb_{1-x}Eu_xTe$ system is readily available in the literature [28] (see also Table 2.4 and §2.2). Band parameters for the 2D PbTe quantum wells are calculated from the projections and cross section of 3D band parameters for bulk PbTe, as discussed before.

The relative energies of the longitudinal- and oblique- subband edges (bound state levels) are calculated using a square well approximation (SWA) in the present study. A more elaborate method to calculate these energy levels is the envelope function approximation (EFA) that takes into account the non-parabolic energy dispersion relation and Krönig-Penney type boundary conditions [30].

The SWA is a sufficient approximation for our present work, because: (1) Our PbTe MQW samples have relatively small quantum well widths ($d_W \sim 20$ Å) and very large barrier layer widths ($d_B \sim 410$ Å). Therefore, the overlap of the wave functions between two adjacent quantum well layers is negligibly small, and (2) The bound state levels calculated by the square well approximation are in good agreement with those obtained by the EFA for $d_W = 20$ Å and $d_W = 53$ Å as shown in the Table 2.5, which proves that the much simpler SWA method (simpler than the EFA method) is adequate for the present work.

The determination of the temperature dependence of the conduction band offset, necessary for the calculation of the bound state levels by the SWA, is described below. The temperature dependence of the L-point band gap in the bulk $Pb_{1-x}Eu_xTe$ system is given by the following empirical formula for $x < 0.05$ [29]: †

$$E_g(x,T) = 190\text{meV} + 0.51\text{meV} \cdot T(K)^2 \frac{1 - 9.8x}{T(K) + 56} + x \cdot 5880\text{meV}. \qquad (2.30)$$

Table 2.5: Calculated energies of the subband edges measured from the band edges of bulk PbTe [units: meV].

	type of subband	EFA [14, 17]	SWA
$d_W = 20$Å			
conduction band	oblique	139	148
	longitudinal	74	76
valence band	longitudinal	−60	−63
	oblique	−123	−123
$d_W = 53$Å			
conduction band	longitudinal (n=2)	88	86
	oblique	78	87
	longitudinal (n=1)	24	22
valence band	longitudinal (n=1)	−18	−18
	oblique	−74	−75
	longitudinal (n=2)	−	−71

A simple extrapolation of Eq. 2.30 to $x = 0.073$, the typical Eu content for our $Pb_{1-x}Eu_xTe$ barrier layer, suggests the following effects: (1) the temperature dependence of the band gap becomes less significant as x increases and approaches 0.073; and (2) for $x = 0.073$, Eq. 2.30 predicts $E_g = 656$ meV at 300 K, which is slightly higher than, but very close to, our experimental value of 630 meV, that is determined from infrared absorption spectra [16], despite the fact that x for our barrier layer is outside of the range of validity of Eq. 2.30. In addition, Eq. 2.30 predicts $E_g = 626$

†Recently, the authors of Ref. [29] reported the updated version for Eq. 2.30 [31],

$$E_g(x,T) = 189.7\text{meV} + 0.48\text{meV} \cdot T(K)^2 \frac{1 - 7.56x}{T(K) + 29} + x \cdot 4480\text{meV}. \tag{2.31}$$

This equation predicts significantly smaller energy gaps for $x > 0.01$ than Eq. 2.30. It is found that Eq. 2.30 provides a better fit to the experimental results reported in Ref. o[29] as well as to our own results [16] on $Pb_{1-x}Eu_xTe$ than Eq. 2.31, if we assume $x \approx 0.073$ for our samples. The main discrepancy comes from the ambiguous determination of x that is in turn used for the determination of E_g via Eqs. 2.30 or 2.31. In the present chapter, we use Eq. 2.30 since it predicts more consistent values of E_g than Eq. 2.31 if we assume $x \approx 0.073$ for our samples as was determined originally [15]. In the next chapter, we will see that the value for x for our samples should be updated to 0.09 according to the newly obtained relation between x and d (lattice constant) [32]. For this case ($x \approx 0.09$), Eq. 2.31 is found to be more consistent with the observed experimental results than Eq. 2.30. Therefore, we will use this revised equation in the next chapter where $x \approx 0.09$ is assumed for our samples.

meV at 77 K which is still close to the room temperature value of 630 meV. Thus, we assume that the experimentally determined band gap of our barrier material (630 meV) is temperature independent in our calculation of subband energy levels. We use Eq. 2.30 to describe the temperature dependence of the band gap for bulk PbTe. The ratio of the conduction band offset (ΔE_c) to the band gap difference between PbTe and $Pb_{1-x}Eu_xTe$ (ΔE_g) is chosen to be 0.55, based on the previously published data [30].

2.4 Experimental results and their theoretical interpretations

The samples, characterized in the previous section and discussed in more detail in this section, were grown using the Molecular Beam Epitaxy (MBE) technique by Dr. Ted Harman at MIT Lincoln Lab.[15]. The modulation doping scheme was employed for carrier injection, introducing Bi (n-type) impurities into the $Pb_{1-x}Eu_xTe$ barrier layers. As mentioned before, modulation doping minimizes the impurity scattering within the quantum wells, leading to high carrier mobilities, especially at low temperatures. The Seebeck coefficient, electrical conductivity, and Hall coefficient were measured on our best sample (T-225) and on a high quality MBE-grown bulk sample (T-168) as a function of temperature in the range 80 K to 580 K. In evaluating the Hall carrier concentration and the electrical conductivity, the sum of the thicknesses of the quantum well part only, rather than the thickness of the whole superlattice including barrier layers, was used as the thickness the sample for our calculations of electrical conductivities and Hall carrier concentrations in order to determine the properties of the quantum wells themselves. Below, each 2D thermoelectric property is discussed separately in some detail.

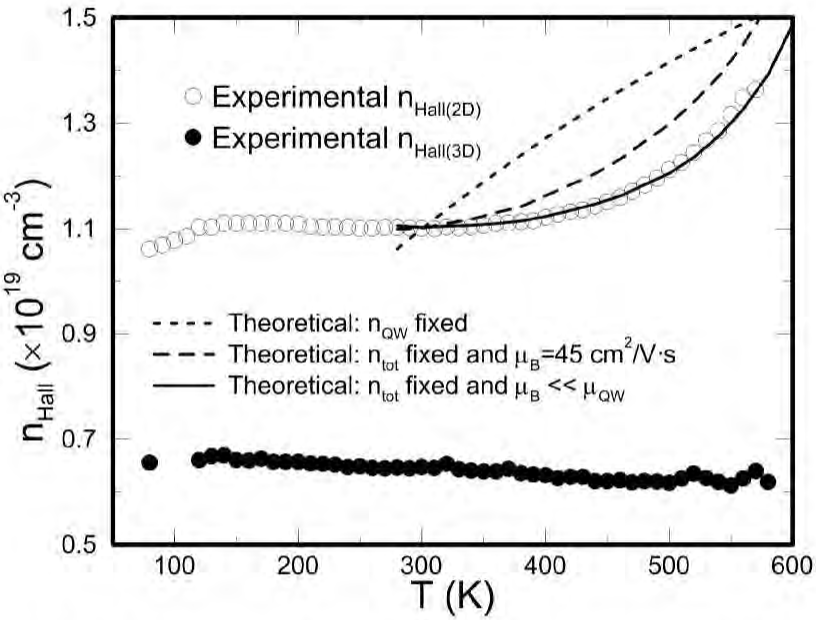

Figure 2-11: Hall carrier concentration as a function of temperature T for a (111) oriented n-type PbTe MQW sample (open circles) and an MBE grown n-type bulk PbTe sample (closed circles). The results for three different model calculations are also shown in the figure; short-dashed line : results assuming $n_{\rm QW}$ is fixed at 6.9×10^{18} cm^{-3}; solid line : results assuming $n_{\rm tot}$ is fixed at 1.15×10^{19} cm^{-3} and $\mu_{\rm B} = 0$ cm^2/V·s; long-dashed line : results assuming $n_{\rm tot}$ is fixed at 1.12×10^{19} cm^{-3} and $\mu_{\rm B} = 45$ cm^2/V·s, where $\mu_{\rm B}$ is the carrier mobility for the barrier layers. Calculations are made assuming $m^*_\Sigma = 2.0\,m$, where m^*_Σ is the density-of-state mass for the Σ valence band. See text for the other assumptions used in these calculations.

2.4.1 Hall carrier concentration

The Hall carrier concentrations for both the bulk and MQW samples mentioned above are plotted as a function of temperature in Fig. 2-11. These quantities are denoted by $n_{\rm Hall(3D)}$ and $n_{\rm Hall(2D)}$, respectively, hereafter. In the experiment, the Hall voltage and the electrical conductivity were measured along the quantum well planes, while the magnetic field (0.35 T) was applied perpendicular to the plane for the Hall coefficient measurement ($\omega_c\tau \ll 1$). Our formulation for $n_{\rm Hall}$ derived in the previous section assumes the low field (high temperature) limit. Choosing the criterion $\omega_c\tau < 0.1$ for the low field limit, our formulation is valid only above 280 K for the MQW sample. Thus our discussion for the modeling of $n_{\rm Hall(2D)}$ is restricted to temperatures above 280 K.

In Fig. 2-11, we find that $n_{\rm Hall(3D)}$ (closed circles) is almost insensitive to tempera-

ture over the measured temperature range. This is a typical behavior for a degenerate semiconductor, where no impurity levels exist below the conduction-band edge [24]. Since bulk n-type PbTe is a single-band material, the interpretation of the experimental data is straightforward. The experimental results suggest no freezing out of the carriers at low temperatures (down to 80 K) and a negligible density of thermally-excited carriers across the band gap, even at high temperatures (up to 580 K). Thus the actual concentration of the conduction carriers n_{3D} is determined to be 6.5×10^{18} cm^{-3} in this sample and n_{3D} is constant as a function of temperature in the range 80-580 K.

For the 2D MQW sample T-225, we find that, although $n_{Hall(2D)}$ is almost constant below room temperature, it increases rapidly with temperature above 450 K, reaching $n_{Hall(2D)} = 1.4 \times 10^{19}$ cm^{-3} at 580 K. Intuitively, this behavior may be interpreted as the increasing occupation of n_{obliq} relative to that of n_{longt} as the temperature is increased, assuming that the total concentration of the electrons bound to the quantum wells $n_{QW} = n_{longt} + n_{obliq}$ is conserved, since the value for the apparent $n_{Hall(2D)}$ increases with increasing occupation of n_{obliq} as shown in Eq. 2.29. However, it turns out that this model doesn't explain the observed behavior for $n_{Hall(2D)}$ properly, as shown by the short-dashed line in Fig. 2-11 for $n_{QW} = 6.9 \times 10^{18}$ cm^{-3}.

The successful modeling of $n_{Hall(2D)}$ as a function of temperature is achieved when the conservation of all the carriers n_{tot} in the superlattice is considered,

$$n_{tot} \equiv n_{QW} - p_{QW} + (n_B - p_B)\frac{d_B}{d_W}, \tag{2.32}$$

where p_{QW} is the concentration of holes bound to the quantum wells in the valence band, and n_B and p_B are electron and hole concentrations for the barrier layer, respectively. The multiplicative factor (d_B/d_W) for n_B and p_B is needed in Eq. 2.32, since n_B and p_B refer to the carrier densities (in cm^{-3}) for the barrier layers that are calculated using the sum of the d_B in the superlattice as the thickness of the sample, whereas n_{tot}, n_{QW} and p_{QW} refer to the carrier density (in cm^{-3}) calculated using the sum of the d_W as the thickness of the sample. Using the value for the band

offset given in the previous section ($\Delta E_c = 170$ meV at 300 K), p_{QW} is found to be negligible compared to n_{QW} up to 600 K, whereas $p_B \times (d_B/d_W)$ becomes important above ~450 K for sample T-225. $n_B \times (d_B/d_W)$ is found to be comparable to n_{QW} over the whole temperature range that was investigated. n_B is calculated considering a 3D parabolic energy band having the same density-of-states effective mass as bulk PbTe for simplicity. The band edge effective masses for $Pb_{1-x}Eu_xTe$ found from the parameters used for the EFA calculation [29] and those determined by the cyclotron resonance experiments [31] are similar to the bulk effective masses for PbTe that are used in the present study [28] (see §2.2.3).

As we mentioned in §2.2, we don't have sufficient knowledge about the valence band structure for $Pb_{1-x}Eu_xTe$ alloys at high temperature ($T > 450$ K), not to mention the valence band structure of PbTe/$Pb_{1-x}Eu_xTe$ superlattices, to make a detailed calculation of the carrier density above 450 K. Therefore, we make a naive guess here. It is known for bulk PbTe that the Σ valence band crosses the L valence band around 450 K, leading to a temperature independent energy gap [24]. Let's also assume that the Σ band of $Pb_{1-x}Eu_xTe$ alloys has the same feature, and that the quantum wells at the Σ-point in the Brillouin zone are not formed due to the insufficient valence band offset. Instead, we allow some freedom of adjusting the value of the 3D density-of-states mass for the Σ band for the whole PbTe/$Pb_{1-x}Eu_xTe$ superlattice to fit the experimental data, and then we compare the density-of-states mass obtained from the fitting with the literature value for the density-of-states mass of the Σ band for bulk PbTe. Study of the thermoelectric properties of p-type PbTe MQWs may shed light on the temperature of the crossing of the Σ and L valence bands for the PbTe/$Pb_{1-x}Eu_xTe$ superlattices [39].

For the reason stated above, we assume the relative position of the Σ band edge for $Pb_{1-x}Eu_xTe$ is the same as that for PbTe in the present work. We also assume a parabolic energy band for the Σ-valleys, and use the density-of-states mass for these valleys (m^*_Σ) as a fitting parameter. The best fit to the experimental results is obtained for $m^*_\Sigma = 2.0\ m$, as shown by the solid curve in Fig. 2-11. This m^*_Σ value for our superlattice sample is a little higher than the previously reported values for

m^*_Σ for bulk PbTe ($m^*_\Sigma \approx 1.0$–$1.4\ m$).

In the above modeling procedure, we assumed that the carrier mobilities for the barrier layers are negligible. The successful modeling of $n_{\mathrm{Hall(2D)}}$ with this assumption suggests that this is indeed the case (see the solid curve in Fig. 2-11). This result, however, is somewhat contradictory to the fact that a MBE-grown bulk $Pb_{1-x}Eu_xTe$ ($x \approx 0.073$) film *has* a mobility (denoted by μ_B) 45 $cm^2/V{\cdot}s$ [15]. However, the results of the theoretical modeling using $\mu_B = 45\ cm^2/V{\cdot}s$ do not fit the experimental results even in the vicinity of 300 K, which is the temperature at which μ_B was determined in Ref. [15], as shown by the long-dashed line in Fig. 2-11. This discrepancy is possibly due to the different electronic state for the $Pb_{1-x}Eu_xTe$ layers in MQWs than for bulk $Pb_{1-x}Eu_xTe$, caused by a lack of the local charge neutrality in the barrier layers (i.e., due to the increased ionized impurity scattering, for example).

One may wonder why the thermal excitation across the band gap is important for the MQW sample but not important for bulk PbTe. This is due to the difference in the position of chemical potentials in these two kinds of samples. According to our model, the chemical potential for the bulk sample lies 82 meV *above* the conduction band edge at 600 K, whereas the chemical potential for the MQW sample lies 70 meV *below* the longitudinal subband edge (which corresponds to 22 meV below the conduction band edge in the band diagram for bulk PbTe). Since, at 600 K, the highest valence band is the Σ band for both bulk and MQW samples, this difference in the chemical potential is caused by the large difference in the electronic density of states near the conduction (sub)band edge between the bulk and MQW samples. The larger the density of states at the conduction band edge is, the lower the position of chemical potential is in order to keep the carrier concentration at a given value. The lower the chemical potential is, the more the thermal excitation of carriers occurs, due to the large density-of-states mass for the Σ valence band.

2.4.2 Carrier mobility

Plotted in Fig. 2-12 are results for the Hall carrier mobility μ_{Hall} as a function of temperature for the MQW sample (open circles) as well as for the MBE grown bulk

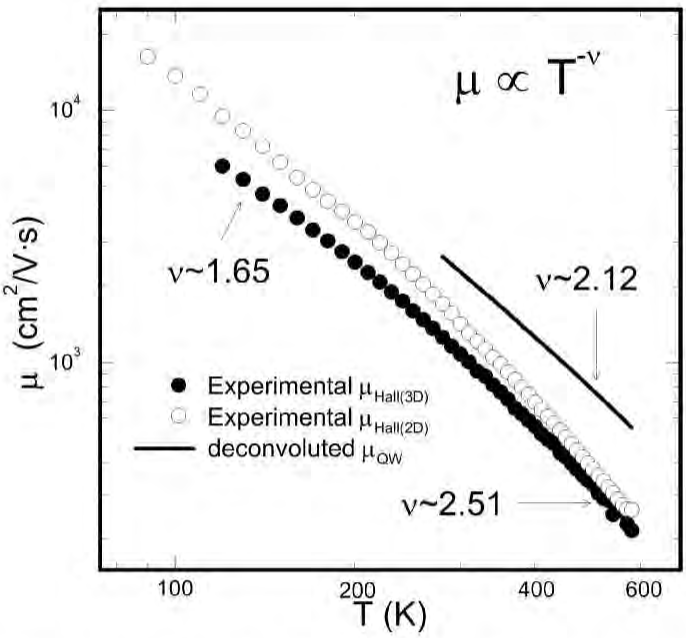

Figure 2-12: Hall and actual carrier mobilities as a function of temperature T for the (111) oriented n-type PbTe MQW (T-225) and a similarly grown bulk PbTe sample. The closed and open circles respectively denote the Hall carrier mobilities for the bulk sample and the Hall carrier mobilities for the MQW sample. The deconvolved actual mobilities for the MQW sample discussed in the text is shown by the solid curve. Note that the Hall mobilities for the bulk sample should be very close to the actual carrier mobilities as discussed in the text.

PbTe sample (closed circles) discussed in the previous subsection. For the bulk sample, $\mu_{\rm Hall}$ is very close to the actual mobility μ, so that it is not necessary to make further corrections to $\mu_{\rm Hall}$ to deduce the actual μ. For the MQW sample, $\mu_{\rm Hall}$ is not equal to $\mu_{\rm W}$, where $\mu_{\rm W}$ is the actual carrier mobility for the quantum wells. Here, we estimate $\mu_{\rm W}$ via the relation $\mu_{\rm W} = \sigma/en_{\rm QW}$, where $n_{\rm QW}$ is obtained from the theoretical modeling of $n_{\rm Hall}$ shown in the previous subsection (see the solid line in Fig. 2-11).

The actual mobilities for the bulk and MQW samples are found to obey the following general formula [24],

$$\mu \propto T^{-\nu}, \tag{2.33}$$

where ν depends weakly on temperature. For the bulk sample, ν is found to increase with temperature. Starting from $\nu = 1.65$ at low temperature (~100 K), ν reaches

2.51 at high temperature (> 300 K), which is consistent with the previously observed results for PbTe [24]. It is known that the longitudinal acoustic phonon deformation potential (LADP) scattering gives $\nu = 1.5$ in the limit of non-degenerate statistics. The generally observed result for bulk PbTe, $\nu = 2.5$, is believed to be the result of the combination of the following factors [26, 27] : (1) LADP scattering of the conduction carriers, (2) polar optical phonon scattering of the conduction carriers, and (3) the temperature dependence of the effective mass. However, the theoretical modeling considering all the above factors explicitly didn't reproduce the correct $\nu = 2.5$ dependence [40]. Therefore, we conclude that the correct modeling of the temperature dependence of the mobility for bulk PbTe would require knowledge of temperature dependence of the overlap integral for the lattice part of the Bloch function and a more exact treatment of the optical phonon frequency ω_0 including the charge screening effect on the reduction of the value for ω_0 [41]. For the MQW sample, we find $\mu_W \sim T^{-2.1}$ above 280 K. This value for ν ($\nu \approx 2.1$) is a little lower than that for the bulk sample ($\nu \approx 2.5$), implying somewhat different scattering mechanisms between the 3D and 2D systems. Generally, the energy dependence of the relaxation time τ is closely related to the density of states (DOS) for the charged carrier as a function of energy. For example, the $\tau \sim E^{-1/2}$ dependence for the LADP scattering of the carriers comes from the $E^{1/2}$ dependence of the DOS function for a 3D parabolic band. Since the electronic DOS is constant with energy for a 2D parabolic band, a model calculation of τ including only the LADP scattering mechanism in a 2D electron gas should also be constant with energy for a parabolic dispersion relation. Another reason for the different values in ν between the 3D and 2D transport is that interface scattering at the well-barrier boundary interface may play some role for carrier scattering in 2D MQW samples.

It is seen that the actual carrier mobility for the MQW sample is enhanced over that for the bulk sample, consistent with the quantum confinement of the carriers and the use of modulation doping. The ratio of μ_W to the bulk mobility μ is found to be about 2 at 300 K, and this ratio increases slightly with temperature in the range 280-580 K. Since our formulation for n_{Hall} breaks down below 280 K, values

for μ_W are not calculated below 280 K. However, a simple extrapolation of μ_W to lower temperatures implies that μ_W is higher than the bulk mobility μ even at low temperatures (down to ~100 K).

We find that the carrier mobility (1170 $cm^2/V{\cdot}s$ at 300 K) for our MBE-grown bulk sample is somewhat lower than the generally known mobility for bulk PbTe with a similar doping level (1500 $cm^2/V{\cdot}s$ at 300 K for $n_{3D} \sim 10^{19}$ cm^{-3}) [28]. The observed lower mobility for our MBE-grown sample is due to some extrinsic factors such as the lattice imperfections caused by the strain effect that is typically found in the MBE-grown films. However, it is worth noting that: (1) the Hall mobility (μ_{Hall}) of our MQW sample (1420 $cm^2/V{\cdot}s$) is found to be higher than the Hall mobility for the similarly grown and similarly doped bulk PbTe sample (1170 $cm^2/V{\cdot}s$) and (2) the actual carrier mobility μ_W deduced for our MQW sample (2180-2350 $cm^2/V{\cdot}s$) turns out to be even higher than the values of mobilities generally known for high-quality bulk PbTe (1500-1700 $cm^2/V{\cdot}s$) at 300 K. More detailed studies have to be carried out in the future to reveal the exact mechanism for the observed enhancement of μ_W in PbTe MQWs.

2.4.3 Seebeck coefficient

The measured Seebeck coefficient $S(T)$ is also plotted as a function of temperature in Fig. 2-13, together with the results of our theoretical models. The theoretical S above 280 K was calculated for $n_{tot} = 1.15 \times 10^{19}$ cm^{-3}, assuming the model explained in §2.4.1, including the 3D parabolic bands which take care of n_B and p_B. The theoretical S below 280 K was calculated for a constant n_{QW} at 6.9×10^{18} cm^{-3}, which is the estimated density of carriers bound to the quantum well at 300 K. It turned out that the thermal excitation of carriers across the band gap has a negligible effect on $S(T)$ up to 400 K. Although the actual n_{QW} may change as a function of temperature below 280 K, the effect of a variation of n_{QW} on $S(T)$ is found to be minor at least for n_{QW} up to $\sim 1.1 \times 10^{19}$ cm^{-3}, which is the value for n_{tot} that we can assume as the upper bound for n_{QW} at low temperatures (see §2.4.1).

In Fig. 2-13 we find that the experimental Seebeck coefficient increases almost

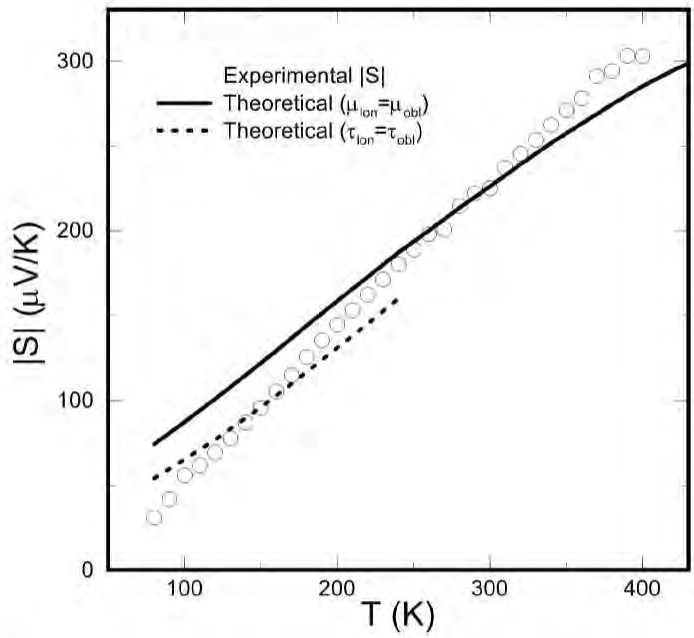

Figure 2-13: Absolute value of the Seebeck coefficient for the n-type PbTe MQW sample (T-225) as a function of temperature (open circles). The solid line shows the theoretical results assuming $\mu_{\rm longt} = \mu_{\rm obliq}$, whereas the dashed line shows the results assuming $\tau_{\rm longt} = \tau_{\rm obliq}$. See text for the other assumptions used in the calculation of S.

linearly with temperature, whereas our theoretical results assuming $\mu_{\rm longt} = \mu_{\rm obliq}$ have a somewhat weaker temperature dependence. Our analysis of the observed experimental results is divided into three temperature regimes.

First, near room temperature (280 K $< T <$ 350 K), we obtain excellent agreement between theory and experiment. Not only the magnitude of the Seebeck coefficient but also the observed slope (dS/dT) show good agreement between theory and experiment. Thus, we find that the condition $\mu_{\rm longt} = \mu_{\rm obliq}$ is consistent with experimental results in this temperature range.

Second, at low temperatures ($<$ 280 K), our model overestimates the Seebeck coefficient. We believe that the main reason for this discrepancy is that the condition $\mu_{\rm longt} = \mu_{\rm obliq}$ is no longer valid at low temperatures. For example, at 100 K ($k_BT =$ 8.6 meV), we find that the energy difference between the longitudinal- and oblique-subband edges ($\Delta E_{\rm longt-obliq}$) is 94 meV. In this situation, since the Fermi energy for sample T-225 lies near the oblique subband edge according to our model [see Fig. 2-15(c)], the Seebeck coefficient for this sample should be dominated by the contribution

from the longitudinal subband only. We find that the condition $\tau_{\rm longt} = \tau_{\rm obliq}$ (instead of $\mu_{\rm longt} = \mu_{\rm obliq}$) is more consistent with the experimental results at low temperatures ($\sim$150 K), as shown by the dashed line in Fig. 2-13. It should be noted that there are no *a priori* reasons that $\tau_{\rm longt}/\tau_{\rm obliq}$ should be constant as a function of temperature.

In the third regime of temperature in our analysis ($>$ 350 K), our model underestimates the values of the Seebeck coefficient. One reason for this discrepancy would be due to the non-parabolic energy bands in actual PbTe samples. The increased density of electronic states for the non-parabolic energy bands at higher energies absorbs a large number of conduction electrons, pushing the chemical potential lower in energy to keep the total number of carriers ($n_{\rm tot}$) unchanged. The lowered chemical potential increases the magnitude of S via Eq. 2.19. In Chapter 3, we will discuss more detailed mechanisms of the observed enhancement in S for the PbTe/$Pb_{1-x}Eu_xTe$ MQWs including the non-parabolic energy bands generally needed to describe the energy dispersion relations for PbTe, and some specific scattering mechanisms such as longitudinal acoustic phonon deformation potential scattering and polar optical phonon scattering. It turns out that the scattering of electrons due to the polar optical phonons has some role in enhancing the values of S at high temperatures as we discuss in Chapter 3.

2.4.4 $Z_{\rm 2D}T$

The dimensionless thermoelectric figure of merit within the quantum well $Z_{\rm 2D}T$ is determined experimentally using the measured S and σ, as shown in Fig. 2-14. Also shown in the figure by the dashed line is the ZT for the MBE-grown bulk sample (T-168) discussed in the previous sections, denoted by ZT(bulk).

In calculating $Z_{\rm 2D}T$, κ_e is estimated through the Wiedemann-Franz law. The Lorenz number L_0 at each temperature is determined via Eqs. 2.24 and 2.25, using ζ^* obtained for the fixed $n_{\rm tot}$ at 1.15×10^{19} cm^{-3} above 280 K, and for the fixed $n_{\rm QW}$ at 6.9×10^{18} cm^{-3} below 280 K. In this calculation, the ratio $\mu_{\rm obliq}/\mu_{\rm longt}$ is changed linearly with temperature from 0.55 (below 150 K, corresponding to the condition $\tau_{\rm longt} = \tau_{\rm obliq}$) to 1 (above 280 K, corresponding to the condition $\mu_{\rm longt} = \mu_{\rm obliq}$).

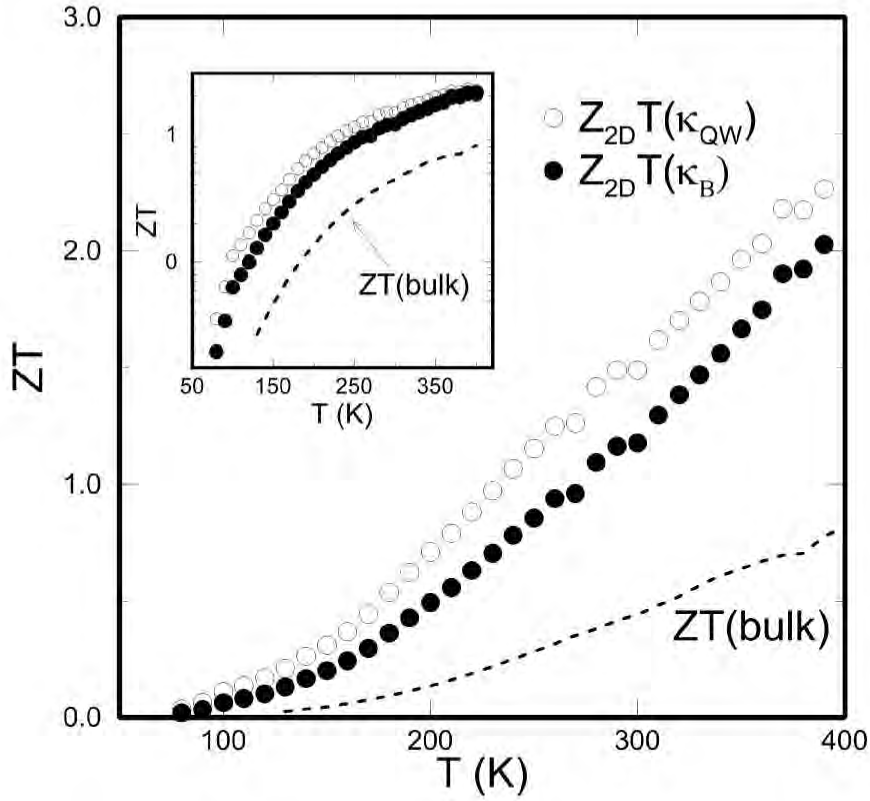

Figure 2-14: Estimated $Z_{2D}T$ using the experimental values for S and σ for the n-type PbTe MQW sample (T-225) as a function of temperature. Two different estimations are made on the lattice thermal conductivity (κ_{ph}) for the quantum well: (1) $\kappa_{ph} = \kappa_B$, where κ_B is the bulk value for the lattice thermal conductivity, is assumed (closed circles) and (2) $\kappa_{ph} = \kappa_{QW}$, where κ_{QW} is given by Eq. 2.34, is assumed (open circles). The dashed line represents the experimentally determined ZTs for the MBE-grown n-type bulk PbTe for comparison. The inset shows the semi-log plot of the same data.

Two different choices are made for the lattice thermal conductivity $\kappa_{\rm ph}$. First, the measured bulk values ($\kappa_{\rm B}$) found in the literature [42] are used. The resultant $Z_{\rm 2D}T$ for this choice of $\kappa_{\rm ph}$ is denoted by $Z_{\rm 2D}T(\kappa_{\rm B})$. Second, we estimate $\kappa_{\rm ph}$ within the quantum well assuming the phonon mean free path ℓ is limited by the quantum well thickness $d_{\rm W}$ using the following equation [11, 12, 14, 17],

$$\kappa_{\rm ph} = \frac{1}{3} C_{\rm v} v \ell \approx \frac{1}{3} C_{\rm v} v d_{\rm W} \equiv \kappa_{\rm QW}, \tag{2.34}$$

where $C_{\rm v}$ is the constant volume specific heat and v is the sound velocity. $Z_{\rm 2D}T$ as determined with this second assumption is denoted by $Z_{\rm 2D}T(\kappa_{\rm QW})$. For bulk PbTe at 300 K, we find the following values in the literature [33, 42] : measured thermal conductivity for undoped bulk PbTe $\kappa = 19.6$ mW/cm·K, constant pressure specific heat $C_p = 1.23$ J/cm^3·K, and the group velocity for the transverse mode of the acoustic phonon $v_T = 1.6 \times 10^5$ cm/s.[†] Using these values for $\kappa_{\rm ph}$, $C_{\rm v}$, and v in Eq. 2.34, respectively, we obtain $\ell = 30$ Å. Since ℓ typically varies as T^{-1} and $d_{\rm W} = 19$ Å for our sample T-225, we can expect a reduction of $\kappa_{\rm ph}$ from the bulk value up to 400 K if the assumption that the value of ℓ is limited by the value of $d_{\rm W}$ is valid.

In Fig. 2-14, we find that $Z_{\rm 2D}T$ increases almost linearly with temperature above 200 K, exceeding $Z_{\rm 2D}T = 2$ at 400 K. Simple extrapolation $Z_{\rm 2D}T$ to higher temperatures implies that even higher $Z_{\rm 2D}T$s may be possible above 400 K. ZTs within

[†]Using the value of v_T for the substitution of v in Eq. 2.34 contains some subtle problem as stated below. Generally, we have distinct values for group velocity for each longitudinal and transverse polarizations of the pertinent acoustic phonon mode. The lattice contribution to the specific heat $C_{\rm v}$ also has contributions from each polarization of the acoustic phonon mode. Therefore, the equation for $\kappa_{\rm ph}$ should be more rigorously,

$$\kappa_{\rm ph} = \frac{1}{3} \sum_i C_{\rm v}^i v_i \ell_i, \tag{2.35}$$

where $C_{\rm v}^i$ is the contribution to $C_{\rm v}$ from the ith polarization of the acoustic phonon ($C_{\rm v} = \sum_i C_{\rm v}^i$), and v_i and ℓ_i are the group velocity and phonon mean free path for the ith polarization of the pertinent acoustic phonon mode, respectively. The subtlety comes from the fact that there is no simple relation between ℓ_is for the different polarizations of the acoustic phonon. For this reason, we content ourselves with the simple treatment of $\kappa_{\rm ph}$ that is shown in this section, and look to more rigorous treatment in the future, where even the energy dependence of the ℓ_is could be incorporated into the model that predicts the values of $\kappa_{\rm ph}$.

the quantum well, as compared to those for the bulk, are enhanced by a factor of more than 2 over the whole measured temperature range (80-400 K), irrespective of the choice for $\kappa_{\rm ph}$. It is also noted that the difference between $Z_{\rm 2D}T$ and ZT(bulk), $\{Z_{\rm 2D}T - ZT({\rm bulk})\}$, increases with increasing temperature, whereas the ratio of $Z_{\rm 2D}T$ to ZT(bulk) decreases with increasing temperature (see the semi-log plot in the inset of Fig. 2-14). The effect of limiting ℓ by $d_{\rm W}$, as judged from the comparison between $Z_{\rm 2D}T(\kappa_{\rm QW})$ and $Z_{\rm 2D}T(\kappa_{\rm B})$, is found to be rather small due to the already small values for ℓ in bulk PbTe (comparable to the quantum well widths $d_{\rm W}$) at relatively high temperatures ($\ell \approx 45$ Å at $T = 200$ K).

It should be noted that a good measure for the actual device performance of the thermoelectric superlattices is the figure of merit for the whole superlattice $Z_{\rm 3D}T$. To estimate the optimum $Z_{\rm 3D}T$ in PbTe/$Pb_{1-x}Eu_xTe$ MQWs, quantitative studies of $\kappa_{\rm ph}$ for the whole superlattice sample are necessary. It is noted that there already exists well established theoretical models to describe $\kappa_{\rm ph}$ for the whole superlattice in the GaAs/AlAs system [43]. If a similar type of model is developed for PbTe/$Pb_{1-x}Eu_xTe$ MQWs, the integration of such a model with the currently studied power factor ($S^2\sigma$) should provide reliable estimates for $Z_{\rm 3D}T$.

For the reason mentioned above, most of the later chapters of this thesis are devoted to the investigation of $Z_{\rm 3D}T$. In Chapter 4, we will extend our theoretical models described in this chapter to calculate $Z_{\rm 3D}T$ of the GaAs/AlAs superlattice, where we will also propose the new concept of Carrier Pocket Engineering (CPE) to design superlattices with an enhanced value of $Z_{\rm 3D}T$. In Chapter 5, we will apply the concept of CPE to the Si/Ge superlattice and show that even larger values for $Z_{\rm 3D}T$ would be possible in Si/Ge superlattices than in GaAs/AlAs superlattices. In Chapter 7, we will see yet other systems of interest, namely PbTe-based quantum-dot superlattices, whose values of $Z_{\rm 3D}T$ are experimentally found to be enhanced relative to those for the corresponding bulk PbTe for given carrier concentrations, and the theoretical predictions of enhanced $Z_{\rm 3D}T$ in (001) oriented short period PbTe/EuTe superlattices and in (111) oriented Bi/(111)$Pb_{1-x}Eu_xTe$ superlattices.

2.5 Discussion

2.5.1 Optimum doping levels for (111) oriented PbTe MQWs

It is of interest to examine how close the doping level for T-225 is to the optimum doping level. Shown in Figs. 2-15(a)-(c) are $Z_{2D}T$ calculated as a function of ζ^* at 300, 200 and 100 K, respectively, together with the experimentally estimated $Z_{2D}T$s using $\kappa_{ph} = \kappa_B$. For theoretical calculations in Fig. 2-15, two assumptions are made for κ_{ph} ($\kappa_{ph} = \kappa_B$ and $\kappa_{ph} = \kappa_{QW}$). The magnitudes for μ_{longt} and μ_{obliq} are decided so that our model particularly developed for T-225 may predict the total mobility equal to μ_W deduced in the previous section, assuming: (1) $\mu_{longt} = \mu_{obliq}$ above 280 K, (2) $\tau_{longt} = \tau_{obliq}$ below 150 K, and (3) a linear temperature dependence for μ_{obliq}/μ_{longt} connecting the above two conditions between 150 K and 280 K, as described in §2.4.4 when calculating L_0 for T-225. Also shown in the figures are values of ζ^* for $n_{QW} = 6.9 \times 10^{18}$ cm^{-3} and $n_{QW} = 1.1 \times 10^{19}$ cm^{-3}, as well as the electronic density of states as a function of energy (right scale) to show the positions for the longitudinal- and oblique- subband edges. The actual n_{QW} for T-225 below 300 K is expected to be between the above two values of n_{QW} from the argument in the previous section, whereas, at 300 K, n_{QW} should be close to 6.9×10^{18} cm^{-3}, since it is at this temperature that the value of n_{QW} is most reliably determined by the experiments (see §2.4.1).

Figure 2-15(a) shows that the doping level for T-225 is almost optimized at 300 K. The figure also suggests that the maximum $Z_{2D}T(\kappa_{QW})$ would be higher than $Z_{2D}T(\kappa_B)$ by 16 %. Figure 2-15(b) shows that the doping level for T-225 is still close to the optimum level even at 200 K, suggesting that only incremental increases of $Z_{2D}T$ are possible by further adjusting the doping levels at this temperature. A more significant increase (49 %) in the value of $Z_{2D}T(\kappa_{QW})$ relative to the value of $Z_{2D}T(\kappa_B)$ is expected at 200 K than at 300 K, since the lower the temperature, the larger the value of ℓ (i.e., the effect of limiting the value of ℓ by the value of d_W is large). Figure 2-15(c) shows that there are two distinct values of ζ which give a local maximum for $Z_{2D}T$s at 100 K. We have investigated the temperature dependent behavior of these

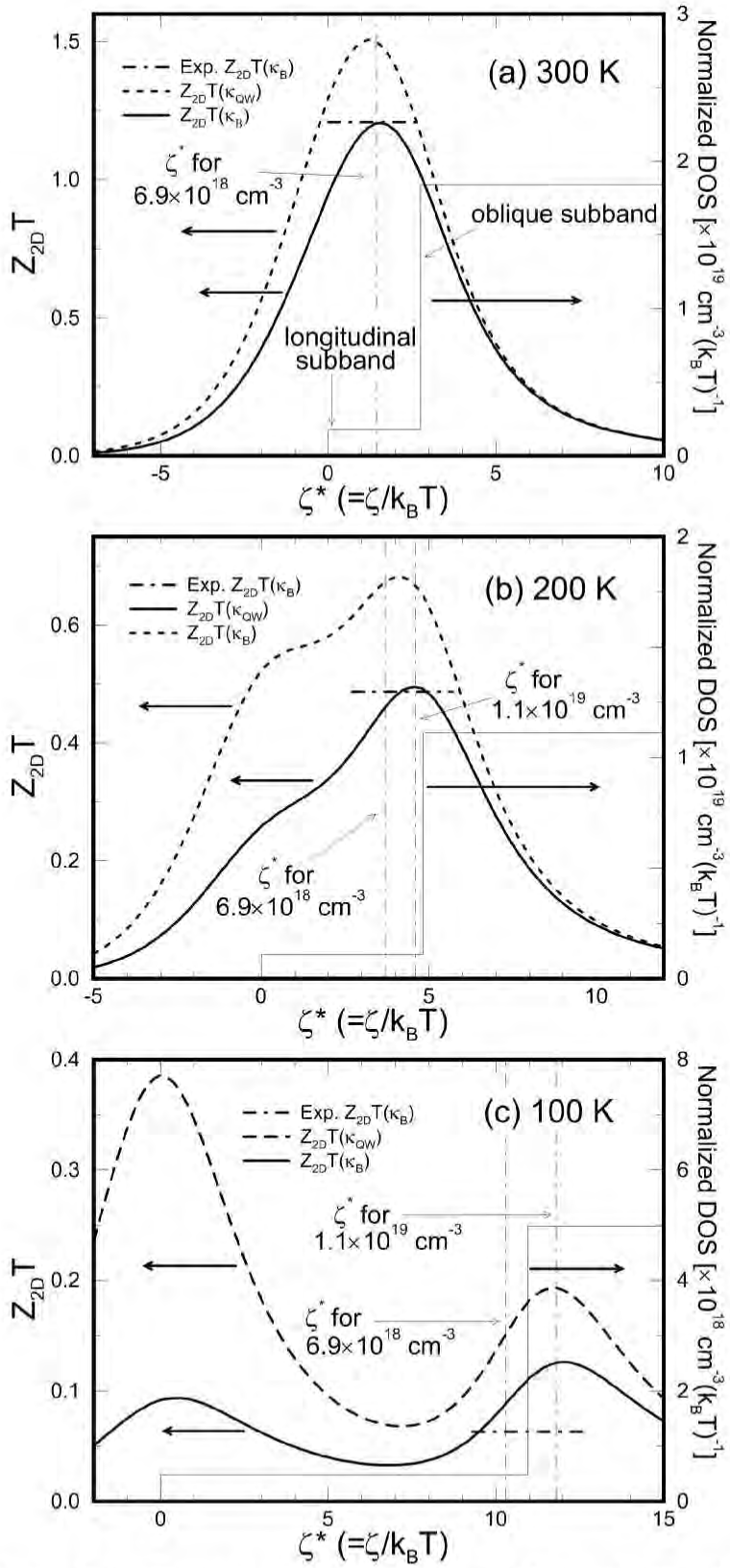

Figure 2-15: Calculated $Z_{2D}T$ as a function of the reduced chemical potential at 300 K (a), 200 K (b), and 100 K (c), for (111) oriented PbTe MQWs ($d_W = 20$ Å and $\Delta E_c \approx 170$ meV at 300 K). Shown by the solid line is $Z_{2D}T(\kappa_B)$ where $\kappa_{ph} = \kappa_B$ is assumed, whereas the results assuming $\kappa_{ph} = \kappa_{QW}$, $Z_{2D}T(\kappa_{QW})$, are plotted by the dashed line. The value for $Z_{2D}T(\kappa_B)$ obtained from the experimental S and σ at each temperature is also indicated by the horizontal dot-dashed line for comparison.

two peaks. For $Z_{2D}T(\kappa_B)$, we find that the second peak (near the oblique subband edge) is always higher than the first peak (near the longitudinal subband edge) down to 77 K, whereas for $Z_{2D}T(\kappa_{QW})$ the first peak exceeds the second peak below 180 K. Thus, if the reduction of κ_{ph} due to the interfacial scattering of phonons is sufficiently effective in PbTe MQWs, the carrier concentration that gives the optimum value of $Z_{2D}T$ at 100 K ($Z_{2D}T \sim 0.4$) should be relatively low ($\sim 5\times10^{17}$ cm^{-3}).

2.5.2 Expected properties for (001) oriented PbTe MQWs

It is of great interest to explore the optimum performance of PbTe MQWs allowing freedom in the choice of the growth direction of the MQWs as well as freedom in changing the doping levels. The (001) oriented MQWs are chosen in this subsection as a prototype for a single-subband 2D system which is expected be better in thermoelectric properties than multiple-subband systems. Recently, such (001) oriented lead chalcogenides MQW samples have been grown on (001) oriented KCl substrates [44]. Large enhancements in Seebeck coefficient and electrical conductivity are indeed observed in (001) oriented PbS/EuS MQWs relative to those for the similarly grown thick layer of PbS [44], which is consistent with our prediction in this subsection. Other examples for a single-subband 2D system that are of more practical interest include Bi quantum wells grown along the trigonal direction [37]. In Chapter 7, we will discuss the prediction of enhanced $Z_{3D}T$s (thermoelectric figure of merit for the whole superlattice) in Bi/(111)$Pb_{1-x}Eu_xTe$ superlattices and (001) oriented PbTe/$Pb_{1-x}Eu_xTe$ short period superlattices.

In the present subsection, the quantum well thickness (d_W) is chosen to be 20 Å for the calculation to compare the results with those for the (111) oriented MQWs. The values for μ_W obtained for the (111) oriented MQWs are used without any further correction for the (001) oriented MQWs above 280 K, and below 280 K extrapolated values for μ_W are used, assuming that μ_W obeys the same power law of temperature as above 280 K (see Eq. 2.33).

Plotted in Fig. 2-16 is $Z_{2D}T$ as a function of ζ^* for the (001) oriented MQWs at 300 K both for $\kappa_{ph} = \kappa_B$ and for $\kappa_{ph} = \kappa_{QW}$. Also shown in the figure are the

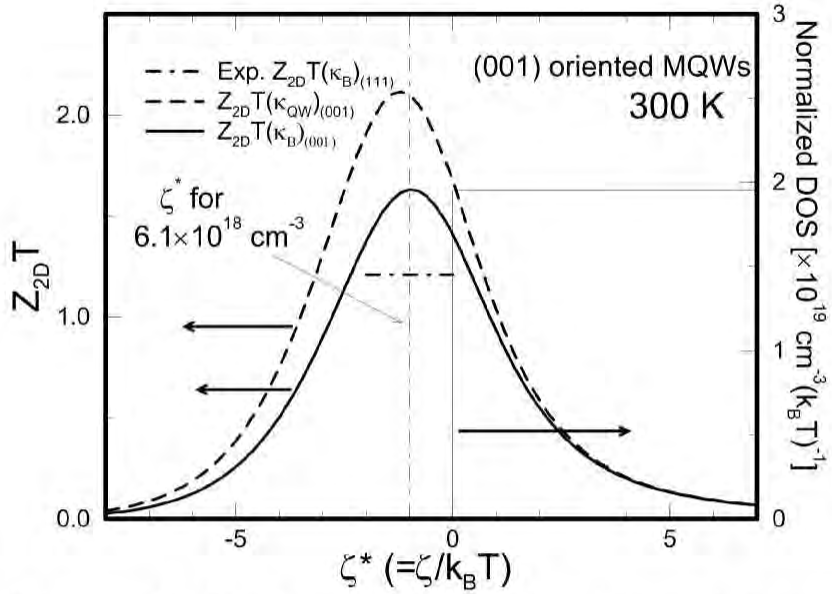

Figure 2-16: Calculated $Z_{2D}T$ as a function of the reduced chemical potential for (001) oriented PbTe MQWs at 300 K (d_W = 20 Å). Shown by the solid line is $Z_{2D}T(\kappa_B)$ where $\kappa_{ph} = \kappa_B$ is assumed, whereas the results assuming $\kappa_{ph} = \kappa_{QW}$, $Z_{2D}T(\kappa_{QW})$, are plotted by the dashed line. The value for $Z_{2D}T(\kappa_B)$ obtained from the experimental S and σ for the (111) PbTe MQWs at 300 K is also shown by the horizontal dot-dashed line for comparison.

optimum doping level for $Z_{2D}T(\kappa_B)$, the electronic density of states as a function of ζ^* (right scale), and the value for the optimum $Z_{2D}T(\kappa_B)$ in (111) oriented MQWs for comparison. We find in Fig. 2-16 that the optimum $Z_{2D}T(\kappa_B)$ for the (001) oriented MQWs [denoted by $Z_{2D}T(\kappa_B)_{(001)}$] is about 36 % higher than that for the (111) oriented MQWs [denoted by $Z_{2D}T(\kappa_B)_{(111)}$] at 300 K. [We, hereafter, denote the quantities for the (001) and (111) oriented MQWs by the subscripts '(001)' and '(111)', respectively.] If ℓ is limited by d_W at this temperature, the optimum $Z_{2D}T(\kappa_{QW})_{(001)}$ is further increased relatively to $Z_{2D}T(\kappa_B)_{(111)}$ by about 30 %, the absolute value of $Z_{2D}T(\kappa_{QW})_{(001)}$ exceeding 2.

Some qualitative features found at 300 K are also observed at lower temperatures. For example, the optimum ζ^* is always found to lie near the conduction subband edge, which is typical of single-subband MQWs. A large enhancement of $Z_{2D}T$ in (001) oriented MQWs relative to $Z_{2D}T_{(111)}$ is found at low temperatures irrespective of the choice for κ_{ph} (see Fig. 2-17). In Fig. 2-17, we plot together the temperature dependences of the theoretical $Z_{2D}T$ at the optimum doping levels for both the (111)

and (001) oriented MQWs as well as the experimental $Z_{2D}T_{(111)}$ for sample T-225. We find that $Z_{2D}T_{(001)}/Z_{2D}T_{(111)}$ is always greater than 1 and increases as T is decreased. The effect of ℓ being limited by d_W is seen by comparing $Z_{2D}T(\kappa_{QW})$ to $Z_{2D}T(\kappa_B)$. We find larger absolute increases in $Z_{2D}T$ by this effect in the (001) oriented MQWs than in the (111) MQWs. To conclude our discussions here: (1) for a given value of d_W, (001) oriented PbTe MQWs always have larger values for $Z_{2D}T$ at the optimum carrier concentration than (111) oriented PbTe MQWs, and (2) the advantage of making (001) oriented PbTe MQWs would be even greater as the value of κ_{ph} is reduced from the bulk value κ_B, for example, due to the increased interface scattering of phonons.

In addition to the above conclusions for the expected properties for the (001) oriented PbTe MQWs, we can see, in Fig. 2-17, the various features that are discussed in the preceding sections. To summarize: (1) the doping level for the sample T-225 seems already optimized for $Z_{2D}T(\kappa_B)$ near and below room temperature; (2) the theoretically optimum $Z_{2D}T(\kappa_{QW})_{(111)}$ deviates from the experimental $Z_{2D}T(\kappa_{QW})_{(111)}$ for sample T-225 below 180 K because of the transition of the value of ζ for the optimum $Z_{2D}T(\kappa_{QW})_{(111)}$ from the vicinity of the oblique subband edge to the vicinity of the longitudinal subband edge; (3) large enhancements in $Z_{2D}T$ relative to the values of $Z_{2D}T_{(111)}$ are expected by making (001) oriented PbTe MQWs; and (4) the effect of ℓ being limited by the value of d_W on increasing $Z_{2D}T$ is larger for the (001) oriented MQWs than for the (111) oriented MQWs.

2.6 Conclusions

In this chapter, the temperature dependences of the dimensionless thermoelectric figure of merit $Z_{2D}T$ and the related transport coefficients are investigated experimentally as well as theoretically using the constant relaxation time approximation for n-type PbTe MQW structures up to 580 K.

The conversion of the low field Hall carrier concentration to the actual carrier concentration is found to be essential in explaining the observed experimental data

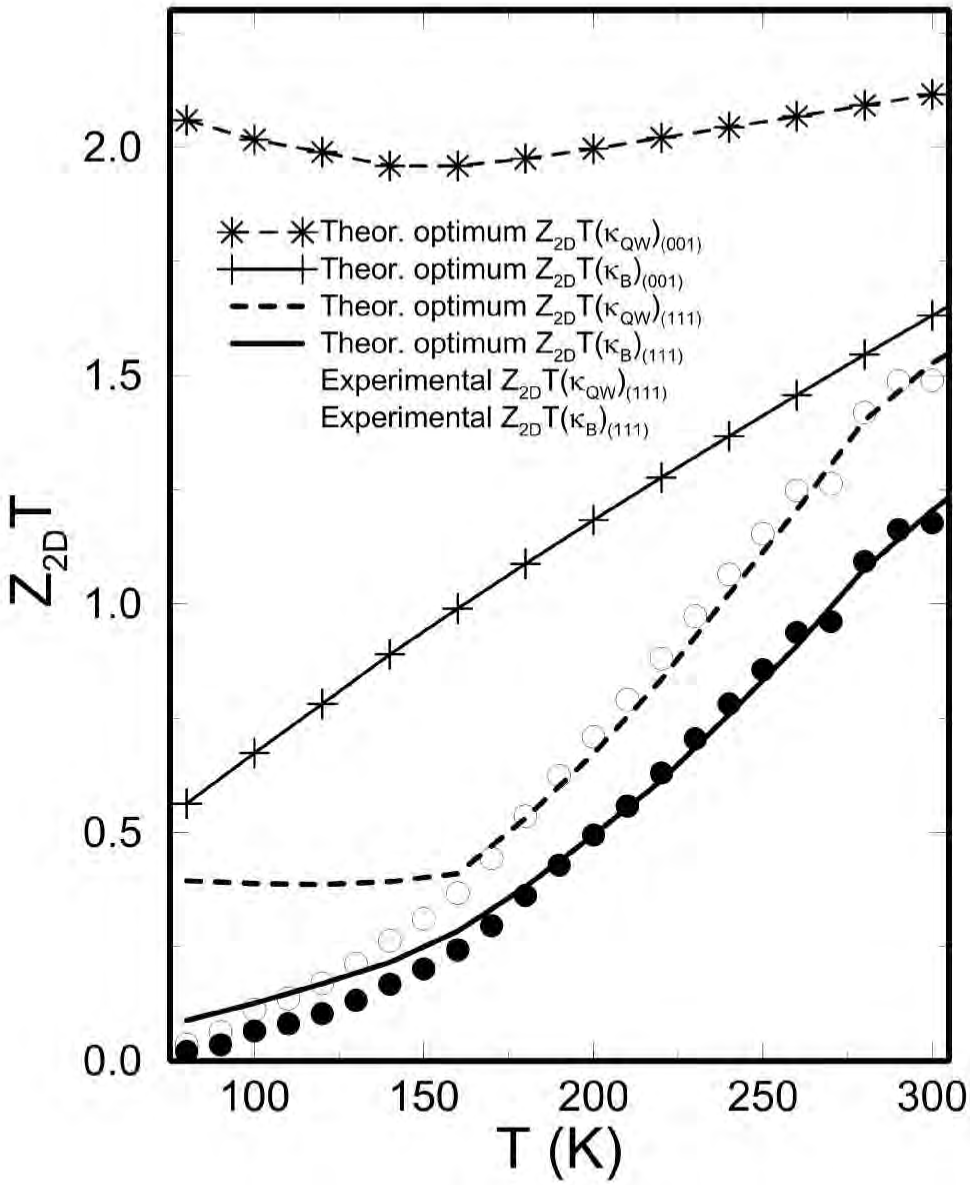

Figure 2-17: Calculated optimum $Z_{2D}T$s as a function of temperature for (111) oriented PbTe MQWs and (001) oriented MQWs with $d_W = 20$Å. The values for $Z_{2D}T$s are calculated both for $\kappa_{ph} = \kappa_B$ and for $\kappa_{ph} = \kappa_{QW}$ (see text). Also shown in the figure are the experimentally determined $Z_{2D}T$s assuming $\kappa_{ph} = \kappa_B$ (closed circles) and assuming $\kappa_{ph} = \kappa_{QW}$ (open circles) for comparison.

as well as to assess the actual carrier mobility in 2D MQW systems. The actual carrier mobilities of the (111) oriented PbTe MQWs are found to be much larger than those of the similarly grown bulk PbTe films, consistent with the quantum confinement of the conduction carriers and the use of modulation doping.

Various thermoelectric properties are investigated as a function of temperature for the (111) oriented PbTe MQWs. It is found that the inclusion of a 3D electronic density of states for the barrier layer as a charge reservoir for the quantum well is necessary for the successful modeling of $n_{\mathrm{Hall(2D)}}$. For the Seebeck coefficient, not only the absolute values for S, but also their slopes (dS/dT) are successfully modeled near room temperature assuming the condition $\mu_{\mathrm{longt}} \approx \mu_{\mathrm{obliq}}$. The condition $\tau_{\mathrm{longt}} \approx \tau_{\mathrm{obliq}}$ is found to be consistent with the measured S around 150 K. A smooth transition between these conditions can be assumed for the successful modeling of S from low (~100 K) to high (~350 K) temperatures. Detailed investigations of the effects of the non-parabolic energy bands as well as the effects of the specific scattering mechanisms to increase S have to be carried out to quantify the experimentally observed S above 350 K and below 200 K that are not in quantitative agreement with the theoretical models introduced in this chapter. The extension of our models, including the effects of specific scattering mechanisms to predict the enhanced themoelectric power S in (111) oriented n-type PbTe/PbEuTe MQWs, are carried out in the next chapter.

The model calculation was extended to predict the optimum thermoelectric properties of the (001) oriented MQWs. Two assumptions are made for the value of lattice thermal conductivity, i.e. $\kappa_{\mathrm{ph}} = \kappa_{\mathrm{B}}$ and $\kappa_{\mathrm{ph}} = \kappa_{\mathrm{QW}}$. The optimum $Z_{\mathrm{2D}}T$ for the (001) oriented MQWs is found to be always larger than that for the (111) oriented MQWs over the whole temperature range that is investigated, assuming that the carrier mobilities for the (001) oriented MQWs are equal to those for the (111) oriented MQWs. Our model predicts that the effect of limiting the value of phonon mean free path ℓ to the value of quantum well width d_{W} on increasing $Z_{\mathrm{2D}}T$ is larger for the (001) oriented quantum wells than for the (111) oriented quantum wells. Hence, the value for $\{Z_{\mathrm{2D}}T(\kappa_{\mathrm{QW}})_{(001)} - Z_{\mathrm{2D}}T(\kappa_{\mathrm{B}})_{(001)}\}$ is found to be always larger than that for $\{Z_{\mathrm{2D}}T(\kappa_{\mathrm{QW}})_{(111)} - Z_{\mathrm{2D}}T(\kappa_{\mathrm{B}})_{(111)}\}$ in the temperature range investigated (80 K $< T <$

340 K). Above 340 K, the experimental $Z_{2D}T_{(111)}$s are found to exceed the theoretical values for $Z_{2D}T_{(111)}$s, probably due to the effect of the non-parabolic energy band, which is not included in our model in this chapter (see §2.4.3).

The importance of investigating the figure of merit for the whole superlattice $Z_{3D}T$ needs more emphasis and will guide our work in the later chapters. More quantitative assessments of the prospects for enhanced $Z_{3D}T$ await : (1) improved models for the thermal conductivity for the whole superlattice, (2) the incorporation of band broadening effects due to overlapping wavefunctions between adjacent quantum wells, and (3) a more rigorous treatment for the relaxation time τ, including specific scattering mechanisms, which has been done in the next chapter for a 2D electron gas of isolated quantum wells as in PbTe MQWs. Concurrently, experimental effort is also needed to reduce the thickness of the barrier layers and to increase the potential barrier height in the barrier layers to increase the degree of quantum confinement of charged carriers. These experiments have to be carried out using single subband systems such as (001) oriented PbTe/$Pb_{1-x}Eu_xTe$ short period superlattices or trigonally oriented Bi/(111)$Pb_{1-x}Eu_xTe$ superlattices in order to obtain a large thermoelectric figure of merit for the whole superlattice, denoted by $Z_{3D}T$.

Chapter 3

Thermoelectric properties of n-type $PbTe/Pb_{1-x}Eu_xTe$ multiple quantum wells II — Solution of the Boltzmann equation including specific scattering mechanisms —

In this chapter, a detailed theoretical investigation is carried out to reveal the mechanism of the enhanced thermoelectric power S in (111) oriented n-type $PbTe/Pb_{1-x}Eu_xTe$ multiple-quantum-wells (MQWs) ($x \simeq 0.09$), that is discussed in the previous chapter. Our model in this chapter includes the following specific scattering mechanisms: longitudinal acoustic phonon deformation potential scattering and polar optical phonon scattering. The model treats the scattering of the two-dimensionally confined electrons in the quantum wells by the three-dimensional phonons. An enhancement in S, that is observed experimentally in the previous chapter, is now predicted theoretically, despite the lifting of the conduction band valley degeneracy, that would

decrease the magnitude of S [22]. Excellent agreement between the experimental and theoretical results has been obtained over a wide temperature range (80–400 K). In the low temperature regime ($\sim$100 K), the polar optical phonons are found to be more effective in scattering carriers in the oblique L-point valleys than in scattering carriers in the longitudinal L-point valley, making the resulting S somewhat suppressed in this temperature regime. In the high temperature regime ($\geq$300 K), the polar optical phonon scattering generally contributes to increasing S due to the particular shape of the distribution function associated with it. It is emphasized that our theoretical model requires virtually no fitting parameters. The excellent agreement between the theoretical and experimental results suggests the validity of our model for the enhanced thermoelectric figure of merit in two-dimensional structures and the reliability of the values of the parameters for the superlattice deduced from other independent measurements, such as Hall carrier concentrations and infrared absorption spectra to measure the values of the energy band gaps.

3.1 Introduction

There has been considerable interest in the thermoelectric properties of low-dimensional systems, such as two-dimensional quantum wells [14–18, 20–22, 37–39, 45–49], and one-dimensional quantum wires [12, 19, 50–52] since Hicks and Dresselhaus predicted that the thermoelectric figure of merit (ZT) for such low-dimensional systems should be substantially enhanced relative to the corresponding bulk materials as the size of the sample is reduced to the nm (or Å) range [12, 14]. This idea was first demonstrated experimentally by Harman *et al.* [15] and Hicks *et al.* [16] using MBE grown (111) oriented PbTe/$Pb_{1-x}Eu_xTe$ multiple-quantum-well (MQW) samples as we discussed in Chapter 2. The observed enhanced thermoelectric properties in this system was first interpreted in terms of the constant relaxation time approximation (CRTA), assuming various values for the ratio of the carrier mobilities between the longitudinal valley and the oblique valleys (see Chapter 2 and §3.4.1) [16, 38]. More recently, D. A. Broido and T. L. Reinecke calculated room temperature values of the

thermoelectric transport coefficients for the (111) oriented PbTe MQWs, including specific scattering mechanisms (longitudinal acoustic phonon deformation potential scattering and polar optical phonon scattering), but assuming a parabolic energy dispersion relation and using the approximation of isotropic constant energy surfaces. They pointed out that the Seebeck coefficient for the PbTe MQW samples should be largely suppressed due to the lifting of the valley degeneracy between the longitudinal and oblique valleys in (111) oriented PbTe MQW samples [22]. However, this latter point was inconsistent with the observed enhancement in the thermoelectric power in the PbTe/$Pb_{1-x}Eu_xTe$ MQW system grown by Harman *et al.* that was discussed in the previous chapter [15, 16]. The main discrepancy comes from the fact that some parameter values used in Broido's work (such as the barrier height for the PbTe quantum well) were not appropriate for describing the properties of the specific samples grown by Harman *et al.* [49]. Thus, it has not been possible to make a direct comparison between the theoretical results by Broido *et al.* [22] and the experimental results by Harman *et al.* [15] and Hicks *et al.* [16].

In the present chapter, we address the issue why the thermoelectric power in n-type (111) oriented PbTe/$Pb_{1-x}Eu_xTe$ MQWs is enhanced in spite of the lifting of the conduction band valley degeneracy in this system. Specifically, we perform a detailed theoretical investigation of the Seebeck coefficient (thermoelectric power) in Pb/$Pb_{1-x}Eu_xTe$ MQWs using the most appropriate, as well as the most updated, band parameters and carrier concentrations to describe the properties of sample T-225 in Ref. [15], so that a direct comparison can be made with the experimental studies. For example, the Eu content for sample T-225 in Ref. [15] ($x \simeq 0.073$) is now updated to a new value $x \simeq 0.09$ according to the most recent data for the lattice constant as a function of x for $Pb_{1-x}Eu_xTe$ alloy [32] and the x-ray data for sample T-225 (see the footnote on page 99). Other improvements in our models over the ones by Broido and Reinecke include consideration of the effects of the non-parabolicity for the energy bands and of the anisotropic constant energy surfaces. The effect of the anisotropic constant energy surface is taken into account by retaining up to the second order term in the Legendre polynomial expansion of the perturbation function

$\phi(\mathbf{k})$ as we will discuss in this chapter. It should be noted that all the parameters used in this study are readily available in the literature in terms of the band parameters for bulk PbTe [28] or $Pb_{1-x}Eu_xTe$ alloys [29–31] (also see §2.2). Thus, our theoretical analysis requires virtually no fitting parameters, except that the number of carriers in the sample has to be determined by an independent experimental technique such as a Hall coefficient measurement [38]. We believe that such investigations should be of great value not only for acquiring a firm understanding of the physics of the low-dimensional thermoelectricity, but also for developing an innovative strategy for designing even better thermoelectric materials using low-dimensional structures in the future.

In the subsequent sections, we will introduce the theoretical formalism for the Boltzmann equation in §3.2 and show the process of the numerical calculation in §3.3. Then, we will discuss the results of our calculation in §3.4 making the comparison with the experimental results that were introduced in Chapter 2. Finally, we will summarize our discussion in this chapter in §3.5.

3.2 Theoretical formalism

A detailed and yet comprehensive review of the Boltzmann equation and semi-classical electron transport theory is given by B. R. Nag [53]. In this section, we will summarize the essence of the Boltzmann transport theory that is needed to understand the subsequent sections of this chapter.

3.2.1 Solution of Boltzmann Equation

The non-equilibrium distribution function for electrons in an electric field $\mathbf{E}$ is obtained by solving the Boltzmann equation,

$$\frac{\partial f(\mathbf{k})}{\partial t} = -\frac{e\mathbf{E}}{\hbar} \cdot \nabla_{\mathbf{k}} f(\mathbf{k}) + \partial_c f(\mathbf{k}) = 0 \tag{3.1}$$

where e is the electron charge (negative number), $\hbar$ is the Planck constant divided by 2π, $\mathbf{k}$ is the electron wave vector, $f(\mathbf{k})$ is the non-equilibrium electron distribution function, and $\partial_c f(\mathbf{k})$ is the collision term defined by,

$$\partial_c f(\mathbf{k}) = -\left(\frac{V_c}{8\pi^3}\right)\int [f(\mathbf{k})\{1-f(\mathbf{k}')\}S(\mathbf{k},\mathbf{k}') - f(\mathbf{k}')\{1-f(\mathbf{k})\}S(\mathbf{k}',\mathbf{k})]\, d\mathbf{k}'. \quad (3.2)$$

Here, V_c is the sample volume and $S(\mathbf{k},\mathbf{k}')d\mathbf{k}d\mathbf{k}'$ is the scattering probability per unit time that an electron within an infinitesimal volume $d\mathbf{k}$ around $\mathbf{k}$ will be scattered into an infinitesimal volume $d\mathbf{k}'$ around $\mathbf{k}'$ in k space. Since the distribution function $f(\mathbf{k})$ reduces to the Fermi-Dirac distribution function $f_0(E_\mathbf{k}) = [1-\exp\{-(E_\mathbf{k}-\zeta)/k_BT\}]^{-1}$ in the limit of $\mathbf{E}=\mathbf{0}$, $S(\mathbf{k},\mathbf{k}')$ and $S(\mathbf{k}',\mathbf{k})$ have to satisfy the following relation,

$$f_0(E_\mathbf{k})\{1-f_0(E_{\mathbf{k}'})\}S(\mathbf{k},\mathbf{k}') - f_0(E_{\mathbf{k}'})\{1-f_0(E_\mathbf{k})\}S(\mathbf{k}',\mathbf{k}) = 0, \quad (3.3)$$

which expresses the detailed balance principle and is used to express $S(\mathbf{k}',\mathbf{k})$ in terms of $S(\mathbf{k},\mathbf{k}')$.

For the case of a two-dimensional electron gas which we will consider in the present chapter, we substitute $A/4\pi^2$ for the factor $V_c/8\pi^3$ in Eq. 3.2, where A is the area of the sample, and the integration is carried out over two-dimensional k space.

3.2.2 Scattering probability

The scattering probability per unit time $S(\mathbf{k},\mathbf{k}')$ is given by the Fermi golden rule,

$$S(\mathbf{k},\mathbf{k}') = \frac{2\pi}{\hbar}\left|\langle\mathbf{k}'\left|H'\right|\mathbf{k}\rangle\right|^2 \delta(E_{\mathbf{k}'} - E_\mathbf{k} \mp \hbar\omega) \quad (3.4)$$

where ω is the phonon frequency and the plus and minus signs in the δ-function stand for the phonon emission and absorption processes, respectively. The explicit expressions for the matrix element $|\langle\mathbf{k}'|H'|\mathbf{k}\rangle|$ for the case of a three-dimensional isotropic crystal are given in Table 3.1 for longitudinal acoustic phonon deformation potential scattering (LADP) and polar optical phonon scattering (POP) [53]. For the expressions for other scattering mechanisms, readers are referred to Refs. [40, 53, 54].

Table 3.1: Matrix element $|\langle \mathbf{k}' | H' | \mathbf{k} \rangle|$ for selected scattering mechanisms in 3D isotropic crystal, where $\mathbf{q} = \mathbf{k}' - \mathbf{k}$ [53].

Type of scattering	Expression
LADP	$\Xi \left(\frac{\hbar}{2V_c \rho \omega_{\mathbf{q}}} \right)^{\frac{1}{2}} S_c(\mathbf{q}, \lambda) \, (\mathbf{e}_{\mathbf{q}} \cdot \mathbf{q}) \left[n(\omega_{\mathbf{q}}) + \frac{1}{2} \pm \frac{1}{2} \right]^{\frac{1}{2}}$
POP	$\frac{\lvert e \rvert}{q} \left(\frac{1}{\epsilon_\infty} - \frac{1}{\epsilon_S} \right)^{\frac{1}{2}} \left(\frac{\hbar \omega_0}{2V_c} \right)^{\frac{1}{2}} \left[n(\omega_0) + \frac{1}{2} \pm \frac{1}{2} \right]^{\frac{1}{2}} S_c(\mathbf{q}, \lambda)$
Ionized impurity	$\frac{Ze^2}{V_c \, \epsilon_S} \frac{1}{\lvert \mathbf{k} - \mathbf{k}' \rvert^2 + \lambda^{-2}}$

Meanings of symbols:

Ξ	- Acoustic phonon deformation potential
ρ	- Density of the sample
V_c	- Sample volume
$\mathbf{e}_{\mathbf{q}}$	- Polarization vector of the lattice wave
ϵ_∞	- High frequency dielectric constant
ϵ_S	- Static dielectric constant
$\omega_{\mathbf{q}}$	- Acoustic phonon frequency for wave vector $\mathbf{q}$
ω_0	- Optical phonon frequency
$n(\omega)$	- Occupation number $n(\omega) = [\exp(\hbar\omega / k_B T) - 1]^{-1}$ for phonons with frequency ω
λ	- Debye screening length
$S_c(\mathbf{q}, \lambda)$	- Screening factor $S_c(\mathbf{q}, \lambda) = q^2 (q^2 + \lambda^{-2})^{-1}$
Z	- Ionicity of an impurity atom

In the present chapter, we consider the scattering of the two-dimensionally confined electrons due to the three-dimensional phonons to model the transport coefficients for the two-dimensionally confined electron gas [22]. We note that a state for a two-dimensionally confined electron can be specified by an in-plane wave vector $\mathbf{k}_{||}$, whereas a state for a phonon is specified by a three-dimensional phonon wave vector $\mathbf{q}$, which will be decomposed into an in-plane component $\mathbf{q}_{||}$ and a perpendicular component q_z for our convenience in carrying out the calculation. The scattering mechanisms explicitly considered in the present work are : 1) longitudinal acoustic phonon deformation potential scattering (LADP) and 2) polar optical phonon scattering (POP). These are the two main scattering mechanisms dominant in bulk PbTe from relatively low (~77 K) to relatively high temperatures (>400 K) [28].

Assuming that the overlap integral for the lattice part of the Bloch function is equal to unity (plane wave approximation), the squared scattering matrix elements for the two-dimensionally confined electrons due to the above mentioned scattering mechanisms are expressed as [54],

$$\left|\langle \mathbf{k}'_{||} \left| H'_{ac} \right| \mathbf{k}_{||} \rangle\right|^2 = \frac{\Xi^2 k_B T}{4\pi\rho\upsilon^2 A} \int_{-\infty}^{\infty} |G(q_z)|^2 \, dq_z \, \delta(\mathbf{k}'_{||} - \mathbf{k}_{||} \mp \mathbf{q}_{||}) \tag{3.5}$$

for LADP and

$$\left|\langle \mathbf{k}'_{||} \left| H'_{op} \right| \mathbf{k}_{||} \rangle\right|^2 = \frac{e^2\hbar\omega_0}{4\pi A} \left(\frac{1}{\epsilon_\infty} - \frac{1}{\epsilon_S}\right) \int_{-\infty}^{\infty} \frac{|G(q_z)|^2 \, dq_z}{\left|\mathbf{q}_{||}\right|^2 + q_z^2} \times [n(\omega_0) + \frac{1}{2} \mp \frac{1}{2}] \delta(\mathbf{k}'_{||} - \mathbf{k}_{||} \mp \mathbf{q}_{||}) \tag{3.6}$$

for POP, where Ξ, ρ, υ, ϵ_∞, ϵ_S, ω_0 and $n(\omega_0)$ are, respectively, the acoustic phonon deformation potential, the mass density of the sample, the speed of sound, the high frequency dielectric constant, the static dielectric constant, the optical phonon frequency and the occupation number $n(\omega_0) = [\exp(\hbar\omega_0/k_B T) - 1]^{-1}$ for phonons with frequency ω_0. Here $G(q_z)$ is defined by

$$G(q_z) = \int_{-\infty}^{\infty} \psi_z^*(z) e^{iq_z z} \psi_z(z) \, dz, \tag{3.7}$$

where $\psi_z(z)$ is the normalized wave function in the confinement direction (z direction) that is obtained by solving the Schrödinger equation for a square well potential. It is noted that the elastic approximation ($E_{\mathbf{k}} = E_{\mathbf{k}'}$) and the high temperature approximation for the number of phonons $n(\omega) \simeq k_B T/\hbar\omega$ are used to describe the acoustic phonon scattering (see Eq. 3.5). However, the full inelastic scattering scheme is utilized to describe the optical phonon scattering, as discussed in §3.3.3 and Appendix D

3.2.3 Thermoelectric power

Once the non-equilibrium distribution function $f(\mathbf{k})$ is obtained by solving the Boltzmann equation, the Seebeck coefficient S (thermoelectric power) is readily calculated using the following equations [53],

$$S = \frac{1}{eT}\frac{\mathbf{L}_{2\mathrm{D}}^{(1)}}{\mathbf{L}_{2\mathrm{D}}^{(0)}}, \tag{3.8}$$

and

$$\mathbf{L}_{2\mathrm{D}}^{(\alpha)} = e\int \frac{d\mathbf{k}_{||}}{2\pi^2} f(\mathbf{k}_{||})\mathbf{v}(\mathbf{k}_{||})\{E(\mathbf{k}_{||}) - \zeta\}^{\alpha}, \tag{3.9}$$

for $\alpha = 0, 1$, where $\mathbf{v}(\mathbf{k}_{||})$ and $E(\mathbf{k}_{||})$ are, respectively, the velocity and the energy of the electron in a state $\mathbf{k}_{||}$.

For a multiple subband system like the PbTe/$Pb_{1-x}Eu_xTe$ MQWs, the transport tensors $\mathbf{L}_{2\mathrm{D}}^{(\alpha)}$ for $\alpha = 0, 1$ are calculated for each subband separately, and the results are summed together for substitution in Eq. 3.8 to obtain S for the whole system.

3.3 Method of calculation

3.3.1 Model system

The model system for the present calculation is the (111) oriented PbTe/$Pb_{1-x}Eu_xTe$ multiple-quantum-wells (MQWs) where $x \simeq 0.09$ and the thicknesses of PbTe and $Pb_{1-x}Eu_xTe$ layers are $\simeq$ 20 Å and $\simeq$400 Å, respectively (sample T-225 that is discussed in the previous chapter and in Ref. [15]). The details of the experimental

results, including the sample structure, growth conditions, and various transport measurements for this sample are discussed in chapter 2 and are published elsewhere [15, 16].

All the band parameters necessary for the numerical calculation of the transport coefficients of the PbTe quantum wells are readily available in the literature [28–31]. In particular, the following values are used in the present calculation from Ref. [22] : the anisotropic effective masses at 300 K, $m_t = 0.034\,m$ (transverse component) and $m_l = 0.35\,m$ (longitudinal component), $\hbar\omega_0 = 14$ meV, $\epsilon_S = 414\,\epsilon_0$ and $\epsilon_\infty = 33\,\epsilon_0$, where ϵ_0 is the dielectric constant of the vacuum, $\Xi = 25$ eV, and $\rho v^2 = 486$ meV/Å^3, where the sound velocity v is directionally averaged. To account for the temperature dependent properties described in the present chapter, the temperature dependences of the bulk effective masses and band gap energy are obtained from Refs. [28] and [31], respectively (also see §2.2).

The bound state levels for the quantum well are calculated by solving the Schrödinger equation for a square well potential using the empirical relation $\Delta E_c/\Delta E_g = 0.55$ where ΔE_c is the conduction band offset and ΔE_g is the difference in energy band gap between $Pb_{1-x}Eu_xTe$ and PbTe as we discussed in Chapter 2 [30]. The non-parabolicity of the energy dispersion relation for the confined electronic states is taken into account using the form $\hbar^2k^2/2m^* = E(1+\tilde{\alpha}E) \equiv \gamma(E)$ [53], where E is the kinetic energy for the electron and $\tilde{\alpha}$ is the inverse of E_g. The value of E_g used in our calculation for the ith subband is the energy difference between the valence- and conduction- band bound state levels for the pertinent subband, denoted by E_g^{l-l} and E_g^{o-o} for the longitudinal (l) subband and the oblique (o) subbands, respectively.

3.3.2 Chemical potential

The chemical potential ζ for the model system is determined by considering the conservation of the total number of carriers per superlattice period ($d_W + d_B$) [38]

(also see §2.4.1 and §3.4.1),

$$n_{\rm tot} \equiv n_{\rm QW} - p_{\rm QW} + (n_{\rm B} - p_{\rm B})\frac{d_{\rm B}}{d_{\rm W}}, \tag{3.10}$$

where $n_{\rm tot}$ is the apparent total carrier density per quantum well defined by Eq. 3.10, $n_{\rm QW}$ ($p_{\rm QW}$) and $n_{\rm B}$ ($p_{\rm B}$) are the concentrations of electrons (holes) bound to the quantum wells and those delocalized throughout the barrier layer unbound to the quantum wells, respectively. It should be noted that the carrier densities $n_{\rm QW}$ and $p_{\rm QW}$ are calculated using the quantum well thickness (denoted as $d_{\rm W}$), whereas $n_{\rm B}$ and $p_{\rm B}$ are calculated using the barrier layer thickness (denoted as $d_{\rm B}$), and hence we obtain the factor $d_{\rm B}/d_{\rm W}$ in Eq. 3.10. We further note that the carrier densities $n_{\rm QW}$ and $p_{\rm QW}$ have contributions from both the longitudinal valley and the oblique valleys that originate from the four L-point valleys in the Brillouin zone for bulk PbTe, and that the carrier density $n_{\rm B}$ is associated with the L-point carriers in the conduction band of the $Pb_{1-x}Eu_xTe$ barrier layer and $p_{\rm B}$ is associated with the L- and Σ-point carriers in the valence band of the $Pb_{1-x}Eu_xTe$ barrier layer. In our model system, $p_{\rm QW}$ and $p_{\rm B}$ are found to be negligible relative to the other terms up to 400 K [38]. Above 400 K the $p_{\rm B}$ term becomes important due to the large density of states mass ($m_d^* \simeq 1.4$) for the Σ valence band [28] (also see §2.4.1). It was also shown previously that the carrier mobility for the $Pb_{1-x}Eu_xTe$ alloy is greatly reduced relative to that for PbTe [15]. Therefore, we assume that the electrical conduction in our model system is entirely due to the carriers that are bound to the quantum wells in the present calculations.

3.3.3 Numerical solution

Once the chemical potential is determined for our model system, the iterative algorithm is employed for the numerical calculation of the non-equilibrium distribution function $f(\mathbf{k}_{||})$ [53]. Taking the x-axis as the direction of the electric field that is parallel to one of the principal axes of the 2D elliptical constant energy surface and defining the normalized k vector $\mathbf{k}_{||}^*$ and the normalized electric field $\mathbf{E}^*$ by

$\mathbf{k}_{||}^* = (k_{||x}^*, k_{||y}^*) = \left((\frac{m}{m_x})^{1/2} k_{||x}, (\frac{m}{m_y})^{1/2} k_{||y}\right)$ and $E_x^* = (\frac{m}{m_x})^{1/2} E_x$, respectively, we can expand $f(\mathbf{k}_{||})$ as,

$$f(\mathbf{k}_{||}) = f_0(E_{\mathbf{k}_{||}}) - \frac{e\hbar E_x^* k_{||}^*}{m} \left(\frac{\partial f_0}{\partial E_{\mathbf{k}_{||}}}\right) \phi(\mathbf{k}_{||}), \tag{3.11}$$

where $\phi(\mathbf{k}_{||})$ is a perturbation function connected with the application of an electric field and $\phi(\mathbf{k}_{||})$ has the units of time. Using the perturbation function $\phi(\mathbf{k}_{||})$ in Eq. 3.11, the Boltzmann equation (Eq. 3.1) is rewritten as

$$\cos\theta = \frac{A}{4\pi^2} \gamma'(E_{\mathbf{k}||}) \int \frac{1 - f_0(E_{\mathbf{k}'})}{1 - f_0(E_{\mathbf{k}})} S(\mathbf{k}_{||}, \mathbf{k}'_{||}) \{\phi(\mathbf{k}_{||}) - k_{||}^{*\prime}/k_{||}^* \phi(\mathbf{k}'_{||})\} \, d\mathbf{k}'_{||}, \tag{3.12}$$

where $\gamma'(E) = d\gamma(E)/dE$, θ is the angle between the vector $\mathbf{k}_{||}^*$ and the x-axis, and Eq. 3.3 is used to eliminate $S(\mathbf{k}'_{||}, \mathbf{k}_{||})$ in terms of $S(\mathbf{k}_{||}, \mathbf{k}'_{||})$. In solving the Boltzmann equation, the perturbation function $\phi(\mathbf{k}_{||})$ is further expanded using the Legendre polynomials $\mathrm{P}_l(x)$ and the two most significant terms are retained, i.e., $\phi(\mathbf{k}_{||}) = a_1(E)\mathrm{P}_1(\cos\theta) + a_3(E)\mathrm{P}_3(\cos\theta)$, in the iteration procedure. The resultant Boltzmann equation is solved for $a_1(E)$ and $a_3(E)$. The reason that we retain the second term in the expansion of $\phi(\mathbf{k}_{||})$ is to handle the anisotropy of the constant energy surface for the oblique valley accurately in solving the Boltzmann equation. In this way, we can keep the error associated with the numerical calculations to within a few percent. The details of the iteration procedure retaining the second order term in the Legendre polynomial expansion of the perturbation function are summarized in Appendix D.

To complete our calculation for the oblique valleys, the procedure above is repeated for $\mathbf{E}^*$ parallel to the y-axis and the transport coefficients calculated along the x- and y- axes are averaged to yield the final isotropic transport coefficient that is consistent with the cubic symmetry of the model system [53].

3.4 Results of calculation and comparison to the experimental results

3.4.1 Constant relaxation time approximation

In Chapter 2, the enhanced values of the Seebeck coefficient observed in the (111) oriented PbTe/$Pb_{1-x}Eu_xTe$ MQWs were explained qualitatively using the constant relaxation time approximation (CRTA) and the two-band model assuming parabolic energy bands [16, 38] : the total Seebeck coefficient S is given by $(\sigma_1 S_1 + \sigma_2 S_2)/(\sigma_1 + \sigma_2)$ where σ_i and S_i $(i = 1,\ 2)$ are the electrical conductivity and the Seebeck coefficient, respectively, for the ith subband. For the (111) oriented PbTe/$Pb_{1-x}Eu_xTe$ MQWs, the four equivalent L point minima in the 3D Brillouin zone are split into one longitudinal (lowest in energy) and three equivalent oblique pockets in the 2D quantum wells; thus, we associate the longitudinal and the oblique subbands with the first and second subbands in the above-mentioned two-band model.

While the carrier concentration and the Seebeck coefficient of a single band material are functions of only the chemical potential and temperature in the CRTA, we need an additional parameter to model S and n_{Hall} in a two-band model as we discussed in Chapter 2. This additional parameter is the ratio of the carrier mobilities μ (or scattering times τ) between these subbands, namely $\mu_{\mathrm{obliq}}/\mu_{\mathrm{longt}} = (\tau_{\mathrm{obliq}}/m_{\mathrm{obliq}})/(\tau_{\mathrm{longt}}/m_{\mathrm{longt}}) \simeq 0.553\tau_{\mathrm{obliq}}/\tau_{\mathrm{longt}}$ where $m_{\mathrm{longt}} = m_{||t}$ and $m_{\mathrm{obliq}} = 2/(m_{||t}^{-1} + m_{||l}^{-1})$ are the transport masses for the longitudinal subband and oblique subband, respectively. The experimental results for the Seebeck coefficient as a function of Hall carrier concentration are shown in Fig. 3-1 for bulk PbTe and PbTe/$Pb_{1-x}Eu_xTe$ MQWs from Ref. [15] together with the theoretical results obtained using the CRTA with three different assumptions for the mobility ratio [38]. The assumptions used in the CRTA in Fig. 3-1 are obtained for various situations of the intra- and the inter-valley scattering, assuming that the relaxation time τ is inversely proportional to the density of states for electrons as stated below (also see Ref. [38] for details).

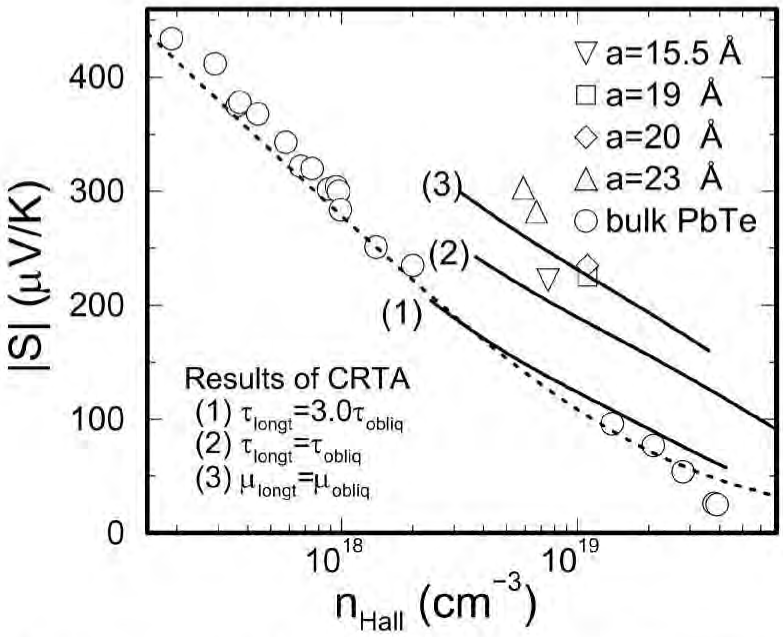

Figure 3-1: The absolute value of the measured Seebeck coefficient as a function of the Hall carrier concentration for bulk PbTe (open circles) and for PbTe/$Pb_{1-x}Eu_xTe$ MQWs of various quantum well thicknesses (other open symbols) at 300 K [38]. The theoretical result for $|S|$ for bulk PbTe using the constant relaxation time approximation (CRTA) and using values of $m_t = 0.034\,m$ and $m_l = 0.35\,m$ for the bulk effective masses is shown by the dashed curve. The theoretical results for PbTe/$Pb_{1-x}Eu_xTe$ MQWs in the CRTA are shown for the following conditions : (1) $\tau_{\rm longt} = 3.0\tau_{\rm obliq}$, intra-valley-scattering being dominant, (2) $\tau_{\rm longt} = \tau_{\rm obliq}$, inter-valley-scattering being dominant, and (3) $\mu_{\rm longt} = \mu_{\rm obliq}$, special case of the inter-valley-scattering (see text for more details).

The physical conditions that lead to various assumptions for the ratio between τ_{longt} and τ_{obliq} are the following. In the relaxation time approximation assuming the elastic scattering of conduction carriers, the relaxation time τ is inversely proportional to the product between the scattering probability $W_{\alpha\beta}$ for an electron in a state in valley α to be scattered into a state in valley β and the density of the electronic states for valley β at energy E [denoted by $\rho_\beta(E)$], where E is the energy of the pertinent electron that is being scattered,

$$\tau_\alpha \sim \frac{1}{\sum_\beta W_{\alpha\beta}\ \rho_\beta(E)}, \tag{3.13}$$

where the summation is taken over all the available valleys (subbands) and the subscript α in τ_α means that the relaxation time being considered is for the carriers in valley α. In the subsequent discussions in this subsection, we assume that $W_{\alpha\beta}$ is constant ($W_{\alpha\beta} = W$), if the scattering of carriers between valley α and valley β is possible, and that $W_{\alpha\beta}$ is zero, if the scattering of carriers between these valleys are impossible, for example, due to a selection rule.

We first consider the case where the electrons are scattered only within the same valley (intra-valley-scattering). In this case, we have $W_{\alpha\beta} = W$, for $\beta = \alpha$, and $W_{\alpha\beta} = 0$, for $\beta \neq \alpha$, where α and β are either the longitudinal valley or one of the oblique valleys. It is noted that $W_{\alpha\beta} = 0$, even if both α and β are the oblique valleys, if α and β represent distinct valleys among the three equivalent oblique valleys. Since the density-of-states effective mass for the longitudinal valley ($0.033\ m$) is about one third of the density-of-states mass for the oblique valley ($0.102\ m$) in 2D, we expect $\tau_{\text{longt}} \approx 3.0\tau_{\text{obliq}}$ in this approximation. This is the condition (1) used in Fig. 3-1.

The second possible assumption is that the electrons are scattered from any one of the valleys to any of the other valleys equally well (inter-valley-scattering). In this case, we have $W_{\alpha\beta} = W$ for any choice of the valleys for α and β, which leads to the condition $\tau_{\text{longt}} = \tau_{\text{obliq}}$. This is the condition (2) used in Fig. 3-1.

The third possible assumption is that some of the inter-valley-scattering have a low probability. For example, it is estimated for bulk PbTe that the relaxation time

τ_{inter} for the inter-valley-scattering among the four equivalent L-point valleys is 20 times larger than that for the intra-valley-scattering τ_{intra} due to a selection rule [24]. It therefore seems plausible that the scattering of carriers among the three equivalent oblique valleys is not allowed by a selection rule, but lowering the symmetry allows the scattering of carriers between the longitudinal- and oblique-valleys. In this case, we have the situation where $W_{\alpha\beta} = 0$ if α and β are both oblique but 'distinct' valleys, and $W_{\alpha\beta} = W$, otherwise. In this situation, using the density-of-states effective masses given above, we obtain $\tau_{\text{longt}} \approx 0.4\tau_{\text{obliq}}$. Using the transport effective masses for the longitudinal valley (0.033 m) and the oblique valley (0.060 m), we find that the mobilities for the longitudinal and the oblique subband carriers are almost equal. This is the condition (3) used in Fig. 3-1.

These three assumptions for the ratio between τ_{longt} and τ_{obliq} are further examined by modeling the observed Hall carrier concentration as a function of temperature as shown in Fig. 3-2. For each of the three cases, the apparent total carrier density n_{tot} was adjusted so that the calculated Hall carrier density matches the experimental Hall carrier density at 300K. As shown in Fig. 3-2, the modeling result using $\mu_{\text{longt}} = \mu_{\text{obliq}}$ again agrees with the observed experimental results best of the three cases considered, as was also found for the modeling of S in Fig. 3-1.

In §2.4.3, we have shown the experimental results for S as a function of temperature for sample T-225 (see Fig. 2-13), and interpreted the results in terms of the constant relaxation time approximation (CRTA) assuming constant n_{QW} below 280 K. On the other hand, the parameter that should be constant in our model is n_{tot} rather than n_{QW}. The successful fitting of the experimental n_{Hall} above 280 K assuming $\mu_{\text{longt}} = \mu_{\text{obliq}}$ is consistent with constant n_{tot} and the value for n_{tot} is estimated to be near 1.15×10^{19} cm^{-3}. Therefore, in this chapter, all the calculations are performed assuming n_{tot} =1.15×10^{19} cm^{-3} that is constant even below 280 K.

A particular interest here is the unexpectedly large value for $\mu_{\text{obliq}}/\mu_{\text{longt}}$ that is obtained from the fitting in CRTA. In this subsection, we have attributed this large value for $\mu_{\text{obliq}}/\mu_{\text{longt}}$ to the consequence of the special case of the inter-valley scattering. We should, however, note that the observed enhancement in S can actually

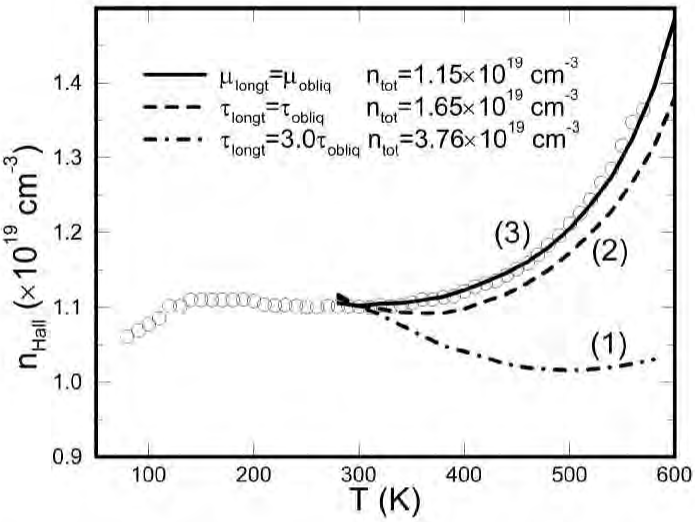

Figure 3-2: The temperature dependence of the Hall carrier concentration for the PbTe/$Pb_{1-x}Eu_xTe$ MQW sample (open circles) for a = 20 Å and assuming that only the carriers confined in the quantum wells contribute to the electrical conduction [38]. The results of the model calculation are plotted for the following assumptions: (1) intra-valley-scattering being dominant, i.e. $\tau_{\rm longt} = 3.0\tau_{\rm obliq}$, (2) inter-valley-scattering being dominant, i.e. $\tau_{\rm longt} = \tau_{\rm obliq}$, (3) the special case of the inter-valley-scattering, where $\mu_{\rm longt} = \mu_{\rm obliq}$.

be understood without including inter-valley scattering in the following subsections. Therefore, the conclusion we can draw here is that the simple density-of-states consideration only for τ does not lead to any physical explanation for the enhanced S that is observed in PbTe MQW samples. A large value for $\mu_{\rm obliq}/\mu_{\rm longt}$ is desirable for obtaining a large value of $Z_{\rm 2D}T$, since the larger the value of $\mu_{\rm obliq}/\mu_{\rm longt}$, the larger the contribution from the oblique subbands to the total $Z_{\rm 2D}T$. Therefore, the reduction of the Seebeck coefficient due to the lifting of the valley degeneracy becomes less important as the value for $\mu_{\rm obliq}/\mu_{\rm longt}$ is increased at higher temperatures. It is of interest to investigate exactly which mechanisms are responsible for the observed values for $\mu_{\rm obliq}/\mu_{\rm longt}$, and hence the enhancement in S for the PbTe/$Pb_{1-x}Eu_xTe$ MQWs relative to that for the corresponding bulk PbTe.

In the next few subsections, we will reveal the exact mechanisms that are responsible for the observed values for $\mu_{\rm obliq}/\mu_{\rm longt}$ and the enhanced values for S. We will first compare the experimental results for sample T-225 with our theoretical results, assuming longitudinal acoustic phonon deformation potential scattering, and polar optical phonon scattering, independently, and then considering both mecha-

nisms acting together.

3.4.2 Seebeck coefficient due to acoustic phonon scattering

Using the elastic and high temperature approximations described in §3.2.2 and considering only the longitudinal acoustic phonon deformation potential scattering, the Boltzmann equation (Eq. 3.12) reduces to the energy-dependent relaxation time $\tau_{ac}(E)$ approximation:

$$\tau_{ac}(E)^{-1} \equiv a_1(E)^{-1} = \frac{(m_x m_y)^{1/2}}{4\pi\hbar^3} \frac{\Xi^2 k_B T}{\rho \upsilon^2} \gamma'(E)^2 \int |G(q_z)|^2 \, dq_z \times 2, \tag{3.14}$$

where the factor 2 at the end of the equation accounts for the phonon absorption and emission processes. Using Eq. 3.14, we can directly investigate the ratio of τ_{ac} between the oblique subbands (denoted by τ_{ac}^{obliq}) and the longitudinal subband (denoted by τ_{ac}^{longt}) for our model system.

If the energy dispersion relation is completely parabolic, the relaxation time τ_{ac} is constant with energy, so that the energy dependent τ formalism basically reduces to the CRTA. In this limit, τ_{ac} is proportional to the product of the density-of-states mass $(m_x m_y)^{1/2}$ and the $|G(q_z)|^2$ integral as seen in Eq. 3.14 [see Eq. 3.7 for the definition of $G(q_z)$]. Using the bulk effective masses at 300 K projected onto the plane of the quantum well, we obtain $m_x = m_y \equiv m_{||t} = 0.034\, m$ for the longitudinal pocket and $m_x \equiv m_{||l} = 0.315\, m$, $m_y \equiv m_{||t} = 0.034\, m$ for each of the oblique pockets. Therefore, the difference in the effective masses accounts for a factor of 0.33 in $\tau_{ac}^{\text{obliq}}/\tau_{ac}^{\text{longt}}$. Another factor comes from the $|G(q_z)|^2$ integral. Since the z component of the electron wavefunction for the longitudinal subband is more confined than that for the oblique subband, the resultant $G(q_z)$, and hence also the $|G(q_z)|^2$ integral, is larger for the longitudinal subband than for the oblique subband (see Fig. 3-3). This accounts for a factor of 3.77 in $\tau_{ac}^{\text{obliq}}/\tau_{ac}^{\text{longt}}$ at 300 K. Therefore the value for $\tau_{ac}^{\text{obliq}}/\tau_{ac}^{\text{longt}}$ assuming a parabolic energy dispersion relation is $0.33 \times 3.77 = 1.26$, which is quite different from the naive assumption $\tau^{\text{obliq}}/\tau^{\text{longt}} = 0.33$ obtained from the density of states factor only. Furthermore, when using a non-parabolic energy dispersion relation, we have an

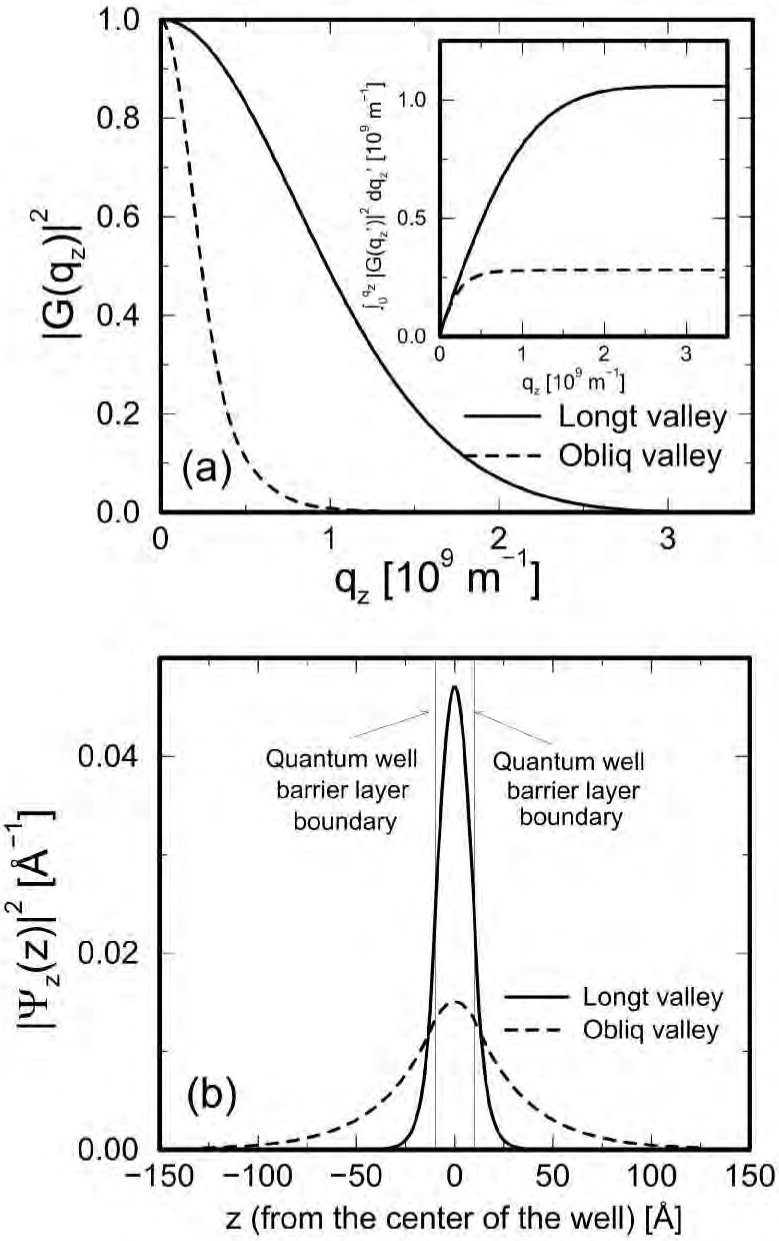

Figure 3-3: (a) $|G(q_z)|^2$ as a function of q_z, where $G(q_z)$ is defined by Eq. 3.7, for the longitudinal (solid curve) and oblique (dashed curve) valleys for our model PbTe/$Pb_{1-x}Eu_xTe$ MQW sample (T-225) at 300 K. The inset shows the integration of $|G(q_z')|^2$ with respect to q_z' from zero to q_z as a function of q_z. Note that such a factor (with $q_z = \infty$) appears in Eq. 3.14. (b) Squared wavefunction $|\psi_z(z)|^2$ for the longitudinal (solid curve) and oblique (dashed curve) valleys for our model PbTe/$Pb_{1-x}Eu_xTe$ MQW sample (T-225) at 300 K as a function of z, which is used for the calculation of $G(q_z)$ in (a). $\psi_z(z)$ is obtained by solving the Schrödinger equation for a square well potential with $d_W = 20$ Å, $d_B = 400$ Å and $\Delta E_c = 150$ meV, where d_W, d_B, and ΔE_c are the quantum well thickness, barrier layer thickness and conduction band offset, respectively.

additional factor of $\gamma'(E)^2$ in Eq. 3.14 where $E = \zeta$ (ζ is the chemical potential) for the longitudinal subband and $E = 0$ (E is at the band edge) for the oblique subband. For our model system at 300 K we find that the Fermi level is 30.15 meV above the longitudinal subband edge and 42.48 meV below the oblique subband edge, where the energy band gaps between the valence and conduction band bound states are 447.69 meV for the longitudinal subband (E_g^{l-l}), and 581.87 meV for the oblique subband (E_g^{o-o}). Since the Fermi energy lies at a degenerate energy (inside the band) only with the longitudinal subband, the additional contribution of the non-parabolicity of the energy bands to $\tau_{ac}^{\text{obliq}}/\tau_{ac}^{\text{longt}}$ becomes important only for the longitudinal subband. For $\zeta = 30.15$ meV and $E_g^{l-l} = 447.69$ meV, we obtain $\gamma'(\zeta)^2 = 1.29$ at 300 K. It turns out that the contribution of the non-parabolicity to $\tau_{ac}^{\text{obliq}}/\tau_{ac}^{\text{longt}}$ is strongly dependent on temperature. For example at 100 K, we find that the Fermi level is 90.6 meV above the longitudinal subband edge and E_g^{l-l} is 382.93 meV, and therefore we get $\gamma'(\zeta)^2 = 2.17$. From this argument, we find that the temperature dependence of $\tau_{ac}^{\text{obliq}}/\tau_{ac}^{\text{longt}}$ mainly comes from the effect of the non-parabolicity of the energy bands (see Fig. 3-4).

Shown in Fig. 3-5 are the experimental Seebeck coefficient (S_{exp}, open circles) as well as the theoretical Seebeck coefficients: 1) considering only the longitudinal acoustic phonon deformation potential scattering (S_{ac}, short-dashed curve) and 2) considering only the polar optical phonon scattering (S_{op}, long-dashed curve). One can see that S_{ac} is smaller than S_{exp} above 200 K, while it is larger than S_{exp} below 150 K. The main reason for the large S_{exp} compared with S_{ac} above 200 K is that the polar optical phonon scattering generally has an effect to increase the value of S as we will discuss in the next subsection. This effect is predominant above 200 K. On the other hand, at lower temperatures ($\leq$ 150 K), the $\gamma(\zeta)^2$ factor in Eq. 3.14 increases for the longitudinal subband, causing $\tau_{\text{ac}}^{\text{longt}}$ to decrease. Hence S_{ac} increases, while in the real sample the polar optical phonons contribute to the preferential scattering of the carriers in the oblique valleys, while leaving the scattering of the carriers in the longitudinal valley relatively unchanged (dominated by the acoustic phonon scattering). This is the mechanism which explains the reduced S_{exp} relative to S_{ac} at

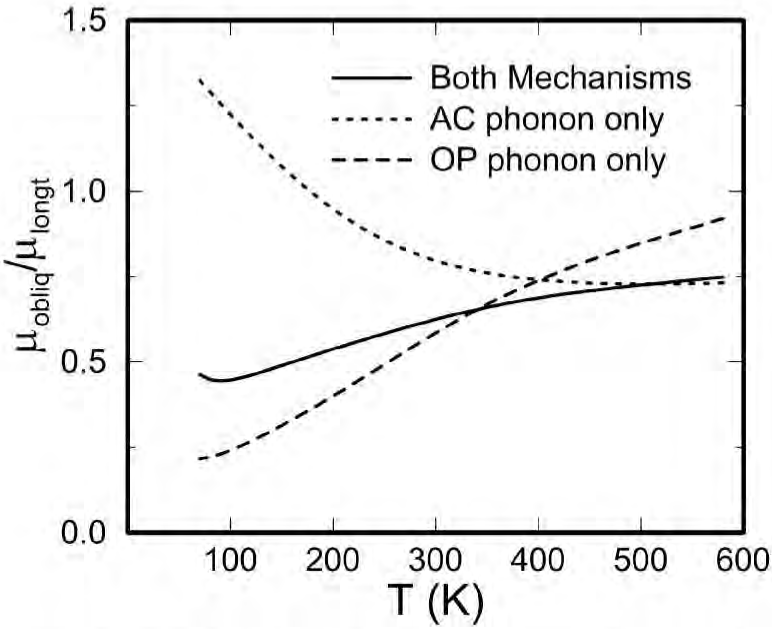

Figure 3-4: Calculated values for the mobility ratio between the carriers in the oblique valley and in the longitudinal valley in (111) oriented PbTe/$Pb_{1-x}Eu_xTe$ MQWs when : (1) only the longitudinal acoustic phonon deformation potential scattering (LADP) is considered (short-dashed curve), (2) only the polar optic phonon scattering (POP) is considered (long-dashed curve), and (3) both LADP and POP are considered (solid curve).

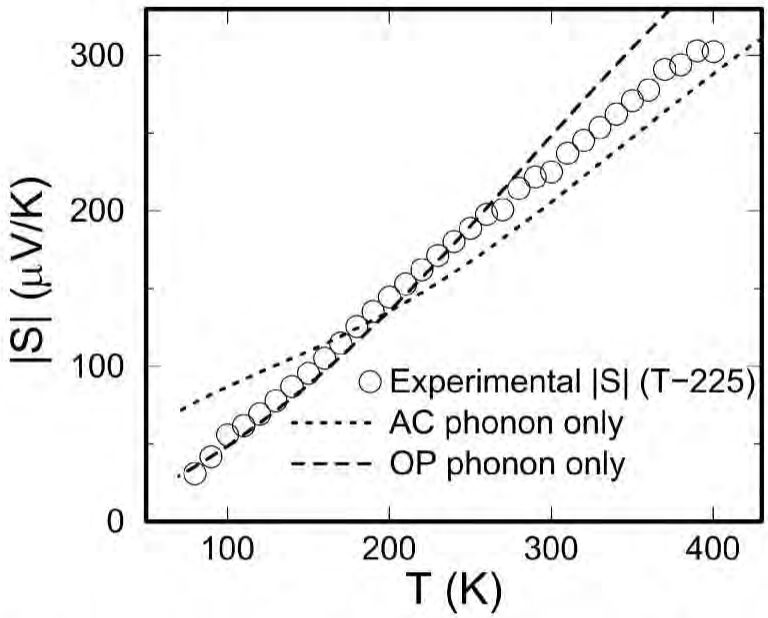

Figure 3-5: Absolute value of the Seebeck coefficient for the PbTe/$Pb_{1-x}Eu_xTe$ MQW sample (T-225) as a function of temperature (open circles) together with the theoretical results (1) considering only longitudinal acoustic phonon deformation potential scattering (short-dashed curve) and (2) considering only polar optic phonon scattering (long-dashed curve).

low temperatures ($\leq$ 150 K).

3.4.3 Seebeck coefficient due to optical phonon scattering

The Seebeck coefficient S calculated considering polar optical phonon scattering only (denoted by $S_{\rm op}$) is also shown in Fig. 3-5 (long-dashed curve) as a function of temperature. The calculated ratio of the mobilities $\mu_{\rm obliq}/\mu_{\rm longt}$ when only the polar optical phonon scattering is considered [denoted by $(\mu_{\rm obliq}/\mu_{\rm longt})_{\rm POP}$] is also plotted as a function of temperature in Fig. 3-4 (long-dashed curve). We find that $(\mu_{\rm obliq}/\mu_{\rm longt})_{\rm POP}$ is also a strong function of temperature and this ratio becomes as small as 0.25 below 100 K. This observation proves the postulate in the previous subsection that the polar optical phonons are more effective in scattering carriers in the oblique valleys than scattering carriers in the longitudinal valley at low temperatures in our model system. Another observation is that although the value for $(\mu_{\rm obliq}/\mu_{\rm longt})_{\rm POP}$ is 0.6$\sim$0.9 for temperatures above 300 K (i.e., $\mu_{\rm obliq} < \mu_{\rm longt}$), where we should be reminded that

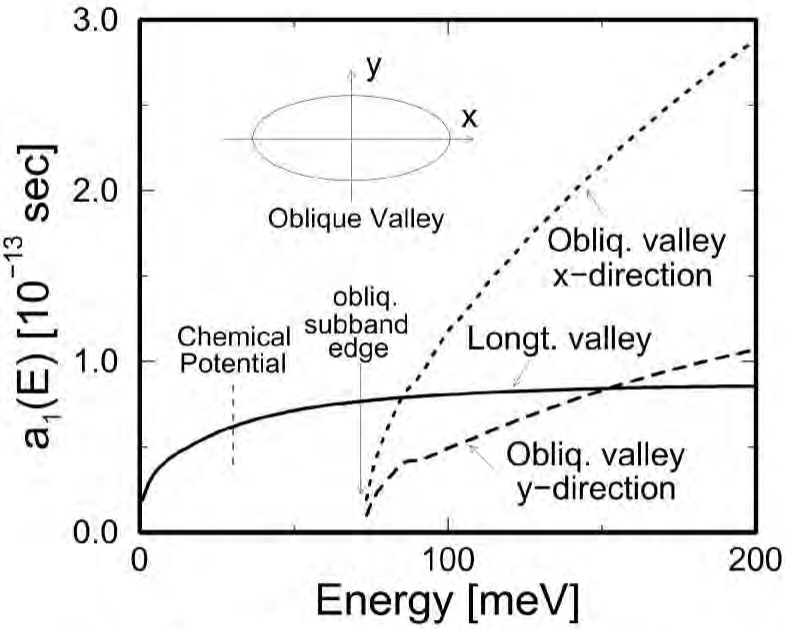

Figure 3-6: The coefficient for the first order term in the Legendre polynomial expansion of the perturbation function $\phi(\mathbf{k}_|)$, $a_1(E)$, as a function of energy at 300 K (see text). The solid, short-dashed and long-dashed curves denote the functions determined for $a_1(E)$ for the longitudinal valley, the oblique valley along the x direction and the oblique valley along the y direction, respectively. Also indicated on the figure are the energy values for the chemical potential and the oblique subband edge.

$\mu_{\text{obliq}} \geq \mu_{\text{longt}}$ was consistent with the experimental result in the CRTA, the resulting S_{op} calculated for our model system turns out to be significantly greater than S_{exp} above 300 K. This apparent discrepancy is resolved if we look at the special shape of the distribution function $f(E)$. Plotted in Fig. 3-6 is the coefficient for the first order term $[a_1(E)]$ of the perturbation function $\phi(\mathbf{k})$ as a function of energy at 300 K. Since $a_1(E)$ (which is interpreted as the scattering time τ in a naive sense) increases with increasing energy near the band edge, we can expect S_{op} to become significantly larger than S_{exp} if the chemical potential ζ is near (or below) the band edge and the width of the rising edge of the $a_1(E)$ function is larger than the magnitude of the thermal energy $k_{\text{B}}T$.

3.4.4 Seebeck coefficient due to both the longitudinal acoustic phonons and the polar optical phonons

When we consider both longitudinal acoustic phonon deformation potential (LADP) scattering and polar optical phonon (POP) scattering and we then calculate the Seebeck coefficient for both of these scattering mechanisms acting at the same time ($S_{\rm tot}$), we simply add the contributions from these scattering mechanisms to the total scattering probability per unit time (Eq. 3.4) and use the iterative approach described in the previous section and Appendix D. The resulting $S_{\rm tot}$ calculated in this way is plotted as a function of temperature in Fig. 3-7 (solid curve) together with the experimental result ($S_{\rm exp}$, open circles). We note that the agreement in Fig. 3-7 between the theoretical and the experimental results is fairly good for the wide temperature range from 80 K to 400 K based on literature values for the band parameters and with no adjustable parameters that are fitted by the model. The good agreement between the theoretical and experimental results indicates the reliability of the parameters deduced from the previous measurements [15] and analyses [38], such as carrier concentrations, lattice constants and energy band gaps, and the validity of the basic idea proposed by Hicks and Dresselhaus [12, 14] which predicts enhanced thermoelectric properties for low-dimensional systems, if the original model calculation is properly refined to include the appropriate scattering mechanisms.

3.5 Conclusions

In this chapter, a theoretical investigation of the thermoelectric power S in (111) oriented PbTe/$Pb_{1-x}Eu_xTe$ multiple-quantum-wells (MQWs) has been performed to reveal the mechanism of the observed enhancement in S in this system. The enhancement in S in this system is observed in spite of the lifting of the valley degeneracy between the longitudinal and oblique valleys at the L-point in the Brillouin zone, which would tend to reduce S. We have considered the effects of longitudinal acoustic phonon deformation potential scattering and the effects of polar optical phonon

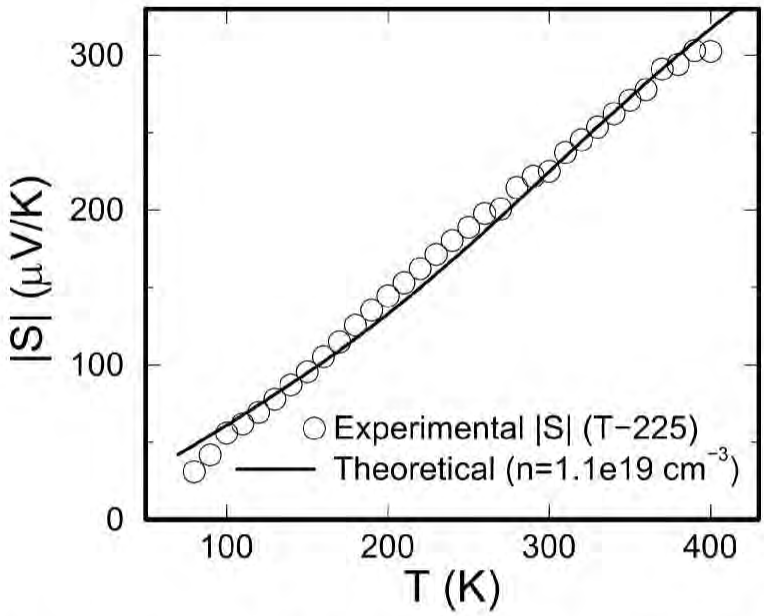

Figure 3-7: Absolute value of the Seebeck coefficient for the PbTe/$Pb_{1-x}Eu_xTe$ MQW sample (T-225) as a function of temperature (open circles) together with the theoretical results obtained for $|S|$ considering both longitudinal acoustic phonon deformation potential scattering and polar optical phonon scattering (solid curve).

scattering on the two-dimensionally confined electrons in the quantum wells. In the low temperature regime (~100 K), we find that polar optical phonons are more effective in scattering the carriers in the oblique valleys than in scattering carriers in the longitudinal valley. Since the occupation of the oblique valleys is small at low T, the resulting thermoelectric power is relatively small. However, in the high temperature regime (≃300 K), where there is more occupation of the oblique valleys, the dominance of the polar optical phonon scattering is found to contribute to increasing S because of the particular shape of the distribution function created by polar optical phonon scattering. Our theoretical result for the two scattering mechanisms acting together yields good agreement with the experimental results over a wide temperature range (80-400 K) without the use of any fitting parameters. It is hoped that the knowledge acquired through this study will contribute to deepening our understanding of the fundamental physics of low-dimensional thermoelectric phenomena, as well as allowing us to plan a new strategy for designing useful thermoelectric materials using low-dimensional structures in the future. Such attempts are made to some ex-

tent in the subsequent chapters, where we develop a new concept of "Carrier Pocket Engineering" to design materials with large values of $Z_{3D}T$ (thermoelectric figure of merit for the whole superlattice).

Chapter 4

Concept of Carrier Pocket Engineering and Enhanced $Z_{3D}T$ in GaAs/AlAs Superlattices

In this chapter, we will develop a new concept of Carrier Pocket Engineering which provides a general guideline for designing a superlattice structure that has an enhanced value of the thermoelectric figure of merit for the whole superlattice, denoted by $Z_{3D}T$. We will also apply this concept to GaAs/AlAs superlattices, where we will find that a large enhancement in $Z_{3D}T$ is achieved relative to the corresponding $Z_{3D}T$s for bulk GaAs and AlAs, despite the fact that neither of these constituent materials is a good thermoelectric material in the bulk form ($Z_{3D}T \approx 0.0085$ for both materials). It turns out that the large enhancement in $Z_{3D}T$ is possible only if the structures and the properties of the superlattices are designed carefully according to the proposal described in this chapter. Our scheme here includes the extension of our models developed previously (see Chapters 2 and 3) that predict an enhanced thermoelectric figure of merit for isolated quantum wells (denoted by $Z_{2D}T$) to models that predict a figure of merit for the whole superlattice (denoted by $Z_{3D}T$), using the Krönig-Penney model to predict the energy dispersion relations for carriers that propagate in the z-direction (parallel to the superlattice growth direction), i.e., E_z vs. k_z. Various superlattice parameters [superlattice growth direction, well- and barrier-

layer thicknesses, and carrier concentrations (or equivalently the position of the chemical potential)] are explored to optimize the value of $Z_{3D}T$, including quantum wells formed at various high symmetry points in the Brillouin zone. The highest room temperature $Z_{3D}T$ obtained for GaAs/AlAs superlattices using the theoretical models developed in this chapter is larger than 0.40 at the optimum carrier concentrations for either (001) or (111) oriented GaAs(20 Å)/AlAs(20 Å) superlattices. Such a value of $Z_{3D}T$ for GaAs(20 Å)/AlAs(20 Å) superlattices is about 50 times greater than that for the corresponding bulk GaAs (or AlAs) obtained using the same basic model to predict the values for the thermoelectric figure of merit $Z_{3D}T$.

4.1 Introduction

There have been an increasing number of studies of the enhanced thermoelectric figure of merit ZT ($Z = S^2\sigma/\kappa$), where S is the Seebeck coefficient, σ is the electrical conductivity, κ is the thermal conductivity, and T is the temperature, for a material in the form of a multiple-quantum-well (MQW) or superlattice structure [11–22, 39, 55–57]. There are currently two main trends in this research area for designing superior thermoelectric materials using superlattice structures whose thermoelectric figure of merit $Z_{3D}T$ is enhanced relative to the corresponding constituent bulk materials. The first of these trends takes advantage of the enhanced density of states for electrons near the Fermi level due to the reduced dimensionality [11–22, 39] as we discussed in Chapters 2 and 3 for isolated quantum wells (denoted hereafter as the "quantum well approach"). The second of these utilizes the potential barriers in the superlattice structures (as realized by the barrier layers) as an effective energy filter to screen out the low energy carriers to achieve an enhanced value of the Seebeck coefficient that results from the favorable change in the functional form of the relaxation time function $\tau(E)$ as a function of energy, as a result of energy filtering [55–57] (denoted hereafter by "potential barrier approach"). In the quantum well approach, the transport coefficients for the samples, that are prepared in the form of multiple-quantum-wells, are studied along the plane of the quantum wells, whereas, in the potential barrier

approach, the transport coefficients are usually studied in a direction perpendicular to the layers of the superlattices (i.e., parallel to the superlattice growth direction).

In this chapter (and also throughout this thesis), our main focus is on the utilization of the quantum well approach to design superlattice structures that have enhanced values of $Z_{3D}T$. However, we also, occasionally, use the idea of the potential barrier approach, whenever needed (see §7.1, for example). In the quantum well approach, thick barrier layers are employed conventionally, to spatially separate the neighboring quantum wells in order to minimize the overlap of wavefunctions between them. Therefore, we have been primarily interested in the properties of the quantum wells themselves rather than the properties of the whole superlattice in this approach. As we have discussed in Chapters 2 and 3, the main strategies in the quantum well approach include : 1) enhancing the value of the Seebeck coefficient relative to that for the corresponding bulk material at a given carrier concentration due to the enhanced density of states near the band edge (within the order of k_BTs) relative to that for the corresponding bulk materials, 2) increasing the lattice thermal resistivity due to the boundary scattering of phonons at the barrier-well interfaces, and 3) enhancing the electron carrier mobility by using the δ- and modulation doping techniques. It is noted that although a fairly large enhancement (by a factor of several) is predicted for $Z_{2D}T$ relative to $Z_{3D}T$ of the corresponding bulk materials in the quantum well approach, there has been little work on predicting an equally large enhancement in $Z_{3D}T$ for the whole superlattice.

In the following sections of this chapter, we will first describe the concept of the Carrier Pocket Engineering that can be used to design superlattice structures which have large values of the thermoelectric figure of merit for the whole superlattice, denoted by $Z_{3D}T$ (§4.2). Our basic models in the quantum well approach that are developed previously (as in Chapters 2 and 3) are now properly extended to include the effect of the tunneling of the carriers between the neighboring quantum wells, using the Krönig-Penney model along the superlattice growth axis, and the parasitic thermal conduction in the barrier layers that would decrease the values of $Z_{3D}T$ but has no effect on the values of $Z_{2D}T$. It is noted that the tunneling of carriers between

the quantum wells through the barrier layers causes the broadening of the density-of-states function DOS(E) near the band edge, which leads to a 2D-to-3D dimensional transition in the thermoelectric properties. Hence, although the values of $Z_{3D}T$ for the superlattice tend to increase with decreasing thickness of the constituent layers of the superlattice as far as the effect of tunneling of the carriers between the layers is negligible, thinning the layers of the superlattice beyond some critical thickness which represents the 2D-to-3D transition of the electronic transport properties of the superlattice would actually lead to a reduction of the Seebeck coefficient and of the resultant value of $Z_{3D}T$ for a given carrier concentration due to the broadening of the DOS(E) function near the band edge. Such effects of the band edge broadening of the DOS(E) function on reduction of the values for the Seebeck coefficient, i.e., the 2D-to-3D transition of the electronic properties of the superlattice, are studied carefully in §4.4, after developing a general scheme of our modeling procedure in §4.3. It is shown, considering only the Γ-subband in the superlattice (which is found at the center of the Brillouin zone), that the band edge broadening effect that would reduce the value of $Z_{3D}T$, is not appreciable for layer thicknesses as small as 20 Å, where equal thicknesses are assumed between the GaAs and AlAs layers. The resultant $Z_{3D}T$ for such a Γ-point superlattice [GaAs(20 Å)/AlAs(20 Å)] is enhanced more than ten times relative to the corresponding $Z_{3D}T$ for bulk GaAs or AlAs at 300 K. In §4.5, we will consider the possibility of having yet another degree of freedom to enhance $Z_{3D}T$, i.e. the possibility of controlling the relative contributions from the Γ-, X- and L-valleys in the conduction band to optimize the resultant value of $Z_{3D}T$. Such an optimization process for the material properties of the superlattice is carried out by changing the parameters for the superlattice, such as the well- and barrier-layer thicknesses, the growth orientation of the superlattices, lattice strain effects at the well-barrier interfaces (see Chapter 5), and/or the spatial profile of the dopant impurities that are introduced in the superlattice, including use of δ-doping and modulation doping schemes (see Chapter 6).

One of the interesting features in the optimization process for the superlattice parameters for getting an enhanced value of $Z_{3D}T$, using the GaAs/AlAs superlat-

tices, is that we can design the structures of the superlattice in such a way that both GaAs and AlAs layers can serve as the layers for the quantum wells, i.e., the electrons in the Γ- and L-valleys are confined in the GaAs layers, whereas the electrons in the X-valleys are confined in the AlAs layers. We call the conditions giving rise to having both constituent layers contributing to the thermoelectric transport as the "Carrier Pocket Engineering condition", hereafter. Having the Carrier Pocket Engineering condition is shown to be advantageous for obtaining large values of $Z_{3D}T$ in designing superlattice structures. It is also expected that the scattering probabilities for the conduction electrons under the Carrier Pocket Engineering condition should be reduced (hence the mobility should be increased) since the electron wavefunctions for the Γ- and L-valleys are spatially separated from those for the X-valleys in real space, which reduces the probabilities of inter-valley scattering of electrons between [Γ,L]-valleys and X-valleys.

4.2 Carrier Pocket Engineering Concept

In this section, we will describe the concept of Carrier Pocket Engineering, which is used to optimize the superlattice structures for the maximum values of $Z_{3D}T$ using a given set of constituent materials. In general, such an optimization process is performed by changing some parameters that are under the control of the materials designer. For the simplest case of a one-band bulk material, the only parameter that one can vary at one's will is the chemical potential ζ. For the case of a one-band model for an isolated 2D quantum well, one obtains the freedom of changing the quantum well thickness d_W in addition to the chemical potential ζ, so that the optimum value of $Z_{2D}T$ is calculated as a function of d_W. It is then shown that the smaller the value of d_W is, the larger the optimum value of $Z_{2D}T$ in this simple model [14, 17].[†] The optimization process for such a simple case of one-band materials/systems is described in §4.2.1. The situation of our optimization process gets a little more complicated, if

[†]Here, an assumption is made that the carrier mobility μ for the quantum well is independent of the quantum well thickness d_W.

more than one (sub)band are contributing to the thermoelectric transport. However, the optimization process for such a multi-(sub)band system is still conceptually simple if one can change the relative energies for the available (sub)band edges independently. In §4.2.2, we will consider such a case of a two-band model, and derive a condition for having the largest value of $Z_{2D}T$ for an isolated quantum well in a two-band model for a given value of d_W, assuming that we can change the relative energies of the two (sub)bands freely. There, we will find that the value of $Z_{2D}T$ in two-(sub)band systems (or any dimensional ZT in the corresponding two-band systems, including $Z_{3D}T$ and $Z_{1D}T$) becomes a maximum, when the energies of these two (sub)bands are completely degenerate. Having known this condition, our problem of getting the largest value of $Z_{3D}T$ using superlattice structures is practically reduced to the problem of developing an experimental methodology to make the available (sub)bands degenerate as much as possible by changing various parameters of the superlattices, such as the values of the quantum well layer thickness (d_W) and the barrier layer thickness (d_B), and the superlattice growth orientation. More precisely, the value of the optimum $Z_{3D}T$ for a given superlattice system is a function of other properties of the superlattice as well, such as the lattice thermal conductivity and the carrier mobilities of each available (sub)band, in addition to the degeneracy condition mentioned above. Therefore, we will encounter a number of competing processes when optimizing the value of $Z_{3D}T$ using the Carrier Pocket Engineering concept. The resolution of these competing processes in order to obtain the largest value of $Z_{3D}T$ is one of the main themes in this chapter.[†]

[†]For example, if the thicknesses for the well and barrier layers that produce the desired (perfect) degeneracy among all the available (sub)bands in multi-(sub)band systems are described by a relatively small value of d_W and a relatively large value of d_B, it is not clear whether or not the value of the resultant optimized $Z_{3D}T$ will further increase by making the value of d_B smaller (so that the phonon mean free path ℓ is limited by an even smaller value of d_B). Since, in this case, we may lose the perfect degeneracy among the available (sub)bands (which tends to decrease the optimum value of $Z_{3D}T$ for a given value of κ_{ph}), but the merit of having smaller phonon mean free path ℓ (i.e., reduced value for κ_{ph}) may outweigh the demerit of not having perfect degeneracy among the available subbands. Another example of a competing process in the optimization of $Z_{3D}T$ comes from the 2D-to-3D transition in the thermoelectric properties of the superlattices. For a given value of d_W, in a system of two-dimensional superlattices, the effective electronic density of states of the carriers for the whole superlattice generally increases with decreasing thickness of the barrier layers (denoted by d_B) from a sufficiently large value to relatively small values. However, below some

The purpose of the this section is to develop a general and systematic approach to devise an implementation methodology to maximize $Z_{3D}T$ using superlattice structures. The details of the actual implementation of the Carrier Pocket Engineering concept for a given system of interest are largely dependent on the properties of the constituent materials of the given superlattice systems. Therefore, the most appropriate version of the implementation methodology for the concept has to be developed individually for each superlattice system of interest. For GaAs/AlAs superlattices (§4.3-§4.6), our main focus in the actual implementation of the concept is in the establishment of the "Carrier Pocket Engineering condition" as discussed in §4.1, where various available conduction band valleys (Γ-, X-, and L-valleys) in GaAs and AlAs are carefully engineered (by varying the thicknesses of GaAs and AlAs layers and examining representative superlattice growth orientations) in such a way that both GaAs and AlAs layers contribute to the thermoelectric transport so that the effect of parasitic thermal conduction in the barrier layers is minimized. On the other hand, in Si/Ge superlattice systems (Chapter 5 and 6), our main emphases are the utilization of "lattice strain engineering" (Chapter 5) and "doping impurity engineering" (Chapter 6) that provide additional degrees of freedom to optimize the properties (thermal, mechanical, and electronic) of the superlattice to achieve the highest value of $Z_{3D}T$. The possibilities of the application of the Carrier Pocket Engineering concept to other systems of interest, such as Bi/(111)$Pb_{1-x}Eu_xTe$ superlattices, are also discussed in Chapter 7.

4.2.1 Optimum ZT for one-band materials

The expressions for the Seebeck coefficient S, electrical conductivity σ, and electronic contribution to the thermal conductivity κ_e are very generally given in terms of the transport $\mathbf{L}^{(\alpha)}$ tensors ($\alpha = 0, 1, 2$), as summarized below. The tensor quantities corresponding to the above transport coefficients σ, S and κ_e are denoted by $\boldsymbol{\sigma}$, $\mathbf{S}$

critical thickness denoted by d_B^*, the tunneling of carriers between the neighboring quantum wells becomes appreciable and the resultant value of $Z_{3D}T$ decreases as a whole as the value of d_B is decreased below the critical value d_B^*, due to the large broadening in DOS(E) function near the band edge as we discuss in §4.4.

and $\mathbf{K}_e$, respectively, and are given by [3, 17],

$$\boldsymbol{\sigma} = \mathbf{L}^{(0)} \tag{4.1}$$

$$\mathbf{S} = -\left(\frac{1}{eT}\right)(\mathbf{L}^{(0)})^{-1}\mathbf{L}^{(1)} \tag{4.2}$$

$$\mathbf{K}_e = \left(\frac{1}{e^2T}\right)(\mathbf{L}^{(2)} - \mathbf{L}^{(1)}(\mathbf{L}^{(0)})^{-1}\mathbf{L}^{(1)}) \tag{4.3}$$

where the $\mathbf{L}^{(\alpha)}$s ($\alpha = 0,\ 1,\ 2$) are defined by,

$$\mathbf{L}^{(\alpha)}(\zeta) = e^2 \int \frac{d\mathbf{k}}{4\pi^3}\left(-\frac{\partial f}{\partial \varepsilon}\right)\tau(\mathbf{k})\,\mathbf{v}(\mathbf{k})\mathbf{v}(\mathbf{k})\,(\varepsilon(\mathbf{k}) - \zeta)^{\alpha} \tag{4.4}$$

for 3D bulk materials. In Eq. 4.4, the integration with respect to $\mathbf{k}$ extends over the entire region of the first Brillouin zone for the particular band of interest. For 2D quantum wells and 1D quantum wires, the factor $(4\pi^3)^{-1}$ in Eq. 4.4 is replaced by $(2\pi^2 d_{\mathrm{W}})^{-1}$ and $(\pi d_{\mathrm{W}}^2)^{-1}$, respectively, where d_{W} denotes the thickness of the quantum wells or wires, and the integration extends over the entire region of the corresponding two- or one-dimensional Brillouin zones, respectively. That the region of integration extends over the entire Brillouin zone implies that $\mathbf{L}^{(\alpha)}(\zeta)$ in Eq. 4.4 has contributions from all the equivalent valleys that belong to the same band index. Therefore, even if the contribution to $\mathbf{L}^{(\alpha)}(\zeta)$ from one particular valley is described by an anisotropic tensor (i.e., $L_{xx}^{(\alpha)} \neq L_{yy}^{(\alpha)}$ or $L_{xx}^{(\alpha)} \neq L_{zz}^{(\alpha)}$, when $\mathbf{L}^{(\alpha)}$ is diagonalized by rotating the coordinate axes), the final $\mathbf{L}^{(\alpha)}(\zeta)$, after summing the contributions to $\mathbf{L}^{(\alpha)}(\zeta)$ from all the equivalent valleys, may become isotropic. Therefore, we define the terms "isotropic systems" or "isotropic materials" as denoting systems that have isotropic $\mathbf{L}^{(\alpha)}(\zeta)$. For such isotropic systems, their $\mathbf{L}^{(\alpha)}$ tensors ($\alpha = 0,\ 1,\ 2$) reduce to scalar quantities and are evaluated easily in terms of the Fermi-Dirac related integrals $F_i(\zeta^*)$ ($i = -1/2,\ 0,\ 1/2,\ 1,\ \cdots$)

$$F_i \equiv F_i(\zeta^*) = \int_0^{\infty} \frac{\eta^i d\eta}{e^{(\eta-\zeta^*)} + 1}, \tag{4.5}$$

where ζ^* is the reduced chemical potential defined by ζ/k_BT, assuming a parabolic energy dispersion relation and using the constant relaxation time approximation. The explicit forms for the scalar quantities $L^{(\alpha)}$ ($\alpha = 0,\ 1,\ 2$) for the isotropic systems, where components of $\mathbf{L}^{(\alpha)}$ are given by $L_{ij}^{(\alpha)} = \delta_{ij} L^{(\alpha)}$ (δ_{ij} is Kronecker's delta), are summarized below for the case of 2D quantum wells [17]. Similar expressions for 3D bulk materials and 1D quantum wires are found in Ref. [17], and are reproduced in Appendix A.

$$L_{\rm 2D}^{(0)}(\zeta) = D_{\rm 2D}\, F_0 \equiv D_{\rm 2D}\, L_{\rm 2D}^{*(0)}(\zeta), \tag{4.6}$$

$$L_{\rm 2D}^{(1)}(\zeta) = D_{\rm 2D}\ (k_BT)\ (2F_1 - \zeta^* F_0) \equiv D_{\rm 2D}\ (k_BT)\ L_{\rm 2D}^{*(1)}(\zeta), \tag{4.7}$$

$$L_{\rm 2D}^{(2)}(\zeta) = D_{\rm 2D}\ (k_BT)^2 \left(3F_2 - 4\zeta^* F_1 + \zeta^{*2} F_0\right) \equiv D_{\rm 2D}\ (k_BT)^2\ L_{\rm 2D}^{*(2)}(\zeta), \tag{4.8}$$

where

$$D_{\rm 2D} = N \times \frac{e}{2\pi d_{\rm W}} \left(\frac{2k_BT}{\hbar^2}\right) \left\{m_{l(\rm 2D)} m_{t(\rm 2D)}\right\}^{\frac{1}{2}} \mu. \tag{4.9}$$

In Eq. 4.9, μ is the electron or hole mobility and N is the number of the equivalent valleys for the band of interest in the first Brillouin zone. We define the "star"ed quantities $L_{\rm 2D}^{*(\alpha)}(\zeta)$ ($\alpha = 0,\ 1,\ 2$) by Eqs. 4.6–4.8 for later convenience when discussing $Z_{\rm 2D}T$ for the two-band systems of isolated quantum wells (§4.2.2).

Using the above equations and assuming the freedom of changing ζ without affecting other band parameters, one can show that $Z_{\rm 2D}T$ for a one-band 2D quantum well, where there is only one band contributing to $Z_{\rm 2D}T$, is expressed in terms of the dimensionless quantity $B_{\rm 2D}$ [17],

$$B_{\rm 2D} = \frac{N}{2\pi d_{\rm W}} \left(\frac{2k_BT}{\hbar^2}\right) \left\{m_{l(\rm 2D)} m_{t(\rm 2D)}\right\}^{\frac{1}{2}} \frac{k_B^2 T \mu}{e\kappa_{\rm ph}}, \tag{4.10}$$

as

$$Z_{\rm 2D}T = \frac{B_{\rm 2D} \left(\frac{2F_1}{F_0} - \zeta^*\right)^2 F_0}{B_{\rm 2D} \left(2F_2 - \frac{4F_1^2}{F_0}\right) + 1}, \tag{4.11}$$

which is a function of the reduced chemical potential ζ^* only.

It is also easy to show that there is a one-to-one correspondence between the value of $B_{\rm 2D}$ and the optimum value for $Z_{\rm 2D}T$. The larger the value of $B_{\rm 2D}$, the larger the

optimum value of $Z_{2D}T$ when the position of the chemical potential is optimized. The same basic argument is also true for 3D bulk materials and 1D quantum wires, where the corresponding expressions for $Z_{3D}T$, $Z_{1D}T$, B_{3D} and B_{1D} as well as the expressions for various transport coefficients, for all one-, two- and three-dimensions, are summarized in Appendix A from Ref. [17].

From the above argument, when trying to find or design materials/systems with large values of ZT using various 3D, 2D and 1D one-band systems, one should look for materials that have large values of B_X where $X = 1D$, 2D or 3D for the corresponding dimensional systems, respectively, i.e., a large density-of-state effective mass, a large carrier mobility and a small lattice thermal conductivity.

4.2.2 ZT for two-band materials

The transport coefficients σ, S and κ_e for two- (or multi-) band materials are still obtained by Eqs. 4.1–4.3, if the transport tensors $\mathbf{L}^{(\alpha)}$ ($\alpha = 0, 1, 2$) in Eqs. 4.1–4.3 are interpreted as the sums of $\mathbf{L}^{(\alpha)}$s ($\alpha = 0, 1, 2$) that are evaluated for each (sub)band separately using a one-band model, where the chemical potential for each (sub)band is measured from its own (sub)band edge individually. In this subsection, we will derive a general expression for $Z_{2D}T$ for a two-band system of isolated quantum wells for a given value of d_W, and we will derive the conditions for the band offset energy ΔE^{2-1} between these two (sub)bands (see Fig. 4-1) in order to have the highest value of $Z_{2D}T$. It turns out that, in this simple two-band model of isolated quantum wells, one can obtain the highest value of $Z_{2D}T$ when the band offset energy is zero ($\Delta E^{2-1} = 0$). The proof of this condition is provided at the end of this subsection. In deriving these expressions and conditions, we will have 2D quantum well systems in mind, since these provide the basic models based on which more practical (and more complicated) models for $Z_{3D}T$ for the whole superlattice (including the effects of the parasitic thermal conduction in the barrier layers and the tunneling of the carriers through the barrier layers) are developed in subsequent sections and chapters. However, the general argument in this subsection is equally applicable to other dimensional systems (3D and 1D) with straightforward modifications of the equations

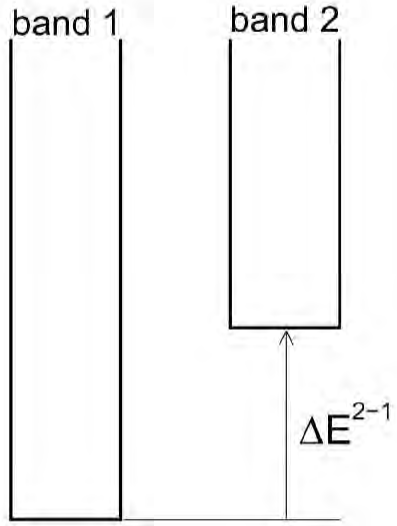

Figure 4-1: Schematic diagram to show the definition of ΔE^{2-1} in the two-band model. ΔE^{2-1} is the energy of the (sub)band edge 2 measured from the band edge of (sub)band 1.

(in most cases, switching the subscript from '2D' to '3D' or to '1D' suffices for these modifications). Assuming that the system that we are working on is isotropic in the pertinent dimension [†] (therefore the tensor quantities in Eqs. 4.1–4.3 reduce to scalars), the general expression for $Z_{2D}T$ for 2D quantum wells with two (sub)bands contributing the thermoelectric transport (two-band model) is given by,

$$Z_{2D}T = \frac{\left(L_{tot}^{(1)}\right)^2}{e^2 T \kappa_{ph} L_{tot}^{(0)} + L_{tot}^{(0)} L_{tot}^{(2)} + \left(L_{tot}^{(1)}\right)^2}, \tag{4.12}$$

where $L_{tot}^{(\alpha)}$s (α = 0, 1, 2) [scalar quantities representing the total transport-related tensor $\mathbf{L}^{(\alpha)}(\zeta)$ for a two-band material] are given by the sum of the contributions to the total $L^{(\alpha)}$ quantities from (sub)band 1 and (sub)band 2, respectively. These contributions, denoted by $L_{2D}^{(\alpha)[1]}$ and $L_{2D}^{(\alpha)[2]}$, respectively, ($L_{tot}^{(\alpha)} = L_{2D}^{(\alpha)[1]} + L_{2D}^{(\alpha)[2]}$) are calculated for each subband separately according to Eqs. 4.6–4.8. To have better perspectives for our argument here, we express $Z_{2D}T$ for the pertinent two-band

[†] i.e., isotropic in 2D in the present example.

system in terms of $L^{*(\alpha)}$ quantities ($\alpha = 0, 1, 2$) introduced in Eqs. 4.6–4.8,

$$Z_{2D}T = \frac{\left(L_{tot}^{*(1)}\right)^2}{(B_{2D}^{tot})^{-1} L_{tot}^{*(0)} + L_{tot}^{*(0)} L_{tot}^{*(2)} + \left(L_{tot}^{*(1)}\right)^2}, \tag{4.13}$$

where

$$L_{tot}^{*(\alpha)} = (1 - \gamma_D)\, L_{2D}^{*(\alpha)}(\zeta) + \gamma_D L_{2D}^{*(\alpha)}(\zeta - \Delta E^{2-1}), \tag{4.14}$$

($\alpha = 0, 1, 2$) and

$$B_{2D}^{tot} = B_{2D}^{[1]} + B_{2D}^{[2]}. \tag{4.15}$$

In Eqs. 4.14 and 4.15, ζ is chemical potential, ΔE^{2-1} is the energy of the band edge for (sub)band 2 measured from the band edge of (sub)band 1 (see Fig. 4-1), $\gamma_D = D_{2D}^{[2]} / \left(D_{2D}^{[1]} + D_{2D}^{[2]}\right)$, where $D_{2D}^{[1]}$ and $D_{2D}^{[2]}$ are calculated using Eq. 4.9 for (sub)band 1 and (sub)band 2, respectively, and $B_{2D}^{[1]}$ and $B_{2D}^{[2]}$ are similarly calculated using Eq. 4.10 for each (sub)band, respectively.

Now, in the subsequent part of this subsection, we will prove that a maximum value for $Z_{2D}T$ in this two-band model is obtained when $\Delta E^{2-1} = 0$. In doing this, we first note that Eq. 4.13 reduces to the result of the one-band model that is given by Eq. 4.11, if the two bands in question are sufficiently separated in energy ($\Delta E^{2-1} \to \pm\infty$), since whichever the band that has the higher energy than the other does not contribute to the transport in this limit.[†] Second, we note that Eq. 4.13 also reduces to the one-band limit (Eq. 4.11), when $\Delta E^{2-1} = 0$, where B_{2D} in Eq. 4.11 is given by B_{tot} in Eq. 4.15. The optimum value for $Z_{2D}T$ in this two-band degenerate limit is larger than those for the corresponding one-band limits ($|\Delta E^{2-1}| \to \infty$) since B_{2D}^{tot} is larger than both $B_{2D}^{[1]}$ and $B_{2D}^{[2]}$.

[†]It is easy to see that Eq. 4.13 reduces to Eq. 4.11, when ΔE^{2-1} goes to ∞, where B_{2D} is given by $(1 - \gamma_D)B_{2D} = B_{2D}^{[1]}$. The same is true for $\Delta E^{2-1} \to -\infty$, where B_{2D} in Eq. 4.11 is given by $\gamma_D B_{2D} = B_{2D}^{[2]}$. In order to show this, one may want to redefine the chemical potential by $\tilde{\zeta} \equiv \zeta + \Delta E^{2-1}$, so that we obtain

$$L_{tot}^{*(\alpha)} = (1 - \gamma_D)\, L_{2D}^{*(\alpha)}(\tilde{\zeta} - \Delta E^{2-1}) + \gamma_D L_{2D}^{*(\alpha)}(\tilde{\zeta}). \tag{4.16}$$

Letting $\Delta E^{2-1} \to -\infty$ in Eq. 4.16, one obtains $L_{tot}^{*(\alpha)} = \gamma_D L_{2D}^{*(\alpha)}(\tilde{\zeta})$.

The rest of the proof is concentrated on showing that $Z_{2D}T$ in the degenerate two-band limit ($\Delta E^{2-1} = 0$) is at a local extremum with respect to a small variation in ΔE^{2-1}. Hence, the optimum value (in terms of changing ζ) of $Z_{2D}T$ is a maximum (in terms of changing ΔE_{2-1}) at $\Delta E^{2-1} = 0$ as shown in Fig. 4-2. First, we assume that $\Delta E^{2-1} = 0$ and $Z_{2D}T$ for the system that we are working on is optimized with respect to chemical potential ζ, so that the derivative of $Z_{2D}T$ with respect to chemical potential ζ vanishes.

$$\delta_\zeta(Z_{2D}T) = 0$$

$$= Z_{2D}T \left\{ \frac{2\,\delta_\zeta L_{tot}^{*(1)}}{L_{tot}^{*(1)}} - \frac{(B_{2D}^{tot})^{-1}\,\delta_\zeta L_{tot}^{*(0)} + L_{tot}^{*(0)}\,\delta_\zeta L_{tot}^{*(2)} + \delta_\zeta L_{tot}^{*(0)}\,L_{tot}^{*(2)} - 2L_{tot}^{*(1)}\,\delta_\zeta L_{tot}^{*(1)}}{(B_{2D}^{tot})^{-1}\,L_{tot}^{*(0)} + L_{tot}^{*(0)}L_{tot}^{*(2)} - \left(L_{tot}^{*(1)}\right)^2} \right\}$$

$$= Z_{2D}T \left\{ \frac{2\,\delta_\zeta L_{2D}^{*(1)}}{L_{2D}^{*(1)}} - \frac{(B_{2D}^{tot})^{-1}\,\delta_\zeta L_{2D}^{*(0)} + L_{2D}^{*(0)}\,\delta_\zeta L_{2D}^{*(2)} + \delta_\zeta L_{2D}^{*(0)}\,L_{2D}^{*(2)} - 2L_{2D}^{*(1)}\,\delta_\zeta L_{2D}^{*(1)}}{(B_{2D}^{tot})^{-1}\,L_{2D}^{*(0)} + L_{2D}^{*(0)}L_{2D}^{*(2)} - \left(L_{2D}^{*(1)}\right)^2} \right\}, \tag{4.17}$$

where the last equality is obtained since $L_{tot}^{*(\alpha)} = L_{2D}^{*(\alpha)}$ ($\alpha = 1, 2, 3$) for $\Delta E^{2-1} = 0$ (see Eq. 4.14). Now, we consider the variation in $Z_{2D}T$ with respect to a small variation of ΔE^{2-1}, denoted by $\delta_\Delta(Z_{2D}T)$,

$$\delta_\Delta(Z_{2D}T)$$

$$= Z_{2D}T \left\{ \frac{2\,\delta_\Delta L_{tot}^{*(1)}}{L_{tot}^{*(1)}} - \frac{(B_{2D}^{tot})^{-1}\,\delta_\Delta L_{tot}^{*(0)} + L_{tot}^{*(0)}\,\delta_\Delta L_{tot}^{*(2)} + \delta_\Delta L_{tot}^{*(0)}\,L_{tot}^{*(2)} - 2L_{tot}^{*(1)}\,\delta_\Delta L_{tot}^{*(1)}}{(B_{2D}^{tot})^{-1}\,L_{tot}^{*(0)} + L_{tot}^{*(0)}L_{tot}^{*(2)} - \left(L_{tot}^{*(1)}\right)^2} \right\}$$

$$= Z_{2D}T\,\gamma_D \left\{ \frac{2\,\delta_\Delta L_{2D}^{*(1)}}{L_{2D}^{*(1)}} - \frac{(B_{2D}^{tot})^{-1}\,\delta_\Delta L_{2D}^{*(0)} + L_{2D}^{*(0)}\,\delta_\Delta L_{2D}^{*(2)} + \delta_\Delta L_{2D}^{*(0)}\,L_{2D}^{*(2)} - 2L_{2D}^{*(1)}\,\delta_\Delta L_{2D}^{*(1)}}{(B_{2D}^{tot})^{-1}\,L_{2D}^{*(0)} + L_{2D}^{*(0)}L_{2D}^{*(2)} - \left(L_{2D}^{*(1)}\right)^2} \right\}, \tag{4.18}$$

where $\delta_\Delta L_{2D}^{*(\alpha)}$ ($\alpha = 1, 2, 3$) in the last expression denotes $\delta_\Delta\{L_{2D}^{*(\alpha)}(\zeta - \Delta E^{2-1})\}$ ($\alpha = 1, 2, 3$), i.e., the variation in $L_{2D}^{*(\alpha)}(\zeta - \Delta E^{2-1})$ for a small variation in ΔE^{2-1}, and the second equality also follows from Eq. 4.14. Now, we would like to finish our proof here by noting $\delta_\Delta\{L_{2D}^{*(\alpha)}(\zeta - \Delta E^{2-1})\} = -\delta_\zeta\{L_{2D}^{*(\alpha)}(\zeta - \Delta E^{2-1})\}$ ($\alpha = 1, 2, 3$). There-

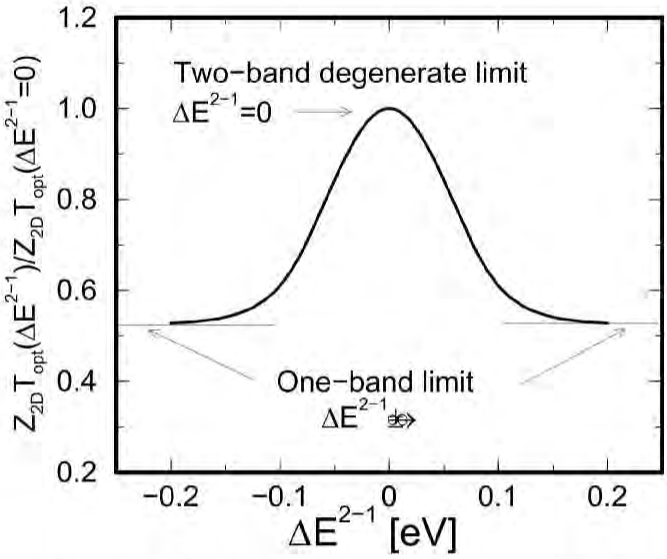

Figure 4-2: A plot to show that the optimum value for $Z_{2D}T$ in a two-band model is maximized at $\Delta E^{2-1} = 0$. The parameters for the two bands in this calculation are chosen such that $B_{2D}^{[1]} = B_{2D}^{[2]}$ and $\{(m_x m_y)^{1/2}/m\}\,(\mu/\kappa_{ph}) = 2.75$ $[\frac{\text{cm}\cdot\text{mW}}{\text{V}\cdot\text{s}\cdot\text{K}}]$. The value of $Z_{2D}T$ in the two-band model reduces to the corresponding one-band values in the limit $\Delta E^{2-1} \to \pm\infty$.

fore, comparing the last expression of Eq. 4.17 with the last expression of Eq. 4.18, we find $\delta_{\Delta}(Z_{2D}T) = 0$.

4.2.3 General guideline for the implementation of the Carrier Pocket Engineering concept using superlattice structures

Having known the condition to have the optimum values for $Z_{2D}T$ in the one-band model and that the optimum values of $Z_{2D}T$ in the two-band model is at maximum when $\Delta E^{2-1} = 0$,[†] we would like to propose general guidelines for designing superlattice structures using the Carrier Pocket Engineering concept to obtain enhanced values of $Z_{3D}T$. It is emphasized again that $Z_{3D}T$ (thermoelectric figure of merit for the whole superlattice) is the quantity we would like to ultimately optimize, though

[†]The physical reason for this is that changing the value of ΔE^{2-1} from zero is equivalent to partially changing the value of the chemical potential ζ in a one-band model from the optimum value (see §4.2.2).

we used the $Z_{2D}T$ quantity (thermoelectric figure of merit within the quantum wells) in the previous subsections to illustrate the idea of the optimization process. We will occasionally use such 2D quantities and their variations in this subsection as well, because the extension of our model for $Z_{3D}T$ for the whole superlattice is based on the models for $Z_{2D}T$ for isolated quantum wells. Thus, the knowledge acquired in the previous subsections, in studying the optimization condition for $Z_{2D}T$ for one- and two-band materials, should be also useful in considering the optimization process for $Z_{3D}T$ for the whole superlattice, at least qualitatively, as we discuss below.

The first step in implementing the superlattice design strategy using the concept of Carrier Pocket Engineering is the selection of materials for the constituent layers of the superlattice. In the discussion of the one-band model in §4.2.1, we have shown that the optimum value for ZT (either $Z_{3D}T$, $Z_{2D}T$ or $Z_{1D}T$) is closely related to the value of the corresponding B_X quantities, where X = 3D, 2D or 1D. The larger the value of B_X, the larger the optimum value of ZT for the corresponding dimensional system. Therefore, we should select the constituent materials for the superlattice among those that have large values of B_X quantities (X = 3D, 2D or 1D) (large values of the density-of-states effective mass and of the carrier mobility, and a small value of the lattice thermal conductivity). The materials that have a large value of the density-of-state mass and a large value of the carrier mobility at the same time are usually realized by both having a multiple number of equivalent valleys in the Brillouin zone for the pertinent conduction or valence band and having a large anisotropy in the constant energy ellipsoids for these valleys. The multiplicity in the number of equivalent valleys is directly proportional to the value of B_X (X = 1D, 2D, 3D) as in Eq. 4.10, and a large anisotropy in the constant energy surfaces provides large values in the following mass ratio that is also proportional to the value of B_X for a given value for the relaxation time τ,

$$\frac{(m_x m_y)^{\frac{1}{2}}}{m^*_{\rm trp}} \equiv \frac{(m_x m_y)^{\frac{1}{2}}}{2}\left(\frac{1}{m_x}+\frac{1}{m_y}\right), \tag{4.19}$$

for isolated 2D quantum wells, and

$$\frac{(m_x m_y m_z)^{\frac{1}{2}}}{m^*_{\rm trp}} \equiv \frac{(m_x m_y m_z)^{\frac{1}{2}}}{3}\left(\frac{1}{m_x}+\frac{1}{m_y}+\frac{1}{m_z}\right), \tag{4.20}$$

for 3D bulk materials. In Eqs. 4.19 and 4.20, m_x, m_y and m_z are x, y and z components of the diagonalized effective mass tensor (by rotating the coordinate axes), respectively, and $m^*_{\rm trp}$ is the directionally-averaged transport effective mass for the set of pertinent equivalent valleys. Large values of such mass ratios contribute to increasing the values of B_X (X = 1D, 2D, 3D), since the carrier mobility μ is inversely related with the transport effective mass $m^*_{\rm trp}$. Another factor that contributes to increasing the value of B_X (X = 1D, 2D, 3D) is provided by having a small value of the lattice thermal conductivity $\kappa_{\rm ph}$. Small values of $\kappa_{\rm ph}$ are usually realized in materials that consist of heavy atoms (since such crystals usually have relatively small sound velocities) or by alloying the material with atoms that have the same valence state as the host material (isoelectronic alloying) to increase the alloy scattering of phonons. However, for our goal of enhancing the value of $Z_{\rm 3D}T$ using superlattice structures, the values of lattice thermal conductivity $\kappa_{\rm ph}$ can be controlled by the structural properties of the superlattice, where the phonon mean free path ℓ may be limited by the thicknesses of the the well- and barrier- layers (denoted by $d_{\rm W}$ and $d_{\rm B}$, respectively). We denote such a technique of reducing the value of $\kappa_{\rm ph}$ through the structural design of the superlattice as "lattice engineering" or "phonon engineering" as we discuss in §4.3.3 and §5.2. Therefore, we do not specifically require, at this stage, the small "bulk" values for $\kappa_{\rm ph}$ for the constituent materials of the superlattices. Having small values of $\kappa_{\rm ph}$ in the bulk form is advantageous only in the sense that it gives us more freedom in designing superlattice structure to optimize $Z_{\rm 3D}T$ without paying too much attention to the conditions necessary to reduce the values for $\kappa_{\rm ph}$ using the lattice engineering approach.

The second step in the implementation of the concept of Carrier Pocket Engineering is to look at the higher energy valleys (or lower energy valleys for p-type materials) that do not contribute to the thermoelectric transport in the bulk form, but may be

made to contribute in the form of a superlattice as a result of the application of the Carrier Pocket Engineering concept. To make the argument concrete, we use the band energy gap diagram for bulk $Ga_{1-x}Al_xAs$ alloys as a function of Al content x (Fig. 4-4) that is found in §4.3.2. For the limiting cases of $x = 0$ (pure GaAs) and $x = 1$ (pure AlAs), we find that the conduction band minima lies at Γ- and X-points in the Brillouin zone, respectively (see Fig. 4-4). These (Γ- and X-valleys) are the valleys, in the bulk form, that contribute to the transport properties in GaAs and AlAs, respectively, with n-type doping. On the other hand, when designing superlattice structures for enhanced values of $Z_{3D}T$, we should not exclude the possibility to have all the available Γ- L- and X-valleys made to contribute to the thermoelectric transport for the whole superlattice. Shown in Table 4.1 are the bulk band parameters for GaAs and AlAs that are determined for each valley type (Γ-, L- or X-valleys) separately, together with the values of B_{3D} and the optimum values of $Z_{3D}T$, calculated using these band parameters for each valley minima.† A heuristic argument is made here by considering a situation where all the valley types in the conduction band of GaAs or AlAs are made completely degenerate in a gedanken experiment to achieve the degenerate condition discussed in §4.2.2. In this case, as we discussed in §4.2.2, the value for the total B_{3D} (denoted by B_{3D}^{tot}) is given by the sum of the contributions from all the valley types, i.e., $B_{3D}^{tot} = B_{3D}^{\Gamma} + B_{3D}^{L} + B_{3D}^{X}$. Therefore, we obtain $B_{3D}^{tot} = 0.0116$ and $B_{3D}^{tot} = 0.0030$ for GaAs and AlAs, respectively, whose corresponding values for $Z_{3D}T$ are 0.112 and 0.0313, respectively. These values are to be compared with $Z_{3D}T = 0.0085$, the value of $Z_{3D}T$ for bulk GaAs or AlAs, including only Γ- and X-valleys, respectively, which are the valleys actually contributing to the thermoelectric transport in bulk GaAs and AlAs, respectively.

There are two reasons why the values for $Z_{3D}T$ for the actual GaAs/AlAs superlattices should be enhanced relative to those for the 3D degenerate limit discussed above. The first reason is that the lattice thermal conductively κ_{ph} for the superlattice

†Note that the calculations are made for a set of the equivalent valleys (thus B_{3D} includes the factor N, which is the number of the equivalent valleys), not for a single valley of the particular band.

Table 4.1: Bulk band parameters at various symmetry points for GaAs and AlAs at 300 K [58, 59]. The values for the energy band gap for each valley are measured from the top of the valence band at the Γ-point in the Brillouin zone. See Table 4.2 for the lattice properties of these materials.

Material	GaAs	AlAs	$Ga_{0.55}Al_{0.45}As$
Parameters for Γ valley ($N = 1$)			
m^Γ/m (effective mass)	0.067	0.150	0.104
m^Γ_{trp}/m (transport mass)	0.067	0.150	0.104
μ_Γ [cm^2/V·s] (electron mobility)	3000	2200	700
E^Γ_g [eV]	1.424	2.96	1.985
$B^\Gamma_{\text{3D}} \sim \left(m^\Gamma\right)^{3/2} \frac{\mu_\Gamma}{\kappa_{\text{ph}}}$	7.96×10^{-4}	9.47×10^{-4}	1.46×10^{-3}
$Z^\Gamma_{\text{3D}}T$	0.00850	0.0101	0.0155
Parameters for L valley ($N = 4$)			
m^L_t/m (transverse component)	0.0754	0.0964	0.0849
m^L_l/m (longitudinal component)	1.9	1.9	1.9
$m^L_{\text{trp}}/m \left[\frac{m}{m^L_{\text{trp}}} = \frac{m}{3}\left(\frac{2}{m^L_t} + \frac{1}{m^L_l}\right)\right]$	0.111	0.141	0.124
μ_L [cm^2/V·s] (electron mobility)	950	320	100
E^L_g [eV]	1.705	2.41	~2.0
$B^L_{\text{3D}} \sim N\left\{\left(m^L_t\right)^2 m^L_l\right\}^{1/2} \frac{\mu_L}{\kappa_{\text{ph}}}$	6.04×10^{-3}	1.26×10^{-3}	2.89×10^{-3}
$Z^L_{\text{3D}}T$	0.0610	0.0134	0.0301
Parameters for X valley ($N = 3$)			
m^X_t/m (transverse component)	0.23	0.19	0.212
m^X_l/m (longitudinal component)	1.3	1.1	1.21
$m^X_{\text{trp}}/m \left[\frac{m}{m^X_{\text{trp}}} = \frac{m}{3}\left(\frac{2}{m^X_t} + \frac{1}{m^X_l}\right)\right]$	0.317	0.262	0.292
μ_X [cm^2/V·s] (electron mobility)	400	180	75
E^X_g [eV]	1.91	2.168	1.985
$B^X_{\text{3D}} \sim N\left\{\left(m^X_t\right)^2 m^X_l\right\}^{1/2} \frac{\mu_X}{\kappa_{\text{ph}}}$	4.81×10^{-3}	7.97×10^{-4}	3.24×10^{-3}
$Z^X_{\text{3D}}T$	0.0492	0.00852	0.0337

Table 4.2: Lattice properties for bulk GaAs, AlAs and $Ga_{0.55}Al_{0.45}As$ alloy at 300 K [58, 59].

Property at 300 K	GaAs	AlAs	$Ga_{0.55}Al_{0.45}As$
Lattice constant a [Å]	5.6533	5.6611	5.6568
Specific heat C_p [$J\,m^{-3}K^{-1}$]	1.795	1.732	1.766
Speed of sound			
$v_{[100]}$ ($\|\|$ to [100]) [$\times 10^3$m/s]	4.76	5.7	5.13
$v_{[110]}$ ($\|\|$ to [110]) [$\times 10^3$m/s]	5.26	6.2	5.64
$v_{[111]}$ ($\|\|$ to [111]) [$\times 10^3$m/s]	5.42	—	—
κ_{ph} [$W\,m^{-1}K^{-1}$]	44.05	90.91	10.91
Phonon mean free path †			
$\ell_{[100]}$ ($\|\|$ to [100]) [Å]	155	276	36
$\ell_{[110]}$ ($\|\|$ to [110]) [Å]	140	254	33

† Calculated using the kinetic formula (Eq. 2.34), where the values for C_p and the average values for v between $v_{[100]}$ and $v_{[110]}$ in this table are used for C_v and v.

is greatly reduced relative to the corresponding bulk values that are given in Table 4.2. In §4.3.3, we will see that the value of κ_{ph} for a GaAs(20 Å)/AlAs(20 Å) superlattice is 7.3 W/m·K, which is a factor of 6 and 12 reduction relative to κ_{ph} for bulk GaAs and AlAs, respectively. Therefore, if we incorporate the effect of boundary scattering of phonons into our heuristic model of 3D degenerate bands, where the new model including the effect of boundary scattering of phonons is denoted by "degenerate 3D superlattice limit" (in the sense that the electronic properties of the superlattice are still three-dimensional), the values for the "effective" B_{3D}^{tot} of our model system increase by factors of 6 and 12, i.e., $B_{3D}^{tot} = 0.07$ ($Z_{3D}T = 0.507$) and $B_{3D}^{tot} = 0.037$ ($Z_{3D}T = 0.308$) for GaAs and AlAs, respectively. The second reason that we should obtain larger values of $Z_{3D}T$ in the actual GaAs/AlAs superlattices than those in the degenerate 3D bulk limit comes from the quantum confinement effect for the conduction carriers, which tends to increase the value of the Seebeck coefficient for a given carrier concentration. To estimate the upper bound for such a quantum confinement effect for the conduction carriers, we define the "degenerate 2D superlattice limit" by the following conditions : 1) the conduction carriers are completely confined in each

conduction layers [therefore, the DOS(E) function for each subband contributing to the thermoelectric transport has a sharp step with a step height given by $\frac{(m_x m_y)^{1/2}}{\pi\hbar^2(d_W+d_B)}$], 2) the value of κ_{ph} is reduced due to the boundary scattering of phonons as we discuss in §4.3.3, and 3) all the available subbands are degenerate with one another. Since all the carriers are completely confined in the well layers in the degenerate 2D superlattice limit, we can still use Eqs. 4.10 and 4.11 to estimate the figure of merit for the whole superlattice ($Z_{3D}T$) if we replace d_W in the denominator of B_{2D} (Eq. 4.10) by $(d_W + d_B)$ and the contributions from all the available conduction band valleys to B_{2D} are summed together. We denote the B_{2D} obtained in this way for the degenerate 2D superlattice limit by B_{3D}^{*tot} and the contribution to B_{3D}^{*tot} from each available (sub)band by $B_{3D}^{*\langle\text{subband name}\rangle}$.† For (001) oriented GaAs/AlAs superlattices, since the three equivalent X-valleys in the bulk form split into one longitudinal valley (denoted by the X_l-valley) and two transverse valleys (denoted by the X_t-valleys), as we discuss in §4.5.1, we have $B_{3D}^{*tot} = B_{3D}^{*\Gamma} + B_{3D}^{*X_l} + B_{3D}^{*X_t} + B_{3D}^{*L}$ in the degenerate 2D superlattice limit. For (111) oriented GaAs/AlAs superlattices, since the four equivalent L-valleys in the bulk material split into one longitudinal valley (denoted by the L_l-valley) and three oblique valleys (denoted by the L_o-valleys), as we discuss in §4.5.2, we have $B_{3D}^{*tot} = B_{3D}^{*\Gamma} + B_{3D}^{*X} + B_{3D}^{*L_l} + B_{3D}^{*L_o}$ in the degenerate 2D superlattice limit. The values for each $B_{3D}^{*\Xi}$ ($\Xi = \Gamma$, X, X_l, X_t, L, L_l or L_o) are given in Tables 4.3 and 4.4 for the case of GaAs(20 Å)/AlAs(20 Å) superlattices (see §4.3.4). Using these values for $B_{3D}^{*\Xi}$, we obtain $B_{3D}^{*tot} = 0.210$ ($Z_{3D}T = 0.627$) for a (001) oriented GaAs(20 Å)/AlAs(20 Å) superlattice and $B_{3D}^{*tot} = 0.198$ ($Z_{3D}T = 0.600$) for (111) oriented GaAs(20 Å)/AlAs(20 Å) superlattice in the degenerate 2D superlattice limit. These values are considered to be the upper limit for the actual $Z_{3D}T$ for the superlattices that are calculated using more realistic models as developed in the next section.

†We use subscript '3D' since we are really dealing with the 3D properties (the properties for the whole superlattice) in the degenerate 2D superlattice limit. The degenerate 2D superlattice limit assumes a two-dimensional-like electronic structure for the superlattice, but the resultant transport properties in this limit are all three-dimensional. The term "2D superlattice" in the "degenerate 2D superlattice limit" should not be confused with the 2D properties (the properties within the quantum wells) which is denoted by subscript '2D'.

The third step in the implementation of the Carrier Pocket Engineering concept is the actual design of a specific structure for the system of our choice. As we mentioned in the beginning of this section, the actual design of the superlattice is closely related to the properties of the constituent materials themselves. Therefore, we will discuss the actual implementation strategies for each system of interest separately in the subsequent sections and chapters.

4.3 Implementation of the concept of Carrier Pocket Engineering using GaAs/AlAs superlattices

In this section, we will discuss an example of the actual implementation of the Carrier Pocket Engineering concept using GaAs/AlAs superlattices.

4.3.1 Choice of materials

One of the reasons why we chose GaAs/AlAs superlattice systems as the first example of the application of the Carrier Pocket Engineering concept described in §4.2 is largely due to the availability of the band parameters in this materials system. Other reasons include the feasibility of fabricating actual superlattice samples that are grown by the molecular-beam epitaxy (MBE) technique. GaAs/AlAs superlattices grown by MBE generally have high quality, whose interfaces are often controlled on an atomic scale. The fact that high quality superlattices can be grown out of GaAs and AlAs is partially due to the nearly perfect lattice matching (lattice mismatch = 0.14 %) at the interfaces between GaAs and AlAs (see Table 4.2). The possibility of having high quality samples in this system provides good opportunities for us to test experimentally the theoretical predictions that are made in this chapter. The primary purpose of our modeling $Z_{3D}T$ for GaAs/AlAs superlattices is to illustrate the idea of Carrier Pocket Engineering. The second purpose is to provide predictions of enhanced $Z_{3D}T$ in this system relative to the corresponding bulk values (GaAs and AlAs) so that one can test the idea of Carrier Pocket Engineering experimentally in

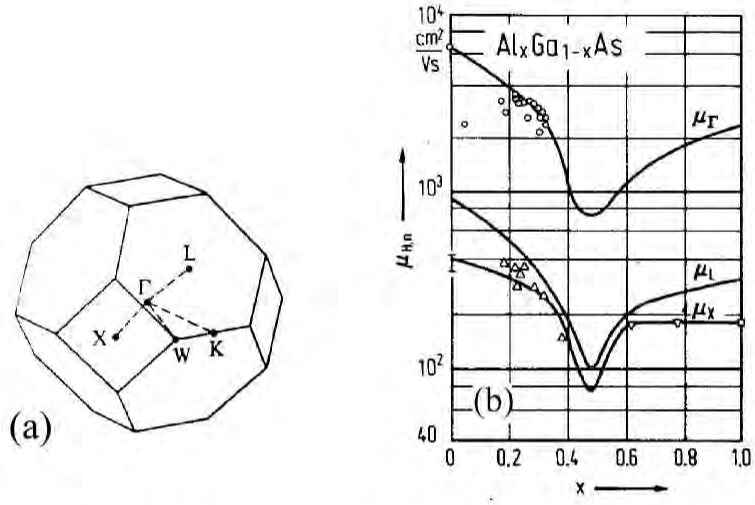

Figure 4-3: (a) The first Brillouin zone for face-centered cubic crystals. The point Γ is at the center of the zone. Various high symmetry points on the zone boundary are indicated by the indices K, L, W and X. (b) Decomposition of the electron Hall mobility into the contributions of the Γ-, L- and X-minima, deduced from the Hall measurements at atmospheric and high pressures. The figure is taken from Ref. [59] (see the references therein for more detail).

the future.

4.3.2 Summary of the bulk properties for GaAs, AlAs and $Ga_{1-x}Al_xAs$ alloys

GaAs and AlAs, or more generally most III-V materials, have a zinc-blende crystal structure whose Bravais lattice is fcc (face-centered cubic). The first Brillouin zone for the fcc lattice is shown in Fig. 4-3(a) together with the symbols Γ, L, X, K and W that denote various high symmetry points in the first Brillouin zone. In these III-V compounds, conduction band extrema lie at the Γ-, L- and X-points in the Brillouin zone. Energy band gaps at these high symmetry points are plotted as a function of Al content x in the bulk $Ga_{1-x}Al_xAs$ alloy in Fig. 4-4(a) [59]. It is noted that the energy band gaps shown in Fig. 4-4(a) are measured relative to the top of the valence band at the Γ-point in the Brillouin zone. It can been seen that the relative orders in energy among these three valley types for pure GaAs ($x = 0$) and AlAs ($x = 1$) are opposite : (from low energy to high energy) $\Gamma \rightarrow L \rightarrow X$ for GaAs and $X \rightarrow L \rightarrow \Gamma$

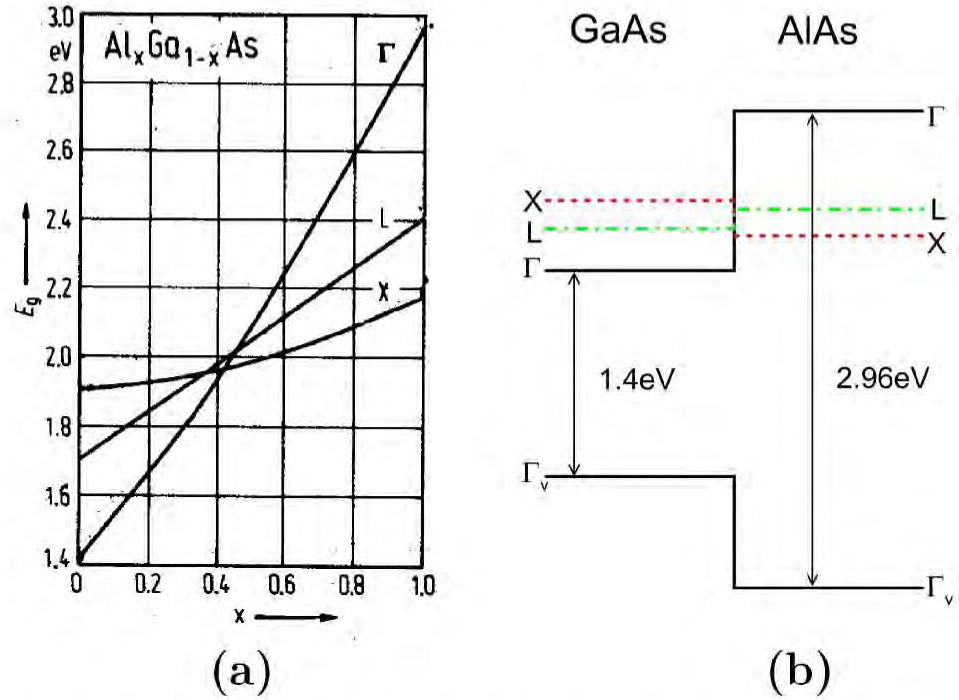

Figure 4-4: (a) Various direct (Γ-point) and indirect (L- and X-points in the Brillouin zone) energy band gaps as a function of Al content x in $Ga_{1-x}Al_xAs$ [59]. All the energy band gaps are measured from the top of the valence band edge at the Γ-point in the Brillouin zone. (b) Conduction band offsets formed for various conduction band valleys between GaAs and AlAs at the GaAs/AlAs interfaces, assuming the empirical relation, $\Delta E_c^{\Gamma} = 0.68\Delta E_g^{\Gamma}$ [58], where ΔE_c^{Γ} is the conduction band offset at the Γ-point in the Brillouin zone and ΔE_g^{Γ} is the difference in the direct (Γ-point) energy band gap between GaAs and AlAs. It is noted that the energy for the X-valley edge in the conduction band is lower in the AlAs layers than in the GaAs layers, whereas the energies for the [Γ,L]-valley edges are lower in the GaAs layers than in the AlAs layers.

for AlAs. Various electronic properties associated with these existing valley types are determined separately by various experimental and theoretical techniques, such as optical absorption/transmission spectroscopy, Hall coefficient measurement under atmospheric and high pressures [see Fig.4-3(b)] [59], and theoretical band calculations, as summarized in Table 4.1 for bulk GaAs, bulk AlAs and a $Ga_{1-x}Al_xAs$ alloy for $x = 0.45$. The bulk properties of n-type semiconductors are governed by the lowest energy conduction band extremum, i.e., the Γ-valley for GaAs and X-valleys for AlAs. Thermoelectric properties for these crystals are generally poor because of the large values of lattice thermal conductivity $\kappa_{\rm ph}$ (44 W/m·K and 91 W/m·K for GaAs and AlAs, respectively, at 300 K), and the small value of the density-of-states mass for GaAs ($m^*_\Gamma/m = 0.067$), or the small value for the carrier mobility for AlAs ($\mu_X = 180$ $cm^2/V{\cdot}s$) as shown in Tables 4.1 and 4.2. Either of these combinations (a large value for $\kappa_{\rm ph}$ and a small value for m^*_Γ, or a large value for $\kappa_{\rm ph}$ and a small value for μ_X) leads to a small value of $Z_{\rm 3D}T$ ($Z_{\rm 3D}T = 0.0085$) for these crystals as shown in Table 4.1. Enhancements in $Z_{\rm 3D}T$ would be expected if we mix GaAs with AlAs to form a solid solution of $Ga_{1-x}Al_xAs$ alloys, because the energies for the valley edges at the Γ-, L- and X-points in the Brillouin zone become very close one another for $x \approx 0.45$ in the $Ga_{1-x}Al_xAs$ alloy, as we can see in Fig. 4-4(a). Moreover, the lattice thermal conductivity $\kappa_{\rm ph}$ for $Ga_{1-x}Al_xAs$ alloys is found to be largely reduced, due to the alloy scattering of phonons, relative to the corresponding bulk values for pure GaAs and AlAs solids. Therefore, an enhancement in the figure of merit $Z_{\rm 3D}T$ in $Ga_{1-x}Al_xAs$ alloys is also expected through the reduction of the lattice thermal conductivity $\kappa_{\rm ph}$. However, it turns out that $Ga_{1-x}Al_xAs$ alloys are not good thermoelectric materials because the carrier (electron) mobility μ for $Ga_{1-x}Al_xAs$ alloys is significantly reduced due to the increased inter-valley scattering and the alloy scattering of the carriers as x (in $Ga_{1-x}Al_xAs$) approaches 0.45, where the energies of all the valley edges become very close to one another [59]. The effect of such a reduction in μ due to the inter-valley scattering in $Ga_{1-x}Al_xAs$ alloys is shown in Fig. 4-3(b), where the carrier mobilities for each valley are deduced by decomposing the experimental Hall mobilities measured under atmospheric and high pressures [59]. Because of such reductions in

μ, the resultant value for $Z_{3D}T$ for $Ga_{1-x}Al_xAs$ alloys ($x \approx 0.45$) is not so large as would be anticipated [calculated $Z_{3D}T$ at 300 K is 0.076 assuming that all the available valleys are degenerate (see Table 4.1)], despite the complete degeneracy among all the Γ-, L- and X-valley types in our model for $Ga_{1-x}Al_xAs$ alloy ($x = 0.45$), as well as the large reduction in lattice thermal conductivity κ_{ph} due to the alloy scattering of phonons. Nevertheless, it should be noted that the value for $Z_{3D}T$ obtained for $Ga_{1-x}Al_xAs$ alloys ($x \approx 0.45$) is still significantly larger than the corresponding value for $Z_{3D}T$ for pure GaAs and AlAs crystals, where only the lowest lying Γ- or X-valleys can contribute to the thermoelectric transport, respectively ($Z_{3D}T = 0.0085$ at 300 K).

Since the reduction in μ due to the inter-valley scattering and alloy scattering is the main cause for the poor thermoelectric properties in the $Ga_{1-x}Al_xAs$ alloys, the key idea to make this material system (i.e., the materials composed of GaAs and AlAs) into a good thermoelectric material with enhanced values of $Z_{3D}T$ is to implement some mechanisms that minimize the effect of inter-valley scattering and alloy scattering of the conduction electrons. In this regard, we show a conduction band offset diagram for GaAs/AlAs heterostructures in Fig. 4-4(b), and propose an idea of using superlattice structures to design good thermoelectric materials that have enhanced values of $Z_{3D}T$ relative to those of the corresponding constituent materials for the superlattice in bulk form. The conduction band offsets shown in Fig. 4-4(b) are determined by the empirical relation, $\Delta E_c^{\Gamma} = 0.68\Delta E_g^{\Gamma}$ [58], where ΔE_c^{Γ} is the conduction band offset at the Γ-point in the Brillouin zone and ΔE_g^{Γ} is the difference in the direct energy band gap between bulk GaAs and AlAs at the Γ-point in the Brillouin zone. As shown in Fig. 4-4(b), one can find that the valley minima at the X-point in the Brillouin zone lie lower in energy in AlAs than in GaAs, whereas it is in GaAs rather than in AlAs that the valley minima at the Γ- and L-points in the Brillouin zone are lower in energy. Therefore, if the superlattices are made using GaAs and AlAs constituent materials, quantum wells are formed in both the GaAs and AlAs layers, where the quantum wells formed in the GaAs layers are due to the conduction band offsets at the Γ- and L-valleys in the Brillouin zone and the

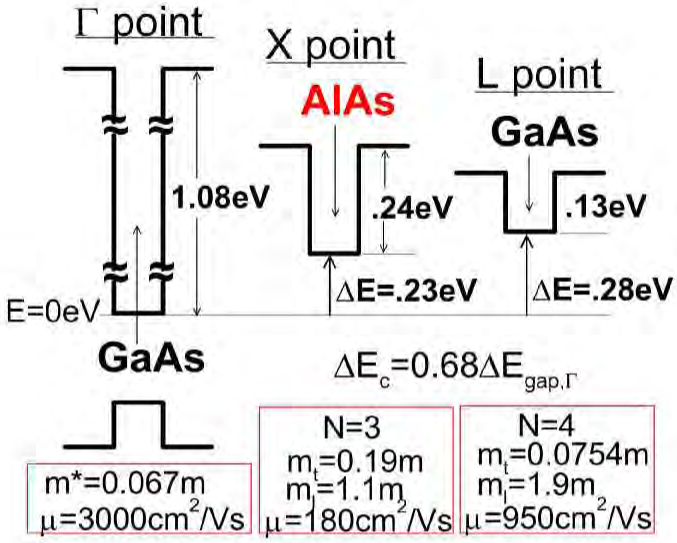

Figure 4-5: Schematic diagram to show the quantum wells formed at various high symmetry points in the Brillouin zone for the GaAs/AlAs superlattice. It is noted that the quantum wells for X-valleys and those for Γ- and L-valleys are formed in the AlAs and GaAs layers, respectively. Thus, it is suggested that the carriers in the Γ- and L-valleys are separated from those in the X-valley in real space, so that the effect of inter-valley scattering on reducing the carrier mobilities is minimized.

quantum wells formed in the AlAs layers are due to the conduction band offset at the X-valley in the Brillouin zone. It is, then, probably possible to separate the carriers in the [Γ,L]-valleys from the carriers in the X-valleys *in the real space* to minimize the inter-valley scattering of the carriers between these valleys by using GaAs/AlAs superlattice structures.[†] The quantum wells formed in this way at the Γ-, L- and X-points in the Brillouin zone are schematically drawn in Fig. 4-5 together with the values for the band offset energies, the barrier height energies for the quantum wells, and the values for the components of the diagonalized effective mass tensor and the electron carrier mobilities for the pertinent valley in the quantum well material (GaAs for Γ- and L-valleys and AlAs for X-valleys). It is noted that the subband energies for the quantum wells at the X- and L-points in the Brillouin zone are increased and decreased, respectively, by making the thickness of the AlAs layers smaller (or by making the thickness of the GaAs layers larger). Therefore, the subband energies for

[†]The effect of alloy scattering is also expected to be reduced in GaAs/AlAs superlattices relative to that in $Ga_{1-x}Al_xAs$ alloys ($x \approx 0.45$), while a new mechanism of interface scattering of the conduction electrons would be introduced in the superlattice form.

the quantum wells formed at the X- and L-points in the Brillouin zone are easily made close to each other in energy by changing the relative thicknesses of the GaAs and AlAs layers. In addition, it is also possible to have the energy of the Γ-point subband close to those of the X- and L-point subbands since the small value for the Γ-point effective mass ($m^*/m = 0.067$) suggests that the energy for the Γ-point subband can be increased significantly by making the thickness of the GaAs layers sufficiently small (of the order of 20 Å). Therefore, it is envisaged that at some specific conditions for the GaAs and AlAs layer thicknesses and the superlattice growth orientation, all the subbands derived from the Γ-, X-, and L-valleys in the Brillouin zone become nearly degenerate with one another. Therefore, there is a possibility that the "Carrier Pocket Engineering condition", as mentioned in §4.1, can be achieved in GaAs/AlAs superlattices, which leads to a significant enhancement in $Z_{3D}T$ relative to that for the corresponding bulk materials.

4.3.3 Reduction of κ_{ph} in GaAs/AlAs superlattices

It is known that the lattice thermal conductivity κ_{ph} is greatly reduced in GaAs/AlAs superlattices relative to those for bulk GaAs or AlAs [43, 60, 61]. It was found that the value for κ_{ph}, for GaAs/AlAs superlattices with equal thicknesses for the GaAs and AlAs layers ($d = d_{GaAs} = d_{AlAs}$), decreases with decreasing thickness d of the layers and κ_{ph} approaches the value of κ_{ph} for $Ga_{1-x}Al_xAs$ alloys with $x \approx 0.5$ below $d = 50$ Å [60]. At present, it is not clear whether the value for the lattice thermal conductivity for the superlattices can be smaller than that for $Ga_{1-x}Al_xAs$ alloy ($x \approx 0.5$), though some theoretical and experimental results suggest that it is indeed possible [43, 62]. It was found that the measured lattice thermal conductivities of the GaAs/AlAs superlattices ($d_{GaAs} = d_{AlAs}$) are in qualitative agreement with the kinetic formula introduced in Chapter 2 (Eq. 2.34) where the value for ℓ (phonon mean free path) is substituted by the value of d_{GaAs} (or d_{AlAs}). Listed in Table 4.2 are the parameters needed for the estimation of κ_{ph} using the kinetic formula in Eq. 2.34. Because the values for κ_{ph} obtained by this formula are different between the GaAs layers ($\kappa_{ph} = 5.97$ W/m·K for $\ell = d_{GaAs} = 20$ Å) and the AlAs layers ($\kappa_{ph} = 6.86$

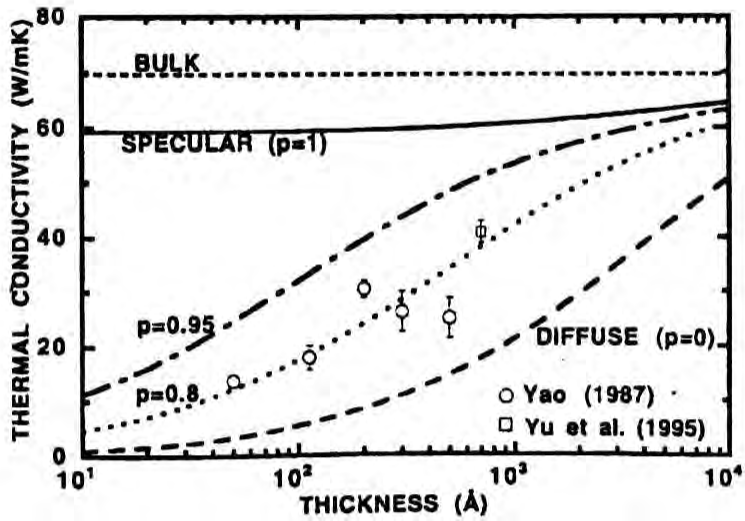

Figure 4-6: The results of the lattice thermal conductivity calculation for GaAs/AlAs superlattices, where equal thicknesses are assumed between the GaAs and AlAs layers ($d_{\mathrm{GaAs}} = d_{\mathrm{AlAs}}$). The calculation was performed by Prof. G. Chen at UCLA based on the Boltzmann transport equation [43]. Also shown in the figure are experimental results obtained for GaAs/AlAs superlattices with $d_{\mathrm{GaAs}} = d_{\mathrm{AlAs}}$ that are published elsewhere [60, 61]. The interface scattering parameter p represents the degree of specularity for phonon reflection or transmission at the GaAs/AlAs interfaces: $p = 1$ implies completely specular interfaces, whereas $p = 0$ implies totally diffuse interfaces.

W/m·K for $\ell = d_{\mathrm{AlAs}} = 20$ Å), the value for κ_{ph} for the whole superlattice should be obtained by the average of these two values for the GaAs and AlAs layers. The values for the lattice thermal conductivity for the equal thickness ($d_{\mathrm{GaAs}} = d_{\mathrm{AlAs}}$) GaAs/AlAs superlattices obtained in this way are 32.1 W/m·K, 16.0 W/m·K and 6.4 W/m·K for $d = 100$ Å, 50 Å and 20 Å, respectively. These values should be compared with the experimental results [60] or the results of more elaborate models of lattice thermal conductivity [43] as discussed below.

Recently, very detailed modeling of the lattice thermal conductivity κ_{ph} of superlattice, based on the Boltzmann transport equation, has been performed by Professor G. Chen at UCLA for GaAs/AlAs superlattices [43]. His model includes the interface scattering parameter p which represent the degree of specularity at the GaAs/AlAs interfaces for the phonon scattering : $p = 1$ implies that interface scattering at the GaAs/AlAs layer boundaries is completely specular, so that any incoming phonons to the interfaces are either transmitted or reflected without any thermalization, whereas

$p = 0$ implies totally diffuse interfaces at the GaAs/AlAs layer boundaries, so that all the phonons colliding at the interfaces are completely randomized. It has been suggested that the atomic scale roughness at the GaAs/AlAs interfaces causes a significant reduction in the lattice thermal conductivity for the whole GaAs/AlAs superlattice, while it has no significant effect on the scattering of the conduction electrons. Therefore, it is proposed that it would be possible to engineer the superlattice material in such a way that it has both a reduced value of $\kappa_{\rm ph}$ and an enhanced value of μ (electron carrier mobility) at the same time, relative to those for the corresponding bulk materials, by combining the technique of the lattice interface engineering with other techniques that would enhance the value of μ such as δ-doping and/or modulation doping techniques [43].

The values for $\kappa_{\rm ph}$ obtained by the calculation described above are shown in Fig. 4-6 [43], for equal thickness ($d_{\rm GaAs} = d_{\rm AlAs}$) GaAs/AlAs superlattices at 300 K, together with some corresponding experimental results for comparison [60, 61]. In Fig. 4-6, we find that the modeling results fit the experimental results very well for $p = 0.8$. Figure 4-6 also shows that the lattice thermal conductivities ($\kappa_{\rm ph}$) for the equal thickness superlattices ($d_{\rm GaAs} = d_{\rm AlAs}$) are reduced from the average bulk value (67.5 W/m·K) between bulk GaAs (44 W/m·K at 300 K) and bulk AlAs (91 W/m·K at 300 K) [denoted by "BULK" in Fig. 4-6] to a value of 17 W/m·K for the GaAs(100 Å)/AlAs(100 Å) superlattice (reduction by a factor of 4 relative to the above averaged value for $\kappa_{\rm ph}$ between bulk GaAs and AlAs), and $\kappa_{\rm ph}$ is further reduced to 7.3 W/m·K for the GaAs(20 Å)/AlAs(20 Å) superlattice (factor of 9 reduction relative to the averaged value between bulk GaAs and AlAs) at 300 K.

We will use the above modeling results ($p = 0.8$) for equal thickness ($d_{\rm GaAs} = d_{\rm AlAs}$) superlattices in our calculation of $Z_{\rm 3D}T$ for GaAs/AlAs Γ-point superlattices (see §4.4). In §4.5, where the optimization of the superlattice structure and the conditions for having the "Carrier Pocket Engineering condition" (see §4.2) are discussed by considering small variations in the superlattice structures from its optimum GaAs(20 Å)/AlAs(20 Å) structure, we will use $\kappa_{\rm ph} = 7.3$ W/m·K for the value of the lattice thermal conductivity for the whole superlattice in our calculation, which is the

values of $\kappa_{\rm ph}$ for the GaAs(20 Å)/AlAs(20 Å) superlattice as shown above.

4.3.4 Krönig-Penney model and calculation of $Z_{3D}T$ for the whole superlattice

We assume the following form for the energy dispersion relation for each subband that is formed in the superlattice for which we would like to calculate the various transport coefficients and the thermoelectric figure of merit for the whole superlattice $Z_{3D}T$:

$$E(k_x,\ k_y,\ k_z) = \frac{\hbar^2 k_x^2}{2m_x} + \frac{\hbar^2 k_y^2}{2m_y} + E_z(k_z), \tag{4.21}$$

where the z axis is here taken to be parallel to the superlattice growth axis, y axis is chosen in such a way that the main axis of the constant energy ellipsoid in the bulk form which is connected with the subband that we are considering now, lies in the $k_y k_z$-plane. The function $E_z(k_z)$ in Eq. 4.21 is obtained by solving a simple one-dimensional Krönig-Penney model [63] as described below. The derivation of Eq. 4.21 is straightforward and exact, if (1) the principal axes for the constant energy ellipsoid of the pertinent conduction band valley in the bulk form for the quantum well and barrier materials coincide with our choice of the xyz-coordinate axes, and (2) the quantum well and barrier materials that compose the pertinent superlattice have the same values for m_x and m_y, i.e., $m_{x,\rm W} = m_{x,\rm B}$ and $m_{y,\rm W} = m_{y,\rm B}$, where subscripts W and B denote the well and barrier layers, respectively. For the general case of $m_{i,\rm W} \neq m_{i,\rm B}$, where $i =$ 'x' or 'y', Eq. 4.21 is not exact even if the principal axes for the constant energy ellipsoids for the corresponding bulk materials coincide with our xyz-axes. The exact form of the energy dispersion relation for the superlattice in this case is given by

$$E(k_x,\ k_y,\ k_z) = \frac{\hbar^2 k_x^2}{2m_{x,\rm W}} + \frac{\hbar^2 k_y^2}{2m_{y,\rm W}} + E_z(k_x,\ k_y,\ k_z), \tag{4.22}$$

where E_z is not a function of only k_z, but a function of all k_x, k_y and k_z. In the present work, calculations of transport coefficients for GaAs/AlAs superlattices are

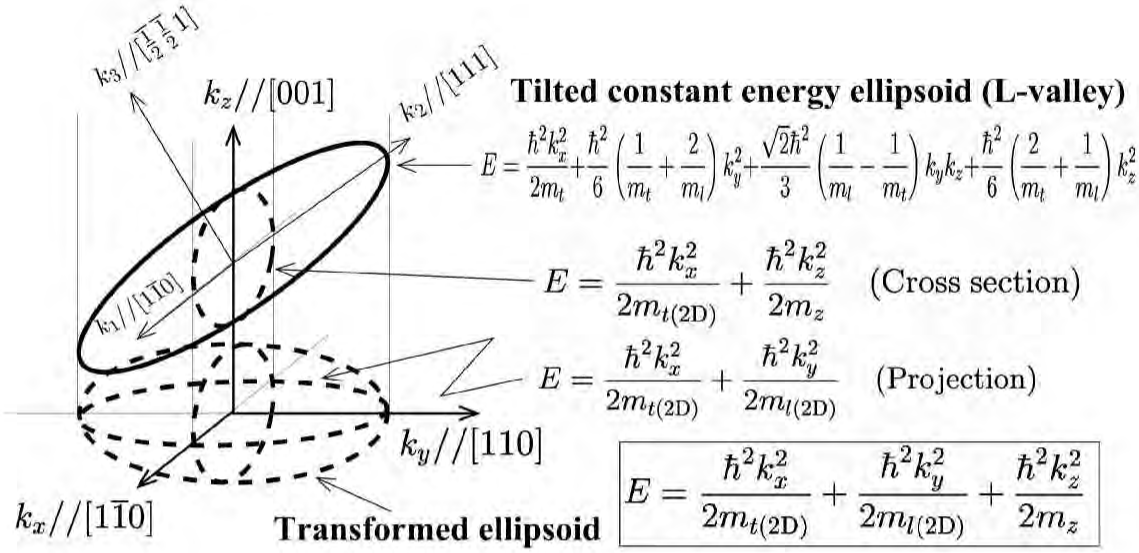

Figure 4-7: Schematic diagram to show how to construct the projected components [$m_{t(2D)}$ and $m_{l(2D)}$] and the cross-sectional component (m_z) for the effective mass tensor **M** for the L-point valley along the [111] direction in the Brillouin zone in (001) oriented GaAs/AlAs superlattices.

made using the approximate form of the energy dispersion relation Eq. 4.21, where the $E_z(k_x,\, k_y,\, k_z)$ term in Eq. 4.22 is approximated by $E_z(k_z) \equiv E_z(0,\, 0,\, k_z)$.[†]

When the principal axes of the pertinent constant energy ellipsoids do not coincide with our xyz-coordinate, but have a tilted angle with our xyz-coordinate, the tilted ellipsoids are transformed into some equivalent ellipsoids whose principal axes coincide with our xyz-axes. Such transformed ellipsoids are constructed from the projected and cross-sectional ellipses of the original tilted ellipsoid as schematically shown in Fig. 4-7. Such a transformation of the constant energy ellipsoids preserves the volume inside the ellipsoid (hence, the density of states for electron is conserved under such transformations) and provides an exact form for the electronic energy dispersion relation of the superlattice, if the electronic bound states formed in the quantum

[†]For the case of $m_{x,\mathrm{W}} \neq m_{x,\mathrm{B}}$ and/or $m_{y,\mathrm{W}} \neq m_{y,\mathrm{B}}$, the exact solution for the function $E_z(k_x,\, k_y,\, k_z)$ is still given by solving Eqs. 4.25-4.27, but the conduction band offset ΔE_c in Eq. 4.27 is replaced with

$$\left[\Delta E_c + \frac{\hbar^2 k_x^2}{2}\left(\frac{1}{m_{x,\mathrm{B}}} - \frac{1}{m_{x,\mathrm{W}}}\right) + \frac{\hbar^2 k_y^2}{2}\left(\frac{1}{m_{y,\mathrm{B}}} - \frac{1}{m_{y,\mathrm{W}}}\right)\right].$$

Therefore, for the case of $m_{x,\mathrm{W}} = m_{x,\mathrm{B}}$ and $m_{y,\mathrm{W}} = m_{y,\mathrm{B}}$, the dependence of $E_z(k_x,\, k_y,\, k_z)$ on k_x and k_y vanishes, and Eq. 4.21 becomes exact, i.e., $E_z(k_z) \equiv E_z(0,\, 0,\, k_z) = E_z(k_x,\, k_y,\, k_z)$.

wells are sufficiently isolated, i.e., if the potential barrier height for the barrier layer is infinitely high or/and the thickness of the barrier layer is infinitely large so that the overlap of the wavefunctions between the neighboring quantum wells is completely negligible. It is noted that the components of the effective mass tensor m_x, m_y and m_z that define the transformed constant energy ellipsoid (see Fig. 4-7) are given by $m_{t(2D)} = \mathrm{M}_{xx}$, $m_{l(2D)} = \mathrm{M}_{yy}$ and $m_z^{-1} = (\mathbf{M^{-1}})_{zz}$, i.e., $m_{t(2D)}$ and $m_{l(2D)}$ are obtained from the diagonal xx and yy components of the effective mass tensor $\mathbf{M}$ for the original tilted constant energy ellipsoid, respectively, and m_z is obtained by the *inverse* of the diagonal zz component of the *inverse* effective mass tensor $\mathbf{M^{-1}}$ for the original tilted constant energy ellipsoid [64].[†] Since the projected constant energy ellipse in this transformation is elongated along the k_y-axis in the k_xk_y-plane in our choice of xyz-coordinate, the values for m_x and m_y in Eq.4.21 are given by $m_{t(2D)}$ (transverse component for the 2D effective mass tensor) and $m_{l(2D)}$ (longitudinal component for the 2D effective mass tensor), respectively. In Tables 4.3 and 4.4, we summarize the formulae that relate the projected effective mass components $m_{t(2D)}$, $m_{l(2D)}$ and the cross-sectional effective mass component m_z, as discussed above, to the transverse (m_t) and the longitudinal (m_l) components of the diagonalized effective mass tensor $\mathbf{M}$ for the original tilted constant ellipsoids,[‡] for various conduction band valleys found in (001) and (111) oriented GaAs/AlAs superlattices, together with the values for $m_{t(2D)}$, $m_{l(2D)}$ and m_z that are used in the actual calculations of the thermoelectric figure of merit $Z_{3D}T$ in the later sections of this chapter.

Now, for the GaAs/AlAs superlattices, the calculation of the energy dispersion relation along the z axis [$E_z(k_z)$ in Eq. 4.21] is carried out for each conduction band valley at various high symmetry points (Γ-, X-, and L-points) in the Brillouin zone separately, using the Krönig-Penney model [63]. Requiring the conservation of the particle (electron) flux along the z axis, we apply the following boundary conditions

[†]It is noted that the mass tensors $\mathbf{M}$ and $\mathbf{M^{-1}}$ here are *not* diagonalized by rotating the coordinate axes as we did for the transport $\mathbf{L}^{(\alpha)}$ ($\alpha = 0, 1, 2$) tensors in §4.2.1.

[‡]The effective mass tensor $\mathbf{M}$ in this sentence *is* diagonalized by rotating the coordinate axes.

Table 4.3: Band parameters for various conduction band valleys in (001) oriented GaAs/AlAs superlattices. ΔE_{edge} denotes the energy for the pertinent conduction valley edge measured from the bottom of the Γ-valley in the conduction band of bulk GaAs and ΔE_c denotes the conduction band offset for the pertinent valley. X_l and X_t denote the longitudinal (main axis of the ellipsoid $\parallel$ to the superlattice growth axis) and transverse (main axis of the ellipsoid $\perp$ to the superlattice growth axis) X-valleys, respectively.

Band Parameter		Γ-valley	X_l-valley	X_t-valley	L-valley
Equations that relate $m_{t(2D)}$, $m_{l(2D)}$ and m_z to m_t and m_l					
$m_{t(2D)}$	$[M_{xx}]$	m_t	m_t	m_t	m_t
$m_{l(2D)}$	$[M_{yy}]$	m_t	m_t	m_l	$\frac{2m_l+m_t}{3}$
m_z^{-1}	$[(\mathbf{M}^{-1})_{zz}]$	m_t^{-1}	m_l^{-1}	m_t^{-1}	$\frac{1}{3}\left(\frac{1}{m_l}+\frac{2}{m_t}\right)$
Values used in the present work for GaAs [a]					
$m_{t(2D)}/m$		0.067	0.23	0.23	0.0754
$m_{l(2D)}/m$		0.067	0.23	1.3	1.292
m_z/m		0.067	1.3	0.23	0.111
Values used in the present work for AlAs [a]					
$m_{t(2D)}/m$		0.150	0.19	0.19	0.0964
$m_{l(2D)}/m$		0.150	0.19	1.1	1.299
m_z/m		0.150	1.1	0.19	0.141
Other parameters and properties					
N [b]		1	1	2	4
Conduction layer		GaAs	AlAs	AlAs	GaAs
μ_{bulk} [c]	[cm^2/V·s]	3000	180	180	950
ΔE_c [a]	[eV]	1.084	0.242	0.242	0.132
ΔE_{edge} [a]	[eV]	0	0.234	0.234	0.284
B_{3D}^* [d]		2.65×10^{-2}	4.51×10^{-3}	2.17×10^{-2}	1.57×10^{-1}
Z_{3D}^*T [e]		0.102	0.0181	0.0840	0.495

[a] Based on the data found in Ref. [58]. Values are given in terms of the free electron mass m.
[b] The number of equivalent valleys.
[c] Data taken from Ref. [59]. Also see Fig. 4-3(b).
[d] Contribution to the $B_{3D}^{*\text{tot}}$ quantity in the "degenerate 2D superlattice limit" that is defined in §4.2.3 (see p.164), for the (001) oriented GaAs(20 Å)/AlAs(20 Å) superlattice.
[e] The optimum value for $Z_{3D}T$ that corresponds to the value of B_{3D}^*, obtained using Eq. 4.11 (also see Appendix A).

Table 4.4: Band parameters for various conduction band valleys in (111) oriented GaAs/AlAs superlattices. ΔE_{edge} denotes the energy for the pertinent conduction band valley edge measured from the bottom of the Γ-valley in the conduction band of bulk GaAs and ΔE_c denotes the conduction band offset for the pertinent valley. L_l and L_o denote the longitudinal (main axis of the ellipsoid $\parallel$ to the superlattice growth axis) and oblique (main axis of the ellipsoid oblique to the superlattice growth axis) L-valleys, respectively.

Band Parameter		Γ-valley	X-valley	L_t-valley	L_o-valley
Equations that relate $m_{t(2D)}$, $m_{l(2D)}$ and m_z to m_t and m_l					
$m_{t(2D)}$	$[M_{xx}]$	m_t	m_t	m_t	m_t
$m_{l(2D)}$	$[M_{yy}]$	m_t	$\frac{2m_l+m_t}{3}$	m_t	$\frac{8m_l+m_t}{9}$
m_z^{-1}	$[(\mathbf{M^{-1}})_{zz}]$	m_t	$3\left(\frac{1}{m_l}+\frac{2}{m_t}\right)^{-1}$	m_l	$9\left(\frac{1}{m_l}+\frac{8}{m_t}\right)^{-1}$
Values used in the present work for GaAs [a]					
$m_{t(2D)}/m$		0.067	0.23	0.0754	0.0754
$m_{l(2D)}/m$		0.067	0.943	0.0754	1.697
m_z/m		0.067	0.317	1.9	0.084
Values used in the present work for AlAs [a]					
$m_{t(2D)}/m$		0.150	0.19	0.0964	0.0964
$m_{l(2D)}/m$		0.150	0.797	0.0964	1.700
m_z/m		0.150	0.262	1.9	0.108
Other parameters and properties					
N [b]		1	3	1	3
Conduction layer		GaAs	AlAs	GaAs	GaAs
μ_{bulk} [c]	[cm^2/V·s]	3000	180	950	950
ΔE_c [a]	[eV]	1.084	0.242	0.132	0.132
ΔE_{edge} [a]	[eV]	0	0.234	0.284	0.284
B^*_{3D} [d]		2.65×10^{-2}	2.77×10^{-2}	9.24×10^{-3}	1.35×10^{-1}
$Z^*_{3D}T$ [e]		0.102	0.106	0.0375	0.437

[a] Based on the data found in Ref. [58]. Values are given in terms of the free electron mass m.
[b] The number of equivalent valleys.
[c] Data taken from Ref. [59]. Also see Fig. 4-3(b).
[d] Contribution to the $B^{*\text{tot}}_{3D}$ quantity in the "degenerate 2D superlattice limit" that is defined in §4.2.3 (see p.164), for the (111) oriented GaAs(20 Å)/AlAs(20 Å) superlattice.
[e] The optimum value for $Z_{3D}T$ that corresponds to the value of B^*_{3D}, obtained using Eq. 4.11 (also see Appendix A).

at the GaAs/AlAs interfaces [65],

$$\Psi_{\mathrm{GaAs}} = \Psi_{\mathrm{AlAs}}, \tag{4.23}$$

$$\frac{1}{m_{z(\mathrm{GaAs})}} \frac{d\Psi_{\mathrm{GaAs}}}{dz} = \frac{1}{m_{z(\mathrm{AlAs})}} \frac{d\Psi_{\mathrm{AlAs}}}{dz}, \tag{4.24}$$

where Ψ_{GaAs} and Ψ_{AlAs} denote the electron wavefunction for the pertinent conduction band valley for the GaAs and AlAs layers, respectively, and $m_{z(\mathrm{GaAs})}$ and $m_{z(\mathrm{AlAs})}$ are the cross-sectional component of the effective mass tensor $\mathbf{M}$ as discussed above.

The energy dispersion relation along the z axis $[E_z(k_z)]$ under the boundary conditions given by Eqs. 4.23 and 4.24 is obtained by numerically solving (see Fig. 4-8) the following equation for E_z for a given value of k_z [63, 65],

$$\frac{1}{2}\left\{\frac{m_{z,\mathrm{W}}Q_z}{m_{z,\mathrm{B}}K_z} - \frac{m_{z,\mathrm{B}}K_z}{m_{z,\mathrm{W}}Q_z}\right\} \sinh Q_z d_{\mathrm{B}} \sin K_z d_{\mathrm{W}}$$

$$+\cosh Q_z d_{\mathrm{B}} \cos K_z d_{\mathrm{W}} = \cos k_z (d_{\mathrm{W}} + d_{\mathrm{B}}) \tag{4.25}$$

where K_z and Q_z are given by,

$$K_z = \frac{\sqrt{2m_{z,\mathrm{W}}E_z}}{\hbar}, \tag{4.26}$$

$$Q_z = \frac{\sqrt{2m_{z,\mathrm{B}}(\Delta E_c - E_z)}}{\hbar}. \tag{4.27}$$

In Eqs. 4.25-4.27, ΔE_c is the conduction band offset for the pertinent valley between the well and barrier layers, d_{W} is the thickness of the quantum well layers (the thickness of the GaAs layers for [Γ,L]-valleys, or the thickness of the AlAs layers for X-valleys), d_{B} is the thickness of the barrier layers (the thickness of the AlAs layers for [Γ,L]-valleys, or the thickness of the GaAs layers for X-valleys), $m_{z,\mathrm{W}}$ and $m_{z,\mathrm{B}}$ are the cross-sectional components of the effective mass tensor along the k_z-axis for the quantum well layers and the barrier layers, respectively, as mentioned above.

Once the energy dispersion relations for all the available subbands (Eq. 4.21) are obtained in this way, various transport coefficients are calculated using the transport

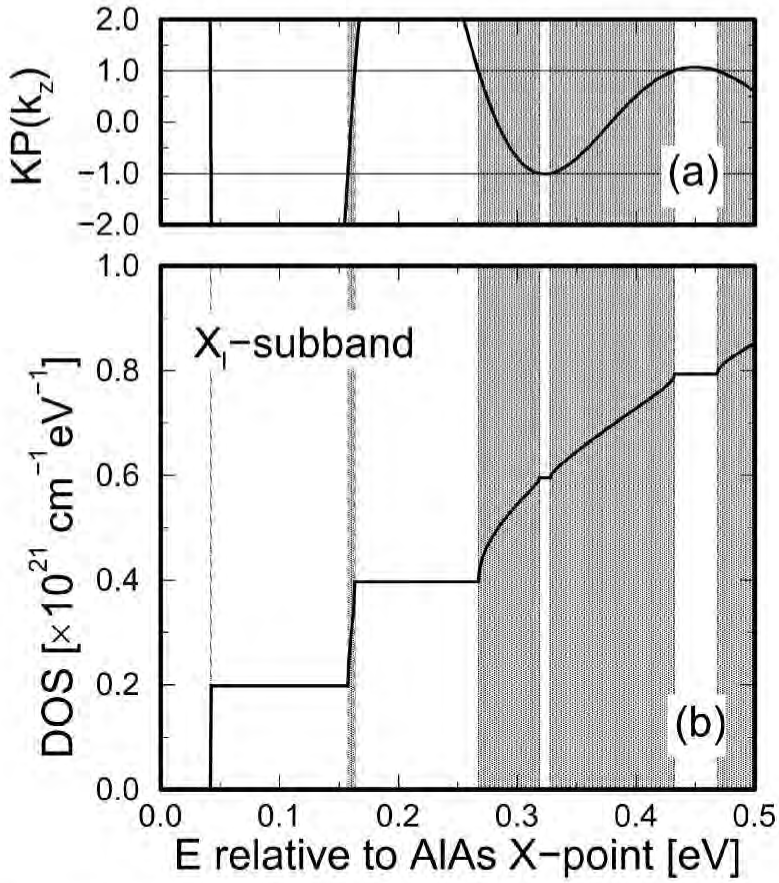

Figure 4-8: (a) Plot of the left hand side of Eq. 4.25 [denoted by KP(k_z)] as a function of energy (E_z in Eqs. 4.26 and 4.27) relative to the X-valley edge in bulk AlAs, where Eq. 4.25 is solved for the subband derived from the longitudinal X-valleys in the (001) oriented GaAs(20 Å)/AlAs(20 Å) superlattice. The shaded region denotes the range in energies where a solution of Eq. 4.25 exists. (b) The resultant electronic density of states for the X_l-subband in the (001) oriented GaAs(20 Å)/AlAs(20 Å) superlattice as a function of energy, which is given by the energy dispersion relation in the form of Eq. 4.21. It is noted that the functional form for the DOS(E) vs. E is identical with that for k_z vs. $E_z(k_z)$ in the extended zone scheme, because the electronic density of states ("per" and "as a function of" energy) for a given value of k_z does not depend on the value of k_z itself (i.e., constant with each allowed vale of k_z).

$\mathbf{L}^{(\alpha)}$ tensors as shown in Eqs. 4.1-4.4. Since the in-plane components of the transport $\mathbf{L}^{(\alpha)}$ tensors for the whole superlattice are usually isotropic, these tensors are represented by scalar quantities $L_{\mathrm{SL}}^{(\alpha)}$. The contribution from each available subband to the total $L_{\mathrm{SL}}^{(\alpha)}$ quantities for the whole superlattice [denoted by $L_{\mathrm{SL}}^{(\alpha)\mathrm{tot}}$] [†] is given by,

$$L_{\mathrm{SL}}^{(\alpha)}(\zeta) \equiv \sum_{k_z} \tilde{L}_{\mathrm{2D}}^{(\alpha)}\left(\zeta - E_z(k_z)\right) = \frac{1}{\tilde{N}_s} \sum_{k_z} L_{\mathrm{2D}}^{(\alpha)}\left(\zeta - E_z(k_z)\right), \tag{4.28}$$

where $\tilde{N}_s$ is the number of superlattice periods, $\tilde{L}_{\mathrm{2D}}^{(\alpha)}$ and $L_{\mathrm{2D}}^{(\alpha)}$ in Eq. 4.28 are given by Eqs. 4.6-4.9, but the d_{W} in the denominator of Eq. 4.9 is replaced with $\tilde{N}_s\left(d_{\mathrm{W}} + d_{\mathrm{B}}\right)$ and $\left(d_{\mathrm{W}} + d_{\mathrm{B}}\right)$, respectively, and the summation is over all the values of k_z that satisfy the periodic boundary condition $\exp\left(ik_z\tilde{N}_s(d_{\mathrm{W}} + d_{\mathrm{B}})\right) = 1$ in the extended zone scheme $(-\infty < k_z < \infty)$. In the present work, we take the limit $\tilde{N}_s \to \infty$ for ease of the numerical calculation,

$$\begin{aligned} L_{\mathrm{SL}}^{(\alpha)}(\zeta) &= \frac{1}{\tilde{N}_s \Delta k_z} \sum_{k_z} L_{\mathrm{2D}}^{(\alpha)}\left(\zeta - E_z(k_z)\right) \Delta k_z \\ &= 2 \times \frac{\left(d_{\mathrm{W}} + d_{\mathrm{B}}\right)}{2\pi} \int_0^{\infty} L_{\mathrm{2D}}^{(\alpha)}(\zeta - E_z) \frac{d\,k_z}{d\,E_z} dE_z, \end{aligned} \tag{4.29}$$

where the factor 2 in the last expression comes from the fact that $L_{\mathrm{2D}}^{(\alpha)}\left(\zeta - E_z(k_z)\right)$ is an even function of k_z, and Δk_z is the interval between the allowed k_zs that satisfy the periodic boundary condition $[\Delta k_z = \frac{2\pi}{\tilde{N}_s(d_{\mathrm{W}}+d_{\mathrm{B}})}]$. Since the inverse function of $E_z(k_z)$ has a same functional form as the density of states function DOS(E) because the number of available electronic states within an constant energy interval ΔE for a given value of the allowed k_z (that satisfies the periodic boundary condition) is constant with energy as well as with the value of k_z (see Fig 4-8), we finally obtain

---

[†] $L_{\mathrm{SL}}^{(\alpha)\mathrm{tot}} = \sum_{\text{available subband}} L_{\mathrm{SL}}^{(\alpha)}$.

the following form for the contribution to the $L_{\rm SL}^{(\alpha)\rm tot}(\zeta)$ from the pertinent subband :

$$L_{\rm SL}^{(\alpha)}(\zeta) = \frac{1}{D_{\rm SL}} \int L_{\rm 2D}^{(\alpha)}(\zeta - E) \frac{d\,{\rm DOS}(E)}{d\,E} dE, \tag{4.30}$$

where $L_{\rm 2D}^{(\alpha)}$ is obtained using the superlattice period $(d_{\rm W} + d_{\rm B})$ instead of $d_{\rm W}$ in Eq. 4.9 as we did in Eqs 4.28 and 4.29 above, ${\rm DOS}(E)$ is the density of states as a function of energy for the whole superlattice for the pertinent subband, and $D_{\rm SL}$ is the step height in the density-of-states function ${\rm DOS}(E)$ for the pertinent subband [see Fig. 4-8(b)] given by,

$$D_{\rm SL} = N \times \frac{(m_{t({\rm 2D})} m_{l({\rm 2D})})^{\frac{1}{2}}}{\pi(d_{\rm W} + d_{\rm B})\hbar^2}. \tag{4.31}$$

The formalism developed here accounts for the effect of the band edge broadening in the ${\rm DOS}(E)$ function on the resulting transport coefficients for the whole superlattice for each subband. The final $L_{\rm SL}^{(\alpha)\rm tot}(\zeta)$s for the whole superlattice are obtained by summing together the $L_{\rm SL}^{(\alpha)}$ contributions from all the subbands that are here evaluated separately.

Finally, the resulting thermoelectric properties for the whole superlattice, for various superlattice periods and superlattice growth directions, are calculated as a function of carrier concentration and temperature, using Eqs. 4.1-4.4 (see §4.4 and §4.5).

4.4 $Z_{\rm 3D}T$ for the Γ-point superlattices

In this section, we will show the result of our calculation including only the Γ-point subband (we denote the superlattice with this assumption as the Γ-point superlattice, hereafter). Such investigations are important because : (1) the transport properties of most GaAs/AlAs superlattices are determined by the Γ-point subband, since the lowest lying subband in these superlattices is usually the Γ-subband, if the thickness of the GaAs layer is larger than 30 Å, and (2) we are also interested in how much enhancement in $Z_{\rm 3D}T$ we can get relative to that of the corresponding constituent bulk materials only due to the effect of the quantum confinement of carriers to enhance the value of S and the effect of boundary scattering of phonons to reduce the

lattice thermal conductivity κ_{ph}, i.e., without having the "Carrier Pocket Engineering condition" that is discussed in §4.1.

Shown in Fig. 4-9(a) is the calculated density of states for the Γ-point subband for GaAs/AlAs superlattices with equal thicknesses for the GaAs and AlAs layers. We find that the density of states near the band edge increases significantly with decreasing superlattice period ($d_{GaAs} + d_{AlAs}$) from 160 Å to 40 Å [see the inset of Fig. 4-9(a)]. It is noted that the broadening of the Γ-point subband becomes comparable to the thermal energy at room temperature (26 meV) for GaAs(20 Å)/AlAs(20 Å) superlattice. Since the broadening effect in the DOS(E) function near the band edge becomes appreciable for superlattice periods ($d_{GaAs} + d_{AlAs}$) below 40 Å, the resultant Seebeck coefficient for a given carrier concentration ($n = 10^{18}$ cm^{-3}) has a peak around ($d_{GaAs} + d_{AlAs}$) = 40 Å [see Fig 4-9(b)]. The decrease in S with decreasing ($d_{GaAs} + d_{AlAs}$) below 40 Å is interpreted as the result of a 2D-to-3D transition of the electronic transport properties of GaAs/AlAs superlattices that results from the increased carrier tunneling between the adjacent quantum wells formed at the Γ-point in the Brillouin zone (within the GaAs layers in real space) for GaAs/AlAs superlattices.

The thermoelectric figure of merit for the whole superlattice $Z_{3D}T$ for GaAs/AlAs Γ-point superlattices are calculated by combining the data for κ_{ph} as a function of the thicknesses of the GaAs and AlAs layers ($d_{GaAs} = d_{AlAs}$) that are discussed in §4.3.3 [43] and the models for the transport coefficients that are developed in §4.3.4. Values of $\Delta E_c = 1$ eV and $\mu = 3000$ cm^2/V·s are used for the conduction band offset at Γ-valley and for the carrier mobility, respectively, for the GaAs/AlAs Γ-point superlattices. The results thus obtained for $Z_{3D}T$ normalized to the corresponding value for bulk GaAs at 300 K [denoted by $(ZT)_{bulk}$] are plotted in Fig. 4-10 as a function of d_W, where the value of $Z_{3D}T$ is optimized with respect to the chemical potential ζ for each value of d_W. It is noted that $(ZT)_{bulk}$ for bulk GaAs is as small as 0.0085 at the optimum carrier concentration ($n = 1.5\times10^{18}$ cm^{-3}), whereas $Z_{3D}T$ for the GaAs(20 Å)/AlAs(20 Å) Γ-point superlattice is more than 0.1 at the optimum carrier concentration ($n = 1.5\times10^{18}$ cm^{-1}) as shown by the solid line in Fig. 4-15

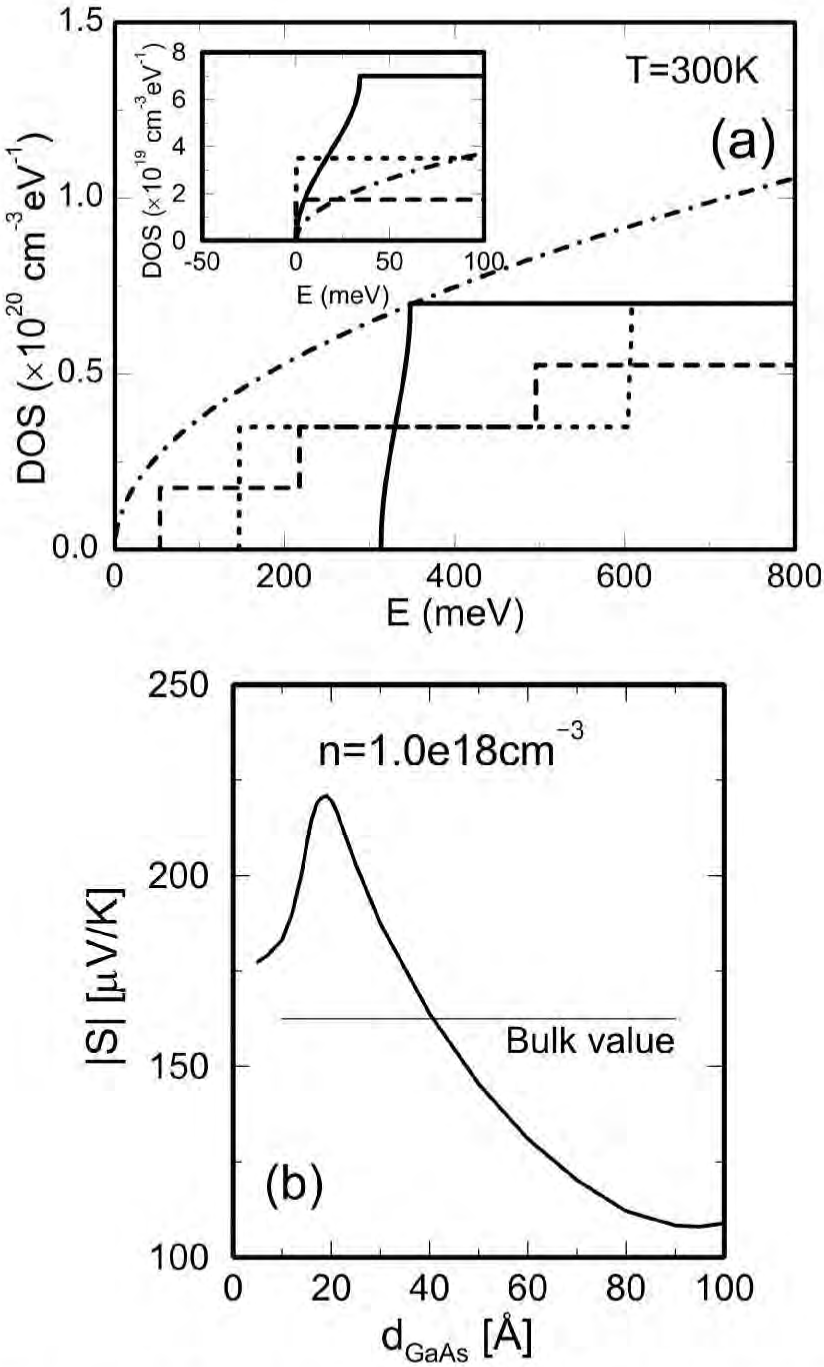

Figure 4-9: (a) Density of states for equal thickness ($d_{\mathrm{GaAs}} = d_{\mathrm{AlAs}}$) GaAs/AlAs Γ-point superlattices as well as for bulk GaAs (dash-dotted line). The quantum well (or barrier layer) thickness, denoted as d_{W} or d_{GaAs}, is chosen to be 20 Å (solid line), 40 Å (short dashed line), and 80 Å (long dashed line). In the inset, each graph is shifted in energy to show the details of the band edge structure. (b) Calculated absolute values for the Seebeck coefficient for the GaAs(20 Å)/AlAs(20 Å) Γ-point superlattice as a function of the quantum well layer thickness d_{W} ($d_{\mathrm{W}} = d_{\mathrm{GaAs}}$). The calculation was made for a fixed value for the carrier concentration $n = 1{\times}10^{18}$ cm^{-3} for the whole superlattice. Also shown in the figure is the bulk (GaAs) value for $|S|$ using the same basic model assuming $n = 1{\times}10^{18}$ cm^{-3}.

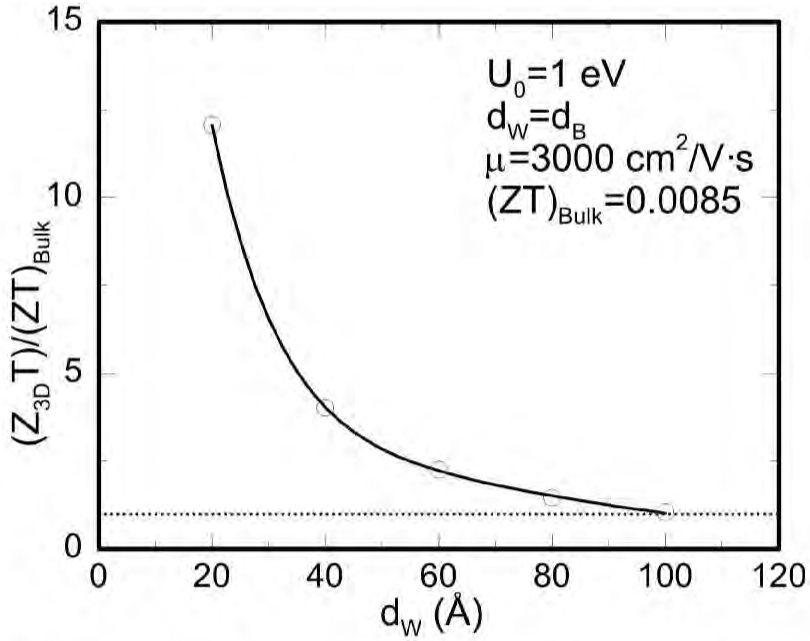

Figure 4-10: Plot of the value of the optimum (with respect to the chemical potential ζ) $Z_{3D}T$ at 300 K, normalized by the corresponding bulk value ($Z_{3D}T = 0.0085$) for GaAs, for equal thickness ($d_{GaAs} = d_{AlAs}$) GaAs/AlAs Γ-point superlattices as a function of the quantum well layer thickness d_W ($d_W = d_{GaAs}$). The calculations shown here are made for the conduction band offset $\Delta E_c = 1$ eV and the (electron) carrier mobility $\mu = 3000$ cm^2/V·s, using the constant relaxation time approximation.

(§4.5.2), which is more than a factor of ten enhancement in $Z_{3D}T$ relative to the corresponding value for bulk GaAs. It is noted that an overall enhancement in $Z_{3D}T$ in GaAs(20 Å)/AlAs(20 Å) Γ-point superlattices is realized due to a combination of the effect of the interface scattering of phonons to reduce κ_{ph}, which account for a factor of about six enhancement in $Z_{3D}T$ relative to the corresponding bulk value, and the effect of quantum confinement of carriers to enhance S, which account for a factor of about two enhancement in the overall $Z_{3D}T$ relative to the corresponding bulk value.

4.5 $Z_{3D}T$ under the Carrier Pocket Engineering condition

In this section, the concept of Carrier Pocket Engineering is applied to GaAs/AlAs superlattices including the contributions from all the Γ-, L- and X-subbands. Then, the optimum structures and orientation for the GaAs/AlAs superlattices are determined to obtain the largest value of $Z_{3D}T$ in this system. The temperature dependence of the resultant values of $Z_{3D}T$ for the (001) and (111) oriented GaAs/AlAs superlattices, and the conditions for having the "Carrier Pocket Engineering condition" (see §4.1) in these superlattices are also discussed in some detail.

4.5.1 $Z_{3D}T$ for the (001) oriented GaAs/AlAs superlattices — optimization of the layer thicknesses —

Shown in Figs. 4-11–4-13 are the calculated density of states for all the available subbands for (001) oriented GaAs(20 Å)/AlAs(20 Å), GaAs(30 Å)/AlAs(20 Å) and GaAs(20 Å)/AlAs(30 Å) superlattices, respectively. By making a superlattice in this orientation, three of the equivalent valleys at the X-point in the Brillouin zone experience a splitting in their valley degeneracy between one longitudinal (main axis of the ellipsoid ∥ to the superlattice growth axis) and two transverse (main axis of the ellipsoid ⊥ to the superlattice growth axis) valleys, denoted by X_l and X_t, respectively. The resultant subbands derived from these valleys are also denoted as X_l- and X_t-subbands, respectively. In Fig. 4-11, we find that the Γ-, X_t- and L-subbands lie very close in energy in the GaAs(20 Å)/AlAs(20 Å) superlattice, and that the energy for the X_l-subband edge is about 50 to 60 meV lower than those for the other subbands. Such a situation doesn't appear to be desirable in obtaining a large value of $Z_{3D}T$, since the mobility for the X-point carriers is relatively low (μ_X = 180 cm^2/V·s at 300 K) compared to the mobilities for the carriers in other subbands (μ_Γ = 3000 cm^2/V·s and μ_L = 950 cm^2/V·s at 300 K) as we discussed in §4.3.2. Nevertheless, we find that, among all the structures considered in this subsec-

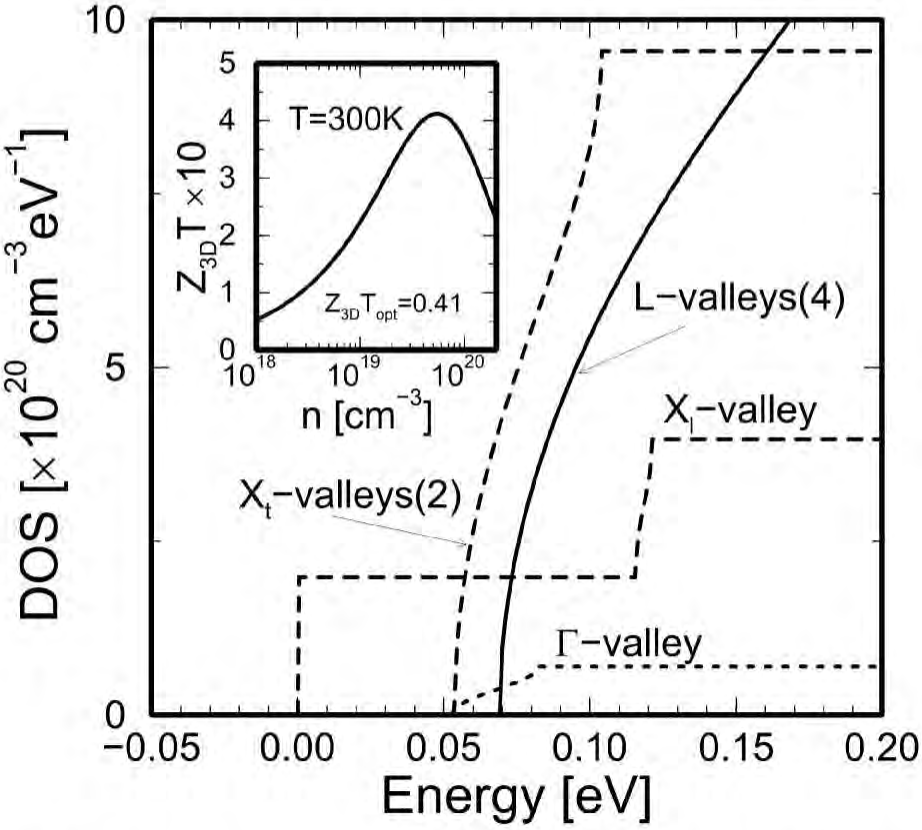

Figure 4-11: Density of states for electrons (DOS) for a (001) oriented GaAs(20 Å)/AlAs(20 Å) superlattice calculated for various subbands derived from Γ-, X_l-, X_t- and L-valleys, as indicated in the figure. The number inside the parentheses denotes the number of equivalent valleys that are degenerate in energy. Therefore, the DOS for X_t-valleys shown here, for example, includes contributions from two equivalent X_t-valleys. The inset shows a plot for the calculated $Z_{3D}T$ as a function of carrier concentration n for this superlattice at 300 K. The position of the chemical potential ζ that gives the optimum value of $Z_{3D}T$ (denoted as $Z_{3D}T_{opt}$) is $\zeta = 0.083$ eV on the main scale.

tion for the (001) oriented superlattices (see Figs. 4-11–4-13), the highest $Z_{3D}T$ occurs in the GaAs(20 Å)/AlAs(20 Å) superlattice ($Z_{3D}T = 0.41$ at 300 K for $n = 5\times10^{19}$ cm^{-3}). Also shown in the insets of Figs. 4-11–4-13 are the calculated values of $Z_{3D}T$ as a function of carrier concentration for each superlattice structure at 300 K. In Figs. 4-11–4-13, we find that the relative energies for the Γ-, X_l-, X_l- and L-subband edges are very sensitive to the thicknesses of the GaAs and AlAs layers for the superlattice. For example, for the GaAs(30 Å)/AlAs(20 Å) superlattice (Fig. 4-12), the lowest lying subband is found to be the Γ-subband. Since the Γ-subband has

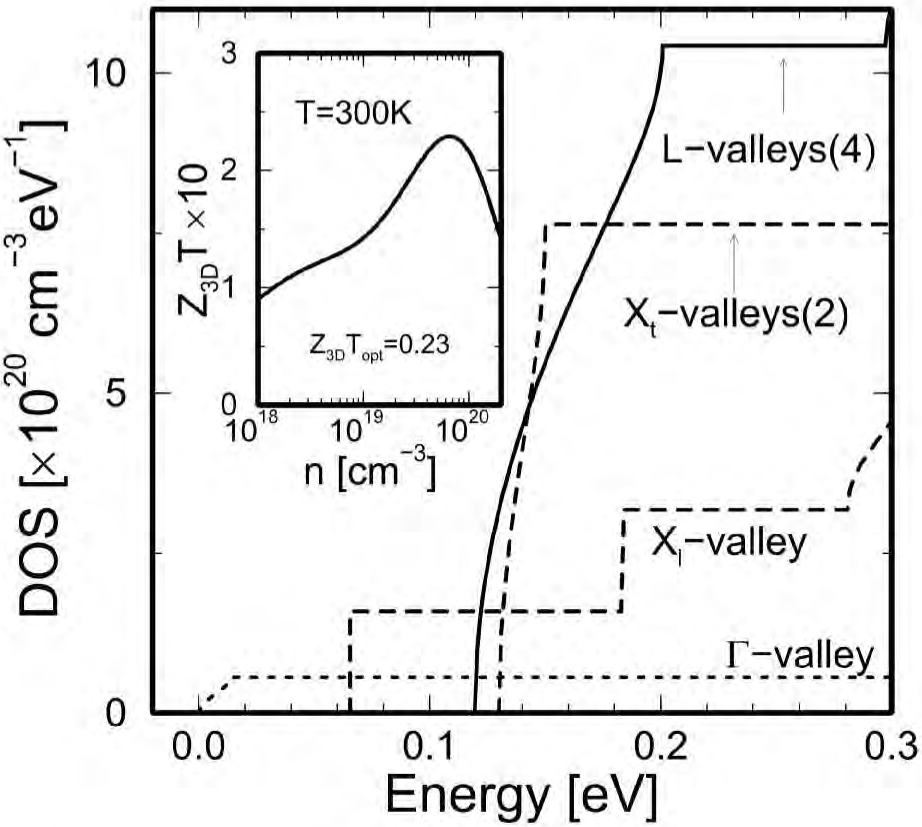

Figure 4-12: Density of states for electrons (DOS) for a (001) oriented GaAs(30 Å)/AlAs(20 Å) superlattice calculated for various subbands derived from Γ-, X_l-, X_t- and L-valleys, as indicated in the figure. The number inside the parentheses denotes the number of equivalent valleys that are degenerate in energy. Therefore, the DOS for X_t-valleys shown here, for example, includes contributions from two equivalent X_t-valleys. The inset shows a plot for the calculated $Z_{3D}T$ as a function of carrier concentration n for this superlattice at 300 K. The position of the chemical potential ζ that gives the optimum value of $Z_{3D}T$ (denoted as $Z_{3D}T_{opt}$) is $\zeta = 0.154$ eV on the main scale.

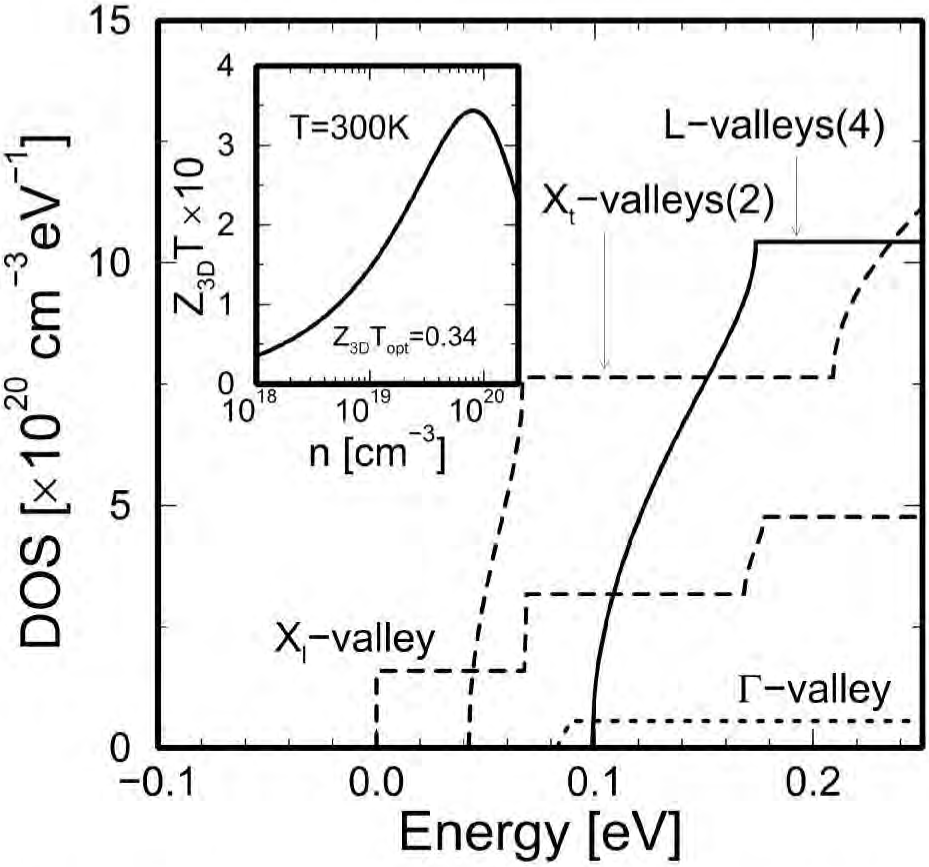

Figure 4-13: Density of states for electrons (DOS) for a (001) oriented GaAs(20 Å)/AlAs(30 Å) superlattice calculated for various subbands derived from Γ-, X_l-, X_t- and L-valleys, as indicated in the figure. The number inside the parentheses denotes the number of equivalent valleys that are degenerate in energy. Therefore, the DOS for X_t-valleys shown here, for example, includes contributions from two equivalent X_t-valleys. The inset shows a plot for the calculated $Z_{3D}T$ as a function of carrier concentration n for this superlattice at 300 K. The position of the chemical potential ζ that gives the optimum value of $Z_{3D}T$ (denoted as $Z_{3D}T_{opt}$) is $\zeta = 0.107$ eV on the main scale.

a relatively large carrier mobility (μ_Γ = 3000 cm^2/V·s) and a relatively small density of states mass (m^*_Γ/m = 0.067), the behavior of the calculated value of $Z_{3D}T$ for this superlattice is similar to those for the corresponding Γ-point superlattice for relatively small carrier concentrations ($n < 1.5\times10^{18}$ cm^2/V·s). For larger carrier concentrations ($n > 3\times10^{18}$ cm^2/V·s), the calculated values of $Z_{3D}T$ for this superlattice are not as large as those for the GaAs(20 Å)/AlAs(20 Å) superlattice, because the contribution from the Γ-subband, which has relatively small values for the Seebeck coefficient at larger carrier concentrations ($n > 3\times10^{18}$ cm^2/V·s), is rather strong. In the case of the GaAs(20 Å)/AlAs(30 Å) superlattice (Fig. 4-13), we find that the energy separation between the [X_l,X_t]-subbands and the [Γ,L]-subbands becomes larger compared to that for the GaAs(20 Å)/AlAs(20 Å) superlattice. Therefore, we observe a moderate decrease in $Z_{3D}T$ for all carrier concentrations below 1.5×10^{20} cm^{-3} in this superlattice relative to the corresponding $Z_{3D}T$s for the GaAs(20 Å)/AlAs(20 Å) superlattice [see the long-dashed line in Fig. 4-15 (§4.5.2)].

4.5.2 $Z_{3D}T$ for the (111) oriented GaAs/AlAs superlattices — optimization of the superlattice growth direction —

It is a crucial question whether the heavy doping condition ($n > 10^{19}$ cm^{-3}), which is required in obtaining the high predicted value of $Z_{3D}T$ ($Z_{3D}T$ = 0.4) at 300 K in the (001) oriented GaAs/AlAs superlattices, is attainable in an actual GaAs/AlAs superlattice. It is known that GaAs can be doped to be a p-type material as heavily as $p = 10^{20}$ cm^{-3} using C (carbon) as a dopant. However n-type doping in GaAs is achieved only up to $n = 5\times10^{18}$ cm^{-3} using Si as a dopant [59]. Therefore, it is of interest to investigate superlattices that are grown in an orientation other than along the (001) direction which may have higher values for the thermoelectric figure of merit $Z_{3D}T$ than those for the (001) oriented GaAs/AlAs superlattices at moderate carrier concentrations ($n = 5\times10^{18}$ cm^{-3}). To address this issue, we have explored various structures of (111) oriented GaAs/AlAs superlattices. In (111) oriented GaAs/AlAs superlattices, four equivalent L-valleys in the bulk form experience the lifting of valley

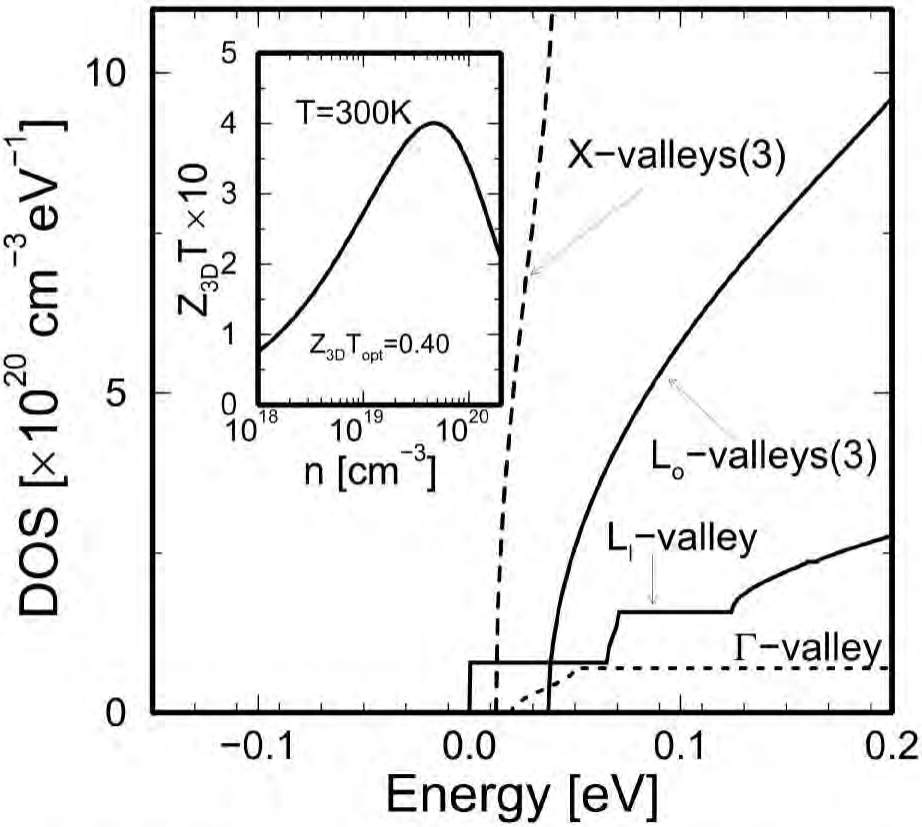

Figure 4-14: Density of states for electrons (DOS) for a (111) oriented GaAs(20 Å)/AlAs(20 Å) superlattice calculated for various subbands derived from Γ-, X-, L_l- and L_o-valleys, as indicated in the figure. The number inside the parentheses denotes the number of equivalent valleys that are degenerate in energy. Therefore, the DOS for L_o-valleys shown here, for example, includes contributions from three equivalent L_o-valleys. The inset shows a plot for the calculated $Z_{3D}T$ as a function of carrier concentration n for this superlattice at 300 K. The position of the chemical potential ζ that gives the optimum value of $Z_{3D}T$ (denoted as $Z_{3D}T_{opt}$) is $\zeta = 0.042$ eV on the main scale.

degeneracy in the superlattice form. Thus, we denote the L-valley(s) whose main axis is parallel and oblique to the superlattice growth direction as (longitudinal) L_l-valley and (oblique) L_o-valleys, respectively, and the resultant subbands as L_l- and L_o-subbands, respectively. On the other hand, three equivalent X-valleys in the bulk form remain equivalent to one another in the (111) oriented superlattices as well. Therefore, the subband derived from the X-valleys (denoted by the X-subband) consists of three equivalent (or degenerate) X-valleys in the superlattice form.

Shown in Fig. 4-14 is the calculated density of states vs. energy for a (111) oriented GaAs(20 Å)/AlAs(20 Å) superlattice. In this structure, since all the Γ-, X- and L-

subbands lie very close in energy, larger values for $Z_{3D}T$ relative to those for the (001) oriented superlattices are expected at lower carrier concentrations ($\sim 5 \times 10^{18}$ cm^{-3}). The calculated $Z_{3D}T$ for the (111) oriented GaAs(20 Å)/AlAs(20 Å) superlattice is plotted as a function of the carrier concentration in the inset of Fig. 4-14, and this $Z_{3D}T$ can be compared with the results for the various (001) oriented superlattices considered in the previous subsection in Fig. 4-15 (long-dash-short-dashed curve). It turns out that the (111) oriented GaAs(20 Å)/AlAs(20 Å) superlattice yields not only as high a $Z_{3D}T$ value as that for the (001) oriented GaAs(20 Å)/AlAs(20 Å) superlattice at the optimum carrier concentrations ($n \sim 5 \times 10^{19}$ cm^{-3} at 300 K), but also a greatly enhanced value for $Z_{3D}T$ ($Z_{3D}T = 0.2$) relative to that for the (001) oriented GaAs(20 Å)/AlAs(20 Å) superlattice ($Z_{3D}T = 0.14$) at moderate carrier concentrations ($\sim 5 \times 10^{18}$ cm^{-3}).

4.5.3 Carrier Pocket Engineering condition in GaAs/AlAs superlattices

We have concluded that a GaAs(20 Å)/AlAs(20 Å) superlattice would provide the optimum structure for obtaining enhanced values of $Z_{3D}T$ in both (001) and (111) oriented superlattices in §4.5.1 and §4.5.2. We have also seen, in §4.5.1, how the relative energies for the Γ-, X_t-, X_l- and L-subbands and the resultant density-of-states function for electrons [DOS(E)] would change as we deviate from the optimum GaAs(20 Å)/AlAs(20 Å) structure to a GaAs(30 Å)/AlAs(20 Å) or a GaAs(20 Å)/AlAs(30 Å) structure in the (001) oriented superlattice system. It is also of our interest to see how the relative energies for the Γ-, X-, L_l- and L_o-subbands and their resultant DOS(E) functions would change in the (111) oriented superlattices, as the structure of the superlattice is changed from the optimum GaAs(20 Å)/AlAs(20 Å) structure to a GaAs(30 Å)/AlAs(20 Å) or a GaAs(20 Å)/AlAs(30 Å) structure. Shown in Figs.4-16 and 4-17 are the calculated density of states for electrons [DOS(E)] for the (111) oriented GaAs(30 Å)/AlAs(20 Å) and GaAs(20 Å)/AlAs(30 Å) superlattices, respectively. The resultant values for $Z_{3D}T$ calculated assuming these structures

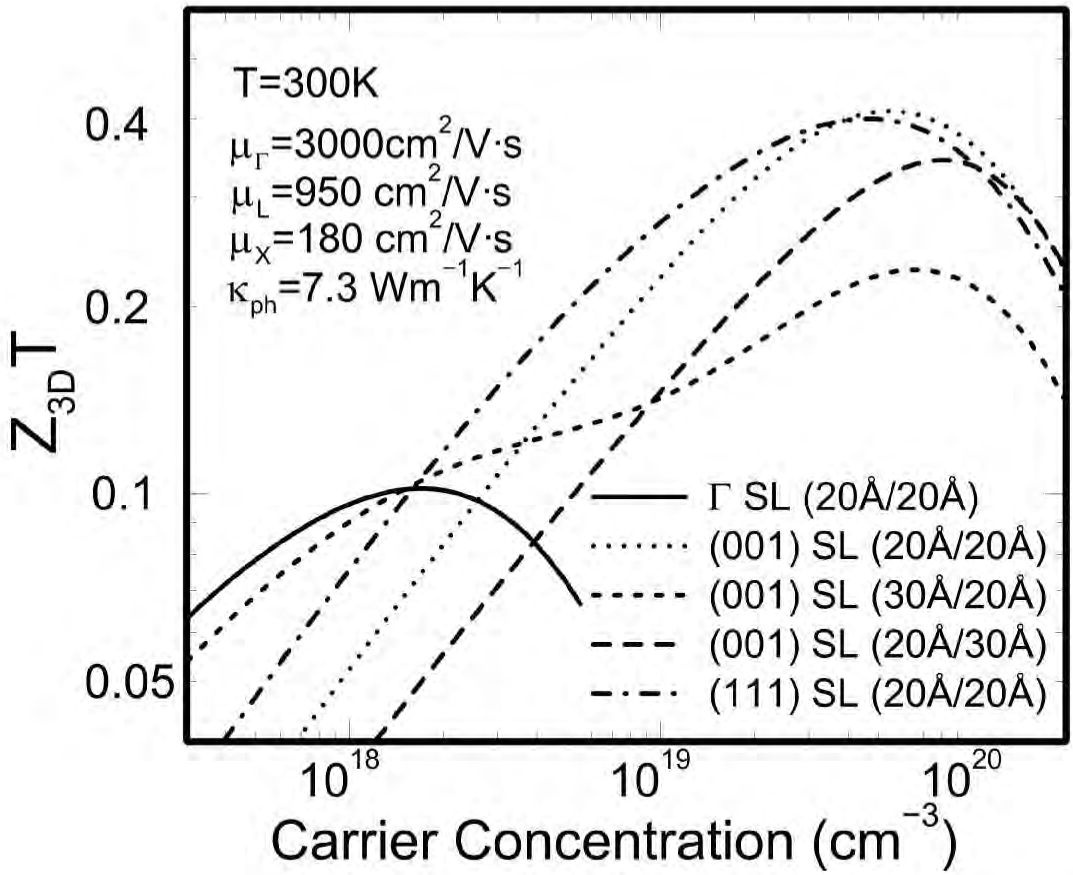

Figure 4-15: Calculated values of $Z_{3D}T$ as a function of carrier concentration for a (001) oriented GaAs(20 Å)/AlAs(20 Å) superlattice (dotted curve), a (001) oriented GaAs(30 Å)/AlAs(20 Å) superlattice (short-dashed curve), a (001) oriented GaAs(20 Å)/AlAs(30 Å) superlattice (long-dashed curve), and a (111) oriented GaAs(20 Å)/AlAs(20 Å) superlattice (long-dash-short-dashed curve). The solid curve denotes $Z_{3D}T$ calculated assuming only carriers in the Γ-point subband for a GaAs(20 Å)/AlAs(20 Å) superlattice.

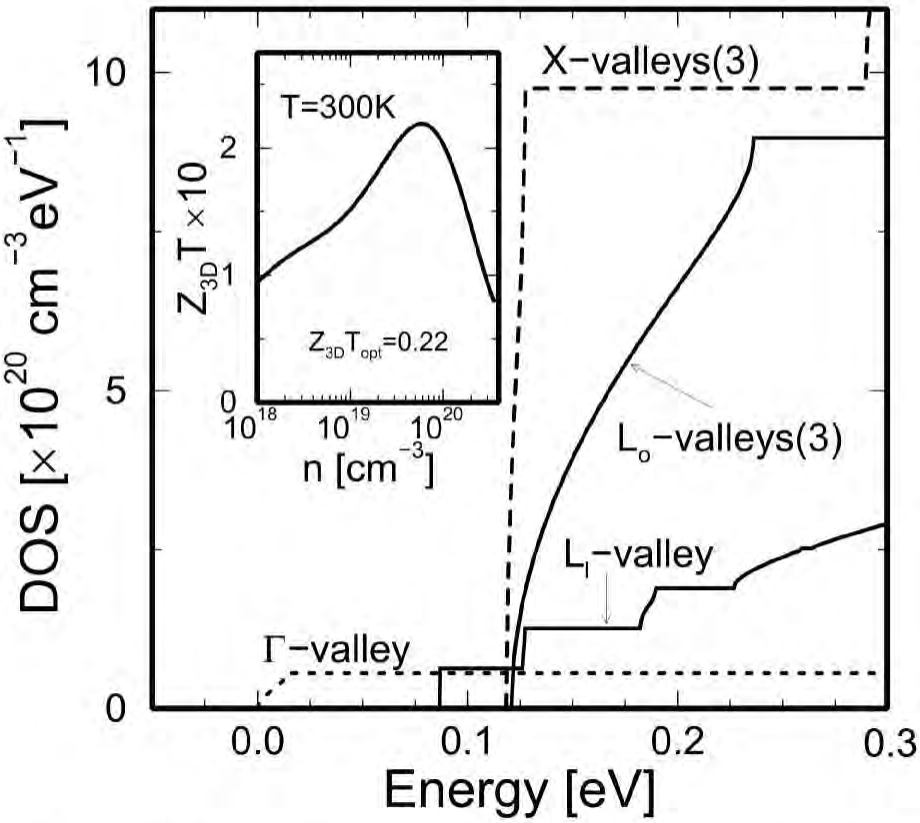

Figure 4-16: Density of states for electrons (DOS) for a (111) oriented GaAs(30 Å)/AlAs(20 Å) superlattice calculated for various subbands derived from Γ-, X-, L_l- and L_o-valleys, as indicated in the figure. The number inside the parentheses denotes the number of equivalent valleys that are degenerate in energy. Therefore, the DOS for L_o-valleys shown here, for example, includes contributions from three equivalent L_o-valleys. The inset shows a plot for the calculated $Z_{3D}T$ as a function of carrier concentration n for this superlattice at 300 K. The position of the chemical potential ζ that gives the optimum value of $Z_{3D}T$ (denoted as $Z_{3D}T_{opt}$) is $\zeta = 0.147$ eV on the main scale.

are also plotted as a function of the carrier concentration in the insets of Figs.4-16 and 4-17, respectively.

It is found that the lowest lying conduction subband in the (111) oriented GaAs(30 Å)/AlAs(20 Å) superlattice (Fig. 4-16) is the Γ-subband as in the (001) oriented GaAs(30 Å)/AlAs(20 Å) superlattice. Therefore, the resultant $Z_{3D}T$s for the (111) oriented GaAs(30 Å)/AlAs(20 Å) superlattice show a similar behavior to that for the (001) oriented GaAs(30 Å)/AlAs(20 Å) superlattice, i.e., the values for $Z_{3D}T$ at smaller carrier concentrations ($n < 1.5\times10^{18}$ cm^{-3}) are relatively large ($Z_{3D}T > 0.1$) as compared to those for the (111) oriented GaAs(20 Å)/AlAs(20 Å) superlattice

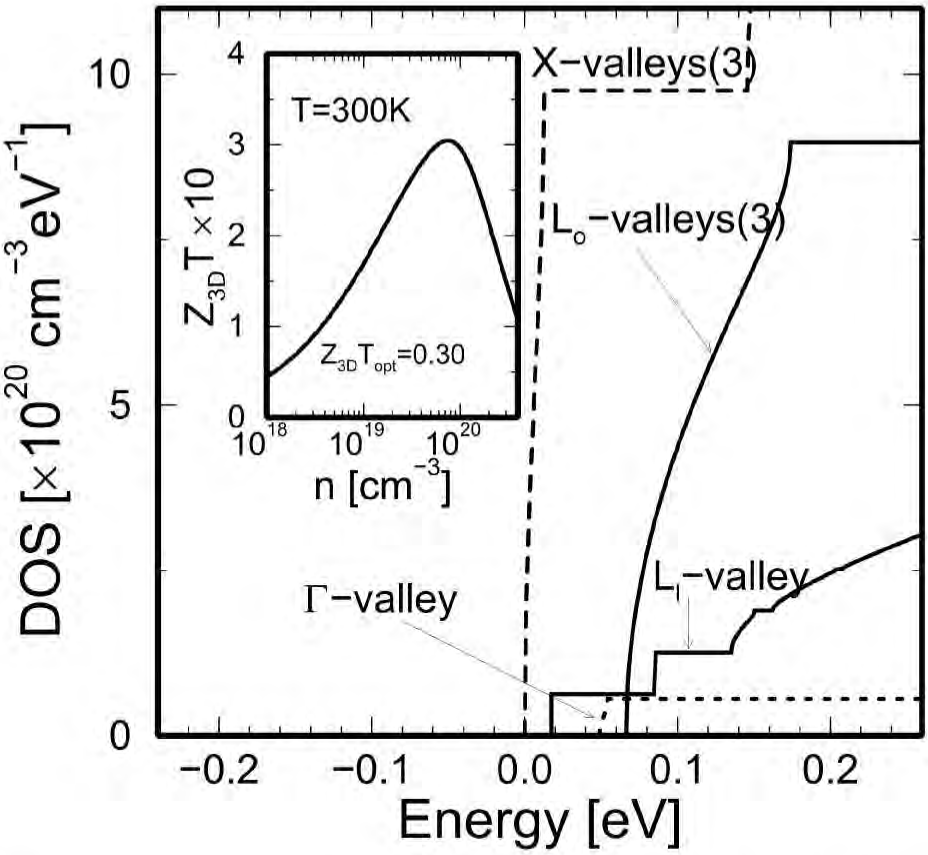

Figure 4-17: Density of states for electrons (DOS) for a (111) oriented GaAs(20 Å)/AlAs(30 Å) superlattice calculated for various subbands derived from Γ-, X-, L_l- and L_o-valleys, as indicated in the figure. The number inside the parentheses denotes the number of equivalent valleys that are degenerate in energy. Therefore, the DOS for L_o-valleys shown here, for example, includes contributions from three equivalent L_o-valleys. The inset shows a plot for the calculated $Z_{3D}T$ as a function of carrier concentration n for this superlattice at 300 K. The position of the chemical potential ζ that gives the optimum value of $Z_{3D}T$ (denoted as $Z_{3D}T_{opt}$) is $\zeta = 0.067$ eV on the main scale.

[because of the relatively large value for the carrier mobility for the Γ-subband (μ_Γ = 3000 cm^2/V·s)]. However, the values for $Z_{3D}T$ at larger carrier concentrations ($n > 2\times10^{18}$ cm^{-3}) for the (111) oriented GaAs(30 Å)/AlAs(20 Å) superlattice are relatively small compared to those for the (111) oriented GaAs(20 Å)/AlAs(20 Å) or GaAs(20 Å)/AlAs(30 Å) superlattices, because a large contribution from the Γ-subband to the total thermoelectric coefficients for the whole superlattice tends to reduce the value of the Seebeck coefficient for the whole superlattice because of the relatively large energy separation between the Γ-subband and other X-, L_l- and L_o-subbands in the (111) oriented GaAs(30 Å)/AlAs(20 Å) superlattice. For the (111) oriented GaAs(20 Å)/AlAs(30 Å) superlattice (see Fig. 4-17), the lowest subband turns out to be the X-subband. Because the carriers occupying the X-subband have relatively low mobilities (μ_X = 180 cm^2/V·s), the resultant values for $Z_{3D}T$ are not as large as those for the (111) oriented GaAs(20 Å)/AlAs(20 Å) superlattice (see the inset in Fig. 4-17).

One may ask how the relative energies for the available subband edges would change when the superlattice period is fixed (i.e., $d_{GaAs} + d_{AlAs}$ = constant) but the relative thicknesses for the GaAs and AlAs layers (denoted by d_{GaAs} and d_{AlAs}, respectively) are varied. Shown in Fig. 4-18 (a) and (b) are the calculated energies for various subband edges in (001) and (111) oriented GaAs/AlAs superlattices for the superlattice period $d_{GaAs} + d_{AlAs}$ = 40 Å, respectively. We find that the Γ-, X- and L-subbands all lie very close in energy for d_{GaAs} around 20 Å in both (001) and (111) oriented superlattices. Therefore, we can conclude that a GaAs(20 Å)/AlAs(20 Å) superlattice indeed provides the optimum structure for the superlattice for obtaining enhanced values of $Z_{3D}T$.

It is of interest to check to what degree the Carrier Pocket Engineering condition as defined in §4.1 is satisfied in the (111) oriented GaAs(20 Å)/AlAs(20 Å) superlattice, where the various available subband edges are closest in energy of all the superlattice structures and orientations for the GaAs/AlAs superlattice considered in this chapter. Plotted in Fig. 4-19(a) are the calculated $Z_{3D}T$s as a function of carrier concentration treating the Γ-, L- (i.e., [L_l,L_o]-) and X-valleys separately

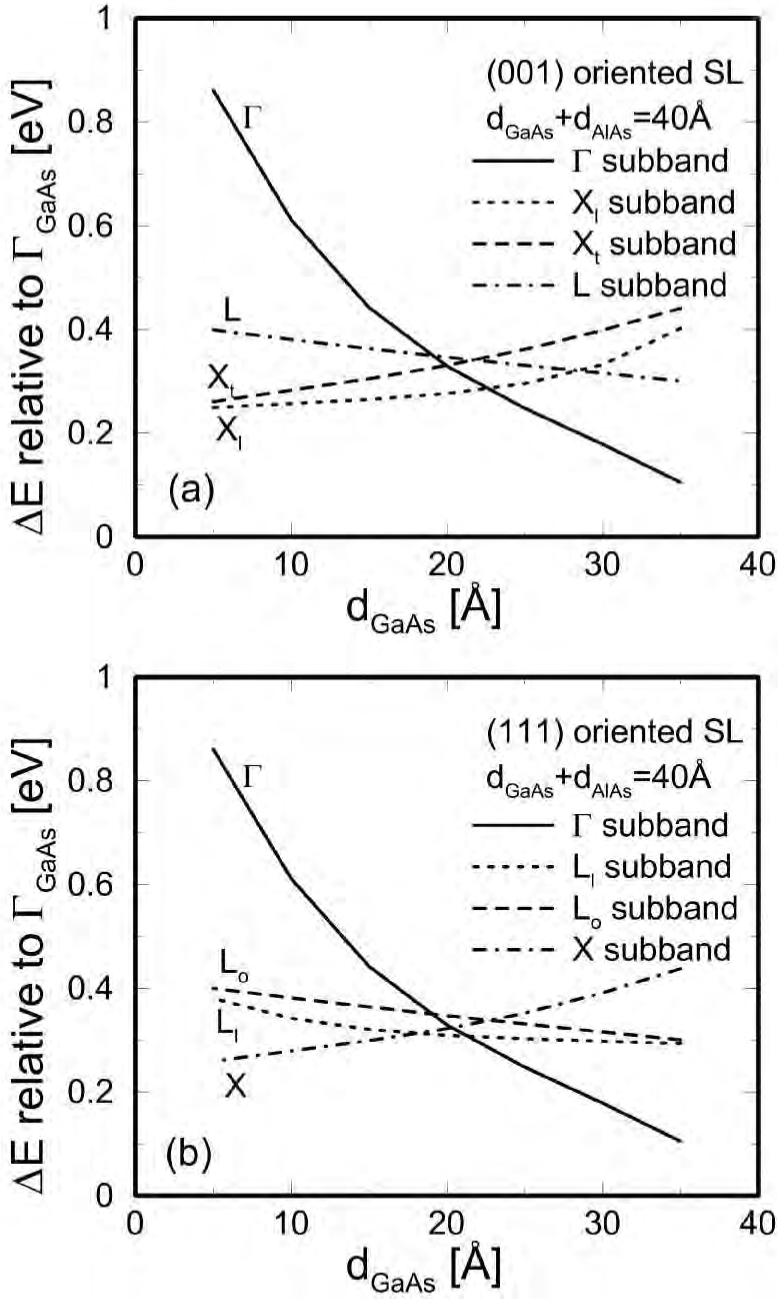

Figure 4-18: Calculated energies for various subband edges for (a) (001) and (b) (111) oriented GaAs/AlAs superlattices, measured from the conduction band edge at the Γ-point in the Brillouin zone for bulk GaAs. The calculated results are obtained for a fixed superlattice period ($d_{\mathrm{GaAs}} + d_{\mathrm{AlAs}}$) = 40 Å. It is noted that the X-point quantum well is formed within the AlAs layers, whereas the Γ- and L-point quantum wells are formed within the GaAs layers. Subscripts l, t and o in X_l, X_t, L_l and L_o denote the orientation of the pertinent conduction band valley: *l*ongitudinal, *t*ransverse, and *o*blique orientations, respectively, relative to the superlattice growth direction.

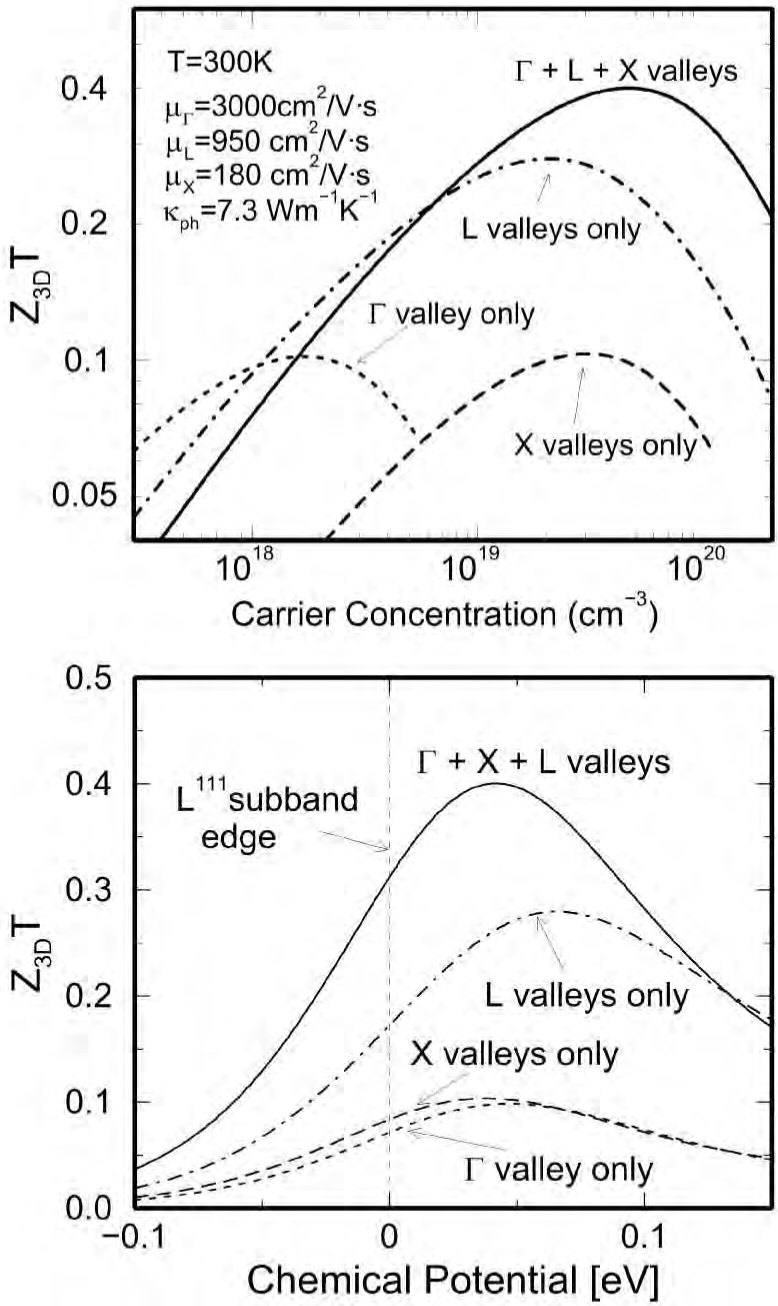

Figure 4-19: (a) Calculated $Z_{3D}T$s for a (111) oriented GaAs(20 Å)/AlAs(20 Å) superlattice as a function of carrier concentration treating Γ- (short-dashed curve), L- (dash-dotted curve) and X-valleys (long-dashed curve), separately, as well as treating all three types of valleys together (solid curve). (b) Calculated $Z_{3D}T$s for a (111) oriented GaAs(20 Å)/AlAs(20 Å) superlattice as a function of chemical potential measured from the longitudinal L-valley subband edge (the lowest conduction subband in energy) treating Γ- (short-dashed curve), L- (dash-dotted curve) and X- (long-dashed curve) valleys separately, as well as treating all three types of valleys together (solid curve).

[denoted by the short-dashed, dash-dotted and long-dashed curves, respectively, in Fig. 4-19(a)] and treating all three types of valleys together (denoted by the solid curve). The calculations are made assuming carrier mobilities of 3000, 950 and 180 $cm^2/V{\cdot}s$ for the Γ-, L- and X-valleys, respectively, and a lattice thermal conductivity of 7.3 W/m·K (see §4.3.2 and §4.3.3) to simulate the thermoelectric properties of (111) oriented GaAs(20 Å)/AlAs(20 Å) superlattices at 300 K. As is clear in Fig. 4-19(a), the optimum value for $Z_{3D}T$ for the (111) oriented GaAs(20 Å)/AlAs(20 Å) superlattice [$Z_{3D}T = 0.4$ at $n = 5{\times}10^{19}$ cm^{-3} given by the solid curve in Fig. 4-19(a)] is obtained not by the contribution from any of the single valley types, but is the result of contributions from all the Γ-, L- and X-valleys to the thermoelectric transport. This last feature can be seen more clearly if we plot the $Z_{3D}T$s as a function of chemical potential [Fig. 4-19(b)], where we find that the extrema of the $Z_{3D}T$s that are calculated by treating each valley type separately occur at similar positions of the chemical potential (within the order of the thermal energy at 300 K), proving the hypothesis of the "Carrier Pocket Engineering condition", i.e., the contributions from all the conduction band valleys add up positively to increase the $Z_{3D}T$ for the whole superlattice if the structure and orientation of the superlattice are carefully optimized.

4.5.4 Temperature dependence of $Z_{3D}T$

It is of practical importance to study the thermoelectric figure of merit $Z_{3D}T$ as a function of temperature, because the value of the optimum $Z_{3D}T$ is usually dependent on temperature. We can use such information about the temperature dependence of $Z_{3D}T$ both to design actual systems for thermoelectric applications in such a way that the system operates at a temperature where the maximum values of $Z_{3D}T$ for the constituent thermoelectric elements are realized and to design the thermoelectric materials in such a way that the value of $Z_{3D}T$ is maximized at a given desired temperature for the pertinent thermoelectric applications.

It turns out that the value of $Z_{3D}T$ generally tends to increase with increasing temperature because the increase in S^2T and the reduction in κ usually overweigh

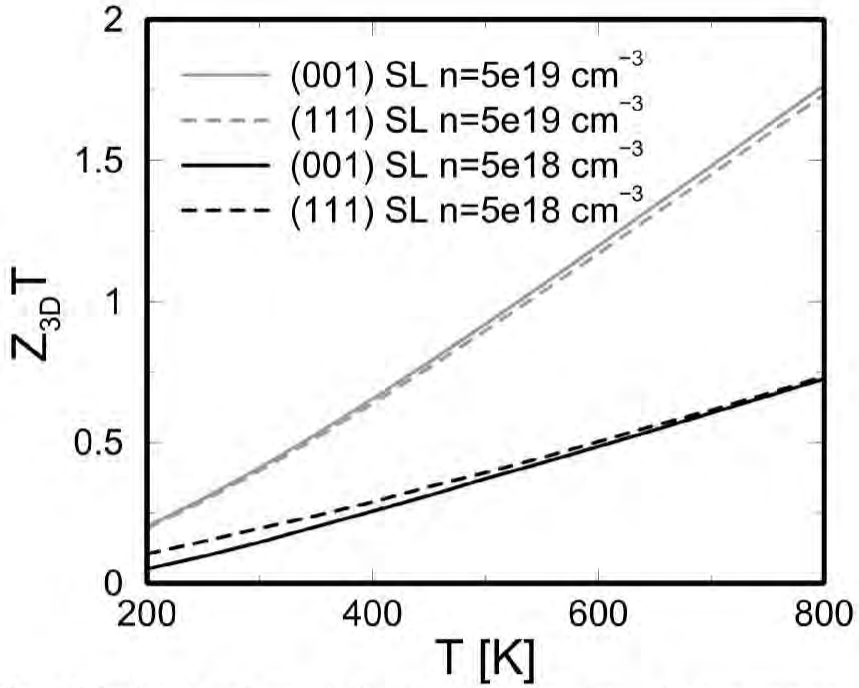

Figure 4-20: Calculated values of $Z_{3D}T$ as a function of temperature for a (001) oriented GaAs(20 Å)/AlAs(20 Å) superlattice (solid curves), and for a (111) oriented GaAs(20 Å)/AlAs(20 Å) superlattice (dashed curves). The results are given for two distinct values for the carrier concentration : $n = 5\times10^{19}$ cm^{-3} (light curves) and $n = 5\times10^{18}$ cm^{-3} (dark curves).

the reduction in σ as the temperature is increased, where ZT is defined by $\frac{S^2\sigma T}{\kappa}$. A peak in $Z_{3D}T$ as a function of temperature usually takes place when the excitation of carriers across the energy band gap (excitation of holes) reduces the magnitude of the Seebeck coefficient at sufficiently high temperature. Another limit for the use of thermoelectric materials at high temperatures is given by the temperature where a structural instability takes place with the given material system, such as interdiffusion phenomena at the well-barrier interfaces for the case of the thermoelectric materials using superlattice structures or the segregation or precipitation of the doping impurities at sufficiently high temperatures.

At present, the modeling of the temperature dependent $Z_{3D}T$ for the GaAs/AlAs superlattices is possible only in a naive sense where some specific temperature dependence of the carrier mobilities is assumed rather arbitrarily. Shown in Fig. 4-20 are examples of such modeling results for $Z_{3D}T$ as a function of temperature for (001) and (111) oriented GaAs(20 Å)/AlAs(20 Å) superlattices. These calculations are

made assuming $\mu \propto T^{-1/2}$ for the temperature dependence of carrier mobility, which is consistent with alloy scattering of the conduction carriers, and for some fixed values of carrier concentrations [$n = 5\times10^{18}$ cm^{-3} (dark curves) and $n = 5\times10^{19}$ cm^{-3} (light curves)]. It is shown that the values of $Z_{3D}T$ increase with temperature under these assumptions. Obviously, more informations on the temperature dependence of the carrier mobility and on the details of the scattering mechanisms are necessary to make more realistic predictions on the thermoelectric figure of merit $Z_{3D}T$ for the GaAs/AlAs superlattices as a function of temperature.

4.5.5 Future work

In the present chapter of this thesis, we have predicted large enhancements in the thermoelectric figure of merit $Z_{3D}T$ for the GaAs/AlAs superlattices relative to those for the corresponding bulk materials (GaAs and AlAs) using a simple model of parabolic energy bands and the constant relaxation time approximation. We have also used the intrinsic lattice mobilities (carrier mobility only due to phonon scattering) for the constituent bulk materials (GaAs and AlAs) to predict the carrier mobility for the superlattice. Although such a choice of our model for the thermoelectric transport and for the values for the carrier mobilities for the superlattice is sufficient to illustrate our main idea of the Carrier Pocket Engineering concept, these simple models are not sufficient to predict reasonably accurate values of $Z_{3D}T$ for the actual GaAs/AlAs superlattices. Therefore, we would like to suggest some improvements for the simple model of $Z_{3D}T$ for the GaAs/AlAs superlattices developed in this chapter, so that one can predict more accurate values for $Z_{3D}T$ for the GaAs/AlAs superlattices in the future.

The first suggestion to improve our current model for $Z_{3D}T$ is to include specific scattering mechanisms as we did for PbTe/$Pb_{1-x}Eu_xTe$ multiple-quantum-wells in Chapter 3. It was found, in §4.5.1-4.5.3, that the optimum values for $Z_{3D}T$ in short period GaAs/AlAs superlattices are obtained at very high carrier concentrations ($n \approx 5\times10^{19}$ cm^{-3}). Under these heavy doping conditions, the scattering of the conduction carriers in the superlattice is expected to be dominated by ionized

impurity scattering. It is noted that inonized impurity scattering has an effect of increasing the value of the Seebeck coefficient through its specific energy dependence of the relaxation time τ ($\tau \sim E^{3/2}$ for 3D systems and $\tau \sim E^2$ for 2D systems, without including the effect of the free carrier screening). However, the values for the carrier mobilities are usually greatly reduced due to the large concentrations of ionized impurities. To overcome such a negative effect of having ionized impurities, the techniques of δ-doping and modulation doping should be considered seriously. Therefore, our improved models to predict more accurate values of $Z_{3D}T$ for the superlattice should include the effect of such doping techniques as well. It is noted that such an improved model for the thermoelectric figure of merit $Z_{3D}T$ for the whole superlattice would suggest yet another version of implementation methodology of the Carrier Pocket Engineering concept for GaAs/AlAs superlattices as discussed in §4.2.3. For example, new superlattices should be designed in such a way that the joint effects of inonized impurity scattering on increasing the values of the Seebeck coefficient and on reducing the values of the carrier mobility have to be optimized to maximize the value of $Z_{3D}T$. Some attempts along these lines to optimize the superlattice structures, including specific scattering mechanisms and the effects of δ- and modulation doping of the carriers, are made in Chapter 5 and 6 using (001) oriented Si/Ge superlattices, and the experimental results are compared with theoretical predictions (Chapter 5).

The second suggestion for future work is the first principles (*ab-initio*) calculation of the band structure and the resultant transport properties for the optimum GaAs(20 Å)/AlAs(20 Å) superlattices, including the above effects of δ- and/or modulation-doped ionized impurities. However, probably, such an investigation should be performed after the investigations using the above simpler models of the thermoelectric transport as well as some preliminary experiments are performed to test the predictions of the simpler models including some experimental investigations to measure the mobilities in model systems.

4.6 Conclusion

In this chapter, we have developed the concept of Carrier Pocket Engineering and applied the concept to GaAs/AlAs superlattices to predict the enhanced thermoelectric figure of merit $Z_{3D}T$ for the whole superlattice relative to the corresponding values for the constituent materials (GaAs and AlAs) in a bulk form. It is found that $Z_{3D}T$ for the Γ-point superlattice could be enhanced by a factor of more than ten relative to that for bulk GaAs. The values for $Z_{3D}T$ under the Carrier Pocket Engineering condition, where all the available conduction subbands are almost degenerate to one another, could be about 50 times as large as that for the corresponding bulk materials. We have also studied the relative contributions from all the available Γ-, X- (X_t- and X_l-) and L- (L_l- and L_o-) subbands to the total thermoelectric figure of merit $Z_{3D}T$ for the whole superlattice. We have explored various superlattice parameters such as the superlattice period, layer thicknesses and the superlattice growth direction to optimize the value of thermoelectric figure of merit $Z_{3D}T$ for the whole superlattice. Values of $Z_{3D}T > 0.4$ are predicted at 300 K for either (001) or (111) oriented GaAs(20 Å)/AlAs(20 Å) superlattices under heavy doping conditions ($\sim 5\times10^{19}$ cm^{-3}), whereas $Z_{3D}T \sim 0.2$ is expected at moderate carrier concentrations ($\sim 5\times10^{18}$ cm^{-3}) for a (111) oriented GaAs(20 Å)/AlAs(20 Å) superlattice, which is still much larger than the corresponding value of $Z_{3D}T$ for bulk GaAs or for bulk AlAs ($Z_{3D}T \sim 0.0085$) at 300 K. Finally some suggestions are made to improve the present simple model of thermoelectric transport for the GaAs/AlAs superlattices so that one can predict more accurate values for the thermelectric figure of merit $Z_{3D}T$ for the actual GaAs/AlAs superlattices including the effect of δ- and modulation doping of the ionized impurities.

Chapter 5

Application of Carrier Pocket Engineering to Si/Ge Superlattices I — Basic Concept and Experimental Proof-of-Principle —

In this chapter, the concept of Carrier Pocket Engineering is applied to strained Si/Ge superlattices to obtain an enhanced thermoelectric figure of merit $Z_{3D}T$. One of the main purposes of this chapter is to develop basic design strategies for semiconductor superlattices that have enhanced values of the thermoelectric figure of merit $Z_{3D}T$ (i.e., design optimization processes for maximizing the value of $Z_{3D}T$), which are particularly suitable for Si/Ge superlattices. A new concept that was developed during such investigations is the use of lattice strain engineering to control the conduction band offsets (§5.3). Aspects of the optimization processes other than the use of lattice strain engineering for enhancing the value of the thermoelectric figure of merit $Z_{3D}T$ are somewhat similar to those developed for GaAs/AlAs superlattices, i.e, the exploration of various geometries and structures for the superlattice to maximize the

value of $Z_{3D}T$ for the whole (3D) superlattice. The resultant value for $Z_{3D}T$ at 300 K, calculated for a strain-symmetrized[†] (111) oriented Si(20 Å)/Ge(20 Å) superlattice is 0.96 (a factor of 70 enhancement relative to the corresponding value for bulk Si), and is shown to increase significantly at elevated temperatures. It is also noted that the optimum value of $Z_{3D}T$ for a (111) oriented Si(20 Å)/Ge(20 Å) superlattice is predicted to be a factor of four larger than the corresponding value of $Z_{3D}T$ for a (001) oriented Si(20 Å)/Ge(20 Å) superlattice, due to the density-of-states factor only.

The second purpose of this chapter is to provide an experimental proof-of-principle study of the concept that is developed in the first half of this chapter. We use (001) oriented Si(20 Å)/Ge(20 Å) superlattices to fulfill this purpose, because high quality samples of Si/Ge superlattice in the (001) orientation are readily available to us through the collaboration with Professor K. L. Wang's group at UCLA. Our future work, after testing our basic concept of enhancing the value of $Z_{3D}T$ with these samples, should be more focused on the experimental proof-of-principle study using (111) oriented Si/Ge superlattices that are predicted to have better thermoelectric properties than (001) oriented Si/Ge superlattices, as mentioned above.

It will be shown that the lowest subband that contributes to the actual thermoelectric transport in a (001) oriented Si(20 Å)/Ge(20 Å) superlattice is a subband that is derived from the two equivalent longitudinal Δ-valleys in the bulk form (denoted as the $\Delta^{\|}$- or Δ^{001}-subband). Since the Δ^{001}-subband has a relatively small density of states for electrons, because of its rather small in-plane effective mass component and a small multiplicity factor, 2, for the number of equivalent valleys, the predicted value for the optimum figure of merit ($Z_{3D}T$) is only 0.24 at 300 K. Therefore, the main purpose of the experimental study of $Z_{3D}T$ using the (001) oriented Si(20 Å)/Ge(20 Å) superlattices is not to obtain a value of $Z_{3D}T$ that is higher than those for any other existing materials (say $Z_{3D}T > 1$), but to test our basic concept of Carrier Pocket Engineering for enhancing the value of $Z_{3D}T$ using low-dimensional structures. We

[†]A strain-symmetrized superlattice means a superlattice that is fully relaxed through lattice strain, i.e., a superlattice whose lattice constant is close to that for the corresponding $Si_{1-x}Ge_x$ alloy with a similar Ge composition x.

also hope to get some feedback from experiment to improve our theoretical models so that they can make more accurate predictions of the values of $Z_{3D}T$ for the Si/Ge superlattice, and to define an improved optimization scheme for designing semiconductor superlattices using Si and Ge with enhanced values of $Z_{3D}T$ relative to their bulk constituents. Such improvements in theoretical modeling, in turn, provide new inputs to the experiments so that rapid progress can be made toward the realization of practically useful thermoelectric materials using superlattice structures.

5.1 Introduction

The use of low-dimensional structures as realized in the form of two-dimensional quantum wells (see Chapters 2, 3 and 4, and references therein) and one-dimensional quantum wires [12, 19, 50–52] has been shown to provide a promising strategy for designing materials with a large value of the thermoelectric figure of merit ZT ($Z = S^2\sigma/\kappa$), where S is the Seebeck coefficient, σ is the electrical conductivity and κ is the thermal conductivity. The original proposal that a large enhancement in ZT should be possible in reduced dimensionalities was made by Hicks and Dresselhaus at MIT using simple models of isolated systems of 2D quantum wells and 1D quantum wires [12, 14]. Although this is a reasonable model for isolated quantum wire arrays [50–52] and multiple quantum wells (MQWs) with very thick and/or infinitely high (potential) barriers [15, 16, 38, 66], refinement of the model has been needed to describe the thermoelectric properties of other quasi-two-dimensional systems, such as MQWs with finite barrier heights and thicknesses, including the effects of the tunneling of the carriers through the barrier layers and of parasitic thermal conduction in the barrier layers (see Chapter 4 and references therein). It is these latter systems that are currently of interest for actual thermoelectric applications.

In Chapter 4, attempts to model such *three-dimensional* $Z_{3D}T$s of the superlattices are performed using short period GaAs/AlAs superlattices. There, we have first considered the effect of the coupling for the Γ-valleys only, between the well (GaAs) and the barrier (AlAs) layers (denoted as a Γ-point superlattice), on the thermoelec-

tric properties of the superlattices, and then we have also extended our models to include the contributions from other X- and L-valleys in the Brillouin zone [48]. It is shown that $Z_{3D}T$ for the Γ-point superlattice could be more than ten times larger than that for the corresponding bulk GaAs, and that $Z_{3D}T$ for the (001) or (111) oriented GaAs(20 Å)/AlAs(20 Å) superlattices under the "Carrier Pocket Engineering condition"[†] (see §4.1 and §4.5.3 for the definition and discussion of the "Carrier Pocket Engineering condition", respectively) is shown to be enhanced by a factor of about 50 relative to the corresponding value of $Z_{3D}T$ for bulk GaAs [48]. It has also been shown that, in order to obtain such a large enhancement in $Z_{3D}T$, the geometry and structure of the superlattices (such as the layer thicknesses and the superlattice growth direction) have to be carefully optimized so that both the GaAs and AlAs layers can be utilized as the conduction channels for electrons that are contributing to the thermoelectric transport. We refer to such a design process by the term "Carrier Pocket Engineering" [48].

In this chapter, the concept of Carrier Pocket Engineering is applied to the Si/Ge superlattices. Since bulk Si and Ge have their conduction band minima at the Δ- and L-points in the Brillouin zone, respectively (the number of the equivalent sites at these high symmetry points are 6 and 4, respectively), the Si/Ge superlattice should provide an ideal system for exploring actual applications of the Carrier Pocket Engineering concept for obtaining enhanced values of $Z_{3D}T$. Other reasons to study the thermoelectric properties of Si/Ge superlattices include : 1) the bulk SiGe alloy is already a good thermoelectric material, and there is a good chance that SiGe in a superlattice form could be an even better thermoelectric material than bulk SiGe alloys; 2) the reduction of the lattice thermal conductivity κ_{ph} due to the boundary scattering of phonons and due to the existence of threading dislocations has been studied extensively in Si/Ge superlattices [62, 67] (see §5.2); and 3) the effect of uniaxial lattice strain at the Si/Ge interfaces [68, 69] provides an additional degree

[†]In short, the "Carrier Pocket Engineering" condition is satisfied when the superlattice structures are designed in such a way that the sum of contributions from all the Γ-, X- and L-valleys are maximized.

of freedom to control the conduction band offsets for the mini-band formation in a superlattice as we discuss in §5.3.

We organize this chapter of the thesis in the following way. We will first review the effect of boundary scattering of phonons and the effect of threading dislocations on reducing the value of lattice thermal conductivity $\kappa_{\rm ph}$ in the Si/Ge superlattices in §5.2. In §5.3, we will explain how the uniaxial lattice strain created at the Si/Ge interfaces would alter the conduction band structures for bulk Si and Ge. The resultant shifts in the energies for the conduction band valleys can be used as an additional tool to control the magnitude of the conduction band offsets for the superlattice. In §5.4, we will show the predictions of our theoretical models for the enhanced values of $Z_{\rm 3D}T$s using the simple models of the constant relaxation time approximation and parabolic energy bands.

§5.5–§5.9 are devoted to showing the results of our experiments on the (001) oriented Si(20 Å)/Ge(20 Å) superlattices that are grown by the molecular-beam epitaxy technique. We will first show the problem that we encountered during the measurement of the Seebeck coefficient S for (001) oriented Si(20 Å)/Ge(20 Å) superlattices grown on (001) oriented Si substrates, where the measured value for $-S$ starts to shoot up toward positive infinity below 200 K (§5.6.2). Our original interpretations for this effect of negative S shooting up below 200 K include the large parallel transport contributions from the buffer layer and/or substrate, and the effect of the floating potential due to the *pn*-junction that is created at the interface between the SiGe graded buffer layer and the (001) Si substrate. The third possibility for this effect of negative S shooting up is the phonon drag effect, where the conduction electrons in the superlattice part of the sample are affected by the directional flow of phonons that are induced from the phonon distribution in the substrate.

It turns out that the effect of negative S shooting up below 200 K is completely eliminated by the use of a Si-on-insulator (SOI) substrate for the growth of the SiGe buffer layer, probably because the SiO_2 layer in the SOI substrate provides good isolation, both electrically and thermally, between the film (superlattice+buffer layer) and the base Si substrate on top of which layers of (001) Si and SiO_2 insulator are

grown to form the SOI substrate (see Fig. 5-12). However, the disappearance of the effect of negative S shooting up for the films grown on SOI does not necessarily mean that there is no parallel electrical conduction in the buffer layer and the substrate. In this regard, we have studied, in §5.8, a set of thin [25 periods of Si(20 Å)/Ge(20 Å) superlattice layers] and thick [100 periods of Si(20 Å)/Ge(20 Å) superlattice layers] samples to subtract out the contributions from the buffer layer and substrate to the measured thermoelectric transport coefficients. We have then deduced the net contribution (to the measured thermoelectric coefficients) from the superlattice part of the sample only (§5.8). It turns out that the values of the thermoelectric coefficients, that are obtained after the subtraction process, differ by 5–10 % from the values without (or before) the subtraction process. Since the subtraction process itself may introduce a similar amount of errors (5–10 %) to the resultant values for the net contribution from the superlattice part of the sample only, through unintentional fluctuations in the materials properties between the two samples used for the subtraction process, the resultant values obtained by the subtraction process have to be examined with some care. Our overall conclusion is that the dominant contribution to the measured thermoelectric transport properties for the 100 periods Si(20 Å)/Ge(20 Å) superlattices comes from the superlattice part of the sample, not from the buffer layer and/or substrate part of the sample.[†]

Detailed results for our experimental proof-of-principle study using (001) oriented Si(20 Å)/Ge(20 Å) superlattices grown on (001) Si substrates and those grown on SOI (Si-on-insulator) substrates are given in §5.6 and §5.7, respectively, where excellent agreement between theory and experiment are obtained for the Seebeck coefficient S as a function of temperature without use of any fitting parameters. In §5.9, we will further examine the values obtained for S and μ_{Hall}, where μ_{Hall} is the Hall carrier mobility, as a function of the carrier concentration at 300 K. These results are compared with the theoretical predictions using the semi-classical models that are developed in Chapter 6.

[†]The contribution from the buffer layer and/or substrate to the measured thermoelectric transport coefficients is estimated to be 5–20 % depending on the carrier concentration of the sample.

It is hoped that the experimental verification of the theoretical prediction for the thermoelectric transport properties in the (001) oriented Si/Ge superlattices, as we did in §5.6–§5.9 in this chapter, would also provide a basis for the development of improved theoretical models for the (111) oriented Si/Ge superlattices, whose optimum value of $Z_{3D}T$ [for a Si(20 Å)/Ge(20 Å) superlattice] is predicted to be four times larger than the corresponding value of $Z_{3D}T$ for a (001) oriented Si(20 Å)/Ge(20 Å) superlattice, using a simple model based on the constant relaxation time approximation.

5.2 Reduced lattice thermal conductivity κ_{ph} in Si/Ge superlattices

In this section, we will review the research performed by other researchers on the thermal conductivity for $Si_{1-x}Ge_x$ alloys (§5.2.1) and for Si/Ge, $Si/Si_{1-x}Ge_x$ superlattices (§5.2.2). Although the main theme of this thesis is on the modeling and experimental-proof-of principle study of the power factor $S^2\sigma$ part of the thermoelectric figure of merit $Z_{3D}T$ for the superlattice structures, we will deviate a little, in this section, from the main stream of this thesis, and discuss another strategy for enhancing the values of $Z_{3D}T$ using superlattice structures, namely, enhancing $Z_{3D}T$ through the reduction of the lattice thermal conductivity κ_{ph}.

We first discuss, in §5.2.1, the reduction of κ_{ph} observed in $Si_{1-x}Ge_x$ alloys relative to those for bulk Si and Ge. Although the detailed mechanisms for the reduction of κ_{ph} in $Si_{1-x}Ge_x$ alloys (i.e., alloy scattering and impurity scattering of phonons) are considered to be distinct from those in the Si/Ge superlattices (interface and impurity scattering of phonons, and phonon scattering due to defects and threading dislocations), the understanding of the mechanisms for the reduced κ_{ph} in $Si_{1-x}Ge_x$ alloys should also provide some insight into the mechanisms for the reduced κ_{ph} in Si/Ge superlattices. The main finding in §5.2.1 is that the reduction of κ_{ph} in $Si_{1-x}Ge_x$ alloys takes place not only due to the alloy scattering of phonons, but also due to

the impurity scattering of phonons for heavily doped $Si_{1-x}Ge_x$ alloy samples. Since the optimum doping levels for Si/Ge superlattices for thermoelectric applications are predicted to be relatively high ($n = 10^{19}\sim10^{20}$ cm^{-3}), the importance of the impurity scattering on reducing κ in $Si_{1-x}Ge_x$ alloys suggests that a new concept of the "dopant impurity" engineering can be developed for Si/Ge superlattices. In this "dopant impurity" engineering concept, the dopant impurities are introduced into the superlattice structures in such a way that the values of κ_{ph} for the superlattices are reduced due to the impurity scattering of phonons, but the values of the carrier mobility for the superlattices are not reduced appreciably by the large dopant concentrations due to some special doping techniques, such as δ- and modulation doping techniques. Since, to the author's knowledge, such an approach of using "doping impurity" engineering to enhance the values of $Z_{3D}T$ in the low-dimensional systems has not yet been pursued by any researchers in the field of low-dimensional thermoelectricity, any pioneering work in this research area is greatly encouraged for the further development of low-dimensional thermoelectricity.

The second subsection in this section is devoted to a review of recently published work, both in theory and in experiment, on the thermal conductivity of Si/Ge superlattices. It is experimentally observed [62, 67, 70–72] and theoretically predicted [73–76] that the lattice thermal conductivities κ_{ph} for Si/Ge and $Si/Si_{1-x}Ge_x$ superlattices are significantly reduced from the corresponding values for bulk Si and Ge. In some cases, the values of κ_{ph} for Si/Ge or $Si/Si_{1-x}Ge_x$ superlattice samples are even lower than the corresponding values of κ_{ph} for $Si_{1-x}Ge_x$ alloys, where x is close to 0.5 [62, 67, 70–72]. Since the values of κ_{ph} for these superlattice samples crucially depend on the quality of the superlattice samples, it is essential to use high-quality, well-characterized superlattice samples for the experiment of the in-plane and cross-plane thermal conductivity measurements in order to identify the possible mechanisms that are responsible for the observed reduction in κ_{ph} for Si/Ge and $Si/Si_{1-x}Ge_x$ superlattices. Our ultimate goal in this research sub-field is to understand the detailed mechanisms that are responsible for the reduction of κ_{ph} in Si/Ge and $Si/Si_{1-x}Ge_x$ superlattices and use the knowledge acquired to engineer superlattice structures in

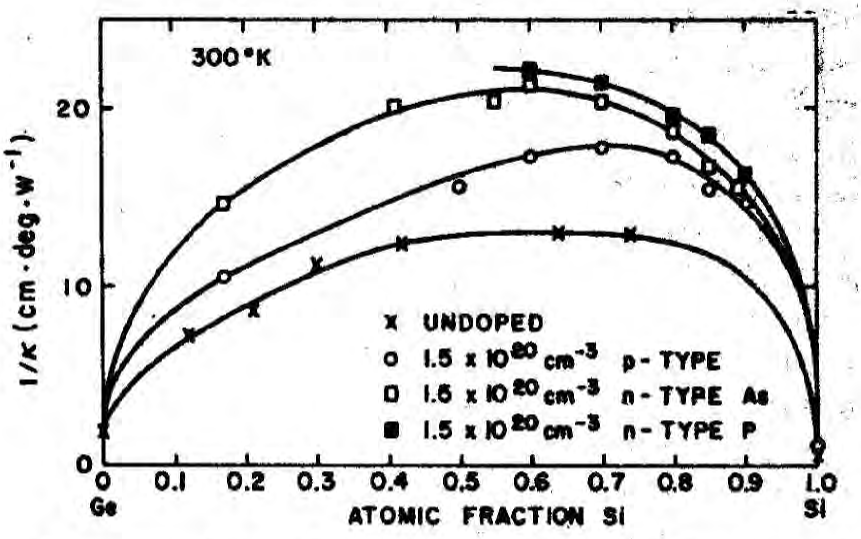

Figure 5-1: Compositional dependence of the thermal resistivity (denoted by $1/\kappa$) of $Si_{1-x}Ge_x$ alloys as a function of $(1-x)$ at 300 K for undoped ($n \sim 2\times10^{18}$ cm^{-3}) samples and for samples doped to $n \sim 1.5\times10^{20}$ cm^{-3} with B, As and P [77].

such a way that the reduction of $\kappa_{\rm ph}$ is maximized, while the reduction in μ (carrier mobility) is minimized. One way to achieve this goal is to utilize atomically rough interfaces in the superlattice structures that are effective in scattering phonons, but have little effect on scattering electrons (or holes), as suggested by Prof. G. Chen at UCLA [43]. Another way is probably to utilize other defect structures, such as threading dislocations which are routinely found in the actual Si/Ge and $Si/Si_{1-x}Ge_x$ superlattice samples, that are effective in scattering phonons, but may not be as effective in scattering electrons (or holes). The concept of reducing the values of $\kappa_{\rm ph}$ using superlattice structures, often denoted by "interface engineering", "lattice engineering" or "phonon engineering" has to be eventually integrated into the concept of Carrier Pocket Engineering to design superlattice structures which maximize $Z_{\rm 3D}T$.

5.2.1 $\kappa_{\rm ph}$ for $Si_{1-x}Ge_x$ alloys

The thermal conductivities of $Si_{1-x}Ge_x$ alloys were studied experimentally by Dismukes *et al.* [77] as early as the 1960s, and were recently reviewed by Wang *et al.* [78]. Examples of the experimental results by Dismukes *et al.* are reproduced in Figs. 5-1 and 5-2, where the values of the thermal resistivity ($1/\kappa$) are plotted as a function

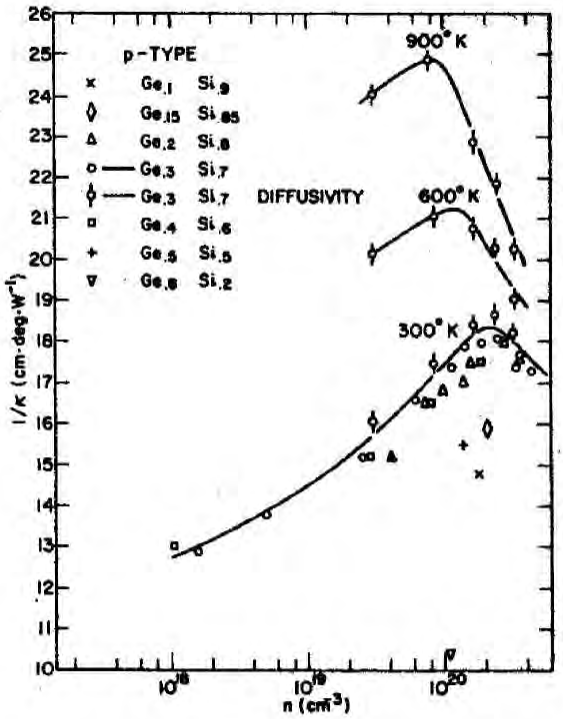

Figure 5-2: The thermal resistivity of p-type $Si_{1-x}Ge_x$ alloys as a function of carrier concentration with temperature and alloy composition as parameters [77].

of Si composition $1-x$ (Fig. 5-1) and as a function of the dopant (carrier) concentration n (Fig. 5-2). In Fig. 5-1. we find that the values of the thermal conductivity κ for $Si_{1-x}Ge_x$ alloys are greatly reduced from the corresponding values for bulk Si ($\kappa \approx 150$ W/m·K) and for bulk Ge ($\kappa \approx 60$ W/m·K). We find the values of $\kappa_{\rm ph}$ for $Si_{1-x}Ge_x$ $x \approx 0.5$ alloys are approximately 8 W/m·K for undoped alloys and can be smaller than 5 W/m·K for heavily doped alloys ($n \sim 1.5\times10^{20}$ cm^{-3}). It is noted that the electronic contribution to the thermal conductivity (denoted by κ_e) is only on the order of 10 % of the total thermal conductivity, even for the heavily doped samples. Therefore, reducing the values of $\kappa_{\rm ph}$ by increasing dopant concentrations, due to the increased impurity scattering of phonons, outweighs the increase in κ due to the increased values of κ_e that are caused by the increased carrier concentrations. Such an effect of doping impurities on reducing the value of κ is more clearly seen in Fig. 5-2, where the measured values of the thermal resistivity $1/\kappa$ for p-type $Si_{1-x}Ge_x$ alloys are plotted as a function of carrier concentration n for several different temperatures and Ge compositions x. We find that the values of κ^{-1} first increase with increasing n

and reach the maximum at $n = 8\times10^{19}$–2×10^{20} cm^{-3}, depending on the temperature, and then decrease with further increasing n due to the increasing contribution of κ_e to the total thermal conductivity κ.

Theoretical models for the thermal conductivity (as well as for the other thermoelectric transport coefficients) for n-type $Si_{1-x}Ge_x$ alloys have been presented by C. B. Vining recently [79], where good agreement between experiment and theory has been found by considering phonon-phonon, point defect, and electron-phonon scattering for phonons.

5.2.2 κ_{ph} for Si/Ge superlattices

Research on the reduced thermal conductivities in Si/Ge and Si/$Si_{1-x}Ge_x$ superlattices were started only recently, both theoretically [43, 73–76, 80] and experimentally [62, 67, 70–72]. In most cases, experiments were performed by measuring the values of κ along the superlattice growth direction (denoted by the cross-plane thermal conductivity $\kappa_\perp$), whereas it is the κ parallel to the plane of the superlattice (denoted by the in-plane thermal conductivity $\kappa_{||}$) that we need for modeling and the experimental determination of the enhanced thermoelectric figure of merit $Z_{3D}T$ along the plane of the superlattice. Shown in Fig. 5-3 is one of the few published examples of in-plane thermal conductivity $\kappa_{||}$ measurements of the Si/Ge superlattices as a function of the superlattice period $(d_W + d_B)$ [72], where the values of $\kappa_{||}$ are calculated by us, by multiplying the published data for the thermal diffusivity at 300 K, that were obtained by the AC calorimetry measurements by R. Venkatasubramanian *et al.* [72], using values of the heat capacity and the mass density obtained by averaging the published values of these quantities for bulk Si and for bulk Ge. The Si/Ge superlattice samples that were used in this AC calorimetry experiment were prepared by chemical vapor deposition on GaAs substrates using a Ge buffer layer [72]. It is noted that neither the orientation of the superlattices nor the thicknesses for the well and barrier layers (denoted by d_W and d_B, respectively) are reported in this paper [72]. The authors of Ref. [72] found that there are three distinct regimes for $\kappa_{||}$ as a function of $(d_W + d_B)$ in Fig. 5-3, and each regime of $\kappa_{||}$ is interpreted

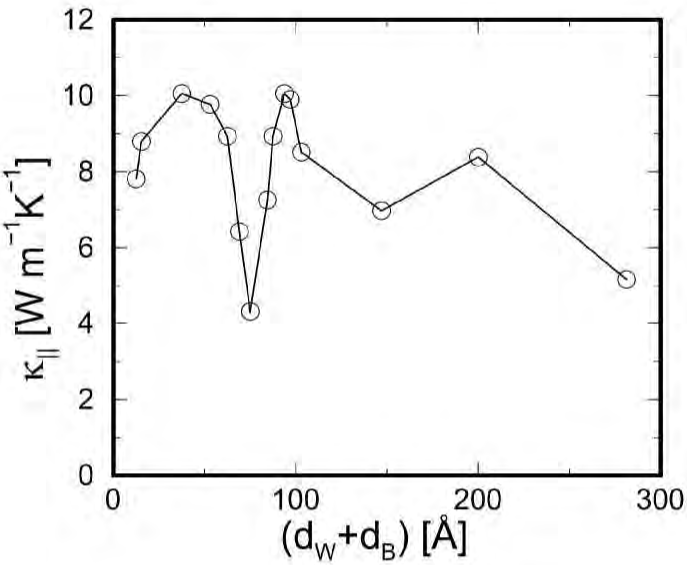

Figure 5-3: The in-plane thermal conductivity $\kappa_{||}$ for CVD-grown Si/Ge superlattices at 300 K as a function of the superlattice period $(d_W + d_B)$ that is obtained by multiplying the published thermal diffusivity data [72] by the average values of the heat capacity and the mass density obtained from published bulk Si and Ge data (see text for more detail).

as follows : (1) When $(d_W + d_B) < 35$ Å, the value of $\kappa_{||}$ decreases with decreasing the value of $(d_W + d_B)$. This decrease in $\kappa_{||}$ is attributed to the increased interface scattering of phonons, that is well-known in GaAs/AlAs superlattices, as was discussed in §4.3.3 [43]. (2) For 35 Å $< (d_W + d_B) < 100$ Å, there is a minimum in $\kappa_{||}$ at $(d_W + d_B) \approx 65$ Å. This minima in $\kappa_{||}$ is attributed to localization-like effects of phonons [80] that are similar to localization effects observed in electrons [81] and photons [82]. (3) When $(d_W + d_B) > 100$ Å, the thermal conductivity decreases with increasing $(d_W + d_B)$. This effect is attributed to increasing dislocation densities as the superlattice period $(d_W + d_B)$ increases, which is consistent with the result of cross-plane thermal conductivity $\kappa_{||}$ measurements, as we will see below.

The experiments on the cross-plane thermal conductivity $(\kappa_\perp)$ measurement can be performed in a much more reliable way than the in-plane thermal conductivity measurement, because the geometrical configuration in the cross-plane measurement of $\kappa_\perp$ for Si/Ge superlattices allows one to use the 3ω-technique [83, 84] that can be performed without removing the substrate and the buffer layer part of the sample from the superlattice, whereas an in-plane $\kappa_{||}$ measurement generally requires a free-

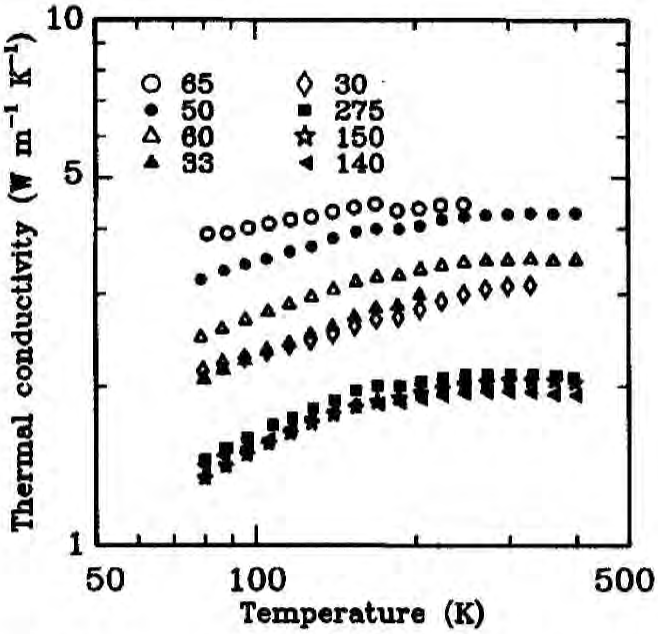

Figure 5-4: Results for the cross-plane thermal conductivity $\kappa_\perp$ as a function of temperature for various CVD-grown Si/Ge superlattice samples, published by S.-M. Lee *et al.* [62]. The 3ω-technique [83, 84] was utilized in this measurement of the cross-plane $\kappa_\perp$. Each symbol in the figure is labelled by the superlattice period $(d_W + d_B)$ measured in Å.

standing sample of Si/Ge superlattices. It is, however, noted that there is a variation of the 3ω-technique, the so-called "2-wire 3ω method", that has been developed by the group of Prof. G. Chen at UCLA [76], which allows one to measure the in-plane $\kappa_{||}$ of the superlattice samples without removing the substrate and buffer layer part of the samples. This 2-wire 3ω-technique, however, has not yet been applied to the Si/Ge superlattices, because our MBE-grown Si/Ge superlattices, that were grown by Prof. K. L. Wang's group at UCLA, are too thin for an accurate determination of the values of $\kappa_{||}$ by this variation of the 3ω-technique.

Examples of the cross-plane thermal conductivity measurements for CVD-grown Si/Ge superlattices are reproduced in Fig. 5-4 from Ref. [62], where the values of $\kappa_\perp$ are plotted as a function of temperature for various values of the superlattice period $(d_W + d_B)$. In Fig. 5-4, the ratio between the well(Si)- and barrier(Ge)-layer thicknesses (d_W/d_B) is varied from one sample to another, with values ranging from $d_W/d_B = 0.88$ [for the sample with $(d_W+d_B) = 65$ Å] to $d_W/d_B = 3.88$ [for the sample with $(d_W + d_B) = 60$ Å]. We find that the values of $\kappa_\perp$ decrease with decreasing

superlattice period $(d_W + d_B)$ below $(d_W + d_B) = 65$ Å, whereas the values of $\kappa_\perp$ for the samples with $(d_W + d_B) > 140$ Å are smaller than those of any superlattice sample with $(d_W + d_B) < 65$ Å. The authors of Ref. [62] attributed the effect of reduced $\kappa_\perp$ for relatively larger superlattice period $[(d_W + d_B) > 140$ Å] to the increased dislocation densities as the value of the superlattice period $(d_W + d_B)$ gets larger, but there is also an argument that is against this interpretation of the reduced $\kappa_\perp$ for the larger superlattice periods $[(d_W + d_B) > 140$ Å] (see Ref. [70] for more detail).

Yet another method to estimate the values of the in-plane thermal conductivity of $\kappa_{||}$ was developed by T. Borca-Tasciuc in the group of Prof. G. Chen at UCLA [85]. According to this method, the cross-plane thermal conductivity $\kappa_\perp$ of the Si/Ge superlattice samples is measured by the 3ω-technique, as a function of temperature as discussed above. The resultant experimental results for $\kappa_\perp$ are fitted using Prof. G. Chen's model for the thermal conductivity of superlattice structures, using the specularity constant p as a fitting parameter [76] (see also §4.3.3). Then, the specularity constant obtained in this fitting of $\kappa_\perp$ is used to predict the in-plane thermal conductivity using the same basic models for the in-plane thermal conductivity $\kappa_{||}$ that were also developed by Prof. G. Chen [43]. An example of such estimation of the in-plane thermal conductivity $\kappa_{||}$ using a high-quality MBE-grown Si/Ge superlattice sample is shown in Fig. 5-5. The superlattice sample used for this analysis (sample JL156) was grown on a (001) Si substrate using a $Si_{1-x}Ge_x$ graded buffer layer [86], and the thicknesses for the quantum wells (Si) and barrier layers (Ge) for this sample were both determined to be 22 Å [67, 70]. The reasons why this specific superlattice sample (JL156) is chosen for the analysis of the in-plane thermal conductivity $\kappa_{||}$ using Prof. G. Chen's models [43, 76] include the facts that : (1) a relatively small density of threading dislocations was found in this (JL156) Si/Ge superlattice sample ($\sim 1.5 \times 10^4$ lines/cm^{-2}) [67, 70], and that (2) this superlattice sample is undoped. Because of these reasons, the properties of this superlattice sample are expected to be compatible with the assumptions made in Prof. G. Chen's models for the superlattice thermal conductivity [43, 76]. In Fig. 5-5, we find that the best fit to the cross-plane thermal conductivity for sample JL156 is obtained for the spec-

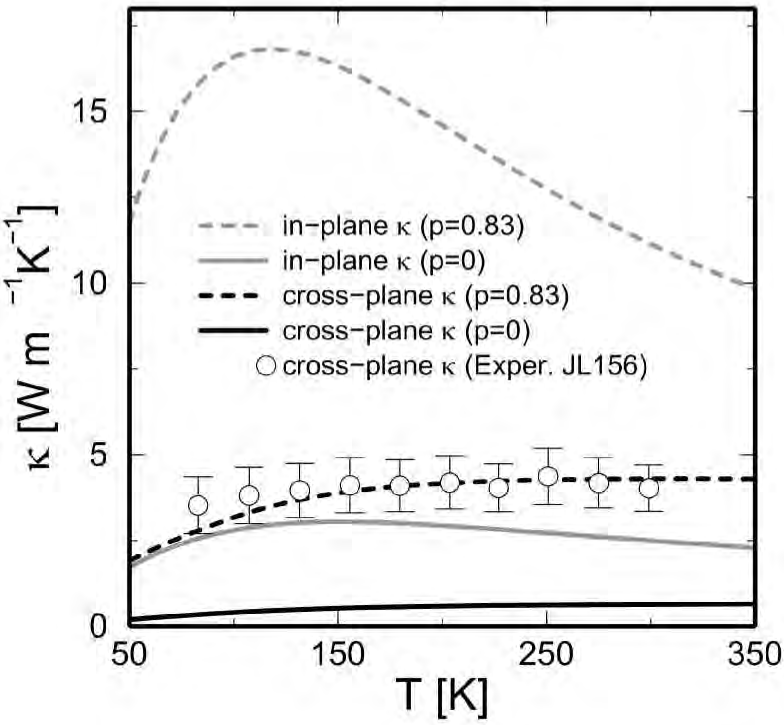

Figure 5-5: Fitting analysis using Prof. G. Chen's model [76], performed by T. Borca-Tasciuc in Prof. G. Chen's group at UCLA, of the cross-plane thermoelectricity $\kappa_{\perp}$ for an MBE-grown Si/Ge superlattice sample (JL156, $d_{\mathrm{W}} + d_{\mathrm{B}} = 44$ Å) (black dashed curve). The specularity parameter obtained in this fitting analysis of the experimental $\kappa_{\perp}$ ($p = 0.83$) is also used to predict the values of the in-plane thermal conductivity $\kappa_{||}$ as a function of temperature for sample JL156 (grey dashed curve) [43]. The results of the calculations for $\kappa_{\perp}$ and $\kappa_{||}$ using $p = 0$ (completely diffuse interfaces) for the specularity parameter are also shown by the black and grey solid curves, respectively, for comparison.

ularity constant $p = 0.83$, which is consistent with the value of p obtained for the GaAs/AlAs superlattices that was discussed in §4.3.3. Using this value ($p = 0.83$) for the specularity constant, the values for the in-plane thermal conductivity $\kappa_{\parallel}$ of this superlattice sample (JL156) are predicted to be two to five times larger than those for the cross-plane thermal conductivity $\kappa_{\perp}$. It is noted again that such an estimation of the in-plane thermal conductivity for superlattice samples is still in a developmental stage. A more accurate determination of the in-plane thermal conductivity for the Si/Ge and other superlattice systems awaits the development of more detailed theoretical models, including an accurate description of the effects of the threading dislocations found in the superlattice structures on the value of the resultant thermal conductivity (both in the in-plane and in the cross-plane directions) of the superlattice samples and the development of several experimental techniques that can directly measure the in-plane thermal conductivity of the superlattices to cross check the measured values and the theoretically predicted values of the in-plane and cross-plane thermal conductivities of the superlattice samples.

5.3 Conduction band structures for bulk Si and Ge, and the effect of uniaxial strain on the valley energies

In this section, we will discuss the effect of the uniaxial lattice strain on the energy of the Δ- and L-valleys in the conduction band of bulk Si and Ge. We will then discuss how to use such an effect to optimize the properties of the superlattices to achieve enhanced values of $Z_{3D}T$ in these superlattices.

5.3.1 Band structures of bulk Si and Ge

Figure 5-6 is a schematic diagram showing the conduction band structures for bulk Si and Ge. We find that Si and Ge have the lowest conduction band minima at the Δ-point [a point between Γ and X in Fig. 4-3(a)] and the L-point [also see Fig 4-

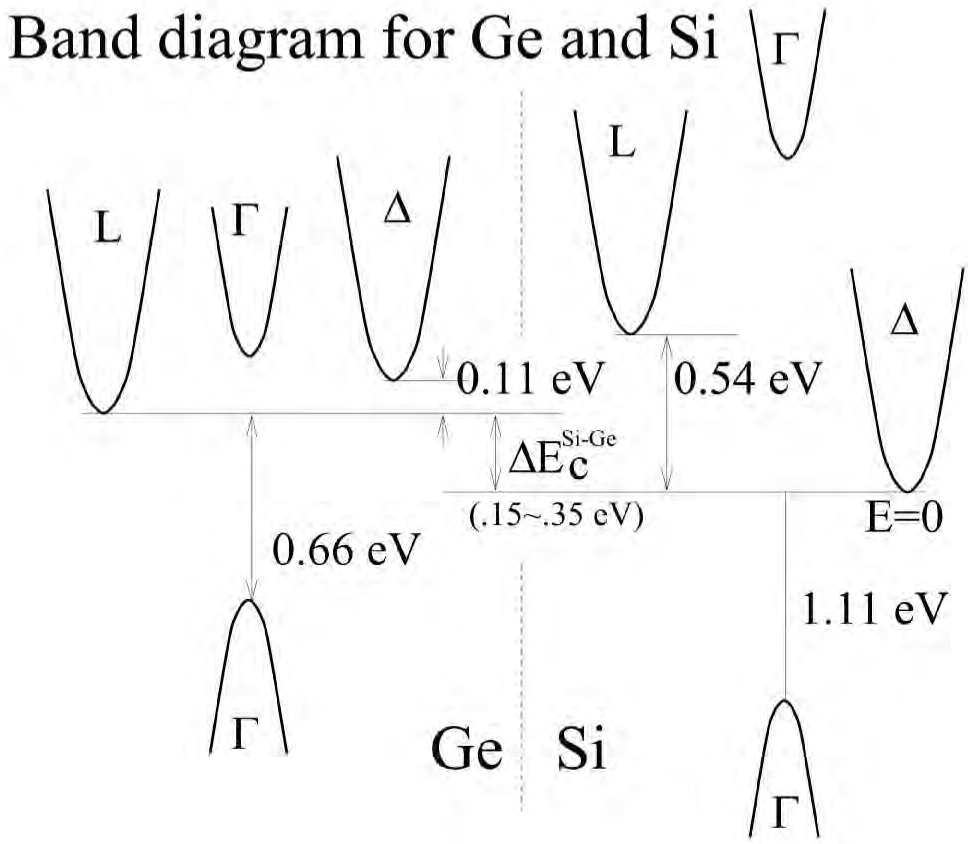

Figure 5-6: Schematic band diagram to show the relative energies between the various conduction band minima for bulk Si and Ge. The actual values for the conduction band offset $\Delta E_c^{\mathrm{Si-Ge}}$ (defined in the figure) range between 0.15 and 0.35 eV, according to the magnitude of the hydrostatic component of the lattice strain. ($\Delta E_c^{\mathrm{Si-Ge}} = 0.25$ eV is used for the conduction band offset in the calculation shown in this chapter.)

3(a)] in the Brillouin zone, respectively. When an interface is created between Si and Ge, the value for the conduction band offset between the Si Δ-point and the Ge L-point (denoted by $\Delta E_c^{\text{Si-Ge}}$) in the absence of uniaxial strain ranges between 0.15 eV to 0.35 eV, depending on the hydrostatic component of the lattice strain in the superlattice [68]. In the present work, we use a value of 0.25 eV for $\Delta E_c^{\text{Si-Ge}}$. It turns out that the final results of the calculated values for the thermoelectric transport coefficients are rather insensitive to the value of $\Delta E_c^{\text{Si-Ge}}$ used in the calculation. Since the primary purpose of this chapter is to investigate how the concept of Carrier Pocket Engineering applies to the Si/Ge superlattice system, we did not try to optimize the value used for $\Delta E_c^{\text{Si-Ge}}$ in our calculations.

5.3.2 Effect of uniaxial strain for the *L*- and Δ-valleys in Si/Ge superlattices

Uniaxial strain due to the lattice mismatch at the Si/Ge interfaces leads to a splitting of the conduction bands that are degenerate in the absence of strain [69]. These splittings (denoted as $\Delta E_c^{\langle\text{valley name}\rangle}$) are expressed with respect to the average band position, which is shifted only by the hydrostatic component of the strain. When the uniaxial strain along the (001) direction is applied to a Si or Ge crystal, as is realized in each layer of Si and Ge in a (001) oriented Si/Ge superlattice, the conduction band minima at the Δ-point (called the Δ-valleys) split according to (the energy of the L-point valley extrema is not affected in this case) [69],

$$\Delta E_c^{001} = \frac{2}{3}\Xi_u^{\Delta}(\epsilon_{\perp} - \epsilon_{||}) \tag{5.1}$$

$$\Delta E_c^{100,010} = -\frac{1}{3}\Xi_u^{\Delta}(\epsilon_{\perp} - \epsilon_{||}), \tag{5.2}$$

where the superscripts to ΔE_c denote the alignment direction for the pertinent valley, Ξ_u^{Δ} is the strain deformation potential for the Δ-valley (likewise, the notation Ξ_u^{L} is used to denote the strain deformation potential for the L-valley), and $\epsilon_{\perp}$ ($\epsilon_{||}$) is the component for the lattice strain tensor perpendicular (parallel) to the interface,

as defined below. Similarly, under uniaxial strain along the (111) direction, as is realized in (111) oriented Si/Ge superlattices, the energies of the Δ-point valleys are not affected, while the energy of the L-point valleys splits according to [69],

$$\Delta E_c^{111} = \frac{2}{3}\Xi_u^L(\epsilon_\perp - \epsilon_{||}) \tag{5.3}$$

$$\Delta E_c^{\bar{1}\bar{1}1,\bar{1}1\bar{1},1\bar{1}\bar{1}} = -\frac{2}{9}\Xi_u^L(\epsilon_\perp - \epsilon_{||}). \tag{5.4}$$

The values for $\epsilon_\perp$ and $\epsilon_{||}$ are calculated assuming that the lateral lattice constant ($||$ to the interfaces) for the strained layer is equal to that of the substrate, where a linear interpolation scheme is utilized to determine the lattice constant for a $Si_{1-x}Ge_x$ substrate via $\epsilon_\perp = (a_\perp - a_0)/a_0$, and $\epsilon_{||} = (a_{||} - a_0)/a_0$. Here, a_0 is the lattice constant for the layer in the absence of lattice strain, and $a_{||}$ (taken to be the lattice constant for the substrate in the present calculation) and $a_\perp$ are the lattice constants parallel and perpendicular to the interfaces, respectively, for the strained layer under consideration [69]. In the present work, the values for $a_\perp$ are calculated according to

$$a_\perp = a_0\left\{1 - D\left(a_{||}/a_0 - 1\right)\right\}, \tag{5.5}$$

where $D = 2\left(c_{12}/c_{11}\right)$ and $D = 2\left(c_{11} + 2c_{12} - 2c_{44}\right)/\left(c_{11} + 2c_{12} + 4c_{44}\right)$ for the (001) and (111) oriented superlattices, respectively. The values for the elastic constants c_{11}, c_{12}, c_{44} and other parameters that are used in the present calculations are summarized in Table 5.1.

5.4 Theoretical prediction of enhanced $Z_{3D}T$

5.4.1 (001) oriented Si/Ge superlattices

Shown in Fig. 5-7(a) is the effect of the uniaxial lattice strain on the position of the Δ-valley minima calculated for the (001) oriented Si/Ge superlattices grown on (001) $Si_{0.5}Ge_{0.5}$ and on (001) Si substrates. When the superlattice is grown on a

Table 5.1: List of parameters used in the present calculation for Si/Ge superlattices.

Band Parameter	Si	Ge
a_0 [Å][a]	5.4307	5.6579
m_t/m [a]	0.19	0.082
m_l/m [a]	0.92	1.59
band minima	Δ	L
N [b]	6	4
μ [cm^2/V·s][c]	1350	3600
$\kappa_{\rm ph}$ [W/m·K][d]	7.3	
$\Delta E_c^{\rm Si-Ge}$ [eV][e]	0.25	
c_{11}	1.675	1.315
c_{12}	0.650	0.494
c_{44}	0.801	0.684
Ξ_u^{Δ} [eV]	9.16	9.42
Ξ_u^{L} [eV]	16.14	15.13

[a] Data taken from Ref. [87].

[b] Number of equivalent valleys.

[c] Bulk carrier mobilities at 300 K. Data taken from Ref. [87].

[d] Value of the lattice thermal conductivity used in the present calculations for the Si/Ge superlattices. The experimental values found in the literature are somewhat smaller than this value (see Ref. [62]). Thus, the resultant values for $Z_{\rm 3D}T$ obtained in our calculation are conservative.

[e] Conduction band offset between the average position for Si Δ-valleys and the average position for Ge L-valleys. The literature values for $\Delta E_c^{\rm Si-Ge}$ are between 0.15 eV and 0.35 eV [68], depending on the hydrostatic component of the strain in the superlattice.

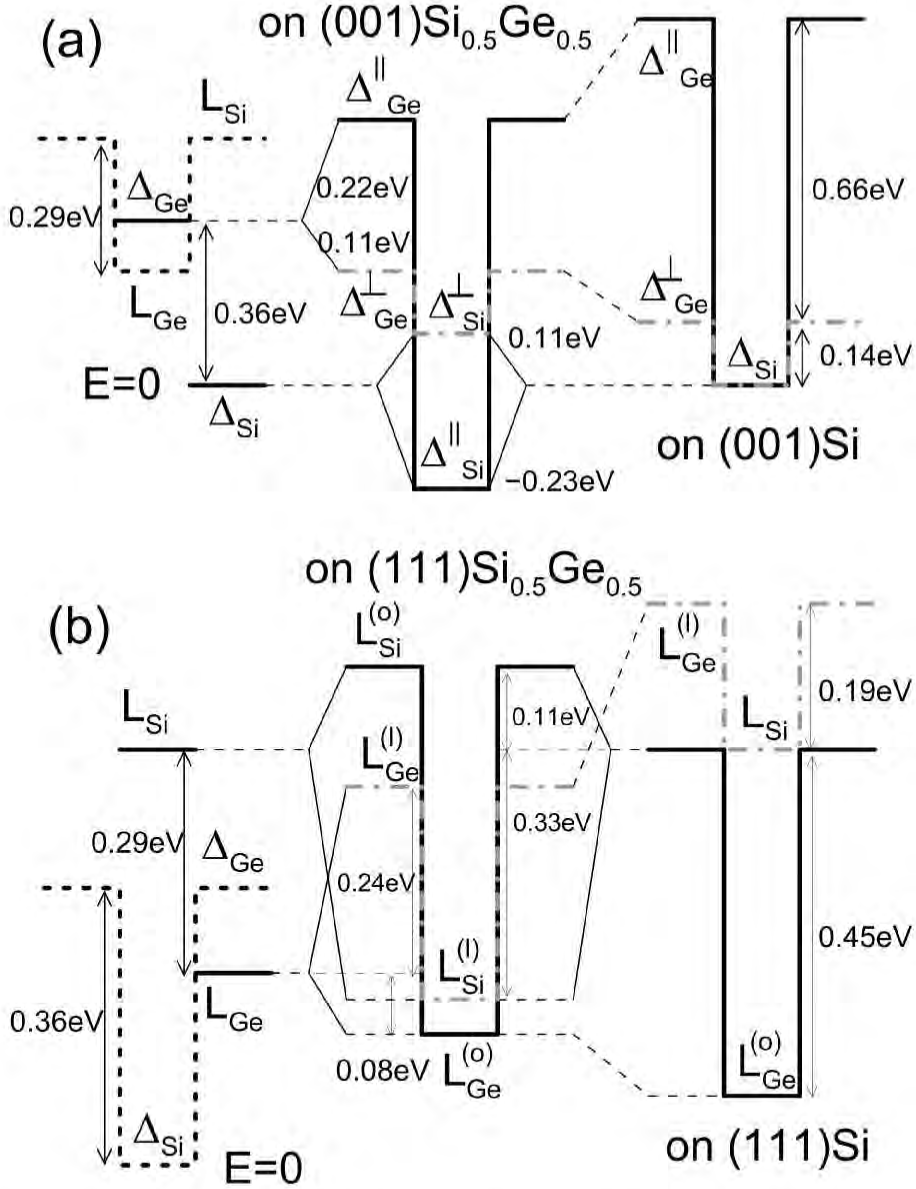

Figure 5-7: Conduction band offset diagrams for (a) (001) and (b) (111) oriented Si/Ge superlattices. The band offsets formed at the Δ^{001}- and $\Delta^{100,010}$-valleys (denoted by $\Delta^{||}$ and $\Delta^{\perp}$, respectively) and at the L^{111}- and $L^{\overline{1}11,\overline{1}1\overline{1},1\overline{1}\overline{1}}$-valleys (denoted by $L^{(l)}$ and $L^{(o)}$, respectively) are shown by the black solid and the grey dash-dotted lines in (a) and (b), respectively. The left, middle, and right diagrams denote the band offsets for the unstrained layers, for a superlattice grown on a $Si_{0.5}Ge_{0.5}$ substrate, and for a superlattice grown on a Si substrate, respectively. The band offsets at the L- and Δ-points in the Brillouin zone are also shown by the black dashed lines in the left hand diagrams of (a) and (b), respectively, for comparison.

(001) $Si_{0.5}Ge_{0.5}$ substrate, the Si and Ge layers experience tensile and compressive stresses, respectively. Therefore, the energy for the Ge (Si) Δ^{001}-valley is shifted upward (downward) and the Ge (Si) $\Delta^{100,010}$-valley is shifted downward (upward), which makes the effective barrier height larger (smaller) for the quantum well derived from the Δ^{001}-valley ($\Delta^{100,010}$-valley). Here, the superscript on Δ denotes the orientation along which the pertinent valley is aligned. The resulting density of states for electrons, shown in Fig. 5-8(a), is calculated for a (001) oriented Si(20 Å)/Ge(20 Å) superlattice grown on a (001) $Si_{0.5}Ge_{0.5}$ substrate, where the thicknesses for the Si and Ge layers (20 Å) are chosen so that the resulting optimum value for $Z_{3D}T$ is maximized. It is noted that the quantum wells for the Δ- and L-valleys are formed in the Si and Ge layers, respectively. Therefore, there is a possibility for the realization of the "Carrier Pocket Engineering condition" (§4.1) for the (001) oriented Si/Ge superlattice. However, for this particular case, L-point carriers make a negligible contribution to the transport, because the energy for the L-point subband edge is very high (~200 meV above the edge of the subband derived from the $\Delta^{100,010}$-valleys). The resultant $Z_{3D}T$ calculated with this superlattice structure is 0.24 at 300 K, which is rather small, although it is much larger than the value of the corresponding $Z_{3D}T$ for bulk Si ($Z_{3D}T = 0.014$ at 300 K).

We propose the following two approaches that can be used to increase the values of $Z_{3D}T$ even further for the Si/Ge superlattices. The first method is to grow the superlattice on a (001) oriented Si substrate so that the effective barrier height for the quantum wells derived from the Δ^{001}-valley will be enhanced due to the compressive stress on the Ge layer [see the right hand diagram in Fig. 5-7(a)]. Under these circumstances, the Δ^{001}-valley and $\Delta^{100,010}$-valleys in the Ge layer are shifted to higher and lower energies, respectively, because of the uniaxial strain along the (001) direction, while the Si Δ-valleys are left degenerate (since the Si layer is unstrained). The resultant density of states for a Si(20 Å)/Ge(20 Å) superlattice grown on a (001) Si substrate is shown in Fig. 5-8(b). With this design of the superlattice, the subband levels associated with the Δ^{001}-valley and the $\Delta^{100,010}$-valleys, respectively, stay very close to each other in energy, because the large effective mass along the (001) direction

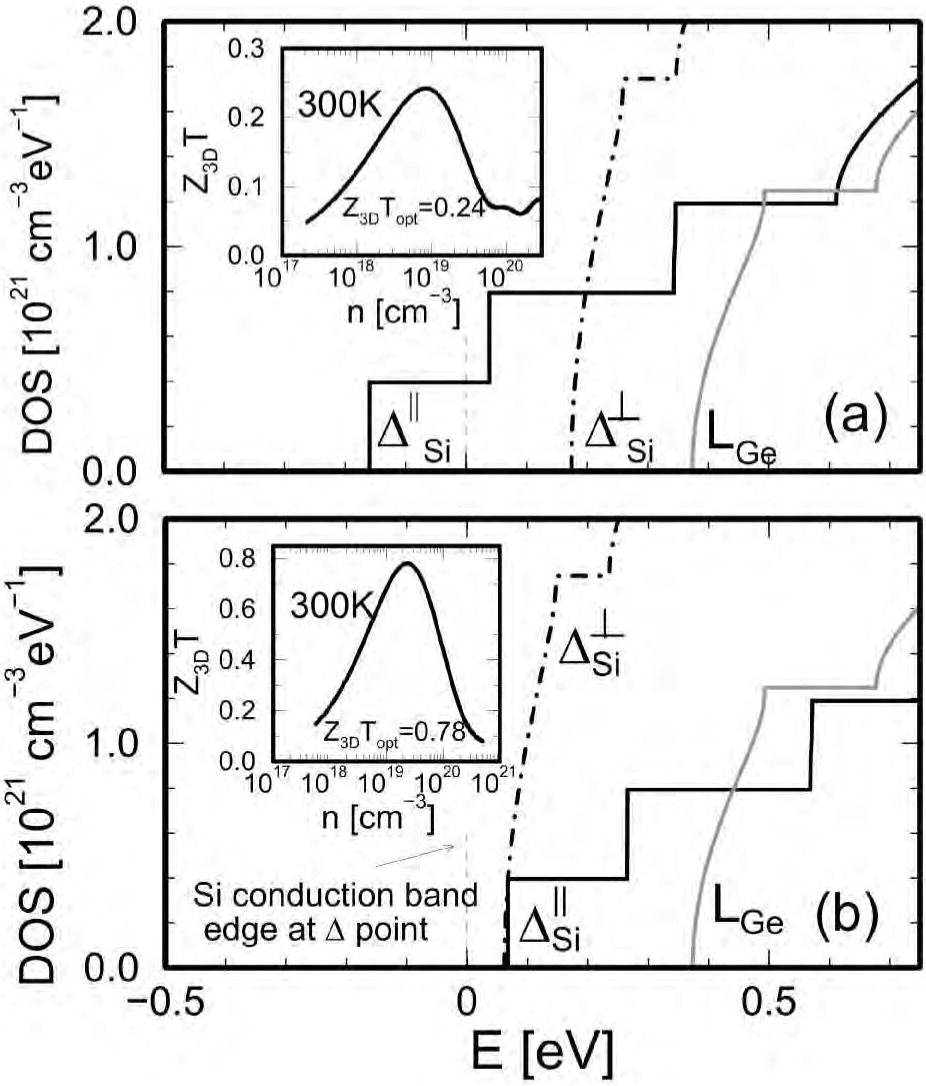

Figure 5-8: Density of states for electrons in (001) oriented Si/Ge superlattices as a function of energy relative to the Δ-point of bulk Si calculated for the subbands derived from the Δ^{001}- (solid curve), $\Delta^{100,010}$- (dash-dotted curve) and L- (grey-solid curve) point valleys: (a) a Si(20 Å)/Ge(20 Å) superlattice grown on a (001) oriented $Si_{0.5}Ge_{0.5}$ substrate, (b) a Si(20 Å)/Ge(20 Å) superlattice grown on a (001) oriented Si substrate. The calculated value of $Z_{3D}T$ as a function of the carrier concentration is shown in the inset of each figure. The chemical potential ζ that gives the optimum value of $Z_{3D}T$ (denoted by $Z_{3D}T_{opt}$) is at the band edge of the $\Delta^{||}$-subband for both (a) and (b). See the caption in Fig. 5-7 for the meaning of the symbols $\Delta^{\perp}_{Si}$, $\Delta^{||}_{Si}$ and L_{Ge}.

(confinement direction) for the Δ^{001}-valley is compensated by the large barrier height when forming subband levels for the quantum well. The resulting value for $Z_{3D}T$ calculated for this superlattice is 0.78 at 300 K [see the inset of Fig. 5-8(b)], which represents more than a factor of three enhancement relative to the corresponding value for $Z_{3D}T$ for the superlattice grown on a (001) $Si_{0.5}Ge_{0.5}$ substrate. One drawback for this design of the superlattice is that the superlattice is not strain-symmetrized, i.e. the lattice constant for a fully relaxed Si(20 Å)/Ge(20 Å) superlattice, which is considered to have the same lattice constant as the $Si_{0.5}Ge_{0.5}$ alloy, is different from the lattice constant for the substrate (Si in this case). Thus, a Si(20 Å)/Ge(20 Å) superlattice can be grown on a (001) oriented Si only up to a certain critical thickness (of the order of 10 to 100 Å) before a large number of crystalline defects and dislocations are introduced, when the superlattice is fully relaxed.

5.4.2 (111) oriented Si/Ge superlattices

The second method that can be used to increase the values of $Z_{3D}T$ for the Si/Ge superlattice is to grow the superlattice in the (111) direction [see Fig. 5-7(b) for the conduction band offsets for the L-valleys]. For a superlattice grown in this way, the subbands derived from the Δ-valleys of Si and Ge remain degenerate due to the symmetry only. The resulting value for $Z_{3D}T$ for the (111) oriented Si(15 Å)/Ge(20 Å) superlattice grown on a (111) oriented $Si_{0.5}Ge_{0.5}$ substrate is calculated to be 0.98 at 300 K [see Fig. 5-9(a)], which is a factor of 4 enhancement relative to the value of $Z_{3D}T$ calculated for a (001) oriented Si(20 Å)/Ge(20 Å) superlattice grown on a (001) oriented $Si_{0.5}Ge_{0.5}$ substrate. It is noted that although the Si(15 Å)/Ge(20 Å) superlattice doesn't have a completely strain-symmetrized structure, since $d_{Si} \neq d_{Ge}$, where d_{Si} and d_{Ge} are thicknesses for the Si and Ge layers, respectively, the corresponding values for $Z_{3D}T$ calculated for a completely strain-symmetrized (111) oriented Si(20 Å)/Ge(20 Å) superlattice are found to have similar values to those for the Si(15 Å)/Ge(20 Å) superlattice (see §5.4.3).

An even larger value of $Z_{3D}T$ is expected if the superlattice is designed in such a way that the subbands derived from the Δ-valleys and the $L^{\overline{1}\overline{1}1,\overline{1}1\overline{1},1\overline{1}\overline{1}}$-valleys stay

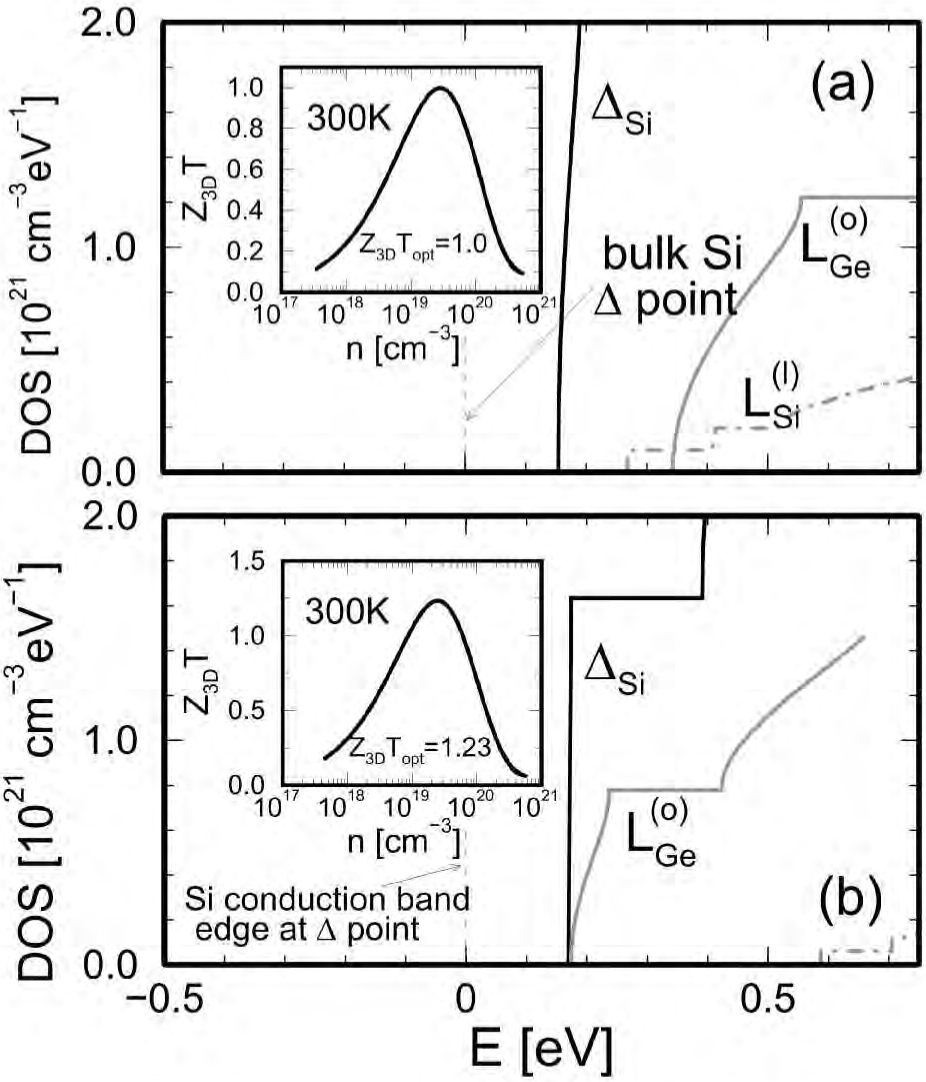

Figure 5-9: Density of states for electrons in (111) oriented Si/Ge superlattices as a function of energy relative to the Δ-point of bulk Si calculated for the subbands derived from the L^{111}- (grey dash-dotted curve), $L^{\overline{1}\overline{1}1,\overline{1}1\overline{1},1\overline{1}\overline{1}}$- (grey solid curve), and Δ- (solid curve) point valleys: (a) a Si(15 Å)/Ge(20 Å) superlattice grown on a (111) oriented $Si_{0.5}Ge_{0.5}$ substrate, (b) a Si(15 Å)/Ge(40 Å) superlattice grown on a (111) oriented Si substrate. The calculated value of $Z_{3D}T$ as a function of the carrier concentration is shown in the inset of each figure. The chemical potential ζ that gives the optimum value of $Z_{3D}T$ (denoted by $Z_{3D}T_{opt}$) is at the band edge of the Δ-subband for both (a) and (b). See the caption in Fig. 5-7 for the meaning of the symbols Δ_{Si}, $L_{Si}^{(l)}$ and $L_{Ge}^{(o)}$.

very close to each other in energy. This situation is conceptually realized by growing a Si(15 Å)/Ge(40 Å) superlattice on top of a (111) oriented Si substrate [see Fig. 5-7(b) (the right hand diagram) and Fig. 5-9(b) for the band offsets and resulting electronic density of states as a function of energy, respectively]. Since the Ge layers in this superlattice are compressively strained while the Si layer is unstrained, only the Ge L-point valleys are split into a L^{111}-valley (higher in energy) and $L^{\overline{1}\overline{1}1,\overline{1}1\overline{1},1\overline{1}\overline{1}}$-valleys (lower in energy). The resulting value for $Z_{3D}T$ calculated for this structure is 1.25, which is a factor of five enhancement relative to the corresponding value of $Z_{3D}T$ for the Si(20 Å)/Ge(20 Å) superlattice grown on a (001) oriented $Si_{0.5}Ge_{0.5}$ substrate. It should be noted that the growth of such a non-symmetrized superlattice is not yet possible with the current MBE technology. The realization of such superlattices awaits future developments in material science.

5.4.3 Temperature dependence of $Z_{3D}T$

It is of practical interest to see how the value of $Z_{3D}T$ increases as the temperature is increased. Shown in Fig. 5-10 is the calculated value for $Z_{3D}T$ as a function of temperature for a strain-symmetrized (001) oriented Si(20 Å)/Ge(20 Å) superlattice grown on a (001) oriented $Si_{0.5}Ge_{0.5}$ substrate as well as for a strain-symmetrized (111) oriented Si(20 Å)/Ge(20 Å) superlattice grown on a (111) oriented $Si_{0.5}Ge_{0.5}$ substrate. The calculation was made assuming a $T^{-\nu}$ dependence for the value of μ with $\nu = 1$ (empirical result for bulk Si) and $\nu = 1.5$ (acoustic phonon deformation potential scattering), where μ is the electron mobility. We also assume that the value of κ_{ph} for the Si/Ge superlattices (see Table 5.1) is constant with temperature, since the length for the phonon mean free path ℓ is limited by the thicknesses of the Si and Ge layers. In Fig. 5-10, we find that the value of $Z_{3D}T$ increases significantly as the temperature is increased for the strain-symmetrized (111) oriented Si(20 Å)/Ge(20 Å) superlattice, so that $Z_{3D}T \simeq 1.5$ is predicted at ~600 K for such a superlattice.

It turns out that (see §5.6–§5.9 and Chapter 6), the dominant scattering mechanism for an actual (001) oriented Si(20 Å)/Ge(20 Å) superlattice (for $n > 1\times10^{18}$ cm^{-3}) is ionized impurity scattering. Although ionized impurity scattering has an effect of

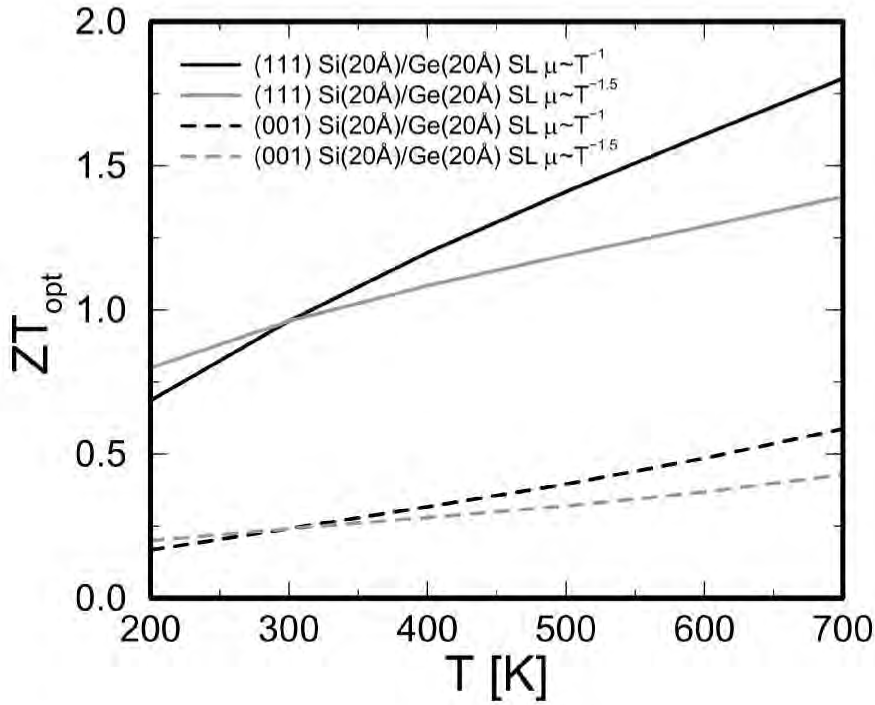

Figure 5-10: Calculated values for the optimized $Z_{3D}T$s for the strain-symmetrized (001) oriented Si(20Å)/Ge(20Å) superlattices grown on a (001) oriented $Si_{0.5}Ge_{0.5}$ substrate (dashed curves) and for the strain-symmetrized (111) oriented Si(20Å)/Ge(20Å) superlattices grown on a (111) oriented $Si_{0.5}Ge_{0.5}$ substrate (solid curves). The temperature dependence for $\mu/\kappa_{\rm ph}$ is taken to be $T^{-1.5}$ (grey curves) and T^{-1} (solid curves).

increasing the value of the Seebeck coefficient through its $\tau \sim E^{3/2}$ dependence for the relaxation time τ for electrons, where E is the energy of the electrons measured from the pertinent band edge, it also has an effect of reducing the value of carrier mobility μ relative to the values obtained without ionized impurity scattering as realized in lightly doped or undoped samples ($n < 1\times10^{17}$ cm^{-3}). In Chapter 6, we will see that the effect of ionized impurity scattering should be greatly reduced by introducing the δ- and modulation doping schemes to dope carriers into the superlattices.

5.5 Experimental procedure and description of samples

In §5.5.1, we describe the design of our samples that are used for our experimental proof-of-principle study (§5.6 §5.9) to test the basic concept developed in §5.4. We will then explain how our experiments are performed using these samples in §5.5.2, whose experimental results are shown in §5.6–§5.9, later in this chapter.

5.5.1 Description of samples

High quality (001) oriented Si(20 Å)/Ge(20 Å) superlattice samples that are used for the experimental proof-of-principle study in this chapter were fabricated by Dr. J. L. Lin in the group of Prof. K. L. Wang at UCLA. These samples are grown by the molecular-beam epitaxy (MBE) technique using a $Si_{1-x}Ge_x$ graded buffer layer on top of a (001) oriented Si or SOI (Si-on-insulator) substrate, where the Ge composition x is gradually increased from 0 to 0.5 across the thickness (1-2 μm) of the buffer layer (see Figs. 5-11 and 5-12).

The structures of these samples are schematically drawn in Figs. 5-11 and 5-12, where one set of samples (JL167 and JL169) are grown on top of (001) oriented Si substrates (see Fig. 5-11) and the other set of samples (JL193, JL194, JL197 and JL199) are grown on top of (001) oriented SOI (Si-on-insulator) substrates using thinner buffer layers than those used for samples JL167 and JL169 (see Fig. 5-12).

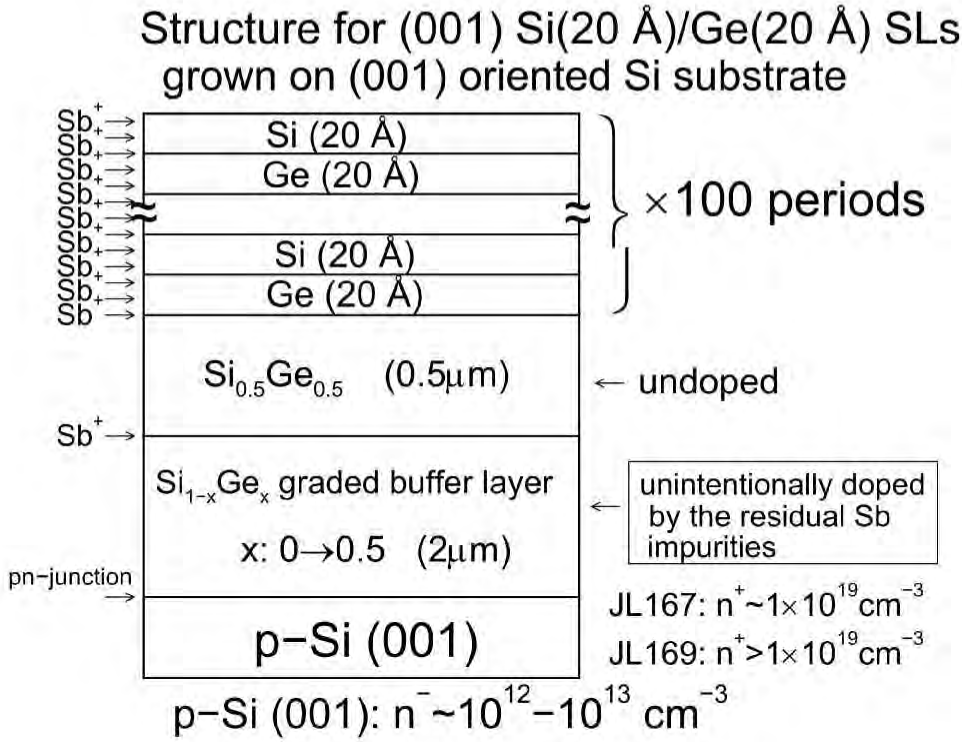

Figure 5-11: A schematic diagram to show the sample structure for the Si(20 Å)/Ge(20 Å) superlattices grown on (001) oriented Si substrates (samples JL167 and JL169). These superlattice samples were grown by Dr. J. L. Liu at UCLA. The dopant concentrations (denoted by n^+) for these samples are approximately 1×10^{19} cm^{-3}, but the n^+ for sample JL169 is supposed to be higher than that for sample JL167. The (001) Si substrate at the bottom of the figure is slightly p-type doped ($n^- \sim 10^{12}$–10^{13} cm^{-3}). Since the $Si_{1-x}Ge_x$ ($x : 0 \rightarrow 0.5$) graded buffer layer is slightly doped n-type due to the residual Sb surfactant impurities, a pn-junction is formed at the interface between the $Si_{1-x}Ge_x$ ($x : 0 \rightarrow 0.5$) graded buffer layer and the (001) oriented p-type Si substrate, which should provide good electrical insulation between the film (superlattice+buffer layer) and the substrate. See §5.6 for the experimental results on the various transport coefficients for these samples.

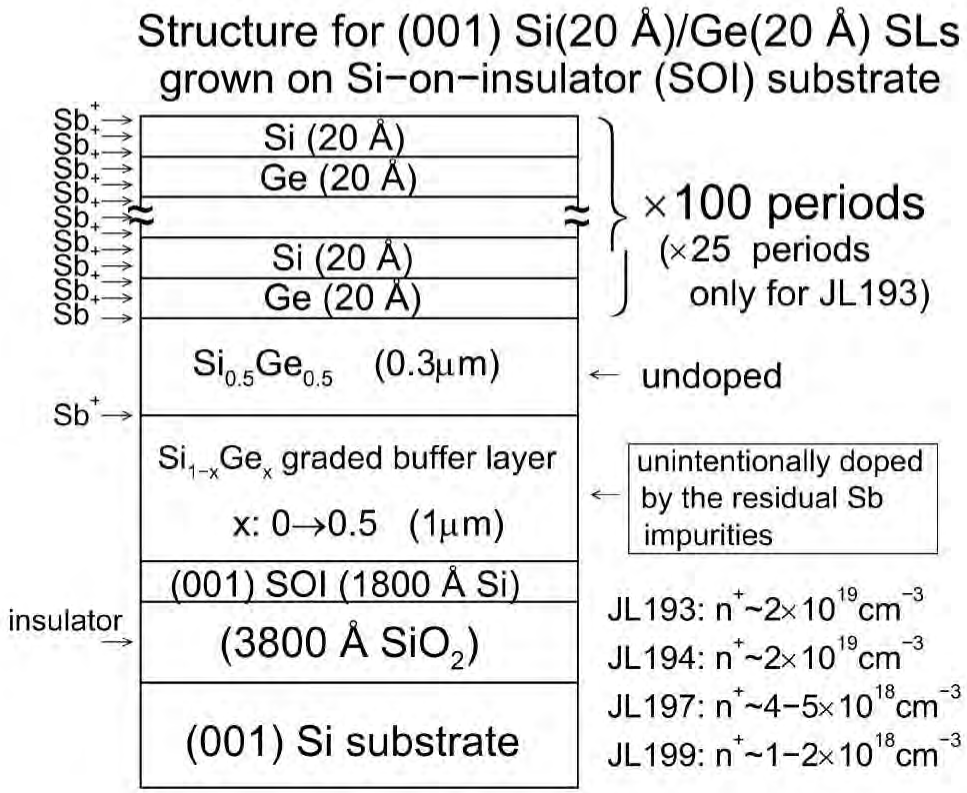

Figure 5-12: A schematic diagram to show the sample structure for the Si(20 Å)/Ge(20 Å) superlattices grown on (001) oriented SOI (Si-on-insulator) substrates (samples JL193, JL194, JL197 and JL199). These superlattice samples were grown by Dr. J. L. Liu at UCLA. The dopant concentrations (denoted by n^+) for these samples are in the range between 1×10^{18} cm^{-3} and 2×10^{19} cm^{-3}. These samples are provided to avoid the effect of the value of $-S$ shooting up below 200 K as discussed in §5.6.2. A SOI (Si-on-insulator) substrate is composed of 1800 Å of a (001) oriented Si layer on top of a 3800 Å SiO_2 layer, where the SiO_2 layer is grown on top of the (001) oriented Si substrate as well. This 3800 Å SiO_2 layer should provide perfect electrical insulation between the film (the layers above the 1800 Å Si layer in the above figure) and the (001) oriented Si substrate underneath the 3800 Å SiO_2 layer. In additon, a 3800 Å SiO_2 layer is considered to provide good thermal insulation between the film and substrate as well, as discussed in §5.6.2 and §5.7.2. See §5.7 for the experimental results on the various transport coefficients for these samples.

For both sets of samples, the actual Si(20 Å)/Ge(20 Å) superlattices are grown on top of an undoped $Si_{0.5}Ge_{0.5}$ buffer layer (0.3-0.5 μm in thickness) that is grown on top of the $Si_{1-x}Ge_x$ ($x : 0 \rightarrow 0.5$) graded buffer layer mentioned above. Shown in Fig. 5-13 are examples of the cross-sectional TEM micrographs for these samples (these specific pictures are taken for sample JL167), which show high crystalline quality for these samples and atomically sharp, and flat interfaces at the Si/Ge boundaries.

The fabrication processes for these superlattices are briefly explained as follows. First, a layer of $Si_{1-x}Ge_x$ ($x : 0 \rightarrow 0.5$) graded buffer layer is grown on top of a (001) oriented Si or SOI (Si-on-insulator) substrate using Sb (antimony) as a surfactant (using the surfactant-mediated growth technique) [86]. The $Si_{1-x}Ge_x$ ($x : 0 \rightarrow 0.5$) graded buffer layer grown in this way typically has a very small threading dislocation density (1.5×10^4 cm^{-3}) and has atomically smooth surfaces, whose surface roughness is estimated to be 20 Å from a number of AFM studies (20 μm $\times$ 20 μm in area) for similarly grown samples [86]. Second, a homogeneous, undoped $Si_{0.5}Ge_{0.5}$ buffer layer (0.3-0.5 μm in thickness) is grown on top of the $Si_{1-x}Ge_x$ ($x : 0 \rightarrow 0.5$) graded buffer layer. It is noted that a sheet of Sb impurities, that were used as a surfactant for the growth of the $Si_{1-x}Ge_x$ ($x : 0 \rightarrow 0.5$) graded buffer layer, remain at the interface between the $Si_{1-x}Ge_x$ ($x : 0 \rightarrow 0.5$) graded buffer layer and the undoped $Si_{0.5}Ge_{0.5}$ buffer layer, whereas no surfactant is used for the growth of the undoped $Si_{0.5}Ge_{0.5}$ homogeneous buffer layer. There are the following two roles for the undoped $Si_{0.5}Ge_{0.5}$ homogeneous buffer layer: (1) Since the Sb surfactant impurities that are used for the growth of the $Si_{1-x}Ge_x$ ($x : 0 \rightarrow 0.5$) graded buffer layer act as an n-type dopant, an undoped $Si_{0.5}Ge_{0.5}$ layer is nessesary to establish good electrical isolation between the graded buffer layer and the superlattice part of the sample. (2) Since the top surface of the $Si_{1-x}Ge_x$ ($x : 0 \rightarrow 0.5$) graded buffer layer is highly strained due to the rapid (though continuous) change in the lattice constant across the thickness of the buffer layer, an additional layer of homogeneous $Si_{0.5}Ge_{0.5}$ (0.3-0.5 μm in thicknes) is needed to obtain a (001) surface of $Si_{0.5}Ge_{0.5}$ that is fully relaxed through the lattice strain for the growth of strain-symmetrized (001) oriented Si/Ge superlattices. Finally, structually strain-symmetrized Si(20 Å)/Ge(20 Å) superlattices [with 100 periods,

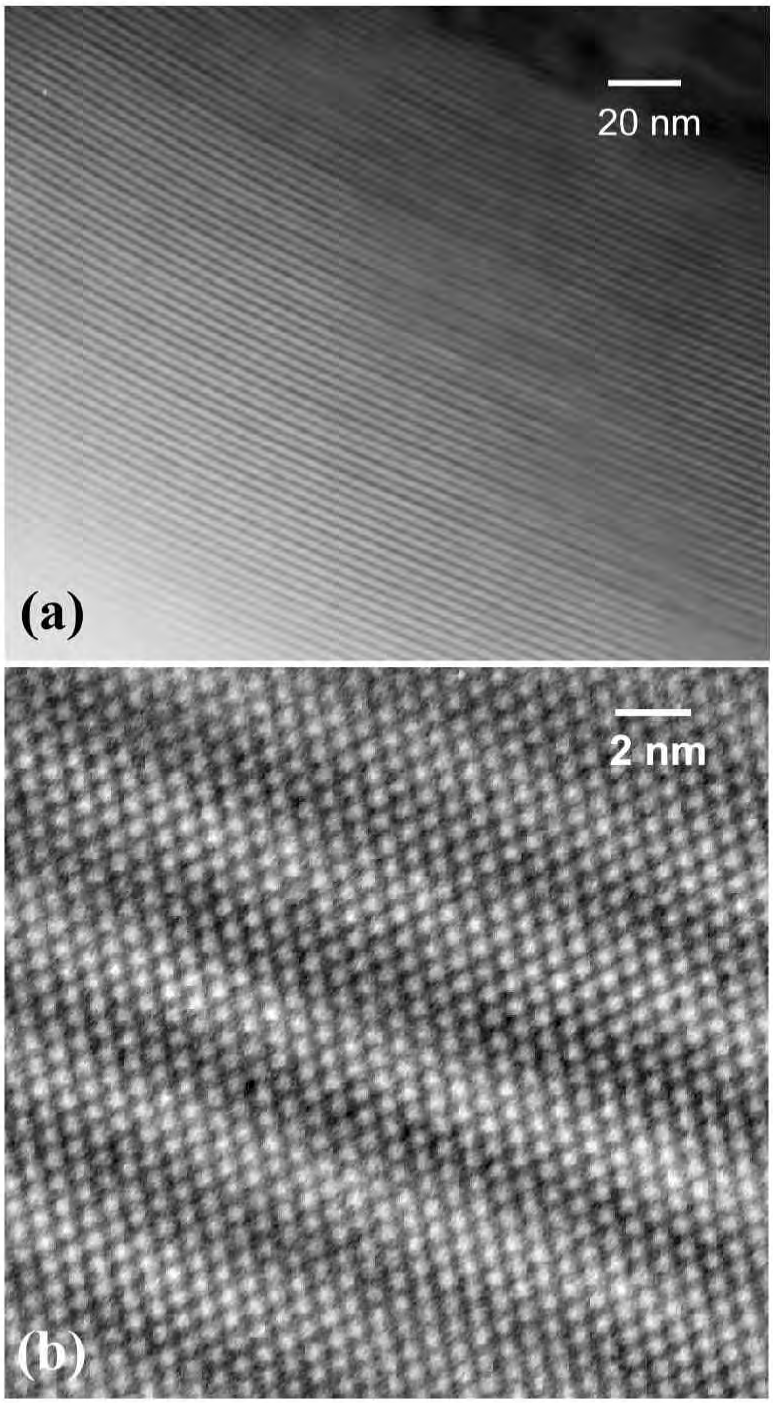

Figure 5-13: TEM (transmission electron microscope) cross-sectional micrographs for a (001) oriented Si(20 Å)/Ge(20 Å) superlattice grown on a SiGe graded buffer layer on top of a (001) oriented Si substrate (sample JL167), showing (a) a wide area of the cross section and (b) a high (atomic) resolution image. TEM images shown here were produced by Dr. T. Radetic in the group of Prof. R. Gronsky in the University of California at Berkeley.

except for sample JL193, where only 25 periods of the Si(20 Å)/Ge(20 Å) layers] were grown on top of the undoped (001) oriented $Si_{0.5}Ge_{0.5}$ buffer layer.

The growth temperature for the Si(20 Å)/Ge(20 Å) layers is chosen to be 500 °C for samples JL167 and JL169. The growth temperature used for the growth of Si(20 Å)/Ge(20 Å) layers in more recent samples (JL193, JL194, JL197 and JL199) is reduced to 350 °C to provide sharper Si/Ge interfaces in the superlattice by minimizing interdiffusion problems.

The samples provided to us by the UCLA group are homogeneously doped throughout the whole thickness of the Si(20 Å)/Ge(20 Å) superlattice part of the sample during the growth process. The doping levels of the samples are in the range between 1×10^{18} cm^{-3} and 2×10^{19} cm^{-3}, where Sb impurities are used as an n-type dopant. In the future, efforts should be expended experimentally on using δ- and/or modulation doping of the Si/Ge superlattices, since the values of $Z_{3D}T$ for the samples that are δ- or modulation-doped in the Ge layers are predicted to be significantly enhanced relative to the values of the corresponding $Z_{3D}T$ for the homogeneously doped samples as we discuss in Chapter 6.

5.5.2 Experimental procedure

The measurements of various transport coefficients [electrical conductivity (denoted by σ), Seebeck coefficient (denoted by S) and Hall carrier density (denoted by n_{Hall})] for the samples described in §5.5.1 are performed using a home-made multi-purpose probe that is specially designed for transport measurements (see Fig. 5-14), in the temperature range between 4.2 K and 400 K. On some occasions, a Quantum Design SQUID magnetometer (systems $MPMS_2$ and $MPMS_{XL}$), equipped with a custom-made probe specially designed for transport measurements, was also used for our convenience in making the measurements.

For all the transport measurements, electrical contacts were made with Sb (5%) doped In (indium) solder using an ordinary soldering iron between the sample and the gold wire leads (or thermocouple junctions). The electrical contacts made in this way show an ohmic behavior in their I-V characteristics with a contact resistance

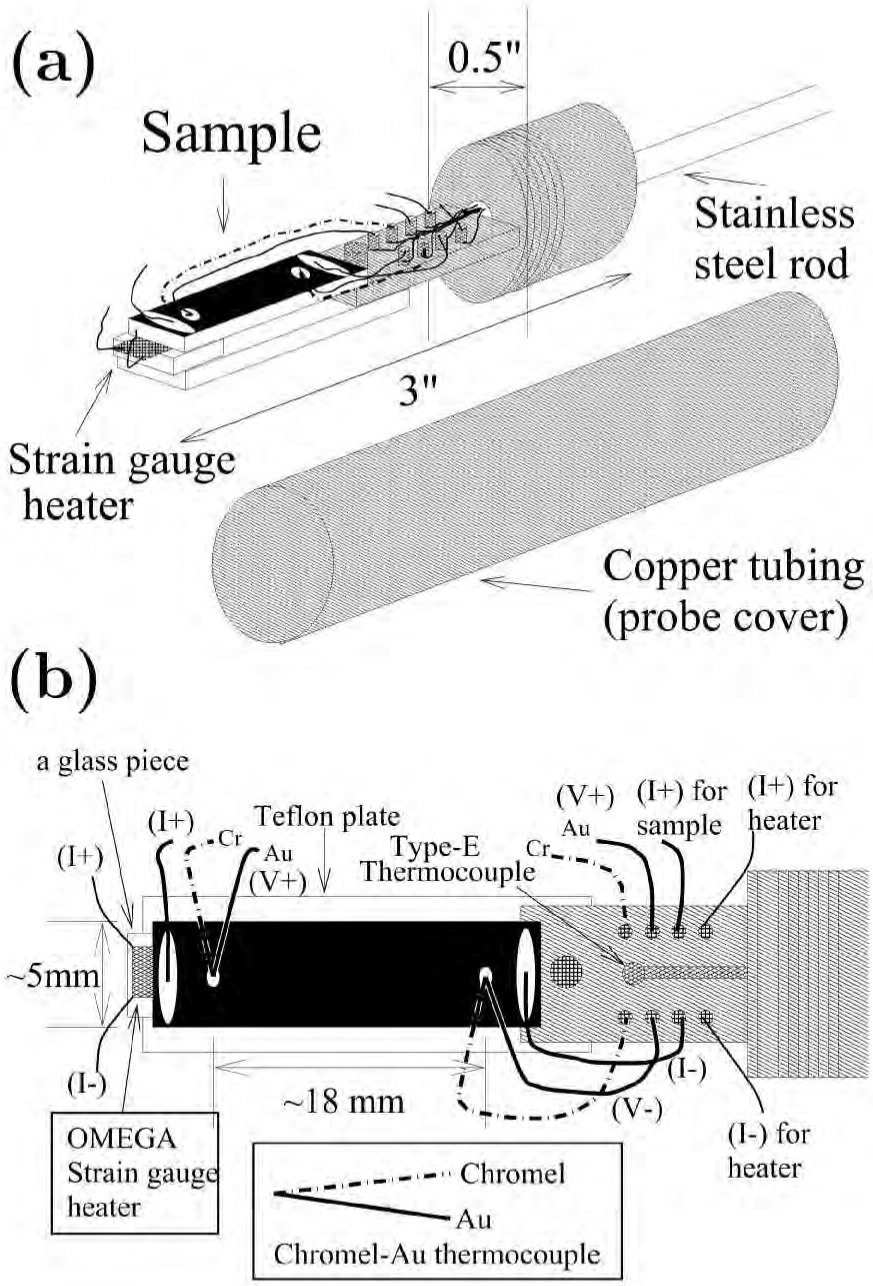

Figure 5-14: A schematic illustration of the home-made probe for transport measurements that is used in the present work: (a) probe head mounted with a sample and (b) top view of (a).

of 10–60 Ω. A typical size of the samples used for the conductivity and Seebeck measurements is 5 mm (width) × 25 mm (length) × 4000 Å (thickness). The thickness given here is the thickness for the superlattice part of the samples only (see Figs. 5-11 and 5-12), which is used for the calculation of the experimental conductivities σ and Hall carrier concentrations n_{Hall} of the various samples. The physical thickness of the samples including the (001) oriented Si substrate, on top of which a buffer layer and a Si(20 Å)/Ge(20 Å) superlattice are grown, is 0.4 mm. A conventional four probe technique is utilized for the resistivity measurements using an electrical current of typically 0.1 mA. For all the transport measurements using the home-made probe (see Fig. 5-14), the temperature of the sample was varied by inserting the probe head into a liquid He (helium) Dewar, where a natural temperature gradient between 4.2 K and 280 K is maintained from the bottom of the Dewar (liquid He temperature) to the top of the Dewar (ambient temperature). This temperature gradient is used to attain a desired temperature between 4.2 K and 280 K. For temperatures higher than 280 K, the probe head is heated up to 400 K in a tube furnace. For the measurement of the Seebeck coefficient above room temperature, a flexible belt-shaped electrical heater was utilized instead of the tube furnace, since the belt-shaped heater provided a better thermal stability between 280 K and 400 K.

The measurements of the Seebeck coefficient are performed using two pairs of Chromel-Au(0.07 at.% Fe) thermocouples, where each thermocouple junction is attached to a sample using Sb (5 %) doped In (indium) solder as mentioned above, and using a separation between these two contacts of ~18 mm [see Fig. 5-14(b)]. A typical size of the contacts made in this way is 0.5 mm in the diameter. The temperatures of the sample at each contact are measured with respect to that of a small copper block [7 mm (width) × 20 mm (length) × 1.5 mm (thickness)] that is attached to the probe head [see Fig. 5-14]. It is noted that there is another (Type-E, Nickel-Chromium vs. Copper-Nickel) thermocouple which is attached to the copper block that measures the temperature of the probe head with respect to the ice point. Therefore, the absolute temperature for the sample can be determined by combining the temperature measured by the Type-E thermocouple and the temperature (difference) measured

by the Chromel-Au(0.07 at.% Fe) thermocouple that is attached to the sample.

Once the two pairs of Chromel-Au(0.07 at.% Fe) thermocouples are attached to the sample in this way, the sample is mounted on the probe head in such a way that one end of the sample (substrate) touches the copper block and the other end of the sample is placed on top of a glass piece, where an OMEGA strain gauge (OMEGA SG-1.5/120-LY11, 120 Ω) is clamped between the sample and the glass piece. The OMEGA strain gauge here will be used as a heater for the Seebeck coefficient measurement. The probe head prepared in this way is finally capped with a copper tube [see Fig. 5-14(a)], sealed with a Teflon tape and evacuated to a reduced pressure for the Seebeck coefficient measurement at low temperatures ($T < 100$ K), where the effect of parisitic thermal conduction through the He (helium) gas at low temperatures is minimized.

For each point of the measurement as a function of temperature, we had waited for a sufficient amount of time (typically more than 10 minutes) before taking a set of ΔV vs. ΔT data, so that the temperature in the probe head is equilibrated. An incrementing electrical current is, then, passed through the strain gauge heater in a stepwise way from 0 mA to 22.4 mA in a few steps, which corresponds to a power of 60 mW. This sequence of events typically creates a temperature difference of 0.1–1 K across the two thermocouple junctions on the sample. The temperatures at the two thermocouple junctions and the Seebeck voltage induced across the sample are simultaneously measured in each plateau reagion of the current profile that is applied to the strain gauge heater, where Au (gold) leads for the thermocouple are used for the Seebeck voltage measurement across the sample as well [see Fig. 5-14(b)]. It is noted that the contribution of the Seebeck voltage induced in the Au wires during the measurement is negligible compared to the Seebeck voltage induced in the sample. ΔV vs. ΔT data taken in this way, where ΔV and ΔT are the induced sample's Seebeck voltage and the corresponding temperature difference between the two thermocouple junctions, respectively, is plotted on a screen by the use of a computer. The values for the resultant Seebeck coefficient are then determined from the linear regression of these data. The curves obtained for ΔV vs. ΔT are usually very linear as they

are recorded, but on some occasions several data points that were taken immediately after the steps (jumps) in the applied current profile are eliminated before taking the linear regression, in order to obtain a better linearity in ΔV vs. ΔT curves.

After measuring the electrical conductivity σ and the Seebeck coefficient S as a function of temperature in this way, the very same piece of the sample that was used for the σ and S measurements is cut into a square shape (5 mm$\times$5 mm) for the Hall coefficient measurement. An electrical contact is made at each corner of the square samples using Sb (5 %) doped In (indium) solder as mentioned above, where an electrical current of 1-5 mA is passed through the sample along the diagonal axis and the voltages are measured along the other diagonal axis (in the direction perpendicular to the current direction). Both the direction of the applied magnetic field B (0.25-0.3 T) and the direction of the applied electrical current I are flipped at each point of the measurement, so that the net contribution of the Hall voltage can be subtracted out from the four combinations of measurements using $\pm B$ and $\pm I$. The same pieces of the samples used for the Hall coefficient measurements are also used for the resistivity measurements using the van der Pauw method at some selected temperatures. It turns out that the resistivities measured by the van der Pauw method are occasionally 5-10 % lower than the resistivitiy measured by the conventional four probe method. In the event that the values differ from one another, the values for the electrical resistivity determined by the four probe method are calibrated according to the values obtained by the van der Pauw method.

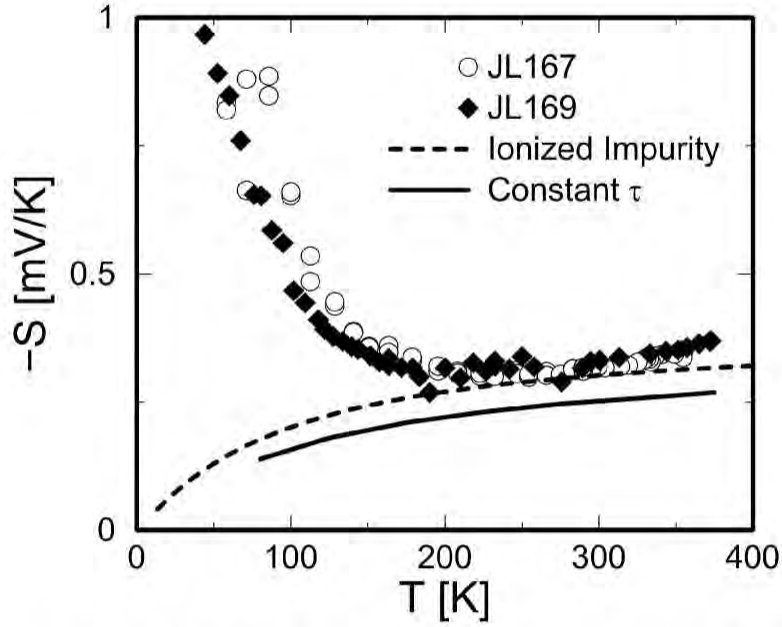

Figure 5-15: Seebeck coefficient as a function of temperature measured for samples JL167 (open circles) and JL169 (filled diamonds), together with theoretical results obtained for $n = 4\times10^{18}$ cm^{-3} using (1) the constant relaxation time approximation (solid curve) and (2) semiclassical models including ionized impurity scattering as the dominant scattering mechanism (see Chapter 6). The most probable explanation for the rapid increase in the measured Seebeck coefficient $|S|$ is due to the phonon drag effect at the current stage of the investigation (see §5.6.2 and Fig. 5-18 for more discussion).

5.6 Experimental Proof-of-Principle Study using (001) oriented Si(20 Å)/Ge(20 Å) superlattices grown on (001) Si substrates

5.6.1 S, σ and n_{Hall} for samples JL167 and JL169

Shown in Figs. 5-15–5-17 are the Seebeck coefficient S, Hall carrier density n_{Hall} and electrical conductivity σ for samples JL167 and JL169 (see §5.5.1) measured as a function of temperature in the temperature range between 4.2 K and 400 K, together with the results of semiclassical models, including ionized impurity scattering as the dominant scattering mechanism, that are developed in Chapter 6. In Fig. 5-15, we find that the measured Seebeck coefficients for samples JL167 and JL169 have almost identical values and behaviors as each other from 50 to 380 K, despite the belief

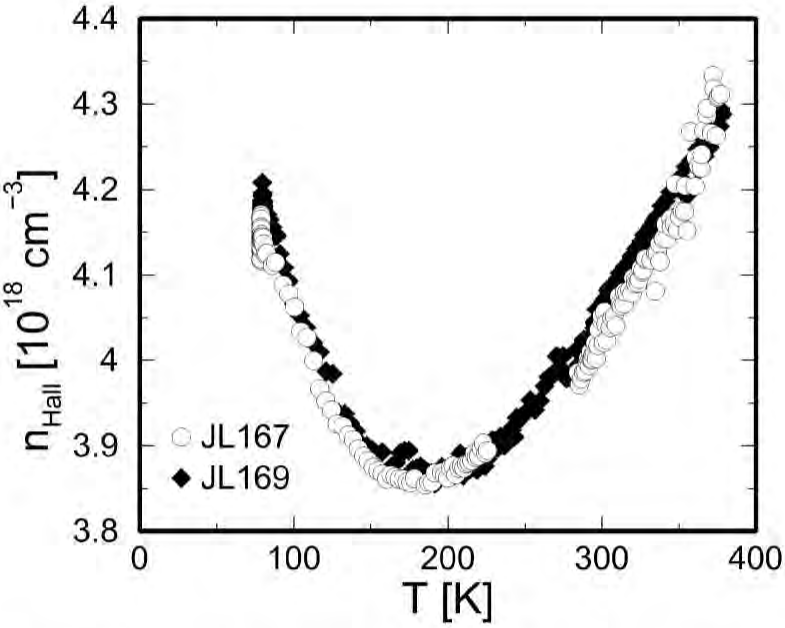

Figure 5-16: Hall carrier concentration as a function of temperature measured for samples JL167 (open circles) and JL169 (filled diamonds). The Hall coefficient measurements shown here are performed using an electrical current of 5 mA and a magnetic field of 0.26 T. The sizes of the samples that are used in these measurements are typically 5 mm × 5 mm.

that the dopant concentration for sample JL169 ($n^+ > 1\times10^{19}$ cm^{-3}) is higher than that for sample JL167 ($n^+ \approx 1\times10^{19}$ cm^{-3}). This discrepancy is partly clarified by looking at the data for the Hall carrier concentration as a function of temperature for samples JL167 and JL169, as shown in Fig. 5-16, where we find that samples JL167 and JL169 virtually have the same carrier concentration, i.e., $n_{\rm Hall} \approx 4 \times 10^{18}$ cm^{-3}, for the entire range of temperature that is investigated (80 K $< T <$ 380 K). The observed magnitudes for the Seebeck coefficient (denoted by $|S|$ or $-S$, since S for an n-type material is a negative number) are found to decrease slowly with decreasing temperature above 250 K, and to increase rapidly with decreasing temperature as T is lowered further below 200 K (see Fig. 5-15).

The results for the theoretical models shown in Fig. 5-15 are obtained for $n = 4\times10^{18}$ cm^{-3} without the use of any fitting parameters, where n is the estimated carrier concentration for samples JL167 and JL169 (see Fig. 5-16 for the measured Hall carrier concentrations as a function of temperature), using (1) the constant relaxation time approximation (solid curve in Fig. 5-15) and (2) semiclassical models including

ionized impurity scattering as the dominant scattering mechanism for electrons (long-dashed curve Fig. 5-15) as we discuss in Chapter 6. While it is found, in Fig. 5-15, that the constant relaxation time approximation underestimates the magnitude of the measured Seebeck coefficient over the entire range of temperature that is investigated ($40\ \mathrm{K} < T < 380\ \mathrm{K}$), the semiclassical model, including ionized impurity scattering as the dominant scattering mechanism, predicts almost correct values for the measured Seebeck coefficient above 200 K. The origin of the other marked feature in Fig. 5-15, i.e., the increasing value of $|S|$ with decreasing temperature below 200 K, will be discussed separately in §5.6.2.

Shown in Fig. 5-17 are the measured electrical conductivities σ as a function of temperature for samples JL167 and JL169. It turns out that the semi-classical models that are developed in Chapter 6, including ionized impurity scattering as the dominant scattering mechanism, do not reproduce the correct magnitudes for the measured electrical conductivity, i.e., the predicted values for the electrical conductivity are about twice larger than the measured conductivity. We attribute the difference between the measured and predicted values for the electrical conductivity (or equivalently for the carrier mobility since the carrier concentrations for sample JL167 and JL169 are found to be rather insensitive to the temperature) to some extrinsic scattering mechanisms that are not included in the semi-classical models that are developed in Chapter 6. These extrinsic scattering mechanisms include : (1) interfacial and/or alloy scattering at the Si/Ge interfaces, (2) scattering due to the structural defects and/or dislocations that are introduced into the superlattice structures during the growth process, such as the threading dislocation as we discussed in §5.2, and (3) scattering due to the fluctuations in the thicknesses of the Si and Ge layers, which would introduce a spatial fluctuation in the bound state energies for the conduction electrons that serve as additional scattering potentials for the conduction electrons.

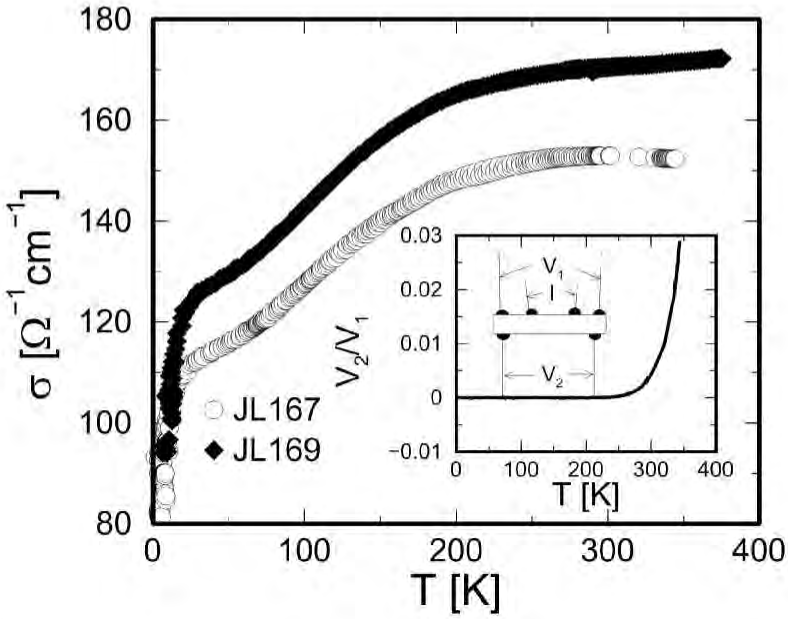

Figure 5-17: Electrical conductivity as a function of temperature for samples JL167 (open circles) and JL169 (filled diamonds). The experimental Hall carrier mobilities obtained for samples JL167 and JL169 are 239 $cm^2/V{\cdot}s$ and 266 $cm^2/V{\cdot}s$, respectively, at 300 K. These values are to be compared with the theoretically predicted value of 556 $cm^2/V{\cdot}s$ (for the both samples) obtained for a homogeneously doped Si(20 Å)/Ge(20 Å) superlattice ($n = 4{\times}10^{18}$ cm^{-3}) using the semi-classical models that are developed in Chapter 6. The origin for this difference in the mobility between theory and experiment is attributed to some extrinsic scattering mechanisms that are not included in the model : interfacial and alloy scattering at the Si/Ge interfaces, scattering due to the structural defects and dislocations (such as the threading dislocation discussed in §5.2), and fluctuations in the Si and Ge layer thicknesses in the superlattice part of the sample. The inset shows a special configuration for the measurement of the electrical conductivity σ, where the voltages induced on the back side (substrate side) of the sample (denoted by V_2) are monitored during the measurement of σ for the superlattice part of the sample (the voltage measured for this purpose is denoted by V_1), to make sure that the parallel transport contribution from the substrate is absent.

5.6.2 Origin of the increasing $|S|$ below 200 K

Now, what happens with the values of the measured S below 200 K? In Fig. 5-15, we saw that the value of $|S|$, where S is the Seebeck coefficient, goes up rapidly with decreasing temperature below 200 K. Our previous interpretations of this effect include the parallel transport contribution from the buffer layer and/or the substrate (see §5.8 for a discussion of the effect of parallel transport contributions from the buffer layer and/or the substrate). However, we now think that the parallel transport in the buffer layer and/or substrate does not provide sufficient reasons for the increasing values of $|S|$ below 200 K that are observed in Fig. 5-15, because : (1) First of all, since the substrate is slightly p-type doped, if there is any parallel transport contribution from the substrate, it should tend to decrease the value of the measured $|S|$ rather than increase (because the superlattice part of the sample is n-type doped). (2) The carriers in the buffer layer tend to freeze out at low temperatures, because the carrier concentration in the buffer layer should be relatively small ($n < 1 \times 10^{18}$ cm^{-3}) [the $Si_{1-x}Ge_x$ (x : 0 $\rightarrow$ 0.5) graded buffer layer is slightly (and unintentionally) doped by the residual Sb surfactant impurities]. Therefore, the parallel transport contribution from the buffer layer should also tend to decrease and eventually go to zero at sufficiently low temperatures. To test this hypothesis, we have measured the voltage induced on the back side of the sample (substrate side of the sample) during the measurement of the electrical conductivity, as schematically shown in the inset of Fig. 5-17. It is noted that, in the parallel conductor model, the voltage induced on the back side (substrate side) of the sample has to be equal to the voltage induced on the film side of the sample, hence $V_2/V_1 = 1$ in the plot shown in the inset of Fig. 5-17. Since the voltages observed during the experiment on the back side (substrate side) of the sample are, at most, only a few percent of the voltage measured on the superlattice side of the sample, the electrical insulation between the top of the film and the bottom of the substrate is substantial. Therefore, we must conclude that the parallel conduction phenomena are not present in the substrate, or, at most, it has only a negligible effect on the measured thermoelectric transport coefficients,

such as the Seebeck coefficient S and the electrical conductivity σ. To make sure that the parallel transport contribution in the buffer layer is absent (or negligible) as well, we have developed, in §5.8, a method to subtract the buffer layer contribution to the measured thermoelectric transport coefficients to deduce the net values of the thermoelectric transport coefficients for the superlattice part of the sample only, where we indeed find that the subtraction of the buffer layer contribution to the measured thermoelectric transport coefficients doesn't change the qualitative features of the measured Seebeck coefficient S and the electrical conductivity σ as a function of temperature.[†]

Another mechanism that would be responsible for the observed increase in $|S|$ with decreasing temperature below 200 K is the phonon drag effect [88–90].[‡] The basic mechanism of the phonon drag effect is summarized as the process of transporting phonons by the conduction electrons [90]. Therefore, if the phonon drag effect is present in the sample, applying an electric field in the absence of a thermal gradient will create a directional flow of phonons. The reciprocal statement of this is that if a directional flow of phonons is present in the sample while there is no external electric field (in the sample), it creates an electrical current. In the normal situation for the measurement of the Seebeck coefficient, where the electric circuit used for the measurement is an open circuit (since the internal resistance of the voltmeter is assumed to be infinity), an electrical current created by the directional flow of phonons accumulates electrical charge at the edge of the sample, which, in turn, creates an internal electric field in the sample in such a way that it exactly cancels the current created by the directional flow of the phonons. The internal voltage established across the sample in this way is the phonon drag contribution to the Seebeck voltage. The Seebeck coefficient in bulk Si and Ge that is caused by the phonon drag effect typically

[†]These studies are carried out using one of the newer set of samples of (001) oriented Si(20 Å)/Ge(20 Å) superlattices (JL193 and JL194) that are grown on (001) oriented SOI (Si-on-insulator) substrates (see §5.8).

[‡]The author acknowledges that the possibility of the phonon drag effect as a mechanism for the observed increase in $|S|$ for samples JL167 and JL169 below 200 K arose during the author's discussion with Professor H. Ehrenreich at Harvard University in February, 2000. A preliminary account of the same discussion also took place with Dr. A. Yamamoto at ETL (Electrotechnical Laboratory), Tsukuba, Japan, during the author's visit to ETL in summer 1999.

follows a $T^{-\nu}$ behavior at low temperatures, where T is the temperature and ν is a positive number between 1 and 2.5 [88, 89]

Shown in Fig. 5-18(a) are exactly the same data as those that are plotted in Fig. 5-15, but the values of the $|ST|$ product, instead of the values of $|S|$, are plotted as a function of temperature, where S is the Seebeck coefficient and T is the temperature. The behavior of the $|ST|$ product as a function of temperature for bulk Ge [88] and bulk Si [89] was extensively studied by Geballe *et al.* in relation to the phonon drag effect. An example of such a study is reproduced in Fig. 5-18(b), where the values of the measured $|ST|$ product for n-type doped bulk Si with $n = 2.2\times10^{18}$ cm^{-3} (sample 126) and 2.7×10^{19} cm^{-3} (sample 140) (here, n is the donor concentration) are plotted as a function of temperature. It is noted that an almost temperature independent behavior is observed in the $|ST|$ product as a function of temperature for our samples JL167 and JL169 in the temperature range between 40 K and 200 K as in Fig. 5-18(a), and for the n-type bulk Si with $n = 2.2 \times 10^{18}$ cm^{-3} (sample 126) in the temperature range between 25 K and 60 K as in Fig. 5-18(b). This behavior in the $|ST|$ product corresponds to a $|S| \sim T^{-1}$ dependence in the Seebeck coefficient. The resemblance in behavior and the actual values of the $|ST|$ product as a function of temperature, between our samples (JL167 and JL169) and the n-type bulk Si with $n = 2.2 \times 10^{18}$ cm^{-3} (sample 126) measured by Geballe *et al.* [89], strongly suggests that the dominant mechanism for the observed increase in the value of $|S|$ at low temperatures ($T < 200$ K) for samples JL167 and JL169 is the phonon drag effect.

It is noted that the effect of the increasing value of $|S|$ is not present in the newer set of Si/Ge superlattice samples (JL194, JL197 and JL199) that are provided by Dr. J. L. Liu at UCLA as shown in Fig. 5-21 (see §5.7.2). We attribute the absence of the effect of increasing $|S|$ (with decreasing T) below 200 K in samples JL194, JL197 and JL199, to the absence of the phonon drag effect in these samples. The fact that the phonon drag effect is present in some Si/Ge superlattice samples, but not in others, suggests that the directional, off-balanced distribution of phonons that is necessary for the phonon drag effect to be observed, is created by some extrinsic mechanisms in samples JL167 and JL169. For the case of samples JL167 and JL169,

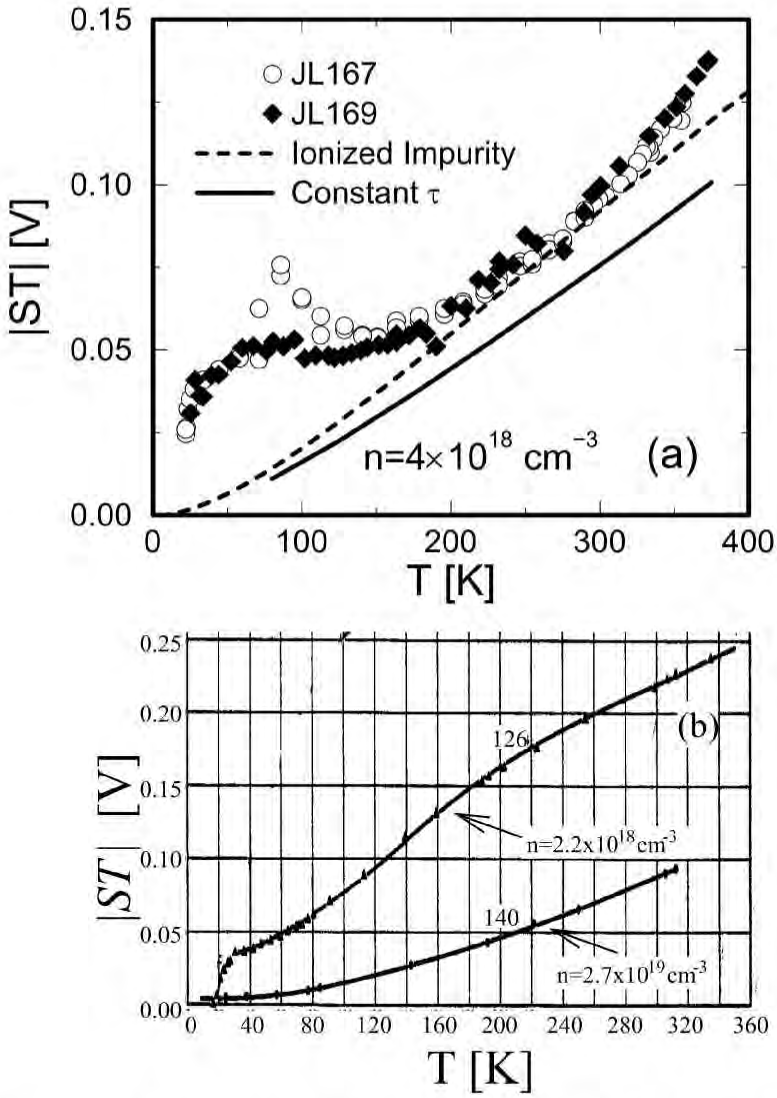

Figure 5-18: (a) Absolute values of the ST product, where S is the Seebeck coefficient and T is the temperature, that are measured for samples JL167 (open circles) and JL169 (filled diamonds) as a function of temperature. Also shown are the theoretical results assuming $n = 4\times10^{18}$ cm^{-3} in the constant relaxation time approximation (solid curve) and in the semi-classical model (long-dashed curve) that is developed in Chapter 6, where the dominant scattering mechanism is ionized impurity scattering. It is noted that the theoretical models used here do not include the phonon drag effect explicitly. (b) A typical phonon drag effect observed in bulk Si (after Geballe *et al.* [89]), where absolute values for the ST product are plotted as a function of temperature for samples with $n = 2.2\times10^{18}$ cm^{-3} (sample 126) and with $n = 2.7\times10^{19}$ cm^{-3} (sample 140) (here, n is the donor concentration). The resemblance between our results in (a) and the results by Geballe *et al.* in (b) [see the results for sample 126] strongly suggests that the observed effect of increasing $|S|$ below 200 K in samples JL167 and JL169 (see Fig. 5-15) is due to the phonon drag effect.

a $Si_{1-x}Ge_x$ ($x : 0 \rightarrow 0.5$) graded buffer layer is directly grown on top of a (001) oriented Si substrate. Therefore, the directional (off-balanced) distribution of phonons is induced in the superlattice part of the samples by the the directional (off-balanced) distribution of phonons in the Si substrate, where such a directional (off-balanced) distribution of phonons is present due to the nature of the bulk Si crystal, as we have seen in Fig. 5-18(b). On the other hand, for the case of JL194, JL197 and JL199, a $Si_{1-x}Ge_x$ ($x : 0 \rightarrow 0.5$) graded buffer layer is grown on top of a (001) oriented SOI substrate. Since the SOI substrate has a 3800 Å thick SiO_2 layer between the Si substrate and the superlattice part of the sample, a structural discontinuity is introduced between the superlattice part and the (001) oriented Si substrate below the SiO_2 layer (see Fig. 5-12). Therefore, a directional flow of phonons (or an off-balanced distribution of phonons) that is present in the Si substrate below the SiO_2 layer does not affect the phonon distribution above the SiO_2 layer. In this way, the superlattice part of the sample retains a balanced (locally equilibrated) distribution of phonons, and hence the absence of the phonon drag effect in samples JL194, JL197 and JL199 can be explained.

5.6.3 $S^2\sigma$ and $Z_{3D}T$ for samples JL167 and JL169

Plotted in Fig. 5-19, are the experimentally determined thermoelectric power factor $S^2\sigma$ for samples JL167 and JL169, which are obtained by combining the experimental data for the electrical conductivity σ and the Seebeck coefficient S that are shown in §5.6.1. As we have discussed in §5.6.2, the cause for the observed rise in $S^2\sigma$ below 200 K in these samples is attributed to a phonon drag effect that induced from the Si substrate. Therefore, we do not discuss this effect any further in this subsection. For temperatures between 200 K and 330 K, the experimental values for $S^2\sigma$, for both samples JL167 and JL169, agree very well with theoretical predictions using semi-classical models that are developed in Chapter 6, where Matthiessen's rule

$$\frac{1}{\tau_{\text{tot}}(E)} = \frac{1}{\tau_{\text{imp}}(E)} + \frac{1}{\tau_{\text{ac}}(E)} + \frac{1}{\tau_{\text{ext}}} \tag{5.6}$$

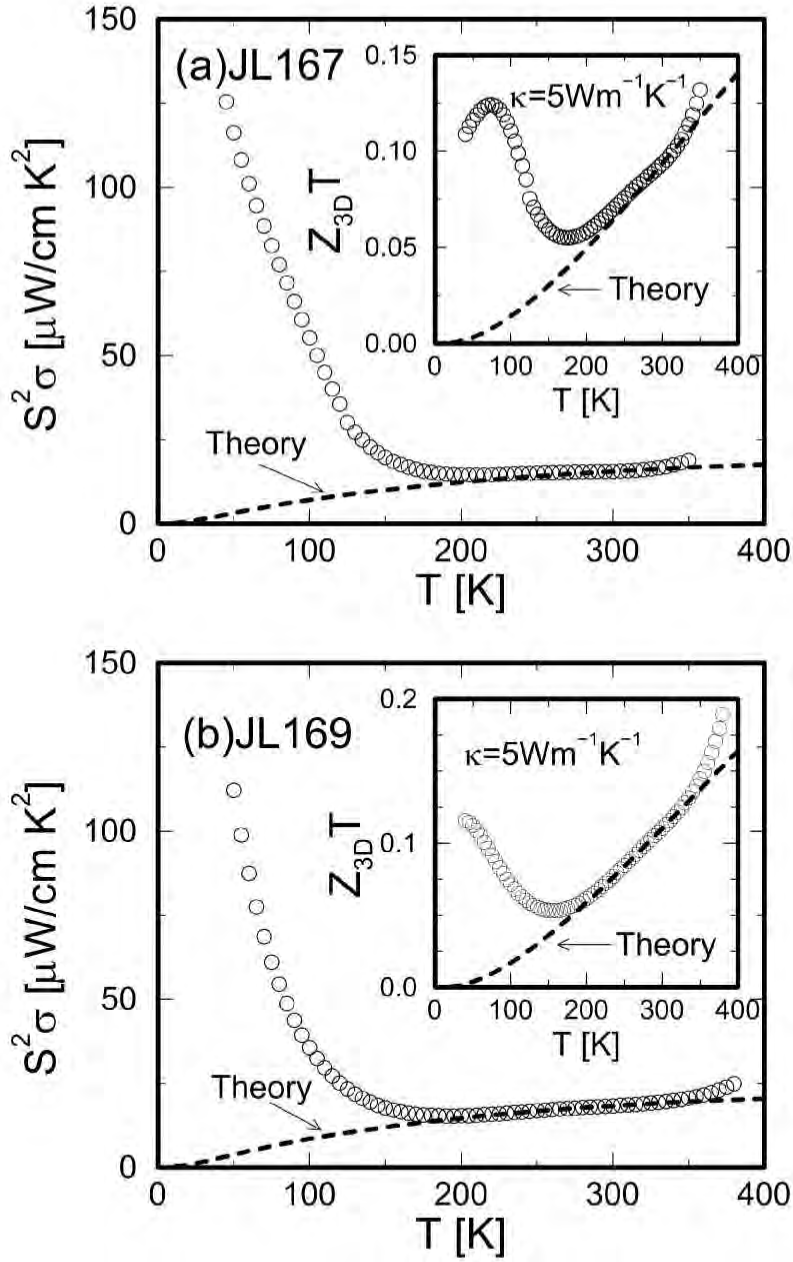

Figure 5-19: Experimentally determined thermoelectric power factor $S^2\sigma$ as a function of temperature for (a) sample JL167 and (b) sample JL169, together with the results of semi-classical models developed in Chapter 6, assuming $n = 4\times10^{18}$ cm^{-3}, and using Matthiessen's rule (Eq. 5.6) as explained in the footnote on page 252. Also shown in the inset of each figure is the estimated $Z_{3D}T$ as a function of temperature, using $\kappa = 5$ W/m·K for the value of the thermal conductivity. It is noted that the electronic contributions to the thermal conductivity κ_e for samples JL167 and JL169 are estimated to be less than 0.1 W/m·K at 300 K using the measured electrical conductivity data (Fig. 5-17) and the Wiedemann-Franz law.

is employed to take into account the extrinsic scattering mechanisms (τ_{ext}) discussed in §5.6.1.[†] For temperatures above 330 K, the experimentally determined values for $S^2\sigma$ are a little larger than the values predicted in theory using the semi-classical models. The origin of such an increase in the experimental $S^2\sigma$ relative to the theoretical prediction above 330 K is due to the corresponding increase in the measured Seebeck coefficient S above 330 K (i.e., not due to the increase in the electrical conductivity σ). The exact mechanism for such an increase in $|S|$ above 330 K is not known at present, but since we have observed a similar behavior of increasing $|S|$ above 300 K in the newer set of samples that are grown on (001) oriented SOI substrates (samples JL194, JL197 and JL199), we will discuss the possible mechanisms for this effect later (see §5.7.2). Therefore, the good agreement between the theoretical predictions and the experimental results for the temperature dependence of the Seebeck coefficient S and the thermoelectric power factor $S^2\sigma$[‡] using samples JL167 and JL169 basically completes the experimental proof-of-principle study of the enhanced thermoelectric properties in the (001) oriented Si(20 Å)/Ge(20 Å) superlattices in the temperature range between 200 K and 330 K.

However, some subtle questions remain about the observed agreement between theory and experiment in the present work using samples JL167 and JL169: (1) First of all, what would be the values of the Seebeck coefficient for the (001) oriented Si(20 Å)/Ge(20 Å) superlattices for temperatures below 200 K if the phonon drag effect were not present? Is there any good agreement between theory and experiment for the values of the Seebeck coefficient of the superlattice below 200 K in this case? (2) Is the phonon drag effect, which is observed to lead to a significant increase in the values of the measured S below 200 K, really absent in the superlattice above 200 K?

[†] $\tau_{imp}(E)$ and $\tau_{ac}(E)$ are the relaxation times as a function of electron energy (measured from the pertinent band edge) for ionized impurity scattering and longitudinal acoustic phonon deformation potential scattering, respectively, and τ_{ext} is the relaxation time that takes into account the extrinsic scattering mechanisms that are discussed in §5.6.1. $\tau_{imp}(E)$ and $\tau_{ac}(E)$ are calculated, at each temperature, using the semi-classical models developed in Chapter 6 without the use of any fitting parameters, whereas the value of τ_{ext} is obtained by fitting the experimental data at 300 K using Matthiessen's rule.

[‡] In modeling the values of the thermoelectric power factor $S^2\sigma$, our theoretical models include the extrinsic scattering mechanisms that are discussed in §5.6.1 through Matthiessen's rule (see Eq. 5.6 and the footnote on page 252).

or are the observed values of S above 200 K actually the result of a combination of both the normal Seebeck coefficient (without the phonon drag effect) and the contribution from the phonon drag effect? (3) Are the parallel transport contributions from the buffer layer and/or the substrate, which is mentioned in §5.6.2, really negligible in the temperature range investigated (from 4.2 K to 400 K) in samples JL167 and JL169? If not, do such contributions account for the slight increases in S from the theoretical values above 330 K that are observed in Fig. 5-15? In order to clarify questions (1) and (2) above, we study below a new set of samples that are grown on (001) oriented SOI (Si-on-insulator) substrates (samples JL194, JL197 and JL199). As we mentioned in §5.6.2, the effect of phonon drag on increasing the values of the measured $|S|$ at low temperatures ($T < 200$ K) is not present in these samples. Therefore, we can also assume that the phonon drag effect is not present in the Seebeck measurements above 200 K as well in these samples. Moreover, since SOI substrates should provide perfect electrical insulation between the superlattice part of the sample and the base (001) Si substrate below the 3800 Å SiO_2 layer (see Fig. 5-12), we can at least exclude the possibility of having the parallel transport contributions from the Si substrate (but not from the SiGe buffer layer) in these superlattice samples. We had originally expected that the Si(20 Å)/Ge(20 Å) superlattices grown on (001) oriented SOI substrates might not have as high values for the carrier mobility as those grown on (001) oriented Si substrates. However, the experimental investigations in this chapter have shown that the values for the measured Hall mobilities for samples JL194, JL197 and JL199 [superlattices grown on (001) oriented SOI substrates] are consistent with those for samples JL167 and JL169 [superlattices grown on (001) oriented Si substrates], suggesting that the structural qualities for samples JL194, JL197 and JL199 are equivalently as high as those for samples JL167 and JL169. Regarding the third question above, we have assessed the amount of parallel transport contribution from the buffer layer or/and substrate to the measured thermoelectric transport coefficients, using a set of thin and thick superlattice samples that are grown using identical growth conditions, and this issue is discussed in §5.8.

Finally, our ultimate goal in this whole project is to obtain an enhanced value

of $Z_{3D}T$. The determination of reliable values of $Z_{3D}T$ for our Si/Ge superlattice samples (JL167 and JL169) is not easy, since the actual temperature dependence of the in-plane thermal conductivity for the superlattice itself is not known at a satisfactory level at present in these samples (see §5.2). However, previous results of theoretical and experimental investigations indicate that the thermal conductivity κ for a short period Si/Ge superlattice ($d_{Si} + d_{Ge} < 100$ Å, where d_{Si} and d_{Ge} are the thicknesses for the Si and Ge layers in the superlattice, respectively) is in the range between 1 W/m·K and 10 W/m·K at room temperature [62, 67], and the value of κ is relatively temperature insensitive between 77 K and 300 K. We, therefore, use the temperature independent value of $\kappa = 5$ W/m·K to make an order of magnitude estimate for the temperature dependence of $Z_{3D}T$ for the samples investigated in this section (JL167 and JL169). Shown in the insets of Fig. 5-19(a)(b) are the results of such estimations of $Z_{3D}T$ as a function of temperature for samples JL167 and JL169, respectively. It will be found, in §5.9, that the doping levels for these samples are almost optimized. Therefore, no significant improvements in the value of $Z_{3D}T$ are expected by adjusting the doping levels in these samples any further. Instead, the values of $Z_{3D}T$ for our Si(20 Å)/Ge(20 Å) superlattice samples should be increased from the present experimental values by improving the structural qualities of the samples, for example, by reducing the interface roughness at the Si/Ge boundaries and/or minimizing the structural defect and dislocation densities that are introduced into the superlattice structures during the growth processes. In Chapter 6, we will see that the calculated values for the carrier mobility for a homogeneously doped Si(20 Å)/Ge(20 Å) superlattice should be a factor of two to three larger than the values obtained in the experiment. Therefore, if we could remove the sources of extrinsic scattering mechanisms for the conduction carriers that are discussed in §5.6.1, the value of $Z_{3D}T$ for the (001) oriented Si(20 Å)/Ge(20 Å) superlattice could perhaps be increased up to ~0.22 at 300 K as we discuss in Chapter 6. It will be also shown in Chapter 6 that the values of the carrier mobility for δ- or modulation-doped Si(20 Å)/Ge(20 Å) superlattices [in the (001) orientation] should be enhanced by a factor of more than two relative to those for the corresponding mobility cal-

culated for a homogeneously doped (001) oriented Si(20 Å)/Ge(20 Å) superlattice. Hence a resultant value of $Z_{3D}T \approx 0.5$ might be expected in a δ-doped (001) oriented Si(20 Å)/Ge(20 Å) superlattice at 300 K using $\kappa = 5$ W/m·K for the thermal conductivity. It should be noted that the values of $Z_{3D}T$ can be further increased by growing the superlattices in a (111) orientation as we discussed in §5.4.2, where the value of $Z_{3D}T$ for the (111) oriented Si(20 Å)/Ge(20 Å) superlattice is predicted to be enhanced by a factor of four relative to the corresponding value of $Z_{3D}T$ for a (001) oriented Si(20 Å)/Ge(20 Å) superlattice at 300 K using the constant relaxation time approximation. Since the basic concept for enhancing the values of $Z_{3D}T$ using the (111) oriented Si/Ge superlattices, as discussed in §5.4.2, is still valid, irrespective of the details of the specific scattering mechanisms, we can expect a significantly larger value for $Z_{3D}T$ ($Z_{3D}T \approx 2.0$ at 300 K) in a δ-doped (111) oriented Si(20 Å)/Ge(20 Å) superlattice.

5.7 Experimental proof-of-principle study using (001) oriented Si(20 Å)/Ge(20 Å) superlattices grown on (001) SOI (Si-on-insulator) substrates

In the previous section, we have shown results for the experimental proof-of-principle study on Carrier Pocket Engineering using (001) oriented Si(20 Å)/Ge(20 Å) superlattice samples that were grown on (001) oriented Si substrates (samples JL167 and JL169). We have seen that the agreement between theory and experiment is fairly good in the temperature range between 200 K and 330 K. However, a large phonon drag contribution to the measured Seebeck coefficient S, which is produced by an off-balanced, directional distribution of phonons in the superlattice part of the sample that is believed to be induced by a similar (off-balanced, directional) distribution of phonons in the substrate, makes the experimental verification of the theoretical prediction of the Carrier Pocket Engineering concept very difficult below 200 K with these samples (JL167 and JL169). We have also raised an issue that parallel trans-

port contributions from the buffer layer and/or substrate may have some effect on the measured thermoelectric transport coefficients for the Si/Ge superlattice samples. A goal of the present section is, therefore, to clarify these issues and to complete the experimental proof-of-principle study for the homogeneously doped (001) oriented Si(20 Å)/Ge(20 Å) superlattices. In addition to this goal, attempts are also being made to determine both the thermal conductivity κ and the electronic transport coefficients S and σ using the same superlattice samples that were cut out from the same original piece of MBE-grown superlattice. As an example of this line of research, we discuss the recent results of the cross-plane thermal conductivity ($\kappa_\perp$) measurements, in §5.7.1, that were performed in Prof. G. Chen's group at UCLA recently [70].

Our future experimental studies should be focused on the study of the δ- and modulation doping effect to further increase the values of $Z_{3D}T$ and on the experimental proof-of-principle study using the (111) oriented Si/Ge superlattices, where an additional factor of four enhancement in the values of $Z_{3D}T$ relative to those for the (001) oriented Si/Ge superlattices in the optimized superlattice structures is expected, based on calculations using the constant relaxation time approximation, as we discussed in §5.4.2.

5.7.1 Cross-plane thermal conductivity κ for samples JL194, JL197 and JL199

Before showing the results of our experiments for the temperature-dependent Seebeck coefficient $S(T)$, the electrical conductivity $\sigma(T)$ and the Hall carrier concentration $n_{\text{Hall}}(T)$ in §5.7.2, we would like to introduce the results of recent measurements of the temperature dependence of the cross-plane thermal conductivity $\kappa_\perp(T)$ that were performed by T. Borca-Tasciuc in the group of Prof. G. Chen at UCLA. These measurements were performed using a 3ω-method [83] for identical samples (JL194, JL197 and JL199) to those that we used for the measurements of the temperature dependence of S, σ and n_{Hall} in §5.7.2.

Shown in Fig. 5-20 are the results of the measured temperature dependence of

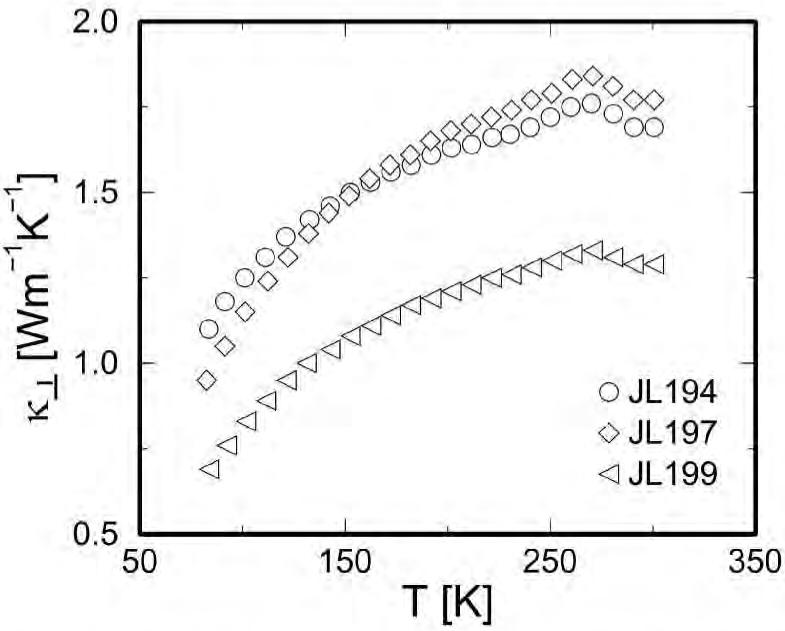

Figure 5-20: The temperature dependence of the thermal conductivity κ along the superlattice growth axis (denoted as the cross-plane thermal conductivity $\kappa_\perp$) measured for sample JL194 (open circles), JL197 (open diamonds) and JL199 (open triangles) as a function of temperature. The measurements are performed by T. Borca-Tasciuc in the group of Prof. G. Chen at UCLA using a 3ω-method [83]. It is noted that the values for $\kappa_\perp$ obtained in this measurement cannot be used for $\kappa(T)$ in the estimation of $Z_{3D}T$ in our experiment since the thermoelectric power factor $S^2\sigma$ for these samples is measured along the plane of the superlattice.

the cross-plane lattice thermal conductivity $\kappa_{\perp}(T)$, where the thermal conductivities of the samples are measured along the superlattice growth direction (perpendicular to the plane of the superlattice, denoted as the cross-plane thermal conductivity) for samples JL194, JL197 and JL199. In these experiments, the values of the thermal conductivity (along the superlattice growth axis) for the superlattice part of the sample only are evaluated using a bare buffer layer sample [the samples without Si/Ge superlattice layers, but with both a $Si_{1-x}Ge_x$ ($x : 0 \rightarrow 0.5$) graded buffer layer and an undoped $Si_{0.5}Ge_{0.5}$ homogeneous buffer layer (see Fig. 5-12)] as the reference substrate in the 3ω-method [83].

In Fig. 5-20, we see a large decrease in the cross-plane thermal conductivity κ for the Si/Ge short period superlattice samples (JL194, JL197 and JL199) relative to the bulk values of the thermal conductivity for Si (κ = 150 W/m·K at 300 K) and Ge (κ = 60 W/m·K at 300 K) [87]. Also a notable feature in Fig. 5-20 is that the measured cross-plane thermal conductivities $\kappa_{\perp}(T)$ are found to decrease with decreasing temperature, whereas the thermal conductivity for a bulk material usually increases with decreasing temperature in this temperature range, since the phonon mean free path in a 3D material usually increases with decreasing temperature.

Although the values of $\kappa(T)$ required for the estimation of the thermoelectric figure of merit $Z_{3D}T$ for the Si/Ge superlattices (JL194, JL197 and JL199) are those for the in-plane thermal conductivity (denoted by $\kappa_{||}$) rather than those for the cross-plane thermal conductivity (denoted by $\kappa_{\perp}$) that are shown in Fig. 5-20, it is hoped that the further analysis of the preliminary cross-plane thermal conductivity in the Si/Ge superlattices will also provide some insight into $\kappa_{||}(T)$ for the in-plane thermal conductivity of the Si/Ge superlattices. For example, theoretical models for the lattice thermal conductivity in both in-plane and cross-plane directions may be developed in such a way that improved estimates for the in-plane thermal conductivity $\kappa_{||}(T)$ can be obtained from the experimental fitting of the cross-plane thermal conductivity only. At the same time, efforts should be continued for an experimental determination of $\kappa_{||}(T)$ to be used in a fully experimental determination of $Z_{3D}T$ for the whole Si/Ge superlattices.

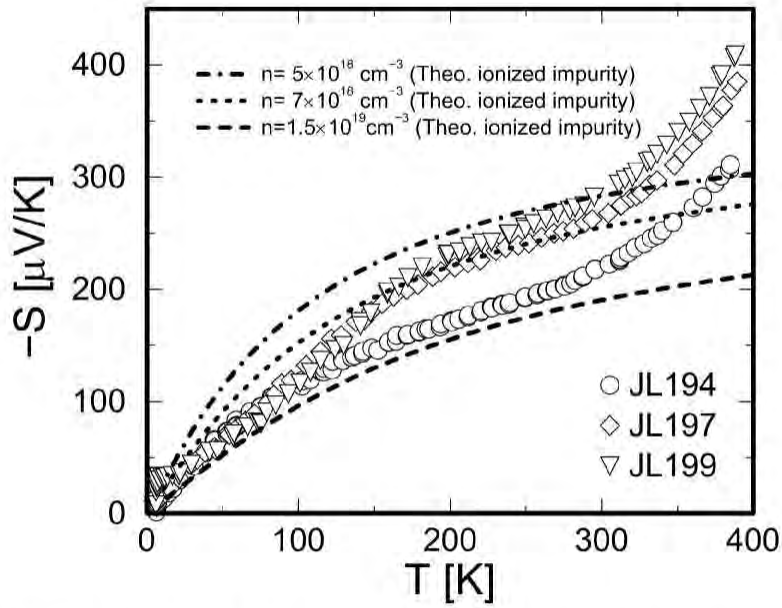

Figure 5-21: Seebeck coefficient as a function of temperature measured for samples JL194 (open circles), JL197 (open diamonds) and JL199 (open triangles), together with the results of semi-classical models developed in Chapter 6, for $n = 5\times10^{18}$ cm^{-3} (dot-dashed curve), 7×10^{18} cm^{-3} (short-dashed curve) and 1.5×10^{19} cm^{-3} (long-dashed curve), without the use of any fitting parameters. Note that the effect of $|S|$ shooting up below 200 K, which is found in samples JL167 and JL169 (see Fig. 5-15), is absent in these samples. The possible reasons for the marked increase in the value of $|S|$ above 300 K include (1) the scattering of electrons due to optical phonons that may become dominant above 300 K and (2) the increasing occupation of the $\Delta_{Si}^{\perp}$-subband by conduction electrons with increasing temperature above 300 K in the actual samples [see Fig. 5-8(a)].

5.7.2 S, σ and n_{Hall} for samples JL194, JL197 and JL199

Shown in the Figs. 5-21–5-23 are the Seebeck coefficient S, electrical conductivity σ, and Hall carrier density n_{Hall} for samples JL194, JL197 and JL199 (see §5.5.1), measured as a function of temperature in the temperature range between 4.2 K and 400 K, together with the results of semi-classical models, which include ionized impurity scattering as the dominant scattering mechanism, that are developed in Chapter 6. In Fig. 5-21, we find that the measured values for the Seebeck coefficient $S(T)$ are in fair agreement with the values predicted by theory, where the theoretical values of S are calculated assuming $n = 5\times10^{18}$ cm^{-3} (dash-dotted curve), 7×10^{18} cm^{-3} (short-dashed curve) and 1.5×10^{19} cm^{-3} (long-dashed curve) (see Fig. 5-23 for the measured Hall carrier concentrations for samples JL194, JL197 and JL199). We find that the

agreement between theory and experiment in Fig. 5-21 is semi-quantitative in the temperature range between 180 K and 300 K, where we conclude that our theoretical models developed in Chapter 6 successfully describe the properties of (001) oriented Si(20 Å)/Ge(20 Å) superlattices that are used in the present study (JL194, JL197 and JL199). In the temperature range below 180 K, the values of the measured Seebeck coefficient are somewhat smaller than the theoretically predicted values. This discrepancy is probably due to the presence of additional scattering mechanisms that are not included in our semi-classical models developed in Chapter 6. The presence of such additional scattering mechanisms is already evident in the measured electrical conductivity data as a function of temperature as shown in Fig. 5-22, where the measured values for the electrical conductivity for samples JL197 and JL199 are a factor of two to three smaller than the theoretically predicted values (see §5.9 and Chapter 6). If these additional scattering mechanisms, as discussed in §5.6.1, have a $\tau \sim E^r$ dependence, with the value of r smaller than 3/2,[†] it is understandable that the values of the measured S for samples JL197 and JL199 are reduced relative to the theoretically predicted values below 180 K.

Now, the resolution of the physical origin for the observed increase in the measured $|S|$ above 300 K in these samples (see Fig. 5-21) is a more difficult task. The possible explanations for this effect at the present stage of the investigation include (1) a parallel transport contribution from the buffer layer and/or substrate, (2) increased contribution from optical phonon scattering of the conduction electrons, and (3) increased occupation of the $\Delta_{Si}^{\perp}$-subband (see Fig. 5-8) by the conduction electrons in the actual samples above 300 K than those predicted by our model calculation based on the Krönig-Penney model (see §5.4.1). The possibility (1) above is discussed in some detail in §5.8, where a set of thin and thick samples, that are grown using identical growth conditions, are utilized to evaluate the net contribution from the superlattice part of the sample only to the measured thermoelectric transport coefficients by subtracting the measured thermoelectric transport coefficient for the thinner

[†]Here, $r = 3/2$ corresponds to ionized impurity scattering in a 3D material. In a strict 2D limit, we obtain $r = 2$ if the screening effect due to the free carriers is absent (see Chapter 6).

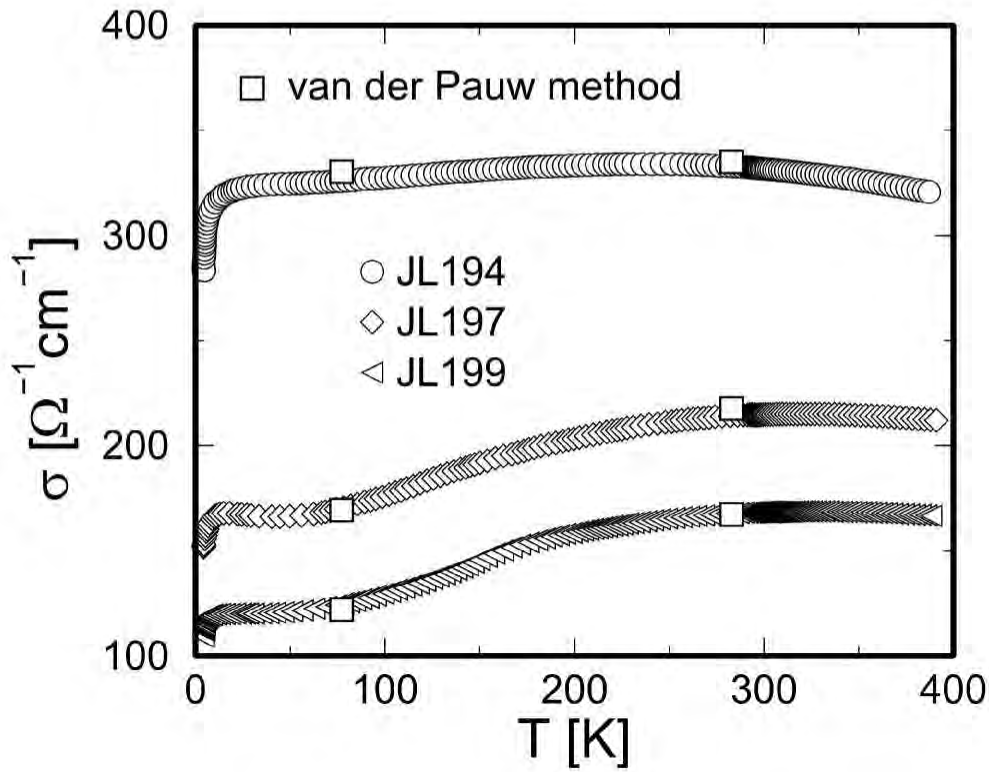

Figure 5-22: Electrical conductivity σ as a function of temperature for samples JL194 (open circles), JL197 (open diamonds) and JL199 (open triangles). The values for σ that are determined by the van der Pauw method are also indicated in the figure by the open square symbols for selected temperatures (77 K and 283 K). The experimental Hall carrier mobilities obtained for samples JL194, JL197, and JL199 are 138 $cm^2/V{\cdot}s$, 192 $cm^2/V{\cdot}s$, and 210 $cm^2/V{\cdot}s$, respectively, at 300 K. These values are to be compared with the theoretically predicted values of 406 $cm^2/V{\cdot}s$, 488 $cm^2/V{\cdot}s$ and 528 $cm^2/V{\cdot}s$ obtained for $n = 5{\times}10^{18}$ cm^{-3}, $n = 7{\times}10^{18}$ cm^{-3} and $n = 1.5{\times}10^{19}$ cm^{-3}, respectively (see Fig. 5-23 for the experimental Hall carrier densities for samples JL194, JL197 and JL199), for homogeneously doped (001) oriented Si(20 Å)/Ge(20 Å) superlattices using the semiclassical models that are developed in Chapter 6. The differences in the values between the theoretical and experimental mobilities are attributed to some extrinsic scattering mechanisms that are not included in the model : (1) interfacial and alloy scattering at the Si/Ge interfaces, (2) scattering due to structural defects and dislocations (such as the threading dislocation discussed in §5.2), and (3) fluctuations in the Si and Ge layer thicknesses in the superlattice part of the sample as we discussed in §5.6.1.

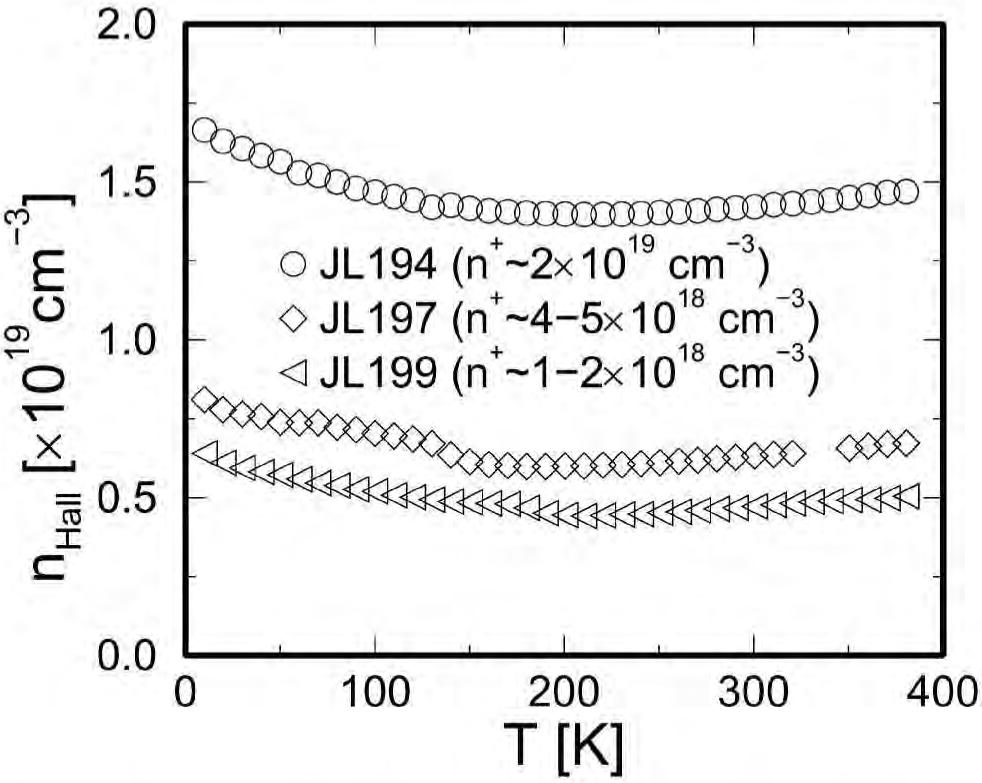

Figure 5-23: Hall carrier concentration as a function of temperature measured for samples JL194 (open circles), JL197 (open diamonds) and JL199 (open triangles). The Hall coefficient measurements shown here are performed using an electrical current of 1.25–2.5 mA and a magnetic field of 0.3 T. The sizes of the samples that are used in these measurements are typically 5 mm × 5 mm.

sample from that for the thicker sample. We find that the feature of increasing $|S|$ above 300 K is still observed in the net contribution to $|S|$ from the superlattice part of the sample only. Therefore, we conclude that the parallel transport contributions from the buffer layer and/or substrate are not responsible for the measured increase in $|S|$ above 300 K. The second mechanism to increase the value of $|S|$ (increased contribution of optical phonon scattering) is found in the measured Seebeck coefficient for the (111) oriented PbTe/$Pb_{1-x}Eu_xTe$ multiple-quantum-well samples as we discussed in Chapter 3 (§3.4.3), where polar optical phonon scattering, which becomes important above ~280 K for the oblique subband [the subband that is derived from the three equivalent (oblique) ⟨111⟩-valleys (see the inset in Fig. 2-10)], has an effect to increase the value of the measured Seebeck coefficient above 300 K. Since polar optical phonons are not present in the Si/Ge superlattices, the inclusion of the non-polar optical phonon scattering mechanism into our semi-classical models may provide improved agreement between theory and experiment for the (001) oriented Si(20 Å)/Ge(20 Å) superlattice samples above 300 K. The third possibility for the cause of the observed increase in $|S|$ above 300 K was attributed above to the increased occupation of the $\Delta_{Si}^{\perp}$-subband by the conduction electrons. This effect is critically related to the band structure (relative energies between the available subbands) of the Si/Ge superlattice. Since our calculations of the subband energies and band broadening effects for the Si/Ge superlattices using the Krönig-Penney model predict only an approximate band structure for the Si/Ge superlattices, first-principles (*ab-initio*) calculations of the band structure for the Si/Ge superlattices, assuming the particular structures and appropriate parameters to describe the properties of samples JL194, JL197 and JL199, may shed light on a more accurate determination of the values for the relative energies and band edge effective masses for the available subbands in the Si/Ge superlattices, which can be used for more accurate predictions of the values for the measured Seebeck coefficient above 300 K.

5.7.3 $S^2\sigma$ and $Z_{3D}T$ for samples JL194, JL197 and JL199

Shown in Fig. 5-24 are the thermoelectric power factors $S^2\sigma$ as a function of tem-

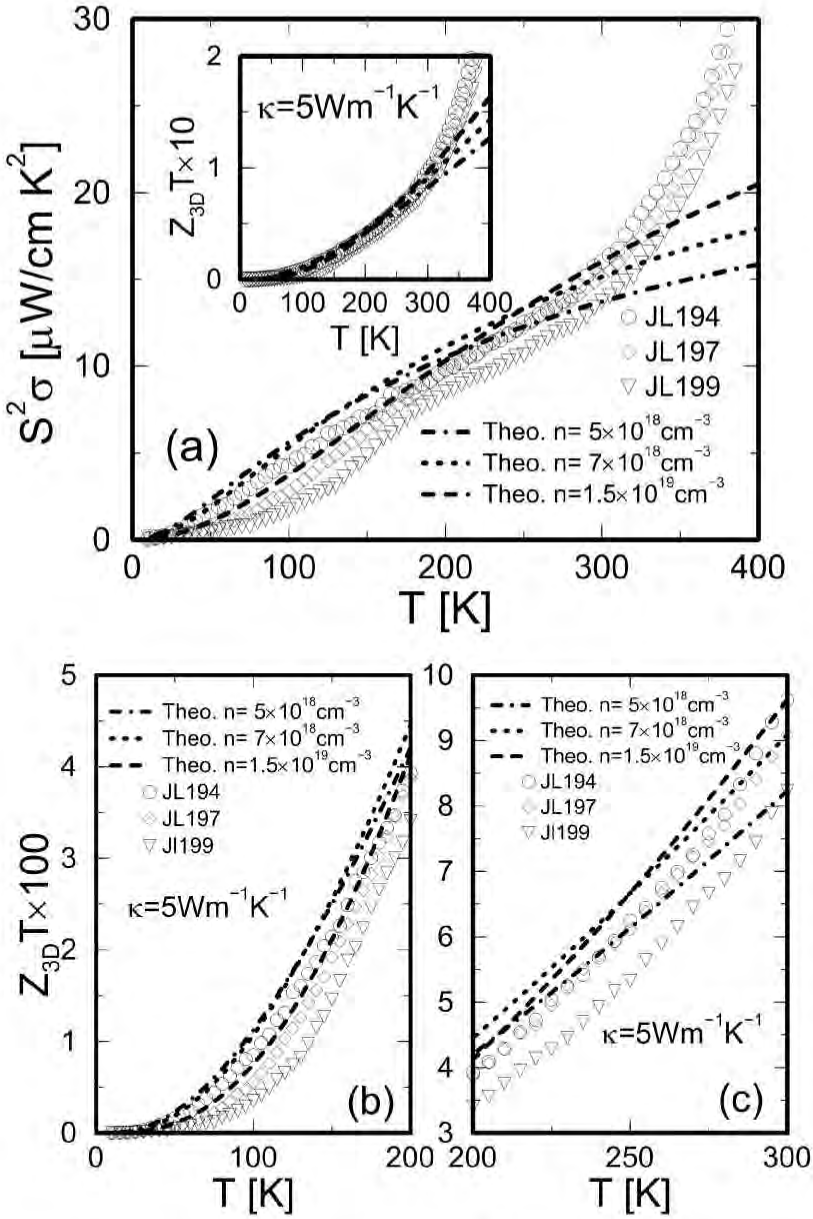

Figure 5-24: (a) Thermoelectric power factor $S^2\sigma$ as a function of temperature measured for samples JL194 (open circles), JL197 (open diamonds) and JL199 (open triangles), together with the results of the semi-classical models that are developed in Chapter 6, for $n = 5\times10^{18}$ cm^{-3} (dot-dashed curve), 7×10^{18} cm^{-3} (short-dashed curve) and 1.5×10^{19} cm^{-3} (long-dashed curve). It is noted that the theoretical values here are obtained using Matthiessen's rule (Eq. 5.6) to take into account the extrinsic scattering mechanisms that are present in the actual superlattice samples such as those used in the present study (see the footnote on page 252 in §5.6.3). The inset shows the plots of estimated values of $Z_{3D}T$ for these samples as a function of temperature using $\kappa = 5$ W/m·K for the thermal conductivity, together with the theoretical results using the same value for κ ($\kappa = 5$ W/m·K). The close-ups of the plot in the inset of (a) for temperatures below 300 K are shown in (b) and (c).

perature for samples JL194, JL197 and JL199, that are obtained using the measured values for S and σ as we discussed in §5.7.2. Also shown in Fig. 5-24 are the results of the semi-classical models that are developed in Chapter 6 using Matthiessen's rule (Eq. 5.6) to take into account the extrinsic scattering mechanisms that are not included in the model (but are present in the actual samples) as discussed in §5.6.3 (see the footnote on page 252). Shown in the inset of Fig. 5-24 are the estimated values of $Z_{3D}T$ as a function of temperature for these samples using $\kappa = 5$ W/m·K for the in-plane thermal conductivity (see §5.7.1). As we discussed in §5.6.3 and §5.7.1, exact values of the in-plane thermal conductivity for Si/Ge superlattices (and hence, those for samples JL194, JL197 and JL199) are not yet known. The Wiedemann-Franz law together with the measured electrical conductivities σ tells us that the thermal conductivities for samples JL194, JL197 and JL199 are dominated by the lattice contribution. Since the previous experiments [62, 67] and theoretical predictions [43, 76] suggest that the temperature dependence of the lattice thermal conductivity κ_{ph} for the superlattice samples is rather weak, we use the constant value of $\kappa = 5$ W/m·K for the thermal conductivity in estimating the value of $Z_{3D}T$ of the Si(20 Å)/Ge(20 Å) superlattice in this subsection.

We find two main features in Fig. 5-24. First, both the experimental and theoretical values for the thermoelectric power factor $S^2\sigma$ are not sensitive to the doping level of the samples in the range of carrier concentration between $n = 5\times10^{18}$ cm^{-3} and $n = 1.5\times10^{19}$ cm^{-3}. This is because the carrier concentration for the homogeneously doped (001) oriented Si(20 Å)/Ge(20 Å) superlattices is already optimized in this range of carrier concentration to obtain the largest value of $Z_{3D}T$ as we will see in §5.9. Further enhancement in the value of $Z_{3D}T$ in the (001) oriented Si/Ge superlattice system is expected if the extrinsic scattering mechanisms (see §5.6.1) that are present in the actual superlattice samples (JL194, JL197 and JL199) are eliminated by improving the structural qualities of the samples. In Chapter 6, we will also see that the introduction of δ- and modulation doping schemes would increase the values of the carrier mobility by a factor of two relative to those for the corresponding homogeneously doped samples. Therefore, as we discussed in §5.6.3, the highest value

of $Z_{3D}T$ expected in a (001) oriented Si(20 Å)/Ge(20 Å) superlattice should reach about 0.5 at 300 K by the use of the δ- and modulation doping schemes and having perfect structural qualities for these superlattices.[†]

The second feature noticeable in Fig. 5-24 is the marked increase in the values of the thermoelectric power factor $S^2\sigma$ and the figure of merit $Z_{3D}T$ above 300 K. We already know that the origin of such increases in $S^2\sigma$ and $Z_{3D}T$ are the increased values in the Seebeck coefficient S and not due to an increase in the electrical conductivity σ as we discussed in §5.7.2. Therefore, some efforts should be given to reveal the exact mechanisms responsible for the observed increase in $|S|$ above 300 K that are found in the homogeneously doped (001) oriented Si(20 Å)/Ge(20 Å) superlattices.

5.8 Assessment of the parallel transport contributions from the buffer layer and substrate

In §5.6 and §5.7, we frequently encountered a difficulty in determining the net contribution from the superlattice part of the sample to the measured thermoelectric transport coefficients S, σ and n_{Hall}. The assessment of the parallel transport contributions from the buffer layer and/or substrate is important not only for evaluating the net properties of the superlattice part of the sample to test the theoretical predictions made in §5.4 and in Chapter 6, but also for keeping ourselves from being misled by the apparent artifact of the experiment, such as the effect of $|S|$ shooting up below 200 K that was observed in §5.6.2. Another thing we are particularly interested in, in this section, is to verify whether the observed marked increase in the measured $|S|$ above 300 K in our superlattice samples is due to the properties of the superlattices themselves, or due to the result of the parallel transport effect from the buffer layer or/and substrate.

We will first study the properties of the bare buffer layer sample (JL200) in §5.8.1.

[†]Readers should be reminded that we have also discussed in §5.4.2 that the values of $Z_{3D}T$ are expected to be enhanced even further (by a factor of four) in the (111) oriented Si(20 Å)/Ge(20 Å) superlattices relative to the corresponding value in the (001) Si(20 Å)/Ge(20 Å) superlattices, using the constant relaxation time approximation.

This sample has both a $Si_{1-x}Ge_x$ ($x : 0 \rightarrow 0.5$) graded buffer layer (unintentionally doped n-type due to the residual Sb surfactant) and an undoped homogeneous $Si_{0.5}Ge_{0.5}$ buffer layer (see Fig. 5-12), that are grown under the identical growth conditions as those used for the buffer layer growth for samples JL193, JL194, JL197 and JL199, but does not have the Si(20 Å)/Ge(20 Å) superlattice part of the sample. We will examine the results of the electrical conductivity measurement and the Seebeck coefficient measurement for this sample, which will provide the basis for the later assessment of the parallel transport contribution from the buffer layer and/or substrate in §5.8.3. We will then study, in §5.8.2, the properties of a Si(20 Å)/Ge(20 Å) superlattice sample which has only 25 periods of Si(20 Å)/Ge(20 Å) superlattice layers (sample JL193), but otherwise was grown using the identical growth conditions as those used for sample JL194. We will see that the apparent (i.e., as-measured) thermoelectric properties of sample JL193 (25 periods) are more severely affected by the parallel transport contribution from the buffer layer or/and substrate than for sample JL194 (100 periods). However, after subtracting the parallel transport contribution from the buffer layer and/or substrate using the parallel conductor model, the values of the thermoelectric transport coefficients attributed to the 25 periods of the superlattice part of sample JL193 show reasonable agreement with the corresponding values for sample JL194 (100 periods). Finally, in §5.8.3, we will estimate the amount of parallel transport contributions from the buffer layer and/or substrate for all the samples we have studied in §5.7 at 300 K, and we conclude that the parallel transport contributions from the buffer layer and/or substrate are not the dominant contributions to the measured thermoelectric properties, but cannot be ignored completely for the (001) oriented Si(20 Å)/Ge(20 Å) superlattice samples that have less than 100 superlattice periods.

5.8.1 Properties of the bare buffer layer[†]

Shown in Fig. 5-25 is the two-dimensional (sheet) electrical conductivity for a bare

[†]The author acknowledges S. B. Cronin at MIT for his experimental assistance in this subsection.

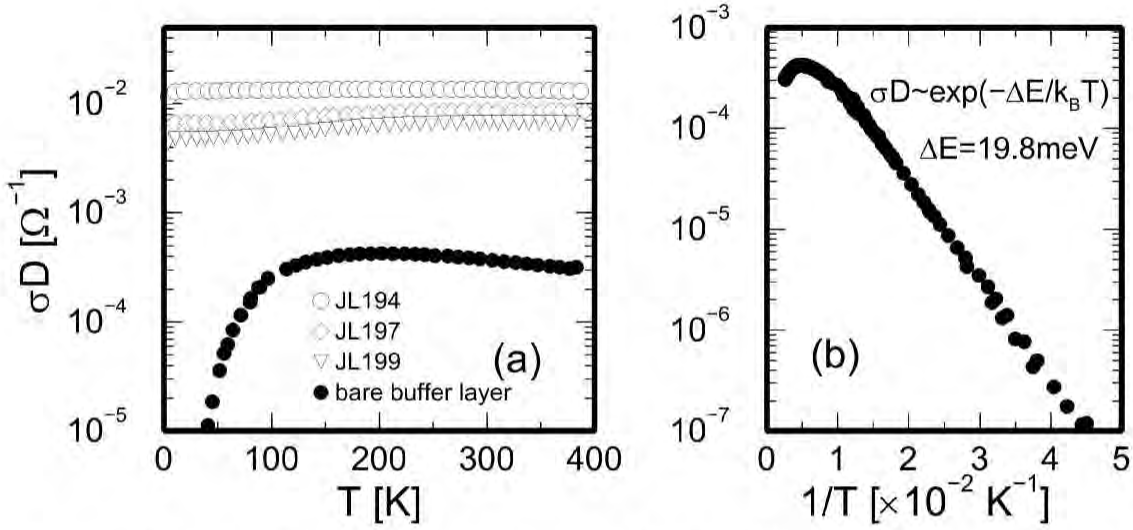

Figure 5-25: (a) Two-dimensional sheet conductivity (denoted as σD, where σ is the three-dimensional electrical conductivity and D is the thickness of the sample used for the calculation of σ) as a function of temperature for a bare buffer layer sample (JL200) that is grown on a SOI (Si-on-insulator) substrate (filled circles). Also shown in the figure are the two-dimensional sheet conductivities σD for samples JL194 (open circles), JL197 (open diamonds) and JL199 (open triangles) that are discussed firstly in §5.7.2. (b) Arrhenius plot of σD for the bare buffer layer sample (JL200). The activation energy obtained for conduction carriers below 100 K is 19.8 meV.

buffer layer sample (JL200) [a sample that has identical buffer layers as those used for the growth of samples JL194, JL197 and JL199, but does not have the superlattice part of the sample] as a function of temperature, together with the corresponding two-dimensional conductivities for the (001) oriented Si(20 Å)/Ge(20 Å) superlattice samples that are examined in §5.7 (samples JL194, JL197 and JL199). The two-dimensional electrical conductivity here means the *electrical conductance per unit area*, which is obtained by multiplying the normal three-dimensional electrical conductivity σ by the sample thickness D that was used for obtaining the values of σ experimentally (therefore, we denote the two-dimensional electrical conductivity by σD). It is noted that the two-dimensional conductivity σD is an additive quantity between the different samples in the parallel conductor model, assuming that the two samples have the same length and width, but can have different thicknesses, as

each other.[†] For example, if we consider a parallel conductor consisting of samples A and B [assuming that both A and B have the same length and width (but may have different thicknesses)], the total two-dimensional conductivity σD for the parallel conductor is the sum of σD's for samples A and B. The reason why we use the two-dimensional electrical conductivity σD instead of the three-dimensional σ is that the parallel transport contribution from the buffer layer and/or substrate is directly visible in the simultaneous plot of the two-dimensional conductivities for the superlattice samples and for the bare buffer layer sample, as we can see in Fig. 5-25(a). In Fig. 5-25, we find that the values of the two-dimensional electrical conductivity for the bare buffer layer sample are a factor of ten to twenty smaller than those for the Si(20 Å)/Ge(20 Å) superlattice samples (JL194, JL197 and JL199) that are studied in §5.7. If our parallel conductors model is strictly valid, this is exactly the contribution from the buffer layer and/or substrate to the measured electrical conductivity [assuming that the buffer layers in the Si(20 Å)/Ge(20 Å) superlattice samples have the identical electrical properties as the bare buffer layer sample (JL200)]. However, there is also a possibility that the intrinsic properties of either the buffer layer or the Si(20 Å)/Ge(20 Å) superlattice part of the sample may be altered due to the presence of the interface between them, i.e., the possible carrier transfer phenomena and/or band bending effect at the superlattice-buffer layer interface may alter the properties of either (or both) of them, for example. Therefore, we will postpone our assessment of the buffer layer and/or substrate contributions to the measured thermoelectric transport coefficients for the Si(20 Å)/Ge(20 Å) superlattices until we examine the transport properties of the "fewer-period" Si(20 Å)/Ge(20 Å) superlattice sample (sample JL193) in §5.8.2, where the properties of a Si(20 Å)/Ge(20 Å) superlattice sample which has only 25 periods of Si(20 Å)/Ge(20 Å) superlattice layers (sample JL193) are studied and compared with the properties of a 100-period superlattice sample (sample JL194) that was grown under the identical growth conditions as those for the 25-period superlattice (JL193). Another feature that we find in Fig. 5-25 is

[†]The parallel conductor model here denotes an electric circuit in which two conductors are connected together in parallel so that their conductances add.

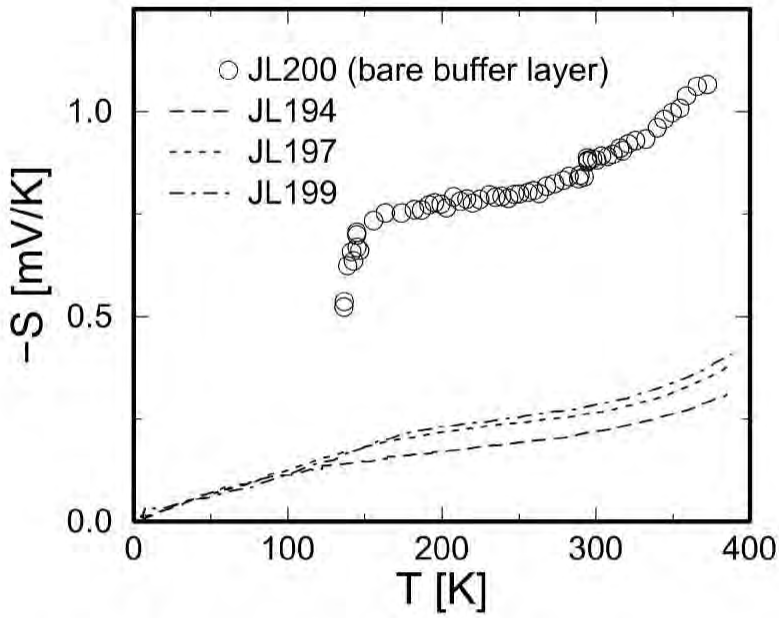

Figure 5-26: Seebeck coefficient as a function of temperature for a bare buffer layer sample (JL200) that is grown on a SOI (Si-on-insulator) substrate (open circles). Also shown in the figure are the measured Seebeck coefficients for samples JL194 (long-dashed curve), JL197 (short-dashed curve) and JL199 (dash-dotted curve), for comparison (these samples are grown on buffer layers that are identical to that grown for sample JL200).

that the bare buffer layer sample (JL200) experiences carrier freeze-out phenomena below 100 K [see Fig. 5-25(b) for the Arrhenius plot]. The activation energy obtained from the Arrhenius plot of the two-dimensional conductivity data [Fig. 5-25(b)] is 19.8 meV.

Shown in Fig. 5-26 is the measured Seebeck coefficient as a function of temperature for the bare buffer layer sample JL200 (open circles) together with the Seebeck data for samples JL194, JL197 and JL199. We find the following features for the Seebeck coefficient $|S|$ of the bare buffer layer sample in Fig. 5-26 : (1) The measured values of the Seebeck coefficient for the bare buffer layer sample are three to four times larger than those for the superlattice samples (JL194, JL197 and JL199) in the temperature range between 140 K and 380 K, which is consistent with the expected doping levels for the bare buffer layer sample ($n < 10^{18}$ cm^{-3}). (2) The measured Seebeck coefficient for the bare buffer layer sample is relatively temperature insensitive between 150 K and 300 K, and (3) the magnitude of the Seebeck coefficient $|S|$

increases with increasing temperature above 300K. The possible explanation for (2) and (3) is that the chemical potential ζ for the bare buffer layer sample is pinned between the impurity level [$\sim$20 meV below the conduction band edge as we determined in Fig. 5-25(b)] and the conduction band edge, for temperatures between 150 K and 300 K, but ζ moves below the impurity level energy (~ -20 meV) above 300 K. It is noted that the Seebeck coefficient S is not a directly additive quantity between the different samples in the parallel conductors model. Therefore, we cannot directly subtract the buffer layer (or substrate) contribution to the measured Seebeck coefficient from the as-measured values of the Seebeck coefficient for the superlattice samples (JL194, JL197 and JL199). Instead, we should consider the transport coefficient $S\sigma D$, that is connected with the energy current carried by the conduction electrons, for the subtraction (or estimation) of the buffer layer and/or substrate contribution to the measured Seebeck coefficient for the Si(20 Å)/Ge(20 Å) superlattice samples, as we discuss in §5.8.3.

5.8.2 Properties of the Si/Ge superlattice with a fewer number of periods (sample JL193)

Our main purpose to study the properties of a Si(20 Å)/Ge(20 Å) superlattice with a fewer number of superlattice periods (25 periods for sample JL193 in contrast to 100 periods for sample JL194) is to examine whether or not any interfacial effects are evident in the measured thermoelectric properties of the Si(20 Å)/Ge(20 Å) superlattice samples, which may alter the electronic properties of the superlattice part of the sample and/or the properties of the buffer layer. If any interfacial effect is present in these samples, the measured thermoelectric properties for a thinner superlattice samples (a fewer number of superlattice periods) should be seriously affected by the interfacial phenomena, and then the parallel conductor model that is explained in §5.8.1 (and further discussed in §5.8.3) is not valid for subtracting out the net contributions of the superlattice part of the sample to the measured values of the thermoelectric transport coefficients for the whole sample. However, even in this case, we can still

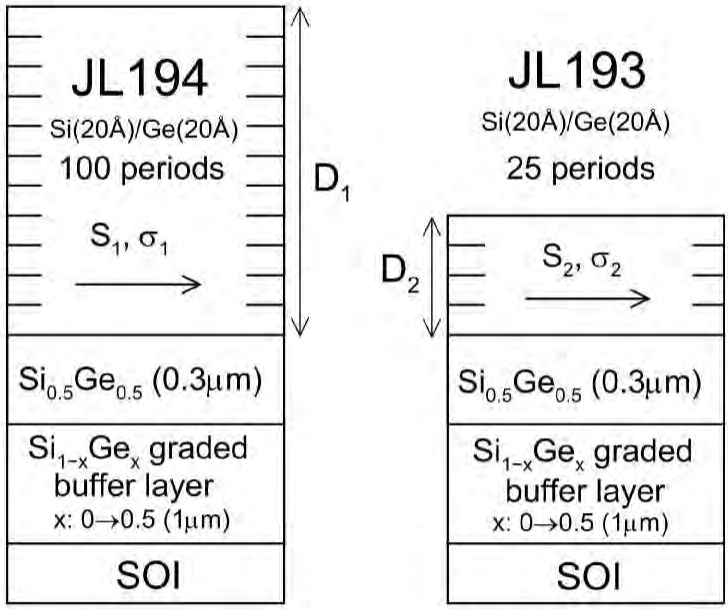

Figure 5-27: Schematic diagram to show the structures of the thin (25 periods) and thick (100 periods) Si(20 Å)/Ge(20 Å) superlattice samples that are used in the present investigation, which are denoted as JL193 and JL194, respectively.

use our parallel conductors model between the 25-period superlattice sample (JL193) and the 100-period superlattice sample (JL194) to evaluate the properties of the top 75 periods of the Si(20 Å)/Ge(20 Å) superlattice in sample JL194, assuming that the electronic properties of the bottom 25 periods of the Si(20 Å)/Ge(20 Å) superlattice part of sample JL194 (and the buffer layer part of the sample) are identical with those for sample JL193.

Shown in Fig. 5-27 are schematic diagrams to show the structure of the thin (25 periods) and thick (100 periods) Si(20 Å)/Ge(20 Å) superlattice samples that are used in this subsection, where one of the samples (JL194) has a larger thickness for the sum of the Si(20 Å)/Ge(20 Å) superlattice layers [Si(20 Å)/Ge(20 Å) × 100 periods = 4000 Å], and the other sample (JL193) has a smaller thickness for the sum of the Si(20 Å)/Ge(20 Å) superlattice layers [Si(20 Å)/Ge(20 Å) × 25 periods = 1000 Å]. These two samples were grown in two consecutive runs using the identical growth conditions. Therefore, we assume that the 25 periods of the Si(20 Å)/Ge(20 Å) superlattice layers in sample JL193 represent identical electronic properties as the initial

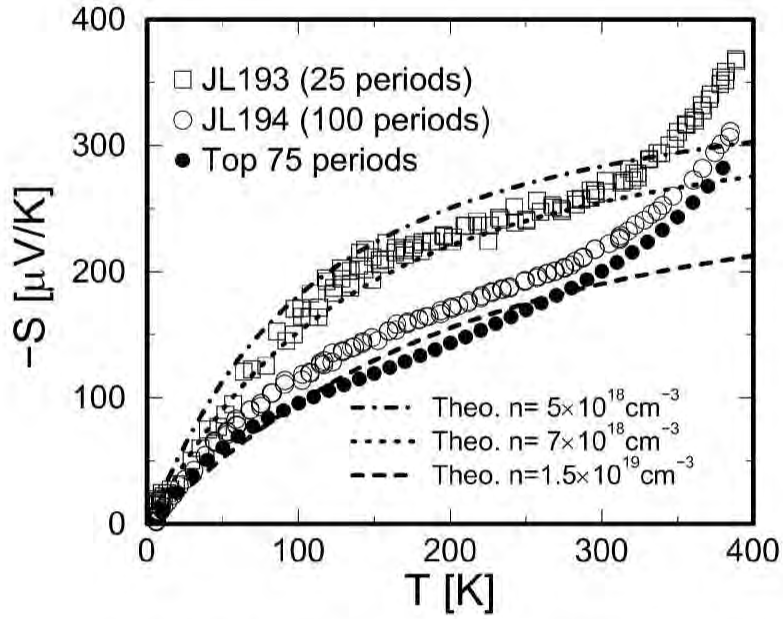

Figure 5-28: Seebeck coefficient as a function of temperature for samples JL193 (open squares) and JL194 (open circles), together with the theoretical results obtained using the semi-classical models that are developed in Chapter 6. The filled circles denote the properties of the top 75 periods of the Si(20 Å)/Ge(20 Å) superlattice part of sample JL194, that are deduced using the subtraction process developed in §5.8.3.

25 periods of the Si(20 Å)/Ge(20 Å) superlattice layers in sample JL194. Since there is no guarantee that such an assumption is valid for the actual pair of samples (JL193 and JL194), we have first to examine the properties of these samples individually with some care.

Shown in Figs. 5-28–5-30 are the Seebeck coefficient S, the Hall carrier concentration n_{Hall} and the electrical conductivity σ as a function of temperature for the 25-period Si(20 Å)/Ge(20 Å) superlattice sample (JL193) together with the corresponding results for the 100-period Si(20 Å)/Ge(20 Å) superlattice sample (JL194) that was grown under the identical growth conditions as those for sample JL193. Also shown in these figures are the properties of the top 75 periods of the Si(20 Å)/Ge(20 Å) superlattice part of the sample for sample JL194 that are deduced using the parallel conductors model for the pair of samples JL193 and JL194 (see §5.8.3 for the discussions of these results). In Fig. 5-28, we find that the values of the measured Seebeck coefficient for the 25-period superlattice sample (JL193) are significantly larger than

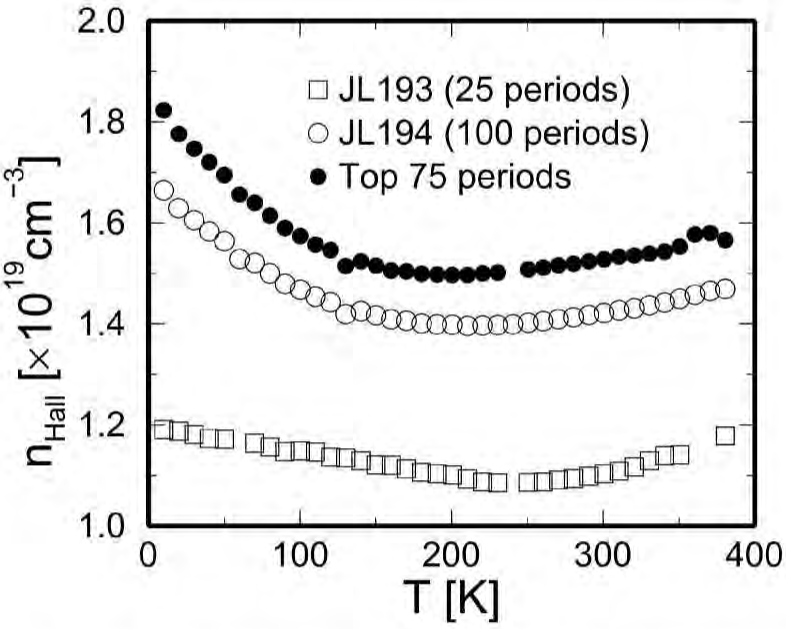

Figure 5-29: Hall carrier concentration n_{Hall} as a function of temperature for samples JL193 (open squares) and JL194 (open circles). The filled circles denote the Hall carrier concentrations deduced for the top 75 periods of the Si(20 Å)/Ge(20 Å) superlattice part of the sample for sample JL194 using the parallel conductor model, as explained in §5.8.3.

the corresponding values for the 100-period superlattice sample (JL194). We can attribute the differences in the measured values for the Seebeck coefficient between samples JL193 (25 periods) and JL194 (100 periods) either to the parallel transport contribution from the buffer layer and/or substrate, or to an unintentional fluctuation in the carrier doping levels along the thickness of the superlattice part of the samples (or attributed to an unintentional scatter in the doping level from one sample to another). Shown in Fig. 5-29 are the Hall carrier concentrations for samples JL193 (25 period) and JL194 (100 periods), where we find that the measured Hall carrier concentrations for the 25-period superlattice sample (JL193) ($n \approx 1.1\times10^{19}$ cm^{-3} at 300 K) are a little lower than those for the 100-period superlattice sample (JL194) ($n \approx 1.4\times10^{19}$ cm^{-3} at 300 K). Although this observation in the Hall carrier concentration is consistent with the Seebeck results shown in Fig. 5-28 (the smaller the carrier concentration, the larger the magnitude of $|S|$), it turns out that this amount of the difference in the carrier concentration does not provide sufficient explanation for the observed difference in the Seebeck coefficient between these two samples (samples

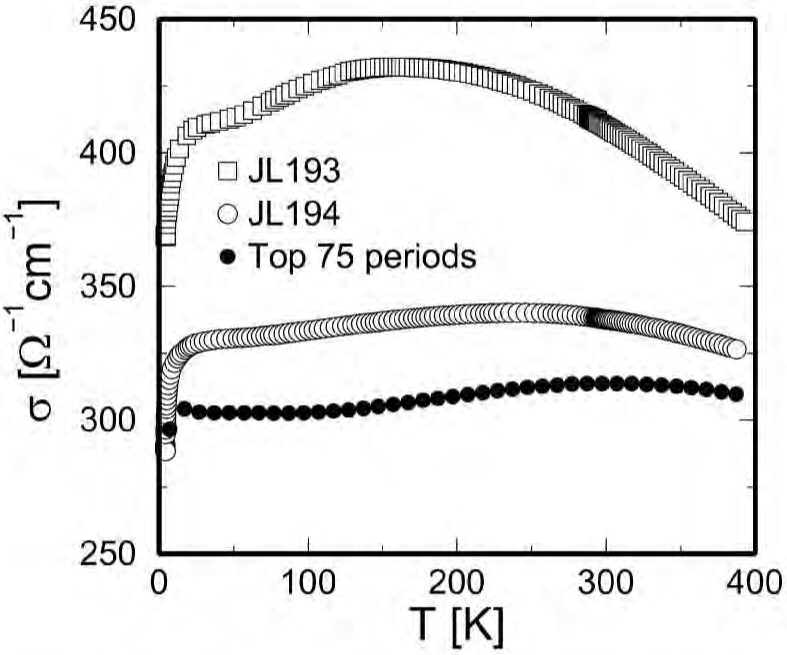

Figure 5-30: Three-dimensional electrical conductivity σ as a function of temperature for samples JL193 (open squares) and JL194 (open circles). The filled circles denote the electrical conductivities deduced for the top 75 periods of the Si(20 Å)/Ge(20 Å) superlattice part of the sample for sample JL194 using the parallel conductors models as explained in §5.8.3.

JL193 and JL194) (see the theoretical results obtained using the semi-classical models in Fig. 5-28, where the value of the carrier concentration predicted for sample JL193 is in the range between $n \approx 5\times10^{18}$ cm^{-3} and $n \approx 7\times10^{18}$ cm^{-3}). Therefore, we conclude that the observed discrepancy between the measured and predicted Seebeck coefficients for the 25-period Si(20 Å)/Ge(20 Å) superlattice sample (sample JL193) is not due to a fluctuation in the carrier concentration between the two samples, but rather is due to the parallel transport contribution from the buffer layer and/or substrate. We will further examine the effect of the parallel transport contribution from the buffer layer and/or substrate in samples JL193 and JL194 in §5.8.3.

The electrical conductivity σ for the 25-period Si(20 Å)/Ge(20 Å) superlattice sample (JL193) is shown in Fig. 5-30 as a function of temperature together with the corresponding results for the 100-period Si(20 Å)/Ge(20 Å) superlattice sample (JL194). It is noted that, as we discussed before, the value of the thickness

that is used to obtain the electrical conductivity σ experimentally is the thickness of the superlattice part of the sample only (i.e., 1000 Å for sample JL193 and 4000 Å for sample JL194). We find that the values for the electrical conductivity obtained for the 25-period superlattice sample (JL193) is significantly larger than the corresponding values for the 100-period superlattice sample (JL194). Since the measured Hall carrier density for the 25-period superlattice sample is *lower* than that for the 100-period superlattice sample (JL194), the resultant difference in the Hall carrier mobility between samples JL193 and JL194 is even larger. The possible causes for the observed enhancement in the carrier mobility for the 25-period superlattice sample (JL193) relative to that for the 100-period superlattice sample (JL194) include a fewer number of structural defects and/or dislocations in sample JL193 (25 periods) than in sample JL194 (100 periods), and/or a smaller density of the ionized impurities in sample JL193 (25 periods) than in sample JL194 (100 periods). The reduced contribution from these scattering mechanisms to the electrical conductivity σ is consistent with the measured electrical conductivity data for sample JL193 (25 periods) as shown in Fig. 5-30. Especially above 200 K, in Fig. 5-30, the observed decrease in σ with increasing temperature is consistent with the increasing contribution from acoustic phonon scattering as the temperature is increased, where other scattering mechanisms (such as scattering due to the structural defects and dislocations and/or ionized impurity scattering) become relatively unimportant.

5.8.3 Assessment of the parallel transport contributions from the buffer layer and/or substrate

In §5.8.1, we have discussed that the two-dimensional electrical conductivity σD and the two-dimensional transport coefficient $S\sigma D$ that is connected with the energy current due to the conduction electrons are additive quantities in our parallel conductors model. It turns out that the Hall carrier density multiplied by the sample thickness D, i.e., $n_{\rm Hall}D$, is also an additive quantity in our parallel conductors model, since the Hall carrier density $n_{\rm Hall}$ is proportional to the Hall conductivity $\sigma_{\rm Hall}$ ($\sigma_{\rm Hall} = j_x/E_y$,

where the external magnetic field $\mathbf{B}$ is applied along the z-direction) for a given value of the external magnetic field B. Therefore, using the parallel conductors model, we obtain the following equations to deduce the net contribution of the superlattice part of the sample only to the measured transport coefficients S, σ and $n_{\rm Hall}$:

$$\sigma_{\rm SL\,only} = \frac{\sigma_1 D_1 - \sigma_2 D_2}{D_1 - D_2}, \tag{5.7}$$

$$S_{\rm SL\,only} = \frac{S_1 \sigma_1 D_1 - S_2 \sigma_2 D_2}{\sigma_1 D_1 - \sigma_2 D_2}, \tag{5.8}$$

$$n^{\rm Hall}_{\rm SL\,only} = \frac{n^{\rm Hall}_1 D_1 - n^{\rm Hall}_2 D_2}{D_1 - D_2}, \tag{5.9}$$

where D_1 and D_2 denote the thicknesses used to obtain the three-dimensional electrical conductivity σ and the Hall carrier density $n_{\rm Hall}$ experimentally for samples 1 and 2, respectively, and the quantities S_1, S_2, σ_1, σ_2, $n^{\rm Hall}_1$ and $n^{\rm Hall}_2$ in Eqs. 5.7–5.9 are defined similarly in the obvious sense (see Fig. 5-27). It is noted that in the specific examples given in this subsection, sample 1 can represent all the superlattice samples (JL193, JL194, JL197 and JL199) and sample 2 represents only the bare buffer layer sample (JL200) [for the subtraction of the buffer layer (and/or substrate) contributions for all the superlattice samples] or the 25-period superlattice sample (JL193) [for the subtraction of the contributions from the bottom 25 periods of the superlattice and the buffer layer (and/or substrate) part of the sample for sample JL194].

Shown in Figs. 5-31 and 5-32 are the two dimensional transport coefficients σD and $S\sigma D$ as a function of temperature, for the bare buffer layer sample JL200 (solid curve), for the 25-period superlattice sample (open squares), and for the 100-period superlattice sample (open circles), to show the relative importance of the parallel transport contributions from the buffer layer and/or substrate to the measured electrical conductivity σ and to the measured Seebeck coefficient S for the Si(20 Å)/Ge(20 Å) superlattice samples assuming that the parallel conductors model is valid. In Fig. 5-31, we find that the parallel transport contribution from the buffer layer or/and substrate to the measured electrical conductivity is relatively small. We estimate the

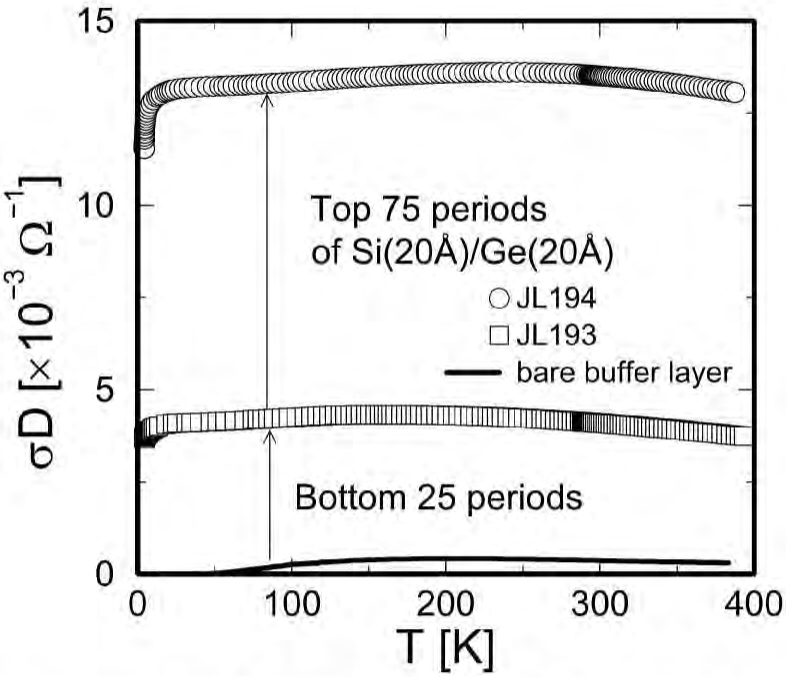

Figure 5-31: Two-dimensional electrical conductivity σD as a function of temperature for sample JL193 (open squares), for sample JL194 (open circles), and for the bare buffer layer sample JL200 (solid curve).

parallel transport contribution from the buffer layer or/and substrate to be 9.1% and 2.8% for samples JL193 and JL194, respectively, at 300 K. On the other hand, the parallel transport contribution to the two-dimensional transport coefficient $S\sigma D$ is relatively large (Fig. 5-32), and it is not in a negligible level anymore for the 25-period superlattice sample (JL193). In fact, this is actually the main cause for the observed discrepancy between the measured and predicted values for S for sample JL193 (25 periods) [see §5.8.2]. Shown in Fig. 5-33 are the results of the subtraction process for the Seebeck coefficient S that is developed in this subsection using the parallel conductor model (Eq. 5.8). We have performed the subtraction process using the following combinations of samples to deduce the values of the Seebeck coefficient for the superlattice part of the sample only for samples JL193 and JL194 : (1) using samples JL193 (25 periods) and JL200 (bare buffer sample) for samples 1 and 2, respectively, in Eq. 5.8 (dot-dashed curve in Fig. 5-33), (2) using samples JL194 (100 periods) and JL200 (bare buffer sample) for samples 1 and 2, respectively, in Eq. 5.8 (dashed curve in Fig. 5-33), and (3) using samples JL194 (100 periods) and JL193 (25 periods) for

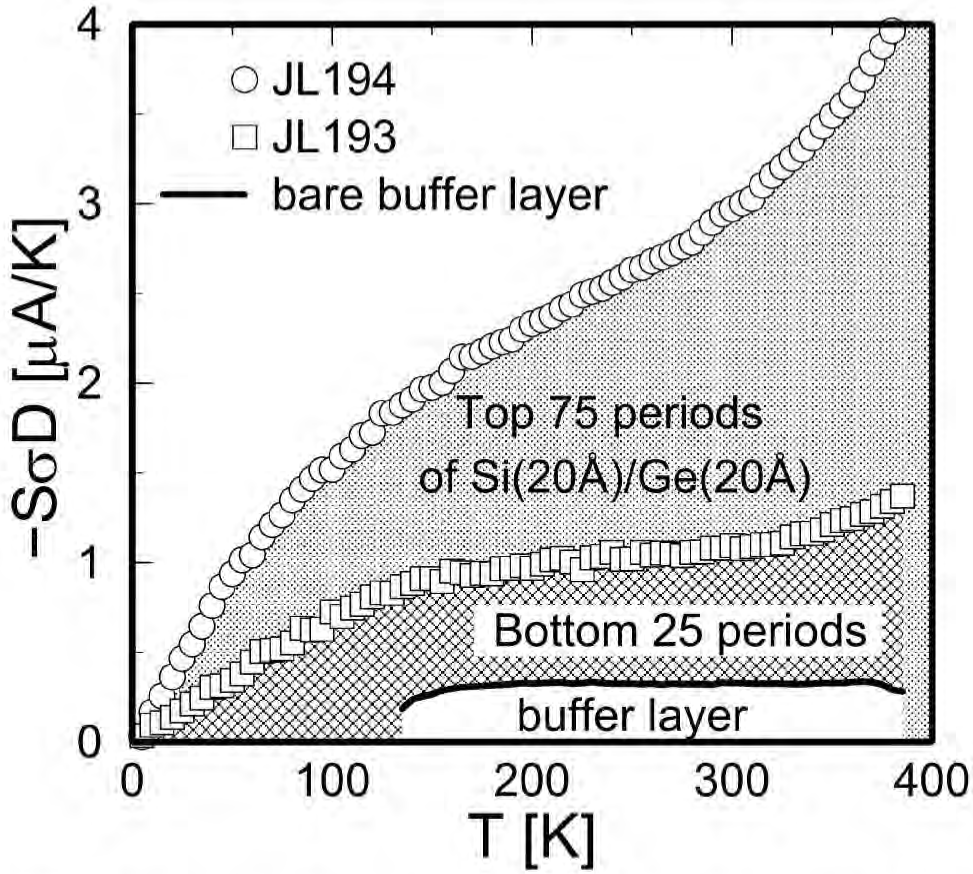

Figure 5-32: Two-dimensional transport coefficient $S\sigma D$ that is connected to the energy current carried by the conduction electrons as a function of temperature for sample JL193 (open squares), for sample JL194 (open circles), and for the bare buffer layer sample JL200 (solid curve).

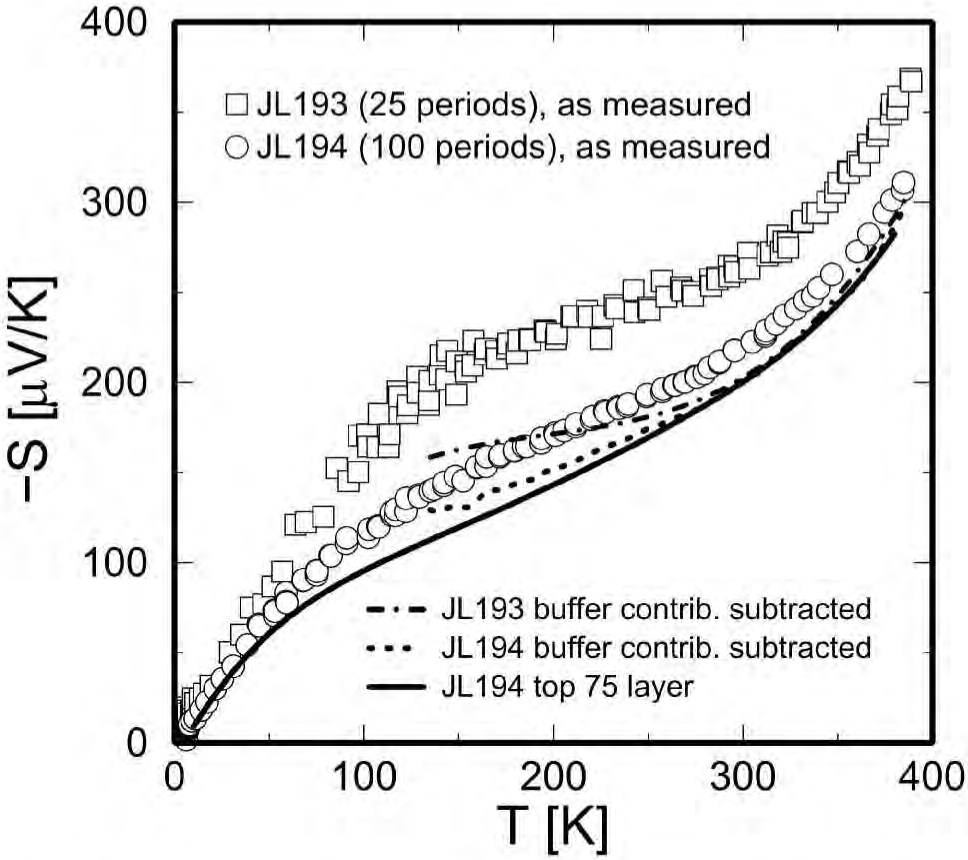

Figure 5-33: Results for the subtraction of the buffer layer contribution to the measured Seebeck coefficient S as a function of temperature. The open squares and open circles denote the measured Seebeck coefficients for samples JL193 and JL194, respectively. The values for the Seebeck coefficient deduced for the superlattice part of the sample only using the parallel conductors model (Eq. 5.8) are also shown for : (1) sample JL193 using the bare buffer layer sample for the subtraction of the buffer layer contribution (dash-dotted curve), (2) sample JL194 using the bare buffer layer sample for the subtraction of the buffer layer contribution (dashed curve) and (3) sample JL194 using the 25-period superlattice sample (JL193) for the subtraction of the contributions from the bottom 25 periods of the superlattice and from the buffer layer part of the sample (solid curve).

samples 1 and 2, respectively, in Eq. 5.8 (solid curve in Fig. 5-33). What we find in Fig. 5-33 are (1) all the curves for the subtracted Seebeck coefficient collapsed into one curve above 280 K and (2) the subtracted values of the Seebeck coefficient deduced for sample JL194 using sample JL200 for the subtraction are similar to those deduced using sample JL193 for the subtraction above 140 K, and (3) the subtracted value of the Seebeck coefficient for sample JL193 is still slightly larger than the corresponding values for sample JL194 below 280 K. However, considering the fact that the measured Hall carrier concentrations for sample JL193 are a little lower than those for sample JL194 (Fig. 5-29), the obtained values for the Seebeck coefficient for sample JL193 after the subtraction process in Fig. 5-33 are in good agreement with the theoretical values obtained using the semi-classical models developed in Chapter 6 for $n = 1.1\times10^{19}$ cm^{-3} below 280 K. (4) The marked feature of increasing $|S|$ with increasing temperature above 300 K that is observed in §5.6.1 and §5.7.2 for all the Si(20 Å)/Ge(20 Å) samples investigated in this chapter is still present even after the subtraction process using any conbinations of the samples given above for samples 1 and 2 used in Eq. 5.8. Therefore, we can conclude that the marked increase in $|S|$ above 300 K that is observed in all the Si(20 Å)/Ge(20 Å) samples investigated in this chapter is not attributed to the parallel transport contribution from the buffer layer or/and substrate, but is a property of the superlattice part of the sample. Since we don't have any conclusive mechanisms for the observed marked increase in $|S|$ above 300 K, future effort should be expended to reveal the exact mechanisms for the observed enhancement in $|S|$ above 300 K in these superlattice samples.

Finally, we summarize, in Tables 5.2 and Table 5.3, the results of the subtraction process for all the superlattice samples grown on SOI substrates that are investigated in this chapter (samples JL193, JL194 JL197 and JL199), using the bare buffer layer sample (JL200) for sample 2 in Eq. 5.8 (except for JL194b in Table 5.3). In these Tables, we can see that the measured electrical conductivities are relatively insensitive to the parallel transport phenomena in the buffer layer and/or subtrate. However, since the measured values for the Seebeck coefficient $|S|$ and the thermoelectric power factor $S^2\sigma$ are sometimes largely affected by the parallel transport phonemena in the

Table 5.2: Thermoelectric properties of various Si(20 Å)/Ge(20 Å) superlattice samples at 300 K (as-measured). The percentage inside the parentheses indicates the estimated portion of the parallel transport contribution from the buffer layer or/and substrate in the measured values of the thermoelectric transport coefficient.

sample name	σD [$\times 10^{-3}$ Ω^{-1}]	$-S$ [μV/K]	$S\sigma D$ [μA/K]
JL199	6.74 (5.6%)	286	1.93 (17.1%)
JL197	8.59 (4.4%)	265	2.28 (14.5%)
JL194	13.51 (2.8%)	220	2.97 (11.1%)
JL193 [a)]	4.09 (9.2%)	267	1.10 (30.1%)
JL200 [b)]	0.37 (100%)	882	0.33 (100%)

[a)]25-period Si(20 Å)/Ge(20 Å) superlattice.
[b)]bare buffer layer sample.

Table 5.3: Thermoelectric properties of various Si(20 Å)/Ge(20 Å) superlattices at 300 K (after subtracting the parallel transport contributions from the buffer layer and/or substrate). The number inside the parentheses is the corresponding as-measured value (the value without the subtraction process) for comparison.

sample name	σ [Ω^{-1}cm^{-1}]	$-S$ [μV/K]	$S^2\sigma$ [μW/cm·K^2]
JL199	159 (169)	251 (286)	10.0 (13.8)
JL197	205 (215)	237 (265)	11.6 (15.1)
JL194	328 (338)	201 (220)	13.3 (16.4)
JL194b [a)]	314 (338)	199 (220)	12.5 (16.4)
JL193 [b)]	372 (409)	206 (267)	15.8 (29.1)

[a)]obtained by subtracting the parallel transport contributions of the bottom 25 periods of the superlattice and of the buffer layer and/or substrate using sample JL193.
[b)]25-period Si(20 Å)/Ge(20 Å) superlattice.

buffer layer and/or substrate, some cautions have to be expended when studying the thermoelectric properties of the Si/Ge superlattices with relatively small numbers of superlattice periods (<50 periods) and/or relatively small values for the carrier concentration ($<10^{19}$ cm^{-3}).

5.9 Summary of the experimental results at 300 K and the effect of the extrinsic scattering mechanisms

In this section, we summarize the experimental results obtained in §5.6–§5.8 for the (001) oriented Si(20 Å)/Ge(20 Å) superlattice samples as a function of carrier concentration n at 300 K. First, in §5.9.1, we examine the experimental Hall mobility $\mu_{\rm Hall}$ as a function of n and estimate the amount of the extrinsic scattering mechanisms contributing to $\mu_{\rm Hall}$ using Matthiesen's rule (Eq. 5.6)

$$\frac{1}{\tau_{\rm tot}(E)} = \frac{1}{\tau_{\rm imp}(E)} + \frac{1}{\tau_{\rm ac}(E)} + \frac{1}{\tau_{\rm ext}}. \tag{5.6}$$

Here, $\tau_{\rm imp}(E)$ and $\tau_{\rm ac}(E)$ are calculated using the semi-classical models without the use of any fitting parameters, but the value of $\tau_{\rm ext}$ is obtained from the fitting of the experimental Hall mobilities. In §5.9.2, we examine how the predicted values for the Seebeck coefficient S are altered if we include the $\tau_{\rm ext}$ contribution into the semi-classical models. Then, these predicted values for $|S|$ including the $\tau_{\rm ext}$ contribution are compared with the *as-measured* experimental values for $|S|$ that are obtained in §5.6–§5.8 and with the values after subtracting the contributions from the buffer layer and/or substrate to deduce the net contribution of the superlattice part of the sample only to the measured S (see §5.8). Finally, in §5.9.3, we show the experimentally deduced thermoelectric power factor $S^2\sigma$ as a function of the carrier concentration n at 300 K. These experimental results (with and without the subtraction process that is developed in §5.8) are compared with the theoretical results that are obtained

using the semi-classical models either without the use of any fitting parameters, or including the τ_{ext} contribution, that is deduced from the fitting of the experimental μ_{Hall} data, to describe the extrinsic scattering mechanisms.

The main purpose of the investigation in this subsection is to provide basic data for the future theoretical investigations to reveal the nature of the extrinsic scattering mechanisms that are found in the (001) oriented Si(20 Å)/Ge(20 Å) superlattice samples as discussed in §5.6.1. The theoretical understanding of the details of the extrinsic scattering mechanisms in the (001) oriented Si(20 Å)/Ge(20 Å) superlattices would, in turn, provide feedback to the experiment for the improvement of the sample properties by removing the extrinsic factors that are responsible for the observed values for τ_{ext}, so that the values for the thermoelectric figure of merit $Z_{\text{3D}}T$ for the (001) oriented Si(20 Å)/Ge(20 Å) superlattices can be increased even further in the future.

5.9.1 Carrier mobility μ as a function of carrier concentration

Shown in the Table 5.4 and plotted in Fig. 5-34 are the results for the experimental Hall carrier mobilities μ_{Hall} at 300 K that are determined for all the (001) oriented Si(20 Å)/Ge(20 Å) superlattice samples discussed in §5.6–§5.8. Also shown in Table 5.4 are the theoretically predicted values for the carrier mobility $\mu_{\text{theo.}}$ using the semiclassical models that are developed in Chapter 6, assuming that the samples are homogeneously doped throughout the superlattice part of the sample, and without the use of any fitting parameters. The values for the relaxation time deduced for the extrinsic scattering mechanisms (denoted as τ_{ext}) [see §5.6.1], that are obtained using the Matthiessen's rule (Eq. 5.6) and fitting the experimental Hall mobility at 300 K for each sample, are also given in Table 5.4. It is noted that the values for $\tau_{\text{imp}}(E)$ and $\tau_{\text{ac}}(E)$, where $\tau_{\text{imp}}(E)$ and $\tau_{\text{ac}}(E)$ denote the relaxation times (as a function of the electron's kinetic energy) associated with ionized impurity scattering and longitudinal acoustic phonon deformation potential scattering, respectively, are calculated

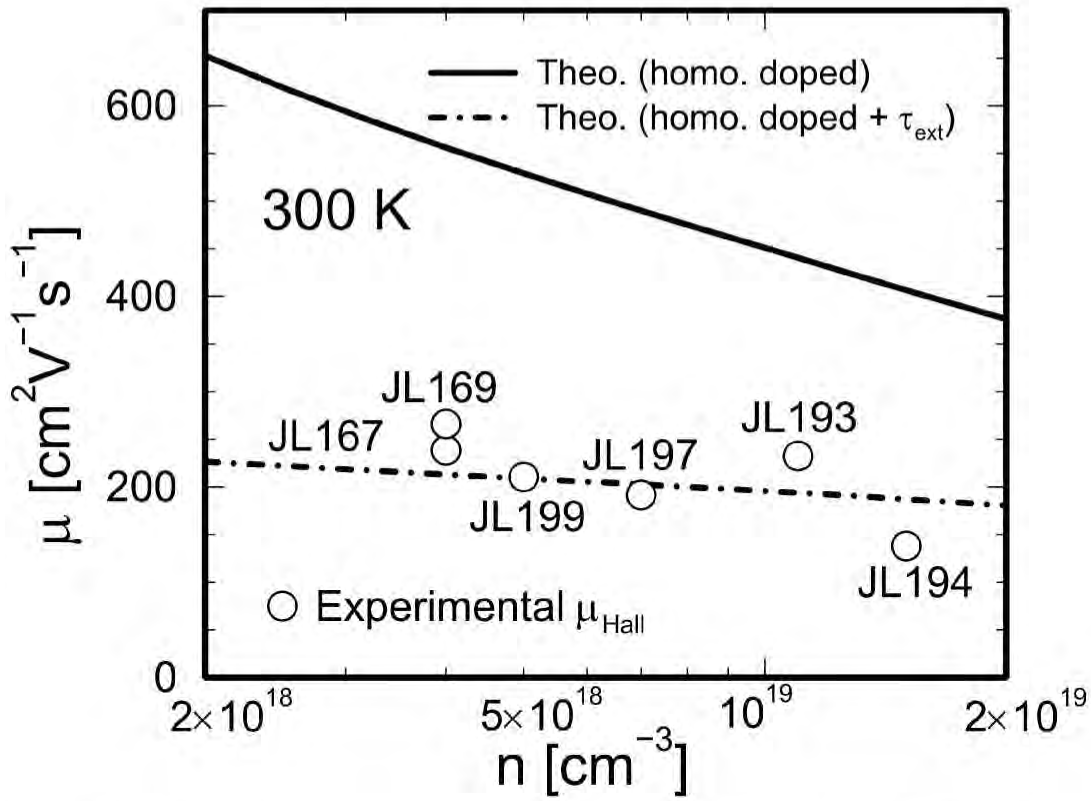

Figure 5-34: Experimentally determined Hall carrier mobility for the (001) oriented Si(20 Å)/Ge(20 Å) superlattices (open circles), that are obtained in §5.6–§5.8, as a function of Hall carrier concentration at 300 K. Also shown in the figure are the theoretically predicated carrier mobilities at 300 K for homogeneously doped (001) oriented Si(20 Å)/Ge(20 Å) superlattices using the semi-classical models developed in Chapter 6 without the use of any fitting parameters (solid curve), and using Matthiessen's rule (Eq. 5.6) to take into account the extrinsic scattering mechanisms that are discussed in §5.6.1 (dot-dashed curve), where a value of $\tau_{ext} = 4\times10^{-14}$ s is chosen from Table 5.4 for the calculation of the theoretical carrier mobilities shown by the dot-dashed curve in the figure.

Table 5.4: The list of the parameters related with the determination of the value of the extrinsic scattering relaxation time τ_{ext} for all the (001) oriented Si(20 Å)/Ge(20 Å) superlattice samples that are investigated in this chapter at 300 K. The symbols n_{Hall}, μ_{Hall}, $\mu_{theo.}$, and τ_{ext} denote the Hall carrier concentration, the Hall carrier mobility, the theoretically predicted value for the carrier mobility using the semi-classical models for homogeneously doped superlattices without the use of any fitting parameters (see Chapter 6), and the relaxation time for the extrinsic scattering mechanisms that is deduced using Matthiessen's rule (Eq. 5.6), respectively.

sample name	n_{Hall} [cm^{-3}]	μ_{Hall} [$cm^2/V{\cdot}s$]	$\mu_{theo.}$ [$cm^2/V{\cdot}s$]	τ_{ext} [s]
JL167	0.4×10^{19}	239	556	4.9×10^{-14}
JL169	0.4×10^{19}	266	556	6.0×10^{-14}
JL199	0.5×10^{19}	210	528	4.1×10^{-14}
JL197	0.7×10^{19}	192	488	3.6×10^{-14}
JL194	1.5×10^{19}	138	406	2.4×10^{-14}
JL193 [a)]	1.1×10^{19}	232	437	5.8×10^{-14}

[a)]25-period Si(20 Å)/Ge(20 Å) superlattice.

using the semiclassical models developed in Chapter 6 without the use of any fitting parameters.

In Table 5.4, we find that the values for τ_{ext} obtained in this way have some scatter, but are approximately constant with respect to the carrier concentration. This is because the extrinsic scattering mechanisms discussed in §5.6.1, i.e., (1) interfacial and/or alloy scattering at the Si/Ge interfaces, (2) scattering due to the structural defects and/or dislocations that are introduced into the superlattice structures during the growth process, such as the threading dislocations, discussed in §5.2, and (3) scattering due to the fluctuations in the thicknesses of the Si and Ge layers, which would introduce a spatial fluctuation in the bound state energies for the conduction electrons (these spatial fluctuations serve as additional scattering potentials for the conduction electrons), are not directly related to the doping level of the superlattice samples. These scattering mechanisms are, however, related to the impurity concentration as a second order effect, since the impurity concentration in the superlattice samples may have some effects on the structural properties of the film. Ignoring these second order effects, we deduce the value for τ_{ext} at 300 K to be around 4×10^{-14} seconds for the (001) oriented Si(20 Å)/Ge(20 Å) superlattice samples that are investigated

in this chapter. We will use this value ($\tau_{ext} = 4\times10^{-14}$ s) for τ_{ext} in the subsequent subsections to model the values of S (Seebeck coefficient) and $S^2\sigma$ (thermoelectric power factor) as a function of carrier concentration at 300 K (also see Fig. 5-34 for the values of the theoretical carrier mobility using $\tau_{ext} = 4\times10^{-14}$ s at 300 K).

5.9.2 Seebeck coefficient *S* as a function of carrier concentration

In the previous subsection (§5.9.1), we have deduced the value for τ_{ext} which is associated with the extrinsic scattering mechanisms, that are present in the actual (001) oriented Si(20 Å)/Ge(20 Å) superlattice samples, from the fitting of the experimental Hall carrier mobility data (see Table 5.4). In this subsection, we are interested in : (1) how the theoretically predicted values for the Seebeck coefficient $|S|$ for the (001) oriented Si(20 Å)/Ge(20 Å) superlattices will be altered by the inclusion of the τ_{ext} factor into the semiclassical models that are developed in Chapter 6, and (2) whether or not the inclusion of the τ_{ext} factor into the models improves the agreement between the experimentally determined values for $|S|$ and the theoretically predicted values for $|S|$.

Plotted in Fig. 5-35 are both the as-measured and the subtracted (see §5.8) experimental Seebeck coefficient as a function of the Hall carrier concentration for the (001) oriented Si(20 Å)/Ge(20 Å) superlattice samples that are investigated in this chapter (open and filled circles, respectively, for the as-measured and subtracted values), together with the theoretical values for the Seebeck coefficient using the semi-classical models developed in Chapter 6 without the use of any fitting parameters (solid curve), and theoretical values using Matthiessen's rule (Eq. 5.6) to take into account the extrinsic scattering mechanisms ($\tau_{ext} = 4\times10^{-14}$ s is chosen from Table 5.4). In Fig. 5-35, we find that while the as-measured values for the experimental Seebeck coefficient (denoted as $S_{a.m.}$) are in good agreement with the theoretical values for the Seebeck coefficient without the use of any fitting parameters (denoted as $S_{homo.}$), the values of the Seebeck coefficient deduced for the net contribution of the superlattice part of

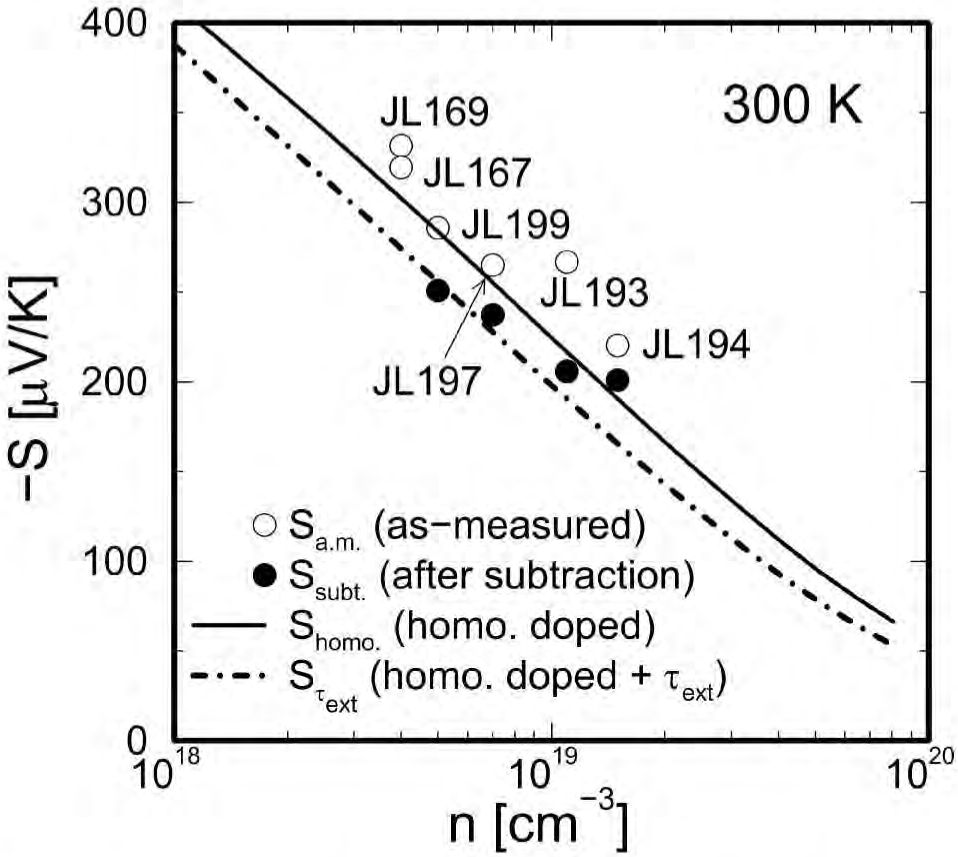

Figure 5-35: The experimentally determined as well as theoretically predicted Seebeck coefficient as a function of carrier concentration at 300 K for the (001) oriented Si(20 Å)/Ge(20 Å) superlattice samples that are investigated in this chapter. The symbols $S_{\text{a.m.}}$ (open circles), $S_{\text{subt.}}$ (filled circles), $S_{\text{homo.}}$ (solid curve) and $S_{\tau_{\text{ext}}}$ (dot-dashed curve) denote the as-measured experimental Seebeck coefficient, the experimental Seebeck coefficient after subtracting the buffer layer and/or substrate contributions, the theoretical Seebeck coefficient using the semiclassical models that are developed in Chapter 6 without the use of any fitting parameters and the theoretical Seebeck coefficient including the τ_{ext} contribution that is obtained from Table 5.4 ($\tau_{\text{ext}} = 4\times10^{-14}$ s is chosen here).

the sample only (denoted as $S_{\text{subt.}}$) (see §5.8) are more consistent with the theoretical values of the Seebeck coefficient including the τ_{ext} factor (denoted as $S_{\tau_{\text{ext}}}$). Since both removing the τ_{ext} contribution and including the parallel transport contribution from the buffer layer and/or substrate have the effect of increasing the values of $|S|$, the apparent agreement between the values of $S_{\text{a.m.}}$ and $S_{\text{homo.}}$ has to be considered as a coincidence. The reasonable agreement between the values for $S_{\text{subt.}}$ and the values for $S_{\tau_{\text{ext}}}$ provides a basis to conclude that our treatments of the parallel transport contribution phenomena from the buffer layer and/or substrate and of the extrinsic scattering mechanisms that are not included in the original semiclassical models developed in Chapter 6, provide some successful approaches to understand the detailed mechanisms of the thermoelectric transport phenomena that are taking place in the actual (001) oriented Si(20 Å)/Ge(20 Å) superlattice samples.

5.9.3 $S^2\sigma$ and $Z_{3\text{D}}T$ as a functiuon of carrier concentration

Shown in Fig. 5-36 are the experimentally as well as theoretically determined thermoelectric power factors $S^2\sigma$ for the (001) oriented Si(20 Å)/Ge(20 Å) superlattice samples that are investigated in this chapter, using the values for μ and S that are plotted in Figs. 5-34 and 5-35, respectively. In Fig. 5-36, we find that, while the as-measured values for $S^2\sigma$ have large scatters in the plot of $S^2\sigma$ vs. n, since the amount of the parallel transport contribution from the buffer layer and/or substrate differs from one sample to another depending on the thickness of the sample (see Tables 5.2 and 5.3), good agreement is found between the theoretically predicted values for $S^2\sigma$ including the τ_{ext} contribution to the semi-classical models that are developed in Chapter 6 and the experimentally determined values for $S^2\sigma$ after the subtraction process that are attributed to the properties of the superlattice part of the sample only, using the parallel conductor model as we developed in §5.8. In addition, we also find that the doping levels for the (001) oriented Si(20 Å)/Ge(20 Å) superlattice samples that are investigated in this chapter are almost in the optimum doping range. Therefore, future experimental work should be expended on improving the structural properties of the superlattice samples to reduce the τ_{ext} contribution to the measured mobility

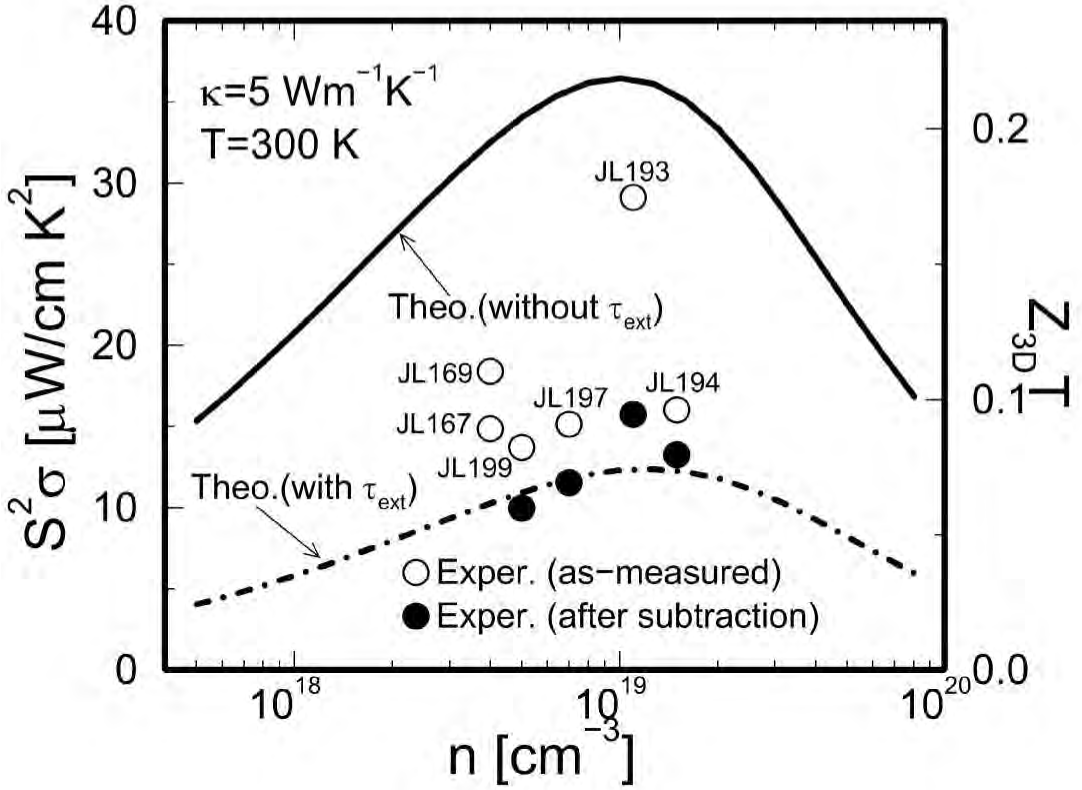

Figure 5-36: The experimentally determined as well as theoretically predicted thermoelectric power factor $S^2\sigma$ (left scale) as a function of carrier concentration at 300 K for the Si(20 Å)/Ge(20 Å) superlattice samples that are investigated in this chapter. The experimental results for $S^2\sigma$ shown here are both as-measured (open circles) and after the subtraction process to deduce the net contribution of the superlattice part of the sample only (filled circles) as discussed in §5.8. The theoretical curves shown here are obtained using semiclassical models that are developed in Chapter 6, without the use of any fitting parameters, assuming homogeneous doping throughout the superlattice part of the sample (solid curve) and using Matthiessen's rule (Eq. 5.6) to take into account the extrinsic scattering mechanisms that are discussed in §5.6.1 (dot-dashed curve), where a value of $\tau_{\rm ext} = 4\times10^{-14}$ s is used for $\tau_{\rm ext}$ (see Table 5.4). The right scale in the figure shows the corresponding values for $Z_{\rm 3D}T$ using $\kappa = 5$ W/m·K for the thermal conductivity.

and/or for developing the δ- and/or modulation doping schemes to enhance the values of the carrier mobility even further, as we discuss in Chapter 6. Readers are also reminded that a large enhancement in the values of $Z_{3D}T$ should furthermore be possible in the (111) oriented Si/Ge superlattice systems where a subband derived from the six equivalent Δ-valleys contributes to the thermoelectric transport for the whole superlattice instead of the two equivalent longitudinal Δ-valleys which contribute to the power factor for the (001) oriented Si/Ge superlattices. The optimum value of $Z_{3D}T$ for a (111) oriented Si(20 Å)/Ge(20 Å) superlattice is predicted to be a factor of four larger than the corresponding value for a (001) oriented Si(20 Å)/Ge(20 Å) superlattice at 300 K using the constant relaxation time approximation as we discussed in §5.4.2.

5.10 Conclusions

In this chapter, the concept of Carrier Pocket Engineering was applied to the strained Si/Ge superlattices to design superlattices with enhanced values of $Z_{3D}T$. The effect of the lattice strain at the Si/Ge interfaces is shown to be utilized as an additional tool to control the conduction band structure of the superlattice. The value of $Z_{3D}T$ calculated for a strain-symmetrized (111) oriented Si(20 Å)/Ge(20 Å) superlattice using the constant relaxation time approximation is 0.96 at 300 K, which represents a factor of four enhancement relative to the corresponding value of $Z_{3D}T$ calculated for a strain-symmetrized (001) oriented Si(20 Å)/Ge(20 Å) superlattice using the same basic models.

The theoretical predictions that are made in the first half of this chapter are tested in the second half of this chapter, which is devoted to an experimental proof-of-principle, using strain-symmetrized (001) oriented Si(20 Å)/Ge(20 Å) superlattice samples that are homogeneously doped throughout the Si/Ge superlattice part of the sample. It turns out that the experimental results obtained in this study are in fair agreement, in the temperature range between 4.2 K and 300 K, with the results of semi-classical models that are developed in Chapter 6, which utilize ionized impurity

scattering as the dominant scattering mechanism. It is also found that the observed increases in S (with decreasing temperature) below 200 K for the samples grown on (001) oriented Si substrates (samples JL167 and JL169) are due to the phonon drag effect, while such an effect is not present in the newer set of samples that are grown on (001) oriented SOI (Si-on-insulator) substrates (samples JL194, JL197 and JL199). We have also found that the measured Seebeck coefficient $|S|$ is enhanced above 300 K relative to the values predicted by theory, and the difference between the values of the measured $|S|$ and the predicted $|S|$ increases with increasing temperature. We have checked that such an increase in $|S|$ above 300 K is not due to the parallel transport contributions from the buffer layer and/or substrate using the parallel conductors model.

Future studies of the enhanced values of $Z_{3D}T$ in the Si/Ge superlattice system should be focused on (1) the effect of δ- and modulation doping on enhancing the values of the carrier mobilities for the Si/Ge superlattices and (2) the experimental proof-of-principle study using the (111) oriented Si/Ge superlattices, where a factor of four enhancement in the value of $Z_{3D}T$ is predicted relative to the (001) oriented Si/Ge superlattice in the optimized superlattice structure using the constant relaxation time approximation.

Chapter 6

Application of Carrier Pocket Engineering to Si/Ge Superlattices II — Detailed modeling and the effect of δ- and modulation doping —

In this chapter, we will develop theoretical models, using the semi-classical Boltzmann transport theory, to predict the values of the transport coefficients for the (001) oriented Si(20 Å)/Ge(20 Å) superlattices that are experimentally investigated in Chapter 5. The basic scheme of the Boltzmann transport theory calculations has been already introduced in Chapter 3, where the thermoelectric transport coefficients for a two-dimensionally confined electron gas for a (111) oriented PbTe(20 Å)/$Pb_{1-x}Eu_xTe$(400 Å) MQW (multiple-quantum-well) sample are calculated assuming longitudinal acoustic phonon deformation potential scattering and polar optical phonon scattering. We have also studied, in Chapter 3, the detailed mechanisms that are responsible for the observed enhancement in $|S|$ (Seebeck coefficient) in the (111) oriented PbTe/$Pb_{1-x}Eu_xTe$ MQWs. The theoretical formalism developed in

Chapter 3 is readily applicable to the (001) oriented Si(20 Å)/Ge(20 Å) superlattices because the z-direction (superlattice growth direction) wavefunction for a (001) oriented Si(20 Å)/Ge(20 Å) superlattice is sufficiently confined within the Si layers so that the overlap of the wavefunction between the two adjacent quantum wells (Si layers) is negligible (see §6.1.2). The detailed differences in theory between the formalism developed in Chapter 3 and that in this chapter are the following : (1) Since we are interested in the *three-dimensional* thermoelectric properties of the Si/Ge superlattices in this chapter (hence, we are interested in the values of $Z_{3D}T$, rather than the values of $Z_{2D}T$ that was the quantity discussed in Chapter 3), we include the thickness of the Ge layers into our formalism when we calculate the transport coefficients in this chapter. (2) The dominant scattering mechanisms included in our models for the (001) oriented Si(20 Å)/Ge(20 Å) superlattices are screened ionized impurity scattering and longitudinal acoustic phonon deformation potential scattering. For PbTe(20 Å)/$Pb_{1-x}Eu_xTe$(400 Å) MQWs, ionized impurity scattering was not important because of their large static dielectric constant ($\epsilon_S \sim 414\epsilon_0$ at 300 K [33]). Instead, polar optical phonon scattering was one of the most dominant scattering mechanisms in PbTe/$Pb_{1-x}Eu_xTe$ MQWs. On the other hand, in the (001) oriented Si(20 Å)/Ge(20 Å) superlattices, polar optical phonon scattering is not important, since both Si and Ge are not polar in nature (elemental semiconductors). Instead, ionized impurity scattering becomes one of the most dominant scattering mechanisms in the Si/Ge superlattices because the static dielectric constants for these materials are relatively small ($\epsilon_S \sim 11.7\epsilon_0$ and $16.1\epsilon_0$ for Si and Ge, respectively [87]),[†] and because general thermoelectric applications require rather large carrier concentrations ($> 5\times10^{18}$ cm $^{-3}$). (3) The effects of the free carrier screening both on ionized impurity scattering and longitudinal acoustic phonon deformation potential scattering are included in this chapter through the inclusion of a Debye screening length λ into our theoretical formalism. (4) The energy dispersion relation for the (001)

[†]As we will see in §6.1.1, the scattering probability $S(\mathbf{k}', \mathbf{k})$ for ionized impurity scattering is proportional to $1/\epsilon_S^2$ besides the density-of-states factor. Therefore, the relative importance of ionized impurity in PbTe/$Pb_{1-x}Eu_xTe$ MQWs, compared to the Si/Ge superlattice, is significantly smaller.

oriented Si(20 Å)/Ge(20 Å) superlattices is assumed to be parabolic, whereas the non-parabolicity in the energy dispersion relations was explicitly considered in the (111) oriented PbTe/$Pb_{1-x}Eu_xTe$ MQWs in Chapter 3.

The organization of this chapter is the following. In §6.1, we will develop the theoretical formalism to calculate the thermoelectric transport coefficients for the (001) oriented Si(20 Å)/Ge(20 Å) superlattices, including ionized impurity scattering and longitudinal acoustic phonon deformation potential scattering as well as considering the effect of the free carrier screening explicitly. In §6.2 and §6.3, we will examine the predicted thermoelectric properties of the (001) oriented Si(20 Å)/Ge(20 Å) superlattices as a function of carrier concentration at 300 K (§6.2), and as a function of temperature for a given carrier concentration ($n = 1.5\times10^{19}$ cm^{-3}). Both in §6.2 and in §6.3, the effects of the δ- and modulation-doping techniques on enhancing the values of the carrier mobility and the resultant values of $Z_{3D}T$ are studied theoretically, using the models developed in §6.1.

We find that the predicted values for the carrier mobility for the δ- and modulation doped superlattices are enhanced significantly relative to the corresponding values of the mobility predicted for the homogeneously doped (001) oriented Si(20 Å)/Ge(20 Å) superlattices, while the values of the Seebeck coefficient are almost unaffected by the specific doping schemes considered for carrier injection. Therefore, we conclude that the thermoelectric properties of the actual (001) oriented Si(20 Å)/Ge(20 Å) superlattices should be accordingly enhanced by introducing the δ- and modulation doping techniques for carrier doping. Finally, in §6.4, we remind ourselves that a really interesting materials system to study using the concept of the Carrier Pocket Engineering (see Chapter 4) is the (111) oriented Si/Ge superlattices, where a factor of four enhancement is predicted in the values of $Z_{3D}T$ for a (111) oriented Si(20 Å)/Ge(20 Å) superlattice relative to the corresponding values of $Z_{3D}T$ for a (001) oriented Si(20 Å)/Ge(20 Å) superlattice using a simple model based on the constant relaxation time approximation, as we discussed in §5.4.2.

6.1 Theoretical formalism

As we mentioned in the introductory statement, the basic scheme for solving the Boltzmann equation is described in Chapter 3. Therefore, those readers who are not familiar with the Boltzmann transport theory are referred to Chapter 3.

6.1.1 Solution of the Boltzmann equation

We have seen in §5.4 that, in our model system of (001) oriented Si(20 Å)/Ge(20 Å) superlattices, the lowest lying conduction subband is the $\Delta^{\parallel}_{\mathrm{Si}}$-(or Δ^{001}-)subband, which has isotropic 2D constant energy ellipses in the two-dimensional Brillouin zone. Since both ionized impurity scattering and longitudinal acoustic phonon scattering can be considered as an elastic scattering event,[†] except at very low temperatures (<10 K), the Boltzmann equation (Eq. 3.12) using the perturbation function $\phi(\mathbf{k}_{||})$ that is connected with the non-equilibrium distribution function $f(\mathbf{k}_{||})$ (see Eq. 3.11)[‡] reduces to

$$\cos\theta = \frac{A}{4\pi^2}\int S(\mathbf{k}_{||},\mathbf{k}'_{||})\{\phi(\mathbf{k}_{||})-\phi(\mathbf{k}'_{||})\}\,d\mathbf{k}'_{||}, \tag{6.1}$$

where A is the lateral area of the pertinent two-dimensionally confined electron gas, $\mathbf{k}_{||}$ and $\mathbf{k}'_{||}$ are the 2D wave vectors to describe the states of the confined electrons before and after the scattering event, respectively, and θ is the polar angle for $\mathbf{k}_{||}$ that is measured from the x-axis. In deriving Eq. 6.1, we have omitted the factor $\gamma'(E_{\mathbf{k}||})$ in Eq. 3.12, since we are dealing with parabolic energy bands. Though the range of the integration, in Eq. 6.1, extends over the entire 2D Brillouin zone, the actual integration can be performed along the curve of the constant energy ellipse owing to the δ-functions found in the equations describing $S(\mathbf{k}_{||},\mathbf{k}'_{||})$ (see Eqs. 3.4–3.6).

[†] An elastic scattering event here means a scattering of the electron in which the kinetic energy of the electron is not altered due to the scattering event.

[‡]
$$f(\mathbf{k}_{||}) = f_0(E_{\mathbf{k}_{||}}) - \frac{e\hbar E_x k_{||}}{m^*}\left(\frac{\partial f_0}{\partial E_{\mathbf{k}_{||}}}\right)\phi(\mathbf{k}_{||}), \tag{3.11}$$

where E_x is the magnitude of the electric field that is applied along the x-direction and m^* is the in-plane component of the effective mass tensor for the pertinent 2D system.

As we did in §3.3.3, we expand the perturbation function $\phi(\mathbf{k}_{||})$ using the Legendre polynomials $\mathrm{P}_l(x)$,

$$\phi(\mathbf{k}_{||}) = a_1(E_{\mathbf{k}_{||}})\mathrm{P}_1(\cos\theta) = a_1(E_{\mathbf{k}_{||}})\cos\theta, \tag{6.2}$$

where $E_{\mathbf{k}_{||}}$ is the energy of the electron that is in state $\mathbf{k}_{||}$. In Eq. 6.2, only the first term ($l = 1$) is retained in the Legendre polynomial expansion since the 2D constant energy surface in our model system is spherical (isotropic). Using Eq. 6.2, the Boltzmann equation (Eq. 6.1), under the elastic scattering condition $E_{\mathbf{k}'_{||}} = E_{\mathbf{k}_{||}}$ (i.e., $|\mathbf{k}'_{||}| = |\mathbf{k}_{||}|$), reduces to the energy-dependent relaxation time formalism.

$$\tau(E_{\mathbf{k}_{||}})^{-1} \equiv a_1(E_{\mathbf{k}_{||}})^{-1} = \frac{m^* A}{2\pi\hbar^3}\int_0^{2\pi} |\mathrm{M}(q_{||})|^2\,(1-\cos\alpha)\,d\alpha, \tag{6.3}$$

where α is the angle between $\mathbf{k}_{||}$ and $\mathbf{k}'_{||}$, $\mathbf{q}_{||}$ is the difference between $\mathbf{k}'_{||}$ and $\mathbf{k}_{||}$ ($\mathbf{q}_{||} \equiv \mathbf{k}'_{||} - \mathbf{k}_{||}$), and $\mathrm{M}(q_{||})$ is the scattering matrix element $\mathrm{M}(q_{||}) = \langle \mathbf{k}'_{||}|H'|\mathbf{k}_{||}\rangle$, which depends on only the magnitude of $\mathbf{q}_{||}$ in the specific examples that we are considering in this chapter (see Table 3.1 for the expressions for the scattering matrix element for various scattering mechanisms in a 3D isotropic material). Because $q_{||}$ in Eq. 6.3 is expressed in terms of $k_{||}$ and α ($q_{||} = 2k_{||}\sin\frac{\alpha}{2}$), Eq. 6.3 can be solved without any approximations.

For our model system of (001) oriented Si(20 Å)/Ge(20 Å) superlattices, the squared matrix element for longitudinal acoustic phonon deformation potential scattering (denoted by $|\mathrm{M}_{\mathrm{ac}}(q_{||})|^2$), including the effect of the screening due to the free carriers, is given by [53, 54, 91],

$$|\mathrm{M}_{\mathrm{ac}}(q_{||})|^2 = \left|\langle \mathbf{k}'_{||}\,|H'_{ac}|\,\mathbf{k}_{||}\rangle\right|^2 = \frac{\Xi^2 k_B T}{4\pi\rho\upsilon^2 A}\int_{-\infty}^{\infty} |G(q_z)|^2\, S_c(\mathbf{q},\lambda)\,dq_z \times 2$$

$$= \frac{\Xi^2 k_B T}{2\pi\rho\upsilon^2 A}\int_{-\infty}^{\infty} |G(q_z)|^2\,\frac{q_{||}^2 + q_z^2}{q_{||}^2 + q_z^2 + \lambda^{-2}}\,dq_z \tag{6.4}$$

where λ, Ξ, ρ and υ are, respectively, the Debye screening length (see below), the acoustic phonon deformation potential, the mass density of the sample and the speed

of sound for the pertinent crystal, $G(q_z)$ is the Fourier transform of the squared wavefunction along the z-direction (superlattice growth axis) as defined in Eq. 3.7,[†] and the factor 2 at the end of the third expression accounts for the phonon absorption and emission processes. In deriving Eq. 6.4, the high temperature approximation for the phonon occupation number $n(\omega) = [\exp(\hbar\omega/k_BT) - 1]^{-1} \simeq k_BT/\hbar\omega$ is utilized and the delta function for the momentum conservation (see Eq. 3.5) is omitted, since we have already assumed $\mathbf{q}_{||} = \mathbf{k}'_{||} - \mathbf{k}_{||}$.

The scattering matrix element for ionized impurity scattering [denoted by $\mathrm{M_{imp}}(q_{||})$] is most simply obtained for an isolated singly charged impurity (see Table 3.1) [53, 54, 91].

$$\mathrm{M_{imp}}(q_{||}) = \langle \mathbf{k}'_{||} \left| H'_{imp} \right| \mathbf{k}_{||} \rangle = \frac{e^2}{2\pi\epsilon_S A} \int_{-\infty}^{\infty} \frac{e^{i\mathbf{q}\cdot\mathbf{R}}}{q^2 + \lambda^{-2}} G(q_z)\, dq_z$$

$$= \frac{e^2\, e^{i\mathbf{q}_{||}\cdot\mathbf{R}_{||}}}{2\pi\epsilon_S A} \int_{-\infty}^{\infty} \frac{e^{iq_z R_z}}{q_{||}^2 + q_z^2 + \lambda^{-2}} G(q_z)\, dq_z, \tag{6.5}$$

where ϵ_S is the static dielectric constant for the pertinent materials system and $\mathbf{R}$ is the position of the impurity ion placed in the system. In Eq. 6.5, we have deliberately included the phase factor $e^{i\mathbf{q}\cdot\mathbf{R}}$ to show that the magnitude of the scattering matrix element is dependent on the position of the impurity ion in the z-direction [where R_z is measured from the middle of the quantum well (Si) layers]. For many randomly distributed impurities, the matrix elements $\mathrm{M_{imp}}(q_{||})$ for all impurities are summed together first, and then squared to obtain the squared matrix element $|\mathrm{M_{imp}}(q_{||})|^2$. After considering the phase cancellations for the randomly distributed impurities, we obtain the following expressions for $|\mathrm{M_{imp}}(q_{||})|^2$ for ionized impurity scattering, depending on the specific assumptions for the doping techniques utilized :

(1) **"Homogeneously doped superlattice samples"**, where the ionized impurity dopants are introduced homogeneously throughout the Si(20 Å)/Ge(20 Å) superlat-

[†] $$G(q_z) = \int_{-\infty}^{\infty} \psi_z^*(z) e^{iq_z z} \psi_z(z)\, dz, \tag{3.7}$$

where $\psi_z(z)$ is the wavefunction along the z-direction obtained by solving the Schrödinger equation assuming the Krönig-Penney model (see §6.1.2).

tice layers (denoted by the subscript 'h-doped' below).

$$|\mathrm{M_{imp}}(q_{\|})|^2_{(\mathrm{h-doped})} = \frac{n^{+}_{3\mathrm{D}} e^2}{\pi^2 \epsilon^2 A} \int_{-\infty}^{\infty} \left| \int_0^{\infty} \frac{\cos(q_z R_z)}{q_{\|}^2 + q_z^2 + \lambda^{-2}} \, G(q_z) \, dq_z \right|^2 dR_z, \tag{6.6}$$

where $n^{+}_{3\mathrm{D}}$ is the 3D concentration of ionized impurities (in m^{-3}) for the whole superlattice.

(2) "**Modulation-doped superlattice samples**", where the ionized impurity dopants are introduced only in the Ge layers of the Si(20 Å)/Ge(20 Å) superlattices. Within the Ge layers, the ionized impurities are homogeneously distributed (denoted by the subscript 'm-doped' below),

$$|\mathrm{M_{imp}}(q_{\|})|^2_{(\mathrm{m-doped})} = \frac{n^{+,\mathrm{modu}}_{3\mathrm{D}} e^2}{\pi^2 \epsilon^2 A} \int_{-\infty}^{\infty} \left| \int_0^{\infty} \frac{\cos(q_z R_z)}{q_{\|}^2 + q_z^2 + \lambda^{-2}} \, G(q_z) \, dq_z \right|^2 \Theta(R_z) \, dR_z, \tag{6.7}$$

where $n^{+,\mathrm{modu}}_{3\mathrm{D}}$ is the 3D concentration of the ionized impurities (in m^{-3}) for the modulation-doped layers (Ge layers), and the function $\Theta(R_z)$ is defined by

$$\Theta(R_z) = \begin{cases} 1 & \text{if } R_z \text{ is within the modulation doped layers,} \\ 0 & \text{otherwise.} \end{cases} \tag{6.8}$$

(3) "***δ*-doped superlattice samples**", where the ionized impurity dopants are introduced two-dimensionally in the middle of each Ge layer in the Si(20 Å)/Ge(20 Å) superlattices (denoted by the subscript 'δ-doped' below).

$$|\mathrm{M_{imp}}(q_{\|})|^2_{(\delta-\mathrm{doped})} = \frac{n^{+}_{2\mathrm{D}} e^2}{\pi^2 \epsilon^2 A} \sum_{R_z^{\delta}} \left| \int_0^{\infty} \frac{\cos(q_z R_z^{\delta})}{q_{\|}^2 + q_z^2 + \lambda^{-2}} \, G(q_z) \, dq_z \right|^2, \tag{6.9}$$

where $n^{+}_{2\mathrm{D}}$ is the two-dimensional sheet concentration of ionized impurities (in m^{-2}) that are δ-doped in the Ge layers of the Si(20 Å)/Ge(20 Å) superlattices, and R_z^{δ} is the position (in the z-direction) of the sheet of the ionized impurities that are δ-doped in the Ge layers. In Eq. 6.9, the summation is taken over all the sheets of the δ-doped ionized impurities that exist in the pertinent superlattice.

The Debye screening length λ that is found in Eqs. 6.4–6.7 is obtained by solving the following equation [53] :[†]

$$\frac{1}{\lambda^2} = \frac{e^2}{k_B T \epsilon_S} \left[\frac{\partial\, n_{3D}}{\partial\, \zeta^*} + \frac{n_{3D}\,(n^i_{3D} - n_{3D})}{n^i_{3D}} \right], \tag{6.10}$$

where n^i_{3D} is the concentration of n-type impurities (donors) that may or may not be ionized, and n_{3D} is the 3D carrier concentration for the whole superlattice. In deriving Eq. 6.10, we have neglected the terms associated with hole and acceptor densities (see Ref. [53]), since our model system of [(001) oriented Si(20 Å)/Ge(20 Å) superlattices] is heavily n-typed doped. In the actual calculations in this chapter, we have assumed that the donor impurities are fully ionized (i.e., $n^i_{3D} = n^-_{3D} = n_{3D}$) since the concentrations of the neutral impurities in our model systems are not known. However, once the information on the neutral impurity concentration of our model system is obtained in the future, either experimentally or theoretically, our treatment of the Debye screening length given here should be improved accordingly.

6.1.2 Wavefunction along the superlattice growth direction

As we see in §6.1.1, all the parameters that are necessary to solve the Boltzmann equation for our model system of the (001) oriented Si(20 Å)/Ge(20 Å) superlattices are obtained from the bulk parameters for Si and Ge that are found in the literature [87].[‡] The only exception to this is the $G(q_z)$ function that is defined in Eq. 3.7 which is needed for the calculation of the scattering matrix element (see Eqs. 6.4–6.9). Since the evaluation of $G(q_z)$ requires a knowledge of the wavefunction along the z-direction

[†]This equation assumes that the sample is a homogeneous, isotropic media. The obvious discrepancy between this assumption and the actual superlattice samples has to be resolved in the future.

[‡]In the particular calculations shown in this chapter we have used the following values from Ref. [87] : static dielectric constant $\epsilon_S = 11.7\epsilon_0$ (the value for bulk Si), longitudinal acoustic phonon deformation potential $\Xi = 10$ eV, mass density for the superlattice sample $\rho = 3.827\times10^3$ kg/m^3 (the average value between bulk Si and bulk Ge), speed of sound $v = 5.995\times10^3$ m/s (the average value between bulk Si and bulk Ge). Among these parameters, only the value of Ξ for the superlattice sample may not be guessed directly from the bulk values. Therefore, the actual value of Ξ for the (001) oriented Si(20 Å)/Ge(20 Å) superlattice may differ at most by a factor of two from the value adopted here, i.e., 5 eV $< \Xi <$ 20 eV, which is the range for the various components of Ξ in bulk Si and bulk Ge (see Ref. [87]).

(superlattice growth axis) $\psi_z(z)$, we have to develop a theoretical model to solve for the wavefunction $\psi_z(z)$ for the (001) oriented Si(20 Å)/Ge(20 Å) superlattices.

In the present work, we adopt the Krönig-Penney model to fulfill this purpose for simplicity. For a more rigorous treatment, both the z-direction wavefunction $\psi_z(z)$ (which predicts the distribution of the free carriers along the z-direction) and the conduction band potential profile (which is determined by the distributions of the ionized impurities and of the free carriers) have to be obtained in a self-consistent manner by solving the Schrödinger equation and the Poisson equation simultaneously, including the band bending effect along the z-direction.[†]

Shown in Fig. 6-1(a) is the calculated squared wavefunction $|\psi_z(z)|^2$ along the z-direction as a function of z measured from the center of a quantum well layer (Si layer) using the Krönig-Penney model. In this calculation, the wavefunction $\psi_z(z)$ is obtained by matching the plane wave functions for an energy E_z and a band offset ΔE_c ($\Delta E_c = 0.808$ eV for this particular example) at the well-barrier boundaries according to the boundary conditions given in Eqs. 4.23 and 4.24, where the value of E_z is obtained by solving the Krönig-Penney equation given in Eq. 4.25.[‡] It is found that the predicted value for E_z has a negligible dependence on k_z. Therefore, the particular solution for $\psi_z(z)$ that is shown in Fig. 6-1(a) is obtained for $k_z = 0$. In Fig. 6-1(a), we find that the predicted wavefunction $\psi_z(z)$ has a negligible overlap between neighboring quantum wells. Therefore, we can use the strict 2D formalism to predict the transport properties of the (001) oriented Si(20 Å)/Ge(20 Å) superlattice systems, as we discussed in §6.1.1.

Another thing one should bear in mind is that there is a certain relation between the scattering rate for the conduction electrons in the 2D systems and the degree of quantum confinement for the conduction electrons along the z-direction. Such a relation is evident in Fig. 3-3(a) for a (111) oriented PbTe(20 Å)/$Pb_{1-x}Eu_xTe$(400 Å)

[†]This approach has to be pursued in the future for a more rigorous treatment of the theoretical modeling of the thermoelectric properties for the (001) oriented Si(20 Å)/Ge(20 Å) superlattice systems.

[‡]The value for the z component of the effective mass tensor m_z used here is $m_z = 0.92\,m$ (see §5.3 in Chapter 5).

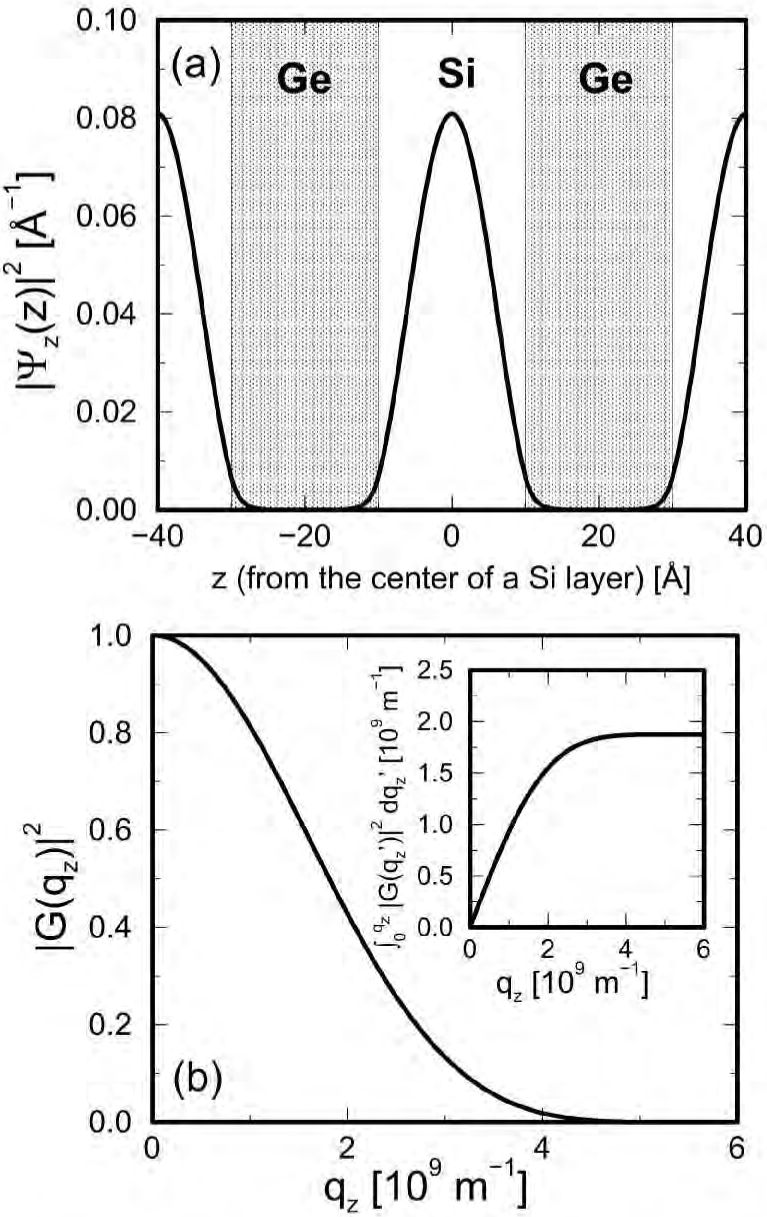

Figure 6-1: (a) Squared wavefunction $|\psi_z(z)|^2$ for a (001) oriented Si(20 Å)/Ge(20 Å) superlattice [$\Delta_{||}$-subband in Fig. 5-8(a)] as a function of z, which is used for the calculation of $G(q_z)$ (the Fourier transform of $|\psi_z(z)|^2$) in (b). $\psi_z(z)$ is obtained by solving the Schrödinger equation using the Krönig-Penney model as discussed in §4.3.4. The calculation was made using the value of the conduction band offset $\Delta E_c = 0.808$ eV and the value of the z component (along the superlattice growth axis) of the effective mass tensor $m_z = 0.92\,m$ (for both Si and Ge layers). (b) $|G(q_z)|^2$ as a function of q_z, where $G(q_z)$ is defined in Eq. 3.7, for the wavefunction given in (a). The inset shows the integration of $|G(q_z')|^2$ with respect to q_z' from zero to q_z as a function of q_z. Note that such a factor (with $q_z = \infty$) appears in the squared matrix element for longitudinal acoustic phonon deformation potential scattering without including the effect of the free carrier screening (see Eq. 3.14).

multiple-quantum-wells, where we have found that the scattering rate for the longitudinal subband is enhanced relative to that for the oblique subband due to the larger values of the $\int_{-\infty}^{\infty} |G(q_z)|^2 dq_z$ factor for the longitudinal subband than for the oblique subband. It is noted that the larger the confinement of the conduction electrons in the z-direction (i.e., the narrower the width of $|\psi_x(z)|^2$), the broader the width of $|G(q_z)|^2$, where the value of $G(q_z)$ at $q_z = 0$, denoted by $G(0)$, is always unity [i.e., $G(0) = \int_{-\infty}^{\infty} |\psi_z(z)|^2 \, dz = 1$]. This indicates that a large quantum confinement does not necessarily imply enhanced thermoelectric properties (since the mobility is reduced due to the increased $\int_{-\infty}^{\infty} |G(q_z)|^2 dq_z$ factor). Therefore, it is necessary to develop an improved optimization process to maximize the value of $Z_{3D}T$, including the nature of the 2D electron gas as discussed above, so that one can predict the most desirable design of the superlattice to obtain the largest value of $Z_{3D}T$ using 2D systems.

6.1.3 Evaluation of the transport coefficients in the relaxation time formalism

Once we obtain the momentum relaxation time function $\tau(E)$ by solving the Boltzmann equation in §6.1.1, we can use the following expressions to evaluate the electrical conductivity σ and the Seebeck coefficient S for our model system of the (001) oriented Si(20 Å)/Ge(20 Å) superlattices:

$$\sigma = \frac{n_{3D} e^2}{m^*} \langle \tau(E) \rangle \tag{6.11}$$

for the electrical conductivity, and

$$S = -\frac{1}{eT} \left\{ \frac{\langle E\tau(E) \rangle}{\langle \tau(E) \rangle} - \zeta \right\} \tag{6.12}$$

for the Seebeck coefficient, where ζ is the chemical potential and $\langle A \rangle$ denotes the following average for the energy dependent quantity A in 2D systems:

$$\langle A \rangle = \frac{\int_0^\infty \left(-\frac{\partial f_0}{\partial E}\right) A(E) E dE}{\int_0^\infty \left(-\frac{\partial f_0}{\partial E}\right) E dE}. \tag{6.13}$$

In Eq. 6.13, $f_0(E)$ denotes the Fermi-Dirac distribution function, and the energy E is measured from the pertinent band edge.

6.2 Predicted values for S, σ and $Z_{3D}T$ for (001) oriented Si(20 Å)/Ge(20 Å) superlattices

— Carrier concentration dependence at 300 K —

In this section, we will examine the results of the theoretical predictions for the thermoelectric properties of the (001) oriented Si(20 Å)/Ge(20 Å) superlattices as a function of carrier concentration n at 300 K. These theoretical predictions are made using the semi-classical models that are developed in §6.1. The effect of δ- and modulation doping techniques on enhancing the values of the carrier mobility μ is also discussed as a function of carrier concentration n at 300 K.

6.2.1 Seebeck coefficient

Shown in Fig. 6-2 are the results of the theoretical calculation of the Seebeck coefficient for (001) oriented Si(20 Å)/Ge(20 Å) superlattices as a function of the carrier concentration n, where (1) homogeneous doping throughout the whole superlattice layers (solid curve), (2) modulation doping only in the Ge layers (dashed curve), and (3) δ-doping at the center of each Ge layer (dash-dotted curve) are assumed, as we discussed in §6.1.1. Also shown in Fig. 6-2 are the experimental results that are obtained in Chapter 5 for the (001) oriented Si(20 Å)/Ge(20 Å) superlattice samples, and the calculated values of $|S|$ using the constant relaxation time approximation for comparison.

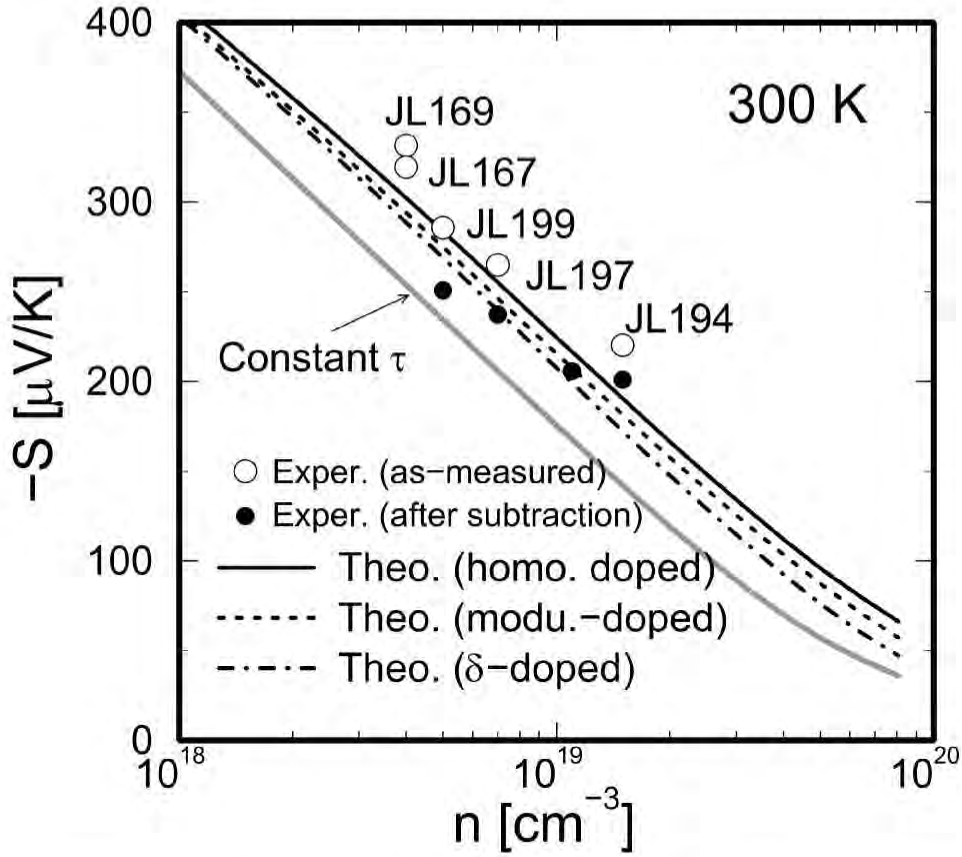

Figure 6-2: The theoretically predicted values for the Seebeck coefficient for (001) oriented Si(20 Å)/Ge(20 Å) superlattices as a function of carrier concentration at 300 K. The calculations were made using the semi-classical models that are developed in §6.1 assuming (1) homogeneous doping throughout the whole superlattice (solid curve), (2) modulation doping only in the Ge layers of the superlattice (dashed curve), and (3) δ-doping in the middle of each Ge layer in the superlattice (dash-dotted curve). Also shown in the figure are the as-measured values for the experimental $|S|$ (open circles), the values for $|S|$ obtained after subtracting the buffer layer and/or substrate contributions (filled circles) as discussed in §5.8, and the values for $|S|$ predicted by the constant relaxation time approximation (gray solid curve) for comparison (see §5.9 for the details of the experimental results).

We find the following features in Fig. 6-2. First of all, the predicted values of $|S|$ that are obtained using the semi-classical models developed in §6.1 are greatly enhanced over the values predicted by the constant relaxation time approximation. This is because the momentum relaxation time $\tau(E)$ predicted using the semi-classical models developed in this chapter is an increasing function of energy. Such a property of the $\tau(E)$ function is mainly caused by the nature of ionized impurity scattering, where a $\tau(E) \sim E^{-3/2}$ dependence is predicted for pure ionized impurity scattering for 3D materials without including the screening effect due to the free carriers. The second feature that is observed in Fig. 6-2 is that although the predicted values for $|S|$ are rather insensitive to the details of the doping techniques that are considered here, they do show some differences among these doping schemes. The main reason for the observed differences in the value of $|S|$ among these three doping techniques comes from the amount of the relative contribution of ionized impurity scattering to the total scattering probability for the conduction electrons. It is predicted that the contribution of ionized impurity scattering to the total scattering probability is the largest in the homogeneously doped samples and is the smallest in the δ-doped samples among the three doping techniques considered here. Therefore the resultant $\tau(E)$ function for the δ-doped superlattice samples is expected to have the weakest energy dependence among those for the three doping schemes considered here.

Although the predicted values for $|S|$ for the δ-doped and the modulation-doped (001) oriented Si(20 Å)/Ge(20 Å) superlattices are found to be smaller than those predicted for the homogeneously-doped samples, if the predicted values for the carrier mobility for the δ-doped and the modulation-doped samples are significantly larger than the corresponding values for the homogeneously doped superlattice samples, we can still achieve enhancements in the thermoelectric power factor $S^2\sigma$ and the resultant $Z_{3D}T$ relative to those predicted for the homogeneously doped samples, by introducing the δ- and/or modulation doping schemes, since the observed differences in the predicted values of $|S|$ between the δ- and modulation-doped samples and the homogeneously doped samples are rather small.

6.2.2 Carrier mobility

Shown in Fig. 6-3 are the theoretically predicted values for the carrier mobility for the (001) oriented Si(20 Å)/Ge(20 Å) superlattice samples that are obtained using the semiclassical models that are developed in §6.1. In obtaining Fig. 6-3, we have also assumed (1) homogeneous doping throughout the superlattice part of the sample (solid curve), (2) modulation doping only within the Ge layers of the sample (dashed curve), and (3) δ-doping only in the middle of each Ge layer of the sample (dash-dotted curve).

As evident in Fig. 6-3, we have found a large enhancement in the predicted values of the carrier mobility for the δ- and modulation-doped (001) oriented Si(20 Å)/Ge(20 Å) superlattice samples relative to the corresponding values for the homogeneously doped samples. It is found that the enhancements in the predicted values of the carrier mobility for the δ-doped or modulation-doped superlattices relative to the corresponding values for the homogeneously doped samples are larger in the heavy doping regime ($n > 5\times10^{18}$ cm^{-3}) than in the light doping regime ($n < 5\times10^{18}$ cm^{-3}). This is because the δ-doped or modulation-doped impurities are screened by the free carriers more strongly than the homogeneously doped impurities in the particular models that we are using to describe the (001) oriented Si(20 Å)/Ge(20 Å) suplerlattices (Krönig-Penney model). We have also assumed a uniform, isotropic medium when calculating the values of the Debye screening length for the Si(20 Å)/Ge(20 Å) superlattices (see footnote on page 300). Plotted in Fig. 6-3 are the calculated values for the Debye screening length λ (using Eq. 6.10) as a function of the carrier concentration at 300 K. We find that the value of λ decreases with increasing carrier concentration. Since the magnitude of the scattering potential created by an ionized impurity decays exponentially with the distance r (where r is measured from the center of the impurity potential) for a distance larger than the Debye screening length, the ionized impurities that are most effective in scattering electrons are those located within the Debye screening length from the center of the electron's wavefunction. Since the position of the δ-doped impurities is 20 Å away from the center of the Si layers in our model for

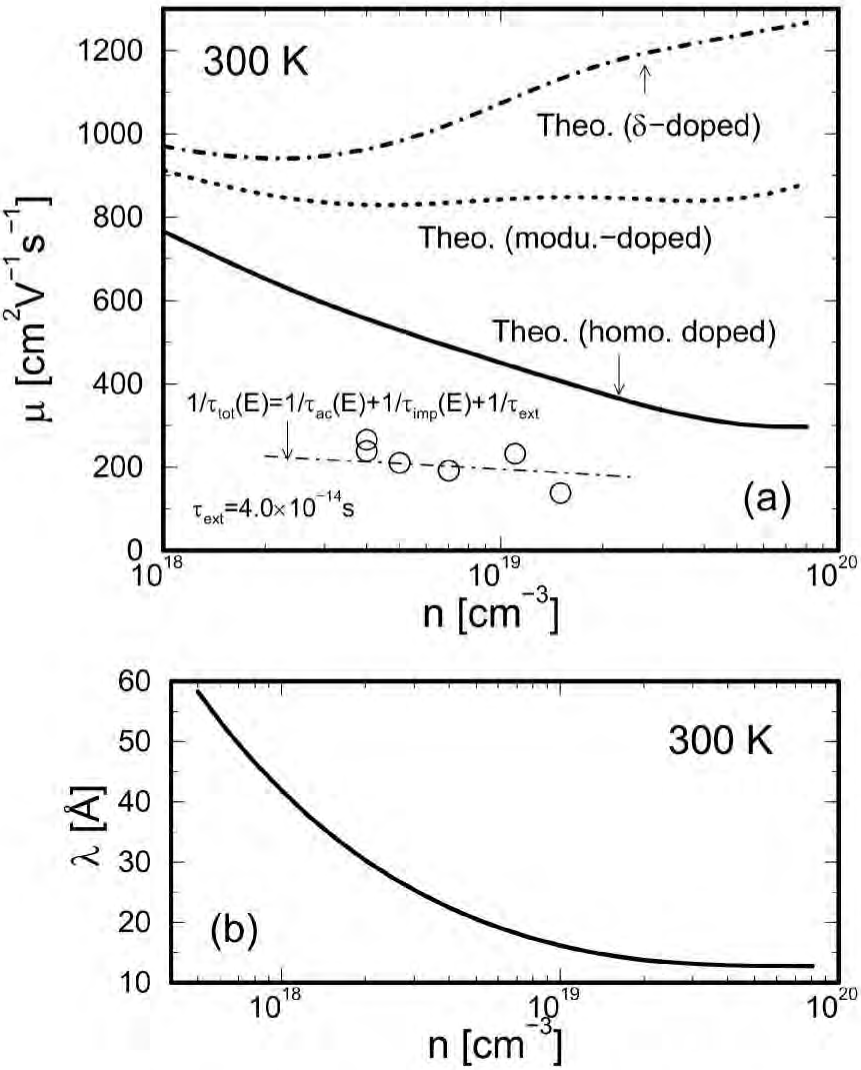

Figure 6-3: (a) The theoretically predicted values for the carrier mobility for (001) oriented Si(20 Å)/Ge(20 Å) superlattices as a function of carrier concentration at 300 K. The calculations were made using the semi-classical models that are developed in §6.1 assuming (1) homogeneous doping throughout the whole superlattice (solid curve), (2) modulation doping only in the Ge layers of the superlattice (dashed curve), and (3) δ-doping in the middle of each Ge layer in the superlattice (dash-dotted curve). Also shown in the figure are the experimental Hall carrier mobilities (open circles) (see §5.9 for more discussion), and the carrier mobilities that are calculated using Matthiessen's rule (Eq. 5.6) to take into account the extrinsic scattering mechanisms that are present in the actual superlattice samples ($\tau_{ext} = 4\times10^{-14}$ s is chosen here) for the homogeneously doped (001) oriented Si(20 Å)/Ge(20 Å) superlattices (thin dash-dotted line), for comparison. (b) Debye screening length as a function of the carrier concentration that is calculated using Eq. 6.10 for a (001) oriented Si(20 Å)/Ge(20 Å) superlattice at 300 K.

the δ-doped Si(20 Å)/Ge(20 Å) superlattices, ionized impurity scattering is expected to be relatively unimportant in the δ-doped samples for carrier concentrations larger than 5×10^{19} cm^{-3}, where the Debye screening length λ is predicted to be smaller than 20 Å [see Fig. 6-3(b)]. This is the reason for the observed increase in the predicted carrier mobility for the δ-doped Si(20 Å)/Ge(20 Å) superlattices in the heavy doping regime ($n > 3\times10^{18}$ cm^{-3}).

6.2.3 $S^2\sigma$ and $Z_{3D}T$

Plotted in Fig. 6-4 are the theoretically predicted values for the thermoelectric power factor $S^2\sigma$ obtained by combining the corresponding results for $|S|$ and σ that are discussed in §6.2.1 and § 6.2.2, respectively. We find that the theoretically predicted values for $S^2\sigma$ for the δ- and modulation-doped (001) oriented Si(20 Å)/Ge(20 Å) superlattices are greatly enhanced relative to the corresponding values predicted for the homogeneously doped superlattices.

The corresponding values of $Z_{3D}T$ for the (001) oriented Si(20 Å)/Ge(20 Å) superlattices assuming the three doping schemes that are discussed in §6.1.1 are also estimated and indicted by the right scale in Fig. 6-4. Since the exact values for the in-plane thermal conductivity are not yet known for the Si/Ge superlattice systems, a constant value of $\kappa = 5$ W/m·K was chosen (rather arbitrarily) to give an order of magnitude estimation for the values of $Z_{3D}T$ for our model system of (001) oriented Si(20 Å)/Ge(20 Å) superlattices. [This value of κ was chosen among the values found in the literature (see §5.2) for the thermal conductivities of $Si_{1-x}Ge_x$ alloys and those for the cross-plane thermal conductivity that was measured for the (001) oriented Si(20 Å)/Ge(20 Å) superlattice samples (see §5.7.1).]

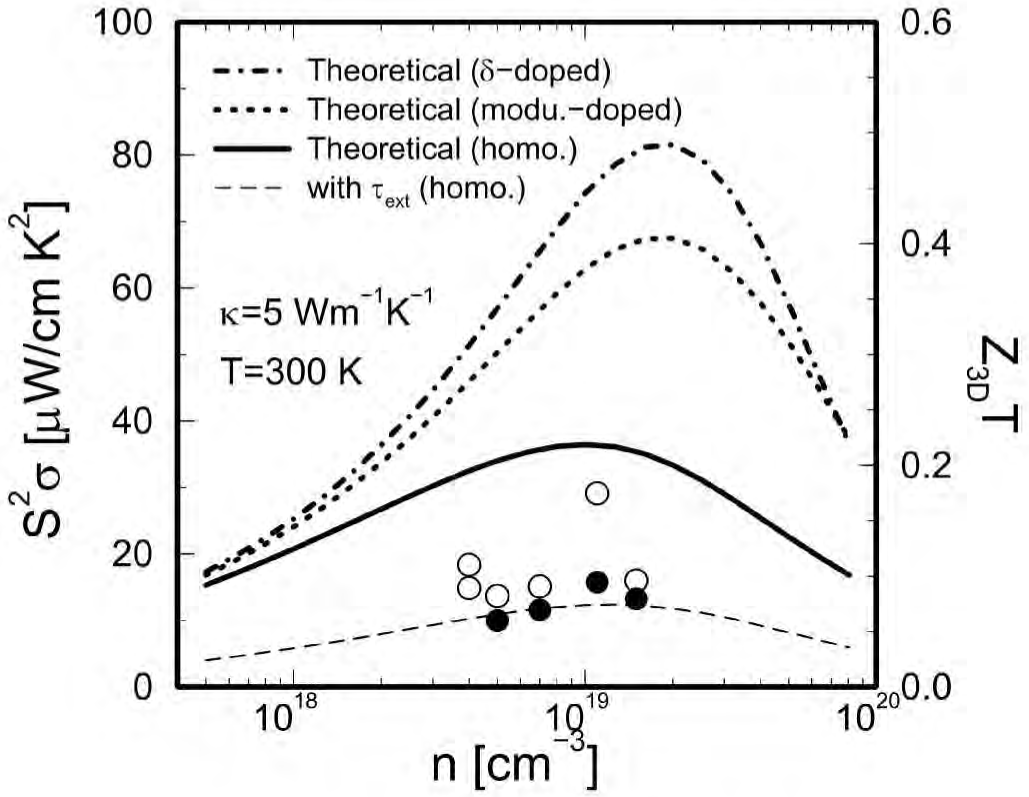

Figure 6-4: The theoretically predicted values for the thermoelectric power factor $S^2\sigma$ for (001) oriented Si(20 Å)/Ge(20 Å) superlattice samples as a function of carrier concentration n at 300 K. These calculations were made using the semi-classical models that are developed in §6.1 assuming (1) homogeneous doping throughout the whole superlattice (solid curve), (2) modulation doping only in the Ge layers of the superlattice (dashed curve), and (3) δ-doping in the middle of each Ge layer in the superlattice (dash-dotted curve). Also shown in the figure are the as-measured values for the experimental $S^2\sigma$ (open circles), the values for $S^2\sigma$ obtained after subtracting the buffer layer and/or substrate contributions (filled circles) (see §5.8), and the values for $S^2\sigma$ obtained using Matthiessen's rule (Eq. 5.6) to take into account the extrinsic scattering mechanisms that are present in the actual superlattice samples (see §5.9 for more discussion) for the (001) oriented homogeneously doped Si(20 Å)/Ge(20 Å) superlattices (thin dash-dotted curve) for comparison (see §5.9.3 for more discussion of the experimental results).

6.3 Predicted values for S, σ and $Z_{3D}T$ for a (001) oriented Si(20 Å)/Ge(20 Å) superlattice

— Temperature dependence study for a given carrier concentration —

In the previous section, we have seen that the theoretically predicted thermoelectric properties for the (001) oriented Si(20 Å)/Ge(20 Å) superlattices are optimized for carrier concentrations between 1×10^{19} cm^{-3} and 2×10^{19} cm^{-3} at 300 K. Therefore, our focus in this section is the temperature-dependent study of the thermoelectric properties of (001) oriented Si(20 Å)/Ge(20 Å) superlattices for a given optimum carrier concentration n, where we choose $n = 1.5\times10^{19}$ cm^{-3} to make the comparison between the theoretical predictions in this section and the experimental results for sample JL194 that we obtained in §5.7.

It is known that the temperature-dependent behavior of $Z_{3D}T$ varies from one material to another. Therefore, the investigation of the temperature-dependent thermoelectric properties of the (001) Si(20 Å)/Ge(20 Å) superlattice would provide us with a basic data on the temperature range in which (001) Si(20 Å)/Ge(20 Å) superlattices are particularly useful for thermoelectric applications. The same basic data on the temperature-dependent thermoelectric properties for (001) oriented Si(20 Å)/Ge(20 Å) superlattices can also be used to improve the optimization scheme for the design of superlattice structures in such a way that the highest value of $Z_{3D}T$ can be obtained in the desired temperature range for specific thermoelectric applications.

6.3.1 Seebeck coefficient

Shown in Fig. 6-5 are the results of the theoretical calculation of the Seebeck coefficient for (001) oriented Si(20 Å)/Ge(20 Å) superlattices as a function of temperature for a given carrier concentration of $n = 1.5\times10^{19}$ cm^{-3}, where (1) homogeneous doping

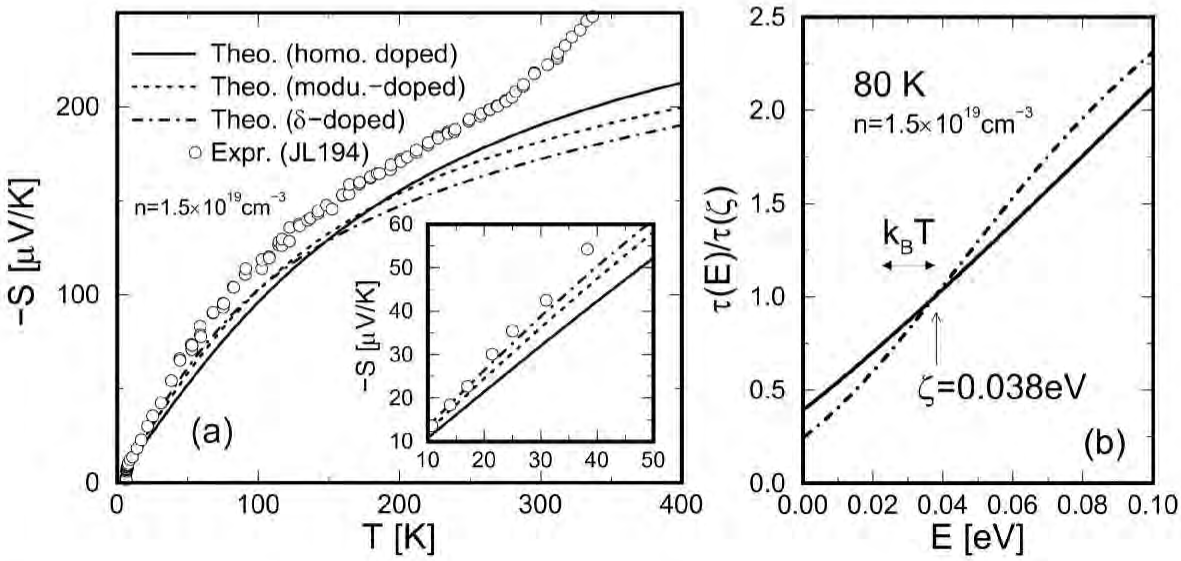

Figure 6-5: (a) The theoretically predicted values of the Seebeck coefficient as a function of temperature for (001) oriented Si(20 Å)/Ge(20 Å) superlattice samples. The calculations were made using the semi-classical models that are developed in §6.1 for $n = 1.5\times10^{19}$ cm^{-3}, where n is the carrier concentration. The following three doping schemes are considered in these theoretical predictions : (1) The model superlattice is homogeneously doped throughout the whole superlattice (solid curve). (2) Only the Ge part (Ge layers) of the model superlattice is homogeneously doped (dashed curve). (3) The model superlattice is doped using the δ-doping technique in the middle of the Ge layers only (dash-dotted curve). Also shown in the figure are the as-measured experimental results for sample JL194 that are discussed in §5.7.2 for comparison. The inset shows a close-up of the main plot in the low temperature regime ($T < 50$ K). (b) The momentum relaxation time $\tau(E)$ as a function of energy that is normalized by the value of $\tau(E)$ at the Fermi energy (chemical potential), which is denoted by $\tau(\zeta)$ [ζ is the chemical potential]. The solid and dash-dotted curves denote the results of calculated $\tau(E)$'s for a homogeneously doped superlattice and for a superlattice that is δ-doped in the middle of the Ge layers only, respectively. It is noted that E is measured from the pertinent band edge.

throughout all superlattice layers (solid curve), (2) modulation doping only in the Ge layers (dashed curve), and (3) δ-doping at the center of each Ge layer (dash-dotted curve) are assumed. Also shown in Fig. 6-5(a) are the experimental results for an MBE-grown (001) oriented Si(20 Å)/Ge(20 Å) superlattice sample with a similar carrier concentration (sample JL194), that is discussed in §5.7, for comparison.

In Fig. 6-5, we find that the predicted values of the Seebeck coefficient for the homogeneously doped superlattice sample are higher than those for the δ-doped and the modulation-doped superlattices above 180 K. This observation is consistent with the fact that the contribution of impurity scattering to the total scattering rate is the largest in the homogeneously doped sample among those for the three doping schemes considered here. On the other hand, the observed results for the Seebeck coefficients below 120 K for the (001) oriented Si(20 Å)/Ge(20 Å) superlattices with these three doping schemes turn out to be rather counter-intuitive, where we find the predicted values of the Seebeck coefficient for the δ-doped and modulation-doped samples are larger than those for the homogeneously doped samples [see the inset of Fig. 6-5(a)]. To resolve this apparent discrepancy, we have examined the energy dependence of the momentum relaxation time $\tau(E)$ in the vicinity of the Fermi energy (chemical potential, which is denoted by ζ) [see Fig. 6-5(b)]. What we find in Fig. 6-5(b) is that although the momentum relaxation time $\tau(E)$ for the δ-doped sample has a weaker energy dependence than the $\tau(E)$ function for the homogeneously doped sample over a large energy scale (on the order of 200 meV at 80 K), only in the vicinity of ζ (chemical potential) and only over a smaller energy scale (of the order of 20 meV), the $\tau(E)$ function for the δ-doped sample is found to have a stronger energy dependence than the $\tau(E)$ function for the homogeneously doped sample. For temperatures above 180 K, since the energy range that contributes to the calculated value of S become sufficiently large, the calculated values for $|S|$ for the homogeneously doped sample become larger than the corresponding values for the δ-doped and the modulation-doped samples.

6.3.2 Carrier mobility

Shown in Fig. 6-3 are the theoretically predicted values for the carrier mobilities for (001) oriented Si(20 Å)/Ge(20 Å) superlattice samples as a function of temperature for a given carrier concentration $n = 1.5\times10^{19}$ cm^{-3}. The calculations are made using the semiclassical models that are developed in §6.1. We have assumed the following three doping scheme in Fig. 6-6 : (1) homogeneous doping throughout the superlattice part of the sample (solid curve), (2) modulation doping only within the Ge layers of the sample (dashed curve), and (3) δ-doping only in the middle of the Ge layers of the sample (dash-dotted curve).

In Fig. 6-6, we find that the predicted values for the carrier mobility for the δ-doped or modulation-doped superlattices increase with decreasing temperature, whereas the predicted values of the carrier mobility for the homogeneously doped superlattices are somewhat temperature independent. In order to clarify the physical origins for the observed behaviors of the predicted values for the carrier mobilities for the (001) oriented Si(20 Å)/Ge(20 Å) superlattices with the three doping techniques considered here, we have also examined the predicted values for the Debye screening length λ of these superlattice samples with $n = 1.5\times10^{19}$ cm^{-3} as a function of temperature, as shown in Fig. 6-6(b). We find, in Fig. 6-6(b), the following two features for the predicted values of λ as a function of temperature : (1) The predicted values for λ are comparable to, but a little smaller than, the value for the distance between the center of the wavefunction (the middle of the Si layers) and the positions of the δ-doped impurities in the Ge-layers (the middle of the Ge layers), in the temperature range that is investigated (10 K $< T <$ 400 K). (2) The predicted values of λ are found to decrease with decreasing temperature from $\lambda \approx 16$ Å at 400 K to $\lambda \approx 13$ Å at 100 K. Since the smaller the value of the Debye screening length, the stronger the effect of the screening due to the free carriers, we estimate that about 40 % of the mobility increase at low temperatures ($T <$ 120 K) for the δ-doped samples (relative to the values of the carrier mobility at $T \approx$ 400 K) comes from the effect of the increased screening due to the free carriers at low temperatures. The other 60 % of the mobility

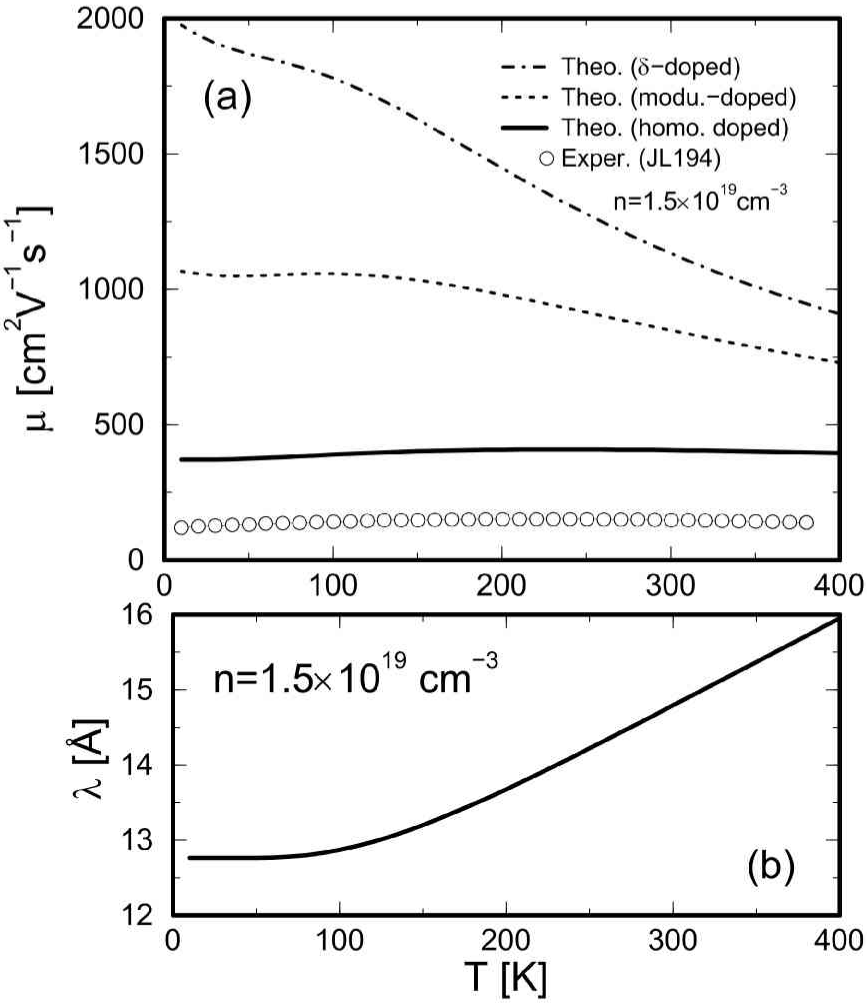

Figure 6-6: (a) The theoretically predicted values for the carrier mobility for (001) oriented Si(20 Å)/Ge(20 Å) superlattices as a function of temperature for a given carrier concentration $n = 1.5\times10^{19}$ cm^{-3}. The calculations were made using the semiclassical models that are developed in §6.1 assuming (1) homogeneous doping throughout the whole superlattice (solid curve), (2) modulation doping only in the Ge layers of the superlattice (dashed curve), and (3) δ-doping in the middle of each Ge layer in the superlattice (dash-dotted curve). Also shown in the figure are the experimental Hall carrier mobilities for a (001) oriented Si(20 Å)/Ge(20 Å) superlattice sample (sample JL194) that was discussed in §5.7, for comparison. (b) Debye screening length as a function of temperature that is calculated using Eq. 6.10 for a (001) oriented Si(20 Å)/Ge(20 Å) superlattice for a given carrier concentration $n = 1.5\times10^{19}$ cm^{-3}.

increase for the δ-doped samples at low temperatures ($T < 120$ K) relative to those at high temperatures ($T \approx 400$ K) is attributed to the reduced phonon contribution to the total scattering rate at low temperatures. For the homogeneously doped samples, the dominant carrier scattering mechanism is ionized impurity scattering arising from impurity ions that are located near the center of the wavefunction (middle of the Si layer) within the distance of the Debye screening length. Furthermore, the phonon contribution to the total scattering rate is negligible even above 300 K. Therefore, we observe a relatively temperature-independent behavior in the theoretically predicted values of the carrier mobility as a function of temperature, as seen in Fig. 6-6(a).

6.3.3 $S^2\sigma$ and $Z_{3D}T$

Finally, plotted in Figs. 6-7 are the theoretically predicted values for the thermoelectric power factor $S^2\sigma$ obtained by combining the corresponding results for $|S|$ and σ that are discussed in §6.3.1 and § 6.3.2, respectively. We find that the theoretically predicted values for $S^2\sigma$ for the δ- and modulation-doped (001) oriented Si(20 Å)/Ge(20 Å) superlattices are greatly enhanced relative to the corresponding values predicted for the homogeneously doped superlattices.

The corresponding values for $Z_{3D}T$ for the (001) oriented Si(20 Å)/Ge(20 Å) superlattices assuming the three doping schemes that are discussed in §6.1.1 are also estimated by combining the predicted values for $S^2\sigma$ that are shown in Fig. 6-7 and a temperature-independent value for the thermal conductivity $\kappa = 5$W/m·K (see the discussion in §6.2.3). These theoretically predicted values for $Z_{3D}T$ for (001) oriented Si(20 Å)/Ge(20 Å) superlattices are plotted in Fig. 6-8 as a function of temperature together with the corresponding experimental results for an MBE-grown (001) oriented Si(20 Å)/Ge(20 Å) superlattice sample (sample JL194) that are discussed in §5.7.3. As is evident in Fig. 6-8, we can expect a large (a factor of two) enhancement in the values of $Z_{3D}T$ for the δ- or modulation-doped(001) oriented Si(20 Å)/Ge(20 Å) superlattice samples relative to the corresponding values for the homogeneously doped (001) oriented Si(20 Å)/Ge(20 Å) superlattice samples.

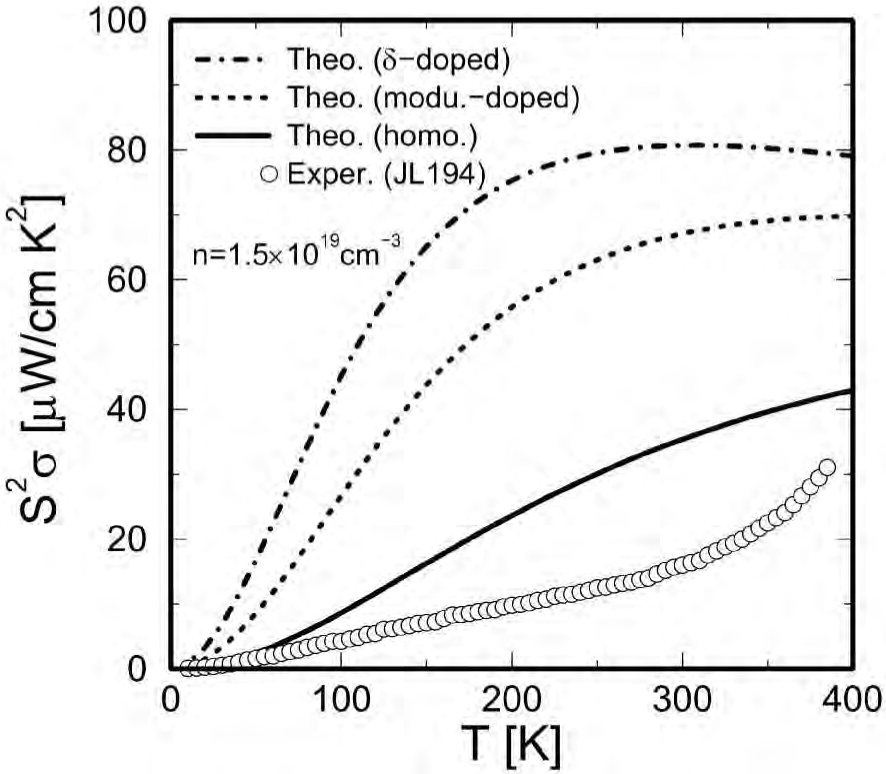

Figure 6-7: The theoretically predicted values for the thermoelectric power factor $S^2\sigma$ for (001) oriented Si(20 Å)/Ge(20 Å) superlattice samples as a function of temperature for a given carrier concentration $n = 1.5\times10^{19}$ cm^{-3}. These calculations were made using the semiclassical models that are developed in §6.1 assuming (1) homogeneous doping throughout the whole superlattice (solid curve), (2) modulation doping only in the Ge layers of the superlattice (dashed curve), and (3) δ-doping in the middle of each Ge layer in the superlattice (dash-dotted curve). Also shown in the figure are the as-measured values for the experimental $S^2\sigma$ for an MBE-grown (001) oriented Si(20 Å)/Ge(20 Å) superlattice sample (sample JL194) that is discussed in §5.7, for comparison.

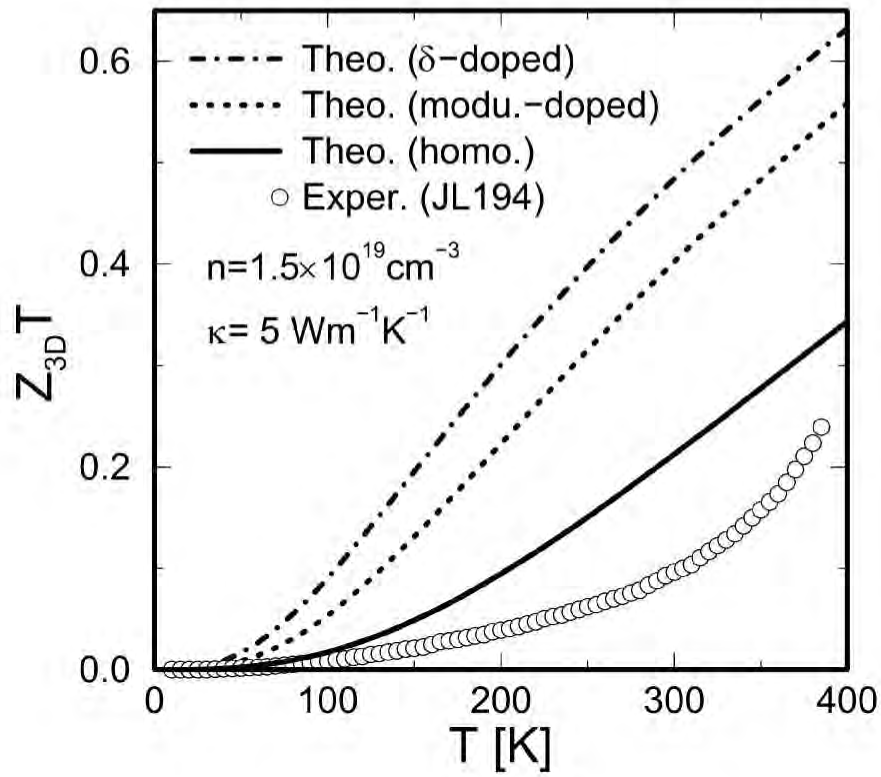

Figure 6-8: The theoretically predicted values for $Z_{3D}T$ for (001) oriented Si(20 Å)/Ge(20 Å) superlattice samples as a function of temperature for a given carrier concentration $n = 1.5\times10^{19}$ cm^{-3}. These calculations were made using the semi-classical models that are developed in §6.1 assuming (1) homogeneous doping throughout the whole superlattice (solid curve), (2) modulation doping only in the Ge layers of the superlattice (dashed curve), and (3) δ-doping in the middle of each Ge layer in the superlattice (dash-dotted curve). The value of the thermal conductivity used to obtained these results is $\kappa = 5$ W/m·K, which is assumed to be temperature independent. Also shown in the figure are the experimentally estimated values of $Z_{3D}T$ using the as-measured values for $S^2\sigma$ for an MBE-grown (001) oriented Si(20 Å)/Ge(20 Å) superlattice sample (sample JL194) that is discussed in §5.7 and using the temperature-independent value of the thermal conductivity $\kappa = 5$ W/m·K, for comparison (also see Fig. 6-7).

6.4 Conclusions

In this chapter, we have developed semi-classical models to predict the thermoelectric properties of the (001) oriented Si(20 Å)/Ge(20 Å) superlattices including ionized impurity scattering and longitudinal acoustic phonon deformation potential scattering. We have considered the following three doping schemes explicitly in our models to predict the effect of the δ- and modulation doping techniques to enhance the values of the carrier mobility relative to those for the homogeneously doped samples : (1) The model superlattice is homogeneously doped throughout the whole superlattice (homogeneously doped samples). (2) The impurity ions are introduced only in Ge layers of the superlattice. Within the Ge layers, the impurity ions are homogeneously distributed (modulation-doped samples). (3) The model superlattice is δ-doped in the middle of each Ge layer (δ-doped samples).

We have seen significant enhancements (a factor of two to three, depending on the temperature and the carrier concentration) in the values of the calculated mobility for the δ-doped or modulation-doped samples relative to the corresponding values for the homogeneously doped samples. The largest value for $Z_{3D}T$ that is obtained for the δ-doped sample at 300 K is 0.49 using a constant $\kappa = 5$ W/m·K for the value of thermal conductivity, which is a factor of more than two enhancement in $Z_{3D}T$ relative to the corresponding value for the homogeneously doped samples ($Z_{3D}T = 0.22$).

Finally, we should be reminded that a practically more interesting material is the (111) oriented Si/Ge superlattices (see §5.4.2). In Chapter 5, we have predicted that the optimum value of $Z_{3D}T$ for a (111) oriented Si(20 Å)/Ge(20 Å) superlattice is a factor of four larger than the corresponding value for a (001) oriented Si(20 Å)/Ge(20 Å) superlattice, using a simple model based on the constant relaxation time approximation. In the future, the semi-classical treatment of the thermoelectric transport coefficients for the (001) oriented Si(20 Å)/Ge(20 Å) superlattices should be extended to predict the thermoelectric properties of the (111) oriented Si/Ge superlattices. Combining the effect of the enhanced density of states near the band edge in the (111) oriented Si/Ge superlattices [relative to the corresponding (001) oriented

Si/Ge superlattices or to the corresponding bulk materials (Si or Ge)] and the effect of enhancing the values of the carrier mobility using the δ- or modulation-doping techniques, we can expect a truly large enhancement in the value of $Z_{3D}T$ [relative to the corresponding values for the (001) oriented Si/Ge superlattices and for the corresponding constituent bulk materials (Si or Ge)] and a practically useful value of $Z_{3D}T$ ($Z_{3D}T \approx 2.0$ at 300 K) in the (111) oriented Si/Ge superlattice systems.

Chapter 7

Other Systems of Interest

In this chapter, we will describe the materials systems that are of interest for future research on the thermoelectricity of low-dimensional or superlattice systems, but are not included in previous chapters of this thesis. In §7.1, we will investigate the mechanisms of the enhanced thermoelectric properties that are experimentally observed in (111) oriented PbTe/Te superlattices [92–94]. These (111) oriented PbTe/Te superlattices, and more recently found (111) oriented $PbSe_{0.98}Te_{0.02}$/PbTe "quantum-dot" superlattices [93–97], are shown to have very large values of $Z_{3D}T$ [$Z_{3D}T = 0.9$ and 1.9 at 300 K and 550 K, respectively, for the $PbSe_{0.98}Te_{0.02}$/PbTe "quantum-dot" superlattices] experimentally, but the mechanisms responsible for the observed enhancements in $S^2\sigma$ and $Z_{3D}T$ are not completely known. In §7.2, we will have a discussion of the thermoelectric properties of the (001) oriented PbTe/$Pb_{1-x}Eu_xTe$ short period superlattices. We have seen in Chapter 2 that the values of the *two-dimensional* $Z_{2D}T$ for (001) oriented PbTe quantum wells (isolated 2D quantum wells) are predicted to be enhanced relative to the corresponding values for the (111) oriented PbTe quantum wells. We are now interested in values of the *three-dimensional* $Z_{3D}T$ (figure of merit for the whole superlattice) for (001) oriented PbTe/$Pb_{1-x}Eu_xTe$ superlattices. We will examine various combinations of quantum well and barrier layer thicknesses, and the magnitude of the conduction band offset (potential barrier height), to maximize the resultant values of the thermoelectric figure of merit $Z_{3D}T$ for the whole superlattice. Finally, in §7.3 we will introduce our recent proposal of developing possible high

$Z_{3D}T$ materials using (111) oriented Bi/$Pb_{1-x}Eu_xTe$ superlattices, where practically useful values of $Z_{3D}T$ ($Z_{3D}T \approx 2$ at 300 K) are predicted using a simple model based on the constant relaxation time approximation.

7.1 Investigation of mechanisms for enhanced thermoelectric properties in PbTe/Te superlattices

In this section, we will investigate various possible mechanisms for the recently discovered enhanced values of $S^2\sigma$ (thermoelectric power factor) and $Z_{3D}T$ in the (111) oriented PbTe/Te superlattice system relative to the corresponding values for bulk PbTe. It is believed that the observed enhancement in $|S|$ in PbTe/Te superlattices shares the same basic physical origins as those that are observed in (111) oriented $PbSe_{0.98}Te_{0.02}$/PbTe "quantum-dot" superlattices [92 96], whose values of $Z_{3D}T$ are shown to be even larger than those for the (111) oriented PbTe/Te superlattices, since the values of the lattice thermal conductivity κ_{ph} are reduced in the $PbSe_{0.98}Te_{0.02}$/PbTe "quantum-dot" superlattices relative to bulk values because of alloy scattering or boundary scattering of phonons at the $PbSe_{0.98}Te_{0.02}$/PbTe interfaces [93, 94]. Therefore, investigation of the mechanisms of the enhanced values of $|S|$ in (111) oriented PbTe/Te superlattices would also provide some insight into the mechanisms of the observed enhancement in the power factor $S^2\sigma$ in (111) oriented $PbSe_{0.98}Te_{0.02}$/PbTe "quantum-dot" superlattices.

We find that, among the various mechanisms which would account for the observed enhancement in S, the energy-dependent τ model ($\tau \sim E^r$) is the most plausible model. In the energy-dependent τ model, the effective scattering parameter r is preferably increased from the value that fits the experimental results for bulk PbTe ($r \approx 0$) due to the additional scattering mechanisms that are introduced into the system by the periodic Te-adsorbed layers. Other transport properties, including the longitudinal magneto-resistance, are also investigated (see §7.1.3).

7.1.1 Introduction

There has been an increasing interest in the enhanced thermoelectric figure of merit ZT ($Z = S^2\sigma/\kappa$), where T is the temperature, S is the Seebeck coefficient, σ is the electrical conductivity, and κ is the thermal conductivity, for a material in the form of a superlattice or multiple-quantum-well (MQW) structure [1-8]. In an early stage of this research area, most work was focused on the study of the enhanced value of ZT only within the quantum well region of the superlattices (denoted by $Z_{2D}T$), that are possible due to the quantum confinement of the conduction carriers (quantum well approach). Another advantage of having a superlattice structure is the reduced lattice thermal conductivity κ_{ph} due to the boundary scattering of phonons at the barrier-well interfaces, which contributes to the enhancement of both $Z_{2D}T$ and $Z_{3D}T$, where $Z_{3D}T$ denotes the figure of merit for the whole superlattice. Recently, the idea of the quantum well approach has been extended to predict enhanced values of $Z_{3D}T$ for short period GaAs/AlAs superlattices [48] (see Chapter 4), which shows that this extended approach is promising for future thermoelectric applications.

Another approach to design a good thermoelectric material using a superlattice structure is the so-called potential barrier model [55, 56] (potential barrier approach). It is suggested that the potential barriers introduced in the superlattice would contribute to a moderate increase in S and a moderate decrease in σ. Then, the overall consequence is a moderately increased $S^2\sigma$ for optimized conditions. The merit of having a reduced κ_{ph} in a superlattice structure should be preserved in the potential barrier approach as well.

Recently, enhanced thermoelectric properties, relative to the corresponding bulk values, were experimentally discovered in MBE-grown, novel lead-chalcogenide-based superlattices, such as in (111) oriented PbTe/Te superlattices or in (111) oriented $PbSe_{0.98}Te_{0.02}$/PbTe "quantum-dot" superlattices [92–96]. It was found that this class of materials has values of the Seebeck coefficient $|S|$ (ranging from $|S| = 80$ μV/K for $n = 4.0\times10^{19}$ cm^{-3} to $|S| = 203$ μV/K for $n = 5.8\times10^{18}$ cm^{-3} at 300 K) that are larger than those for the corresponding bulk PbTe ($|S| = 22$ μV/K for

Table 7.1: Summary of the superlattice parameters and the thermoelectric properties at 300 K for MBE-grown bulk PbTe and PbTe/Te superlattice samples that were used in the present study. Data are taken from Ref. [92].

Sample No.	S [μV/K]	n [cm^{-3}]	μ [cm^2/Vs]	d_{PbTe} [nm]	# of periods
T184	-149	7.3×10^{18}	1200	bulk PbTe	bulk PbTe
T442	-80	4.0×10^{19}	650	21.6	189
T444	-163	1.3×10^{19}	785	26.7	189
T446	-193	8.2×10^{18}	880	29.9	190
T447	-203	5.8×10^{18}	1015	14.8	314

$n = 4.0\times10^{19}$ cm^{-3} and $|S| = 168$ μV/K for $n = 5.8\times10^{18}$ cm^{-3} at 300 K) by the values of 35–58 μV/K for a given carrier concentration at 300 K (see § 7.1.2). The values for the observed Hall carrier mobility for the PbTe/Te superlattices are found to be in the same range as, but slightly smaller than, those for the corresponding PbTe bulk (thick) films. Combining these values for S (Seebeck coefficient) and σ (electrical conductivity), the resultant values for $S^2\sigma$ and $Z_{3\mathrm{D}}T$, estimated using the bulk value for κ_{ph} from the literature ($\kappa_{\mathrm{ph}} = 2$ W/m·K at 300 K), are found to be enhanced by 23 and 25 %, respectively [92–94]. It is noted that the optimum values for $S^2\sigma$ and for $Z_{3\mathrm{D}}T$ occur at slightly higher carrier concentrations for the PbTe/Te superlattices ($n_{\mathrm{opt}}\sim1\times10^{19}$ cm^{-3}) than for the corresponding PbTe bulk (thick) films ($n_{\mathrm{opt}}\sim6\times10^{18}$ cm^{-3}) [92–94].

7.1.2 Experiments and models

The details of the sample preparation are given elsewhere [92]. Briefly, the PbTe/Te multilayer structures were grown by molecular beam epitaxy where the thickness of the PbTe layer was varied from 14.8 to 29.9 nm as shown in Table 1. The thickness of the Te layer is believed to be 2 to 3 mono-layers (ML), since we find that the Te layers are only adsorbed layers on the PbTe surface. The Bi dopants were introduced into the PbTe layers homogeneously to make the material n-type. A summary of the various properties (at 300 K) of the samples that were used in the present study is given in Table 7.1 from Ref. [92].

Shown in Fig. 7-1 is a plot of the experimental Seebeck coefficient as a function of Hall carrier concentration [92] together with the theoretical curves calculated using (a) an energy-dependent τ model, and (b) a potential barrier model, which are described in more detail below. First we discuss the possibility of having an enhanced effective mass, which is relevant to having a quantum confinement of electrons.

In the constant relaxation time approximation, the Seebeck coefficient S and the carrier concentration n for a material with parabolic energy bands are expressed as

$$S = -\frac{k_B}{e}\left(\frac{5F_{3/2}(\zeta^*)}{3F_{1/2}(\zeta^*)} - \zeta^*\right) \quad \text{and} \quad n = \frac{1}{2\pi^2}\left(\frac{2k_BT}{\hbar^2}\right)^{\frac{3}{2}}(m^*)^{\frac{3}{2}}F_{1/2}(\zeta^*), \tag{7.1}$$

respectively, where $F_i(\zeta^*)$ denotes the Fermi-Dirac related integrals defined elsewhere [14]. We find that S is a function of only the reduced chemical potential ζ^* ($\zeta^* = \zeta/k_BT$), whereas the carrier concentration is proportional to the power 3/2 of the density-of-states mass m^* $\left[m^* = N^{2/3}(m_t^2 m_l)^{1/3}\right]$, where N is the number of equivalent valleys in the Brillouin zone. This implies that the increased effective mass along the superlattice growth direction due to quantum confinement could account for the observed enhanced S. However, we exclude this possibility because: 1) we did not observe any difference in the optical band gap between the PbTe/Te superlattices and MBE-grown PbTe, which implies that no quantum confinement is present in these superlattice samples, 2) the periodically-introduced Te layers in the PbTe/Te superlattices are so thin (0.8–1.5 nm) that it is hardly believed that the Te layers behave as either quantum wells or barrier layers, and 3) if the quantum confinement effect is present in (111) oriented PbTe superlattices, the values of $|S|$ are predicted to be reduced, rather than increased, relative to the corresponding values for bulk PbTe at the same carrier concentration because of the lifting of the valley degeneracy as we discuss in §7.2.

Energy-dependent τ model

Since the possibility of having a quantum confinement effect in (111) oriented PbTe/Te superlattices is excluded as discussed above, we can regard our PbTe/Te superlattices

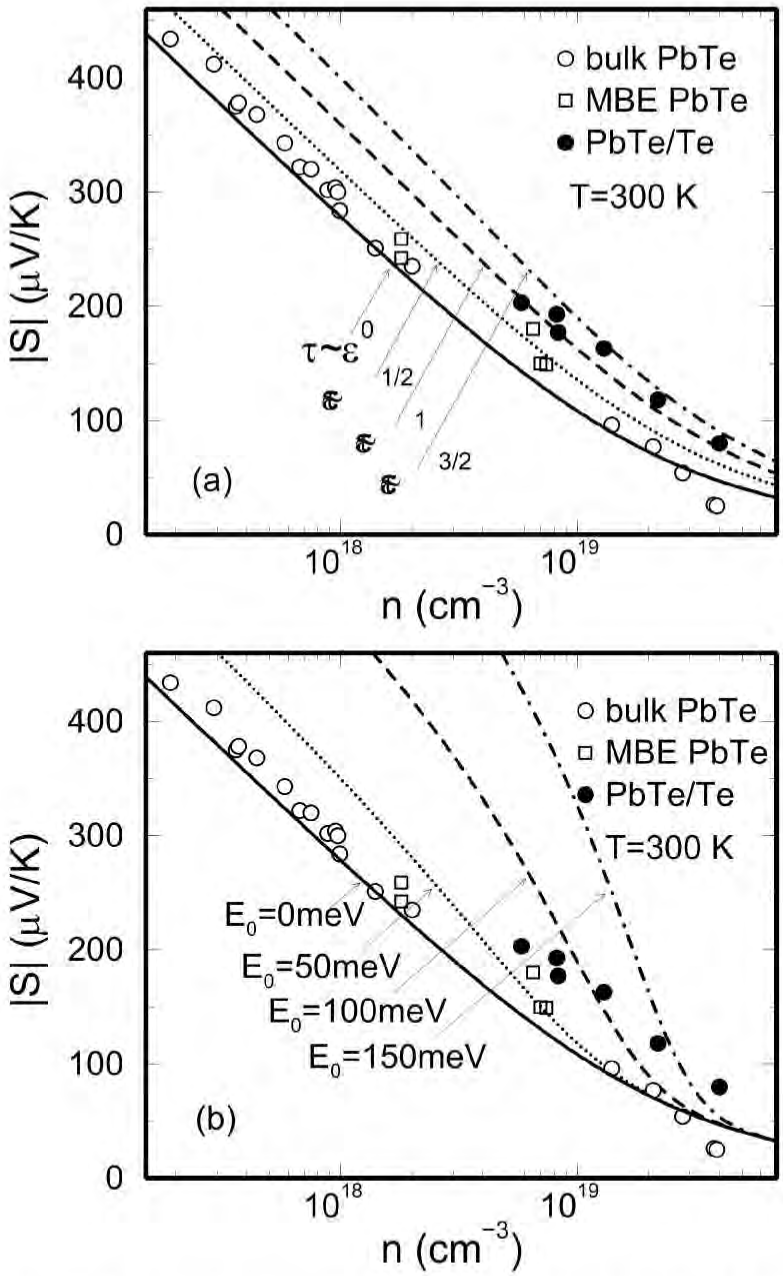

Figure 7-1: Fitting of the experimental data using possible models: (a) Energy-dependent τ with various values of the scattering parameter r. (b) Potential barrier model with various values of the potential barrier energy E_0. The experimental data are taken from Refs. [15] and [92].

as a 3D (bulk) material with some modified scattering mechanisms.

One possibility which may explain the observed enhancement in $|S|$ in a 3D bulk system is the preferably modified energy dependence of τ. Assuming $\tau \sim E^r$, where E is the energy for an electron and r denotes a scattering parameter, S for a bulk semiconductor is expressed as

$$S = -\frac{k_B}{e}\left(\frac{(r+5/2)F_{r+3/2}(\zeta^*)}{(r+3/2)F_{r+1/2}(\zeta^*)} - \zeta^*\right). \tag{7.2}$$

It is known that the scattering parameter r is $-1/2$ for longitudinal acoustic phonon deformation potential scattering, $1/2$ for piezoelectric scattering due to the acoustic phonons, and $3/2$ for ionized impurity scattering. Shown in Fig. 7-1(a) is the theoretical fitting of the experimental data using various values for r. It is found that $r = 1$ to 1.5 would explain the observed enhancement in S, which is well within the range of values for the conventional scattering mechanisms. Therefore, future work should be focused on investigation of the scattering mechanisms associated with the extra Te layers in the PbTe/Te superlattices, since they may modify the details of the scattering mechanisms for the conduction electrons and give the same effect as increasing r (the higher the r, the higher the S for a given ζ^*). Thus, we need to investigate other transport properties such as the longitudinal magneto-resistance of the PbTe/Te superlattices (see §7.1.3) to obtain further information on the scattering mechanisms that are responsible for the enhanced values of $|S|$.

Potential barrier model

We have also considered whether the so-called potential barrier model (PBM), proposed by Rowe *et al.* [55] and Nishio *et al.* [56], could explain the observed enhancement in S for the PbTe/Te superlattice samples. In this model, S is calculated assuming that the relaxation time τ is zero if the energy of the electron E is smaller than some value of the potential barrier energy E_0, and $\tau = \tau_0$ if E is larger than E_0, where τ_0 is assumed to be independent of E for simplicity. Shown in Fig. 7-1(b) are the results of the theoretical fitting to the experimental data using the PBM with

various values for E_0. We find: 1) the PBM with reasonably small values of E_0 (typically $E_0 \simeq 50$ meV) predict a large enhancement in S only at relatively small carrier concentrations n (typically $n < 5{\times}10^{18}$ cm^{-3}) and do not predict a sufficient enhancement at larger carrier concentrations (typically $n > 1{\times}10^{19}$ cm^{-3}) and 2) although the difference in the experimental S between the PbTe/Te superlattice and bulk PbTe at a given n is almost constant as a function of n, the PBM predicts that the difference in S between the samples with and without the potential barriers should decrease with increasing n. Because of these discrepancies, we also conclude that the PBM, at least in its present form, does not describe the observed enhanced thermoelectric properties (Seebeck coefficient) for the PbTe/Te superlattices correctly.

7.1.3 Longitudinal magneto-resistance, magneto-mobility and Hall mobility

Our analysis in the previous subsection suggests that a more detailed study of the transport properties of the PbTe/Te superlattices is needed to collect more information on the details of the scattering mechanisms due to the extra Te layers. Here, we chose to study the longitudinal magneto-resistance for this purpose. Both the magnetic field and the electric current are applied parallel to the plane of the superlattice, i.e., in the $(1\bar{1}0)$ direction. Considering the relative geometries among the four equivalent L-point valleys in this configuration, we can calculate the magneto-conductivity tensor $\boldsymbol{\sigma}(\mathbf{B})$, using an equation of motion for an electron, $e\left(\mathbf{E}+\mathbf{v}\times\mathbf{B}\right) = m\mathbf{v}/\tau$. The longitudinal magneto-resistance ($\Delta R/R_0$, where R_0 is the zero field resistance) is then readily deduced from the magneto-conductivity tensor $\boldsymbol{\sigma}(\mathbf{B})$. This formulation suggests that the coefficient for the B^2 term in the magneto-resistance is related to the carrier mobility $\mu_{\rm M}$ by [25] :

$$\left.\frac{\Delta\rho}{\rho B^2}\right|_{\rm longit.} = \mu_{\rm M}^2 \frac{3K(K-1)^2}{(2K+1)^3}, \quad \text{where} \quad \mu_{\rm M} = \frac{|e|}{3}\left(\frac{2}{m_t}+\frac{1}{m_l}\right)\left(\frac{\langle\tau_{\rm M}^3\rangle}{\langle\tau_{\rm M}\rangle}\right)^{\frac{1}{2}} \quad \text{and} \quad K = \frac{m_l}{m_t}. \tag{7.3}$$

In Eq. 7.3, $\left(\langle\tau_{\rm M}^3\rangle/\langle\tau_{\rm M}\rangle\right)^{1/2} \equiv \tau$ for the constant τ approximation.

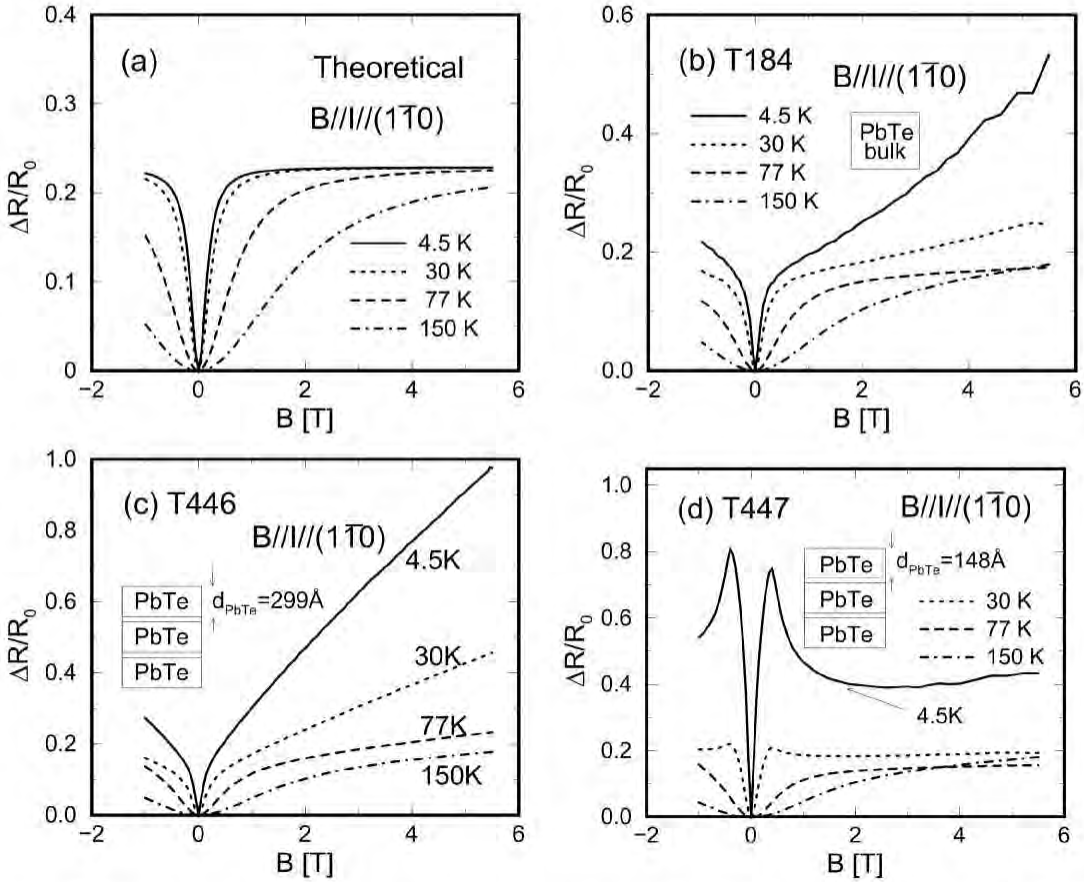

Figure 7-2: The calculated (a) and the experimental [(b), (c) and (d)] results for the longitudinal magneto-resistance for bulk PbTe [(a) and (b)] and for PbTe/Te superlattices (c and d) at various temperatures. See Table 7.1 for the properties of the various samples.

Shown in Fig. 7-2(a) are the results of calculations using the experimentally obtained values for the magneto-mobility $\mu_{\rm M}$ for MBE-grown bulk PbTe (see Fig. 7-3a). The values $\mu_{\rm M} = 5100$, 13100, 38000, and 53000 cm^2/Vs are utilized in these calculations for $T = 150$, 77, 30, and 4.5 K, respectively, under the constant τ approximation. The generic features shown in this figure are: 1) $\sim B^2$ dependence of $\Delta R/R_0$ at small magnetic field B, 2) a saturation behavior of $\Delta R/R_0$ at large magnetic field (this effect is most pronounced at low temperature), and 3) the saturation level for $\Delta R/R_0$ is just above 0.2.

Shown in Fig. 7-2(b) are the experimental results for MBE-grown bulk PbTe (T184). We find the above three generic features in Fig. 7-2(b) for $T = 150$, 77 and 30 K. However, we also see non-generic features, such as the non-saturation effect

of $\Delta R/R_0$, at high magnetic field and at low temperatures (T = 4.5 and 30 K). This discrepancy may be caused by entering the quantizing field regime, which is consistent with the appearance of oscillations in $\Delta R/R_0$ at high B for the T = 4.5 K data. Our semi-classical model is not strictly valid in this regime. Shown in Figs. 7-2(c) and (d) are two typical experimental behaviors observed for the PbTe/Te superlattices (T446 and T447), that are distinct from the generic behavior discussed above. It is noted that most of the other PbTe/Te superlattice samples that were investigated also showed either of these two types of behavior in the longitudinal magneto-resistance measurement.[†] Figure 7-2(c) shows a linearly increasing $\Delta R/R_0$ with magnetic field below T = 30 K, whereas the data in Fig. 7-2(d) show a sharp peak in $\Delta R/R_0$ around 0.3 T which becomes very pronounced below T = 30 K. At present, we do not know the exact origin of these unexpected behaviors in the longitudinal magneto-resistance for PbTe/Te superlattices. However there might be some relation between the observed anomalies in the longitudinal magneto-resistance and the observed enhancements in S for the PbTe/Te superlattices.

Despite the anomalous behaviors discussed above, the behavior of the observed magneto-resistance in the low field regime (typically <0.1 T) is consistent with the transport properties in zero field. Shown in Fig. 7-3(a) are the temperature-dependent mobility deduced from the measured longitudinal magneto-resistance data via Eq. 7.3. We find that the carrier mobility obtained from the Hall measurements (denoted by $\mu_{\rm H}$) [see Fig. 7-3(b)] is in qualitative agreement with the mobility obtained from the longitudinal magneto-resistance measurements (denoted by $\mu_{\rm M}$) [Fig. 7-3(a)].

7.1.4 Conclusions

Various possible mechanisms are investigated to explain the recently discovered enhanced Seebeck coefficient in the (111) oriented PbTe/Te superlattices. The energy dependent τ model ($\tau \sim E^r$) is found to be the most reasonable model among the various theoretical models considered. Thus future research should focus on inves-

[†]Some PbTe/Te samples (T442 and T444) showed behaviors that are more consistent with the generic behavior obtained by the model calculation (Fig. 7-2a) than for samples T446 and T447.

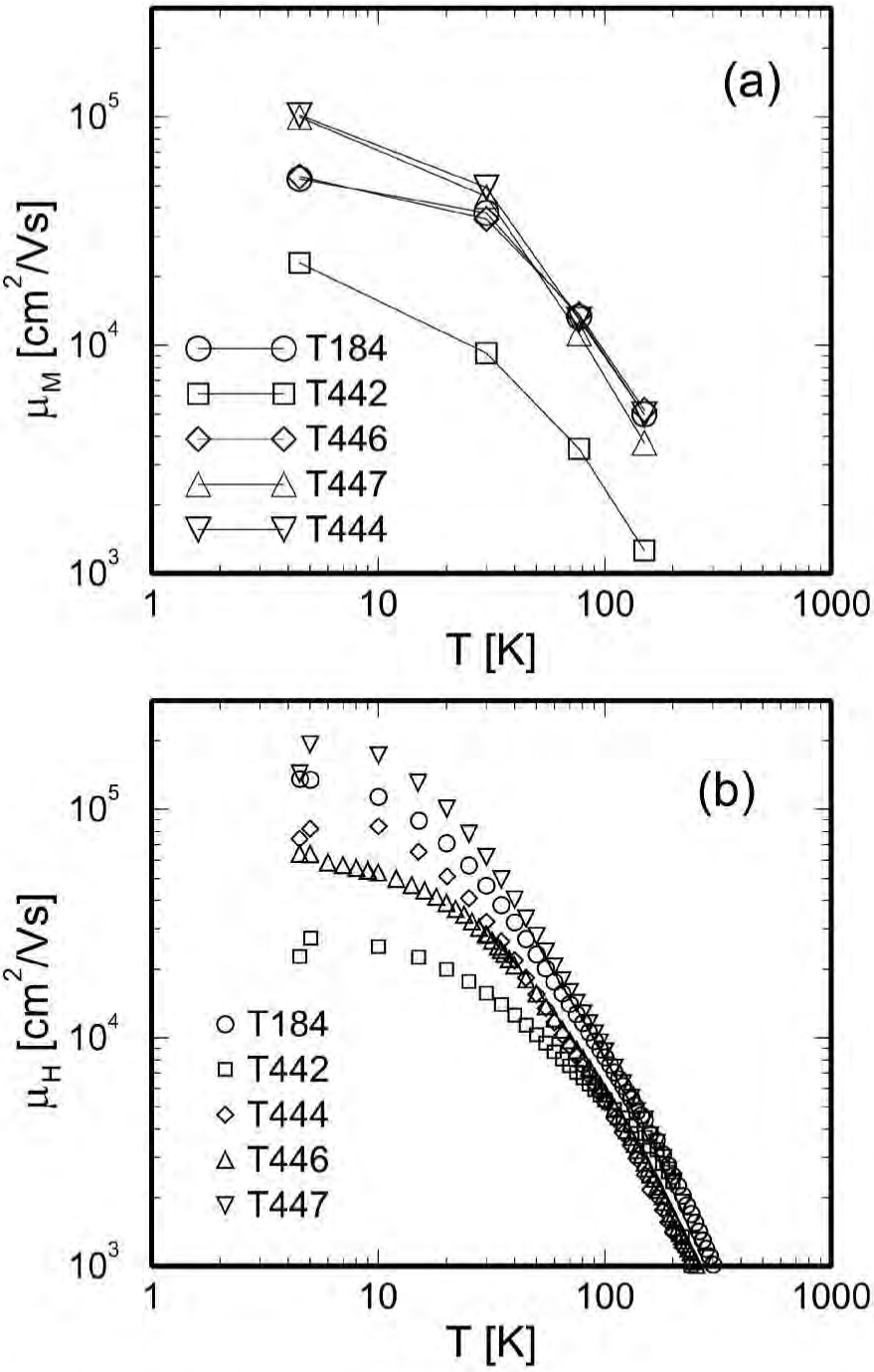

Figure 7-3: (a) Magneto mobility μ_{M} calculated from the longitudinal magneto-resistance measurements via Eq. 7.3 and (b) the experimental Hall carrier mobility μ_{H}, for MBE-grown bulk PbTe (T184) and for four different PbTe/Te superlattices as a function of temperature [98].

tigation of the effective scattering parameter r for the scattering due to the extra Te layers. The longitudinal magneto-resistance of PbTe/Te superlattices has been investigated for this purpose. The low field longitudinal magneto-resistance measurements are found to be consistent with the low field Hall mobility measurements for all the superlattice samples. Some anomalies are found in the measured longitudinal magneto-resistance as a function of magnetic field at low temperatures. The relation between these anomalies and the observed enhanced Seebeck coefficient should be investigated in more detail in the future, especially with regard to possible energy-dependent relaxation time processes.

7.2 (001) oriented PbTe/$Pb_{1-x}Eu_xTe$ short period superlattices

The theoretical modeling of $Z_{3D}T$ for (001) oriented PbTe/$Pb_{1-x}Eu_xTe$ short period superlattices was first started while we were investigating possible mechanisms for the enhanced $S^2\sigma$ and $Z_{3D}T$ that are observed in the (111) oriented PbTe/Te superlattices or in the (111) oriented $PbSe_{0.98}Te_{0.02}$/PbTe "quantum-dot" superlattices, as we discussed in §7.1. In these investigations, we have first considered the quantum confinement effect as a possible mechanism that is responsible for the observed enhancements in $S^2\sigma$ and $Z_{3D}T$ and we have made extensive modeling efforts to test whether or not the quantum confinement effect can account for the observed enhancement in $Z_{3D}T$ in this system. We have specifically used the Krönig-Penney model (see Chapter 4) to model the quantum confinement effect in the PbTe/Te superlattices, where we have assumed that the thin Te layers in the PbTe/Te superlattices provide potential barriers that have relatively large values for the barrier height U_0 ($U_0 > 1$ eV).

What we have found in these modeling efforts, however, was a decrease, rather than an increase, in the values of $Z_{3D}T$, if a quantum confinement effect is present in the (111) oriented PbTe/Te superlattices, because the density of states for electrons

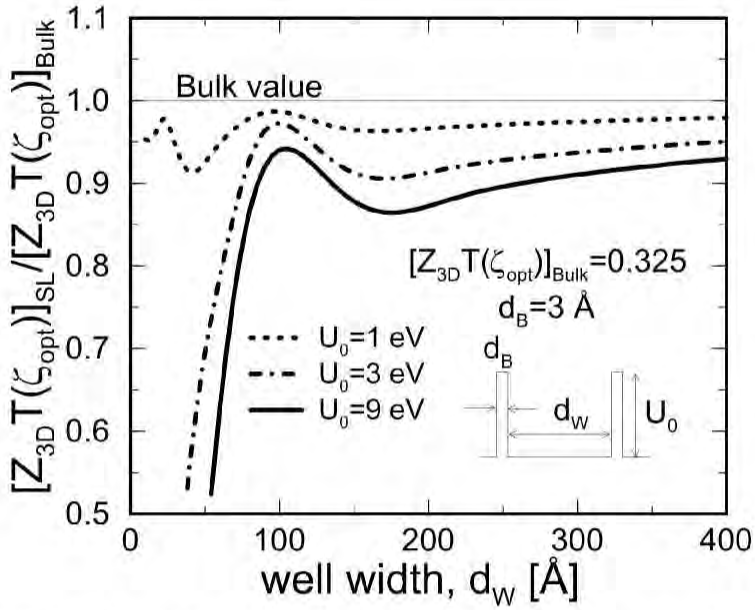

Figure 7-4: Plot of the calculated thermoelectric figure of merit $Z_{3D}T$ at the optimum carrier concentration at 300 K for (111) oriented PbTe-based superlattices (normalized by the corresponding value for bulk PbTe) as a function of the quantum well width d_W. In obtaining these results, a relatively small value for d_B (barrier layer thickness) [d_B = 3 Å], and relatively large values of the potential barrier height U_0 (U_0 = 1, 3, and 9 eV) are utilized to simulate the effect of the extra Te layers in the PbTe/Te superlattice. The calculated values for these (111) oriented PbTe-based superlattices are found to be reduced relative to the corresponding value for bulk PbTe, due to the lifting of the valley degeneracy [22] (see text and Chapter 2 for more discussion), which contradicts the experimental observation in §7.1.

near the band edge is reduced relative to that for the corresponding bulk PbTe due to the lifting of the valley degeneracy [22] (see Chapter 2). Shown in Fig 7-4 are examples of such model calculations, where the optimum values of $Z_{3D}T$ at 300 K [denoted by $Z_{3D}T(\zeta_{opt})$] are plotted as a function of the quantum well width d_W for various values for the potential barrier height U_0. In obtaining the results in Fig. 7-4 (and all the other results shown in this section), we have used values of $m_t = 0.0335\,m$ and $m_l = 0.35\,m$ for the transverse and the longitudinal components of the effective mass tensor, respectively. We have also assumed that both the quantum wells and the barrier layers of the superlattice have the same values for m_t and m_l, respectively, for simplicity, and that the value of the lattice thermal conductivity κ_{ph} for the (111) oriented PbTe/Te superlattices is the same as that for bulk PbTe (κ_{ph} = 2 W/m·K at 300 K). As we have seen in §7.1, the (111) oriented PbTe/Te superlattices that

showed enhanced values of $S^2\sigma$ and $Z_{3D}T$ have PbTe-layer thicknesses (d_W) in the range between 150 Å and 300 Å and the thickness for the Te layers (d_B) is very small (~3 Å). Therefore, using the value of d_B = 3 Å for the barrier layer thickness, the value of $Z_{3D}T$ at the optimum carrier concentration is plotted as a function of the quantum well width (d_W) for U_0 = 1, 3 and 9 eV in Fig. 7-4.

Although the 2D quantum confinement effect didn't turn out to be the mechanism that is responsible for the observed enhancements in $S^2\sigma$ and $Z_{3D}T$ in the (111) oriented PbTe/Te superlattices, the modeling results obtained during this investigation suggested that there are different regimes in geometry and orientation, where the quantum confinement effect could be used for enhancing the values of $Z_{3D}T$ for the whole superlattice in PbTe-based superlattices [or, more broadly, in the lead-chalcogenide-based superlattices, since all the lead-chalcogenides (PbTe, PbSe and PbS) have many properties common to one another]. These regimes, which we have found in our preliminary modeling study, are summarized as follows : (1) Superlattices have to be grown in the (001) orientation to avoid the lifting of the valley degeneracy as we discussed in Chapter 2. (2) Relatively large values of the potential barrier height (conduction band offset) (>0.5 eV) are necessary in order to see a substantial enhancement in the values of $Z_{3D}T$ for the whole superlattice relative to that for the corresponding bulk material. (3) The values for the superlattice period ($d_W + d_B$) have to be smaller ($d_W + d_B \approx 60$ Å) than those we have seen for the (111) oriented PbTe/Te superlattices ($d_W + d_B \approx$ 150–300 Å). It is also noted that, in order to obtain the maximum value of $Z_{3D}T$, the values of d_W and d_B have to be properly optimized for a given value of the potential barrier height U_0 and for a given value of the temperature T as we discussed in Chapter 4. In this section, we show the results of these optimization processes that were performed on (001) oriented PbTe/$Pb_{1-x}Eu_xTe$ short period superlattice systems.

7.2.1 Choice of the barrier material

As we have discussed in Chapter 2, $Pb_{1-x}Eu_xTe$ alloys provide various properties that are ideal for these materials to be used as the barrier layers for the PbTe-based

quantum well superlattices. These properties include (see §2.2) : (1) almost perfect lattice matching between the $Pb_{1-x}Eu_xTe$ homogeneous alloys and PbTe (lattice mismatch < 2 %), and (2) a large controllability for the value of the band offset ΔE_c ($\Delta E_c = U_0$, where U_0 is the potential barrier height) through a change in the value of the Eu content x (the value of ΔE_c can be changed continuously from $\Delta E_c = 0$ eV for $x = 0$ to $\Delta E_c \approx 1$ eV for $x = 1$). In addition, it is also known that various lead-chalcogenide-based superlattices can be grown both in the (111) orientation (see Chapter 2 and the references therein) and in the (001) orientation [44], where a (111) oriented BaF_2 substrate is utilized for the growth of (111) oriented superlattices [15, 39, 92–94] and a (001) oriented KCl substrate is utilized for the growth of (001) oriented superlattices [32, 44, 99–109]. Therefore, it is possible to test experimentally the theoretical predictions made in this section in the future, when suitable growth conditions for the (001) oriented $PbTe/Pb_{1-x}Eu_xTe$ superlattices [or for other (001) oriented lead-chalcogenide-based superlattices] are identified.

7.2.2 Effect of the quantum well and barrier thicknesses on the value of $Z_{3D}T$

Shown in Fig. 7-5 are the calculated values for $Z_{3D}T$ at the optimum carrier concentration [denoted as $Z_{3D}T(\zeta_{opt})$] as a function of d_W (quantum well thickness) and d_B (barrier layer thickness) for (001) oriented $PbTe/Pb_{1-x}Eu_xTe$ superlattices ($x \approx 1$, i.e., $U_0 = 1$ eV is chosen for this specific investigation) at 300 K. In obtaining these results, we have used bulk values for the components of the effective mass tensor ($m_t = 0.0335\, m$ and $m_l = 0.35\, m$), for the lattice thermal conductivity ($\kappa_{ph} = 2$ W/m·K), and for the carrier mobility ($\mu = 1500$ cm^2/V·s), because of the unavailability of values for these parameters for the superlattice systems. We find the following features in Fig. 7-5 : (1) The calculated values for $Z_{3D}T(\zeta_{opt})$ for the (001) oriented $PbTe/Pb_{1-x}Eu_xTe$ superlattices approach the corresponding bulk value for PbTe ($Z_{3D}T = 0.325$) in the limits $d_W \to \infty$ and $d_W \to 0$, for all the values of d_B that were investigated here (3 Å $< d_B <$ 40 Å). (2) There is a minimum in the value

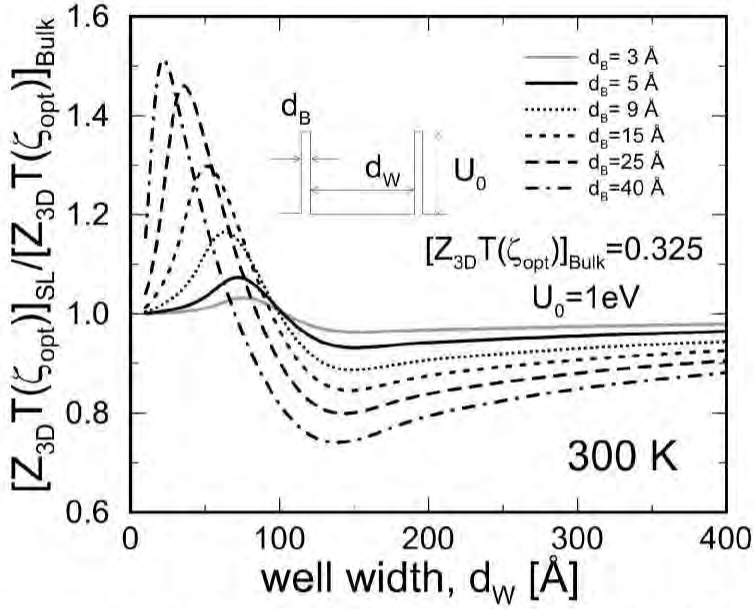

Figure 7-5: The calculated values of the thermoelectric figure of merit $Z_{3D}T$ at the optimum carrier concentration [denoted by $Z_{3D}T(\zeta_{opt})$] (normalized by the corresponding value for bulk PbTe) for (001) oriented PbTe/$Pb_{1-x}Eu_xTe$ superlattices as a function of the quantum well thickness (d_W) and the barrier layer thickness (d_B). These calculations are made using the Krönig-Penney model for $U_0 = 1$ eV, where U_0 is the potential barrier height (conduction band offset).

of $Z_{3D}T(\zeta_{opt})$ as a function of the quantum well width d_W for each value of d_B that was investigated. These minima in $Z_{3D}T(\zeta_{opt})$ are always found in the vicinity of $d_W = 140$ Å, irrespective of the value of d_B (the barrier layer thickness). (3) The maximum value of $Z_{3D}T(\zeta_{opt})$ for a given value of d_B is found to increase as the value of d_B is increased. The value of d_W which gives the maximum in $Z_{3D}T(\zeta_{opt})$ is found to decrease with increasing d_B, but the corresponding value for the superlattice period ($d_W + d_B$), that gives the maximum value of $Z_{3D}T(\zeta_{opt})$, is almost constant with respect to the value of d_B used in this calculation.

7.2.3 Effect of the potential barrier height on the value of $Z_{3D}T$

In §7.2.2, we have seen that the calculated $Z_{3D}T$ for (001) oriented PbTe/$Pb_{1-x}Eu_xTe$ superlattices (where $x \approx 1$ and $U_0 = 1$ eV are assumed) are always maximized when $(d_W + d_B) \approx 60$ Å, irrespective of the value of d_B, and that the larger the

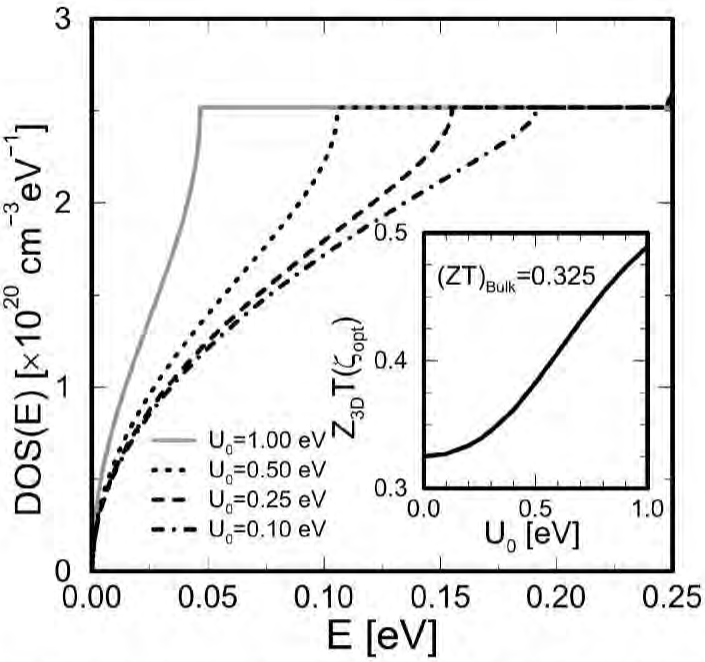

Figure 7-6: The calculated electronic densities of states [denoted by DOS(E)] at 300 K for (001) oriented PbTe (20 Å)/$Pb_{1-x}Eu_xTe$(40 Å) superlattices as a function of energy E that is measured from the pertinent band edge. The grey-solid, short-dashed, long-dashed and dash-dotted curves, respectively, denote the calculated results for the DOS(E) for U_0 = 1.0, 0.5, 0.25 and 0.1 eV, where U_0 is the potential barrier height (conduction band offset). The inset shows a plot of $Z_{3D}T(\zeta_{opt})$ (figure of merit at the optimum carrier concentration) as a function of the potential barrier height U_0 for (001) oriented PbTe (20 Å)/$Pb_{1-x}Eu_xTe$(40 Å) superlattices at 300 K. The positions for the optimum chemical potential ζ_{opt} that gives the largest value of $Z_{3D}T$ for a given value of U_0 are between 0 and 0.05 eV in the main scale of the figure for all the values of U_0 that were investigated (0 eV $< U_0 <$ 1 eV).

value of d_B, the larger the maximum value of $Z_{3D}T$ for U_0 = 1 eV, where U_0 is the potential barrier height (conduction band offset). In this subsection, we are interested in : (1) how would the value of $Z_{3D}T(\zeta_{opt})$ be changed in the (001) oriented PbTe(20 Å)/$Pb_{1-x}Eu_xTe$(40 Å) superlattice system, if the value of the potential barrier height U_0 is reduced from 1 eV (which corresponds to $x \approx 1$)? and (2) what are the values of the optimum carrier density, at 300 K, which give the largest value of $Z_{3D}T$ for the (001) oriented PbTe(20 Å)/$Pb_{1-x}Eu_xTe$(40 Å) superlattices, for some selected values of the potential barrier height U_0 (0 eV $< U_0 <$ 1 eV)?

Shown in Fig. 7-6 are the calculated densities of states as a function of energy (measured from the pertinent band edge) for (001) oriented PbTe(20 Å)/$Pb_{1-x}Eu_xTe$(40 Å) superlattices, where various values for U_0 (potential barrier height) were utilized in

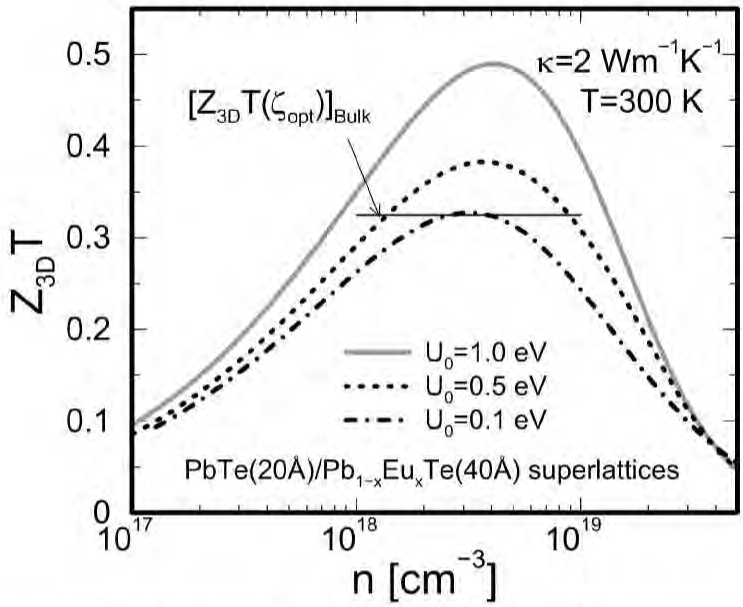

Figure 7-7: The calculated values of $Z_{3D}T$ as a function of the carrier concentration for the (001) oriented PbTe(20 Å)/$Pb_{1-x}Eu_xTe$(40 Å) superlattices at 300 K. The grey-solid, short-dashed and dash-dotted curves denote the calculated $Z_{3D}T$s for U_0 = 1.0, 0.5 and 0.1 eV, respectively, where U_0 is the potential barrier height (conduction band offset). The corresponding value of $Z_{3D}T$ for bulk PbTe at the optimum carrier concentration ($n \approx 3\times10^{18}$ cm^{-3}), which is denoted by $[Z_{3D}T(\zeta_{opt})]_{Bulk}$, is also shown in the figure by the holizontal solid line, for comparison.

these calculations (U_0 = 0.1, 0.25, 0.5 and 1 eV) [see Eq 2.31 for the relation between x and the energy band gap E_g in the $Pb_{1-x}Eu_xTe$ alloy†]. Also plotted in the inset of Fig. 7-6 are the calculated values of $Z_{3D}T(\zeta_{opt})$ at 300 K for (001) oriented PbTe(20 Å)/$Pb_{1-x}Eu_xTe$(40 Å) superlattices as a function of the potential barrier height U_0. We find that the calculated value for $Z_{3D}T(\zeta_{opt})$ is relatively insensitive to the value of U_0 when $U_0 < 0.3$ eV, but increases rapidly with increasing U_0 above $U_0 = 0.3$ eV and approaches the value of $Z_{3D}T(\zeta_{opt}) = 0.54$ above $U_0 = 1$ eV, which is the value for $Z_{3D}T(\zeta_{opt})$ in the strongly confined "degenerate 2D superlattice limit" [see §4.2.3 (page 164)].

Shown in Fig. 7-7 are the calculated values of $Z_{3D}T$ as a function of the carrier concentration n for (001) oriented PbTe(20 Å)/$Pb_{1-x}Eu_xTe$(40 Å) superlattices at

†As we have seen in Chapter 2, the conduction band offset ΔE_c (or the potential barrier height U_0) is related to the difference in the direct energy band gap ΔE_g between the quantum well material (PbTe) and the barrier layer material ($Pb_{1-x}Eu_xTe$) through the empirical relation $\Delta E_c = 0.55\Delta E_g$ [30].

300 K for $U_0 = 1.0$, 0.5 and 0.1 eV, where U_0 is the potential barrier height. We find, in Fig. 7-7, that the values for the optimum carrier concentration n for the largest values of $Z_{3D}T$ are in the range between 2×10^{18} cm^{-3} and 6×10^{18} cm^{-3} for all the investigated values of U_0, and that the largest enhancement in the value of $Z_{3D}T$ due to the quantum confinement effect (relative to the corresponding value for bulk PbTe) can be obtained when the carrier concentration of the superlattice sample is close to the optimum value ($n = 2$–6×10^{18} cm^{-3}) [see, for example, the results of the calculation for $U_0 = 1.0$ eV in Fig. 7-7].

7.3 (111) oriented Bi/$Pb_{1-x}Eu_xTe$ superlattices

Theoretical modeling of the enhanced thermoelectric figure of merit $Z_{3D}T$ in (111) [or triginally] oriented Bi-based superlattices is a natural extention of the theoretical modeling for the (001) oriented PbTe/$Pb_{1-x}Eu_xTe$ superlattices that were discussed in §7.2. Since bulk Bi has only *three* (not four) equivalent L-point valleys that correspond to the three oblique L-valleys in (111) oriented bulk PbTe and $Pb_{1-x}Eu_xTe$ alloys, we can completely avoid the negative effect of lifting the conduction band valley degeneracy (on reducing the value of $Z_{3D}T$) in (111) oriented Bi-based superlattices, where Bi is used for the quantum well material.

In this section, enhanced values of the thermoelectric figure of merit $Z_{3D}T$ are predicted for (111) oriented Bi/$Pb_{1-x}Eu_xTe$ superlattices. The values of $Z_{3D}T$ obtained for $x \approx 1$ superlattices are 2.31, 1.55 and 1.61[†] at 300 K, 150 K and 77 K, respectively, which shows that these materials are promising candidates for thermoelectric elements in the temperature range between 77 K and 300 K. Even with x as small as 0.1, where the conduction band offset ΔE_c is estimated to be 0.25 eV, the predicted values of $Z_{3D}T$s are 1.75, 1.16 and 1.18 at 300 K, 150 K and 77 K, respectively. It is proposed that other families of Bi-based superlattices, such as Bi/(111)CdTe su-

[†]The reason why we have a larger value for the calculated $Z_{3D}T$ at 77 K than at 150 K here is that the phonon mean free path ℓ is assumed to be limited by the thickness of the quantum wells (d_W) or the barrier layers (d_B) below 150 K in our calculation, while the carrier mobility μ is assumed to increase with decreasing temperature according to the experimental results for the bulk mobilities of Bi that are found in the literature (see §7.3.2).

perlattices [110], should also be good candidates for low-temperature thermoelectric elements.

7.3.1 Introduction

The use of superlattice structures to design useful thermoelectric materials with large values of the thermoelectric figure of merit ZT ($Z = S^2\sigma/\kappa$), where T, S, σ and κ are the temperature, Seebeck coefficient, electrical conductivity and thermal conductivity, respectively, has attracted significant interest in the thermoelectric materials community (see previous chapters and the references therein). The basic strategies of enhancing the values of ZT using low dimensional structures are based on: (1) the use of the enhanced density of states for electrons (or holes) near the band edge to increase the magnitude of the Seebeck coefficient $|S|$ at a given carrier concentration, and (2) the use of the increased boundary scattering of phonons at the well-barrier interfaces in the superlattice to reduce the values of the lattice thermal conductivity $\kappa_{\rm ph}$ relative to the corresponding bulk values [12, 14]. Recently, this original proposal of enhancing the values of ZT using the isolated quantum wells and wires, that was made by Hicks and Dresselhaus, has been extended to more realistic systems such as GaAs/AlAs [47, 48, 111] (see Chapter 4) and Si/Ge [111, 112] (see Chapters 5 and 6) short period superlattices, and an enhancement in the three-dimensional thermoelectric figure of merit ($Z_{\rm 3D}T$) for the whole superlattice has been predicted relative to the values of $Z_{\rm 3D}T$ for the corresponding bulk materials.

The key strategy for the successful design of thermoelectric materials using superlattice structures is to find a set of the following two kinds of materials for the quantum well and barrier layer materials : (a) a material with highly anisotropic constant energy surfaces that will be used for the quantum well layers, and (2) a material (for the barrier layers) that is chemically (and structurally) compatible with the well material and has a large energy band gap to provide sufficiently large band offsets for the confinement of the conduction carriers. Bi is an semimetal that has various unique properties, such as a highly anisotropic Fermi surface, large values of the electron and hole mobilities and small values of the lattice thermal conductiv-

ity [52, 113–116]. These features of Bi make it potentially a very interesting material for thermoelectric applications especially in its semiconducting form [20, 37, 113]. The semimetal-semiconductor transition in Bi is believed to be realized using low-dimensional structures such as quantum wells and wires [50, 51, 110, 117]. It has been noted that Bi would have a large thermoelectric figure of merit ($ZT = 2.0$ at 300 K) if it could be made into a single carrier semiconductor by removing its holes [113]. Hicks *et al.* proposed that this should be experimentally realized by making 2D superlattices out of Bi, where Bi serves as the quantum well material [37]. They predicted large values of $Z_{2D}T$ ($Z_{2D}T = 4$ for a well width of 50Å at 300 K) for isolated Bi quantum wells, where $Z_{2D}T$ denotes the figure of merit within the quantum wells. Although the necessity of considering finite barrier widths and finite barrier heights, when predicting values of ZT in such systems, has been pointed out elsewhere [20], there has been no study or proposal on the kind of barrier materials to be used for the Bi superlattices and on the optimum structures (layer thicknesses and the growth orientations) of the superlattices, in order for such superlattices to be practically useful in thermoelectric applications. Several attempts have been made, with some degree of success, to realize the semimetal-semiconductor transition in Bi using reduced dimensionalities [50, 51, 110, 117]. The two-dimensional nature of the electron transport has been also reported experimentally in Bi/(111)PbTe superlattices [118–120].

In the subsequent subsections, we will show the results of our theoretical investigation of the thermoelectric properties of Bi/(111)$Pb_{1-x}Eu_xTe$ superlattices. We choose $Pb_{1-x}Eu_xTe$ alloys for the barrier layer material because : (1) the Bi hexagonal (001) plane has good lattice matching with the $Pb_{1-x}Eu_xTe$ cubic (111) plane (lattice mismatch ~0.3 % and ~2 % at (111)Bi/(111)PbTe and (111)Bi/(111)EuTe interfaces, respectively), (2) since Bi/(111)PbTe superlattices have been already fabricated experimentally in the past [118–120], there is a good chance that one can grow Bi/(111)$Pb_{1-x}Eu_xTe$ superlattices in the near future as well, and (3) the ability of changing the value of the energy band gap from 0.32 eV (PbTe) to 2.2 eV (EuTe) continuously by changing the value of x (see Chapter 2) provides us with a large degree of controllability in the materials design when this material reaches the stage

of actual superlattice fabrication for thermoelectric applications.

7.3.2 Methods of calculation

The calculation of $Z_{2D}T$ for isolated quantum wells of Bi has been reported elsewhere [37]. In the present work, extension of this model is made to include the effects of finite barrier widths and finite barrier heights (Krönig-Penney model) [63], and to include the opposite signs for the electron and hole contributions to the thermoelectric transport (two-band, two-carrier model). For simplicity, we assume parabolic energy bands for both L-point electrons and T-point holes. Since Bi has highly non-parabolic electronic energy dispersion relations, the values for the effective masses are strongly dependent on energy. For example, the band edge effective mass tensor for electrons at low temperatures ($T < 80$) is given by $m_e^x = 0.00119\ m$, $m_e^y = 0.266\ m$ and $m_e^z = 0.00228\ m$, where the x-, y- and z-axes are taken to be parallel to the principal axes of the constant energy ellipsoid, whereas the effective mass tensor at the Fermi energy ($E_F = 23$ meV) is given by $m_{E_F}^x = 0.00651\ m$, $m_{E_F}^y = 1.362\ m$ and $m_{E_F}^z = 0.0101\ m$. In addition, the band edge effective mass for Bi is known to increase rapidly with increasing temperature above 80 K ($m_e^x = 0.00708\ m$, $m_e^y = 1.58\ m$ and $m_e^z = 0.0136\ m$ for $T = 300$ K). In the present calculation, we use the values for the masses at the Fermi-level since they are a conservative choice for the following reasons : (1) The semimetal-semiconductor transition for the Bi/(111)$Pb_{1-x}Eu_xTe$ superlattices leads to an increase in the band edge effective mass, and, at the optimum structure of the superlattices, the energy for the conduction subband edge is always higher than the Fermi energy of bulk Bi. (2) At higher temperatures, the respective values for the band edge mass tensor and the degree of non-parabolicity rapidly increase and decreases with increasing temperature. For example, at 300 K, the values for the band edge effective mass tensor become comparable to the values for the effective masses at the Fermi energy at low temperatures ($T < 77$ K), as is shown above. In fact, the values for $Z_{3D}T$ calculated using the band edge effective masses at 300 K are slightly larger than the values for $Z_{3D}T$ calculated using the Fermi energy values for the effective mass. Therefore, using the values for m_{E_F} for

the estimation of the values of $Z_{3D}T$ at 300 K is conservative.

The value for the lattice thermal conductivity κ_{ph} at 300 K used in the present calculation (see Table 7.2) is determined from the bulk values for Bi and PbTe. These values are in the range between 0.9 W/m·K and 1.7 W/m·K for bulk Bi [121] and 2.0 W/m·K for bulk PbTe [33], respectively. Therefore, we choose an average value between these (κ_{ph} = 1.5 W/m·K), as a conservative estimate of κ_{ph} for Bi/(111)$Pb_{1-x}Eu_xTe$ superlattices at 300 K. It is noted that the actual values for κ_{ph} for the Bi/(111)$Pb_{1-x}Eu_xTe$ superlattices are expected to be significantly smaller than this value (κ_{ph} = 1.5 W/m·K), since the values for κ_{ph} for $Pb_{1-x}Eu_xTe$ alloys should be reduced relative to that for PbTe due to the alloy scattering of phonons. The phonon mean free paths ℓ for bulk Bi and bulk PbTe are estimated to be 10 Å and 30 Å, respectively, at 300 K. Since ℓ has a T^{-1} temperature dependence in a 3D bulk crystal (the dominant scattering mechanism for phonons being other phonons), we also assume that κ_{ph} for the Bi/(111)$Pb_{1-x}Eu_xTe$ superlattices obey this temperature dependence unless ℓ is limited by the boundary scattering of phonons. We estimate the temperature at which ℓ is limited by the boundary scattering of phonons in Bi/(111)$Pb_{1-x}Eu_xTe$ superlattices to be 150 K. We therefore take the value of κ_{ph} to be independent of temperature below 150 K.

Other parameters used in the present study are summarized in Table 7.2. We assume that the conduction and valence band offsets, denoted by ΔE_c and ΔE_v, respectively (as defined in Fig. 7-8), can be approximated by equally splitting the difference in the band energy gap between Bi and $Pb_{1-x}Eu_xTe$, since there is no prior report on the conduction- and valence- band offsets in this system. The band overlap energy Δ_0 for Bi, also defined in Fig. 7-8, is assumed to be temperature dependent (see Table 7.2), whereas the conduction- and valence- band offsets are assumed to be temperature independent.

7.3.3 Results of $Z_{3D}T$ calculation

Shown in Fig. 7-9 are the calculated $Z_{3D}T$ values at the optimum carrier concentration for n-type Bi/(111)$Pb_{1-x}Eu_xTe$ superlattices [denoted by $Z_{3D}T(\zeta_{opt})$] as a function

Table 7.2: Parameters used for $Bi/Pb_{1-x}Eu_xTe$ superlattices.

Effective mass components[a]

	Bi	$Pb_{1-x}Eu_xTe$
m_e^x/m	0.00651	–
m_e^y/m	1.362	–
m_e^z/m	0.0101	0.0372
$m_h^{x,y}/m$	0.0644	–
m_h^z/m [a]	0.696	0.425

Electron and hole mobilities for bulk Bi [52]

$$\mu_e^x[\mathrm{cm}^2/\mathrm{V{\cdot}s}] = 1.05 \times 10^{10}\, T[\mathrm{K}]^{-2.22}$$
$$\mu_e^y[\mathrm{cm}^2/\mathrm{V{\cdot}s}] = 6.91 \times 10^{8}\, T[\mathrm{K}]^{-2.46}$$
$$\mu_h[\mathrm{cm}^2/\mathrm{V{\cdot}s}] = 2.27 \times 10^{9}\, T[\mathrm{K}]^{-2.27}$$

Lattice Thermal conductivity[b]

$$\kappa_{\mathrm{ph}}\ [\mathrm{W/m{\cdot}K}] = \begin{cases} 3.0\ [\mathrm{W/m{\cdot}K}] & (T < 150\mathrm{K}) \\ 4.5 \times 10^2\, T^{-1}\ [\mathrm{W/m{\cdot}K}] & (T > 150K) \end{cases}$$

Overlap energy for bulk Bi (see Fig. 7-8)

$$\Delta_0\ [\mathrm{meV}] = \begin{cases} 38\ [\mathrm{meV}] & (T < 80\mathrm{K}) \\ 38 + 0.044(T-80) & \\ -4.58 \times 10^{-4}(T-80)^2 & (T > 80\mathrm{K}) \\ +7.39 \times 10^{-6}(T-80)^3\ [\mathrm{meV}] & \end{cases}$$

[a)] Electron and hole effective masses. The values for m_e^x/m and m_e^y/m are obtained by projecting the 3D constant energy ellipsoid onto the (111) trigonal (or cubic) plane, whereas the value for m_e^z/m is obtained from the cross section of the constant energy ellipsoid in the xz-(or yz-)plane.

[b)] Conservative estimate for the lattice thermal conductivity for the $Bi/Pb_{1-x}Eu_xTe$ superlattice used for the present calculation (see text).

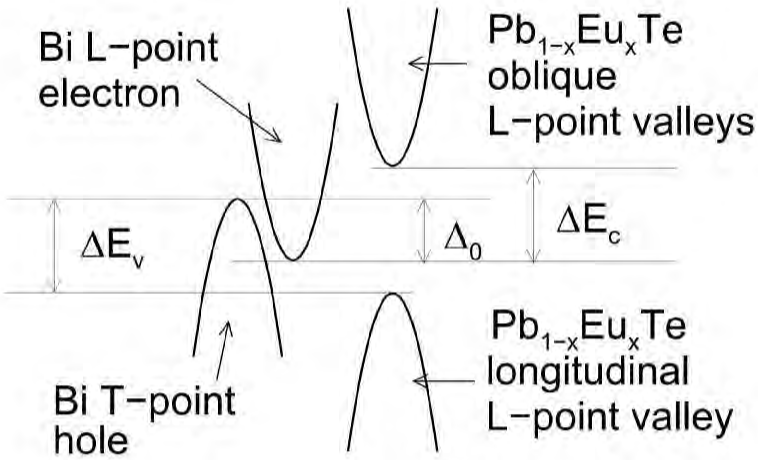

Figure 7-8: Conduction and valence band offset diagrams for (111) oriented $Bi/Pb_{1-x}Eu_xTe$ superlattices. Bi L-point conduction valleys are assumed to be coupled with the oblique L-point conduction band valleys of $Pb_{1-x}Eu_xTe$, whereas the Bi T-point valence band valley is assumed to be coupled with the longitudinal L-point valence band valley of $Pb_{1-x}Eu_xTe$. $\Delta E_c = \Delta E_v$ is assumed in the present work.

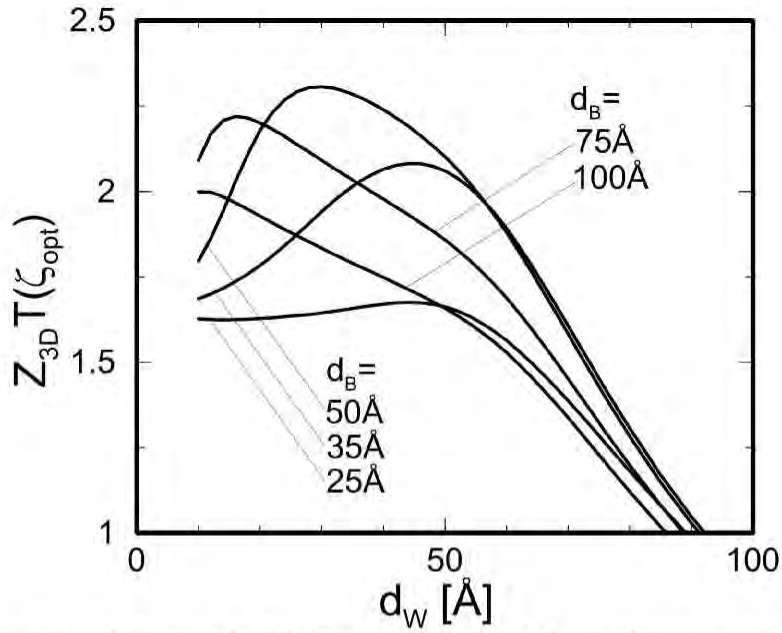

Figure 7-9: Calculated thermoelectric figure of merit at the optimum carrier concentration $Z_{3D}T(\zeta_{opt})$ as a function of the well (Bi) and barrier ($Pb_{1-x}Eu_xTe$) thicknesses (denoted by d_W and d_B, respectively). The conduction band offset ΔE_c and the temperature are taken to be 1 eV (corresponding to $x \approx 1$) and 300 K, respectively.

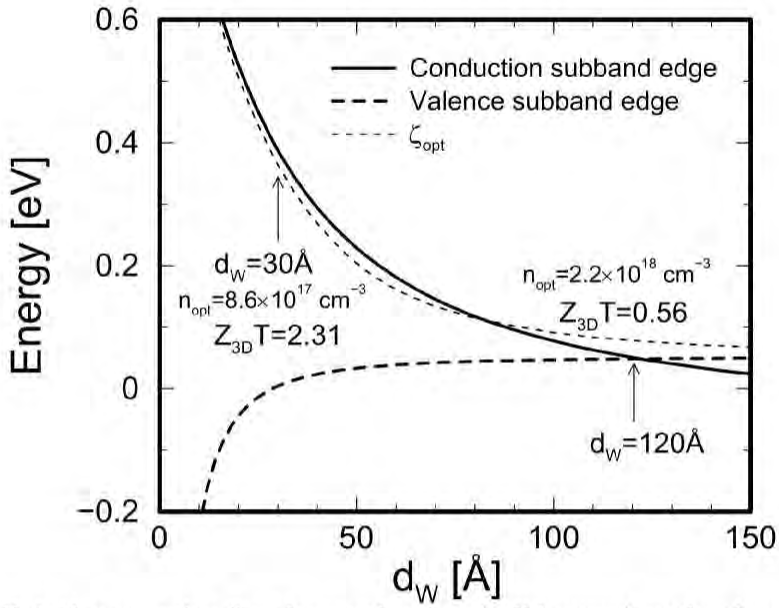

Figure 7-10: Relative energies for the conduction (solid curve) and valence (long-dashed curve) subband edges as a function of quantum well thickness $d_{\rm W}$ for Bi/(111)$Pb_{1-x}Eu_xTe$ superlattices ($x \approx 1$) at 300 K. The conduction and valence band offsets (denoted by ΔE_c and ΔE_v, respectively, and $\Delta E_c = \Delta E_v$ is assumed) and the barrier layer thickness $d_{\rm B}$ are taken to be 1 eV (see text) and 50 Å, respectively. The zero energy in the figure is the mid-point in the overlap energy (Δ_0 = 104 meV at 300 K) between the conduction and valence band for bulk Bi.

of well (Bi) and barrier ($Pb_{1-x}Eu_xTe$) layer thicknesses (denoted by $d_{\rm W}$ and $d_{\rm B}$, respectively). Explicit calculations are made for $x \approx 1$, $\Delta E_c = \Delta E_v = 1$ eV, and $\Delta_0 = 104.2$ meV at 300 K (see Table 7.2). For most of the values of $d_{\rm B}$ considered in Fig. 7-9, we observe that $Z_{\rm 3D}T(\zeta_{\rm opt})$ first increases with decreasing $d_{\rm W}$, reaches a maximum at a certain value for $d_{\rm W}$ (denoted as $d_{\rm W|opt}$) and then decreases with further decrease of $d_{\rm W}$. The first increase in $Z_{\rm 3D}T(\zeta_{\rm opt})$ is due to the increased density of states for electrons [the height of the steps in the electronic density of states is proportional to $(d_{\rm W} + d_{\rm B})^{-1}$], and the decrease in $Z_{\rm 3D}T(\zeta_{\rm opt})$ below $d_{\rm W} = d_{\rm W|opt}$ is due to the increased tunneling of the electrons between the neighboring Bi layers across the barrier layers. The highest value for $Z_{\rm 3D}T$ [$Z_{\rm 3D}T(\zeta_{\rm opt})$=2.31] with the above values for the various band offsets is obtained for $d_{\rm B} = 50$ Å and $d_{\rm W|opt} = 30$ Å at a carrier concentration of 8.6×10^{17} cm^{-3} (see Fig. 7-10). It is noted that for values of $d_{\rm W}$ near $d_{\rm W|opt}$, the Bi/(111)$Pb_{1-x}Eu_xTe$ superlattices are always semiconductors (for any values for $d_{\rm B}$ that are considered in the present study). Even for $d_{\rm W} \approx 70$

Table 7.3: Optimum structures and calculated $Z_{3D}T$s for Bi/$Pb_{1-x}Eu_xTe$ superlattices.

T[K]	d_W[Å]	d_B[Å]	n_{opt}[cm^{-3}]	$Z_{3D}T$
$\Delta E_c = 1.0$ eV ($x \approx 1$)				
300	30	50	8.6×10^{17}	2.31
150	30	60	5.9×10^{17}	1.55
77	28	75	2.6×10^{17}	1.61
$\Delta E_c = 0.5$ eV ($x \approx 0.3$)				
300	26	75	7.9×10^{17}	2.03
150	36	75	5.1×10^{17}	1.34
77	40	85	2.4×10^{17}	1.37
$\Delta E_c = 0.25$ eV ($x \approx 0.1$)				
300	18	85	7.7×10^{17}	1.75
150	36	100	4.7×10^{17}	1.16
77	50	105	2.2×10^{17}	1.18

Å, where the holes in the valence band start to push the position of the optimum chemical potential ζ_{opt} up into the conduction band, the band gap energy for the superlattice is several times as large as the thermal energy ($k_BT = 26$ meV at 300 K). For superlattices with $d_W < 60$ Å, the contribution of holes to the total thermoelectric transport is negligible.

We have also investigated the optimum structures and doping levels that give the largest values for $Z_{3D}T$ at various temperatures (77, 150 and 300 K) and for various values of conduction band offset ($\Delta E_c = 0.25$, 0.5 and 1.0 eV). The investigation and prediction of materials with enhanced values for $Z_{3D}T$ at low temperatures ($T < 150$ K) is important because there are virtually no thermoelectric materials systems at present that are useful at low temperatures, where there exist strong demands for thermoelectric refrigerators to cool high-T_c superconductors. The results for these calculation are summarized in Table. 7.3.

7.3.4 Conclusions

In this section, enhanced values of the thermoelectric figure of merit $Z_{3D}T$ are predicted for n-type Bi/(111)$Pb_{1-x}Eu_xTe$ superlattices at optimal doping concentrations.

The values of $Z_{3D}T$ for $x \approx 1$ superlattices are predicted to be 2.31, 1.55 and 1.61 at 300, 150 and 77 K, respectively. These values for $Z_{3D}T$ are found to depend on the value of the conduction band offset ΔE_c. It is also found that the optimum values for the quantum well and barrier layer thicknesses to obtain the maximum value of $Z_{3D}T$ are also dependent on the value of ΔE_c. It is proposed that Bi/(111)$Pb_{1-x}Eu_xTe$ superlattices are a promising candidate for thermoelectric cooling elements at low temperatures, and other families of Bi quantum well superlattices, such as Bi/(111)CdTe superlattices, should also possess equivalently good qualities for obtaining enhanced values of the thermoelectric figure of merit $Z_{3D}T$.

Chapter 8

Conclusions

Summary of the thesis

In this thesis, we have discussed how one can use low-dimensional structures, especially in the form of two-dimensional superlattices, to design materials with enhanced values of the thermoelectric figure of merit $Z_{3D}T$. The general strategies taken throughout the thesis are the following : (I) explore various combinations of materials for the quantum wells and barrier layers of the superlattice, predicting the optimum structure, orientation, and other properties of the superlattices that provide the maximum value of $Z_{3D}T$ using simple models based on the constant relaxation time approximation; (II) perform an experimental proof-of-principle study to test the theoretical predictions made in the stage (I) investigation above; (III) improve the theoretical models to understand the obtained experimental results and give feedback to experimentalists providing information on what needs to be improved in the experiments in order to achieve even higher experimental values of $Z_{3D}T$; (IV) apply the knowledge acquired about various mechanisms that are responsible for the enhanced values of the thermoelectric figure of merit $Z_{3D}T$ during the stage (I)-(III) investigations of this optimization process, using one materials system for a systematic investigation of the scientific issues, to other materials systems that may be more suitable for achieving even larger values of the thermoelectric figure of merit $Z_{3D}T$. Using the specific examples that were exploited in this thesis, we can exemplify the

above (I)–(IV) investigations in the general optimization strategies taken throughout the thesis, as discussed below.

First, the stage (I) and (II) investigations in the above optimization process were described in Chapter 2 using (111) oriented PbTe(20 Å)/$Pb_{1-x}Eu_xTe$(400 Å) multiple-quantum-well (MQW) samples, where our focus was on the enhanced thermoelectric figure of merit within the quantum wells, denoted by $Z_{2D}T$. We have seen that the models based on the constant relaxation time approximation predicts that larger values of $Z_{2D}T$ are obtainable in the (001) oriented PbTe quantum wells (§2.5.2) than in the (111) oriented quantum wells. This main result of enhanced $Z_{2D}T$ in the (001) oriented PbTe-based multiple-quantum-wells also led us to the theoretical investigation of (001) oriented short-period PbTe/$Pb_{1-x}Eu_xTe$ superlattices (§7.2) to predict enhanced values of $Z_{3D}T$ (figure of merit for the whole superlattice) using the same basic ideas as those used for the prediction of the enhanced $Z_{2D}T$, but including the *three-dimensional* energy dispersion relation, that is obtained using the Krönig-Penney model, and without using the two-dimensional energy dispersion relation that was employed for the prediction of enhanced $Z_{2D}T$. Since the actual samples of (001) oriented PbTe-based quantum wells or (001) oriented PbTe/$Pb_{1-x}Eu_xTe$ short period superlattices were not yet available to us, the experimental proof-of-principle study of the enhanced *two-dimensional* thermoelectric figure of merit $Z_{2D}T$ was performed using MBE-grown (111) oriented PbTe/$Pb_{1-x}Eu_xTe$ multiple-quantum-wells (MQW) [15], where the thicknesses for the barrier ($Pb_{1-x}Eu_xTe$) layers (~400 Å) were much larger than those for the well (PbTe) layers (~20 Å). This experimental investigation can be categorized as a stage (II) investigation of the above general optimization process.

The work performed in Chapter 3 is categorized as a stage (III) investigation of the above optimization process [i.e., improvement of the theoretical models according to the results of the stage (II) investigation above], where we have analyzed the obtained experimental results (enhanced values for the Seebeck coefficient$|S|$) for the (111) oriented PbTe(20 Å)/$Pb_{1-x}Eu_xTe$(400 Å) superlattice (sample T-225) that were obtained in Chapter 2, using the improved theoretical models based on the semi-

classical Boltzmann transport theory, including some specific scattering mechanisms.

The work performed in Chapter 4 is categorized as both the stage (IV) and the stage (I) investigations in the above general optimization strategies, as explained below. In Chapters 2 and 3, we have proved, both experimentally and theoretically, that the basic concept of enhancing the values of $Z_{2D}T$ using low-dimensional structures (which is denoted as the "basic principle of low-dimensional thermoelectricity" in §1.3) can actually work. Therefore, the next step in this line of research was to predict enhanced values of $Z_{3D}T$ (thermoelectric figure of merit for the whole superlattice). In this sense, the work performed in Chapter 4 is categorized as the stage (IV) investigation discussed above (application of the knowledge acquired during the previous investigations to another materials system of interest), because we have applied the knowledge acquired in the study of enhanced $Z_{2D}T$ for PbTe/$Pb_{1-x}Eu_xTe$ MQWs to "another" GaAs/AlAs superlattice system to predict the enhanced *three-dimensional* thermoelectric figure of merit $Z_{3D}T$ for the GaAs/AlAs superlattice system. It is needless to say that Chapter 4 was the stage (I) investigation for the GaAs/AlAs superlattice system, using simple models based on the constant relaxation time approximation.

Since actual GaAs/AlAs superlattice samples, that were specially designed by us to test the theoretical predictions for an enhanced $Z_{3D}T$ in this superlattice system in Chapter 4, were not yet available to us for experiments, we proceeded in our research without performing an experimental proof-of-principle study for the GaAs/AlAs superlattices. The next materials system chosen for the study of enhanced thermoelectric figure of merit $Z_{3D}T$ was the Si/Ge superlattices. The reason why the Si/Ge superlattices were chosen for the topic of our investigation was largely due to the availability of the samples to test the theoretical predictions made by us for this materials system, since (001) oriented Si/Ge superlattice samples were readily available to us through the collaboration with Prof. K. L. Wang's group at UCLA under the MURI[†] program. In addition to that, the general knowledge acquired during the

[†]DOD/ONR MURI : Quantum Structures for Thermoelectric Applications (principal investigator : Prof. Gang Chen at UCLA).

modeling study of GaAs/AlAs superlattices, denoted by the "Carrier Pocket Engineering concept" in Chapter 4, also suggested that Si/Ge superlattices should be a good materials candidate by which we might achieve enhanced values of the thermoelectric figure of merit $Z_{3D}T$. It should be also noted that, during the stage (I) investigation of the Si/Ge superlattices, using simple theoretical models based on the constant relaxation time approximation, we have discovered a new concept of using the lattice strain effects that are experienced by the Si and Ge layers of the superlattice, as an additional parameter to control the conduction band offset to further enhance the values of $Z_{3D}T$ in this superlattice system (Chapter 5).

The second half of Chapter 5, and Chapter 6 are, respectively, devoted to stage (II) and (III), and stage (III) investigations of the general optimization process that is discussed above. In the second half of Chapter 5, we have experimentally tested the theoretical predictions that were made in the first half of Chapter 5. We have used (001) oriented Si/Ge short period superlattices to fulfill this purpose, since (111) oriented Si/Ge superlattice samples were not yet available to us through the collaborations under the MURI program. However, it should be remembered that the predicted values of $Z_{3D}T$ for (111) oriented Si/Ge superlattices [$Z_{3D}T = 0.98$ for a strain symmetrized (111) Si(15 Å)/Ge(20 Å) superlattice at 300 K] was much larger than the corresponding value of $Z_{3D}T$ for (001) oriented Si/Ge superlattices [$Z_{3D}T = 0.24$ for a strain symmetrized (001) oriented Si(20 Å)/Ge(20 Å) superlattice at 300 K] when the structural parameters of the superlattice such as the quantum well and barrier layer thicknesses are optimized. The experimental results obtained during this proof-of-principle study were analyzed using the semi-classical models that were developed in Chapter 6 [stage (III) investigation of the general optimization process that is discussed above]. In Chapter 6, we have extended our theoretical investigations of the enhanced thermoelectric figure of merit $Z_{3D}T$ for the (001) oriented Si/Ge superlattice samples to include the effects of δ- and modulation doping techniques so that further increases in the values of $Z_{3D}T$ for the (001) oriented Si/Ge superlattices were predicted. Thus, this can be regarded as the feedback from the theoretical modeling investigation to the experimental investigation [stage (III) investigation of

the general optimization process that is discussed above]. A natural continuation along this line of the research using the Si/Ge superlattice systems is the stage (IV) investigation of the (111) oriented Si/Ge superlattices, where various knowledge, acquired during the optimization processes for the (001) oriented Si/Ge superlattices, should be incorporated into the future design of (111) oriented Si/Ge superlattice structures, in which the optimum value of the thermoelectric figure of merit for a strain-symmetrized (111) oriented Si(20 Å)/Ge(20 Å) superlattice is predicted to be a factor of four larger than that for the corresponding strain-symmetrized (001) oriented Si(20 Å)/Ge(20 Å) superlattice, using a simple model based on the constant relaxation time approximation.

Beside the above-mentioned mainstream topics of the thesis, we have also discussed the possible mechanisms for the enhanced thermoelectric properties that were observed experimentally in the (111) oriented PbTe/Te and $PbSe_{0.98}Te_{0.02}$/PbTe "quantum-dot" superlattices (§7.1). In this investigation, although we were not able to identify the exact mechanisms that are responsible for the enhanced thermoelectric properties in these systems, the observed experimental results strongly suggested that something other than the quantum confinement effect of the conduction carriers[†] are responsible for the observed enhancement in the thermoelectric properties in these systems. During the effort of explaining the mechanisms for the observed enhanced thermoelectric properties of the (111) oriented PbTe/Te superlattices in terms of the quantum confinement effect, we have found that there should be another regime in structure and orientation of the superlattice where one can utilize the quantum confinement effect of the conduction carriers more effectively for enhancing the thermoelectric properties of the superlattices. Thus, we have investigated, in §7.2, the thermoelectric properties of (001) oriented PbTe/$Pb_{1-x}Eu_xTe$ short period superlattices using simple models based on the constant relaxation time approximation. Fi-

[†]The "quantum confinement effect" here means that the "quantum confinement effect to enhance the density of states using low-dimensional structures" as we discussed in §1.3. There exist other types of quantum confinement effect that may be responsible for the observed enhancement in S in the (111) oriented $PbSe_{0.98}Te_{0.02}$/Te "quantum-dot" superlattices, such as the quantum mechanical confinement of electrons within the quantum dots, which may provide ionized-impurity-like scattering mechanisms that enhance the values of S.

nally, the same line of the research is continued using (111) oriented Bi/$Pb_{1-x}Eu_xTe$ short period superlattices (§7.3), where practically useful values of $Z_{3D}T$ ($Z_{3D}T > 1$) were predicted even at temperatures as low as 77 K.

Future trends

Now, we identify the issues left over for the future work. Probably, the most difficult part of the actual application of low-dimensional structures to enhance thermoelectricity is the fabrication of thick superlattices. Superlattices with a total thickness in the 'mm' range would be required for commercial applications of low-dimensional thermoelectricity, either for refrigeration or power generation applications.[†] Recent trends to overcome this disadvantage of low-dimensional thermoelectricity in actual applications, therefore, include the integration of the thermoelectric elements, that are prepared using superlattice structures, into conventional semiconductor-based integrated circuits, so that the integrated thermoelectric device can "spot-cool" [123] only the part of the given integrated circuit which requires lower temperatures than the rest of the circuit, as in a semiconductor-based solid state laser or an infrared detector.

In order to develop such "spot-cooled" thermoelectric devices using superlattice structures, it is also necessary to develop p-type materials that have as high values of $Z_{3D}T$ as those for the n-type superlattices that were investigated in this thesis, in order to design thermoelectric devices that have a balanced pair of p- and n-type materials (see §1.2). It is possible, in many cases, to use the same general optimization strategies, based on the quantum confinement effect of the conduction carriers

[†]It is noted that Dr. T. C. Harman at MIT Lincoln Lab. has achieved a growth rate as high as 10 μm/hour for the MBE grown $PbSe_{0.98}Te_{0.02}$/PbTe "quantum-dot" superlattices without degrading the thermoelectric properties appreciably from those of the films grown using a standard 1 μm/hour growth rate [122]. It is, however, noted that, even with this unusually high growth rate for the MBE-grown superlattice films, it takes 100 hours (4 days and 4 hours) to grow a 1mm thick (total thickness) superlattice, which indicates that molecular beam epitaxy is an extremely expensive process for fabricating a "low-dimensional" thermoelectric element that can be used in actual thermoelectric applications. It is, therefore, necessary to explore other growth techniques for the superlattices that are much faster and much less expensive than the molecular-beam epitaxy technique, but which can grow superlattices with as high a quality as as those grown by the MBE technique, for the future commercialization of low-dimensional thermoelectricity.

on enhancing the thermoelectric properties of superlattices, as those used for n-type doped semiconducting superlattices in this thesis, for p-type doped semiconducting superlattices as well. However, since many semiconducting materials have their valence band maxima at the center of the Brillouin zone (Γ-point), where the number of the equivalent valley sites is only one, it may be necessary to explore strategies other than those based on the quantum confinement effect to design p-type thermoelectric materials that have enhanced thermoelectric properties relative to conventional p-type thermoelectric materials. Hints along this line of research lie, for example, in p-type $PbSe_{0.98}Te_{0.02}/PbTe$ "quantum-dot" superlattices and/or in novel p-type B_4C/B_9C superlattices [124]. For p-type $PbSe_{0.98}Te_{0.02}/PbTe$ "quantum-dot" superlattices, since most lead-chalcogenide compounds have symmetrical electronic structures between the valence and conduction bands, it is likely that the enhanced thermoelectric properties that are observed in n-type $PbSe_{0.98}Te_{0.02}/PbTe$ "quantum-dot" superlattices, can also be observed in p-type $PbSe_{0.98}Te_{0.02}/PbTe$ "quantum-dot" superlattices. For p-type B_4C/B_9C superlattices, although the exact mechanisms are not yet known, some experimental investigations indicated excellent thermoelectric properties in this superlattice system and these p-type materials have been already used for the experimental evaluation of thermoelectric devices whose p- and n-type legs are designed (and actually fabricated) using the superlattice structures [124, 125]. However, scientific understanding of why these p-type materials yield high $Z_{3D}T$ values remains to be achieved in future studies.

Appendix A

Thermoelectric figure of merit for a one-band material of various dimensions in the constant relaxation time approximation

A.1 Meaning of symbols and values of physical constants

Meaning of symbols

symbol	meaning	units
N	# of equivalent valleys	—
ζ	chemical potential	J
ζ^*	reduced chemical potential $\frac{\zeta}{k_B T}$	—
T	temperature	K
κ_{ph}	lattice thermal conductivity	$\mathrm{W\,m^{-1}K^{-1}}$
μ	carrier mobility	$\mathrm{m^2V^{-1}s^{-1}}$
m_x, m_y, m_z	components of effective mass tensor	kg

List of physical constants

symbol	meaning	value	units
m	free electron mass	9.10956	10^{-31} kg
e	electron charge	1.60219	10^{-19} C
$\hbar$	Planck constant/2π	1.05459	10^{-34} J·s
k_B	Boltzmann constant	1.38062	10^{-23} J K^{-1}

Fermi-related integral function

$$F_j(\zeta^*) = \int_0^\infty \frac{\xi^j d\xi}{e^{(\xi-\zeta^*)}+1},$$

where $j = -\frac{1}{2}, 0, \frac{1}{2}, 1, \frac{3}{2}, \cdots$.

A.2 3D bulk materials

The electrical conductivity σ, the Seebeck coefficient S, the electronic contribution to the thermal conductivity κ_e and the dimensionless thermoelectric figure of merit $Z_{3D}T$ for a one-band bulk material are, respectively, given by

$$\sigma = N \times \frac{e}{3\pi^2}\left(\frac{2k_BT}{\hbar^2}\right)^{\frac{3}{2}}(m_xm_ym_z)^{\frac{1}{2}}\,\mu\left(\frac{3}{2}F_{\frac{1}{2}}\right), \tag{A.1}$$

$$S = -\frac{k_B}{e}\left(\frac{5F_{\frac{3}{2}}}{3F_{\frac{1}{2}}} - \zeta^*\right), \tag{A.2}$$

$$\kappa_e = N \times \frac{k_B^2T}{3\pi^2e}\left(\frac{2k_BT}{\hbar^2}\right)^{\frac{3}{2}}(m_xm_ym_z)^{\frac{1}{2}}\,\mu\left(\frac{7}{2}F_{\frac{5}{2}} - \frac{25F_{\frac{3}{2}}{}^2}{6F_{\frac{1}{2}}}\right), \tag{A.3}$$

and

$$Z_{3D}T = \frac{B_{3D}\left(\frac{5F_{\frac{3}{2}}}{3F_{\frac{1}{2}}} - \zeta^*\right)^2 \frac{3}{2}F_{\frac{1}{2}}}{B_{3D}\left(\frac{7}{2}F_{\frac{5}{2}} - \frac{25F_{\frac{3}{2}}{}^2}{6F_{\frac{1}{2}}}\right)+1}, \tag{A.4}$$

where

$$B_{3D} = \frac{N}{3\pi^2}\left(\frac{2k_BT}{\hbar^2}\right)^{\frac{3}{2}}(m_xm_ym_z)^{\frac{1}{2}}\frac{k_B^2T\mu}{e\kappa_{ph}}. \tag{A.5}$$

A.3 2D isolated quantum wells

The electrical conductivity σ, the Seebeck coefficient S, the electronic contribution to the thermal conductivity κ_e and the dimensionless thermoelectric figure of merit $Z_{1D}T$ for a one-band isolated 2D quantum well are, respectively, given by

$$\sigma = N \times \frac{e}{2\pi d_W}\left(\frac{2k_BT}{\hbar^2}\right)(m_xm_y)^{\frac{1}{2}}\mu F_0, \tag{A.6}$$

$$S = -\frac{k_B}{e}\left(\frac{2F_1}{F_0} - \zeta^*\right), \tag{A.7}$$

$$\kappa_e = N \times \frac{k_B^2T}{2\pi d_W e}\left(\frac{2k_BT}{\hbar^2}\right)(m_xm_y)^{\frac{1}{2}}\mu\left(3F_2 - \frac{4F_1{}^2}{F_0}\right), \tag{A.8}$$

and

$$Z_{2D}T = \frac{B_{2D}\left(\frac{2F_1}{F_0} - \zeta^*\right)^2 F_0}{B_{2D}\left(3F_2 - \frac{4F_1^2}{F_0}\right) + 1}, \tag{A.9}$$

where

$$B_{2D} = \frac{N}{2\pi d_W}\left(\frac{2k_BT}{\hbar^2}\right)(m_xm_y)^{\frac{1}{2}}\frac{k_B^2T\mu}{e\kappa_{ph}}. \tag{A.10}$$

A.4 1D isolated quantum wires

The electrical conductivity σ, the Seebeck coefficient S, the electronic contribution to the thermal conductivity κ_e and the dimensionless thermoelectric figure of merit $Z_{1D}T$ for a one-band isolated 1D quantum wire are, respectively, given by

$$\sigma = N \times \frac{2e}{\pi d_W^2}\left(\frac{2K_BT}{\hbar^2}\right)^{\frac{1}{2}} m_x^{\frac{1}{2}}\mu\left(\frac{1}{2}F_{-\frac{1}{2}}\right), \tag{A.11}$$

$$S = -\frac{k_B}{e}\left(\frac{3F_{\frac{1}{2}}}{F_{-\frac{1}{2}}} - \zeta^*\right), \tag{A.12}$$

$$\kappa_e = N \times \frac{2k_B^2 T}{\pi d_{\mathrm{W}}^2 e}\left(\frac{k_B T}{\hbar^2}\right) m_x^{\frac{1}{2}} \mu \left(\frac{5}{2}F_{\frac{3}{2}} - \frac{9F_{\frac{1}{2}}{}^2}{2F_{-\frac{1}{2}}}\right). \tag{A.13}$$

and

$$Z_{1\mathrm{D}}T = \frac{B_{1\mathrm{D}}\left(\frac{3F_{\frac{1}{2}}}{F_{-\frac{1}{2}}} - \zeta^*\right)^2 \frac{1}{2}F_{-\frac{1}{2}}}{B_{1\mathrm{D}}\left(\frac{5}{2}F_{\frac{3}{2}} - \frac{9F_{\frac{1}{2}}{}^2}{2F_{-\frac{1}{2}}}\right) + 1}, \tag{A.14}$$

where

$$B_{1\mathrm{D}} = N \times \frac{2}{\pi d_{\mathrm{W}}^2}\left(\frac{2k_B T}{\hbar^2}\right) m_x^{\frac{1}{2}} \frac{k_B^2 T \mu}{e\kappa_{\mathrm{ph}}}. \tag{A.15}$$

A.5 Table for Z_XT vs. B_X (X = '1D', '2D' and '3D')

B_X	3D bulk		2D quantum well		1D quantum wire	
(X= 1D, 2D, 3D)	$Z_{3D}T(\zeta^*_{opt})$	ζ^*_{opt}	$Z_{2D}T(\zeta^*_{opt})$	ζ^*_{opt}	$Z_{1D}T(\zeta^*_{opt})$	ζ^*_{opt}
0.00014	0.00150932	2.46233	0.000568229	0.666509	0.000274548	−0.367236
0.00016	0.00172448	2.45991	0.000649373	0.666308	0.000313764	−0.367274
0.00019	0.00204702	2.45633	0.000771073	0.666003	0.000372587	−0.367341
0.00022	0.00236931	2.45275	0.000892756	0.665698	0.000431407	−0.367398
0.00026	0.00279864	2.44802	0.00105497	0.665288	0.00050983	−0.367484
0.00031	0.00333469	2.44215	0.0012577	0.664783	0.000607853	−0.367589
0.00037	0.00397704	2.43516	0.0015009	0.664172	0.00072547	−0.367713
0.00044	0.00472521	2.42712	0.00178455	0.663466	0.000862678	−0.367856
0.00052	0.00557865	2.41803	0.00210861	0.662656	0.00101947	−0.368018
0.00062	0.00664305	2.40684	0.00251349	0.661645	0.00121543	−0.368218
0.00074	0.00791684	2.39365	0.0029991	0.660434	0.00145055	−0.368466
0.00088	0.00939821	2.37857	0.00356528	0.659032	0.00172481	−0.368752
0.00105	0.0111903	2.36071	0.00425228	0.657325	0.00205776	−0.369105
0.00125	0.0132893	2.34028	0.00505978	0.655322	0.00244936	−0.369515
0.0015	0.0158993	2.31557	0.00606806	0.652833	0.0029387	−0.370021
0.00179	0.0189083	2.28798	0.00723615	0.649962	0.00350612	−0.370612
0.00214	0.0225139	2.2561	0.00864376	0.64651	0.00419062	−0.371327
0.00256	0.0268044	2.2197	0.0103298	0.6424	0.00501156	−0.372186
0.00307	0.0319634	2.17794	0.0123726	0.63745	0.00600776	−0.373216
0.00368	0.0380641	2.13109	0.0148095	0.631585	0.00719834	−0.374455
0.00441	0.0452698	2.07889	0.0177167	0.624642	0.00862177	−0.375934
0.00529	0.0538262	2.02078	0.0212082	0.616393	0.0103357	−0.377707
0.00634	0.0638598	1.95702	0.0253557	0.606704	0.012378	−0.379815
0.0076	0.0756703	1.88775	0.0303068	0.595298	0.0148247	−0.382333
0.00911	0.0895168	1.81286	0.0362036	0.581918	0.0177511	−0.385337
0.01093	0.105798	1.73209	0.0432592	0.566211	0.0212701	−0.388932
0.01311	0.124768	1.64615	0.0516379	0.547948	0.0254734	−0.393205

B_X	3D bulk		2D quantum well		1D quantum wire	
(X= 1D, 2D, 3D)	$Z_{3D}T(\zeta^*_{opt})$	ζ^*_{opt}	$Z_{2D}T(\zeta^*_{opt})$	ζ^*_{opt}	$Z_{1D}T(\zeta^*_{opt})$	ζ^*_{opt}
0.01573	0.146875	1.55509	0.0616064	0.526748	0.0305083	−0.398297
0.01887	0.172484	1.4595	0.0734132	0.502334	0.0365187	−0.404334
0.02264	0.202099	1.35958	0.0873954	0.474343	0.043701	−0.411496
0.02716	0.23618	1.25588	0.103894	0.442472	0.0522642	−0.419946
0.03259	0.275332	1.14859	0.123355	0.406365	0.0624836	−0.429931
0.0391	0.320048	1.03833	0.146199	0.365834	0.0746402	−0.441661
0.04692	0.371031	0.925488	0.172989	0.320573	0.089109	−0.455403
0.0563	0.428828	0.810103	0.204258	0.270486	0.106277	−0.471444
0.06755	0.49409	0.692697	0.240626	0.215487	0.126609	−0.490069
0.08105	0.567525	0.573478	0.282789	0.155501	0.150648	−0.511603
0.09725	0.649824	0.452685	0.331478	0.0905561	0.179005	−0.53637
0.11669	0.741688	0.33052	0.387474	0.0207376	0.212364	−0.564675
0.14002	0.843826	0.207124	0.451603	−0.0538206	0.251495	−0.596824
0.16802	0.956948	0.0826311	0.524728	−0.132937	0.297248	−0.633111
0.20162	1.08173	−0.0428247	0.607724	−0.216403	0.350546	−0.673757
0.24194	1.21885	−0.169187	0.701496	−0.303979	0.412394	−0.71898
0.29032	1.36896	−0.296388	0.806953	−0.395427	0.483862	−0.768924
0.34838	1.53272	−0.42439	0.925029	−0.490518	0.566101	−0.823684
0.41805	1.71073	−0.553184	1.05662	−0.589013	0.660296	−0.883288
0.50165	1.90358	−0.68275	1.20263	−0.690675	0.767679	−0.947738
0.60198	2.11185	−0.813117	1.36395	−0.795331	0.889525	−1.01696
0.72237	2.33605	−0.944257	1.54141	−0.902753	1.02709	−1.09085
0.86684	2.57667	−1.0762	1.73582	−1.01279	1.18165	−1.16927
1.0402	2.83419	−1.20896	1.94796	−1.12527	1.35446	−1.25205
1.24824	3.10906	−1.34256	2.17857	−1.24007	1.54676	−1.33902
1.49788	3.40165	−1.477	2.42833	−1.35705	1.75972	−1.42997
1.79745	3.71238	−1.61232	2.6979	−1.4761	1.99448	−1.52472
2.15694	4.04159	−1.74851	2.98788	−1.59713	2.25214	−1.62308
2.58832	4.38959	−1.8856	3.29884	−1.72004	2.5337	−1.72485
3.10598	4.75672	−2.0236	3.63129	−1.84477	2.84012	−1.82985

B_X	3D bulk		2D quantum well		1D quantum wire	
(X= 1D, 2D, 3D)	$Z_{3D}T(\zeta^*_{opt})$	ζ^*_{opt}	$Z_{2D}T(\zeta^*_{opt})$	ζ^*_{opt}	$Z_{1D}T(\zeta^*_{opt})$	ζ^*_{opt}
3.72717	5.14324	−2.16251	3.98574	−1.97123	3.17231	−1.9379
4.4726	5.54943	−2.30233	4.36262	−2.09936	3.53109	−2.04886
5.36711	5.97553	−2.44305	4.76237	−2.22908	3.91722	−2.16256
6.44053	6.42177	−2.58469	5.18536	−2.36037	4.33142	−2.27886
7.72863	6.88838	−2.72724	5.63197	−2.49315	4.77433	−2.39762
9.27435	7.37555	−2.87067	6.10253	−2.62737	5.24656	−2.51873
11.1292	7.88347	−3.015	6.59735	−2.76297	5.74867	−2.64206
13.3551	8.41234	−3.16019	7.11675	−2.89993	6.28117	−2.76752
16.0261	8.96231	−3.30623	7.66098	−3.03818	6.84454	−2.89498
19.2313	9.53355	−3.45312	8.23032	−3.17768	7.43922	−3.02435
23.0775	10.1262	−3.60082	8.82502	−3.31838	8.06562	−3.15555
27.693	10.7404	−3.74934	9.44531	−3.46025	8.72415	−3.28849
33.2316	11.3764	−3.89863	10.0914	−3.60323	9.41516	−3.42308
39.8779	12.0341	−4.04868	10.7635	−3.74731	10.139	−3.55923
47.8535	12.7139	−4.19947	11.4619	−3.89241	10.896	−3.69689
57.4242	13.4157	−4.35099	12.1867	−4.0385	11.6865	−3.83598
68.9091	14.1397	−4.5032	12.9381	−4.18557	12.5108	−3.97643
82.6909	14.886	−4.65609	13.7163	−4.33355	13.3692	−4.11816
99.2291	15.6548	−4.80963	14.5215	−4.48242	14.2619	−4.26114
119.075	16.446	−4.96381	15.3538	−4.63214	15.1892	−4.40528
142.89	17.2599	−5.11861	16.2134	−4.78268	16.1514	−4.55056
171.468	18.0965	−5.274	17.1004	−4.93401	17.1487	−4.6969
205.761	18.9558	−5.42998	18.015	−5.0861	18.1814	−4.84425
246.914	19.8381	−5.5865	18.9573	−5.23891	19.2496	−4.99258
296.296	20.7433	−5.74357	19.9275	−5.39242	20.3537	−5.14183
355.556	21.6716	−5.90115	20.9257	−5.54661	21.4937	−5.29196
426.667	22.6229	−6.05923	21.952	−5.70143	22.67	−5.44295
512	23.5975	−6.21781	23.0065	−5.85688	23.8828	−5.59473
614.4	24.5954	−6.37684	24.0894	−6.01293	25.1321	−5.74728
737.28	25.6166	−6.53635	25.2007	−6.16954	26.4182	−5.90058

Appendix B

Investigation of the thermoelectric properties of the lightly doped, (111) oriented $PbTe(20\ Å)/Pb_{1-x}Eu_xTe(400\ Å)$ multiple-quantum-wells

In this Appendix, we compile a piece of our work that is supplemental to the research discussed in Chapters 2 and 3. The main focus of the investigation in this Appendix is to study "experimentally" the values for the mobility ratio $\mu_{\text{obliq}}/\mu_{\text{longt}}$ that is discussed in Chapters 2 and 3, and to examine whether there is any systematic dependence of the ratio $\mu_{\text{obliq}}/\mu_{\text{longt}}$ on the doping level (carrier concentration) and temperature.

The original manuscript on which this Appendix is based was written as an internal report to Prof. G. Bauer and to Dr. G. Springholz at the Johannes Kepler Universität Linz, in Austria, who had kindly accepted our request of growing the $PbTe/Pb_{1-x}Eu_xTe$ MQW samples for us. It is noted that the work shown in this Appendix was carried out before we started the very elaborate theoretical calculations of

the thermoelectric transport properties of the PbTe quantum wells (including specific scattering mechanisms) that are discussed in Chapter 3. Moreover, it was actually through the work shown in this Appendix that we had realized that we needed something better than a simple model based on the constant relaxation time approximation in order to provide a detailed explanation of the observed enhanced thermoelectric properties in the (111) oriented PbTe(20 Å)/$Pb_{1-x}Eu_xTe$(400 Å) multiple-quantum-wells that are discussed in Chapter 2.

B.1 Introduction

Recently, Harman *et al.* [15] and Hicks *et al.* [16] observed enhanced values of the thermoelectric power ($|S| \approx 225$ μV/K at 300 K) and a large value of the electron Hall carrier mobility ($\mu_{\rm Hall} \approx 1400$ cm^2/V·s at 300 K and $\mu_{\rm Hall} \approx 2\times10^4$ cm^2/V·s at 77 K) for heavily doped MQW samples ($n_{\rm 3D} \approx 1.1\times10^{19}$ cm^{-3} using $d_{\rm W} = 20$ Å for the thickness of the sample) of n-type PbTe(20 Å)/$Pb_{1-x}Eu_xTe$(400 Å) ($x \approx 0.073$[†]). We had been trying to figure out the underlying physics for the rather unusual properties of PbTe MQWs by modeling the thermoelectric power and the Hall carrier concentration as a function of temperature, using the three (sub)band model which utilizes the ratios of mobilities between the longitudinal- and oblique-subbands and between the $Pb_{1-x}Eu_xTe$ barrier layer and the oblique subband in the quantum well as variable parameters. It turned out that it is very difficult to explain the observed thermoelectric power and high mobility at 300 K without assigning as high an electron mobility to the oblique subband carriers as for the longitudinal subband carriers. After having considerable discussions with Professor Henry Ehrenreich at Harvard University on this issue, we realized that it is rather unreasonable to assume such a high mobility for the oblique subband for the following reasons : The relaxation time τ is, assuming that only intra-valley carrier scattering is important, inversely

[†]This value is now updated to be 0.09 (see the footnote on page 99).

proportional to the scattering probability,

$$\tau \sim \frac{1}{W\rho}, \tag{B.1}$$

where W is the squared scattering matrix element and ρ is the density of states for the pertinent electron pocket. The density of states for a single oblique pocket is about 3 times as large as that for the longitudinal pocket in the quantum wells. Therefore, the value for the relaxation time τ for the longitudinal subband should be three times larger than that for the oblique subband, considering the density-of-states factor only. Moreover, the transport effective mass for the oblique subband is about twice as large as that for the longitudinal subband. Therefore, the ratio of mobilities between the longitudinal- and oblique-subbands ($\mu_{\mathrm{longt}}/\mu_{\mathrm{obliq}}$) should be about 6 if we consider the density-of-states factor only. On the other hand, this naive approximation is not correct if (1) inter-valley scattering is the dominant scattering process and/or (2) the value of the scattering matrix element W is different between the longitudinal- and oblique-subbands. The study of the mechanisms that are responsible for the reduction of mobility for the longitudinal subband would provide very useful information for designing a good thermoelectric superlattice, since a large value of the electron mobility for the longitudinal subband would tend to lower the value of the total Seebeck coefficient $|S|$ because the longitudinal subband is assigned a much smaller value of the Seebeck coefficient than the oblique subband, and the total value of the Seebeck coefficient is given as the weighted average of the Seebeck coefficient that is assigned to each subband of the pertinent quantum well, with the electrical conductivity that is also assigned to each existing subband. Therefore, the purpose of the present work is to investigate the values of $\mu_{\mathrm{longt}}/\mu_{\mathrm{obliq}}$ systematically, for a set of well-defined n-type PbTe(20 Å)/$Pb_{1-x}Eu_xTe$(400 Å) multiple-quantum-well samples as a function of the carrier concentration and temperature.

B.2 Theoretical Modeling

Our model for the Seebeck coefficient and the Hall coefficient assumes a parabolic energy band structure with 1) a longitudinal subband, which is derived from the longitudinal L-point valley in bulk PbTe, 2) an oblique subband, which is derived from the three equivalent L-point valleys that are oblique to the superlattice growth axis, and 3) a 3D parabolic band that takes care of the parallel transport contributions from the barrier layers of the superlattice samples. The density of states for the barrier layer was multiplied by $d_{\mathrm{B}}(=$ barrier layer width$)/d_{\mathrm{W}}(=$ quantum well layer width) to take into account the effect of the parallel conduction in the Hall coefficient and the Seebeck coefficient measurements. Each of the subband energies is calculated using the Krönig-Penney model (see Eq. B.7) and using bulk values for the effective masses for PbTe and $Pb_xEu_{1-x}Te$ (see Eqs. B.2–B.5). We assume the constant relaxation time approximation throughout the Appendix, unless mentioned otherwise.

Bulk effective masses for PbTe used in the present work are given by

$$m_t = 0.024 + 3.15 \times 10^{-5} T \tag{B.2}$$

$$m_l = 0.25 + 3.33 \times 10^{-4} T, \tag{B.3}$$

where m_t and m_l denote the transverse and the longitudinal components of the effective mass tensor, respectively.

The bulk effective mass for $Pb_{1-x}Eu_xTe$ ($x \approx 0.08$) is determined from the Seebeck coefficient measurement as a function of temperature for sample MBEG894[†] (see Fig. B-3) in the following way. The experimental results for the Seebeck coefficient for sample MBEG894 are fitted by the theoretical model based on the constant relaxation time approximation using the bulk effective masses of PbTe that are given in Eqs. B.2 and B.3. In this fitting procedure, the total carrier concentration n was used as a fitting parameter, and then the value of n obtained from the fitting of the See-

[†]Sample MBE894 is a MBE grown $Pb_{1-x}Eu_xTe$ ($x \approx 0.08$) bulk (thick) film. The details of the growth conditions and the specifications of the other MBE grown $PbTe/Pb_{1-x}Eu_xTe$ superlattice samples are given in the letter from Dr. G. Springholz as shown in Figs. B-1 and B-2.

Dr.G.Springholz
JOHANNES KEPLER UNIVERSITÄT LINZ
INSTITUT FÜR HALBLEITERPHYSIK,O.UNIV.-PROF. DR. GÜNTHER BAUER
A-4040 Linz, Tel.(0732)2468/9600, Telefax (0732)2468822, e-mail: G.Springholz at hlphys.uni-linz.ac.at

Takaagi Koga
Room No. 13-3005
Massachusetts Institute of Technology
77 Massachusetts Avenue
Cambridge, MA 02139
USA

12.4.1998

Dear Takaagi,

Enclosed I send you the PbTe/PbEuTe MQW samples that I have grown for you. Unfortunately I initialy misinterpreted your requested sample parameters in the sense that I thought that you wanted a total 3D carrier density of 1 x 10^{18} cm^{-3}, instead of this density in the QWs only, so I had to repeat the sample growth. These new samples have this order of carrier density in the QWs assuming that all carriers measeured by Hall effect are located in the quantum wells. The reference PbEuTe sample I grew first had a lattice constant of 6.485 Å, which gives a Eu content of around 8 %, depending on which relationship one uses for the Eu content as a function of lattice constant. I have also made some x-ray diffraction measurements on the MQW samples, which yielded a superlattice period of around 420Å for the measured samples, i.e., a QW thickness of 20 Å. Also I have made quick Hall measurement to roughly determine the carrier density in the QWs taking a total QW thickness of 20Å times the period number of 120, which is the same for all MQW samples. The mobility of the MQW samples seems to be somewhat lower than the values of Ted Harman, and is certainly considerably lower than for pure PbTe layers. This is due to interface scattering and probably some intermixing at the interfaces since the carrier scattering by Eu impurities is rather strong. It is our experience that the mobility in wider quantum wells and/or for barrieres with lower Eu content is much better. Therefore, I have also grown two additional samples one with a 40 Å well width and one with a reduced Eu content in the barrier. Note also that I have intentionally Bi-doped only the PbTe QW region since otherwise for the wide PbEuTe barriers it mavbe not all carriers are transferred to the QW region. However, the PbEuTe barriers have some background doping level due to vacancy incorporation too, which however I have not determined independently. The thickness of the PbEuTe buffer is 1500 Å for all samples. Note also that for the last two samples, the Hall effect measurement yielded somewhat strange result, namely strongly current dependent carrier densities and mobilities and unusually high mobilities as room temperature. This could be due to contact problems. Possibly the Hall measurements are affected stronger by possible parallel conduction channels in the barriers, so I do not trust too much in these values. You have to check again with your Hall measurements. I will also have our technitian make a Hall bar structure from these two samples in order to check what's going on.

Figure B-1: Letter from Dr. G. Springholz about the sample specifications.

The samples I have prepared now are:

sample	d_{QW}	nominal x_{Eu}	$d_{Barrier}$	u_{300K} (cm^2/Vs)	n_{10K} (cm^{-3})
MBEG894 (BiTe=320°C)	-	~8 %	4.1 um(total thickness)	160	-3.3 x 10^{18}
MBEG902 (BiTe=350°C)	20 Å	~8 %	400 Å	265 77K: 2500	-7.1 x 10^{18} -5.1 x 10^{18}
MBEG908 (BiTe=320°C)	20 Å	~8 %	400 Å	300 77K: 2870	-2.0 x 10^{18} -2.2 x 10^{18}
MBEG909 (BiTe=300°C)	20 Å	~8 %	400 Å	288 77K: 3120	-2.0 x 10^{18} -7.1 x 10^{18}
MBEG910 (BiTe=280°C)	20 Å	~8 %	400 Å	215 77K: 2100	-1.1 x 10^{18} -4.7 x 10^{17}
MBEG914 (BiTe=300°C)	20 Å	~6 %	400 Å	2700 (?) 77K: contact problems	-1.7 x 10^{18}
MBEG915 (BiTe=300°C)	40 Å 20Å doped	~8 %	400 Å	2600 (?) 77K: contact problems	-1.3 x 10^{18}

If you have further questions, send me a message by e-mail.

Best regards, also to Millie and Gene,

Yours,

Gunther Springholz

Figure B-2: Letter from Dr. G. Springholz about the sample specifications (continued).

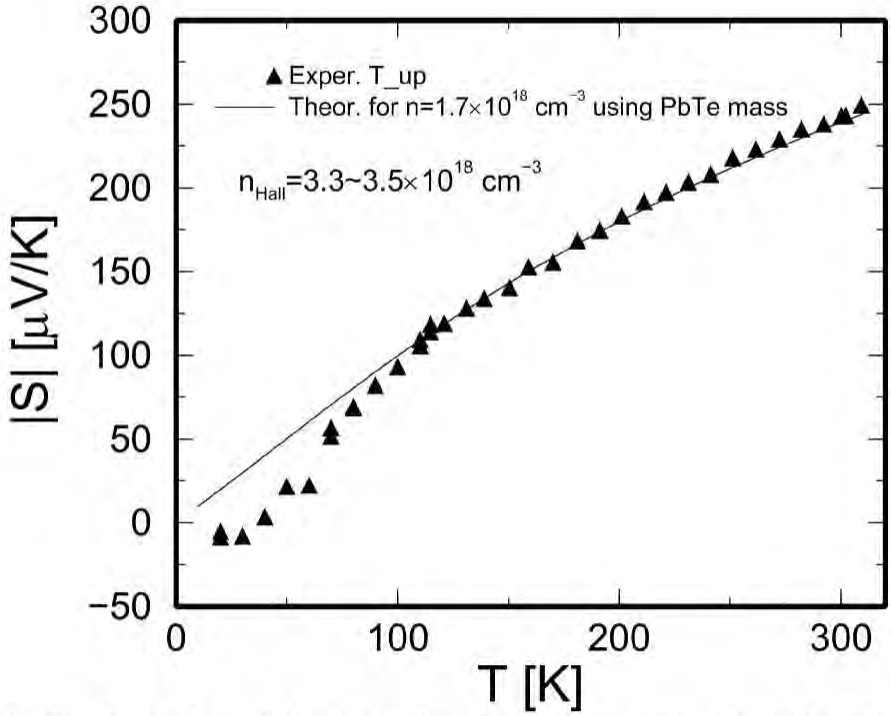

Figure B-3: The Seebeck coefficient as a function of temperature for a MBE-grown bulk (thick) $Pb_{1-x}Eu_xTe$ film ($x \approx 0.08$) sample (sample MBEG894).

beck data was compared with the Hall carrier concentration of the same sample that was obtained in a separate independent experiment. The best fit of the experimental Seebeck coefficient for sample MBEG894 was obtained for $n = 1.7 \times 10^{18}$ cm^{-3} as shown in Fig. B-3. The Hall carrier concentration for this sample is determined to be 3.5×10^{18} cm^{-3} at low temperature (~10 K) [measured by Koga] or 3.3×10^{18} cm^{-3} at room temperature (~300 K) [measured by Springholz]. This means that, assuming the actual carrier density is equal to the Hall carrier density, the density of states for $Pb_{1-x}Eu_xTe$ is about twice as large as that for PbTe. Thus, we assume the effective masses for $Pb_{1-x}Eu_xTe$ to be $2^{2/3}$ (= 1.5874) times as large as those for PbTe.

$$m_t(Pb_{1-x}Eu_xTe) = 1.5874 \times m_t(PbTe) \tag{B.4}$$

$$m_l(Pb_{1-x}Eu_xTe) = 1.5874 \times m_l(PbTe) \tag{B.5}$$

In calculating the bound state energy levels using the Krönig-Penney model, the following boundary conditions are used at the barrier-well interfaces, since the particle

current at the barrier-well interfaces has to be conserved:

$$\Psi_{\mathrm{W}} = \Psi_{\mathrm{B}}, \qquad \frac{1}{m_{\mathrm{W}}}\frac{d\Psi_{\mathrm{W}}}{dz} = \frac{1}{m_{\mathrm{B}}}\frac{d\Psi_{\mathrm{B}}}{dz} \tag{B.6}$$

which yields the Krönig-Penney energy dispersion relation

$$\frac{(Q/m_{\mathrm{B}})^2 - (K/m_{\mathrm{W}})^2}{2(Q/m_{\mathrm{B}})(K/m_{\mathrm{W}})}\sinh Qd_{\mathrm{B}} \sin Kd_{\mathrm{W}} + \cosh Qd_{\mathrm{B}} \cos Ka = \cos k(d_{\mathrm{W}} + d_{\mathrm{B}}) \tag{B.7}$$

where

$$K = \sqrt{2m_{\mathrm{W}}E}/\hbar \qquad \text{and} \qquad Q = \sqrt{2m_{\mathrm{B}}(\Delta E_c - E)}/\hbar. \tag{B.8}$$

In Eqs. B.7 and B.8, ΔE_c is the barrier height (conduction band offset), d_{W} is the quantum well thickness, d_{B} is the barrier layer thickness, m_{W} is the effective mass for the quantum well layer, and m_{B} is the effective mass for the barrier layer. Assuming that we have quantum confinement along the z-axis, the z-component of the effective mass tensor is obtained by the cross section of the ellipsoidal constant energy surface in the k_xk_z-(or k_yk_z-) plane for the quantum well and barrier layer materials, whereas the in-plane components of the effective mass tensor for the 2D quantum well are obtained by the projection of the 3D constant energy surfaces onto the plane of the quantum well (k_xk_y-plane). For the longitudinal subband in the (111) oriented PbTe/$Pb_{1-x}Eu_x$Te MQWs, the projection of the ellipsoidal constant energy surface to the (111) plane coincides with the cross section of the constant energy surface, yielding an isotropic in-plane mass component ($= m_t$) for the quantum well and the z-component of the effective mass equal to m_l. For the oblique subband in the (111) oriented PbTe/$Pb_{1-x}Eu_x$Te MQWs, the z-component of the effective mass tensor is given by

$$m_z^{-1} \equiv m_{\mathrm{W}}^{-1} = \frac{1}{9}\left(\frac{8}{m_{t(3\mathrm{D})}} + \frac{1}{m_{l(3\mathrm{D})}}\right), \tag{B.9}$$

whereas the in-plane components of the effective mass tensor are given by

$$m_x \equiv m_{t(2\mathrm{D})} = m_{t(3\mathrm{D})} \tag{B.10}$$

and

$$m_y \equiv m_{l(2D)} = \frac{8m_{l(3D)} + m_{t(3D)}}{9}. \tag{B.11}$$

We use the following empirical equation for the temperature dependent energy band gap for $Pb_{1-x}Eu_xTe$ [31] :

$$E_g(x,T) = 189.7\text{meV} + 0.48 \cdot T(\text{K})^2 \frac{1 - 7.56x}{T + 29} + 4480 \cdot x \tag{B.12}$$

and the conduction band offset ΔE_c (barrier height for the quantum well) is calculated using the relation [30]

$$\Delta E_c = 0.55 \Delta E_g. \tag{B.13}$$

The values for the total Seebeck coefficient and the Hall carrier concentration for the whole superlattice are calculated using the following equations (multiple carrier model). It is noted that the terms for the barrier layer have to be multiplied by the factor d_B/d_W to take into account the parallel conduction contribution from the barrier layers, yielding

$$S_{\text{total}} = \frac{S_{\text{longt}}\sigma_{\text{longt}} + S_{\text{obliq}}\sigma_{\text{obliq}} + S_{\text{barrier}}\sigma_{\text{barrier}}d_B/d_W}{\sigma_{\text{longt}} + \sigma_{\text{obliq}} + \sigma_{\text{barrier}}d_B/d_W} \tag{B.14}$$

for the Seebeck coefficient. For the Hall carrier density (low field limit), we obtain

$$n_{\text{Hall}} = \frac{(n_{\text{longt}}\mu_{\text{longt}} + n_{\text{obliq}}\mu_{\text{obliq}} + n_{\text{barrier}}\mu_{\text{barrier}}d_B/d_W)^2}{A + B + C}, \tag{B.15}$$

where

$$A = n_{\text{longt}}\mu_{\text{longt}}^2 r_{H\text{longt}}, \tag{B.16}$$

$$B = \frac{4K_{2D}}{(K_{2D}+1)^2} n_{\text{obliq}}\mu_{\text{obliq}}^2 r_{H\text{obliq}}, \tag{B.17}$$

$$C = \frac{3K_{3D}(K_{3D}+2)}{(2K_{3D}+1)^2} n_{\text{barrier}}\mu_{\text{barrier}}^2 r_{H\text{barrier}}d_B/d_W, \tag{B.18}$$

in which $K_{2D} = m_{l(2D)}/m_{t(2D)}$ and $K_{3D} = m_{l(3D)}/m_{t(3D)}$. In Eqs. B.15–B.18, $r_{H\text{longt}}$, $r_{H\text{obliq}}$ and $r_{H\text{barrier}}$ are Hall scattering factors for each subband/layer defined by

$r_H = \langle\tau\rangle^2/\langle\tau^2\rangle$. We further assume $r_{H\text{longt}} = r_{H\text{obliq}} = \frac{3K_{3D}(K_{3D}+2)}{(2K_{3D}+1)^2} r_{H\text{barrier}} = 1$ in the present calculations. The following equations for the Seebeck coefficient for single band materials, assuming the constant relaxation time approximation, are used to calculate the contribution from each subband and barrier layer to the total Seebeck coefficient. For the longitudinal and the oblique subbands

$$S_{2D} = -\frac{k_B}{e}\left(\frac{2F_1(\zeta^*)}{F_0(\zeta^*)} - \zeta^*\right), \tag{B.19}$$

and for the barrier layer

$$S_{3D} = -\frac{k_B}{e}\left(\frac{5F_{3/2}(\zeta^*)}{3F_{1/2}(\zeta^*)} - \zeta^*\right), \tag{B.20}$$

where the reduced chemical potential $\zeta^*(= \zeta/k_BT)$ is measured from each (sub)band edge.

B.3 IR transmission

The IR transmission experiments were carried out on all the samples provided (see Figs. B-4–B-10). For bulk $Pb_{1-x}Eu_xTe$ film (MBEG894), the optical absorption edge occurs near 5000 cm^{-1} (617 meV), corresponding to the Eu content $x \sim 0.085$ according to Eq. B.12. For quantum well samples (Figs. B-5–B-10), three distinct wavenumbers, each associated with optical transition of electrons from the valence band to the conduction band (1) for the longitudinal subband, (2) for the oblique subband and (3) for the $Pb_{1-x}Eu_xTe$ barrier layer, respectively, are found in the transmission spectra. These wavenumbers are compared to the corresponding energy gaps obtained in the theoretical calculation assuming a certain Eu composition x as described in the previous section. The Eu compositions x for which the best agreement between the experiment and theory is obtained are given below.

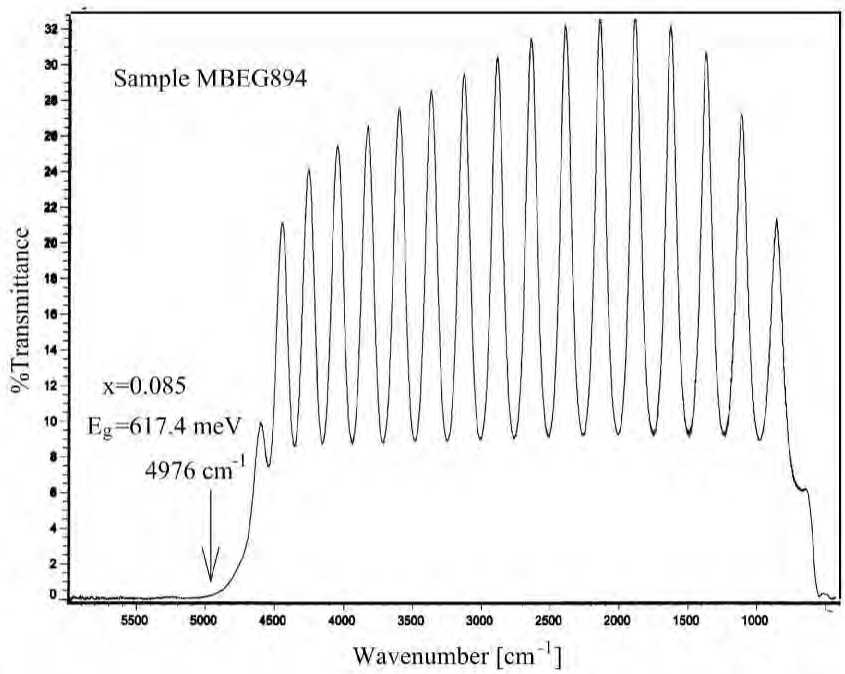

Figure B-4: IR transmission spectrum for a MBE-grown bulk (thick) $Pb_{1-x}Eu_xTe$ film ($x \approx 0.08$) sample (sample MBEG894). The value for the direct energy band gap shown in the figure ($E_g = 617.4$ meV) is obtained for $x = 0.085$ and $T = 300$ K using Eq. B.12.

Sample name	Eu composition x	see Fig.
MBEG902	0.08	B-5
MBEG908	0.092	B-6
MBEG909	0.09	B-7
MBEG910	0.095	B-8
MBEG914	0.065	B-9
MBEG915	0.08	B-10

These results are also consistent with the observations of the spacing of the Fabry-Perot interference fringes in the spectra [32]. The spacing of Fabry-Perot interference fringes in Figs. B-5–B-10 implies the highest refractive indices for samples MBEG902, MBEG914 and MBEG915 whose Eu contents x are among the lowest of all the samples, and the lowest refractive index for sample MBEG910 whose Eu content is among the highest. The refractive indices for samples MBEG909 and MBEG908 are found to be slightly higher than that for MBE910, consistent with a slightly lower Eu content

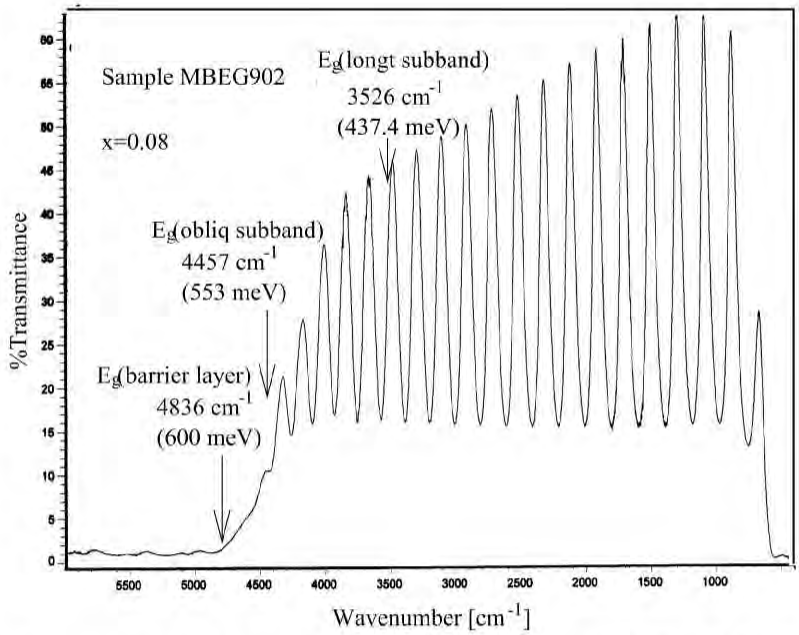

Figure B-5: IR transmission spectrum for a (111) oriented PbTe(20 Å)/$Pb_{1-x}Eu_xTe$(400 Å) multiple-quantum-well sample (MBEG902). The values of the optical energy band gaps given in the figure are obtained by the Krönig-Penney model using Eqs. B.12 and B.13 to calculate the conduction and valence band offsets at $T = 300$ K, where the value of x (Eu content) used in the calculation is also given in the figure ($x = 0.08$).

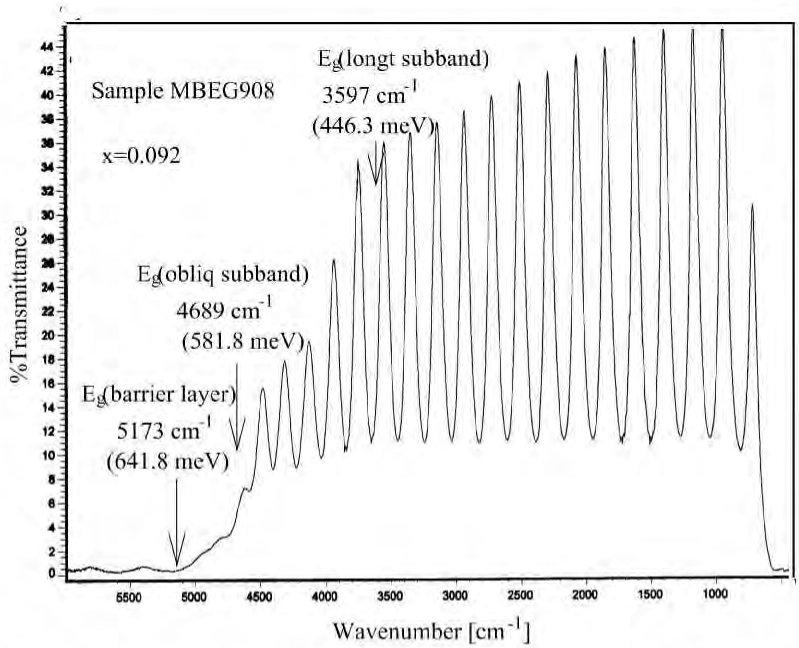

Figure B-6: IR transmission spectrum for a (111) oriented PbTe(20 Å)/$Pb_{1-x}Eu_xTe$(400 Å) multiple-quantum-well sample (MBEG908). The values of the optical energy band gaps given in the figure are obtained by the Krönig-Penney model using Eqs. B.12 and B.13 to calculate the conduction and valence band offsets at $T = 300$ K, where the value of x (Eu content) used in the calculation is also given in the figure ($x = 0.092$).

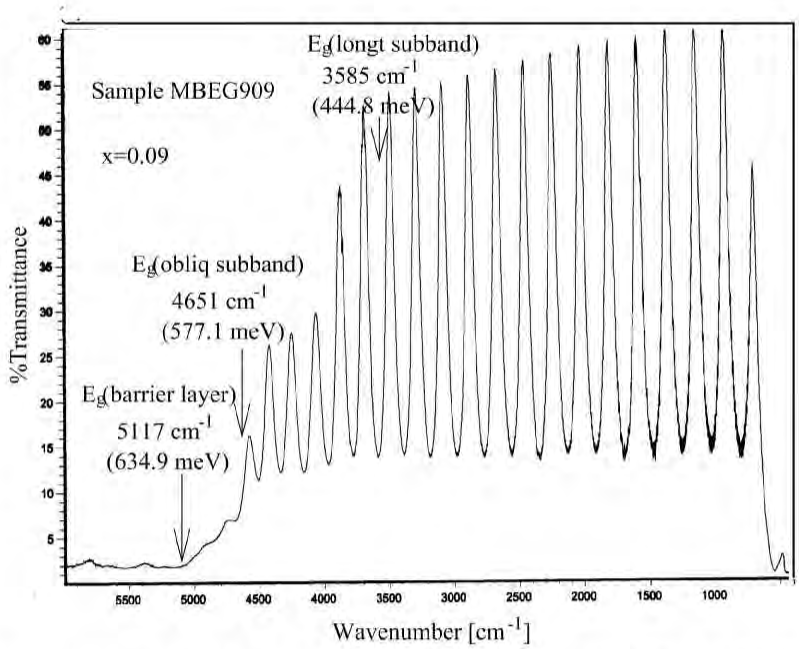

Figure B-7: IR transmission spectrum for a (111) oriented PbTe(20 Å)/$Pb_{1-x}Eu_xTe$(400 Å) multiple-quantum-well sample (MBEG909). The values of the optical energy band gaps given in the figure are obtained by the Krönig-Penney model using Eqs. B.12 and B.13 to calculate the conduction and valence band offsets at $T = 300$ K, where the value of x (Eu content) used in the calculation is also given in the figure ($x = 0.09$).

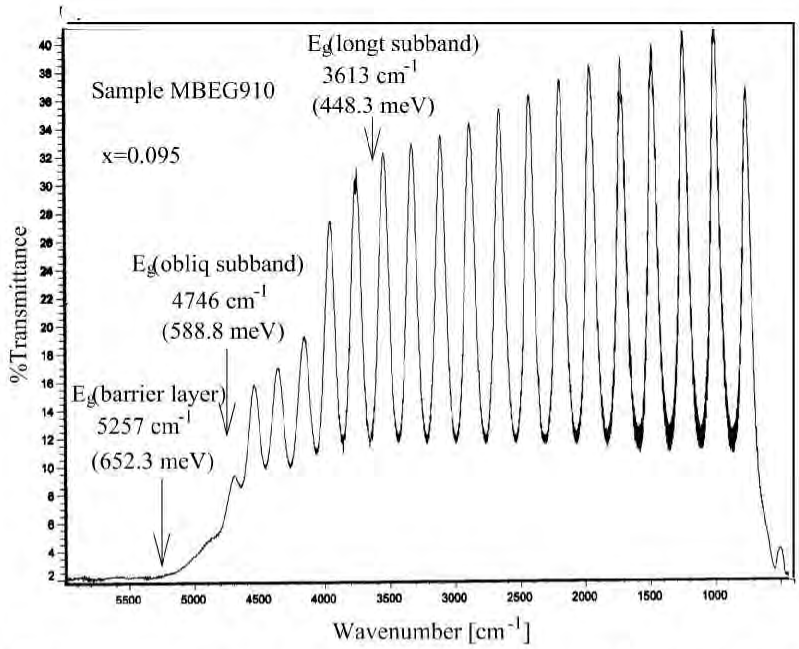

Figure B-8: IR transmission spectrum for a (111) oriented PbTe(20 Å)/$Pb_{1-x}Eu_xTe$(400 Å) multiple-quantum-well sample (MBEG910). The values of the optical energy band gaps given in the figure are obtained by the Krönig-Penney model using Eqs. B.12 and B.13 to calculate the conduction and valence band offsets at $T = 300$ K, where the value of x (Eu content) used in the calculation is also given in the figure ($x = 0.095$).

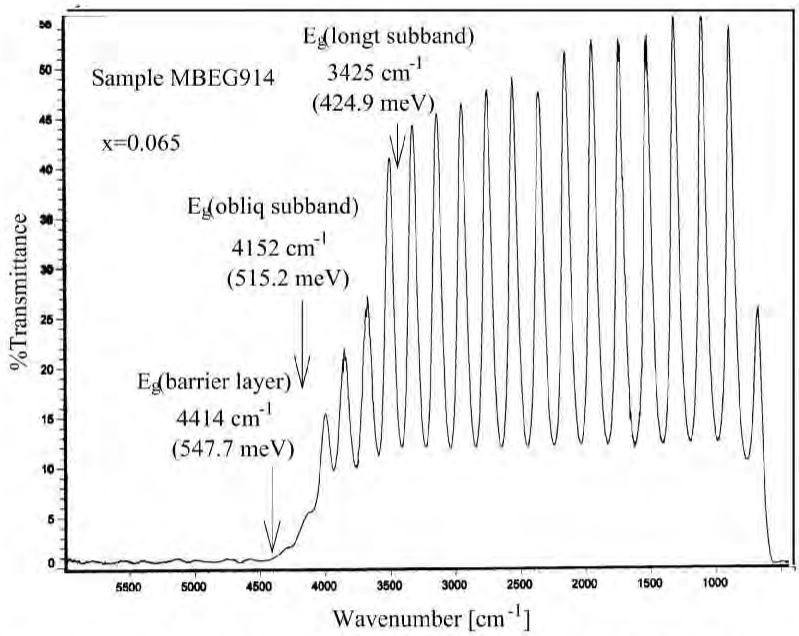

Figure B-9: IR transmission spectrum for a (111) oriented PbTe(20 Å)/$Pb_{1-x}Eu_xTe$(400 Å) multiple-quantum-well sample (MBEG914). The values of the optical energy band gaps given in the figure are obtained by the Krönig-Penney model using Eqs. B.12 and B.13 to calculate the conduction and valence band offsets at $T = 300$ K, where the value of x (Eu content) used in the calculation is also given in the figure ($x = 0.065$).

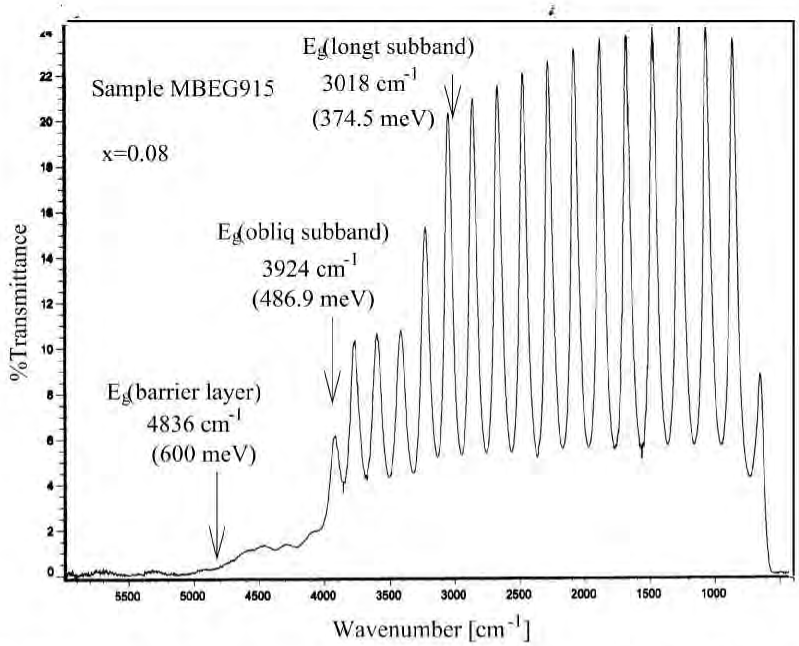

Figure B-10: IR transmission spectrum for a (111) oriented PbTe(20 Å)/$Pb_{1-x}Eu_xTe$(400 Å) multiple-quantum-well sample (MBEG915). The values of the optical energy band gaps given in the figure are obtained by the Krönig-Penney model using Eqs. B.12 and B.13 to calculate the conduction and valence band offsets at $T = 300$ K, where the value of x (Eu content) used in the calculation is also given in the figure ($x = 0.08$).

x for these samples than for MBEG910.

B.4 Hall carrier concentration

Hall coefficient measurements as a function of temperature were carried out for all the quantum well samples. For the bulk $Pb_{1-x}Eu_xTe$ sample (MBEG894), the experimental data were obtained only at low temperature (~10 K) due to the loose contacts during the measurement. The typical samples size is 3×3 mm^2, and a magnetic field of 0.3 T was utilized for these measurements. The pure Hall voltage was separated from the resistive voltage drop by switching the magnetic field between +0.3 T and −0.3 T at each temperature of measurement. Typically, an electrical current of 1–10 μA was used in these measurements.

Shown in Fig. B-11 is the measured Hall carrier density as a function of temperature for samples MBEG902, 908, 909 and 910. The results for samples MBEG914 and 915 are given in Fig. B-24 and Fig. B-26, respectively. It is found that the Hall carrier concentration for all the samples (except for the $Pb_{1-x}Eu_xTe$ bulk sample MBEG894) varies as a function of temperature. In most cases, the Hall carrier density is found to increase above ~ 170 K (MBEG 902, 909, 910, 914 and 915), but in one case (MBEG908), the Hall density decreases with increasing temperature. These apparent changes in Hall density as a function of temperature are not fully consistent with the change in the charge distribution among the three (sub)bands (longitudinal- and oblique- subbands and barrier layer) provided that our theoretical model for the Hall carrier concentration is valid.

The Hall carrier mobilities are shown as a function of temperature in Figs. B-12 and B-13. The Hall mobility for the sample MBEG910 (~2000 cm^2/V·s below 70 K and ~250 cm^2/V·s at room temperature) is found to be the lowest of all the samples in spite of its low carrier concentration, probably because of the large interface scattering due to its rather high Eu content (x = 0.095) for the barrier layer. The highest mobility is found in sample MBEG914 at low temperature (<150 K), consistent with the quantum confinement effect. This sample had the lowest Eu content (x = 0.065)

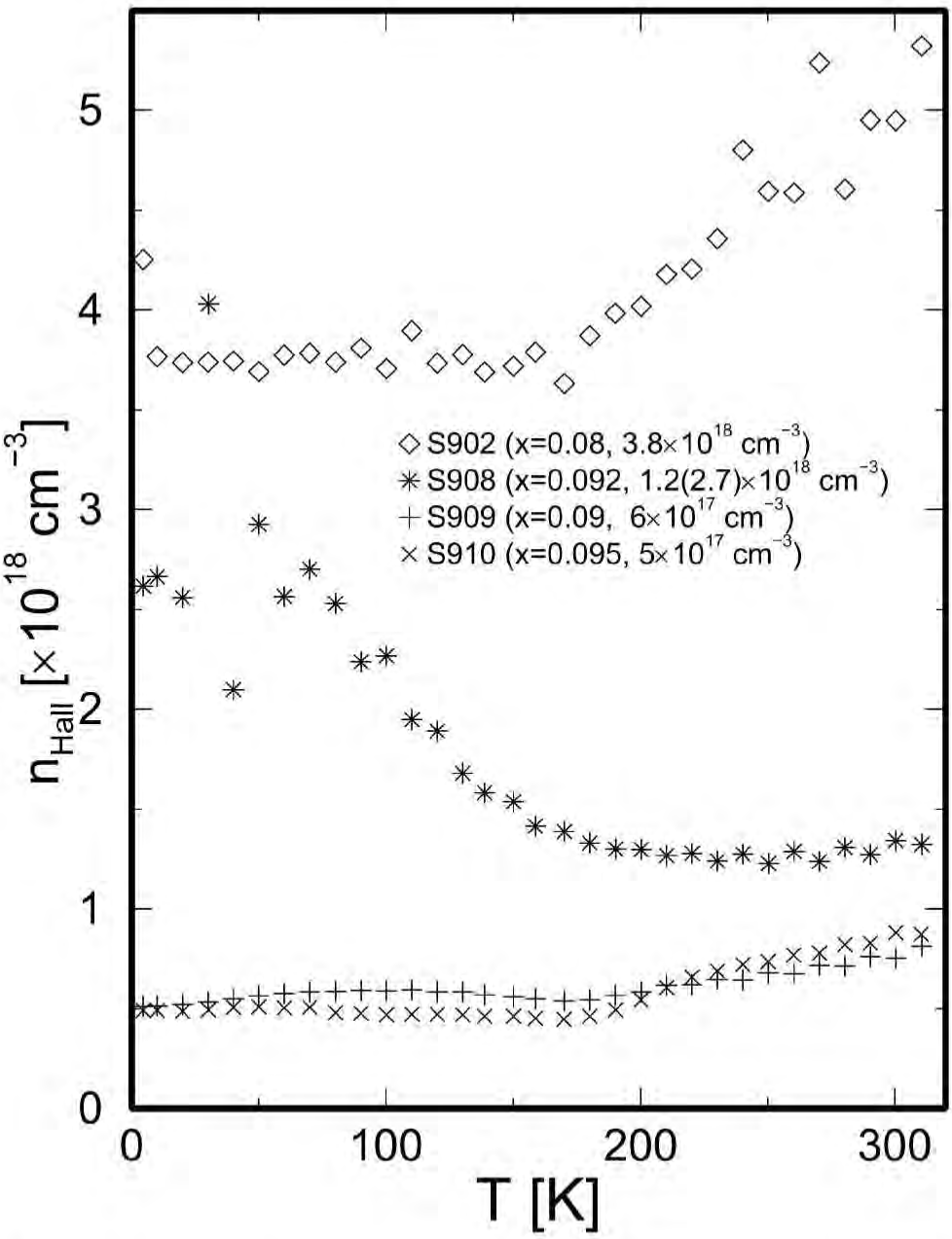

Figure B-11: Hall carrier concentration as a function of temperature for various (111) oriented PbTe(20 Å)/$Pb_{1-x}Eu_xTe$(400 Å) multiple-quantum-well samples.

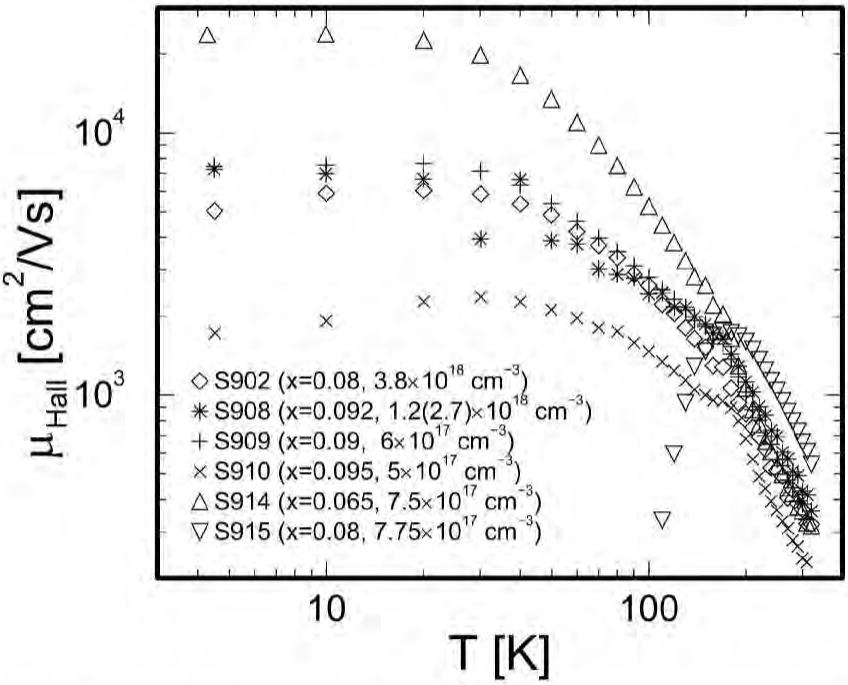

Figure B-12: Hall carrier mobility as a function of temperature for various (111) oriented PbTe(20 Å)/$Pb_{1-x}Eu_xTe$(400 Å) multiple-quantum-well samples.

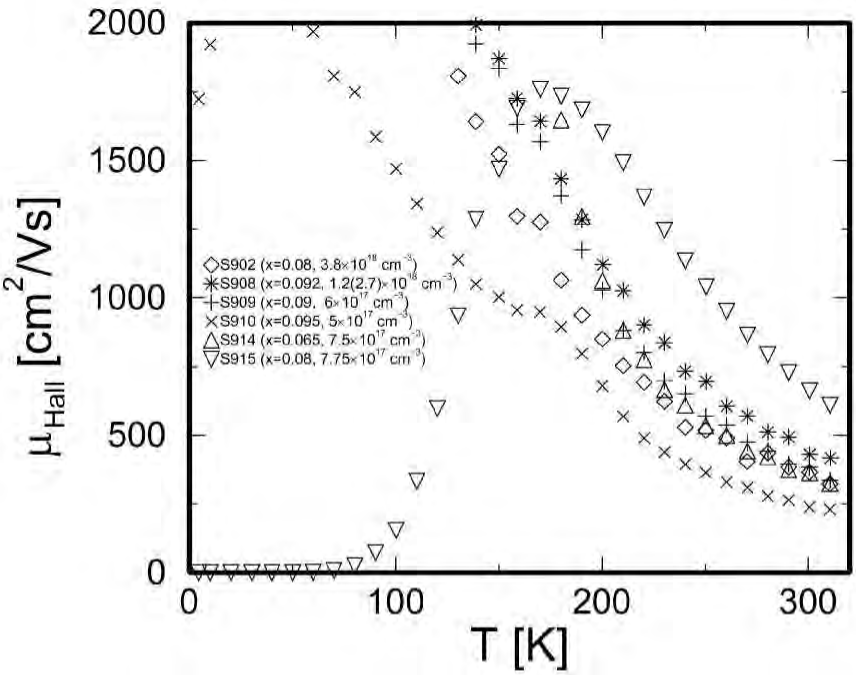

Figure B-13: Hall carrier mobility as a function of temperature for various (111) oriented PbTe(20 Å)/$Pb_{1-x}Eu_xTe$(400 Å) multiple-quantum-well samples (magnified scale).

in the barrier layer. We find a mobility >20000 $cm^2/V{\cdot}s$ for this sample below 20 K. It is estimated that more than 97 % of the carriers are bound to the longitudinal subband for this sample below 100 K. On the other hand, the Hall mobility for this sample at room temperature is found to be rather low (~270 $cm^2/V{\cdot}s$), despite its high mobility at low temperature. This is probably because there are a rather large number of carriers occupying the 3D energy band for the barrier layer at room temperature for this sample. We estimate, in our model, that about 57 % of the total carriers are located in the barrier layer at room temperature in this sample.[†]

Rather peculiar behavior is observed for sample MBEG915. For this sample, the Hall mobility is among the highest of all the samples above 180 K. However, below 170 K, the Hall mobility starts to decrease with decreasing temperature reaching virtually zero mobility at 60 K. This zero mobility is found to be connected to the large (increasing) values of the electrical resistivity at low temperature as shown in Fig. B-14. The Hall carrier concentration remains finite at low temperatures for this sample as shown in Fig. B-26. The increased resistivity at low temperature was also observed during the measurement of the Seebeck coefficient, where the observed ΔV vs. ΔT data at low temperatures ($T < 70$ K) were found to be rather noisy due to the large resistance across the sample (sample MBEG915).

B.5 Seebeck coefficient

B.5.1 MBEG910

Shown in Fig. B-15 is the Seebeck coefficient as a function of temperature for sample MBEG910. The carrier concentration within the quantum well for this sample is determined to be $4.8{\times}10^{17}$ cm^{-3} from the Hall coefficient measurement at low temper-

[†]This conclusion may have to be revised according to the results of the more elaborate theoretical modeling that is performed in Chapter 3. In Chapter 3, we find that polar optical phonon scattering is more effective in scattering the carriers in the oblique subband than in scattering the carriers in the longitudinal subband. Therefore, the observed decrease in the values of the carrier mobility may be attributed to the increasing occupation of the oblique subband by the conduction carriers, where the conduction carrier are more vulnerable to polar optical phonon scattering.

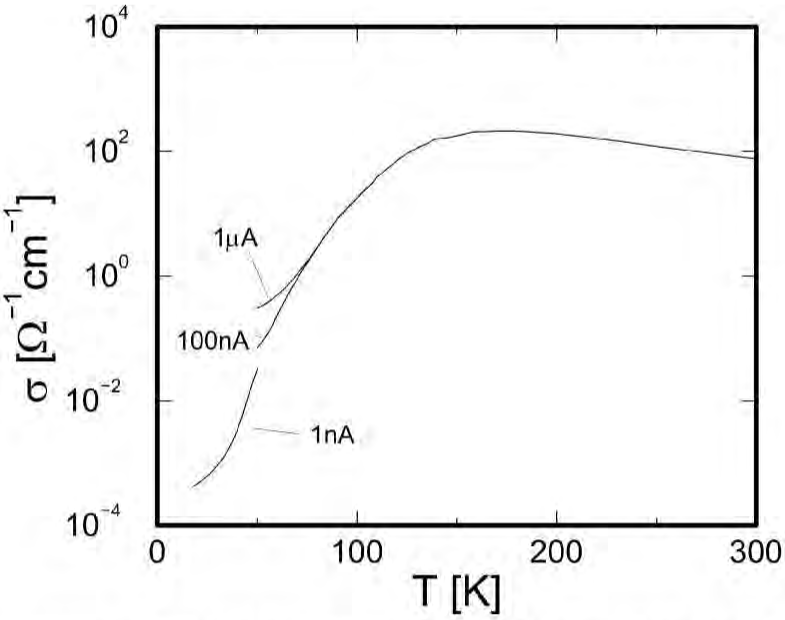

Figure B-14: Electrical conductivity as a function of temperature for a (111) oriented PbTe(20 Å)/$Pb_{1-x}Eu_xTe$(400 Å) multiple-quantum-well sample (MBEG915).

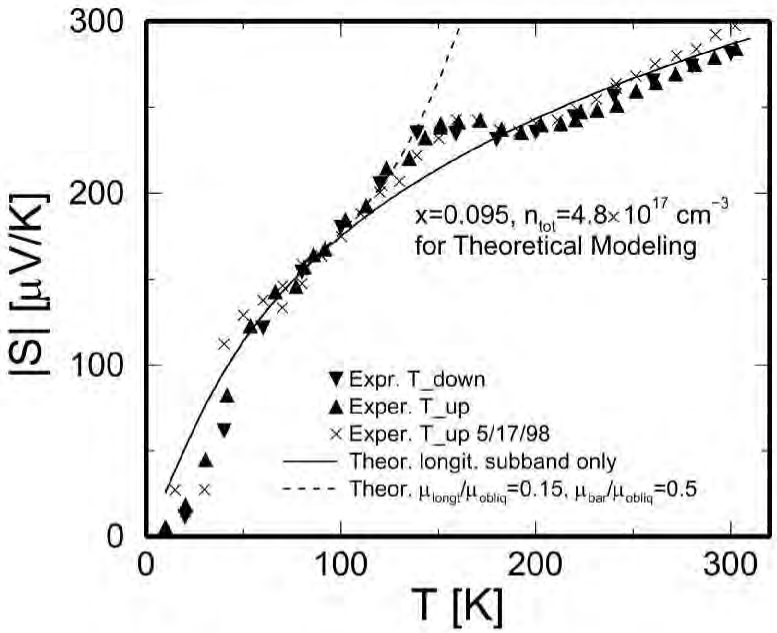

Figure B-15: The Seebeck coefficient as a function of temperature for a (111) oriented PbTe(20 Å)/$Pb_{1-x}Eu_xTe$(400 Å) multiple-quantum-well sample (MBEG910).

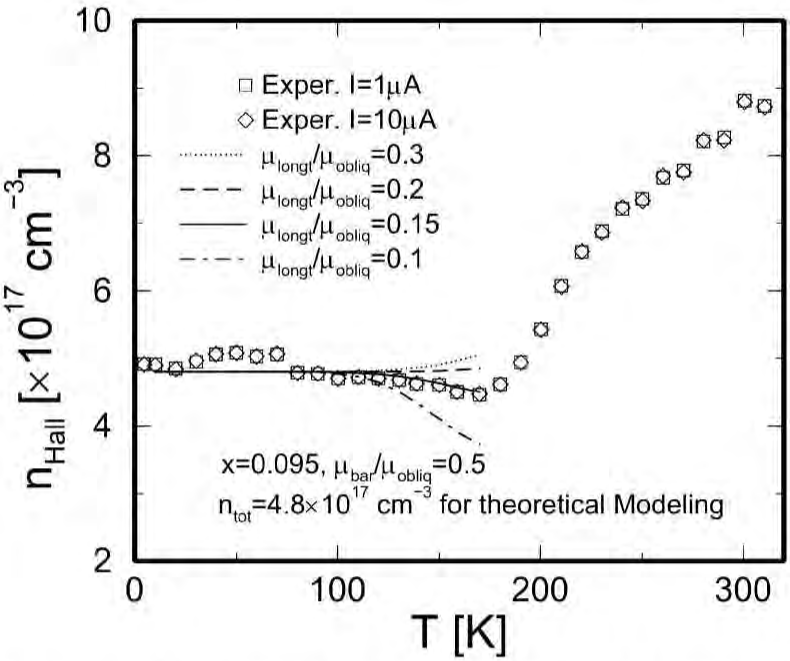

Figure B-16: Hall carrier density as a function of temperature for a (111) oriented PbTe(20 Å)/$Pb_{1-x}Eu_xTe$(400 Å) multiple-quantum-well sample (MBEG910).

ature (see Fig. B-16). We find a small bump in the Seebeck coefficient near 150 K and a small dip in Hall carrier density near 170 K. These bump and dip features may be related to the existence of the oblique subband (see below), but, up to now, we don't have a full explanation for this anomaly. The general behavior of the Seebeck coefficient as a function of temperature is best explained, if we assume that there exists only a longitudinal subband in the quantum well (single subband approximation) [see the solid line in Fig. B-15]. However, this assumption neither explains the origin of the bump, nor the behavior of the Hall carrier concentration above 200 K (see Fig. B-16). Up to now, we have no explanation for this increasing Hall carrier concentration with increasing temperature above 200 K. A similar behavior is also observed for samples MBEG909, 902 and 914 (see Figs. B-18, B-22 and B-24). The low temperature side of the bump in the Seebeck coefficient and the low temperature side of the dip in the Hall carrier concentration are modeled assuming the existence of all three (sub)bands in the model. In this case, we set the total carrier density to be $n_{\rm tot} = 4.8\times10^{17}$ cm^{-3} and allow the distribution of the carriers to change among these three (sub)bands as a

function of temperature according to the Fermi-Dirac distribution function.[†] We find that the oblique subband starts being occupied above 100 K. In Fig. B-16 we show a few modeling results for the Hall carrier mobility as a function of temperature (for $\mu_{\rm lon}/\mu_{\rm obliq} = 0.1$, 0.15, 0.2, 0.3 and $\mu_{\rm bar}/\mu_{\rm obliq} = 0.5$, since the Hall mobility for the $Pb_{1-x}Eu_xTe$ bulk sample MBEG894 is typically half of the Hall mobilities for other quantum well samples near room temperature), among which $\mu_{\rm longt}/\mu_{\rm obliq} = 0.15$ agrees best with the experimental results. In Fig. B-15, we show the modeling results for the Seebeck coefficient for $\mu_{\rm longt}/\mu_{\rm obliq} = 0.15$ and $\mu_{\rm B}/\mu_{\rm obl} = 0.5$ (dashed curve). Thus, the simultaneous modeling of the Seebeck coefficient and Hall carrier concentration is possible below 140 K assuming $\mu_{\rm longt}/\mu_{\rm obliq} = 0.15$.[‡]

B.5.2 MBEG909

The Seebeck coefficient and Hall carrier concentration for sample MBEG909 are shown in Figs. B-17 and B-18, respectively, as a function of temperature. The Hall carrier concentration of this sample is determined to be 5 to 6×10^{17} cm^{-3} at low temperature. The theoretical calculation of the Seebeck coefficient, assuming only the longitudinal subband, is shown by the solid curve in Fig. B-17 for $n_{\rm tot} = 6\times10^{17}$ cm^{-3}. The agreement between the experiment and model calculation is good up to ~130 K, where carriers are predominantly located in the longitudinal subband. Above 140 K, the experimental Seebeck coefficient is higher than the model calculation that was performed including only the longitudinal subband. This is because a large number

[†]In this report, we assumed that the total carrier density $n_{\rm tot}$ that is defined by the following equation is assumed to be constant with temperature considering the charge conservation:

$$n_{\rm tot} = n_{\rm longt} + n_{\rm obliq} + n_{\rm B} \times \frac{d_{\rm B}}{d_{\rm W}},$$

where $n_{\rm longt}$, $n_{\rm obliq}$, and $n_{\rm B}$ are the carrier densities that are attributed to the longitudinal subband, to the oblique subband, and to the barrier layers. The reason we need the factor $\frac{d_{\rm B}}{d_{\rm W}}$ in the above equation is that $n_{\rm B}$ is calculated using the thickness of the barrier layers ($d_{\rm B}$), whereas $n_{\rm longt}$ and $n_{\rm obliq}$ are calculated using the thickness of the quantum well layers ($d_{\rm W}$).

[‡]In Chapter 3, we find that the polar optical phonon scattering, which is the dominant scattering mechanism for the oblique subband, has an effect of increasing the value of the Seebeck coefficient relative to those predicted in the constant relaxation time approximation. Therefore, the actual value of $\mu_{\rm longt}/\mu_{\rm obliq}$, considering the details of the scattering mechanisms, should be larger than the value given here (i.e., $\mu_{\rm longt}/\mu_{\rm obliq} > 0.15$).

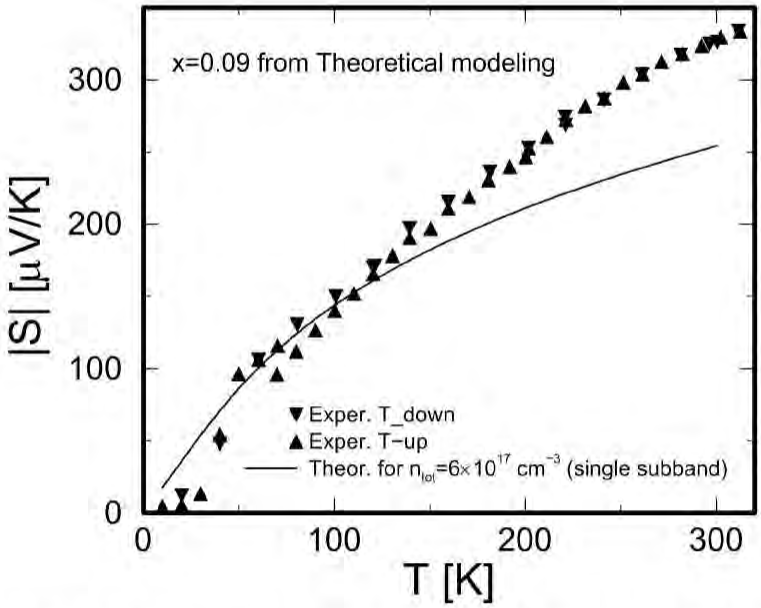

Figure B-17: The Seebeck coefficient as a function of temperature for a (111) oriented PbTe(20 Å)/$Pb_{1-x}Eu_xTe$(400 Å) multiple-quantum-well sample (MBEG909).

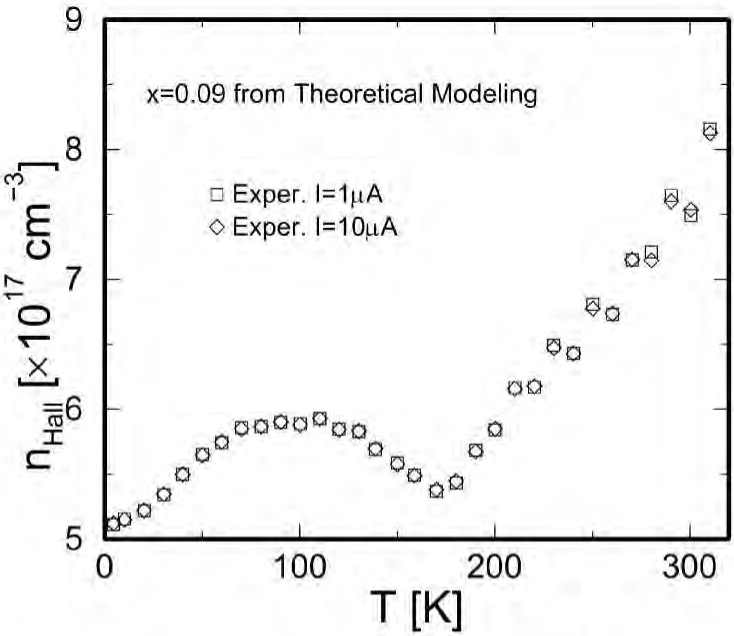

Figure B-18: Hall carrier density as a function of temperature for a (111) oriented PbTe(20 Å)/$Pb_{1-x}Eu_xTe$(400 Å) multiple-quantum-well sample (MBEG909).

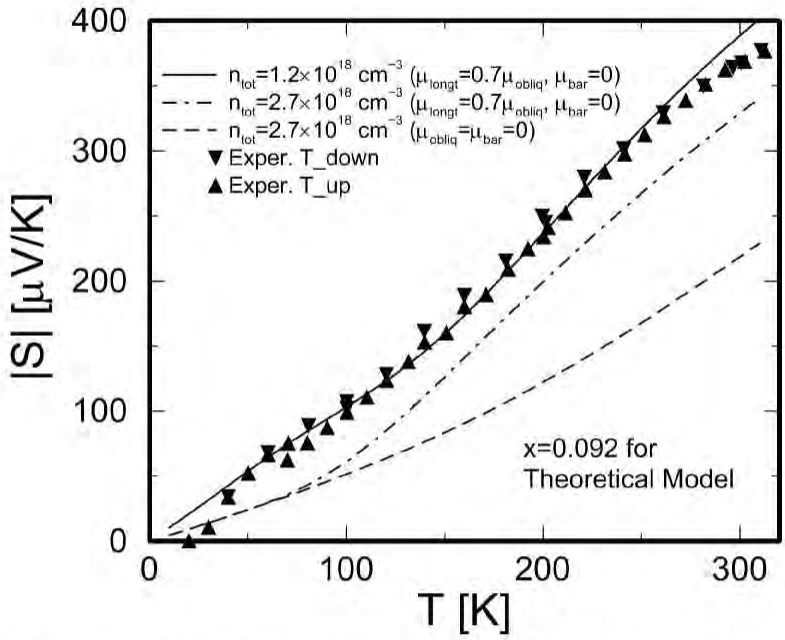

Figure B-19: The Seebeck coefficient as a function of temperature for a (111) oriented PbTe(20 Å)/$Pb_{1-x}Eu_xTe$(400 Å) multiple-quantum-well sample (MBEG908).

of carriers start occupying the oblique subband at this temperature (and the barrier layer at even higher temperature). We found that the simultaneous fitting of the Seebeck coefficient and the Hall carrier concentration is difficult with our three (sub)band theoretical model above 150 K.

B.5.3 MBEG908

The temperature dependence of the Seebeck coefficient and Hall carrier concentration for sample MBEG908 are shown in Figs. B-19 and B-20, respectively, as a function of temperature. The Hall carrier concentration of this sample is found to have a rather peculiar behavior as a function of temperature (see Fig. B-20) compared to those for the other samples. The Hall carrier concentration is determined to be 2.7×10^{18} cm^{-3} and 1.2×10^{18} cm^{-3}, at low temperatures (below 70 K) and at high temperatures (above 180 K), respectively. Therefore, we have made calculations of the Seebeck coefficient both for $n_{\rm tot} = 2.7\times10^{18}$ cm^{-3} and for $n_{\rm tot} = 1.2\times10^{18}$ cm^{-3}, using our three (sub)band model. The best result is obtained for $n_{\rm tot} = 1.2\times10^{18}$ cm^{-3}, assuming $\mu_{\rm longt}/\mu_{\rm obliq} = 0.7$ and $\mu_{\rm B} = 0$ (see Fig. B-19). The modeling result for the

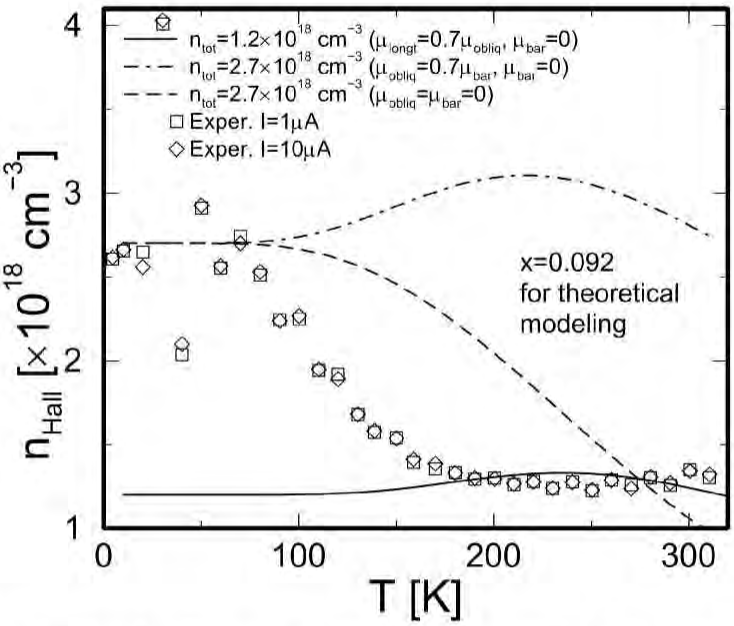

Figure B-20: Hall carrier density as a function of temperature for a (111) oriented PbTe(20 Å)/$Pb_{1-x}Eu_xTe$(400 Å) multiple-quantum-well sample (MBEG908).

Hall carrier concentration with the same assumptions agrees with the experimental result only above 180 K. The theoretical calculation for $n_{\rm tot} = 2.7\times10^{18}$ cm^{-3} agrees poorly with experimental results for any assumptions for the μ's (see Figs. B-19 and B-20).

B.5.4 MBEG902

The Seebeck coefficient and Hall carrier concentration for sample MBEG902 are shown in Figs. B-21 and B-22, respectively, as a function of temperature. For this sample, the carrier concentration is about 3.8×10^{18} cm^{-3} at low temperature (below 170 K) (see Fig. B-22). Therefore, the model calculation of the Seebeck coefficient was carried out for this carrier concentration (Fig. B-21). The ratio of the mobilities between the barrier layer and the oblique subband ($\mu_{\rm B}/\mu_{\rm obliq}$) is set to be 0.5 since the Hall mobility for the bulk $Pb_{1-x}Eu_xTe$ film (MBEG894) was typically half the values of the Hall carrier mobility for the quantum well samples at room temperature (see Fig. B-2). At low temperature, any specific assumptions for the ratio of the mobilities between the barrier layer and the oblique subband ($\mu_{\rm B}/\mu_{\rm obliq}$) have negligible effect

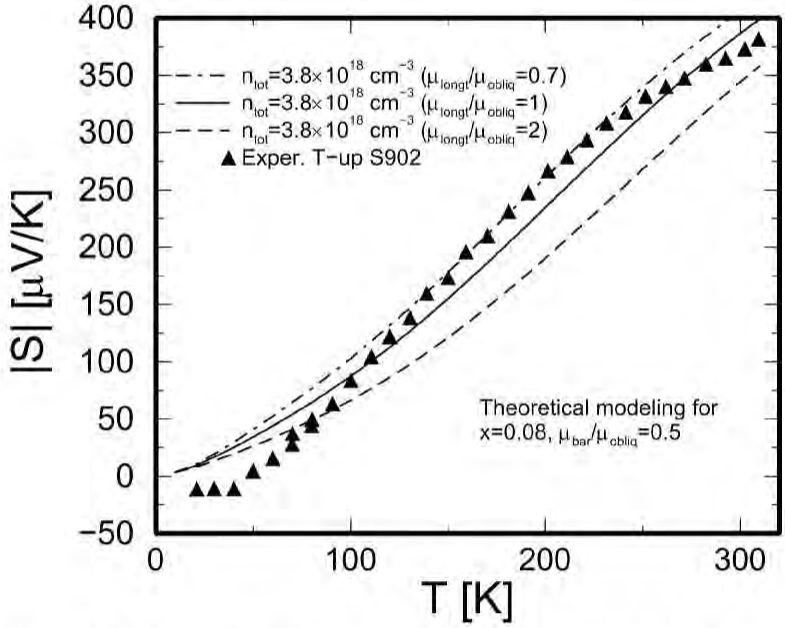

Figure B-21: The Seebeck coefficient as a function of temperature for a (111) oriented PbTe(20 Å)/$Pb_{1-x}Eu_xTe$(400 Å) multiple-quantum-well sample (MBEG902).

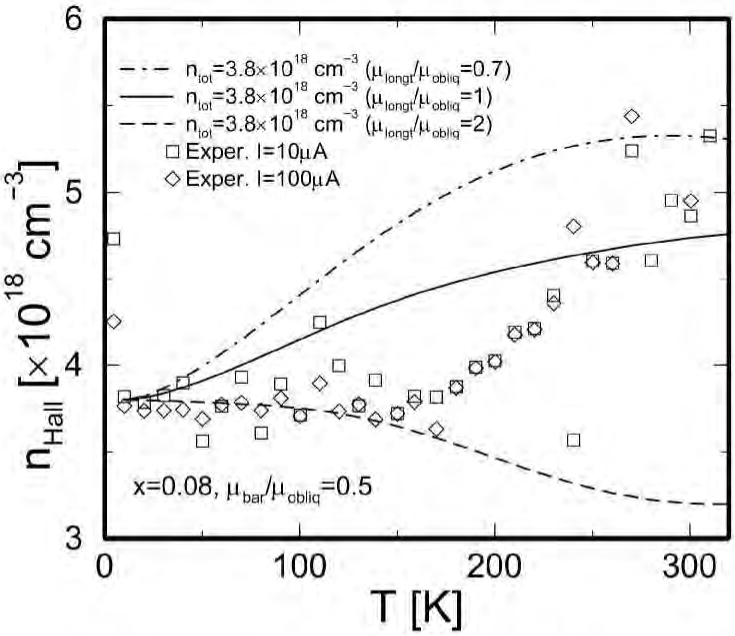

Figure B-22: Hall carrier density as a function of temperature for a (111) oriented PbTe(20 Å)/$Pb_{1-x}Eu_xTe$(400 Å) multiple-quantum-well sample (MBEG902).

on the final modeling results of the Seebeck coefficient or Hall carrier concentration, since the carrier occupation at the barrier layer becomes very small at low temperature. In Fig. B-21, we show the results of three model calculations each assuming $\mu_{\rm longt}/\mu_{\rm obliq} = 0.7$, 1, and 2, respectively. Probably, what is happening here is that at low temperature, the ratio $\mu_{\rm longt}/\mu_{\rm obliq}$ is about 2, which is consistent with the modeling result of the Hall carrier concentration, and this ratio decreases with increasing temperature reaching a value of about 0.7 at ~150 K.† Then, this value will again increase at high temperature (above 230 K). However, this observation of the ratio of mobilities between the longitudinal and the oblique subbands is not consistent with the result for the Hall carrier concentration above 100 K (see Fig. B-22).

B.5.5 MBEG914

The Seebeck coefficient and Hall carrier concentration for sample MBEG914 are shown in Figs. B-23 and B-24, respectively, as a function of temperature. The general behavior of the Seebeck coefficient and Hall carrier concentration is somewhat similar to the results for sample MBEG910, despite the differences in the carrier concentration and the Eu content x between these two samples. In the Seebeck coefficient for sample MBEG914, there is a change of slope around 140 K instead of a bump which was found for sample MBEG910. In the Hall carrier concentration, there is also a dip around 150 K, and the Hall carrier concentration increases with increasing temperature above 150 K as we found for sample MBEG910. The Hall carrier concentration at low temperature (around 50 K) is determined to be 7.5×10^{17} cm^{-3}. Therefore, the theoretical calculation of the Seebeck coefficient is carried out for this carrier concentration. Assuming the same mobilities for the longitudinal- and oblique-subbands and

†The poor agreement between the experimentally determined Seebeck coefficients and the theoretically predicted Seebeck coefficients based on the constant relaxation time approximation here, is somewhat similar to what we observe in Chapters 2 and 3 for the PbTe(20 Å)/$Pb_{1-x}Eu_xTe$(400 Å) MQW sample that was grown by Dr. T. C. Harman at MIT Lincoln Lab. (sample T-225). Therefore, the physical origins for the apparent temperature dependence of the value of the ratio $\mu_{\rm longt}/\mu_{\rm obliq}$, that is obtained by fitting the experimental results using the constant relaxation time approximation, should be resolved by the detailed theoretical modeling including specific scattering mechanisms (longitudinal acoustic phonon and polar optical phonon) as we discuss in Chapter 3.

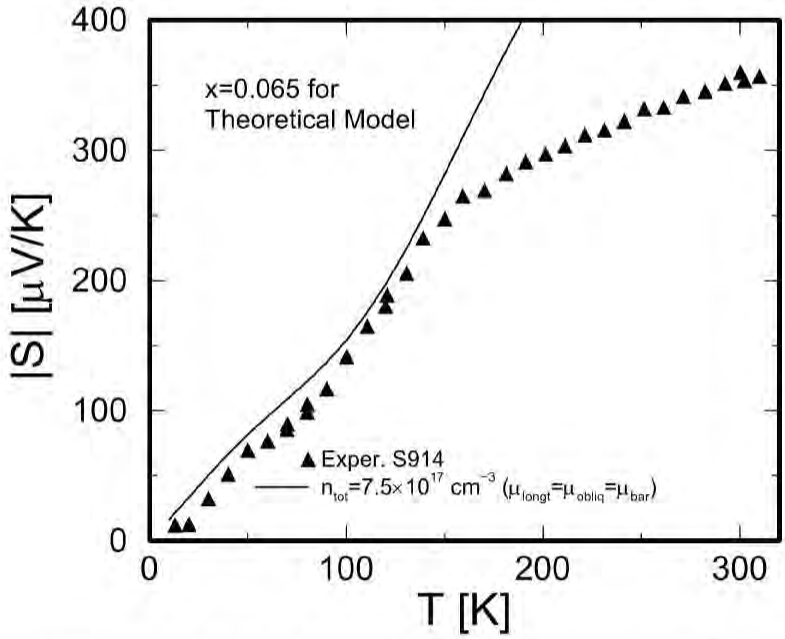

Figure B-23: The Seebeck coefficient as a function of temperature for a (111) oriented PbTe(20 Å)/$Pb_{1-x}Eu_xTe$(400 Å) multiple-quantum-well sample (MBEG914).

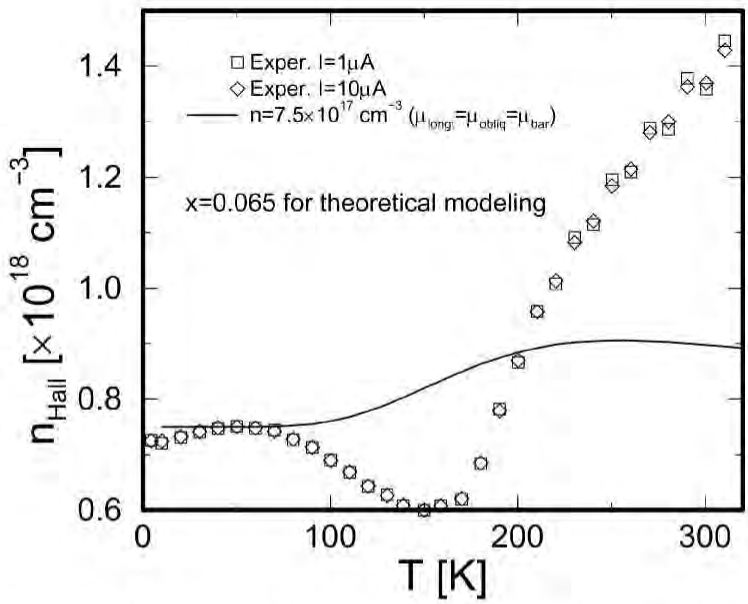

Figure B-24: Hall carrier density as a function of temperature for a (111) oriented PbTe(20 Å)/$Pb_{1-x}Eu_xTe$(400 Å) multiple-quantum-well sample (MBEG914).

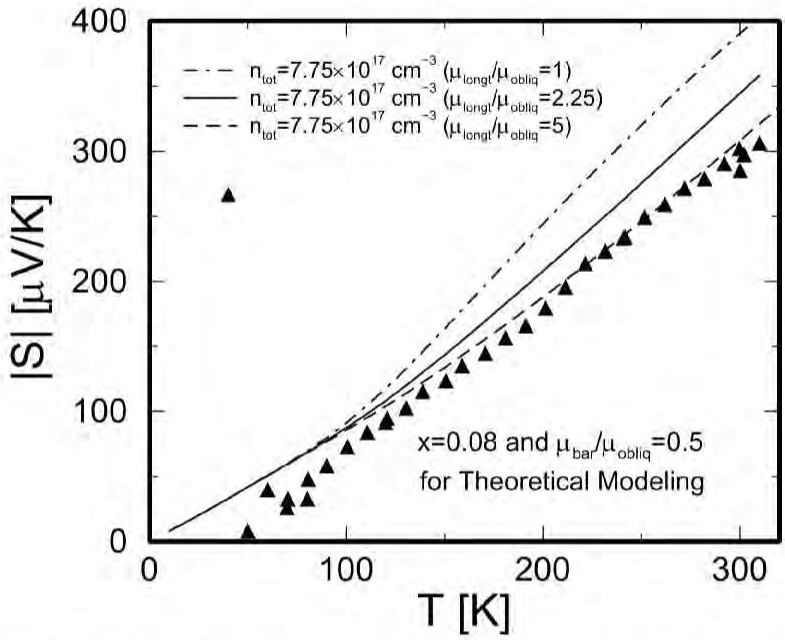

Figure B-25: The Seebeck coefficient as a function of temperature for a (111) oriented PbTe(20 Å)/$Pb_{1-x}Eu_xTe$(400 Å) multiple-quantum-well sample (MBEG915).

for the barrier layer, the experimentally observed Seebeck coefficient is successfully modeled below 130 K. However, the modeling results for the Hall carrier concentration with the same assumptions as in the calculation of the Seebeck coefficient are not completely consistent with the experimental results above 100 K (see Fig. B-24).

B.5.6 MBEG915

The Seebeck coefficient and Hall carrier concentration for sample MBEG915 are shown in Figs. B-25 and B-26, respectively, as a function of temperature. For this sample, the Hall carrier concentration above 130 K (up to 310 K) is best modeled using $n_{\rm tot} = 7.75{\times}10^{17}$ cm^{-3}, $\mu_{\rm longt}/\mu_{\rm obliq} = 2.25$ and $\mu_{\rm B}/\mu_{\rm obliq} = 0.5$. Therefore, we determine the carrier concentration of this sample to be $n_{\rm tot} = 7.75{\times}10^{17}$ cm^{-3}. We have also calculated the Seebeck coefficient as a function of temperature for $n_{\rm tot} = 7.75{\times}10^{17}$ cm^{-3}. We have made three calculations using $\mu_{\rm longt}/\mu_{\rm obliq} = 1$, 2.25, and 5, but we have always assumed $\mu_{\rm B}/\mu_{\rm obliq} = 0.5$. These results are plotted in Fig. B-25 together with the experimental results. We find that the theoretical results assuming $\mu_{\rm longt}/\mu_{\rm obliq} = 5$ agree with the experimental result best of all the

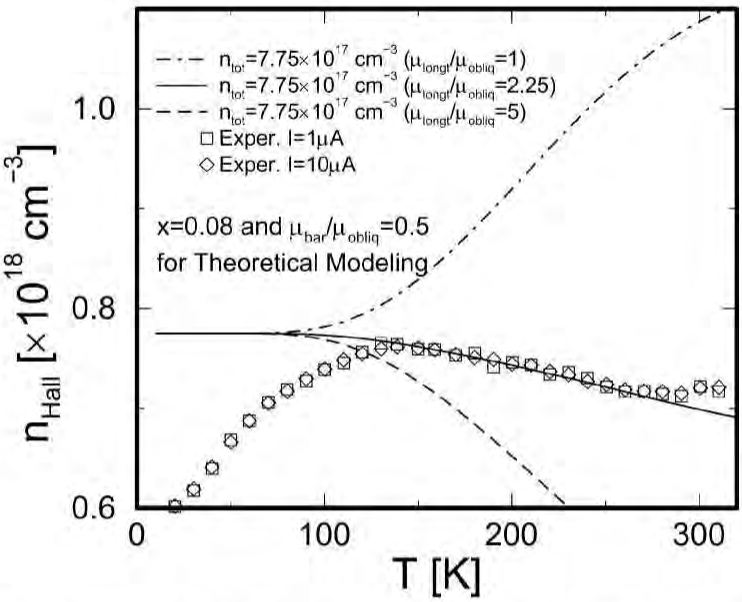

Figure B-26: Hall carrier density as a function of temperature for a (111) oriented PbTe(20 Å)/$Pb_{1-x}Eu_xTe$(400 Å) multiple-quantum-well sample (MBEG915).

assumptions considered here ($\mu_{\rm longt}/\mu_{\rm obliq}$ = 1, 2.25, and 5), whereas the calculation assuming $\mu_{\rm longt}/\mu_{\rm obliq} = 2.25$, which gives the best fit to the Hall carrier concentration, overestimates the values of the actual Seebeck coefficient.

B.6 Summary

For quantum well samples with low carrier concentrations ($<10^{18}$ cm^{-3}), the agreement between the experimental and theoretical results for the Seebeck coefficient is pretty good at low temperatures ($\lesssim$150 K), where the conduction electrons predominantly populate the longitudinal subband. However, the simultaneous modeling of the Seebeck coefficient and the Hall carrier concentration is found to be difficult at high temperatures ($\gtrsim$150 K) where the oblique subband and the 3D energy band for the barrier layers start being occupied. For higher carrier concentrations ($>10^{18}$ cm^{-3}), the behavior of the experimental Seebeck coefficient is successfully modeled over a wide temperature range ($\sim$50 K $< T <$ $\sim$300 K) using our three (sub)band model, assuming the total number of carriers in the superlattice is conserved. We always find poor agreement between experiment and theory when we assume $\mu_{\rm longt}/\mu_{\rm obliq} \approx 6$,

which is the result for the naive intra-valley carrier scattering model, considering the density-of-states factor only. Good agreement between theory and experiment are obtained for values of the ratios of the mobilities $\mu_{\text{longt}}/\mu_{\text{obliq}}$ between 0.7 and 2. Thus, inter-valley scattering of carriers may become important for these quantum wells at high temperature.[†]

[†]This last sentence turns out not to be the case as we discuss in Chapter 3.

Appendix C

Enhanced carrier mobility observed in $PbTe/Pb_{1-x}Eu_x$ Te multiple-quantum-wells (unpublished rebuttal paper to Appl. Phys. Lett.)

Note : the references for this Appendix are given on page 396.

Comment on "Thermoelectric transport in quantum well superlattices"
[Appl. Phys. Lett. 70, 2834 (1997)] (unpublished manuscript)

T. Koga[1], T. C. Harman[2], S. B. Cronin[4] and M. S. Dresselhaus[3,4]

[1]*Division of Engineering and Applied Sciences, Harvard University, Cambridge, MA 02138*

[2]*Lincoln Laboratory, Massachusetts Institute of Technology, Lexington, MA 02173*

[3]*Department of Electrical Engineering and Computer Science and* [4]*Department of Physics, Massachusetts Institute of Technology, Cambridge, MA 02139*

The enhanced thermoelectric figure of merit Z in low dimensional systems has been an

attractive research topic since its first systematic study by Hicks and Dresselhaus [1]. This idea has been experimentally demonstrated in the PbTe/$Pb_{1-x}Eu_xTe$ MQW (multiple-quantum-well) system by Harman *et al.* [2] and Hicks *et al.* [3]. Recently, Broido and Reinecke [4] reported calculations of Z, explicitly taking into account the dependence of the carrier scattering by phonons on energy and quantum well width, and the effects of the multiple-carrier-valley splitting. Their calculations indicated rather small $Z_{2D}T$ values (smaller than the bulk value) for PbTe quantum wells with quantum well widths $d_W < 100$ Å [4]. Their argument for the small $Z_{2D}T$ for PbTe quantum wells is two-fold: (1) the valley degeneracy of multi-valley bulk semiconductors is lifted by the quantum confinement leading to a decrease in the electrical conductivity due to a reduction in carrier density, and (2) qualitatively different scattering rates in superlattices from those in bulk materials cause a decrease in the carrier mobility with decreasing well thickness.

In their calculation of $Z_{2D}T$, the authors assumed an infinite barrier height for the quantum well, which leads to a rather large energy splitting between the longitudinal- and oblique- subbands for PbTe. Based on this assumption, they concluded that the carrier density in the oblique subband becomes negligible for $d_W < 60$ Å. However, the barrier heights for the experimental PbTe quantum wells in the PbTe/$Pb_{1-x}Eu_xTe$ MQWs of Ref. 2 and 3 are in the range of 100–200 meV [5], which leads to much smaller energy splittings between the lowest longitudinal- and oblique- subbands. The optimum carrier doping, the measured Hall mobility and the measured Seebeck coefficient at room temperature, respectively, have the values 1.1×10^{19} cm^{-3}, 1420 $cm^2/V{\cdot}s$ and -225 $\mu V/K$ for the 19 Å quantum wells of the best MQW sample and 7.4×10^{18} cm^{-3}, 1220 $cm^2/V{\cdot}s$ and -149 $\mu V/K$ for the corresponding bulk films in Ref. 2 and 3. For the 19 Å quantum wells, we estimate that about 57 % of the conduction carriers populate the oblique subband at 300 K [3]. Population of the oblique subband contributes importantly to the high power factor ($S^2\sigma = 130$ $\mu W/cm{\cdot}K^2$) through the enhancement of S due to the large density of states of the oblique subband. Therefore, we conclude that the authors' first point mentioned above arises from their unrealistic assumption for the barrier height for the quantum

well.

Plotted in Fig. C-1 is the experimentally obtained Hall carrier mobility $\mu_{\rm Hall}$ as a function of the quantum well width $d_{\rm W}$ for PbTe/$Pb_{1-x}Eu_xTe$ MQWs. Most of the data plotted in Fig. C-1 are taken from Ref. 2, but a few recently obtained data points are also added to the figure. Although higher mobilities for *undoped* PbTe have been obtained [6], our best mobilities for 10^{18}–10^{19} cm^{-3} Bi-doped MBE-grown bulk PbTe films are in the range 960-1230 $cm^2/V{\cdot}s$ at room temperature, as indicated by the shaded pattern in the figure. On the other hand, the mobilities for MQW samples at room temperature are in the range 650–1420 $cm^2/V{\cdot}s$, which show a larger scatter than those for the bulk samples, but cover the entire range for the observed bulk mobilities. From this experimental observation, we conclude that no degradation of carrier mobility is evident for the MQW samples at least as the quantum well width $d_{\rm W}$ is reduced down to 19 Å.

The justification of using S^2n as a measure of the power factor ($S^2\sigma$) in Ref. 3, which is another point being criticized by the authors of Ref. 4, follows naturally from the above argument. Since no obvious degradation of carrier mobility is observed for our MQW samples, S^2n can be used as an equally good measure for $S^2\sigma$. The use of S^2n avoids the difficulties associated with the calculation of the mobility, since an adequate theory of carrier scattering for PbTe quantum wells is not yet available.

The theoretical calculations carried out by Broido and Reinecke [4], which include a detailed treatment for the carrier scattering mechanism to solve the Boltzmann equation, are indeed a good approach to model the thermoelectric transport of MQW systems more quantitatively. However, our analysis given in this short report indicates the importance of performing such calculations using more realistic conditions, such as using a finite barrier height for the quantum well superlattice.

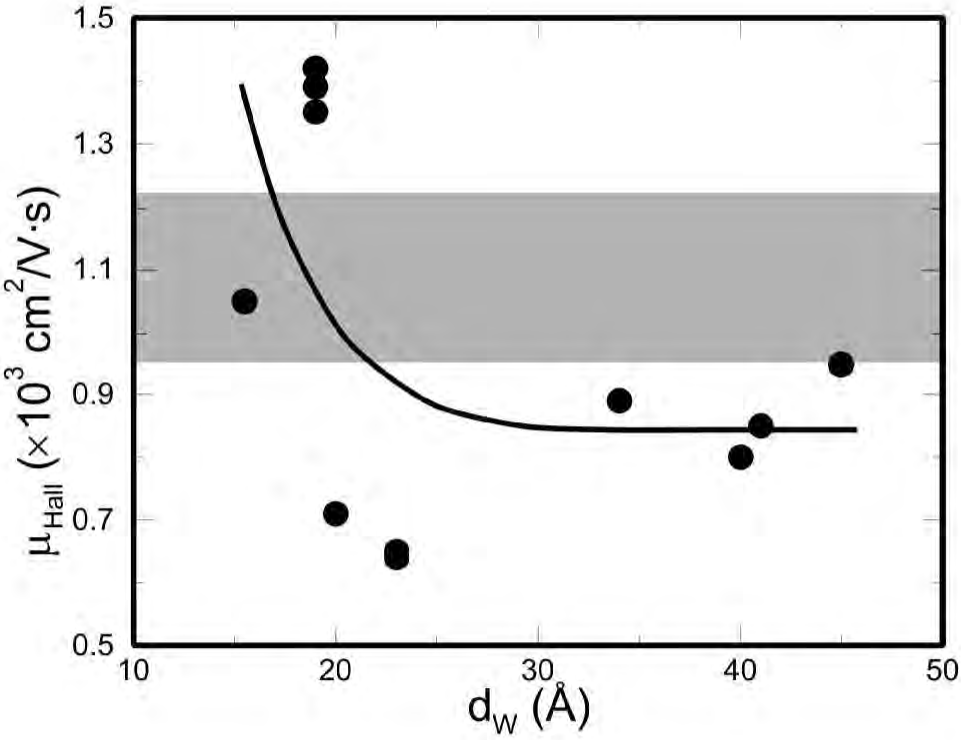

Figure C-1: Hall carrier mobility μ_{Hall} as a function of the quantum well width d_{W} for PbTe/$Pb_{1-x}Eu_xTe$ MQWs at 300 K (closed circles). Most of the data are taken from Ref. 2, but a few more recently obtained results are also added. The shaded region indicates the carrier mobilities for similarly grown bulk PbTe for comparison. The solid line is a guide to the eye.

REFERENCES

[1] L. D. Hicks and M. S. Dresselhaus, Phys. Rev. B **47**, 12727 (1993).

[2] T. C. Harman, D. L. Spears, and M. J. Manfra, J. Electron. Mater. **25**, 1121 (1996).

[3] L. D. Hicks, T. C. Harman, X. Sun, and M. S. Dresselhaus, Phys. Rev. B **53**, R10493 (1996).

[4] D. A. Broido and T. L. Reinecke, Appl. Phys. Lett. **70**, 2834 (1997).

[5] S. Yuan, G. Springholtz, G. Bauer, and M. Kriechbaum, Phys. Rev. B **49**, 5476 (1994).

[6] G. Springholtz, and G. Bauer, J. Cryst. Growth **144**, 157 (1994).

Appendix D

Iteration method to solve the perturbation function $\phi(\mathbf{k}_{||})$

In this Appendix, we will explain how to solve the Boltzmann equation (Eq. 3.12),

$$\cos\theta = \frac{A}{4\pi^2}\gamma'(E_{\mathbf{k}||}) \int \frac{1-f_0(E_{\mathbf{k}'})}{1-f_0(E_{\mathbf{k}})} S(\mathbf{k}_{||}, \mathbf{k}'_{||})\{\phi(\mathbf{k}_{||}) - k_{||}^{*\prime}/k_{||}^{*}\phi(\mathbf{k}'_{||})\}\, d\mathbf{k}'_{||}, \tag{3.12}$$

using the iterative approach for an inelastic (optical phonon) scattering mechanism [53].

In order to solve Eq. 3.12 for the perturbation function $\phi(\mathbf{k}_{||})$, we first expand $\phi(\mathbf{k}_{||})$ in terms of the Legendre polynomials $\mathrm{P}_l(\cos\theta)$, as discussed in §3.3.3, where θ is the polar angle for the wave vector $\mathbf{k}_{||}$:

$$\phi(\mathbf{k}_{||}) = \sum_{l=1,3,\cdots} a_l(E_{\mathbf{k}_{||}})\mathrm{P}_l(\cos\theta). \tag{D.1}$$

In Eq. D.1, only the odd order terms in the Legendre polynomial expansion are retained due to the symmetry of the pertinent problem.

After inserting Eq. D.1 into Eq. 3.12, and integrating over the primed variables, Eq. 3.12 will have the following structure due to the δ-function that is found in the Fermi golden rule [$S(\mathbf{k},\mathbf{k}') = \frac{2\pi}{\hbar}\left|\langle\mathbf{k}'\left|H'\right|\mathbf{k}\rangle\right|^2 \delta(E_{\mathbf{k}'} - E_{\mathbf{k}} \mp \hbar\omega)$] (Eq. 3.4) :

$$
\begin{aligned}
P_1(\cos\theta) \equiv \cos\theta = \quad & a_1(E)A_1(E,\theta) && + \quad a_3(E)A_3(E,\theta) \\
+ \quad & a_1(E+\hbar\omega)A_1^+(E,\theta) && + \quad a_3(E+\hbar\omega)A_3^+(E,\theta) \\
+ \quad & a_1(E-\hbar\omega)A_1^-(E,\theta) && + \quad a_3(E-\hbar\omega)A_3^-(E,\theta),
\end{aligned}
\tag{D.2}
$$

where the first and the second terms are connected with the elastic scattering process of electrons (if we include the elastic scattering mechanisms in the pertinent problem); the first to the fourth terms are connected with the optical phonon absorption process for the electrons that are scattered out of the state $\mathbf{k}_{||}$ and the optical phonon emission process for the electrons that are scattered into the state $\mathbf{k}_{||}$; and the first, the second, the fifth and the sixth terms are connected with the optical phonon emission process for the electrons that are scattered out of the state $\mathbf{k}_{||}$ and the optical phonon absorption process for the electrons that are scattered into the state $\mathbf{k}_{||}$. In Eq. D.2, ω denotes the optical phonon frequency, E denotes the energy of an electron in the state $\mathbf{k}_{||}$ (the subscript in $E_{\mathbf{k}_{||}}$ is dropped for clarity), and only up to third order terms in the Legendre polynomials are retained, since it is exactly what we did in §3.3.3. However, it is also straightforward to extend the formalism in this Appendix to include the terms in the Legendre polynomial expansion to any higher order.

Now, changing the variable according to $x = \cos\theta$ in Eq. D.2, and using the orthogonality relation for the Legendre polynomials,

$$
\int_{-1}^{1} \mathrm{P}_n(x)\mathrm{P}_l(x)dx = \frac{2}{2n+1}\delta_{nl},
\tag{D.3}
$$

we will obtain the following set of two equations that connect the values of $a_1(E)$ and $a_3(E)$ to the values of $a_1(E \pm \hbar\omega)$ and $a_3(E \pm \hbar\omega)$:

$$
\begin{aligned}
\tfrac{2}{3} = \quad & a_1(E)A_{11}(E) && + \quad a_3(E)A_{31}(E) \\
+ \quad & a_1(E+\hbar\omega)A_{11}^+(E) && + \quad a_3(E+\hbar\omega)A_{31}^+(E) \\
+ \quad & a_1(E-\hbar\omega)A_{11}^-(E) && + \quad a_3(E-\hbar\omega)A_{31}^-(E),
\end{aligned}
\tag{D.4}
$$

and

$$
\begin{aligned}
0 = \quad & a_1(E)A_{13}(E) && + \; a_3(E)A_{33}(E) \\
+ \; & a_1(E+\hbar\omega)A^{+}_{13}(E) && + \; a_3(E+\hbar\omega)A^{+}_{33}(E) \\
+ \; & a_1(E-\hbar\omega)A^{-}_{13}(E) && + \; a_3(E-\hbar\omega)A^{-}_{33}(E),
\end{aligned}
\tag{D.5}
$$

where the coefficients A_{11}, A_{31}, A^{+}_{11}, A^{+}_{31}, A^{-}_{11} and A^{-}_{31} in Eq. D.4 are obtained by multiplying $P_1(x)$ to the both sides of Eq. D.2, and using the orthogonality relation Eq. D.3, while the coefficients A_{13}, A_{33}, A^{+}_{13}, A^{+}_{33}, A^{-}_{13} and A^{-}_{33} in Eq. D.5 are obtained by multiplying $P_3(x)$ to the both sides of Eq. D.2, and using the orthogonality relation Eq. D.3.

Now, in order to solve Eqs. D.4 and D.5 for $a_1(E)$ and $a_3(E)$, we use the following iterative approach.

1st iteration

(1) For $E = E_0 < \hbar\omega$ (0th step of the 1st iteration), the values for $a_1(E_0 - \hbar\omega)$ and $a_3(E_0 - \hbar\omega)$ are not *defined*, since $A^{-}_{11}(E_0) = A^{-}_{31}(E_0) = A^{-}_{13}(E_0) = A^{-}_{33}(E_0) = 0$, and the values for $a_1(E_0 + \hbar\omega)$ and $a_3(E_0 + \hbar\omega)$ are not *known* yet. Therefore, we first obtain the approximate values for $a_1(E_0)$ and $a_3(E_0)$ by setting $a_1(E_0 + \hbar\omega) = a_3(E_0 + \hbar\omega) = 0$. The approximate values for $a_1(E_0)$ and $a_3(E_0)$ obtained in this way are denoted by $a^{(1)}_1(E_0)$ and $a^{(1)}_3(E_0)$ [more generally, the approximate solutions for $a_1(E_0)$ and $a_3(E_0)$ after the nth iteration are denoted by $a^{(n)}_1(E_0)$ and $a^{(n)}_3(E_0)$, respectively, as we will see below].

(2) For $E = E_0 + m\,\hbar\omega$ (mth step of the 1st iteration), where $m = 1, 2, 3, \cdots$, the Eqs. D.4 and D.5 connect the values of $a_1(E_0 + m\,\hbar\omega)$ and $a_3(E_0 + m\,\hbar\omega)$ to the values of $a_1(E_0 + (m \pm 1)\hbar\omega)$ and $a_3(E_0 + (m \pm 1)\hbar\omega)$. Since approximate solutions $a^{(1)}_1(E_0 + (m-1)\hbar\omega)$ and $a^{(1)}_3(E_0 + (m-1)\hbar\omega)$ are now known from the $(m-1)$th step of the first iteration, whereas no solutions are yet available for $a_1(E_0 + (m+1)\hbar\omega)$ and $a_3(E_0 + (m+1)\hbar\omega)$, we can obtain the best approximate values for $a_1(E_0 + m\,\hbar\omega)$ and $a_3(E_0 + m\,\hbar\omega)$ (denoted by $a^{(1)}_1(E_0 + m\,\hbar\omega)$ and $a^{(1)}_3(E_0 + m\,\hbar\omega)$, respectively) using the approximate values $a^{(1)}_1(E_0 + (m-1)\hbar\omega)$ and $a^{(1)}_3(E_0 + (m-1)\hbar\omega)$, and by

setting $a_1(E_0+(m+1)\hbar\omega)=a_3(E_0+(m+1)\hbar\omega)=0$, in solving Eqs. D.4 and D.5 for $a_1(E_0+m\,\hbar\omega)$ and $a_3(E_0+m\,\hbar\omega)$.

(3) Repeat (2) incrementing the value of m by 1 until m becomes a sufficiently large number M.

nth iteration ($n>1$)

(1) For $E=E_0<\hbar\omega$ (0th step of the nth iteration), as in the 1st iteration, the values for $a_1(E_0-\hbar\omega)$ and $a_3(E_0-\hbar\omega)$ are not *defined*, since $A^-_{11}(E_0)=A^-_{31}(E_0)=A^-_{13}(E_0)=A^-_{33}(E_0)=0$. However, the values for $a_1(E_0+\hbar\omega)$ and $a_3(E_0+\hbar\omega)$ are now known *approximately* from the $(n-1)$th iteration [i.e., they are given by $a_1^{(n-1)}(E_0+\hbar\omega)$ and $a_3^{(n-1)}(E_0+\hbar\omega)$, respectively]. Therefore, we can obtain *improved* values for $a_1(E_0)$ and $a_3(E_0)$ using the values of $a_1^{(n-1)}(E_0+\hbar\omega)$ and $a_3^{(n-1)}(E_0+\hbar\omega)$ from the $(n-1)$th iteration. The improved values thus obtained for $a_1(E_0)$ and $a_3(E_0)$ after nth iteration are denoted by $a_1^{(n)}(E_0)$ and $a_3^{(n)}(E_0)$, respectively.

(2) For $E=E_0+m\,\hbar\omega$ (mth step of the nth iteration), where $m=1,\,2,\,3,\,\cdots$, the Eqs. D.4 and D.5 connect the values of $a_1(E_0+m\,\hbar\omega)$ and $a_3(E_0+m\,\hbar\omega)$ to the values of $a_1(E_0+(m\pm1)\hbar\omega)$ and $a_3(E_0+(m\pm1)\hbar\omega)$. Since the approximate solutions of $a_1^{(n)}(E_0+(m-1)\hbar\omega)$ and $a_3^{(n)}(E_0+(m-1)\hbar\omega)$, and those of $a_1^{(n-1)}(E_0+(m+1)\hbar\omega)$ and $a_3^{(n-1)}(E_0+(m+1)\hbar\omega)$ are available from the $(m-1)$th step of the nth iteration, and from the $(m+1)$th step of the $(n-1)$th iteration, respectively, we can obtain, using these values, improved values for $a_1(E_0+m\,\hbar\omega)$ and $a_3(E_0+m\,\hbar\omega)$ from Eqs. D.4 and D.5. These improved values for $a_1(E_0+m\,\hbar\omega)$ and $a_3(E_0+m\,\hbar\omega)$, after the nth iteration, are denoted by $a_1^{(n)}(E_0+m\,\hbar\omega)$ and $a_3^{(n)}(E_0+m\,\hbar\omega)$, respectively.

(3) Repeat (2) incrementing the value of m by 1 so long as m does not exceed $M-n+1$ ($m<M-n+2$). It is noted that we cannot perform the $(M-n+2)$th step of the nth ($n>1$) iteration, since the approximate values for $a_1(E_0+(m+1)\hbar\omega)$ and $a_3(E_0+(m+1)\hbar\omega)$ are not available from the $(n-1)$th iteration for $m=M-n+2$.

The iteration process described above is repeated by a sufficiently large number

of $n = N$ times to get good convergence. For the calculations performed in §3.3.3, we have usually obtained a sufficiently good convergence after $N \approx 8$.

Bibliography

[1] N. E. Ashcroft and N. D. Mermin, in *Solid State Physics*, chapter 13, page 257, (Saunders College Publishing, Philadelphia, 1976).

[2] A. F. Ioffe, *Semiconductor Thermoelements and Thermoelectric Cooling* (Infosearch Ltd., London, 1957).

[3] N. E. Ashcroft and N. D. Mermin, in *Solid State Physics*, chapter 12 and 13, (Saunders College Publishing, Philadelphia, 1976).

[4] B. Sherman, R. R. Heikes, and R. W. Ure, J. Appl. Phys. **31**, 1 (1960).

[5] H. J. Goldsmid, *Electronic Refrigeration* (Pion, London, 1986).

[6] G. D. Mahan, Physics Today **March** (1997).

[7] G. D. Mahan, *Solid State Physics* (Academic Press, New York, 1998), Vol. 51. edited by H. Ehrenreich and F. Spaepen.

[8] G. D. Mahan, Proc. Natl. Acad. Sci. USA **93**, 7436 (1996).

[9] G. A. Slack and V. G. Tsoukala, J. Appl. Phys. **76**, 1665 (1994).

[10] G. A. Slack, in *CRC Handbook of Thermoelectrics*, page 407, (CRC Press, New York, 1995). edited by D. M. Rowe.

[11] L. D. Hicks and M. S. Dresselhaus. In *Semiconductor Heterostructures for Photonic and Electronic Applications: MRS Symposia Proceedings, Boston, volume* **281**, edited by C. W. Tu, D. C. Houghton, and R. T. Tung, page 821, Materials Research Society Press, Pittsburgh, PA, 1993.

[12] L. D. Hicks and M. S. Dresselhaus, Phys. Rev. B **47**, 16631 (1993).

[13] D. L. Broido and T. L. Reinecke, Phys. Rev. B **51**, 13797 (1995).

[14] L. D. Hicks and M. S. Dresselhaus, Phys. Rev. B **47**, 12727 (1993).

[15] T. C. Harman, D. L. Spears, and M. J. Manfra, J. Electron. Mater. **25**, 1121 (1996).

[16] L. D. Hicks, T. C. Harman, X. Sun, and M. S. Dresselhaus, Phys. Rev. B **53**, R10493 (1996).

[17] Lyndon D. Hicks. *The effect of quantum-well superlattices on the thermo-electric figure of merit.* PhD thesis, Massachusetts Institute of Technology, June 1996. Department of Physics.

[18] J. O. Sofo and G. D. Mahan, Appl. Phys. Lett. **65**, 2690 (1994).

[19] D. A. Broido and T. L. Reinecke, Appl. Phys. Lett. **67**, 100 (1995).

[20] D. A. Broido and T. L. Reinecke, Appl. Phys. Lett. **67**, 1170 (1995).

[21] P. J. Lin-Chung and T. L. Reinecke, Phys. Rev. B **51**, 13244 (1995).

[22] D. A. Broido and T. L. Reinecke, Appl. Phys. Lett. **70**, 2834 (1997).

[23] C. Kittel, *Introduction to Solid State Physics 7th edition* (John Wiley & Sons, Inc., New York, 1996). p.137.

[24] Y. I. Ravich, B. A. Efimova, and I. A. Simirnov, *Semiconducting Lead Chalcogenides* (Plenum Press, New York, 1970). chapter 3, 4 and 6.

[25] K. Seeger, *Semiconductor Physics – An Introduction –* (Springer-Verlag, Berlin, 1985). chapter 4.

[26] Yu. I. Ravich, B. A. Efimova, and V. I. Tamarchenko, Phys. Stat. Sol. (b) **43**, 11 (1971).

[27] Yu. I. Ravich, B. A. Efimova, and V. I. Tamarchenko, Phys. Stat. Sol. (b) **43**, 453 (1971).

[28] R. Dornhaus, G. Nimtz, and B. Schlicht, *Narrow-Gap Semiconductors* (Springer-Verlag, Berlin, 1985). Springer Tracts in Modern Physics, Volume 98.

[29] S. Yuan, H. Krenn, G. Springholz, and G. Bauer, Phys. Rev. B **47**, 7213 (1993).

[30] S. Yuan, G. Springholz, G. Bauer, and M. Kriechbaum, Phys. Rev. B **49**, 5476 (1994).

[31] S. Yuan, H. Krenn, G. Springholz, Y. Ueta, G. Bauer, and P. J. McCann, Phys. Rev. B **55**, 4607 (1997).

[32] A. Y. Ueta. *MBE Growth and Characterization of $PbTe/Pb_{1-x}Eu_xTe$ Epitaxial Layers.* PhD thesis, the Johannes Kepler Universität Linz, January 1997. Department of Physics.

[33] G. Nimtz, in *Landolt-Bornstein Numerical Data and Functional Relationships in Science and Technology, New Series, Group III: Crystal and Solid State Physics*, page 170, edited by O. Madelung, M. Schultz, and H. Weiss (Springer-Verlag, Berlin, 1983), Vol. 17f.

[34] R. S. Allgaier, J. Appl. Phys. **32**, 2185 (1961).

[35] A. A. Andreev and V. N. Radionov, Soviet Physics-Semicondctor **1**, 145 (1967).

[36] H. Sitter, K. Lischka, and H. Heinrich, Phys. Rev. B **15**, 680 (1977).

[37] L. D. Hicks, T. C. Harman, and M. S. Dresselhaus, Appl. Phys. Lett. **63**, 3230 (1993).

[38] T. Koga, S. B. Cronin, T. C. Harman, X. Sun, and M. S. Dresselhaus. In *Semiconductor Process and Device Performance Modelling: MRS Symposia Proceedings, Boston, volume* **490**, edited by S. T. Dunham and J. S. Nelson, page 263, Materials Research Society Press, Warrendale, PA, 1998.

[39] T. C. Harman, D. L. Spears, D. R. Calawa, S. H. Groves, and M. P. Walsh. In *Proceedings for the 16th International Conference on Thermoelectrics*, page 416, 1997.

[40] A. K. Das and B. R. Nag, J. Phys. Chem. Solids **39**, 259 (1978).

[41] H. Ehrenreich, J. Phys. Chem. Solids **9**, 129 (1959).

[42] J. R. Drabble and H. J. Goldsmid, *Thermal conduction in Semiconductors* (Pergamon Press, New York, 1961). page 180.

[43] Gang Chen, Trans. ASME, Journal of Heat Transfer **119**, 220 (1997).

[44] A. Sipatov, V. Volobuev, A. Fedorov, E. Rogacheva, and I. Krivulkin. In *Proceedings for the 18th International Conference on Thermoelectrics*, 1999.

[45] T. Koga, S. B. Cronin, T. C. Harman, X. Sun, and M. S. Dresselhaus, (1997). unpublished manuscript (reproduced in Chapter 2 in this thesis).

[46] D. A. Broido and T. L. Reinecke, Phys. Rev. B **51**, 13797 (1995).

[47] T. Koga, X. Sun, S. B. Cronin, M. S. Dresselhaus, K. L. Wang, and G. Chen, Journal of computer-Aided Materials Design **4**, 175 (1997).

[48] T. Koga, X. Sun, S. B. Cronin, and M. S. Dresselhaus, Appl. Phys. Lett. **73**, 2950 (1998).

[49] T. Koga, T. C. Harman, S. B. Cronin, and M. S. Dresselhaus, (1997). unpublished manuscript (reproduced in Appendix C in this thesis).

[50] Z. Zhang, J. Y. Ying, and M. S. Dresselhaus, J. Mater. Res. **13**, 1745 (1998).

[51] Z. Zhang, X. Sun, M. S. Dresselhaus, J. Y. Ying, and J. P. Heremans, Appl. Phys. Lett. **73**, 1589 (1998).

[52] Xiangzhong Sun. *The effect of quantum confinement of the thermoelectric figure of merit.* PhD thesis, Massachusetts Institute of Technology, June 1999. Department of Physics.

[53] B. R. Nag, *Electron Transport in Compound Semiconductors* (Springer-Verlag, Berlin, Heidelberg, 1980). Springer Series in Solid-State Sciences 11.

[54] K. Tomizawa, *Numerical Simulation of Submicron Semiconductor Devices* (ARTECH HOUSE, INC., Norwood, 1993).

[55] D. M. Rowe and G. Min. In *Proceedings for 13th International Conference on Thermoelectrics*, page 339, 1994.

[56] Y. Nishio and T. Hirano, Jpn. J. Appl. Phys., Part 1 **36**, 170 (1997).

[57] R. Venkatasubramanian, T. Colpitts, E. Watko, M. Lamvik, and N. El-Masry, Journal of Crystal Growth **170**, 817 (1997).

[58] S. Adachi, J. Appl. Phys. **58**, R1 (1985).

[59] O. Madelung, in *Landolt-Bornstein Numerical Data and Functional Relationships in Science and Technology, New Series, Group III: Crystal and Solid State Physics*, page 136, edited by O. Madelung and M. Schultz (Springer-Verlag, Berlin, 1987), Vol. 22a. and references therin.

[60] T. Yao, Appl. Phys. Lett. **51**, 1798 (1987).

[61] X. Y. Yu, G. Chen, A. Verma, and J. S. Smith, Appl. Phys. Lett. **67**, 3554 (1987).

[62] S.-M. Lee, D. G. Cahill, and R. Venkatasubramanian, Appl. Phys. Lett. **70**, 2957 (1997).

[63] C. Kittel, *Introduction to Solid State Physics 7th edition* (John Wiley & Sons, Inc., New York, 1996). p.180.

[64] Y. M. Lin, (1999). Private communication.

[65] C. Weisbuch and B. Vinter, in *Quantum Semiconductor Structures*, (ACADEMIC PRESS, INC, San Diego, 1991).

[66] T. Koga, T. C. Harman, S. B. Cronin, and M. S. Dresselhaus, Phys. Rev. B **60**, 14286 (1999).

[67] T. Borca-Tasciuc, W. L. Liu, J. L. Liu, T. F. Zeng, D. W. Song, C. D. Moore, G. Chen, K. L. Wang, M. S. Goorsky, T. Radetic, R. Gronsky, X. Sun, and M. S. Dresselhaus. In *Proceedings for the 18th International Conference on Thermoelectrics*, 1999. and references therein.

[68] M. M. Rieger and P. Vogl, Phys. Rev. B **48**, 14276 (1993).

[69] C. G. Van de Walle, Phys. Rev. B **39**, 1871 (1989).

[70] T. Borca-Tasciuc, W. L. Liu, J. L. Liu, T. F. Zeng, D. W. Song, C. D. Moore, G. Chen, K. L. Wang, M. S. Goorsky, T. Radetic, R. Gronsky, T. Koga, and M. S. Dresselhaus, (2000). (unpublished).

[71] G. Chen, S. Q. Zhou, D.-Y. Yao, C. J. Kim, X. Y. Zheng, Z. L. Liu, K. L. Wang, X. Sun, and M. S. Dresselhaus. In *Proceedings for the 17th International Conference on Thermoelectrics*, page 202, 1998.

[72] R. Venkatasubramanian, E. Siivola, and T. Colpitts. page 191, 1998.

[73] P. Hyldgaard and G. D. Mahan, Phys. Rev. B **56**, 10754 (1997).

[74] G. Chen and M. Neagu, Appl. Phys. Lett. **71**, 2761 (1997).

[75] G. Chen, T. Borca-Tasciuc, B. Yang, D. Song, W. Liu, T. F. Zeng, and D.-A. Achimov, Thermal Science & Engineering **7**, 43 (1999).

[76] G. Chen, Phys. Rev. B **57**, 14958 (1998).

[77] J. P. Dismukes, L. Ekstrom, E. F. Steigmeier, I. Kudman, and D. S. Beers, J. Appl. Phys. **35**, 2899 (1964).

[78] K. L. Wang and X Zheng. In *Properties of Strained and Relaxed Silicon Germanium*, edited by Erich Kasper, page 70, INSPEC, the Institution of Electrical Engineers, London, United Kingdom, 1994. EMIS Datareviews Series No. 12.

[79] C. B. Vining, J. Appl. Phys. **69**, 331 (1991).

[80] R. Venkatasubramanian, Phys. Rev. B **61**, 3091 (2000).

[81] P. W. Anderson, Phys. Rev. **109**, 1492 (1958).

[82] D. S. Wiersma, P. Batolini, A. Lagendik, and R. Righini, Nature **390**, 671 (1997).

[83] D. G. Cahill and R. O. Pohl, Phys. Rev. B **35**, 4067 (1987).

[84] D. G. Cahill, Rev. Sci. Instrum. **61**, 802 (1990).

[85] T. Borca-Tasciuc, (2000). Private comunication.

[86] J. L. Liu, C. D. Moore, G. D. U'Ren, Y. H. Luo, Y. Lu, G. Jin, S. G. Thomas, M. S. Goorsky, and K. L. Wang, Appl. Phys. Lett. **75**, 1586 (1999).

[87] O. Madelung, in *Landolt-Bornstein Numerical Data and Functional Relationships in Science and Technology, New Series, Group III: Crystal and Solid State Physics*, page 43 and 87, edited by O. Madelung and M. Schultz (Springer-Verlag, Berlin, 1987), Vol. 22a. and references therin.

[88] T. H. Geballe and G. W. Hull, Physical Review **94**, 1134 (1954).

[89] T. H. Geballe and G. W. Hull, Physical Review **98**, 940 (1955).

[90] J. M. Ziman, in *Principles of the Theory of Solids*, chapter 7, page 244, (Cambridge University Press, New York, 1972).

[91] B. K. Ridley, *Electrons and Phonons in Semiconductor Multilayers* (Cambridge University Press, New York, 1997).

[92] T. C. Harman, D. L. Spears, and M. P. Walsh, J. Electron. Mater. Lett. **28**, L1 (1999).

[93] T. C. Harman, P. J. Taylor, D. L. Spears, and M. P. Walsh. In *Proceedings for the 18th International Conference on Thermoelectrics*, 1999.

[94] T. C. Harman, P. J. Taylor, D. L. Spears, and M. P. Walsh, J. Electron. Mater. Lett. **29**, L1 (2000).

[95] G. Springholz, V. Holy, M. Pinczolits, and G. Bauer, Science **282**, 734 (1998).

[96] V. Holy, G. Springholz, M. Pinczolits, and G. Bauer, Phys. Rev. Lett. **83**, 356 (1999).

[97] M. Pinczolits, G. Springholz, and G. Bauer, Appl. Phys. Lett. **73**, 250 (1998).

[98] T. Koga, T. C. Harman, X. Sun, S. B. Cronin, and M. S. Dresselhaus. In *Thermoelectric Materials 1998 The Next Generation Materials for Small-Scale Refrigeration and Power Generation Applications: MRS Symposia Proceedings, Boston, volume* **545**, edited by T.M. Tritt, H.B. Lyon, G. Mahan Jr., and M.G. Kanatzidis, page 479, Materials Research Society Press, Warrendale, PA, 1999.

[99] A. G. Fedorov, I. A. Shneiderman A. Yu. Sipatov, and E. V. Kaidalova, Journal of Crystal Growth **198/199**, 1211 (1999).

[100] A. Yu. Sipatov, Low Temperature Physics **25**, 376 (1999).

[101] I. V. Kolesnikov and A. Yu. Sipatov, Sov. Phys. Semicond. **23**, 598 (1989).

[102] I. V. Kolesnikov, A. N. Kovalev, A. Yu. Sipatov, V. I. Paramonov, A. I. Fedorenko, and A. E. Yunovich, Sov. Phys. Semicond. **23**, 601 (1989).

[103] A. A. Konchits, I. M. Zaritskii, S. P. Kolesnik, V. A. Stephanovich, O. A. Mironov, S. V. Chistyakov, Yu. Sipatov, and A. I. Fedorenko, Physica C **185-189**, 2737 (1991).

[104] O. A. Mironov, S. V. Chistyakov, I. Yu. Skrylev, A. I. Fedorenko, A. Yu. Sipatov, B. A. Savitskii, L. P. Shpakovskaya, O. N. Nashekina, and M. Oszwaldowski, Superlattices and Microstructures **8**, 361 (1990).

[105] O. A. Mironov, B. A. Savitskii, A. Yu. Sipatov, A. I. Fedorenko, A. N. Chirkin, S. V. Chistyakov, and L. P. Shpakovskaya, JETP Lett. **48**, 106 (1988).

[106] A. Yu. Sipatov, JETP Lett. **68**, 716 (1998).

[107] A. I. Fedorenko, A. G. Fedorov, A. Yu. Sipatov, and O. A. Mironov, Thin Solid Films **267**, 134 (1995).

[108] O. A. Mironov, S. V. Chistyakov, I. M. Zaritskii, A. A. Konchits, S. P. Kolesnik, V. A. Stephanovich, A. Yu. Sipatov, and A. I. Fedorenko, Physica C **180**, 196 (1991).

[109] N. L. Bobrov, L. F. Rybal'chenko, V. V. Fisun, I. K. Yanson, O. A. Mironov, S. V. Chistyakov, V. V. Zorchenko, A. Yu. Sipatov, and A. I. Fedorenko, Sov. J. Low Temp. Phys. **16**, 862 (1990).

[110] C. A. Hoffman, J. R. Meyer, F. J. Bartoli A. Di Venere, X. J. Yi, C. L. Hou, H. C. Wang, J. B. Ketterson, and G. K. Wong. Phys. Rev. B **48**, 11431 (1993). and references therein.

[111] T. Koga, X. Sun, S. B. Cronin, and M. S. Dresselhaus. In *Proceedings for the 18th International Conference on Thermoelectrics*, 1999.

[112] T. Koga, X. Sun, S. B. Cronin, and M. S. Dresselhaus, Appl. Phys. Lett. **75**, 2438 (1999).

[113] C. F. Gallo, B. S. Chandrasekhar, and P. H. Sutter, J. Appl. Phys. **34**, 144 (1963).

[114] M. P. Vecchi and M. S. Dresselhaus, Phys. Rev. B **10**, 771 (1974).

[115] R. T. Isaacson and G. A. Williams, Phys. Rev. **185**, 682 (1969).

[116] J. Heremans and O. P. Hansen, J. Phys. C **12**, 3483 (1979).

[117] M. Lu, R. J. Zieve, A. van Hulst, H. M. Jaeger, T. F. Rosenbaum, and S. Radelaar, Phys. Rev. B **53**, 1609 (1996).

[118] S.-C. Shin, J. B. Ketterson, and J. E. Hilliard, Phys. Rev. B **30**, 4099 (1984).

[119] S.-C. Shin, J. E. Hilliard, and J. B. Ketterson, Thin Solid Films **111**, 323 (1984).

[120] S.-C. Shin, J. E. Hilliard, and J. B. Ketterson, J. Vac. Sci. Technol. A **2**, 296 (1984).

[121] H. Lehmann, in *Landolt-Bornstein Numerical Data and Functional Relationships in Science and Technology, New Series, Group III: Crystal and Solid State Physics*, page 46, edited by O. Madelung, M. Schultz, and H. Weiss (Springer-Verlag, Berlin, 1983), Vol. 17e. and references therin.

[122] T. C. Harman, (1999). Private communication.

[123] C.-J. Kim, G. Chen, and D.-J. Yao. In *MURI : Quantum Structures for Thermoelectric Applications, Second Annual Review*, Los Angels, April 12–13, 1999.

[124] S. Ghamaty and N. Elsner. In *Proceedings for the 17th International Conference on Thermoelectrics*, page 206, 1998.

[125] S. Ghamaty and N. Elsner. In *MURI : Quantum Structures for Thermoelectric Applications, Third Annual Review*, Los Angels, January 25–26, 2000.